

# ORBITAL EXPERIMENT CAPSULE

## FEASIBILITY STUDY FINAL REPORT

VOLUME II

CR 73127

Supporting Technical Studies and Tradeoffs

**HUGHES**

HUGHES AIRCRAFT COMPANY  
SPACE SYSTEMS DIVISION

SEPTEMBER 1967 • NASA Contract NAS 2-4236

HUGHES Reference B2810 • SSD 70385R

FACILITY FORM 562

(ACCESSION NUMBER)

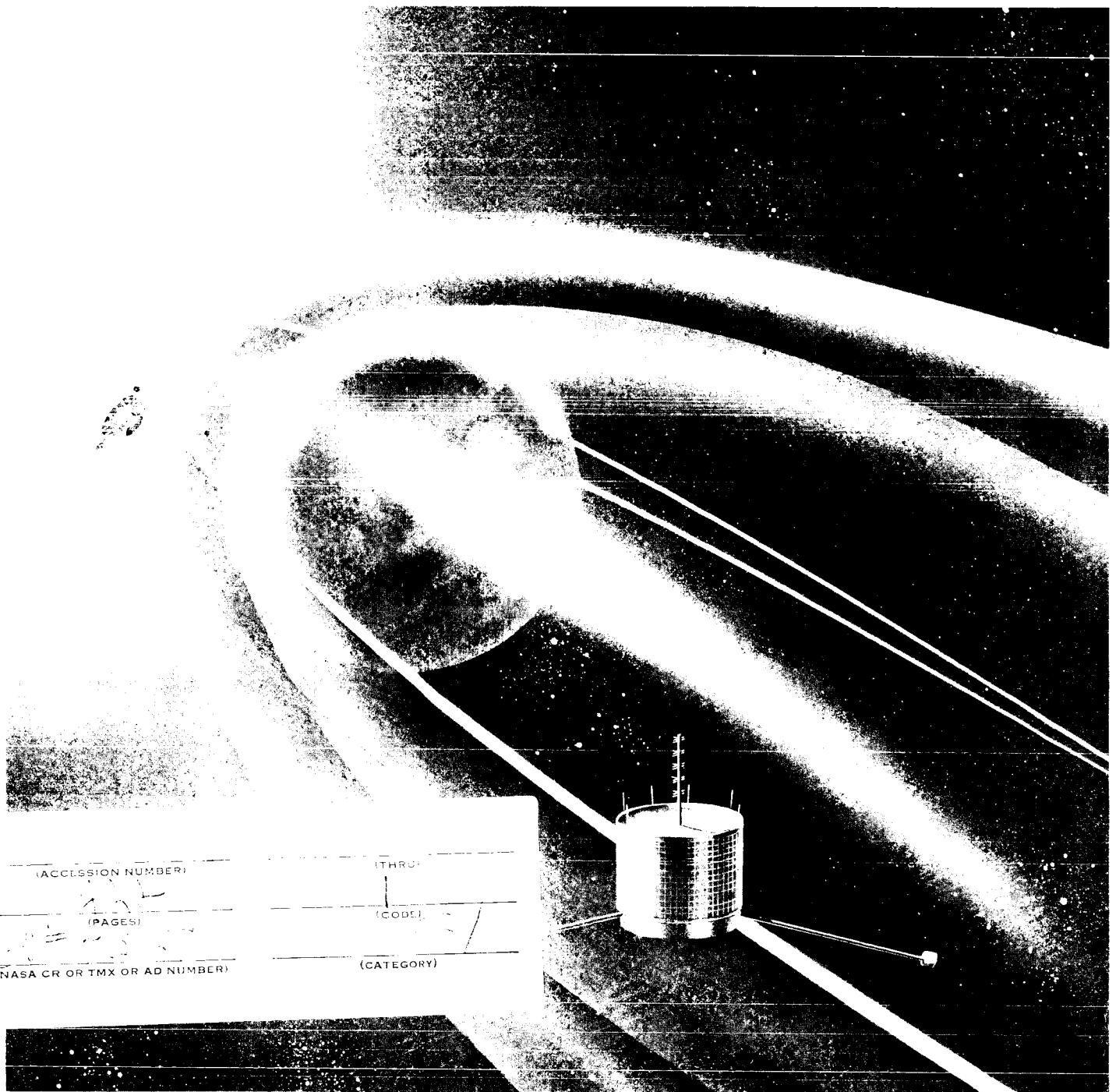
(THRU)

(PAGES)

(CODE)

(NASA CR OR TMX OR AD NUMBER)

(CATEGORY)



# **ORBITAL EXPERIMENT CAPSULE**

**FEASIBILITY STUDY**

**FINAL REPORT**

NASA Contract NAS 2-4236

**VOLUME II**

Supporting Technical Studies and Tradeoffs

**SEPTEMBER 1967**

HUGHES Reference B2810

**HUGHES**

SSD-70385R

HUGHES AIRCRAFT COMPANY  
SPACE SYSTEMS DIVISION

## CONTENTS

	<u>Page</u>
1.0 INTRODUCTION	1-1
2.0 SYSTEMS ANALYSIS	
2.1 Voyager Mission, Mars Environment, and Experiment Requirements	2-3
2.1.1 General	2-3
2.1.2 Voyager Mission Requirements	2-3
2.1.2.1 Preliminary Mission Profile	2-3
2.1.2.2 Launch Environment	2-5
2.1.2.3 Voyager Mission Constraints	2-5
2.1.3 Expected OEC Mission Environment	2-8
2.1.3.1 Interplanetary Environment	2-8
2.1.3.2 Earth Environment	2-10
2.1.3.3 Mars Environment	2-12
2.1.4 Experiments	2-17
2.1.4.1 Orbit Requirements	2-19
2.1.4.2 Experiment Requirements	2-21
2.1.4.3 Data Requirements	2-21
2.1.5 Instruments	2-23
2.1.5.1 Instrument Requirements	2-23
2.1.5.2 Interfacing Constraints	2-28
2.2 Orbit Analysis	2-31
2.2.1 General	2-31
2.2.2 Orbit Characteristics	2-32
2.2.3 Orbit Relationships to Magnetosphere	2-37
2.2.4 Orbital Lifetime	2-45
2.2.5 Differential Drag Effects	2-50
2.2.6 Effect of Solar Perturbations	2-51
2.2.7 Solar Eclipse	2-53
2.2.8 Voyager-OEC Occultation	2-59
2.2.9 Antenna Field of View Requirements	2-60
2.2.9.1 OEC Antenna Coverage	2-61
2.2.9.2 Voyager Antenna Coverage	2-63
2.3 Voyager-OEC Relative Motion	2-69
2.3.1 General	2-69
2.3.2 Voyager Coordinate System	2-71
2.3.3 Relationship of Separation Vector to Voyager	2-72
2.3.3.1 Orientation Constraints	2-73
2.3.4 Kinematics of Separation	2-81
2.4 Separation Studies	2-91
2.4.1 Methods of OEC Separation	2-91
2.4.1.1 Nonspinning Separation	2-91
2.4.1.2 Partial Spin Separation	2-99
2.4.1.3 Separation System Design	2-105

2.4.2	Separation and Spinup Error Analysis	2-115
2.4.2.1	Spinup Error Analysis	2-115
2.4.2.2	Translational Effects of Spinup	2-116
2.4.2.3	Effects of Spinup Thrust Misalignment	2-124
2.4.2.4	Separation Window	2-125
2.4.2.5	Error Sensitivity	2-129
2.4.3	Voyager—OEC Perturbation Study	2-135
2.4.3.1	Voyager Attitude Control	2-137
2.4.3.2	Effect of Limit Cycle on OEC Separation	2-138
2.4.3.3	OEC Induced Perturbations on Voyager	2-138
2.5	Attitude and Orbit Determination	2-141
2.5.1	Requirements for Attitude and Orbit Determination	2-141
2.5.2	Geometry	2-142
2.5.2.1	Voyager Separation Conditions	2-147
2.5.2.2	Motion of Mars About Sun	2-148
2.5.2.3	Orbital Regression	2-148
2.5.3	Determination of Sensor Accuracies	2-148
2.5.4	Attitude and Position Sensors	2-152
2.5.4.1	Sun Sensor	2-152
2.5.4.2	Horizon Sensor	2-153
2.5.5	Determination Process	2-158
2.5.5.1	Attitude Determination	2-158
2.5.5.2	Orbit Determination	2-163
2.6	Attitude Stabilization, Control, and Orbital Maneuver Requirements	2-175
2.6.1	Effects of External Disturbances on Attitude	2-175
2.6.1.1	Solar Pressure Torques	2-177
2.6.1.2	Gravity Gradient Torques	2-180
2.6.1.3	Aerodynamic Torques	2-183
2.6.1.4	Disturbance Torque Summary	2-185
2.6.2	Spinning Body Dynamics	2-185
2.6.2.1	Average Drift Effects	2-185
2.6.2.2	Instantaneous Drift Effects	2-188
2.6.2.3	Effects of Disturbances on OEC Attitude	2-195
2.6.3	Attitude Corrections	2-196
2.6.4	Orbital Maneuvers	2-199
2.6.4.1	Orbit Changes Dynamics	2-199
2.6.4.2	Voyager—OEC Stationkeeping	2-206
2.7	Attitude Stabilization, Control, and Orbit Control Implementation	2-208
2.7.1	OEC Spinup System	2-209
2.7.2	Nutation Damping	2-210
2.7.3	Control Considerations	2-211
2.7.3.1	Attitude Control Techniques	2-211
2.7.3.2	Orbit Control Technique	2-215
2.7.3.3	Operational Characteristics	2-215
2.7.3.4	Attitude and Orbit Control Requirements	2-217



2.8	System Performance	2-222
2.8.1	Mission Summary	2-222
2.8.2	Baseline OEC Selection	2-225
2.8.3	Operation Characteristics	2-225
2.8.4	Sequence of Events	2-227
2.9	References	2-233
3.0	COMMUNICATIONS AND DATA HANDLING STUDIES AND TRADEOFFS	
3.1	General	3-1
3.2	UHF/VHF Relay Link for Primary Data Mode	3-1
3.2.1	Frequency Selection	3-2
3.2.2	Galactic Noise	3-3
3.2.3	Solar Noise	3-3
3.2.4	Summary of Frequency-Dependent Parameters	3-5
3.2.5	Modulation Method	3-5
3.2.6	Coding	3-7
3.2.7	Power Requirements for Alternate Cases in Co-orbital Mode	3-7
3.2.8	Orbit Change Mode	3-7
3.3	S-Band Link for Backup Data Mode	3-11
3.3.1	Analysis and Design	3-11
3.3.2	Modulation Methods	3-15
3.3.3	Data Enhancement Achievable With Coding Techniques	3-15
3.3.4	Command Link	3-19
3.4	Summary	3-21
4.0	CONFIGURATION STUDIES AND TRADEOFFS	
4.1	General	4-1
4.1.1	Experiment Requirements	4-2
4.2	Environmental Considerations	4-3
4.3	Voyager Spacecraft Constraints	4-5
4.4	Gyroscopic Stability Considerations	4-7
4.5	Separation Concepts	4-11
4.6	Solar Power Considerations	4-13
4.7	Boom Considerations	4-13
4.8	Configuration Development	4-17
4.8.1	Configuration A	4-17
4.8.2	Configuration B	4-19
4.8.3	Configuration C	4-19
4.8.4	Configuration D	4-23
5.0	RECOMMENDED CONFIGURATION	5-1
6.0	SUBSYSTEMS STUDIES AND TRADEOFFS	
6.1	Power Subsystem	6-1
6.1.1	General	6-1
6.1.2	Design Concepts	6-1
6.1.2.1	Configuration A	6-1
6.1.2.2	Configuration B	6-1
6.1.2.3	Configuration C	6-3

6.1.3	Solar Panel	6-3
6.1.3.1	Design Considerations	6-3
6.1.3.2	RF Shielding	6-7
6.1.3.3	Solar Panel Voltage Ripple	6-7
6.1.3.4	Solar Panel Weight	6-7
6.1.3.5	Environmental Capabilities	6-9
6.1.4	Battery	6-11
6.1.4.1	Battery Candidates	6-11
6.1.4.2	Selection of Battery	6-13
6.1.4.3	Cell Requirement	6-13
6.1.4.4	Power Demands on Batteries	6-13
6.1.4.5	Battery Characteristics Summary	6-14
6.1.4.6	Cycle Life	6-15
6.1.4.7	Open Circuit Storage During Transit	6-15
6.1.4.8	Battery Capacity and Charge Rate	6-15
6.1.5	Battery Charge-Discharge Controller	6-18
6.1.5.1	Description of Operation	6-18
6.1.5.2	Detail Operational Characteristics	6-18
6.1.5.3	Electronics Characteristics Summary	6-21
6.2	Propulsion Subsystem	6-22
6.2.1	General	6-22
6.2.2	Spinup Systems	6-23
6.2.2.1	Solid Propellant Spinup System	6-23
6.2.2.2	Ammonia Vaporjet Spinup System	6-23
6.2.2.3	Equilibrium Boiling System	6-25
6.2.2.4	Electrically Heated System	6-25
6.2.2.5	Water Heat Source System	6-25
6.2.2.6	Cold Gas (GN <sub>2</sub> ) System	6-27
6.2.3	Attitude Control and Orbit Change Propulsion System	6-28
6.2.3.1	System Considerations	6-31
6.3	Structure Subsystem	6-33
6.3.1	General	6-33
6.3.2	Structure Description	6-33
6.4	Thermal Control Subsystem	6-36
6.4.1	General	6-36
6.4.2	Design Summary	6-36
6.4.3	Solar Panel	6-37
6.4.4	Internal Equipment	6-39
6.4.5	Internal Power Dissipation	6-43
6.4.6	Thermal Model	6-43
6.4.6.1	Thermal Model Results	6-46
6.4.6.2	Transit Phase	6-46
6.4.7	Materials, Hardware, and Weights	6-49
6.4.8	Nomenclature	6-56
6.5	Sensors Subsystem	6-57
6.5.1	General	6-57
6.5.2	Sun Sensors Description	6-57
6.5.3	Horizon Sensor Description	6-61
6.5.4	Reliability	6-66
6.6	References	6-66

7.0	MAGNETIC CONTROL STUDIES	
7.1	Overall Spacecraft Fields	7-1
7.2	Magnetic Environment	7-2
7.3	Magnetic Budgets - Detailed Estimate	7-4
7.4	Achievement of Magnetic Cleanliness - Magnetic Control	7-9
7.5	Accuracy of Measurement	7-11
7.6	Voyager Boom Lengths	7-13
8.0	OEC RELIABILITY	
8.1	Reliability Assessment	8-1
8.2	Reliability of Alternate Modes of Operation	8-1
8.3	Failure Rate Data	8-5
8.4	Critical Unit Reliabilities	8-9
	8.4.1 Tape Recorder	8-9
	8.4.2 Batteries	8-9
	8.4.3 Propulsion	8-10
8.5	Reliability Consideration for Low Temperature Exposure During Eclipse	8-13
APPENDICES		
A.	Attitude Determination	A-1
B.	Orbit Determination	B-1
C.	Effects of Oscillator Drift on Multiple Frequency Shift Keying	C-1
D.	Use of Canopus Sensor as Roll Reference	D-1

## 1.0 INTRODUCTION

This report presents the technical studies and tradeoffs performed during the course of the OEC feasibility study to define the OEC mission design spectrum and the recommended mission conceptual design. The work presented here supports the conclusions and choices described in Volume I, "OEC Feasibility Study Final Report."

The analyses presented in this volume were based on the fundamental mission requirements described in detail in Volume I. These requirements led to the definition of a mission philosophy with a wide range of possibilities. This document explores these possibilities and the various solutions and modes of operation which are possible within the prescribed constraints.

A result of the studies in this volume is a recommended OEC configuration which meets all of the performance requirements outlined by the Ames Research Center. Furthermore, the selected configuration and mission profile incorporate additional flexibility which enhances the mission's scientific objectives.

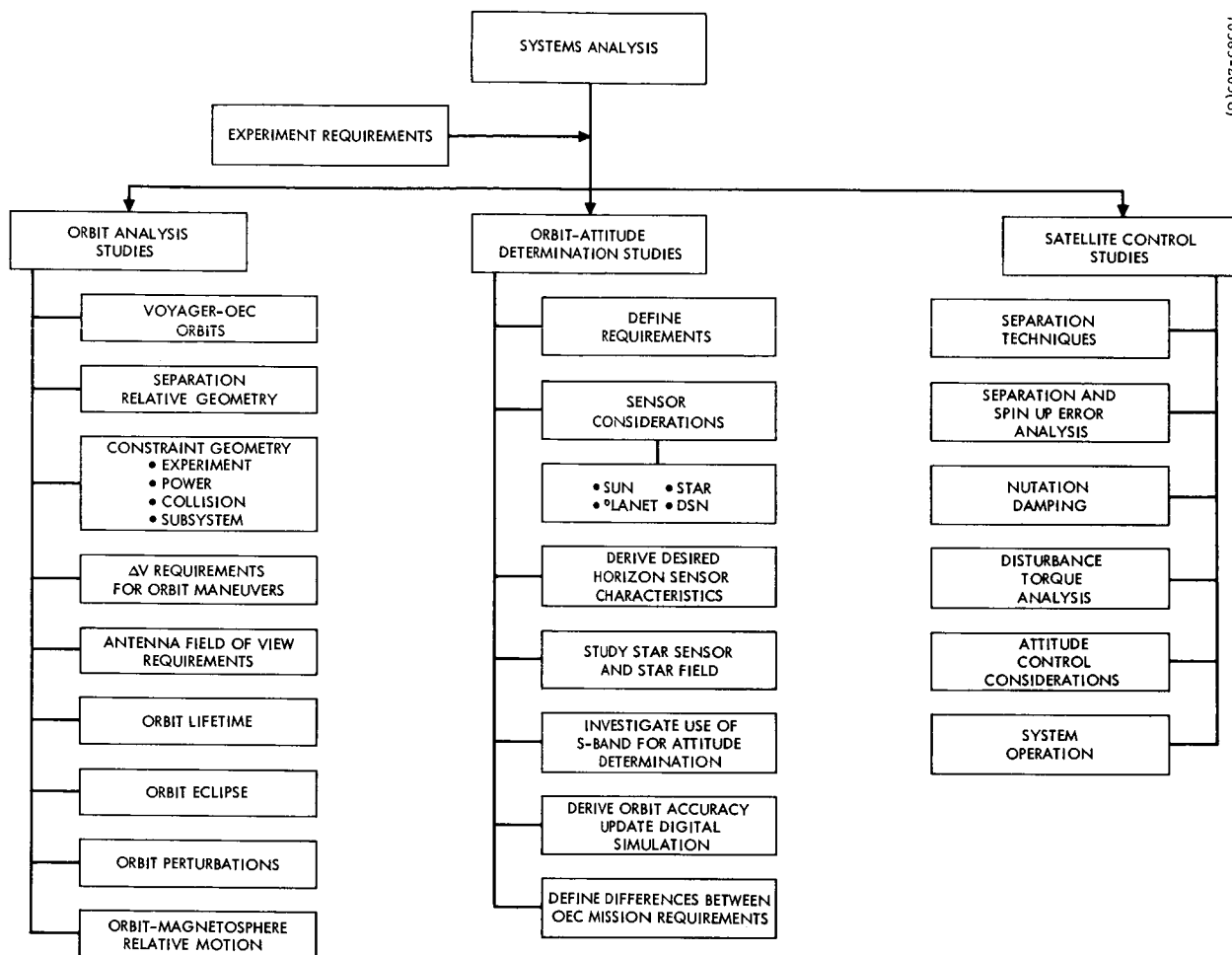
## 2.0 SYSTEMS ANALYSIS

The objective of this feasibility study is to determine whether a satellite can be ejected from the Voyager 1973 Orbiter and positioned in a preferential orbit about Mars. Requirements imposed on the selected orbits dictate that they be suitable to achieve the experimental objectives outlined in the "Specification for an Orbital Experiment Capsule (OEC) Study" as defined by Ames Research Center.

In order to establish the feasibility of such a mission, several conceptual approaches representing the range of viable solutions have been studied. The two mission extremes are defined as a co-orbiter concept and an orbit change concept. In brief, these classifications connote that the OEC will operate in either the same general orbit as the Voyager Orbiter or, by proper maneuvering, be positioned into another selected orbit.

There are several subtleties in the two mission concepts that influence the design of the orbital capsule. This section defines the basic environmental conditions under which any mission must operate, establishes the kinematic as well as dynamic properties of the orbits and satellite, and provides an accurate method of specifying both the position and attitude of the OEC. Ultimately these results establish the points of departure between the various mission approaches and lead to the development of the various experimental capsule designs.

The discussion in this section stems from the early development of a system flow diagram illustrating the important system parameters which are necessary to evaluate the performance of the proposed baseline configuration. Figure 2-1 shows the individual study tasks conducted in the course of the OEC feasibility study. Each of the items is treated in detail in the text, providing the necessary information to arrive at a preferable OEC concept and the associated real time operational performance.



System Task Flow-Diagram

## 2.1 VOYAGER MISSION, MARS ENVIRONMENT, AND EXPERIMENT REQUIREMENTS

### 2.1.1 General

A primary objective of the OEC is to establish a satisfactory orbit about the planet Mars at such an altitude and inclination that scientific measurements of the Martian environment and its relationship to the solar atmosphere can be made. Present estimates of the Martian atmosphere and surface are derived from Earth-based observations. The only attempt at direct measurements was made by the Mariner IV spacecraft. These direct measurements indicated no measurable Martian magnetic field at a distance of 13,200 km from the planet's center. This section describes the characteristic of the Voyager-OEC missions and the scientific experiments which could detect various measurables of the Martian environment.

### 2.1.2 Voyager Mission Requirements

Before discussing the characteristics of the Voyager orbits, the Voyager 1973 Mars mission is summarized. It is important because the OEC must survive the launch and transit phase of the Voyager mission as well as operate independently in orbit about Mars.

#### 2.1.2.1 Preliminary Mission Profile

The OEC/Voyager spacecraft will be assembled, checked out, and launched from Complex 39 at the Kennedy Space Center aboard a Saturn V booster. Figure 2-2 shows the two Voyager spacecraft housed under the Saturn V shroud. Launch and arrival dates satisfying the Voyager mission constraints are 15 July to 3 September 1973 and 4 February to 21 March 1974.

Figure 2-3 is a schematic of the nominal Voyager/OEC flight plan. Launch is initiated with ignition of the first stage. Approximately 2-1/2 minutes after liftoff, S-IC engines are shut down. The S-IC stage is subsequently jettisoned and the S-II stage ignited at approximately 40 miles altitude. Approximately 9 minutes after liftoff, the S-II stage is separated from the S-IVB. The S-IVB is then used to inject the Voyager/OEC payload into parking orbit and is re-ignited at a later point to propel the payload to the desired escape conditions. During the coasting period in the parking orbit, the protective nose fairing and forward portion of the shroud are jettisoned. Following the establishment of the escape conditions, the forward Voyager/OEC spacecraft will be separated, the shroud center-section jettisoned, and the aft Voyager/OEC separated.

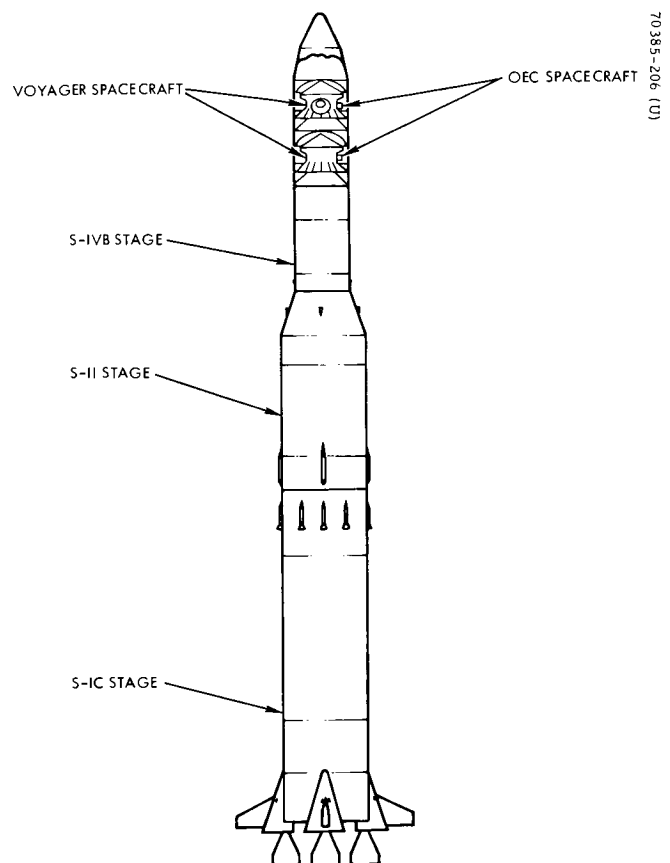


Figure 2-2. Voyager Space Vehicle Configuration

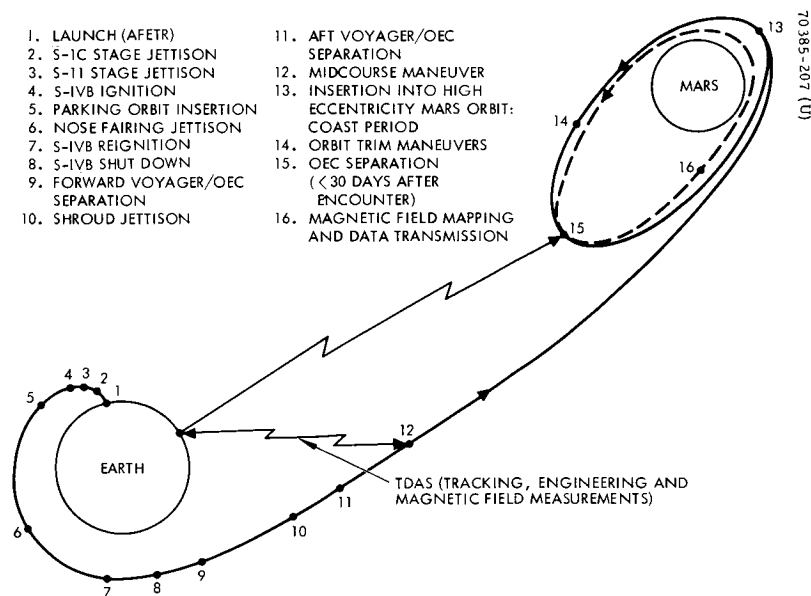


Figure 2-3. Nominal Flight Plan



During the interplanetary transit, midcourse maneuvers will be made to adjust Mars encounter conditions. The interplanetary transit trajectory places the Voyager/OEC vehicle in a Mars flyby trajectory with orbit plane inertial geometry and periapsis location consistent with the Voyager mission requirements. A maneuver initiated relatively near periapsis will establish the desired nominal Mars orbit. The Voyager/OEC vehicle will then be tracked to accurately determine its orbit and to estimate necessary trim maneuvers. This period may extend for several weeks to permit surveillance of possible landing sites for the capsule.\*

A signal sent from the Earth will initiate separation of the OEC from the Voyager.

#### 2.1.2.2 Launch Environment

The OEC environment experienced during launch of the Saturn V must be assessed to enable proper structural capsule design. The maximum acoustic noise level at the forward skirt and payload area of the S-IVB stage is approximately 150 db, referenced to a pressure of 0.0002 microbars. This level is experienced during first stage burn (70 seconds after liftoff) and during the period of high dynamic pressure. In addition, the maximum sound pressure level occurs at 355 to 710 Hz. The maximum axial acceleration of the booster is only 3.7 g at S-IC burnout (i. e., 2-1/2 minutes after launch) and is considerably lower thereafter. In Reference 1, vibration specifications for payloads are given which cover the launch environment. The design specification for random vibration has a maximum spectral density of  $0.2 \text{ g}^2/\text{Hz}$  at a frequency of 200 to 500 Hz.

Since the Saturn V shroud is jettisoned following the establishment of a parking orbit, a benign thermal environment can be maintained during the launch phase, and aerodynamic heating will not be a problem.

#### 2.1.2.3 Voyager Mission Constraints

Table 2-1 lists requirements for the Voyager mission (Reference 1) which are of immediate significance to the OEC mission. The first four requirements listed are extremely important as OEC mission design parameters. They establish the range of altitudes and inclinations in which the OEC must operate. The complete generality exhibited by the range given is shown in Figure 2-4. As shown in a Mars centered coordinate system, the inclination constraints specified in Table 2-1 are equivalent to a 30 to 70 degree range of inclinations to the Martian equatorial plane. The Mars pole is itself inclined to the Mars ecliptic plane by approximately 25 degrees.

By revolving the orbits illustrated about the Martian north pole (for a fixed inclination), the complete generality, taking into account the present uncertainty in the actual orbit nodal crossing, can be envisioned.

---

\* The possibility of delaying separation of the OEC from the Voyager for an extended period of time has a significant implication on the design requirements for eclipse operation.

TABLE 2-1. SOME VOYAGER MISSION CONSTRAINTS

1) Periapsis altitude, $h_p$	$500 \text{ km} \leq h_p \leq 1500 \text{ km}$
2) Apoapsis altitude, $h_a$	$10,000 \text{ km} \leq h_a \leq 20,000 \text{ km}$
3) Orbital inclination to Martian equator, $i$	$i \geq 30$ degrees (landing site constraint)
4) Orbital inclination to ecliptic, $i_e$	$i_e \leq 45$ degrees (Voyager ultra-violet experiment)
5) Latitude of periapsis, $\omega_p$	$-60 \leq \omega_p \leq 40$ degrees over 6 months
6) Voyager operating life in Mars orbit	At least 2 months with design goal of 6 months
7) Voyager minimum planetary quarantine contamination lifetime	50 years
8) Solar eclipse duration, $T_e$	$T_e = 0$ for first 30 days, and minimum (8 percent of orbit period or 60 minutes/orbit) for next 5 months
9) Central angle between sub-periapsis point and nearest terminator, $\lambda_{\omega p}$	$0 \leq \lambda_{\omega p} \leq 45$ degrees for first 3 months, $-30 \leq \lambda_{\omega p} \leq 90$ degrees thereafter
10) Angle between orbit plane and terminator plane, $i_p$	$i_p \geq 30$ degrees for first 3 months, $i_p < 30$ degrees for a total of 1 month over next 3 months
11) Capability is required to rotate periapsis by at least $\pm 20$ degrees from initial (hyperbolic) location.	
12) Capsule de-orbit maneuver shall be performed between 3 and 12 days after orbit insertion. Capability for delaying this operation for 30 days is required.	
13) Unpredictable translational accelerations originating in Voyager shall not exceed a total average value of $0.6 \times 10^{-7} \text{ cm/sec}^2$ (3 $\sigma$ ), time average over 1 hour.	
14) Orbit trim maneuvers may be required for post-lander orbital operations.	

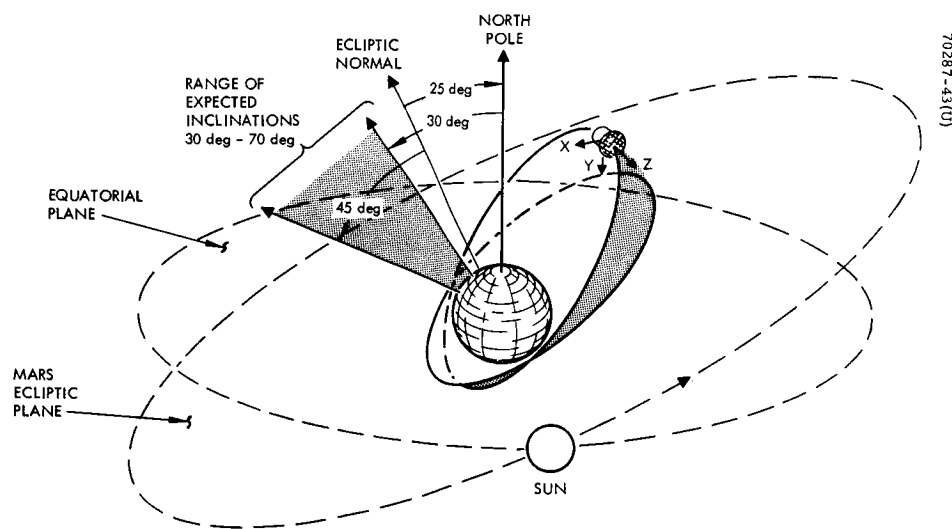


Figure 2-4. Relationship of OEC Orbits to Mars Environment

The Voyager spacecraft is shown in Figure 2-4 with the given XYZ coordinates. Voyager stabilization is provided by an active three axis control system which continuously tracks the sun and the star Canopus.

### 2.1.3 Expected OEC Mission Environment

The anticipated OEC environments include the natural environment as well as that induced from the Voyager bus. Mechanical environments induced during launch and boost phase are not included in this discussion. The effects of the natural environment are reduced somewhat because of the shielding effects of the bus. However, this decrease is partially offset by the secondary radiations from the bus surfaces.

The expected in-transit and orbit environment must also be accounted for in the design of the power source. A power system employing a solar array and batteries is chosen for this mission. In designing the solar array, adequate surface area must be allocated to provide for the degradation due to the space environment.

The conditions of the telluric, interplanetary, and Martian environments to which the spacecraft will be subjected are listed in the following tabulation. The data consists of a brief summary, covering only the conditions that will have an effect on design of the spacecraft and its instrumentation.

#### 2.1.3.1 Interplanetary Environment

##### a) Electromagnetic Radiation (radial from the sun)

- Solar constant  $1.39 \times 10^{-6} \text{ erg cm}^{-2} \text{ sec}^{-1}$  or  $1.39 \times 10^{-5} \text{ lumen m}^{-2}$
- X-rays  $\lambda = 1 \text{ to } 10 \text{ \AA}$ 
  - Quiet sun  $10^{-8} - 10^{-3} \text{ erg cm}^{-2} \text{ sec}^{-1} \text{ \AA}^{-1}$
  - Active sun  $10^{-6} - 10^{-2} \text{ erg cm}^{-2} \text{ sec}^{-1} \text{ \AA}^{-1}$
- $\gamma$ -rays  $\lambda < 1 \text{ \AA}$ 
  - Quiet sun  $< 10^{-8} \text{ erg cm}^{-2} \text{ sec}^{-1} \text{ \AA}^{-1}$
  - Active sun  $< 10^{-5} \text{ erg cm}^{-2} \text{ sec}^{-1} \text{ \AA}^{-1}$
- Ultraviolet  $500 < \lambda < 3000 \text{ \AA}$   
 $5 \text{ ergs cm}^{-2} \text{ sec}^{-1} \text{ \AA}^{-1}$

##### b) Solar Wind (radial with the sun)

- Outside shock front  $N_p = 3 \text{ to } 13 \text{ particles cm}^{-3}$   
at  $300 \text{ to } 800 \text{ km sec}^{-1}$

- For quiet sun  $N_p = 0.3 \text{ to } 10 \text{ particles cm}^{-3} \text{ at } 250 \text{ to } 500 \text{ km sec}^{-1}$
- For active sun  $N_p = 5 \text{ to } 18 \text{ particles cm}^{-3} \text{ at } 400 \text{ to } 900 \text{ km sec}^{-1}$
- Composition
  - 90 percent protons ( $H^+$ )
  - 0 to 10 percent alpha particles ( $He^{++}$ )
  - Unknown percent heavy nuclei ( $Li \rightarrow Fe$ )

- Total solar wind flux, particles  $\text{cm}^{-2} \text{ sec}^{-1}$

	<u>Minimum</u>	<u>Maximum</u>
$H^+$		
Quiet sun	$8.1 \times 10^6$	$9.4 \text{ to } 10^8$
Active sun	$1.8 \times 10^8$	$2.0 \times 10^9$
$He^{++}$ plus heavy nuclei		
Quiet sun	$9 \times 10^5$	$1 \times 10^8$
Active sun	$2 \times 10^7$	$2.2 \times 10^8$

Since the solar wind is a neutral plasma, there is an equal number of low energy electrons. The energy is within the range 1 to 300 ev.

c) Cosmic Ray Radiation

- Solar minimum  $N_c = 0.5\text{-}2 \text{ particles cm}^{-2} \text{ sec}^{-1}$
- Solar maximum  $N_c = 1\text{-}4 \text{ particles cm}^{-2} \text{ sec}^{-1}$
- Energy range
  - 40 mev to  $10^{13}$  mev
  - (predominantly between 1 and  $10^4$  bev)
- Composition
  - Protons ( $H^+$ ) 85 percent
  - Alpha particles ( $He^{++}$ ) 14 percent
  - Heavy nuclei ( $Li \rightarrow Fe$ ) 1 percent

d) Solar Flares

- Overtime period 1967-1968       $2.05 \times 10^{11}$  protons  $\text{cm}^{-2}$  ( $E > 5 \text{ mev}$ )

2.1.3.2 Earth Environment

The earth environment is summarized to illustrate the dynamic variations in the magnetic and electric fields and the trapped radiation zone particle fluxes. This data is used as a basic input parameter in design of the spacecraft for survival in passing through near-earth space.

a) Magnetic Field

- Magnetosphere and magnetopause      Perigee 0.3 gauss at boundary  
2 to 20  $\gamma$
- Transition      5 to 20  $\gamma$  (solar field centered  
around geomagnetosphere)
- Interplanetary  
    Quiet sun      3 to 8  $\gamma$  (average 5.1  $\gamma$ ) at 1 AU  
    direction  
    Active sun      1 to 100  $\gamma$  at 135 degrees tangential  
    to Earth's orbit

b) Outer Magnetosphere

Electrons  $E < 45 \text{ kev}$        $10^{12} - 10^{14} \text{ cm}^{-2} \text{ sec}^{-1}$

(Very sharp rise through magnetopause from transition region —  
about a factor of  $10^3$ )

Add low energy protons and electrons from trapped radiation.

The dynamic changes in the geomagnetic field are shown in Table 2-2.

These variations are due to fluctuations in the solar wind, solar magnetic field, charged particle bombardment, and distortion of the Earth's field due to daily rotation.

TABLE 2-2. VARIATIONS IN GEOMAGNETIC FIELD

Characteristic Time, seconds	Description of Phenomena	Estimated Typical Magnitude, gamma	Buildup Time or Duration	Type of Measurement
$10^{-2}$	Sub-audio frequency fluctuations	0.01 gamma-sec <sup>-1</sup>		Relative
$10^0$	Micropulsations	0.1		
$10^2$	Giant pulsations Sudden commencements	20 20 to 30	Shock front 10 seconds remaining for several hours	
$10^4$	Diurnal variations - increase and decrease of field intensity	30	6 to 12 hours	
$10^6$	Storm-time effects 27 day recurrence effects	< 100	Several hours to several days	
$10^8$	Annual variations	10		Absolute
$10^{10}$	Solar cycle effects Secular variations	25 gamma year <sup>-1</sup>	Steady change throughout year	

c) Trapped Radiation (Magnetosphere)

## • Inner zone

Protons

 $2 \times 10^5$  protons cm<sup>-2</sup> sec<sup>-1</sup>  
 $E > 5$  mev

Electrons

 $3 \times 10^8$  electrons cm<sup>-2</sup> sec<sup>-1</sup>  
 $E > 0.5$  mev

- Outer zone

Protons	$10^4$ protons $\text{cm}^{-2} \text{sec}^{-1}$ $E > 5 \text{ mev}$
Electrons	$10^7$ electrons $\text{cm}^{-2} \text{sec}^{-1}$ $E > 0.5 \text{ mev}$

- Transition region

Electrons	
$E \geq 45 \text{ kev}$	$10^8 \text{ to } 10^9 \text{ cm}^{-2} \text{sec}^{-1}$
$E < 45 \text{ kev}$	$10^9 \text{ to } 10^{12} \text{ cm}^{-2} \text{sec}^{-1}$

The particles are accelerated along the shock wave toward the magnetic tail of the Earth (along diverted solar magnetic field lines).

Standard B-L plots of the trapped radiation fluxes are shown in Figures 2-5 and 2-6.

d) Electric Field

• Field intensity	$1 \text{ to } 2 \text{ mv m}^{-1}$
Occasionally dips to	$600 \text{ to } 800 \text{ mv m}^{-1}$
Occasionally rises to	$2 \text{ mv m}^{-1}$ (very rare)
• Frequency	dc to 80 Hz

These variations occur in the upper regions of the magnetosphere.

### 2.1.3.3 Mars Environment

The dynamic ranges and values of the magnetic field, electric field, and particles associated with the Earth are used and interpreted to represent possible variations in the Martian environment. Generally the dc parameters will be much smaller, but the dynamic variations will be assumed to be the same except for the  $1/r^2$  effect.

**Magnetic Field.** The existence or nonexistence of a magnetic field in the planet Mars is still unknown. There have been no Earth-based observations of radio emissions characteristic of trapped particles and no observed auroral activity characteristic near magnetic poles to indicate any magnetic field. Direct measurements from the Mariner IV spacecraft indicated no magnetic field at a distance of 13,200 km from the center of the planet (altitude of 9800 km). Although the latter measurement did not indicate the presence of any magnetic field, it did establish an upper boundary for the dipole moment of Mars of  $24.2 \times 10^{21} \text{ gauss cm}^3$ , or



$3 \times 10^{-4}$  that of Earth. This would imply a surface magnetic field at the magnetic equator of Mars of only 100 gamma. With the possibility of such a weak field, there is some question as to its source and nature.

There are two possible explanations for the generation of a Martian magnetic field. One, similar to that of the Earth, is that it is internally generated by currents in the core driven by electromotive forces of thermoelectric, electrolytic, or dynamic origin. In this case it is likely that a dipolar magnetic field would exist with the magnetic axis nearly aligned with the axis of rotation of the planet (the Earth's magnetic axis is 11.4 degrees with respect to its axis of rotation, and Jupiter's magnetic axis has been estimated to be at 11 degrees with respect to its spin axis). It is possible that Mars does not have a liquid nickel-iron core, and the magnetism is generated by other internal forces that change in character and act very slowly.

Any weak field generated internally would be greatly affected by the solar wind on the sub-solar side of the planet. Here the magnetic pressure characterized by  $B^2/8\pi$  is balanced by the kinetic or dynamic pressure of the solar wind. The altitude of stagnation is a function of the  $(-1/6)$  power of the solar wind pressure for a dipole field as expressed in the following equation:

$$R = \left[ \frac{M_{\sigma}^2}{4\pi n m v^2} \right]^{1/6} \quad (2-1)$$

where

$M$  = magnetic moment

$1/2 n m v^2$  = solar wind pressure

$R$  = planetary radii

The boundary formed is the magnetopause and the volume is the magnetosphere. Much like the Earth, there would be a comet-like tail resulting from the interaction of the solar wind with the Martian magnetic field lines and atmosphere, stretching the lines and particles in an antisolar direction. The aberration of the tail would vary from 2 to 5 degrees.

The results of assuming the  $M_{\sigma}/M_{\oplus} = 0.0005$  magnetic dipole field are shown in Figure 2-7 as the magnetopause shock front location.

Superimposed on Figure 2-7 is the Mariner IV flight path with respect to Mars. This figure shows that the presence of a magnetosphere and shock wave could go undetected. This weak field would indicate that the solar wind on occasion would act directly with the Martian atmosphere, possibly carrying some of the atmosphere particles into a tail.

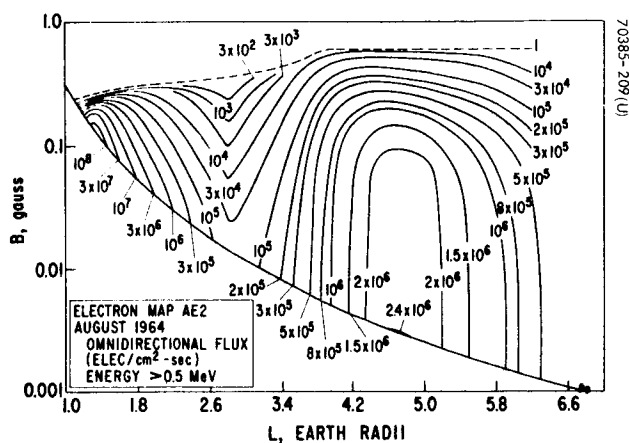


Figure 2-5. Log B-L Flux Map of Electron Environment

Contours are omnidirectional flux above 0.5 Mev. Dotted contour for 1 electron/cm<sup>2</sup>-sec represents limit of map at low altitudes

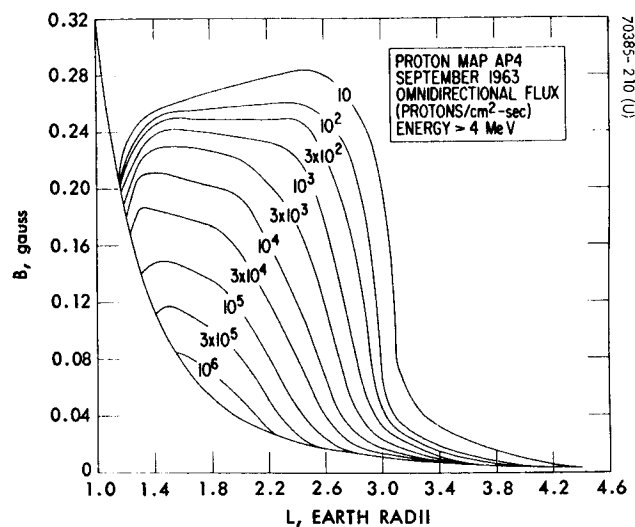


Figure 2-6. B-L Flux Map of Proton Environment

Contours are omnidirectional Flux above 4 Mev.

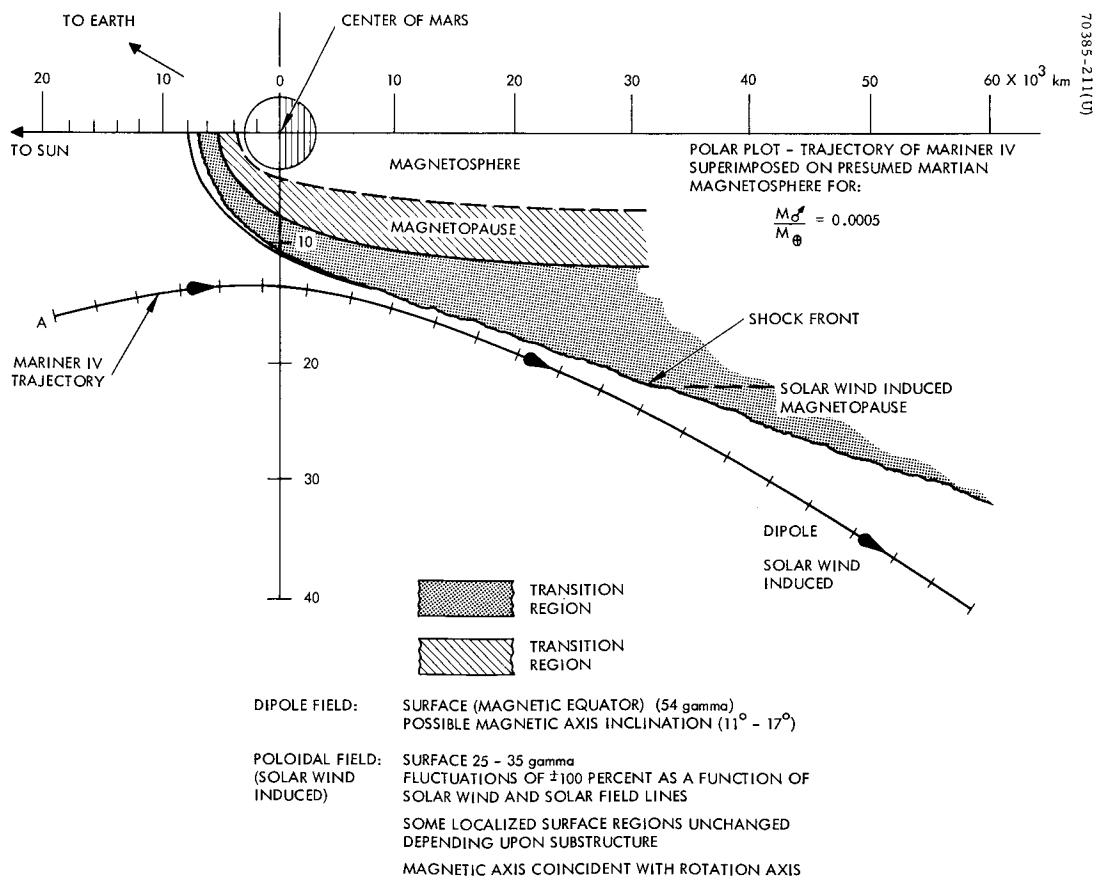


Figure 2-7. Analytical Diagram Used for Inferring Upper Limit to Ratio of Magnetic Dipole Moment of Mars to That of Earth

For the solar wind to push the magnetopause to an altitude of  $10^3$  km, the surface magnetic flux density would have to be about  $54\gamma$ . This value is for a normal solar wind of 4 particles  $\text{cm}^{-3}$  moving at a velocity of  $300 \text{ km sec}^{-1}$ . The magnetic pressure to stagnate the given solar wind at the subsolar point is derived from a magnetic flux density of 25 gamma at the altitude of  $10^3$  km. A change of  $\pm 2$  particles  $\text{cm}^{-3}$  constitutes a change of  $\pm 550$  km in altitude of the magnetopause and a change in flux density of  $\pm 12$  gamma.

The second possibility of the origin of a magnetic field is related to a solar wind induced magnetic field. A solar wind induced field is not a stable field, as is an internally generated dipole. The field is subject to the large fluctuation in magnitude and direction of the solar wind. One possible theory for the formation of very weak magnetic fields of a planet has been developed by T. Gold (Reference 2) in which the solar magnetic lines are piled up around the subsolar point due to the action of the solar wind and a magnetically conductive body, where the magnetic time constant is long compared to the Martian day. The hanging up of solar magnetic lines on the subsolar side of the planet produces a magnetic cavity behind the planet. Since the planet is rotating, the induced magnetic field is characterized by the classical problem of a rotating sphere magnetized from one side only. Here the resulting planetary magnetic field is poloidal; i. e., lines of force are north and south with an intensity that varies with the magnetic pile-up, and hence as a function of the solar wind. No longitudinal component would exist since the planet acts as a diamagnet — a rotating shell magnetized from one direction only.

Because of the presence of an atmosphere, although tenuous, the interaction of the solar wind with the atmosphere particles may result in the Martian magnetic field being confined to an ionosphere.

For either the internally generated field or solar wind induced field, a magnetopause should exist but it may be very close to the surface of the planet. The magnetic moment of Mars would be  $1.33 \times 10^{-4}$  times that of the Earth for the stagnation pressure to be at the surface. The minimum ratio of the Martian magnetic moment to the Earth magnetic moment is calculated assuming no surface effects and that the stagnation point (in a dipole field) would be at the surface. Mariner IV data indicates that the magnetic moment can be no greater than  $3 \times 10^{-4}$  that of the Earth.

Therefore

$$1.3 \times 10^{-4} < \frac{M_{\sigma}}{M_{\oplus}} < 3 \times 10^{-4}$$

Assuming the upper limit and a decrease in the number of solar wind particles to  $2 \text{ cm}^{-3}$ , the radius to the stagnation point moves out to 6200 km from 5500 km. Similarly, an increase in the solar wind particles to  $6 \text{ cm}^{-3}$  drives the stagnation level to 4900 km. These correspond to a 25 percent change in the solar wind velocity.

With the lower limit, the magnetopause is only a few kilometers above the surface and the shock wave would be about 1000 km above the surface. An increase in the solar wind profile would drive the shock wave to the surface, and a decrease would move the shock wave and magnetopause away from the surface.

The numbers quoted are based on a previous expression for the stagnation point in a dipole field. Assuming number density changes in the solar wind, the altitude of the stagnation point can be calculated. This is not necessarily the case for a solar wind induced field where the gradient may be something less than a dipole field.

The actual detection and measurement of a planetary magnetic field is predicated on specific observable signatures that define the shock, transition, and magnetosphere previously described. These signatures are based upon the many measurements and theories associated with the Earth's magnetic field and the interaction of the solar wind and field on it. There are two kinds of measurements that bear on the presences of a magnetic field: 1) direct measurement of the magnetic field by use of magnetometers, and 2) measurement of the charged particle radiation fluxes.

There will be magnetic field changes associated with the bow shock, transition region, magnetopause, and magnetosphere different from the solar or interplanetary field. Associated with the magnetic field are the signatures of charged particles — particularly the electrons. Three main signatures are as follows:

- Change in the solar wind particle flux
- Bursts of electrons near and beyond the shock front. The field lines in the shock front provide an acceleration mechanism for the electrons
- Additional bursts of electrons in the transition region
- Trapped radiation (electrons and protons) in the magnetosphere

Trapped Radiation. Radiation zones similar to the Earth's radiation zones in all probability do not exist near Mars. Because of the very weak magnetic field and if the field is dipolar, any trapped radiation would consist of low energy protons along with electrons. On the other hand, the type of magnetic field such as the solar wind induced field does not provide conjugate points between which the charged particles can be trapped. It is more likely that the presence of charged particles is confined primarily to an ionosphere formed by photoemission from the interaction of the ultraviolet and X-ray with the Martian atmosphere.

Any "trapped" charged particles will be those confined within the areo-magnetospheric tail, in the transition region and in the shock front. Since the magnetospheric boundaries are formed by magnetic pressure balancing the solar wind kinetic pressure, the relative electron (low energy) count is expected to be about the same as for the Earth. The only major difference is the inverse square effect of the solar wind flux.

Induced Environment. During the transit phase of the mission while the OEC is mated to the Voyager bus, the capsule is subject to thermal, vibration, and secondary radiation from the bus. The induced environments from the Voyager Orbiter itself remain to be determined. If RTGs are used as the major Voyager orbiter power system, then the gamma rays and neutrons must also be accounted for in establishing the OEC environment. A typical set of parameters representing

an RTG environment is shown here — the radiation environmental characteristics of the SNAP 27 50-watt RTG at a distance of 1 meter are given:

- Neutrons (3 mev peak) 125 mrem hr<sup>-1</sup>
- Gamma (1 mev mean) 11 mR hr<sup>-1</sup>
- Perpendicular to axis of RTG  
1.7 mR hr<sup>-1</sup>
- Parallel to axis of RTG
- Surface temperature 500° K

#### 2.1.4 Experiments

Scientific experiments applicable to the OEC concept have been considered beyond those designated for fields and particle measurements. The only restriction on the alternate experiments is the budgeted volume, power, and data requirements nominally allocated to the instruments. Some of the experiments that were considered are listed here.

Magnetic Field Mapping. Measurement of the magnetic field of Mars will be made as a function of spatial geometry and time with respect to the planet. Such mapping will include the following:

- a) Map areomagnetosphere boundary
- b) Map field changes through bow shock
- c) Map interplanetary field and planetary field interface along with dynamic changes
- d) Measure small perturbations of the Martian field at values less than 0.25 gamma and at frequencies of 1 to 2 cycles Hz per second
- e) Determine whether field is a dipole, solar wind induced poloidal, or a multipole
- f) Map magnetic field inside the magnetosphere

Electric Field Mapping. When the charged particles of the solar wind penetrate the magnetic field, there is a separation of the electron and protons and subsequent production of an electrostatic field. Similarly, the differential movement of the electrons and protons produces an electric current and an electric field.

As for the magnetic field experiment, the electric field and its variations will be mapped from a dc field to the ac field up to 80 kHz.

Gravity Gradient. One possible experiment that can be conducted by the OEC is measurement of the gravitational fields of the moons of Mars — Phobos and Deimos. Such an experiment would require a flyby distance from the moons of about 100 to 200 km. It would also require very precise orbit timing and orbit correction. A device has been developed (rotating-vibrating mass) that has sufficient sensitivity to perform the necessary measurement. However, the orbit adjustment requirements require further investigation.

Solar Wind Fluxes. Solar wind low energy particle fluxes will be measured outside the influence of the Martian environment. Spatial resolution for such an experiment will vary from fine near the subsolar point to coarse for the antisolar point.

Such continual monitoring of the solar wind in and out of the Martian environmental influence will provide data on the interaction of the solar particles with the Martian atmosphere and the Martian magnetic field. Measurement will be made of the energy spectrum and the fluctuating direction with respect to the sun.

Solar Flare Activity. Since the proposed OEC mission is in or near a solar minimum, it is not likely that many solar flares will occur. However, it is quite likely the ultraviolet and X-ray emissions in the initial rise portion of a flare (even for subflares) may be of sufficient intensity to disturb the Martian ionosphere. It would therefore enhance the overall mission if the radiation output of any solar flare activity in the form of protons, ultraviolet, and X-ray were measured and correlated with other fields and particle measurements near Mars. These measurements would include solar cosmic rays.

"Trapped" Particles. Associated with an areomagnetsphere is the possibility of "trapped" electrons and protons ( $E_e < 100$  kev,  $E_p < 5$  mev) — trapped in the sense of being concentrated in specific spatial location in relation to the magnetosphere. This results largely from the interaction of the solar wind particles with the magnetic and electric fields. Measurement will be made of the energy spectrum and spatial distribution of the electrons as the OEC passes through the magnetosphere — bow shock, transition region, and inner portion — within the orbit capabilities of the OEC. These measurements are not programmed for the Voyager spacecraft.

Atmospheric and Ionospheric Measurement. An indirect measurement of the Martian atmosphere and ionosphere can be made utilizing the occultation of the OEC with the Voyager Orbiter through measurement of the changes in the frequency, phase, and amplitude of a radio signal (a function of the number of particles per cubic centimeter and charge). The surface pressure and profile of the atmosphere can be determined as well as the extent of the ionosphere. These characteristics are also a function of the limb surface roughness in relation to the OEC-Voyager line of sight. Repeated measurements could provide some indication of the areographic distribution of the atmospheric and ionospheric thickness and number density.

Interstellar Cosmic Rays. Energy spectral measurements could be made of cosmic rays with energies  $E > 400$  mev. One possible experiment is the

measurement of  $\text{Be}^{10}$  to obtain possible data that could lead to age dating and formation of the solar system. More general spectral measurements would be possible. In the event of solar flare activity, measurement of a Forbush decrease would be possible to correlate with some Earth based measurements.

Inert Particles. Measurement could be made of the distribution of dust particles "trapped" near Mars. These measurements would provide mass distribution and spatial distribution with respect to the planet. At the same time it is conceivable to be able to obtain data on the influx of dust particles from the solar system. The spinning of the OEC will provide impact data around 360 degrees and data for identifying the direction of maximum intensity.

The experiments listed would be performed after physical separation of the OEC from the Voyager Orbiter. It is possible that two OEC type capsules will be orbiting at the same time, giving rise to the problem of using duplicate experiments or some different experiments to complement one another. This imposes additional requirements on the orbits, data handling, telecommunications, and — as just mentioned — experiment selection.

#### 2.1.4.1 Orbit Requirements

A discussion of the bounds of the possible Martian magnetosphere is repeated here to illustrate the desired range of possible orbits (see Figure 2-8).

Under the present periapsis limit of 500 km, the orbit location as shown in Figure 2-8 would permit measurement of the magnetosphere on the subsolar side of Mars as well as the antisolar side. This, of course, assumes that the maximum magnetic field is that determined from the Mariner IV data. If it is not, then the subsolar pass would measure only the location of a shock wave associated with a solar-induced magnetic field.

The initial position of the orbit must meet the two following conditions:

- 1) The line of the apsides should lead the Mars-sun line by 45 degrees to account for the spatial rotation of the magnetospheric tail during the initial part of the mission.
- 2) The plane of the orbit (the line of the apsides) should be inclined about 5 degrees above or below the Mars orbit plane so as to prevent any eclipsing of the OEC during the initial part of the mission. This orbit constraint may well require adjustment of the OEC orbit and hence require that the OEC have orbit change capability if separation occurs in an unfavorable orbit with respect to making the desirable measurement.

Since the nature of the Martian field is unknown, it is further desirable to be injected into an orbit inclined with the equatorial plane of Mars. Only then could the field be measured as a function of a areographic latitude and permit a differentiation between a dipole field and a solar induced field. The range of desirable inclination lies between 30 and 50 degrees. As the orbit precesses, the values of the fields and particles in the equatorial plane would be obtained.

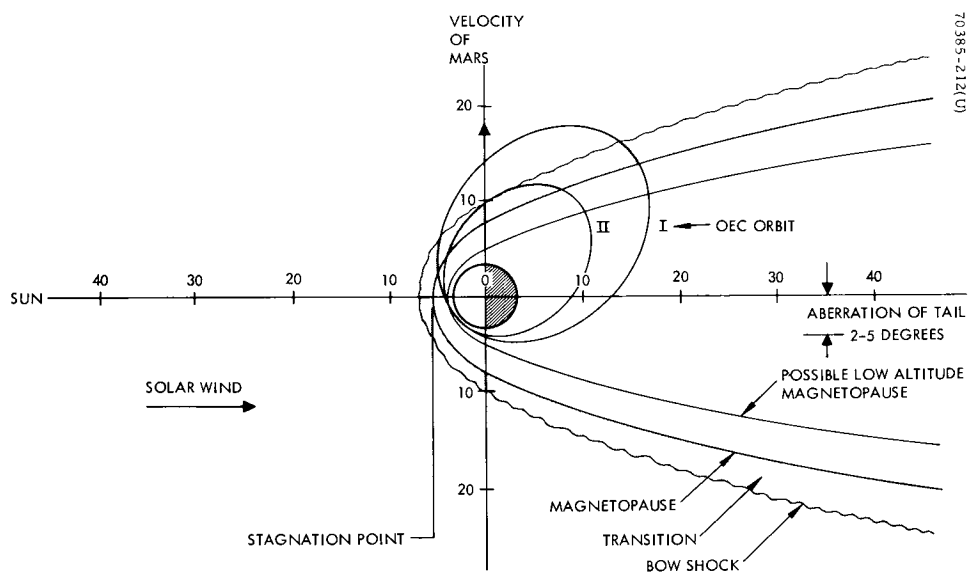


Figure 2-8. Location of OEC Orbit With Respect to Mars Magnetosphere



#### 2. 1. 4. 2 Experiment Requirements

The experiments to be conducted on the OEC depend quite naturally on the actual mission and ultimate orbital characteristics. Once this phase is defined, the desired measurables of the Martian environment are defined and thus both the data acquisition method and finally the associated instrument can be characterized.

The experiments, associated instruments, and data acquisition are based on the mission and orbital characteristics and the range of parameters of the environment to be measured. A number of possible experiments have been mentioned. The number of experiments that can be conducted per mission will be established in part by the OEC spacecraft limitations. These experiments are summarized in Table 2-3, along with the parameters specifying the expected ranges and necessary resolution. The resolution is a function of the dynamic nature of the parameter to be measured and the extent to which the parameter is desired to be known. If small variations are to be measured, as is the desired case for the OEC, greater accuracy is required and therefore a higher number of measurements. The number of measurements for the magnetic field, for example, is assumed to be at one-fourth wave intervals of the highest frequency fluctuation as shown in Table 2-3.

There are a great number of experiments that could be conducted from the OEC. Table 2-3 represents several of the desirable choices. Those identified with an asterisk were considered in the study. The most important experiments are related to measuring the magnetic field, solar plasma and soft electrons, and the electric field. These typical experiments are desirable; however, final selection is dependent on the configuration design, system weights, and total power required.

#### 2. 1. 4. 3 Data Requirements

The amount of data required from each of the experiments listed in Table 2-3 is determined by the sampling interval and the accuracy of the data itself. Because of the dynamic variations of the environment to be measured, the number of samples to be made for each of the experiments is determined as a function of the OEC spin speed and is specified as:

Magnetometer	250 bits/sec
Plasma probe	250 bits/sec
Electric field meter	50 bits/sec

Other experiments that may be utilized would have to have similar data bit rates for real time sensing and transmission, plus similar weight, power, and volume.

Experiment	Range	Resolution	
		Spatial	Measurement
<u>Fields</u>			
• Magnetic*			
Magnetosphere	0 to 100γ 0.5 to 10 <sup>-3</sup> for micropulsations (see Figure 2-3)	~<1/4 wave of fluctuation	<0.25γ (magnitude) <15° direction Development to 0.1 or 0.01γ
Transition	5 to 100γ Compressional fluctuations 0.2 to 1 Hz	~<1/4 wave of fluctuation	
Free space	0.2 to 10γ (quiet) 5 to 100γ (flare)	~<1/4 wave of fluctuation	
• Electric	600 μv m <sup>-1</sup> to 1 mv m <sup>-1</sup> (60 db) over dc to 80 kHz	Same as magnetic	8 bandpass channels ±5 percent bandpass ΔE E ≈ 5 percent <3° direction
<u>Particles</u>			
• Solar wind*	3 × 10 <sup>5</sup> to 1 × 10 <sup>10</sup> cm <sup>-2</sup> sec <sup>-1</sup>	Fine in subsolar direction Coarse in antisolar direction	E/Q ≈ 10 kv to 50 volts
• Near Mars particles*			
Free space	3.5 × 10 <sup>6</sup> to 8.6 × 10 <sup>8</sup> ele. cm <sup>-2</sup> sec <sup>-1</sup>	Uniform sample sector	
Transition region	(Free space flux increased by 10 to 10 <sup>3</sup> behind shock front) E <sub>e</sub> > 80 ev	Uniform samples	ΔE/E ≈ 0.5
• Cosmic			
Protons	E > 40 mev		
α	E > 100 mev	In plane of σ ecliptic - uniform sample sector	
Heavy nuclei	E > 3 gev		
Electrons	E > 1 mev E > 30 mev 50 to 5 × 10 <sup>4</sup> proton cm <sup>-2</sup> sec <sup>-1</sup>		
• Dust particles	F <sub>s</sub> = K10 <sup>-14.54 ± 0.6</sup> m <sup>82</sup> β ≈ -0.5 (Mariner IV) K accounts for nearness to asteroid belt may be near 1	In plane of σ ecliptic 2π - uniform sample sector	mv > 1.5 × 10 <sup>-3</sup> dyne sec
<u>Atmosphere</u>			
• Occultation experiment	Surface pressure 2 to 20 mbar density		1 part 10 <sup>11</sup>
*Primary objectives			

TABLE 2-3. OEC EXPERIMENT REQUIREMENTS

#### 2.1.5 Instruments

The selection of instruments to perform the measurement of a specific experiment is predicated in part by the following factors:

- Accuracy
- Performance (time constant)
- Size, weight, and shape
- Reliability (space proven or experience proven)
- Power requirement

Integration of the experiments on a satellite requires the consideration of several additional factors, such as:

- Interfacing with the satellite and other instruments
- Selection of a location to minimize interference
- Environmental effects

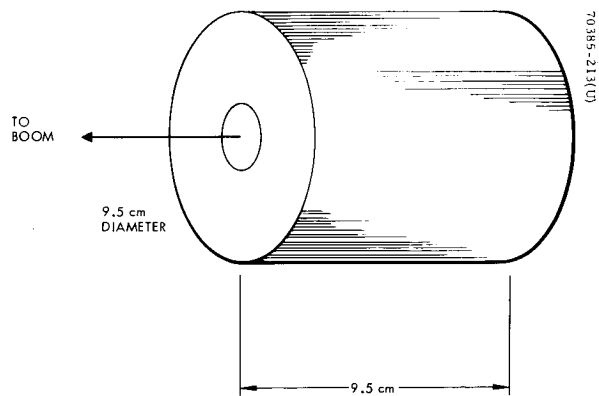
##### 2.1.5.1 Instrument Requirements

A general requirement that applies to all scientific instruments is that they be easily accessible to provide for an interchange of experiments. If at any time throughout the hardware phase it is required to alter the scientific payload, it is desirable to do so with minimal interaction with the overall satellite system. This can be interpreted in terms of designing an adaptable satellite for the various sizes and shapes of typical instruments. The instruments must, however, adhere to the power conditioning system on the satellite.

Some of the instruments considered in this study are listed in Table 2-4, together with a partial list of available instrument characteristics. Satellite scientific payloads can be established by the grouping of various instruments. The differences in payload weight and power for three typical groupings are shown in Table 2-5; the weight varies between 13 and 20 pounds.

To conduct an experimental measurement, each instrument under consideration must be capable of operating over the dynamic range of the specified parameter with sufficiently small response time. Those listed in Table 2-4 represent space proven hardware which has found successful application on the Pioneer VI, IMP I, and OGO-3 spacecraft.

Physical characteristics of the various instruments considered are shown in Figures 2-9 through 2-14.



a) SENSOR ASSEMBLY

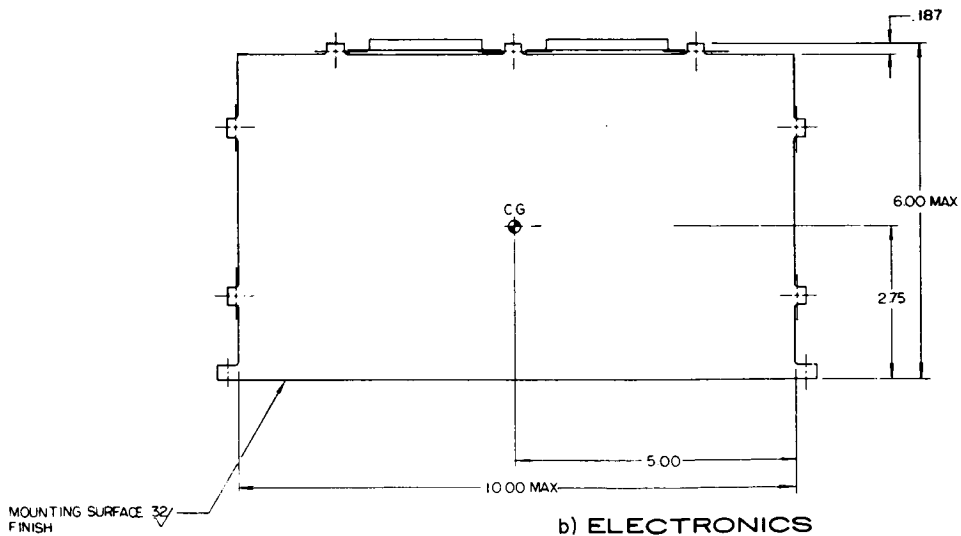
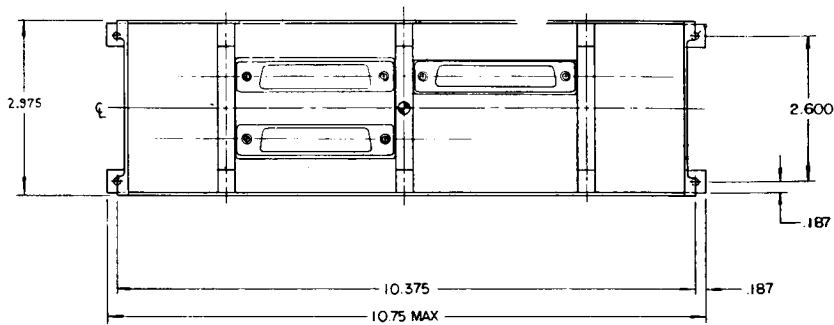


Figure 2-9 Magnetometer

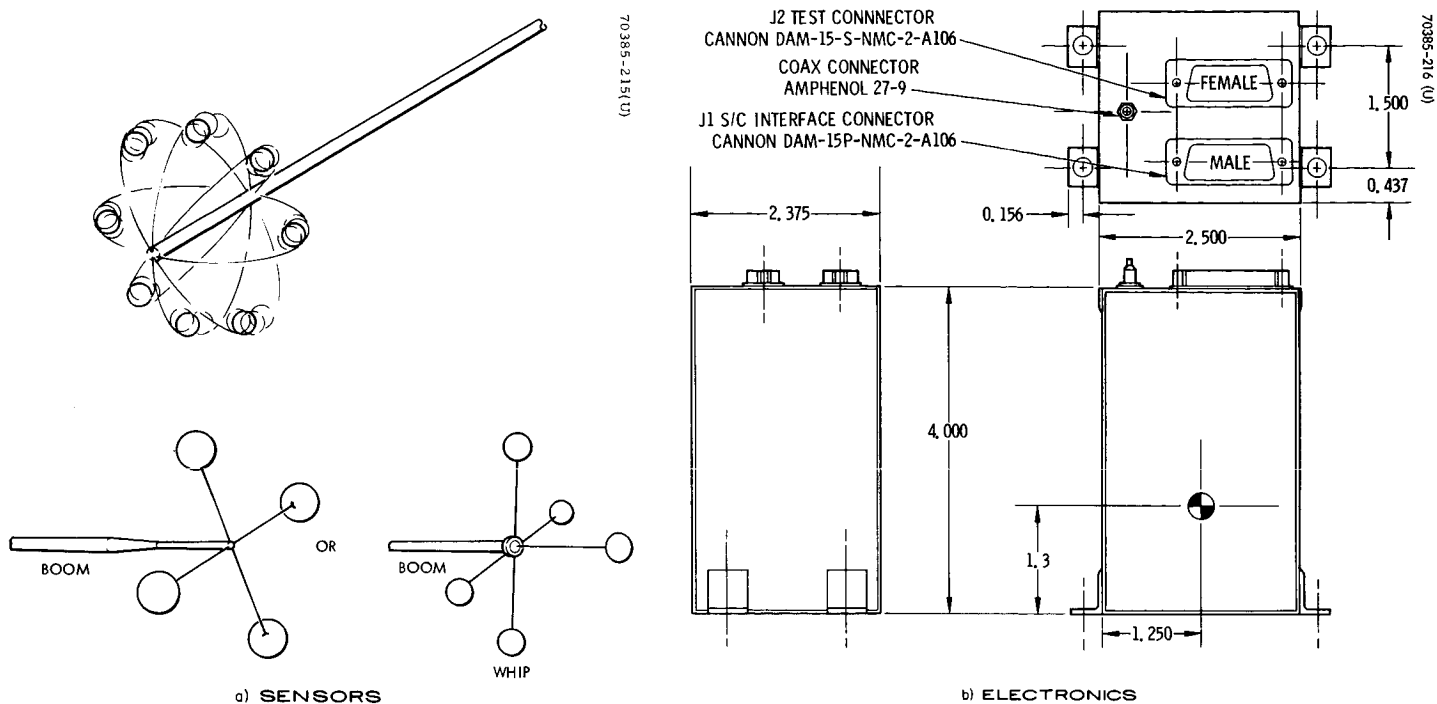


Figure 2-10. Electric Field Meter

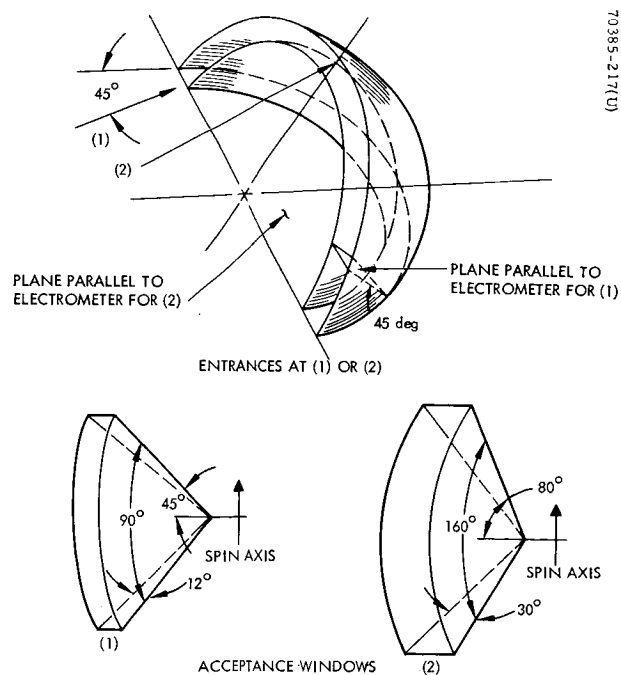


Figure 2-11. Schematic of Solar Plasma and Low Energy Electron Probe Acceptance Windows

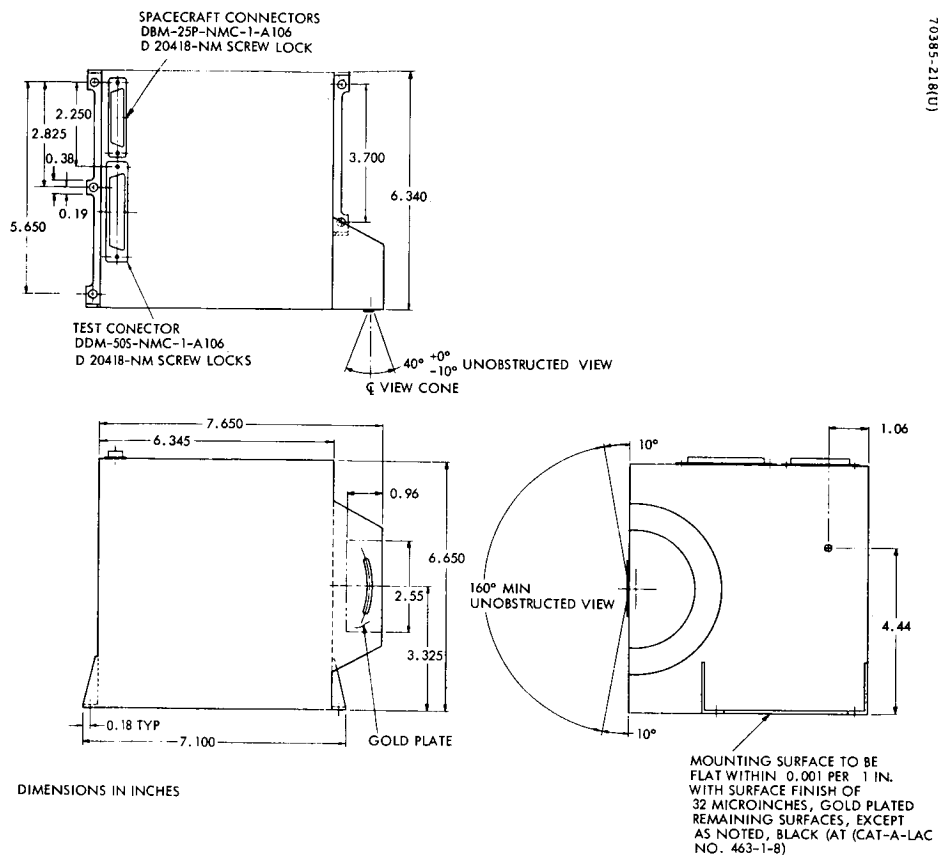


Figure 2-12. Plasma Probe

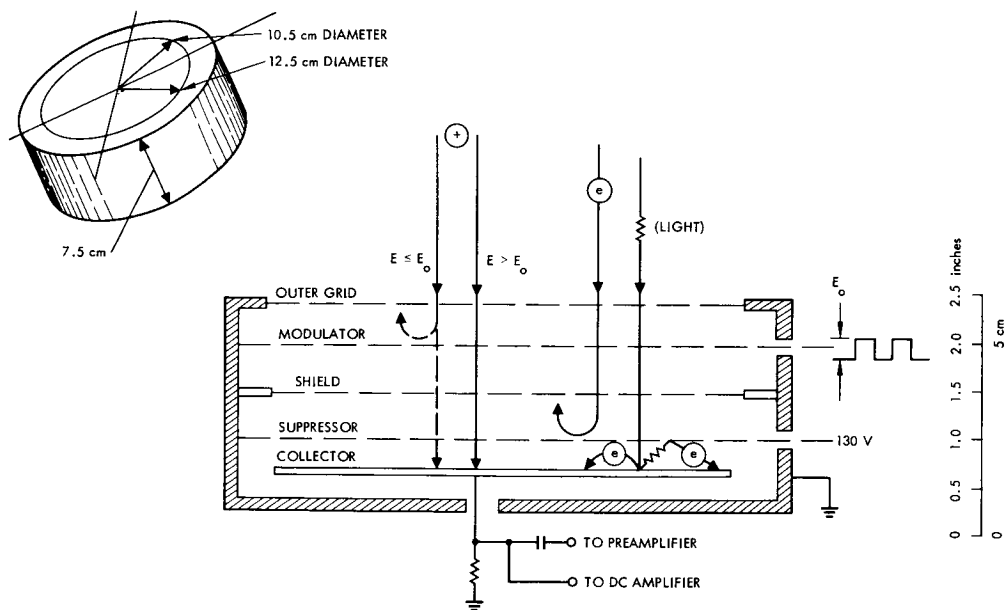


Figure 2-13. Schematic of Faraday Cup

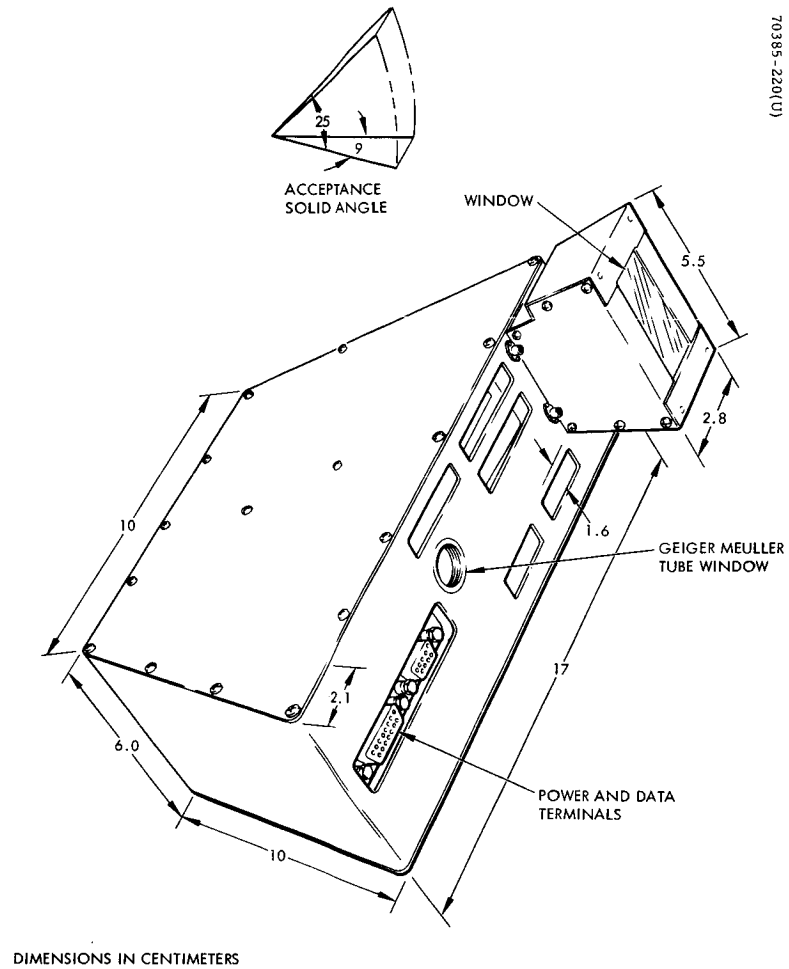


Figure 2-14. Single Direction LEPEDA

TABLE 2-4. OEC INSTRUMENTS

Instrument	Power, watts			Range	Operating Temperature	Input Data		Output Data	Size	Orientation	Experiment Data
	Weight	Ave	Peak			Voltage	Frequency and Waveform				
Flux gate (three component sensor) electronics	0.9 4.7	4.0	7.8	$\pm 100\gamma$	-30° to +80°C -60° to +100°C	28	2400	Digital	See Figure 2-9	Orthogonal — aligned with body axes	Magnetic fields
Search coil (sensor) electronics	1.5 3.5	1.5	2	$\pm 100\gamma$	-30° to +80°C -60° to +100°C	28		Digital	4.1 liters See Figure 2-10	Body axes	
UCLA antenna electronics	1.0			100 $\mu\text{v m}^{-1}$ to 1 $\text{v m}^{-1}$ (80 db)	-60° to +100°C	28				Body axes	Electric fields
Existing antenna (whip) electronics	0.75	0.5		1/f response	-60° to +100°C	28					
Ames curved plate analyzer (Pioneer VI)	6.3	3.5		10-14 to 10 <sup>-9</sup> amp 3 x 10 <sup>5</sup> to 10 <sup>10</sup> ions cm <sup>-2</sup> sec <sup>-1</sup>		28		Digital	See Figure 2-12	Acceptance fan 20° x 160° in plane of spin axis	Solar plasma
Faraday cup (Explorer 18)	4.0	0.5		5 to 3000 ev	-20° to +65°C	28		Digital	See Figure 2-13	Acceptance cone 1 to spin axis	
Ames curved plate analyzer (if combined with solar wind, unit weight and power increased)	8.0	4.0		10-14 to 10 <sup>-9</sup> amp		28		Digital	See Figure 2-12	Acceptance fan 20° x 160° in plane of spin axis	
LEPEDEA (OGO-3)	6.3	2.5		100 ev to 50 kev (electrons) 1 kev to 500 kev (protons)		28		Digital	See Figure 2-14	Acceptance fan 1 to spin axis	Soft electron and protons
Faraday cup (Mariner IV)	2.7	2.6		30 ev to 10 kev	-20° to +65°C	28		Digital	See Figure 2-13	Acceptance cone 1 to spin axis	
Solid state telescope (two required)	5.0	0.8								One 1 to spin axis One 2 to spin axis	
Pulse height analyzer	0.4	2.0							4 x 18 x 25cm		
GM tube array	3.5	2.0								1 to spin axis	Cosmic rays
Neher chamber	2.5	0.2							7.5 cm sphere	Omni	
Coulumb scattering (anton tubes) IMP I	1.5	0.5								Acceptance cone 1 to spin axis	
GM tube array	3.5	2.0		Solar flare spectrum						1 to spin axis	Solar flares
Impact plate				mv > 10 <sup>-5</sup> gm sec	-70° to +125°C	28	2400	Digital		In plane of spin axis	Dust particles
Mariner IV experiment	6	7									Atmosphere

### 2.1.5.2 Interfacing Constraints

Interface requirements fall into two categories: 1) the interface of the scientific instruments with the spacecraft and each other and 2) the interfacing with the environment of the Voyager bus — the latter concerned with the performance and survival of the capsule in the Voyager environment. The more important interface concerns the following:

- Instrument interchangeability
- Adequate acceptance window allowance
- Unobstructed view for instruments



TABLE 2-5. ESTIMATED PAYLOAD WEIGHTS

Instrument	Weight, pounds	Power, watts	
		Average	Payload
Group I			
• ARC flux gate	5.6	4.0	7.8
• Solar plasma and soft electrons	8.0	4.0	
• Electric field meter	3.0	3.0	
	<u>16.6</u>	<u>11.0</u>	<u>7.8</u>
Group II			
• ARC flux gate	5.6	4.0	7.8
• Solar plasma	6.3	3.5	
• Soft electrons	6.3	2.5	
	<u>18.2</u>	<u>10.0</u>	<u>7.8</u>
Group III			
• ARC flux gate	5.6	4.0	7.8
• Search coils	5.0	4.0	
• Solar plasma plus soft electrons	8.0	4.0	
• Electric field meter (simple-whip antenna)	0.75	0.5	
	<u>19.35</u>	<u>12.5</u>	<u>7.8</u>

- Minimizing the magnetic field of the spacecraft
- Minimizing the electrical field of the spacecraft

To meet the requirement of complete instrument interchangeability, a standard power interface must be established. That is, the power conversion from the raw power of the spacecraft, which typically may be at 28 volts dc, will be in the scientific instrument. Power conversion from this fixed level to that required

by a particular instrument is conducted internally as part of the instrument electronics.

The instruments and electronics are to be located within the spacecraft in several bays. These are schematically illustrated in Figure 2-15.

The charged particle detectors are located in the bays at 90 degrees to the line of the boom(s) so that the acceptance angle will not be interfered with by the boom(s) or any other part of the spacecraft. The electronics associated with the boom(s) experiments can be located in bays adjacent to the experiment bays. The magnetometer and electric field meters are to be located on the boom(s) to minimize the influence of the spacecraft fields on the output of the sensors.

Orientation of the various sensors must also be considered. Since the spacecraft is spinning, it is desirable to position the acceptance angle of the charged particle detectors such that the widest angle is in a plane parallel to the spin axis so that sectional samples may be taken during each revolution. The exact section would be known relative to the sun position and could be correlated with the planetary position. (A schematic of the sensor acceptance angle orientation is shown in Figures 2-11 and 2-14.) The resultant orientation of the instrument will have a direct effect on the residual magnetic field in the orientation of the maximum magnetic moment vector.

The windows must be located such that the potential effects of the vehicle on the low energy plasma are minimized. If Faraday cup detectors are used, the windows would have to be larger to accommodate the increased entrance area.

Interface of the electric field meter is primarily in articulating the "dumbbells" into proper orientation during deployment of the magnetometer booms. One is parallel to the spin axis and the other is perpendicular to the spin axis.

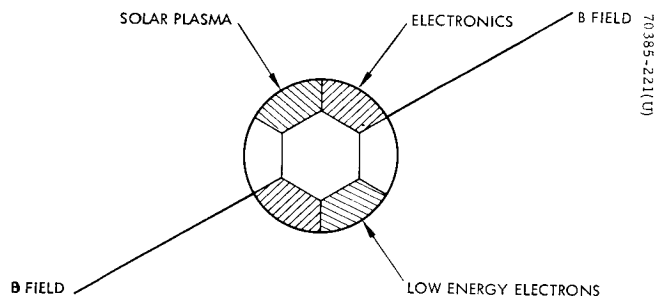


Figure 2-15. Location of Equipment Bays

## 2.2 ORBIT ANALYSIS

### 2.2.1 General

The general requirements for the Voyager mission design specify a large class of possible orbit inclinations as well as orbit characteristics in which the Voyager must operate. Since the Voyager spacecraft serves as a reference platform for the OEC, the variety of altitudes and inclinations must be studied to determine the influence of these orbit parameters on the OEC mission design.

There are two classes of OEC missions that can be described. Each of these in some way reflect into the system design of the capsule and its flexibility.

1) If the Voyager orbits are satisfactory, and the experiment requirements can be met, it is conceivable to envision the OEC as a simple spin stabilized satellite of Mars, maintaining relative ranges with Voyager compatible with a direct continuous short range communication link (i. e. , no planetary occultation of the communication link) and having no control capability other than that designed into the mission to provide initial spinup. This OEC configuration is relatively simple and is suitable for the mission, however, it is directly dependent on Voyager maintaining the same orbit over the 6 months lifetime of OEC. If a direct Earth communication link were included in this OEC design, low data rates could be established independent of Voyager; however, initial orientation becomes very important to ensure an Earth acquisition.

2) If either the proposed Voyager orbits are unsatisfactory or increased flexibility is desired in the design of this mission, then provisions must be made for including an attitude control and orbit change capability. This leads to a more sophisticated satellite design in that independence from the Voyager bus requires a more flexible communication system. Nominally, it is proposed to continue to transmit both experimental and engineering data to Voyager, and through Voyager telemetry to Earth. However, complete autonomy from Voyager can be obtained only by inclusion of a direct OEC/Earth communication link.

The two widely differing preliminary conceptual designs for the OEC noted above were previously introduced as the co-orbital and orbit change systems. The major departure between the alternative OEC concepts is seen to involve the degree of flexibility afforded the satellite to divorce itself from the Voyager mission requirements. For the simplest co-orbital system, i. e. , where the satellite is devoid of propulsive capability and the relative OEC/Voyager distance is constrained to a small value, the OEC mission effectiveness is tied intimately to the Voyager mission requirements. On the other hand, the orbit change concept, which attributes to the satellite the ability to perform gross orbital maneuvers, allows for a degree of independence in optimizing the

on-orbit performance of the satellite. . Although the co-orbital system is simpler, less expensive, and more reliable than the orbit change system, the latter is a considerably more flexible and versatile concept.

The analyses contained in this section cover the scope of such related topics as:

- Description of the orbit characteristics
- Relative relationship between orbits and the Martian magnetosphere
- Effects of orbit decay due to a Martian atmosphere
- Differential drag decay between Voyager and OEC
- Influence of solar gravitational perturbations
- Duration of eclipses of OEC by Mars
- Geometry for occultation of Voyager and OEC
- Field of view requirements for the Voyager - OEC antenna link
- Launch window geometry

### 2.2.2 Orbit Characteristics

The Voyager mission constraints outlined in Section 2.1 indicate that the range of periapsis altitudes and apoapsis altitudes are, respectively,

$$500 \text{ km} \leq h_p \leq 1500 \text{ km}$$

$$10,000 \text{ km} \leq h_a \leq 20,000 \text{ km}$$

The orbital periods of the elliptic orbits are determined from the following equation

$$P = \frac{2\pi}{\sqrt{\mu}} a^{3/2} \quad (2-2)$$

where

$\mu$  = gravitational constant of Mars

$$= 0.428 \times 10^5 \text{ km}^3/\text{sec}^2$$

$a$  = semi-major axis of the orbit, km

and

$$a = \frac{r_p}{(1 - e)} \quad (2-3)$$

where

$r_p$  = radial distance from Mars center to periapsis

$= R_m + h_p$  ( $R_m = 3393$  km)

$e$  = orbit eccentricity

The eccentricity is defined by

$$e = \frac{r_p V_p^2}{\mu} - 1 \quad (2-4)$$

where  $V_p$  = orbital velocity at periapsis.

These equations are evaluated (Reference 3) and the characteristics of the Voyager orbits are established. Figure 2-16 illustrates the period of the orbits as a function of the altitude limitations. For the altitudes given, the possible period varies from 7 to 14 hours. The time along the orbit as referenced to the periapsis is shown as a function of the true anomaly in Figure 2-17. This information is necessary to describe the launch window.

Several additional parameters of importance are represented as a function of position of the OEC in the orbit. These are the velocity, radius vector, angular rate of change of true anomaly, and flight path angle (described from the local horizontal) and are illustrated in Figures 2-17 and 2-18.

The above results are dependent on the general relationship of the various orbits about the planet Mars. In addition, the influence of the planetary oblateness must be accounted for. The net effect is a secular variation which creates a regression of the equatorial node as well as causing the argument of periapsis to either advance or regress, dependent on the orbit inclination. Apsidal rotation is a motion of the line of apsides about the orbit normal.

A derivation of both the nodal and apsidal rotations ( $\dot{\Omega}$  and  $\dot{\omega}$ ) is presented in several texts (Reference 4); a particularly useful form is as follows:

$$\dot{\Omega} = -3\pi J_2 \left[ \frac{R_m}{a(1 - e^2)} \right]^2 \cos i \quad \text{radians per revolution} \quad (2-5)$$

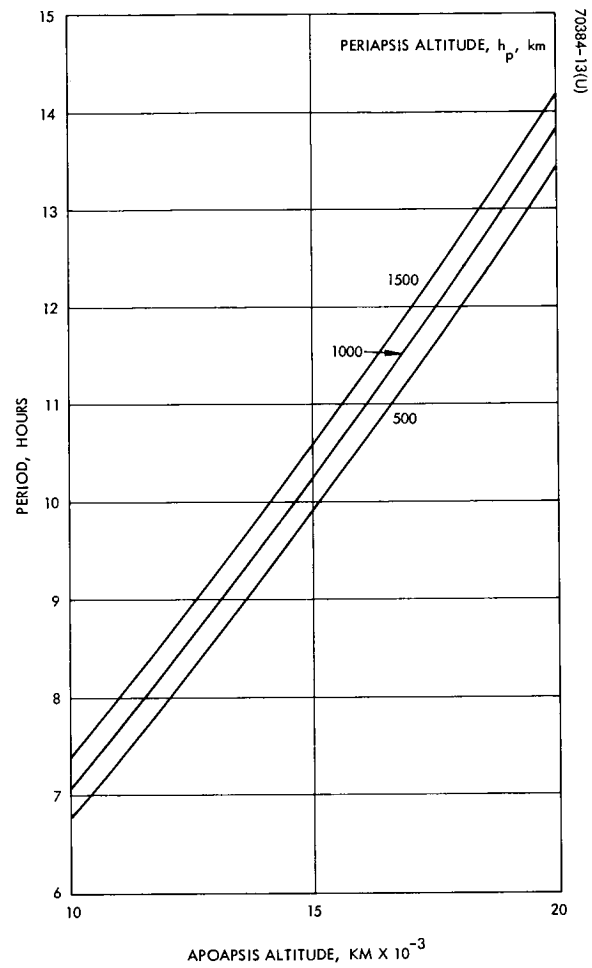


Figure 2-16. Period Versus Apoapsis Altitude

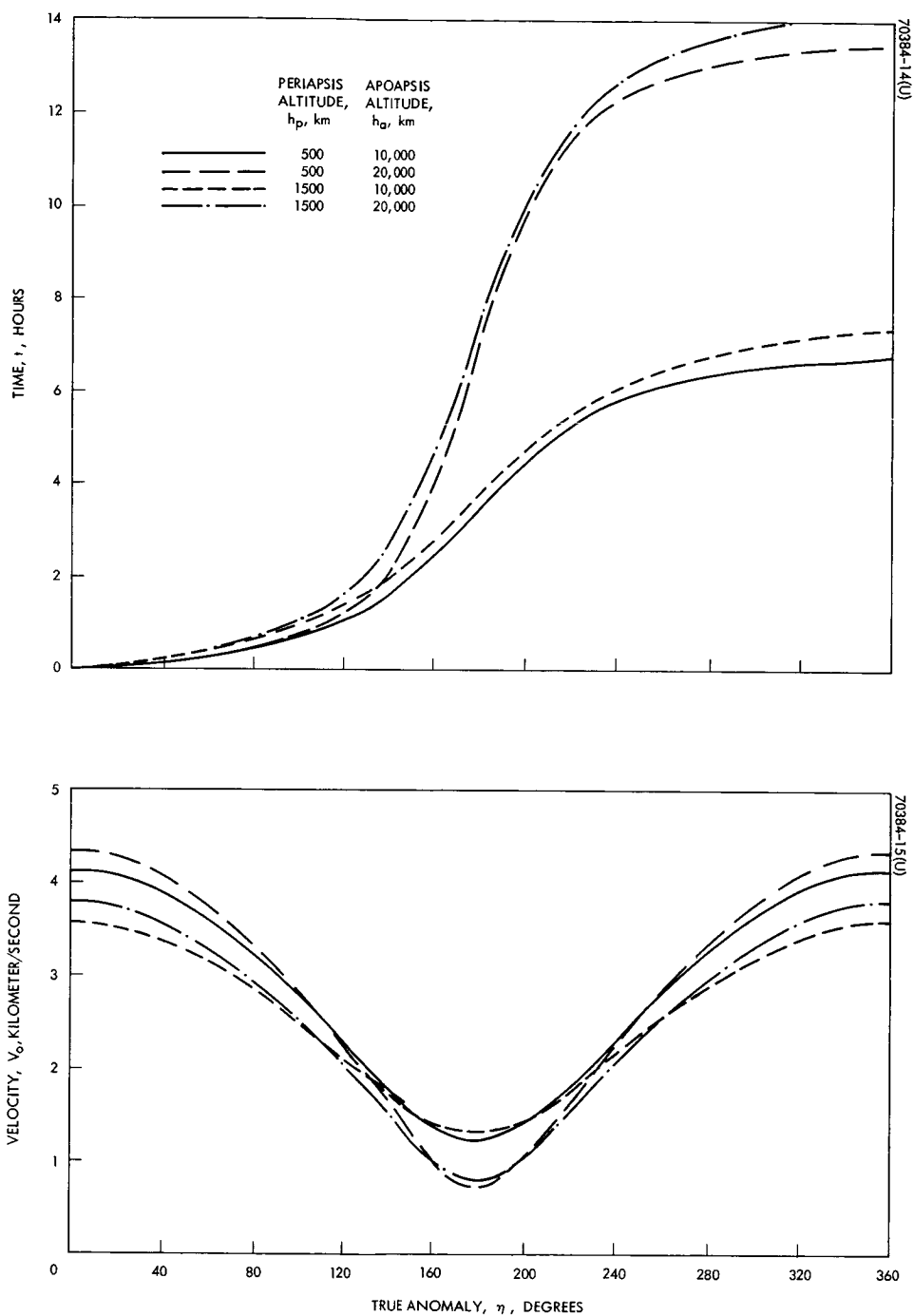


Figure 2-17. Time and Velocity Versus True Anomaly

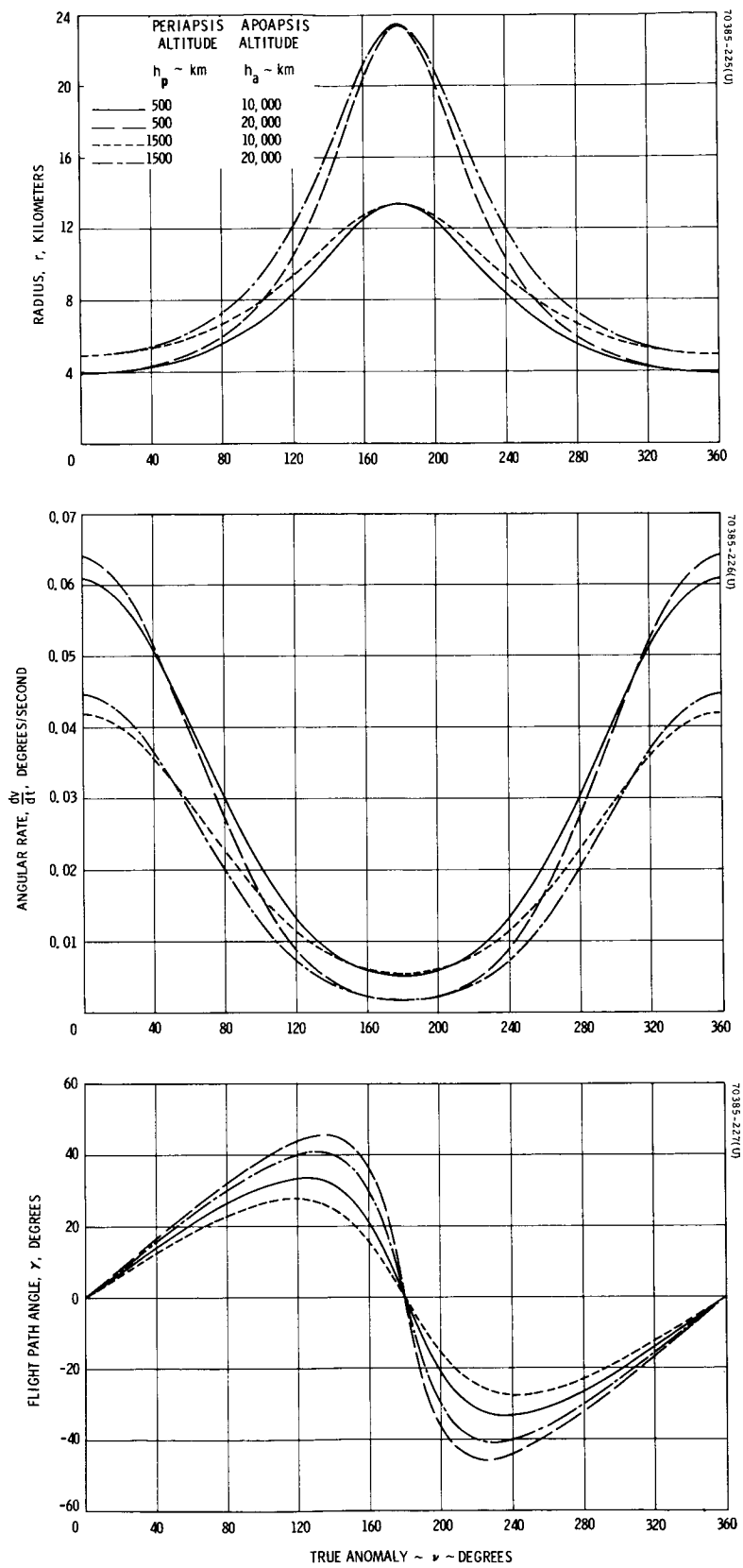


Figure 2-18. Radius, Angular Rate, and Flight Path Angle Versus True Anomaly



$$\dot{\omega} = 3\pi J_2 \left[ \frac{R_m}{a(1-e^2)} \right]^2 (2 - 5/2 \sin^2 i) \quad \text{radians per revolution} \quad (2-6)$$

where  $R_m$  is the radius of Mars, and  $J_2$  is the coefficient of the second spherical gravitational harmonic. Reference 5 states that  $J_2 \cong 1.95 \times 10^{-3} \pm 5 \times 10^{-5}$  for Mars.

Equations 2-5 and 2-6 show that these rotations are relatively strong functions of the semi-major axis (a), eccentricity (e), and orbital inclination with respect to the equator (i). Hence, the effect of the oblate gravitational field on the extent of the mapping of the magnetosphere will depend on the final OEC orbit. This will be treated in the following subsection. Figures 2-19 and 2-20 show the magnitude of these rotations for various orbits of interest. Note that  $|\dot{\Omega}|$  and  $|\dot{\omega}|$  increase as the apoapsis altitude decreases and that  $\dot{\omega}$  changes sign at an inclination of 63.4 degrees.

### 2.2.3 Orbit Relationships to Magnetosphere

The four dimensional characteristics of the Martian magnetosphere imply the desirability of taking measurements over a range of altitudes, latitudes, and inertial longitudes, as well as time. In this discussion, the variation of these quantities over the mission will be described and the implication of these variations on the extent of the mapping discussed.

The relative motion of the OEC orbit and the Martian magnetosphere over the 6-month mission is of sufficient importance to clarify the expected geometrical relationships. Figure 2-21 is a schematic representation of a typical OEC orbit (for either the co-orbital or orbit change system) and its geometrical relationship to the Sun and the magnetosphere. The longitude of periapsis relative to the Sun at epoch is shown as  $\lambda_0$ . Assuming for the moment that the orbit plane is fixed in inertial space, the magnetosphere will rotate (relative to the orbit plane) at the angular rate of Mars around the Sun ( $\lambda_m = 0.53$  deg/day). Over the 6 month mission, this effect will allow the OEC to sample the Mars environment at various longitudes in the magnetosphere and at various altitudes. In particular, periapsis will rotate relative to the magnetosphere a total of 97 degrees.

In fact, the relative rotation will be greater than 97 degrees because of the precession effects mentioned in Section 2.2.2. As indicated, the affect of the oblateness will torque the orbit in such a manner that the mapping will be

---

\* Since  $J_2$  for the Earth is  $1.08 \times 10^{-3}$ , this indicates that Mars is considerably more oblate than the Earth.

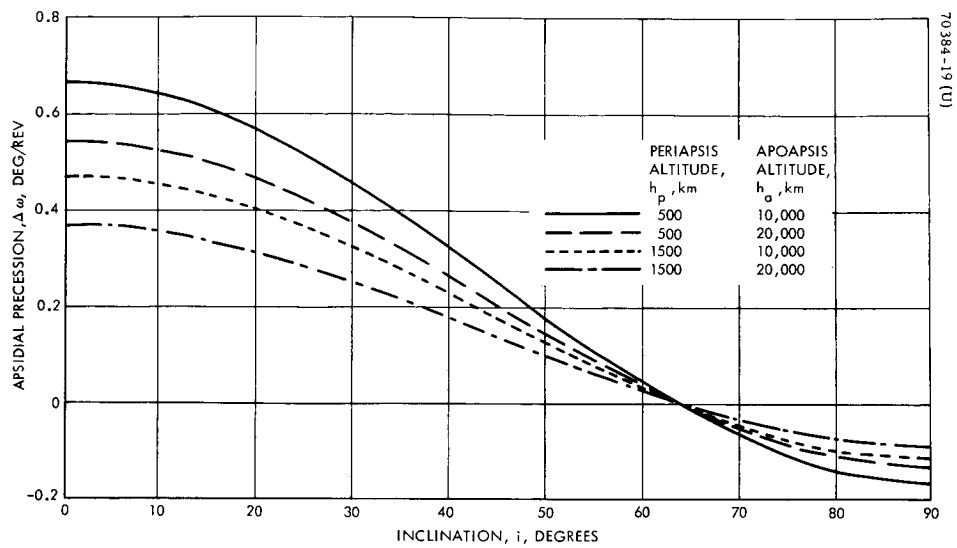


Figure 2-19. Apsidal Precession Versus Inclination

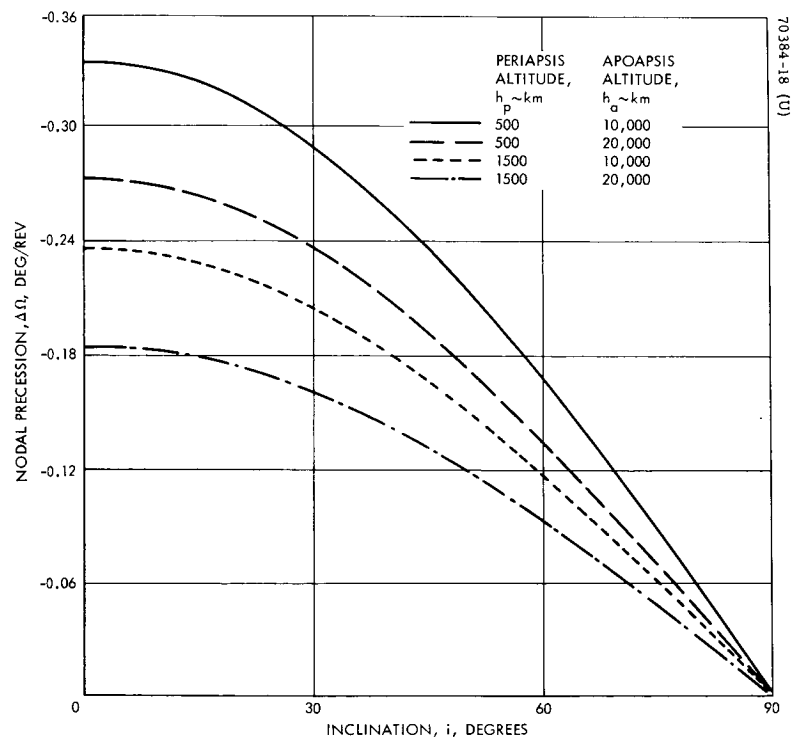


Figure 2-20. Nodal Precession Versus Inclination

more extensive than implied above. To clarify these effects, the results presented in Figures 2-19 and 2-20 are interpreted illustratively.

Figure 2-22 illustrates in two views the effect of the rotation of the apse line for  $i < 64$  degrees. A typical set of conditions is shown with the equatorial plane of Mars inclined  $\sim 25$  degrees to the ecliptic. An assumed magnetospheric boundary is shown and the orbit exaggerated to illustrate the motion. The apsidal rotation vector  $\bar{\omega}$  is illustrated normal to the orbit plane. Motion of the periapsis altitude from point A  $\rightarrow$  D is seen in the side view and in the plane of the orbit. The top view provides a more pictorial illustration. Note that the rotation of the apse line is in the same direction as the  $1/2$  deg/day motion of Mars about the Sun so that when viewing the motion of the magnetosphere rotation, it can readily be seen that periapsis moves in the same direction.

The effect of nodal regression on the orbits is shown in Figure 2-23. The orbit regresses westerly at a rate that is characterized by the specific orbital elements. Both the side and top views illustrate the direction that periapsis moves (from A  $\rightarrow$  D). Regression is symmetrical about the Mars spin axis, but takes on various orientations with respect to the ecliptic normal and hence the magnetosphere.

Figure 2-24 shows a combination of the two effects and indicates the difficulty of establishing an optimum mapping criteria.

In order to display some representative numerical results, assume that periapsis is located at the minimum latitude relative to the Martian equator. Figure 2-25 shows a schematic mercator projection of a typical OEC orbit and the relative motion induced by the oblate gravitational field. Using Figure 2-25 it is relatively easy to demonstrate that the relative longitude ( $\lambda$ ) between periapsis and the Sun is determined from the geometry and given by the expression.\*

$$\lambda \cong \lambda_0 + \left( \dot{\lambda}_m + \frac{24}{P} |\dot{\Omega}| \right) K + \tan^{-1} \left( \operatorname{ctn} \left( \frac{24}{P} \dot{\omega} K \right) \cos i \right) - \pi/2 \quad (2-7)$$

while the periapsis latitude is

$$\Phi = -\sin^{-1} \left( \cos \left( \frac{24}{P} \dot{\omega} K \right) \sin i \right) \quad (2-8)$$

---

\* In Equation 2-6, it has been assumed that the Sun moves at a constant rate in the Martian equator.

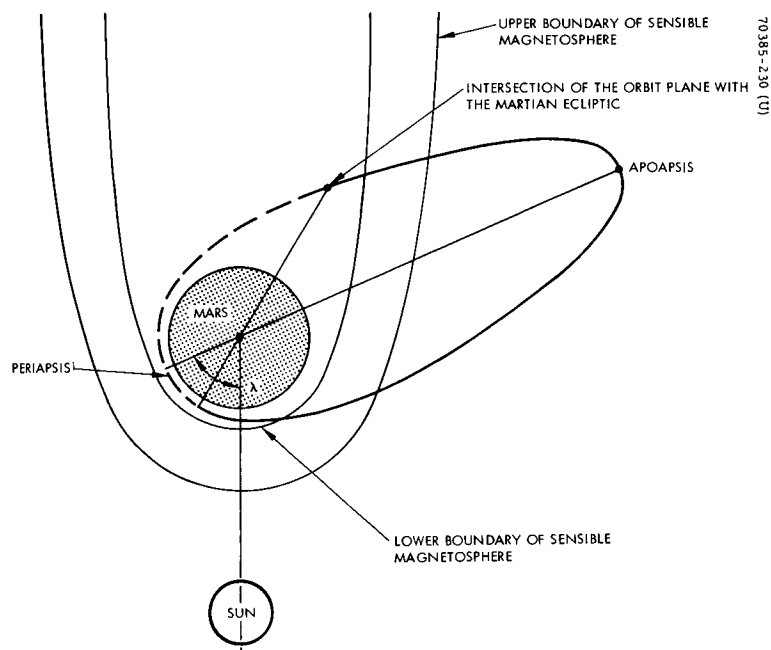


Figure 2-21. Orbit Geometry Relative to Magnetosphere

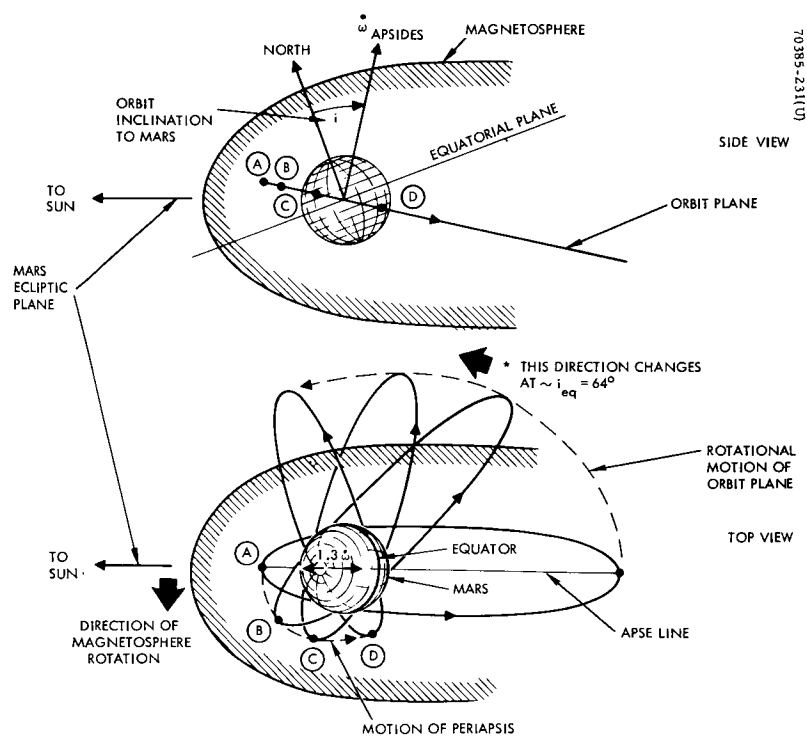


Figure 2-22. Effect of Rotation of Apse Line

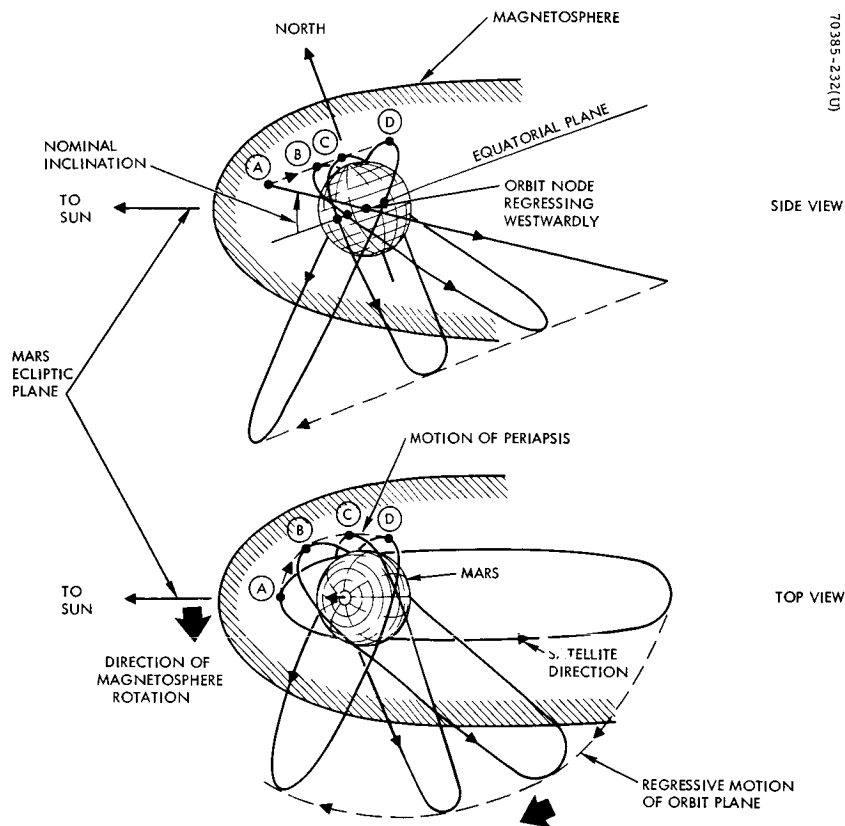


Figure 2-23. Effect of Orbit Regression on Elliptical Orbit

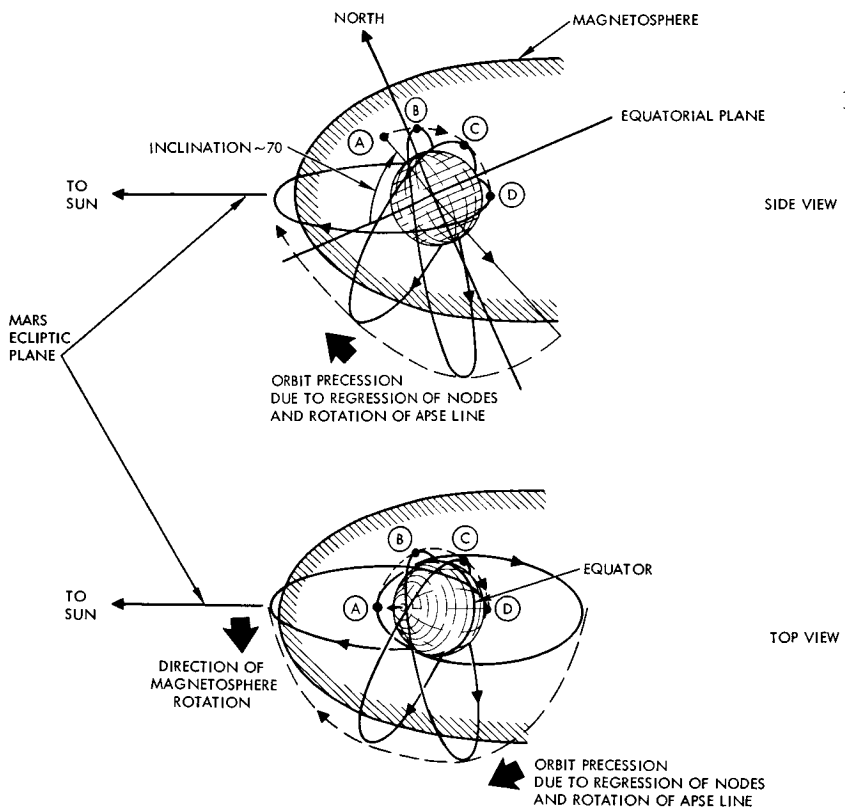


Figure 2-24. Typical Expected Motion of Elliptic Orbit at High Inclination to Equator

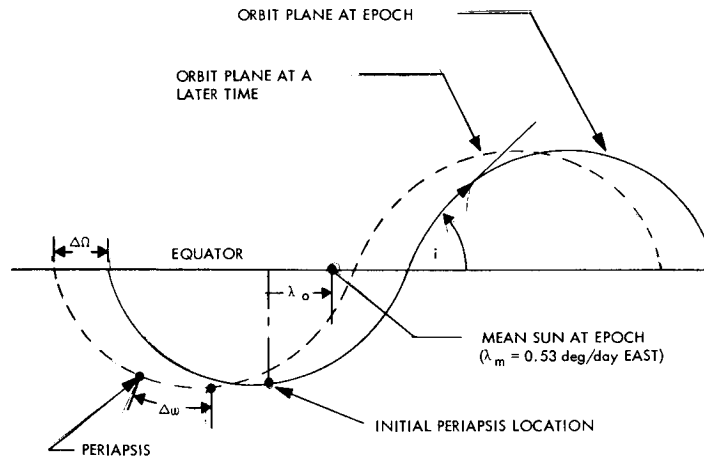


Figure 2-25. Motion of Orbit Plane Due to Oblate Gravitational Field

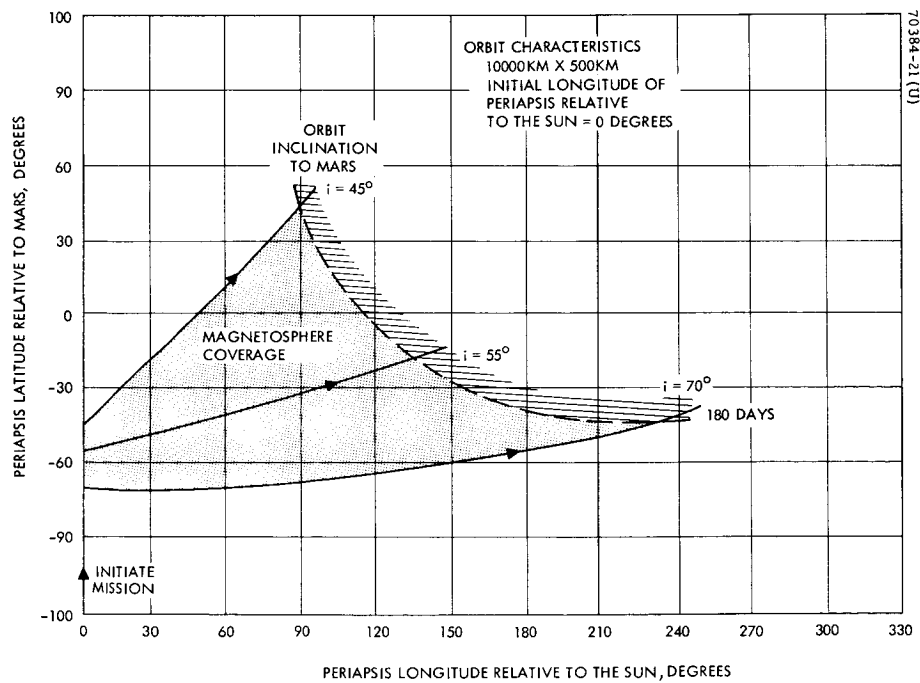


Figure 2-26. Typical OEC Orbit-Magnetosphere Relationship

where

$i$  = orbital inclination to Martian equator

$\dot{\Omega}$  = nodal regression rate, rad/rev

$\dot{\omega}$  = apsidal rotation rate, rad/rev

$K$  = days from epoch

$\lambda$  = longitude of periapsis relative to the Sun, radians

$\phi$  = latitude of periapsis, radians

$P$  = orbital period, hours

Figure 2-26 shows a plot of  $\lambda$  versus  $\phi$  for orbits with the following characteristics:  $h_a = 10,000$  km,  $h_p = 500$  km,  $\lambda_0 = 0$ , and  $i = 45$  degrees, 55 degrees, and 70 degrees. The results indicate that for  $i = 70$  degrees, i. e., the highest orbital inclination consistent with the Voyager mission, periapsis will rotate through an angle of approximately 230 degrees relative to the magnetosphere over the 6 month mission. The latitude variation is  $\approx 28$  degrees. This will allow a relatively large sampling of the magnetic field at the periapsis altitude. These results are illustrated in Figure 2-27. This view indicates how for this typical case, the apoapse might initially protrude above the magnetosphere. As the orbit changes and Mars moves, this reference point rotates through some 200 degrees and never enters the shock region. Periapse always remains at low Mars latitudes. This example does not represent a necessarily desirable feature but in fact points out the kind of phenomena expected and the complexity of arriving at some optimum orbit.

Figure 2-26 also shows the expected types of coverage at the lower inclined orbits. For example, at  $i = 45$  degrees, the longitude variation is not nearly so pronounced, while the latitude variation is somewhat larger. In particular, the total changes in  $\lambda$  and  $\phi$  are 92 and 87 degrees, respectively. The trend of these variations stems mainly from the change in sign of  $\dot{\omega}$  at  $i = 63.4$  degrees.

The results shown in Figure 2-26 are insensitive to changes in periapsis altitude within the assumed altitude regime but will vary considerably with large changes in the apoapsis altitude. Specifically, as the apoapsis altitude increases, the longitude and latitude regions covered will decrease.

Several interpretations of the results can be established. If the magnetosphere is assumed to be symmetrical, then 180 degree variations between the periapsis altitude and the magnetosphere is adequate. Hence, inclinations of greater than 65 degrees to the equator are desirable, for a mission duration of 6 months. For longer durations, the same longitudinal range is obtained at lower inclinations and at increasing latitudes. For the largest expected Voyager inclination of 70 degrees, substantially greater variations in longitude can be achieved at the cost of decreased latitudinal variations.

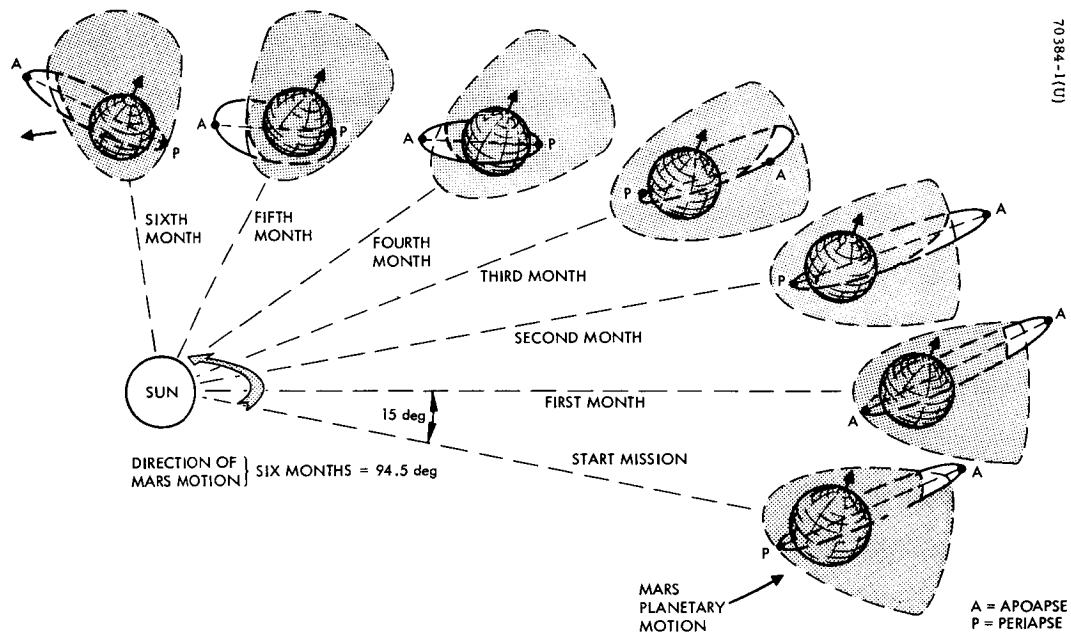


Figure 2-27. Orbit-Magnetosphere Motion



Selection of the proper orbit to optimize the mission objective of mapping the magnetosphere deserves careful consideration. Due to the current general ground rules for the Voyager orbits, it is a very cumbersome task to completely identify these characteristics. The results of this study indicate that, without question, there will be extensive mapping accomplished.

A more complete study is required, but only after the Voyager nominal injection date, node, and other pertinent characteristics have been better defined. At that time, a detailed study could indicate the most desirable orbit inclination to ensure the most complete description of the Martian magnetosphere.

#### 2.2.4 Orbital Lifetime

A definitive study of the OEC mission lifetime has produced several important results. The rationale for this analysis was to determine if the capsule could meet the Voyager mission requirement (Reference 6) of 50 years minimum lifetime. (During the study phase, the requirement was reduced to 10 years.) This subsection discusses these results and presents several conclusions.

The primary perturbation contributing to a finite life for the spacecraft derives from the interaction of the satellite with the atmosphere of Mars. Although the Martian atmosphere is only 1/500 of the mass of the Earth's atmosphere, satellite orbits with extremely low periapsis altitudes will experience appreciable decay over a 50 year period.

Ten atmospheric models are presented in the Voyager Design Specification (Reference 1). In addition, a recent model by D. F. Spencer (Reference 7) was included in a study of the perturbative influence on the orbit. Table 2-6 displays the values of surface density and scale height associated with each atmosphere. This is of particular significance, since a large scale height implies a low density gradient with respect to altitude, and hence a dense atmosphere at high altitudes. This in turn contributes to atmospheric degradation of the orbit at high altitudes and a corresponding decrease in lifetime.

The atmospheric density altitude profile is assumed to be static and exponential in form,\* i. e. ,

$$\rho = \rho_0 e^{-\frac{h}{H}} \quad (2-9)$$

where

$\rho_0$  = surface density

H = scale height

From Reference 8, the lifetime of a satellite interacting with an exponential atmosphere is

---

\*A static atmosphere is defined as one which is invariant with time.

TABLE 2-6. MARTIAN ATMOSPHERIC MODELS

Atmosphere Model	Surface Pressure, millibars	Surface Density, gm/cm <sup>3</sup> × 10 <sup>-5</sup>	Scale Height, km
VM-1	7.0	0.96	14.2
VM-2	7.0	1.85	5.5
VM-3	10.0	1.37	14.3
VM-4	10.0	2.57	5.2
VM-5	14.0	1.91	14.2
VM-6	14.0	3.08	6.1
VM-7	5.0	0.68	14.2
VM-8	5.0	1.32	5.5
VM-9	20.0	2.73	14.2
VM-10	20.0	3.83	6.9
Spencer	6.0	3.00	10.0

Estimates made of the Mars atmosphere from Mariner IV data indicated that

$$\rho_o = 1.5 \times 10^{-5} \text{ gm/cm}^3 \text{ and } H = 9 \text{ km}$$

$$T = \frac{\left(\frac{m}{C_D A}\right) \sqrt{\frac{2\pi}{\mu H}}}{\rho_{P_o}} r_{P_o} \left\{ \frac{e_o^{3/2}}{\sqrt{1-e_o^2}} - \sqrt{\frac{2}{2}} \left[ F(\cos^{-1} e_o, \sqrt{2/2}) - F(\pi/2, \sqrt{2/2}) + 2E(\pi/2, \sqrt{2/2}) - 2E(\cos^{-1} e_o, \sqrt{2/2}) \right] \right\} \times 0.317 \times 10^{-7} \text{ years} \quad (2-10)$$

where

M = OEC mass, 32.12 kg (minimum weight vehicle)

A = 6.0 square meters

$C_D$  = drag coefficient assumed = 2.0

$\mu$  = gravitational constant for Mars

$e_o$  = initial orbital eccentricity

F, E = elliptic integrals of first and second kind

$$\rho_{P_o} = \rho_o \exp \left( \frac{-h_{P_o}}{H} \right), \quad h_{P_o} = \text{periapsis altitude}$$

$$r_{P_o} = h_{P_o} + R_M, \quad (R_M = \text{radius of Mars})$$

In order to determine the variance in the OEC orbital lifetime due to the uncertainty in the knowledge of the Martian atmosphere, lifetimes were determined for all 11 models for a typical orbit and subsequently compared. Figure 2-28 shows the uncertainty regime existing in the lifetime estimate as a function of periapsis altitude for an apoapsis altitude of 20,000 km. The results indicate a large dispersion in the lifetime estimate. In particular, to satisfy the 50-year Voyager mission constraint, the uncertainty in the allowable periapsis altitude is approximately 175 km. The sparsest Martian atmosphere (VM-4) dictates a minimum altitude of 95 km, Spencer's atmosphere requires at least 188 km, while the densest atmosphere (VM-9) requires a periapsis altitude greater than 275 km.

The 50-year OEC orbit lifetime is assumed based on a Voyager mission constraint. A relaxation of this constraint has a negligible effect on the OEC mission design. As shown in Figure 2-28 a 10 percent decrease in periapsis altitude is achievable for an assumed 10-year orbit lifetime. This represents less than a 30 km change in periapsis and is on the order of the orbit determination accuracy.

It is apparent from these results that the OEC could safely descend to about 275 km and suitably meet the lifetime requirements. The possibility of lowering the altitude further is then based on "which is the most realistic atmospheric model." At the present the answer is unavailable; however, more definitive atmospheric information may be available from possible Mariner Mars flyby missions prior to 1972.

Figure 2-29 indicates the minimum periapsis altitude for the range of given atmospheric models as a function of the assumed altitude at apoapse for both a 10 and 50 year lifetime. The fact that the periapsis altitude is not sensitive to the apoapsis altitudes between 10,000 and 20,000 km is apparent. There is a large region of minimum altitude uncertainty, as shown in this figure.

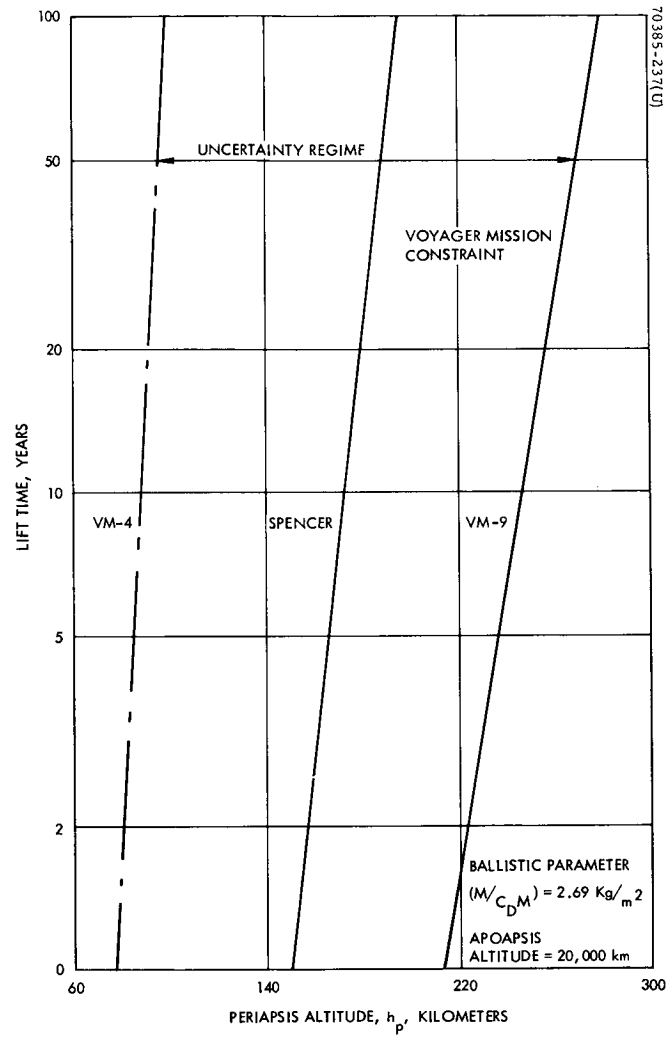


Figure 2-28. OEC Orbit Lifetime

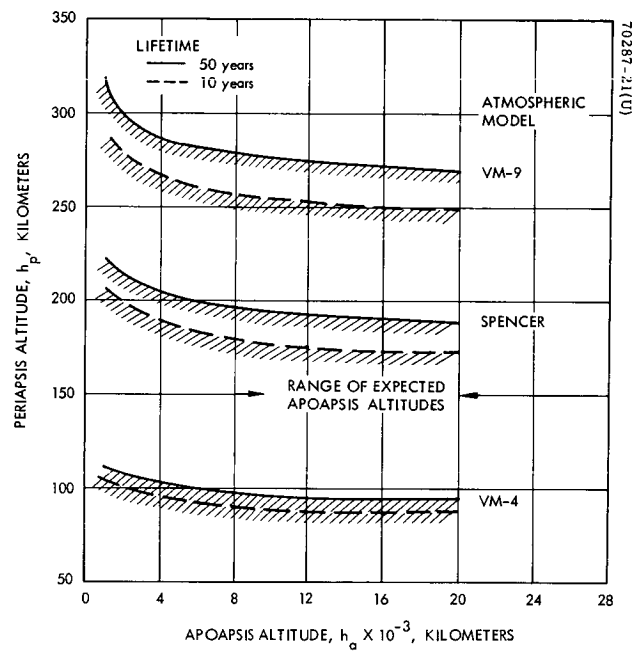


Figure 2-29. Minimum Altitude Limitations

In summary, these results imply that it is reasonable to operate with OEC periapsis altitudes as low as 275 km and to guarantee a 50-year mission lifetime. This is a significant fact if the Martian magnetic field is weak at nominal mission altitudes. As a result of this analysis it appears reasonable to study the possibilities of incorporating orbit change capabilities in the OEC mission.

### 2.2.5 Differential Drag Effects

One of the major areas of concern in the OEC mission is the desire to guarantee that a collision between the OEC and Voyager spacecraft will not take place subsequent to separation. The question of the effect of differential drag on the distance of closest approach of the two vehicles is treated here.

The effect of atmospheric drag on the orbits of the OEC and Voyager spacecraft is to decrease the semi-major axis (or equivalently the energy) and thereby the orbital period (P). Since,

$$P = \frac{2\pi}{\sqrt{\mu}} a^{3/2}$$

where  $\mu$  is the gravitational constant of Mars and  $a$  is the semi-major axis of the orbit, it follows immediately for small perturbations that

$$\delta P = \frac{3}{2} P \frac{\delta a}{a}$$

The change in semi-major axis of a highly elliptic orbit over one complete revolution can be developed from the analysis of Reference 9.

$$\frac{\delta a}{a} = \frac{2\pi}{M/C_D A} \rho_P \sqrt{\frac{a(1-e^2)H}{2\pi e}} \cdot \frac{1+e}{1-e} \quad (2-11)$$

where

$M$  = vehicle mass

$A$  = cross sectional area normal to the velocity vector

$C_D$  = drag coefficient (assumed = 2)

$e$  = orbital eccentricity

$\rho_P$  = atmospheric density at periapsis ( $h_P$ ) =  $\rho_o e^{h_P/H}$

$\rho_o$  = surface density

H = atmospheric scale height

In addition, for small changes in the orbital period, the variation in in-track location ( $\delta S$ ) of the vehicle after a revolution can be accurately approximated by

$$\delta S = V \delta P \quad (2-12)$$

where V is the velocity at epoch. Combining Equations 2-11 and 2-12 yields

$$\delta S = \frac{3\pi}{(M/C_D A)} \cdot P V \rho_P \frac{a(1-e^2)H}{2\pi e} \left( \frac{1+e}{1-e} \right) \quad (2-13)$$

Equation 2-13 shows the effect of atmospheric drag on the in-track location of the satellite in terms of orbital and atmospheric parameters. It is apparent from this equation that  $\delta S$  increases with increasing  $\rho_P$  and hence, to estimate an upper bound on  $\delta S$ , the OEC/Voyager orbit with the lowest periapsis altitude should be considered; i.e., a periapsis altitude of 500 km.

In Section 4.0, 11 Martian atmospheric models are displayed and subsequently compared. It is shown that the most significant atmosphere (VM-9) in terms of orbit degradation is described by the following constants:  $\rho_o = 2.73 \times 10^{-5}$  gm/cm<sup>3</sup> and H = 14.2 km. Assuming, as a representative case, an OEC/Voyager orbit with an apoapsis altitude of 20,000 km, a periapsis altitude of 500 km, i.e., the maximum value of P associated with the range of possible Voyager orbits, taking V equal to the velocity at periapsis, and finally using the values of  $\rho_o$  and H noted in Equation 2-13 gives

$$\delta S(M/C_D A) \cong 72 \times 10^{-3} \text{ kg/m} \quad (2-14)$$

Since  $M/C_D A$  for both the OEC and Voyager is of the order of 15.8 kg/m<sup>2</sup>, it is seen that the in-track displacement from an assumed drag free case is negligibly small. Hence, if the drag free constraints on the mission are adjusted so as to obviate collision, interaction with the Martian atmosphere can be ignored.

#### 2.2.6 Effect of Solar Perturbations

During the operational lifetime of the OEC mission, solar gravitational perturbations act on the capsule. The net effect is a disturbance which tends to change the OEC orbital velocity. In essence the solar perturbation adds and/or subtracts an incremental velocity to the nominal orbit velocity.

The purpose of this discussion is to investigate these effects and in particular relate them to the periapsis altitude. This is an important study since the possibility of planetary contamination must be avoided, and the results of this analysis influence the orbit selection.

A typical orbit with periapsis altitude of 1000 km and apoapsis altitude of 10,000 km is assumed. An attitude orientation is chosen in the worst sense so that the maximum effect of the solar perturbations on the periapsis altitude is found.

Reference 9 shows that the change in periapsis altitude, due to the solar perturbations, per revolution of the satellite is given by

$$\Delta h_p = K_1 \{ \sin 2\gamma \cos 2\hat{\omega} \cos \hat{i} - [\cos^2 \gamma - \sin^2 \gamma \cos^2 \hat{i}] \sin 2\hat{\omega} \} \quad (2-15)$$

where

$$K_1 = \frac{15 \frac{GM_d}{2a_d^3} a \pi e \sqrt{1-e^2}}{n^2} \quad (2-16)$$

$GM_d$  =  $\mu$  of the disturbing body

=  $1.372 \times 10^{11} \text{ km}^3/\text{sec}^2$  for the Sun

$a_d$  = distance of the disturbing body from planet

$\cong 1.5237 \text{ AU}$  for Mars

$a$  = semi-major axis of the OEC orbit

$e$  = eccentricity of the OEC orbit

$n$  = mean angular motion of OEC in its orbit about Mars

$\gamma$  = angle (in the ecliptic) from line of nodes of the OEC orbit to the Mars-Sun line

$\hat{i}$  = inclination of the OEC orbit with respect to Martian ecliptic plane

$\hat{\omega}$  = argument of periapsis with respect to Martian ecliptic plane



Substituting the assumed orbital parameters into Equation 2-16 yields

$$K_1 = \frac{15 (0.566 \times 10^{-14} \text{ sec}^{-2}) (8.91 \times 10^3 \text{ km}) (3.14) (0.505) (0.864)}{6.10 \times 10^{-8} \text{ rad}^2/\text{sec}^2}$$

$$\approx 1.702 \times 10^{-2} \text{ km}$$

Analysis of Equation 2-15 shows that the extreme perturbations correspond to orientations of  $\gamma = 0, 180$  degrees and  $\omega = 45, 135, 225, 315$  degrees. Substitution of these values into Equation 2-15 results in a maximum change in periapsis altitude (per orbit revolution) due to solar perturbations of

$$\Delta h_{P_{\max}} = \pm 1.702 \times 10^{-2} \text{ km/rev}$$

$$= \pm 0.01702 \text{ km/rev}$$

Since the inertial orientation of the orbital plane is constantly changing, the average solar perturbation over the mission will be somewhat less. In any case, the net effect over the 6-month mission lifetime for this typical orbit would be less than 10 km.

The worst case effects of solar perturbations are actually exhibited for missions operating at high apoapsis altitudes along with the lowest periapsis altitudes. The minimum altitude established from the orbit decay studies is approximately 300 km. For a 20,000 km x 300 km orbit, this change in periapsis altitude could be as great as 55 km. By combining this effect with that of atmospheric decay and including some margin, a minimum operating altitude of approximately 350 km (50 year lifetime) is recommended. A somewhat lower altitude is possible for the 10 year lifetime constraint.

### 2.2.7 Solar Eclipse

The eclipse history specified for the Voyager mission at the present time calls for no eclipsing during the first 30 days of operation and no greater than a maximum of 60 minutes per orbit during the succeeding 5 months\* (see Reference 1). Since the OEC may not separate from the Voyager for a period of 30 days, the maximum eclipse duration experienced by either the co-orbital or orbit change systems, over the latter portion of its 6 month operation, might be considerably in excess of this value. The eclipse durations of highly elliptical orbits are a

---

\*Actually, the maximum eclipse after the first 30 days is the minimum of 8 percent of the orbital period and 60 minutes.

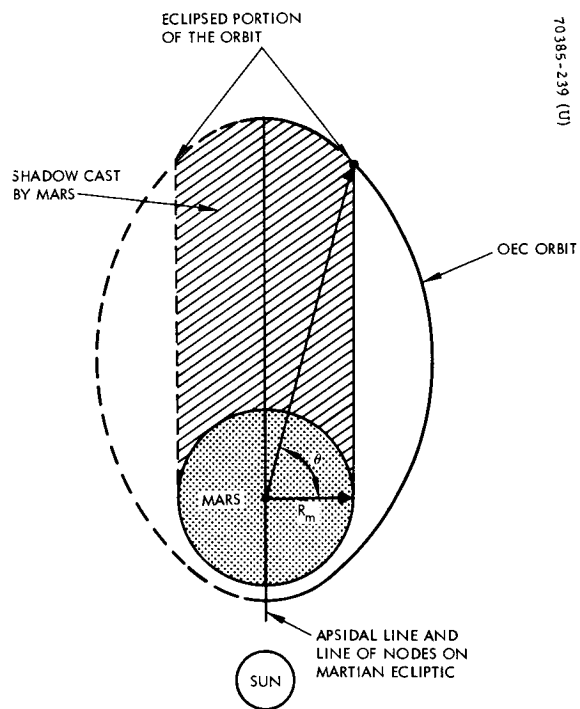


Figure 2-30. Orbital Geometry for Maximum Eclipse Duration

strong function of such quantities as date, argument of periapsis relative to the Martian ecliptic, and orbit node location. Since the Voyager orbit has not been specified to a sufficient degree to guarantee the initial values of these quantities, flexibility demands that the OEC be designed to operate with the thermal and power environment dictated by worst case eclipsing. In addition, it has been ascertained that a preferred initial inertial orientation of the orbit plane exists for sampling the magnetic field, and this orientation will yield the maximum eclipse period per orbit.

The critical orbital orientation is obtained when the apsidal line, the line connecting apoapsis and periapsis, lies in the Martian ecliptic and the Sun lies on the line segment connecting Mars and periapsis. Figure 2-30 displays this worst case geometry. The duration of solar eclipsing,  $T_E$ , for this case is determined from

$$T_E = 2 \left( \frac{P}{2} - t' \right) \quad (2-17)$$

where  $t'$  is the time required by the satellite to travel from periapsis to the point of entry (A) into the shadow. Using Kepler's Equation,  $t'$  can be expressed in terms of the eccentric anomaly  $E$ . In particular,

$$t' = P \left( \frac{E - e \sin E}{2\pi} \right) \quad (2-18)$$

Substitution of Equation 2-17 into 2-18 yields

$$T_E = P \left( 1 - \frac{E - e \sin E}{\pi} \right) \quad (2-19)$$

$E$  is defined in terms of the true anomaly ( $\nu$ ) as

$$E = \cos^{-1} \left( \frac{e + \cos \nu}{1 + e \cos \nu} \right) = \cos^{-1} \left( \frac{e - \sin \theta}{1 - e \sin \theta} \right)$$

and  $\theta$  is as shown on Figure 2-30. At this point, it only remains to determine  $\theta$  in terms of the known orbital parameters in order to completely define the eclipse period. To do so, the radius vector from Mars at point A is introduced:

$$r = \frac{a(1 - e^2)}{1 + e \cos \nu} = \frac{a(1 - e^2)}{1 - e \sin \theta} \quad (2-20)$$

From the figure,

$$R_m = r \cos \theta \quad (2-21)$$

Combining these equations yields

$$R_m = \left( \frac{a(1 - e^2)}{1 - e \sin \theta} \right) \cos \theta$$

or

$$R_m (1 - e \sin \theta) = a(1 - e^2) \cos \theta$$

By regrouping

$$R_m e \sin \theta + a(1 - e^2) \cos \theta = R_m$$

dividing through by

$$\frac{\sqrt{(eR_m)^2 + \left(a(1 - e^2)\right)^2}}{\left(\frac{eR_m}{\sqrt{(eR_m)^2 + \left(a(1 - e^2)\right)^2}}\right) \sin \theta + \left(\frac{a(1 - e^2)}{\sqrt{(eR_m)^2 + \left(a(1 - e^2)\right)^2}}\right) \cos \theta} = \frac{R_m}{\sqrt{(eR_m)^2 + \left(a(1 - e^2)\right)^2}}$$

Recognize that this expression has the form of the trigonometric relationship

$$\sin(\theta + \lambda) = \cos \lambda \sin \theta + \sin \lambda \cos \theta$$

so that by letting

$$\sin \lambda = \frac{a(1 - e^2)}{\sqrt{(eR_m)^2 + \left(a(1 - e^2)\right)^2}} \quad \cos \lambda = \frac{eR_m}{\sqrt{(eR_m)^2 + \left(a(1 - e^2)\right)^2}}$$

then

$$\sin(\theta + \lambda) = \frac{R_m}{\sqrt{(eR_m)^2 + (a(1-e^2))^2}}$$

and

$$\theta = \sin^{-1} \frac{R_m}{\sqrt{(eR_m)^2 + (a(1-e^2))^2}}$$

where

$$\lambda = \tan^{-1} \left( \frac{a(1-e^2)}{eR_m} \right) \quad (2-22)$$

Finally,

$$\theta = \sin^{-1} \left( \frac{1}{\sqrt{e^2 + \frac{a^2(1-e^2)^2}{R_m^2}}} \right) - \tan^{-1} \left( \frac{a(1-e^2)}{eR_m} \right) \quad (2-23)$$

can be written.

Figure 2-31 shows the maximum eclipse duration/orbit versus periapsis altitude for various apoapsis altitudes. It is immediately apparent that these upper bound values can be considerably in excess of the Voyager baseline constraint. In particular, for an orbit with  $h_p = 500$  km and  $h_a = 20,000$  km, the maximum eclipse time is 2.64 hours/rev.<sup>P</sup> For lower values of apoapsis, say,  $h_a = 10,000$  km,  $T_e$  decreases to 1.61 hours/rev, while for lower values of  $h_p$ ,  $T_e$  increases slightly. For  $h_a = 20,000$  km and  $h_p = 300$  km (i.e., the minimum periapsis altitude consistent with the 50 year lifetime constraint),  $T_e = 2.7$  hours/rev. The latter value represents the maximum eclipse duration for the orbit change satellite, unless the altitude is increased above an apoapsis altitude of 20,000 km.

Figure 2-32 shows a representative variation of eclipse duration with time for a 20,000 km by 500 km orbit. The orbit is inclined at 20 degrees to the ecliptic,

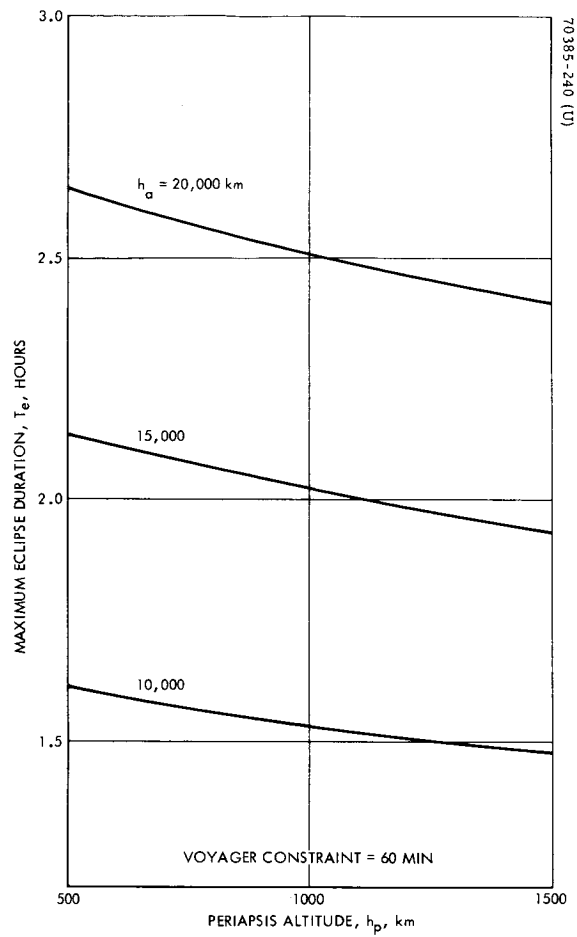


Figure 2-31. Maximum Solar Eclipse

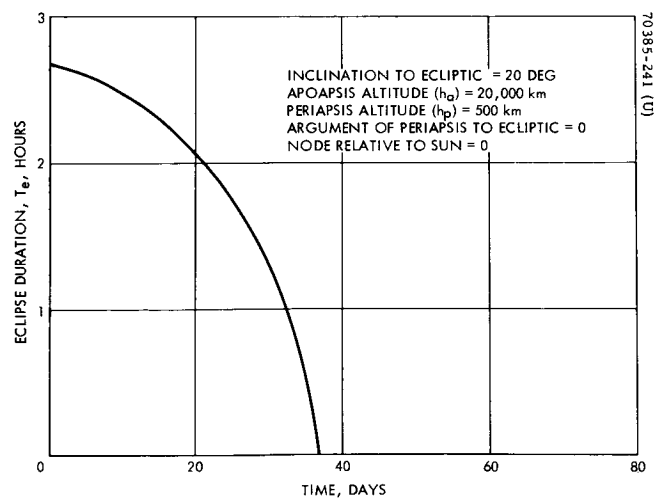


Figure 2-32. Eclipse Duration Versus Time

and its epoch conditions give the maximum eclipse duration. The results show that the period of high eclipsing is experienced for a moderate number of days. For periods greater than a month, the eclipse duration goes to zero and remains so for at least an additional 40 days. Variations of this type are typical for high eccentricity orbits. Although the eclipse distribution is not symmetrical about  $t=0$ , it is reasonable to estimate that eclipse periods of longer than 60 minutes may exist for up to 2 months. This condition probably precludes the possibility of interrupting communication between the OEC and Voyager during these periods. Hence, sufficient battery power should be included for operating the OEC during peak eclipsing.

#### 2.2.8 Voyager-OEC Occultation

Provision for occultation of Voyager or OEC by Mars is a desirable feature in the event that an "Occultation Experiment" is included as a primary experiment. In light of this, it is of interest to determine the communication range requirements necessary to provide this mission feature.

The minimum range which results in planetary occultation is found from observing Figure 2-33 and the following orbital equations:

$$D = 2r \sin \nu \quad (2-24)$$

where  $\nu$  = true anomaly and

$$r = \frac{a(1 - e^2)}{1 + e \cos \nu} = \frac{a(1 - e^2)}{1 + e \left( \frac{R_m}{r} \right)} \quad (2-25)$$

Rewriting yields

$$r = a(1 - e^2) - eR_m \quad (2-26)$$

For the nominal orbit assumed, the characteristic parameters are

$$h_p = 1000 \text{ km}$$

$$h_a = 10,000 \text{ km}$$

$$a = 8.9 \times 10^3 \text{ km} \quad (2-27)$$

$$e = 0.505$$

$$r = 4918 \text{ km}$$

$$\nu = \cos^{-1} \left( \frac{R_m}{r} \right) = 46.2 \text{ degrees} \quad (2-28)$$

and finally the minimum distance is

$$D = 2r \sin \nu$$

$$= 7120 \text{ km} \quad (2-29)$$

Figure 2-34 illustrates the earliest time during the mission at which occultation will occur as a function of the separation velocity. The detailed discussion of the selection of this range of velocities is presented in 2.4. It must be recognized that the consequence of larger injection velocities is that communication power requirements increase. For example, at a separation velocity of 0.1 fps, commensurate with co-orbital mission operation, the maximum communication range requirement is approximately 2700 km. This range is well below the minimum occulting range. If occultation is desirable, a minimum velocity increment of approximately 0.25 fps is required. For example, to produce an occultation during the fifth month,  $\Delta V = 0.3$  fps and the maximum range is 8500 km.

Adding this capability to the simple co-orbiter mission requires additional solar power. For an 8500 km communication range, the power required is nine times that at 2700 km.

For the orbit change mission, with the occultation experiment, it could be desirable to provide immediate occultation. This can be produced by separating with velocities on the order of 1.0 fps. Thus the occultation experiment could be conducted within the first several weeks.

#### 2.2.9 Antenna Field of View Requirements

The complex nature of the orbit motion, as well as the generality of possible orbit characteristics is reflected in the determination of the communication antenna coverage requirements. It is necessary to size the field of view for both the OEC and Voyager to ensure continuity of data transmission.



Both missions discussed require identical antenna coverage. The only difference is that continuous data is transmitted in the co-orbital mode, whereas data is stored on tape and played back at preselected intervals for the orbit change mission.

The three factors that must be considered in designing the antenna coverage are

- 1) Rotation of Voyager as it tracks the Sun and Canopus
- 2) Orientation of the OEC to Voyager in the nominal orbit
- 3) Effects of orbit precession

Figure 2-35 illustrates the effect of Sun's motion. Orbit regression and apsidal rotation have been discussed in Section 2.2.2.

#### 2.2.9.1 OEC Antenna Coverage

Since the OEC is spinning, the required antenna pattern is clearly symmetrical about the spin axis. The angle from the normal to the spin axis to the boundary of the antenna pattern can be computed with the aid of Figure 2-36. Assuming that the spin axis lies within 5 degrees of the normal to the Martian ecliptic (a constraint for both the co-orbital and orbit change systems), the maximum angle between the spin axis and orbit normal is (5 degrees +  $i_e$ ). Since the inclination of the initial orbit plane of Voyager to the Martian ecliptic is constrained to be less than 45 degrees, the aforementioned angle has a maximum initial value of 50 degrees. Neglecting perturbations on the orbit, i.e., assuming that the orbit plane remains fixed in inertial space, the required angle from the spin axis normal is found to be  $\pm 50$  degrees.

This corresponds to a requirement for a "pancake beam," symmetric about the spin axis, and enclosing an elevation angle of 100 degrees.

The regression of the orbit node due to planetary oblateness adds a further degree of complexity to the problem. The oblateness of Mars causes the orbit plane to rotate about the polar axis of the planet and therefore modifies the antenna requirements obtained above. This rotation means the orbit normal will be changing position in inertial space throughout the mission; i.e., the angle  $i_e$  will be a function of time.

Figure 2-20 illustrated the effect of the Martian oblate gravitational field on the node of the orbit with respect to the Martian equator. As seen in Figure 2-37, the motion of the node with respect to the equator ( $\Delta\Omega$ ) causes a corresponding change in the orientation angles relative to the (Martian) ecliptic, i.e.,  $\Omega_o$  and  $i_e$ . The spherical geometry of Figure 2-37 results in the following relationships:

$$\cos i_e = \cos i \cos \epsilon + \sin i \sin \epsilon \cos (\Omega_o - |\Delta\Omega|) \quad (2-30)$$

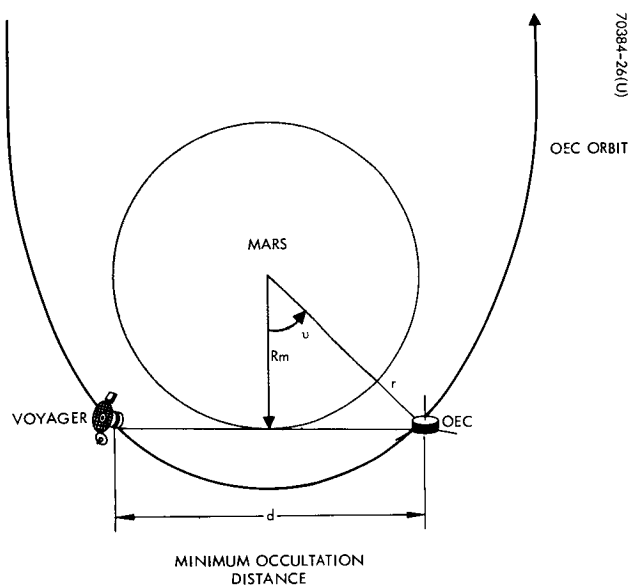


Figure 2-33. Occultation for Two Vehicles in Same Orbit

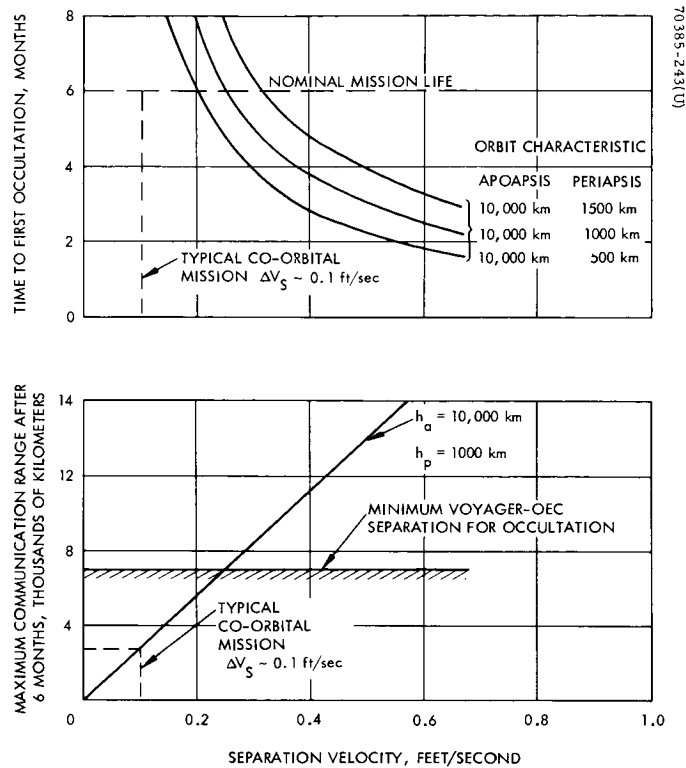


Figure 2-34. Effects of Occultation on Co-orbital Mission Design

- ROTATION RATE =  $1/2^\circ$ /DAY
- IN 6 MONTHS SUN APPEARS TO MOVE  $94^\circ$

- VOYAGER TRACKS SUN AND CANOPUS

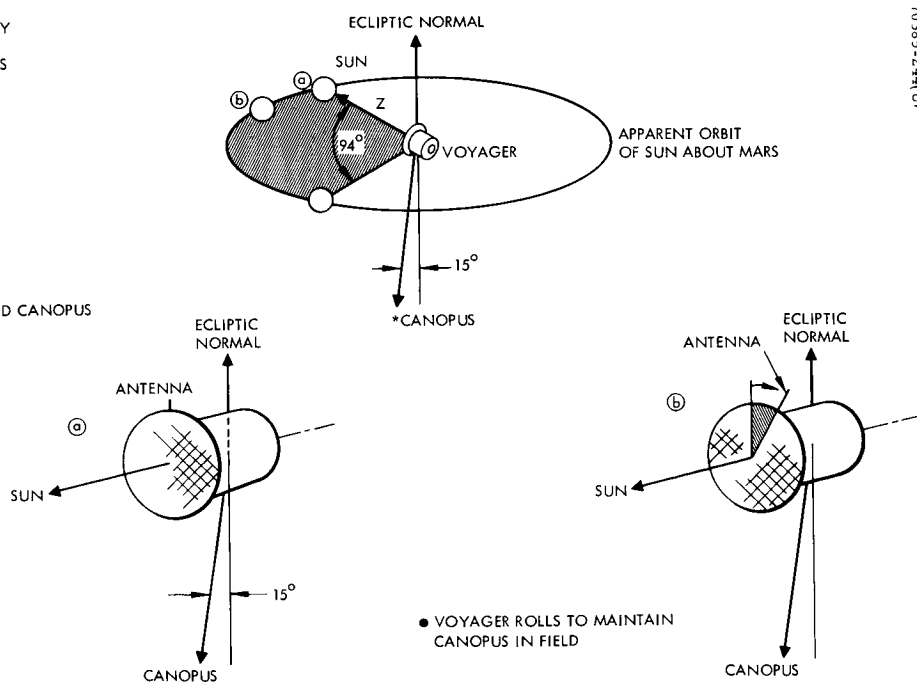


Figure 2-35. Influences on Antenna Coverage

and

$$\sin \Omega_e = \sin (\Omega_{e_0} - \Delta \Omega_e) = \frac{\sin i \sin (\Omega_0 - |\Delta \Omega|)}{\sin i_e} \quad (2-31)$$

where  $\Delta \Omega_e$  is the (westward) displacement of the node along the equator.

Since the nominal Voyager-OEC orbit has not been specified, the antenna pattern which yields the largest field of view requirement is considered. As shown above, the size of the total required elevation angle of the antenna beam is specified by the angle  $2 (i_e + 5 \text{ degrees})$ . Since oblateness causes the angle  $i_e$  to vary throughout the mission, the angle of interest is the maximum value of  $i_e$  obtainable within the range of possible Voyager/OEC orbits. Since the inclination of the initial orbit plane to the ecliptic is constrained to be equal or less than 45 degrees (see Reference 6), it is apparent from Figure 2-37 that the maximum value of  $i$  relative to the Martian equator is 70 degrees, i.e., when  $\Omega_{e_0}$  is zero. With an initial inclination of 70 degrees relative to the equator, Figure 2-20 indicates that nodal regressions as high as 96 degrees are possible during a 6-month mission for certain Voyager orbits. Substitution of the values — i.e.,  $i = 70 \text{ degrees}$ ,  $\Omega_0 = 0$ , and  $|\Delta \Omega| = 96 \text{ degrees}$  — into Equation 2-30 yields an inclination of 74.3 degrees relative to the (Martian) ecliptic after 6 months for this orbit. Hence, the co-orbital OEC configuration requires a 160 degree pancake beam for continuous visibility under all possible orbital conditions.

If plane change maneuvers are not contemplated for the orbit change OEC, then the 160 degree pancake beam antenna will also suffice for this concept. On the other hand, if further analysis indicates that  $i_e$  may be substantially increased above the current Voyager limit, then an isotropic pattern (4 steradians) may be required.

#### 2.2.9.2 Voyager Antenna Coverage

Due to the complexity of this analysis, the Voyager antenna requirements are evaluated on three levels, each succeeding level increasing in complexity. The analysis is based on the co-orbital OEC mission, but conclusions are reached in Level III which apply to the orbit change mission as well.

Level I. The following simplifications are made for this level:

- 1) The perturbations on the orbit are neglected; i.e., the orbit plane remains fixed in inertial space.
- 2) No roll motion is required by the Voyager spacecraft; i.e., assume the star Canopus is located 90 degrees out of the Martian ecliptic and thus is always within the field of view of the Voyager star sensor as the Voyager Z-axis tracks the sun.

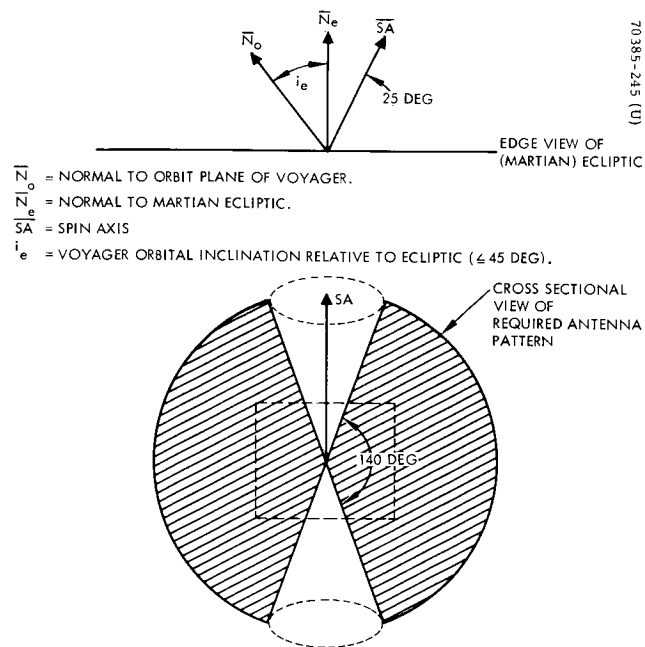
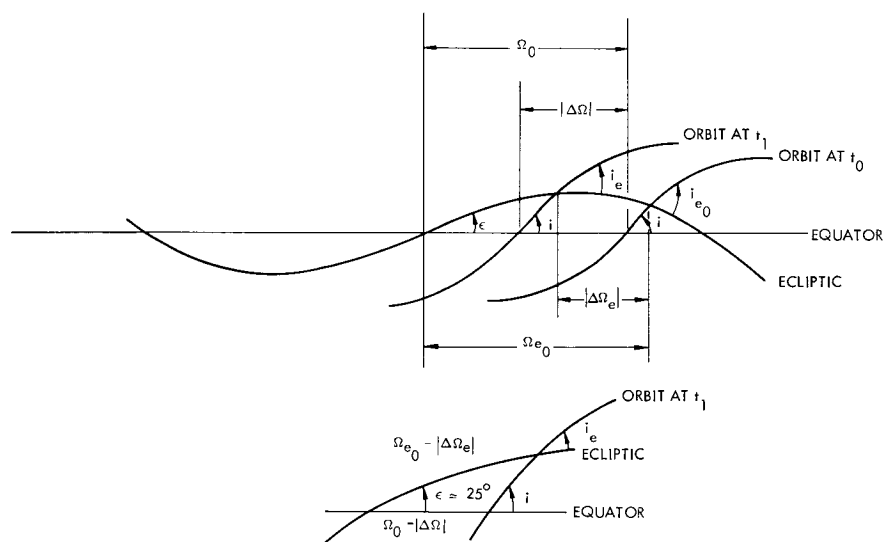


Figure 2-36. Required Antenna Pattern for OEC



NOTE:

$\Omega_0$  AND  $\Delta\Omega$  ARE MEASURED IN THE EQUATORIAL PLANE

$\Omega_{e0}$  AND  $\Delta\Omega_e$  ARE MEASURED IN THE ECLIPTIC PLANE

Figure 2-37. Mercator Projection

Section 2.2.3 indicates the broad aspect variation that must be accommodated during each orbit; i.e., the communication line of sight from Voyager to the OEC moves through all angular directions in the orbit plane during each orbit. Figure 2-38 shows a schematic representation of the communication aspect requirement as related to the Voyager spacecraft. For a single orbit, the antenna coverage required is a beam containing the orbital plane of the OEC about Voyager, i.e., a 360 degree "disc beam" perpendicular to the orbit normal. In order to maintain the Voyager solar array normal to the Sun's rays, the Voyager spacecraft axes are required to rotate about the normal to the ecliptic at approximately one-half degree per day, due to the motion of Mars about the Sun. This motion is equivalent to holding the Voyager spacecraft fixed and rotating the orbit plane (in westerly sense) about the normal to the ecliptic.

Over a 6-month period the required antenna coverage is the superposition of the successive orbit planes formed by rotating the initial orbit plane approximately 90 degrees about the ecliptic normal. The orientation of this required coverage volume relative to the Voyager spacecraft can be determined only if the orientation of the initial orbit plane relative to the ecliptic is completely specified. Since this orientation is unknown at this time, it is necessary to design the antenna pattern such that it will suffice regardless of the orbit eventually selected for the Voyager-OEC mission. In particular, if the node of the orbit relative to the ecliptic is not restricted, then all possible orbit nodes must be considered. This ambiguity of initial orientation corresponds to a full 360 degree rotation of Voyager relative to the orbit plane; consequently, the superposition of the successive orbit planes would form a "pancake beam", symmetric about the normal to the ecliptic and enclosing an elevation angle of twice the angle ( $i_e$ ) between the normal to the ecliptic and the orbit normal (Figure 2-39). Alternately, this pancake beam may be described by an excluded cone of size (90 degrees -  $i_e$ ).

Level II. The orbit perturbations are still neglected, but consideration is given to the fact that Canopus is not 90 degrees out of the Martian ecliptic.

The star Canopus is actually about -75 degrees (in declination) out of the Martian ecliptic plane. The Voyager spacecraft will execute roll maneuvers, about the Z-axis, throughout the mission to retain Canopus within the field of view of the star sensor. In terms of the Voyager body axis system, this corresponds to keeping Canopus in the Y-Z plane at all times throughout the mission, while the Z-axis tracks the sun as shown in Figure 2-35.

Since the Voyager antenna is fixed to the spacecraft, the axis of symmetry of the pattern will move by up to 15 degrees from the ecliptic normal due to these roll maneuvers. Therefore, the excluded cone must be reduced by 15 degrees and, as can be seen in Figure 2-39, the antenna requirements for Level II are equivalent to those of Level I where the excluded cone is now of size (90 degrees -  $i_e$  - 15 degrees).

Level III. The regression of the orbit due to planetary oblateness adds a further degree of complexity to the problem. In particular, the oblateness of Mars causes the orbit plane to rotate about the polar axis of the planet and thereby modifies the antenna requirements obtained above. This rotation means the orbit normal will be changing position in inertial space throughout the mission; i.e., the angle  $i_e$  will be a function of time.

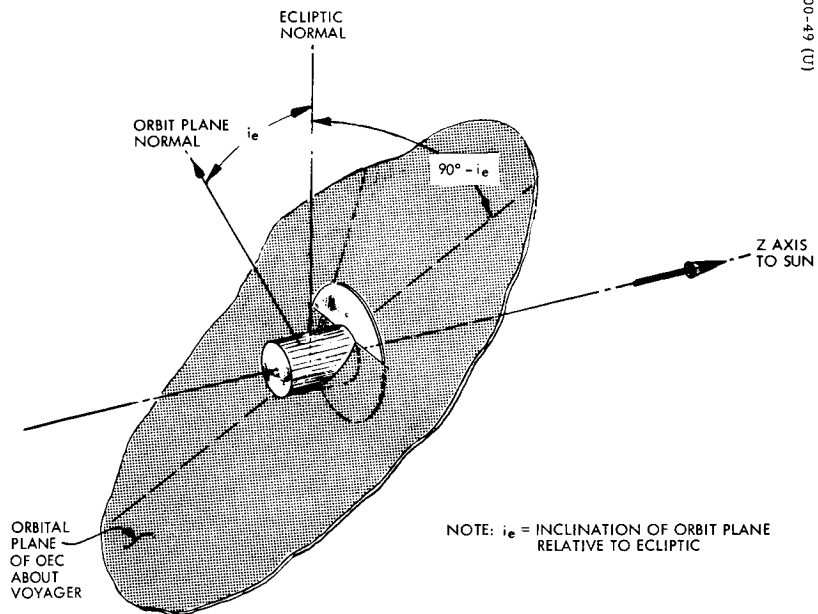
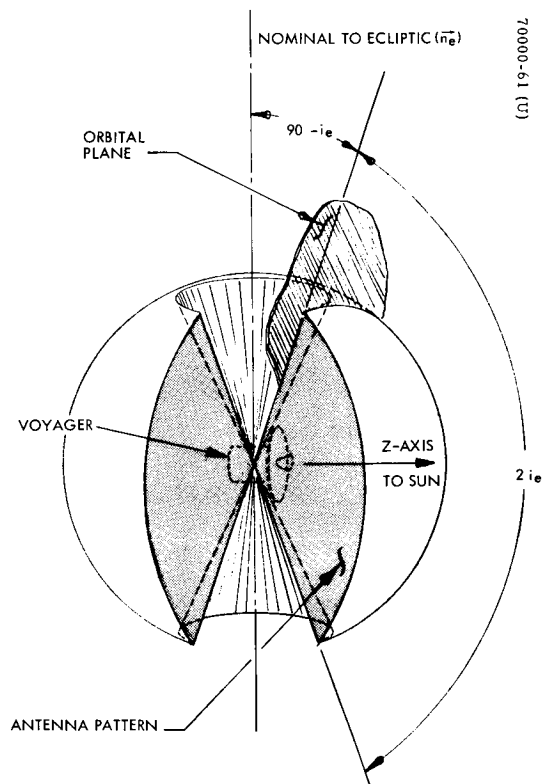


Figure 2-38. Voyager Communications Aspects Over One Orbit



NOTE:  
ROTATION OF ORBITAL PLANE ABOUT Y-AXIS  
SWEEPS OUT VOLUME NOTED AS "SUPERPOSITION  
OF RECEIVING ASPECTS"

Figure 2-39. Level II Antenna Pattern Requirements

Figure 2-20 shows the effect of the Martian oblate gravitational field on the node of the orbit with respect to the Martian equator. As seen in Figure 2-37, the motion of the node with respect to the equator ( $\Omega$ ) causes a corresponding change in the orientation angles relative to the ecliptic, i.e.,  $\Omega_e$  and  $i_e$ . The spherical geometry of Figure 2-37 results in the relationship identified as Equations 2-30 and 2-

The antenna pattern required for an extreme Voyager orbit is now considered. As shown in the Level II discussion, the size of the excluded cone is specified by the angle  $(90 \text{ degrees} - i_e - 15 \text{ degrees})$  or  $(75 \text{ degrees} - i_e)$ . The angle of interest is the maximum value of  $i_e$  obtainable within the range of possible Voyager-OEC orbits. Since the inclination of the initial orbit plane to the ecliptic is constrained to be equal or less than 45 degrees, it is apparent that the maximum value of  $i$  relative to the Martian equator is 70 degrees, i.e., when  $\Omega_{e0}$  is zero. With an initial inclination of 70 degrees relative to the equator, Figure 2-20 indicates that nodal regressions as high as 96 degrees are possible during a 6-month mission for certain Voyager orbits. Substitution of these values —  $i = 70 \text{ degrees}$ ,  $\Omega_0 = 0$ , and  $|\Delta\Omega| = 96 \text{ degrees}$  — into Equation 2-30 yields an inclination of 74.3 degrees relative to the ecliptic after 6 months. Thus, to guarantee continuous communication for the entire realm of Voyager orbits, a  $4\pi$  steradian antenna pattern is required since the excluded cone is specified by  $(75 - 74.3 \text{ degrees}) \approx 0$ . It is apparent that the orbit change mission, with its added uncertainties, will also require a  $4\pi$  steradian antenna pattern unless the orientations of the orbital planes are specified in advance. Figure 2-40 illustrates the expected worst case coverage angles for both vehicles; note that both the Voyager and OEC antenna patterns are symmetrical in the region of the ecliptic normal. This is due to the orientation of OEC of  $<5$  degrees to the ecliptic normal and the Sun-Canopus tracking of Voyager.

For a fully specified initial Voyager orbit there could, of course, be a considerable reduction in the coverage requirements, and the antenna pattern would be nonsymmetrical with respect to the Voyager. The orientation of this field of view with respect to the Voyager is a function of the initial orbital parameters of the orbit and of the initial inertial orientation of the Voyager spacecraft.

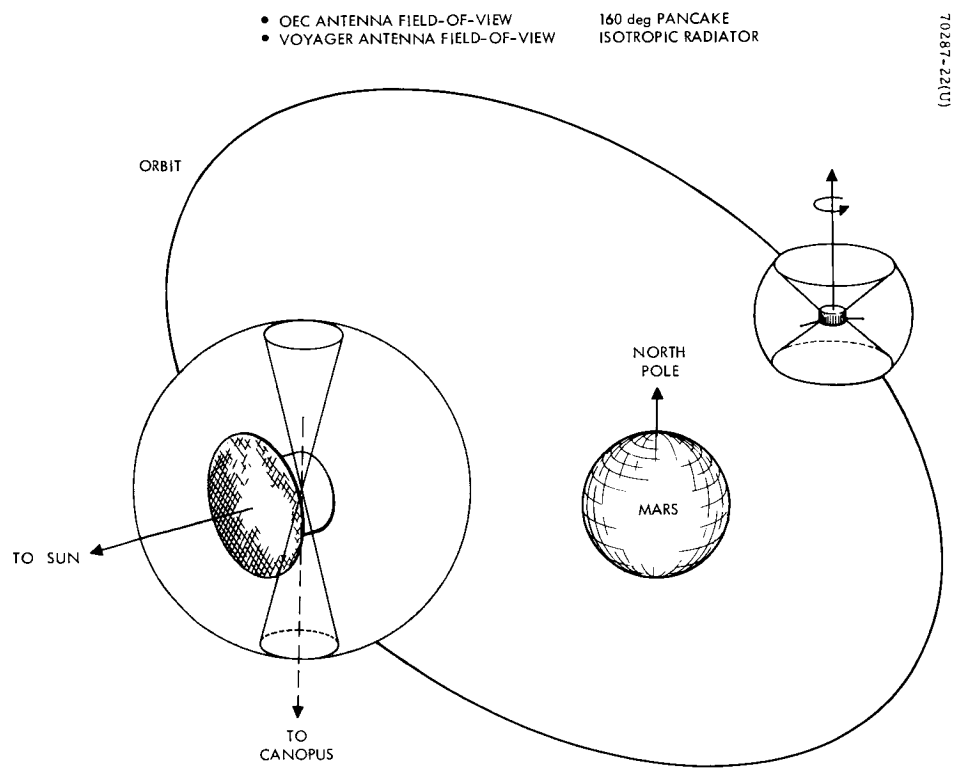


Figure 2-40. Voyager-OEC Antenna Coverage



## 2.3 VOYAGER - OEC RELATIVE MOTION

### 2.3.1 General

The OEC is injected into an orbit about Mars after the mission of the Voyager Lander is completed. There are two constraints imposed on the separation design that are considered for the coorbital missions:

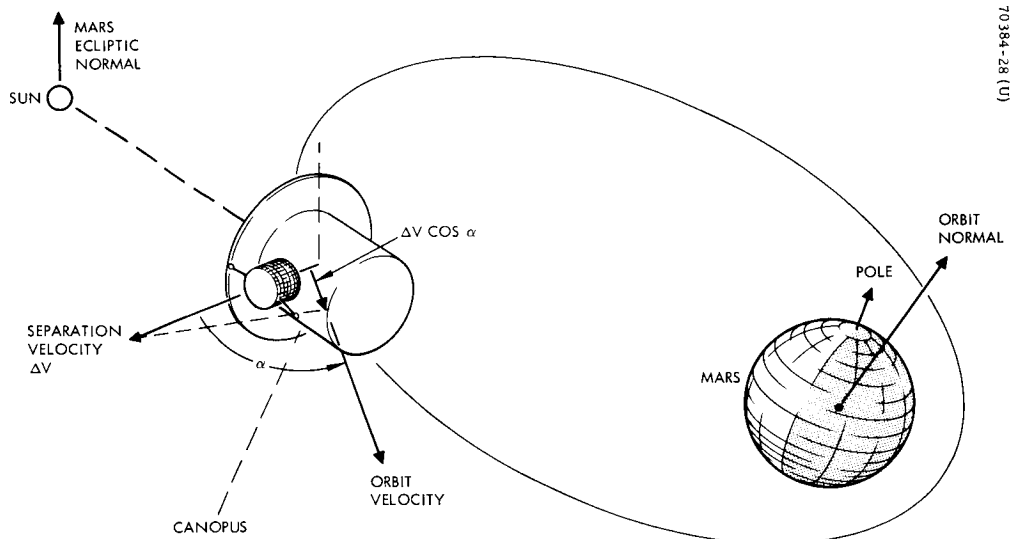
- 1) Guarantee of a noncollision of the OEC with Voyager on the first orbit
- 2) Minimization of the relative separation distance after 6 months to maintain a low mission power requirement for the co-orbiter design

Control over each of these factors is related to the characteristics of the separation system, the separation velocity magnitude, the launch geometry, and the Voyager orbit characteristics which establish the initial launch conditions for OEC.

The objective of the injection is to change the orbital period of the OEC orbit from that of Voyager. This is accomplished by making the orbit velocity of the capsule either greater or smaller than that of Voyager by a desired amount. The actual difference is sized by the factors outlined above and discussed here.

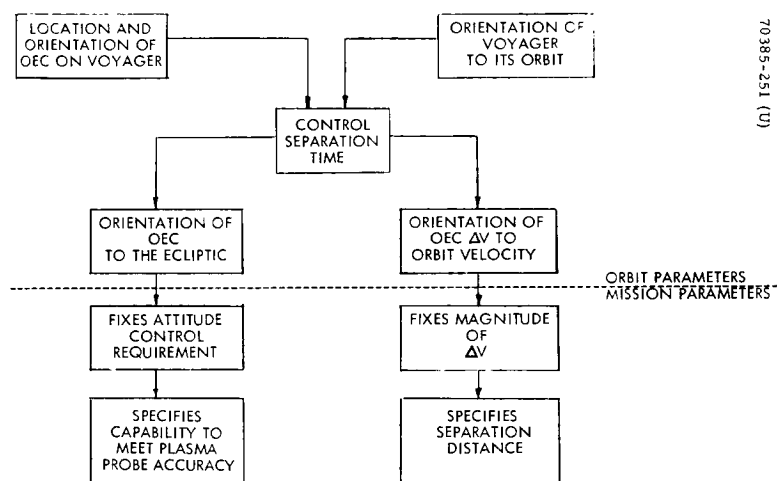
Figure 2-41 illustrates the relationship between the OEC, Voyager, and the orbit parameters. A typical orbit is shown, as well as the geometry with the Mars ecliptic plane. The Voyager orbiter stabilization is provided by an active three axis system which tracks both the Sun and star Canopus. As such, and because the Sun's apparent motion is very slow (0.5 deg/day), the bus is considered a fixed inertial reference platform over a fraction of a day. Referring to Figure 2-16, the range of orbital periods is between 7 and 14 hours. Hence the Voyager tracking motion during the period of an orbit is extremely small and need not be considered in studying the injection phase. However, the relationship of the location of the OEC on the Voyager must be related to the particular orbit to establish the proper separation and initial orientation.

The OEC orbital period is adjusted by selection of the proper position in the orbit to command separation. Control over the period is gained by selection of the angle  $\alpha$  between the separation velocity  $\Delta V$  and the instantaneous orbit velocity of Voyager. By choosing the parallel component of velocity increment along the orbit velocity vector, the desired OEC orbit is established. This value is given by



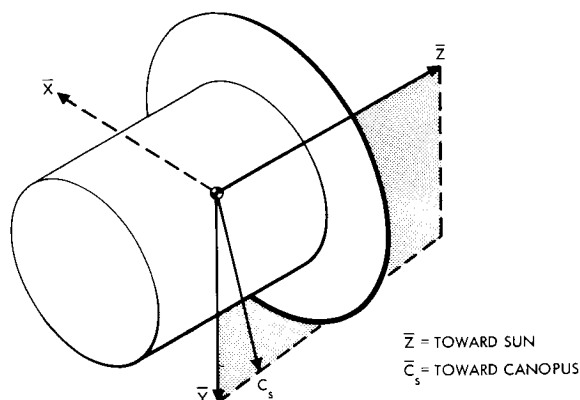
70384-28 (U)

Figure 2-41. Relative Voyager-OEC Motion



70385-251 (U)

Figure 2-42. Geometrical Parameters



70385-252 (U)

Figure 2-43. Voyager Body Axes

$$\Delta V_p = |\Delta V| \cos \alpha \quad (2-32)$$

where

$|\Delta V|$  = magnitude of separation device velocity increment

$\alpha$  = angle between separation vector and orbit velocity vector

The orientation of the OEC spin axis to the ecliptic normal is required to be less than  $\pm 5$  degrees. To meet this specification, the OEC must either be precisely aligned on Voyager and separated extremely close to the ecliptic normal or an attitude correction system must be incorporated. This topic receives considerable attention in Section 2.4.

In order to meet these mission requirements, the orbit injection parameters must be clearly defined. Figure 2-42 shows the interrelationship of the geometrical parameters. By knowledge of the location and orientation of the OEC on Voyager as well as the orientation of Voyager to its orbit, a relationship to the time of separation and the window is established. Given this information as well as the geometry relating Voyager to the ecliptic plane, the angle from the ecliptic normal is found. The Voyager-OEC separation distance is a function of the injection aspect angle to the Mars orbit and the point of separation. Knowledge of these parameters provide a measure of maximum range at the end of the nominal 6-month OEC operation.

The following discussion analyzes in detail the requirements for separation and identifies the range of velocity increments and the geometrical parameters discussed above.

### 2.3.2 Voyager Coordinate System

The Voyager body axes coordinates (X, Y, Z) are defined with the  $\bar{Z}$  axis pointing toward the Sun and with the star Canopus lying in the Y-Z plane at all times (Reference 1). Figure 2-43 is a sketch of the Voyager reference coordinates.

The Voyager, and hence its coordinates, vary with time. In particular, it not only rotates about the normal to the ecliptic while tracking the Sun (a rotation of approximately 1/2 degree per day), but also rolls about the Z-axis to retain Canopus in the Y-Z plane. This system may be defined uniquely in terms of two vectors:

$\bar{C}_S$  = vector from the Voyager spacecraft to Canopus

$\bar{S}$  = vector from the Voyager spacecraft to the Sun

In terms of these unit vectors, the  $\bar{X}$ ,  $\bar{Y}$ ,  $\bar{Z}$  Voyager body axis system is

$$\bar{Z} = \bar{S}$$

$$\bar{X} = \frac{\bar{C}_S \times \bar{S}}{|\bar{C}_S \times \bar{S}|} \quad (2-33)$$

$$\bar{Y} = \bar{Z} \times \bar{X}$$

This body-axis system can be solved in terms of (Earth) ecliptic coordinates. To facilitate matters, the vector  $\bar{S}$  was approximated by the vector from Mars to the Sun and the vector  $\bar{C}_S$  was approximated by the vector from the Sun to Canopus. Using ephemeris data from Reference 10,  $\bar{X}$ ,  $\bar{Y}$ ,  $\bar{Z}$  were obtained in terms of (ecliptic) unit vectors  $\bar{A}$ ,  $\bar{B}$ , and  $\bar{C}$  (see Figure 2-44). For a nominal separation date of 7 March 1974,\* the vectors  $\bar{Z}$  and  $\bar{C}_S$  are

$$\begin{aligned} \bar{Z} &= 0.199 \bar{A} - 0.980 \bar{B} + 0 \bar{C} \\ \bar{C}_S &= -0.0612 \bar{A} + 0.236 \bar{B} - 0.969 \bar{C} \end{aligned} \quad (2-34)$$

Equations 2-33 and 2-34 result in the Voyager body axis being specified by:

$$\begin{aligned} \bar{X} &= -0.980 \bar{A} - 0.199 \bar{B} + 0.013 \bar{C} \\ \bar{Y} &= -0.013 \bar{A} - 0.003 \bar{B} - 0.999 \bar{C} \\ \bar{Z} &= 0.199 \bar{A} - 0.980 \bar{B} + 0 \bar{C} \end{aligned} \quad (2-35)$$

These vectors are used to define the orientation of the OEC with respect to Voyager and the ecliptic.

### 2.3.3 Relationship of Separation Vector to Voyager

In this analysis, the OEC is assumed to be separated radially from the Voyager spacecraft, and hence the direction of the separation is defined by the unit vector

$$\Delta \bar{V} = \cos \Gamma \bar{X} + \sin \Gamma \bar{Y} \quad (2-36)$$

---

\* This data corresponds to the midpoint of the arrival window plus 10 days allowance to initiate the Lander experiment. It is subsequently indicated that the final results are not sensitive to moderate changes in separation date.

where  $\Gamma$  is the angle the separation vector makes with the X-axis of the Voyager body axis system (see Figure 2-45). The OEC spin axis is assumed to be collinear with the separation vector. This is not necessarily the case since it is possible to have other orientation of the spin axis to the separation vector, as discussed in Section 2.4. The solution discussed here does not change; however, the separation vector-spin axis must be redefined. Since the longitudinal axis of the Voyager points at the Sun, the initial spin axis direction is nominally normal to the Sun line. This condition guarantees that the sun sensor (located on the periphery of the OEC) will see the Sun, and hence attitude data will be available immediately after separation and spinup.

### 2.3.3.1 Orientation Constraints

Selection of a preferred location on the Voyager Orbiter requires that the sensitivity of various performance parameters be evaluated for all possible locations  $\Gamma$ . There are four important constraining factors:

- Provision for spin axis attitude alignment to the ecliptic normal of  $< \pm 5$  degrees over the mission
- Provision for a Sun-OEC spin axis angle  $> 75$  degrees for power considerations (this is a less constraining factor than that above)
- Provision for a safe separation and noncollision on the first orbit
- Provision for minimum interaction with Voyager subsystems

Ecliptic Normal Alignment at Separation. Proper positioning of the co-orbital OEC on the Voyager is required to ensure that the spin axis of the OEC is sufficiently near normal to the ecliptic to yield satisfactory power system and plasma probe performance over the life of the mission.

Combining Equations 2-35 and 2-36 enables writing the equation for the spin axis in terms of ecliptic coordinates. For the nominal separation date (7 March 1974), this results in

$$\begin{aligned} \bar{\eta}_S = & \cos \Gamma (-0.980 \bar{A} - 0.199 \bar{B} + 0.013 \bar{C}) \\ & + \sin \Gamma (-0.013 \bar{A} - 0.003 \bar{B} - 0.999 \bar{C}) \end{aligned} \quad (2-37)$$

The angle between the spin axis ( $\bar{\eta}_S$ ) and the normal to the ecliptic ( $\bar{\eta}_e = \bar{C}$ ) is given by the dot product of the two vectors, i. e.,

$$\cos \epsilon_2 = \bar{\eta}_S \cdot \bar{\eta}_e = +0.013 \cos \Gamma - 0.999 \sin \Gamma \quad (2-38)$$

Figure 2-46 presents a plot of this angle,  $\epsilon_2$ , as a function of the position of OEC relative to the Voyager body axis. Although this curve is strictly valid only for the nominal separation date, it has been determined that the results

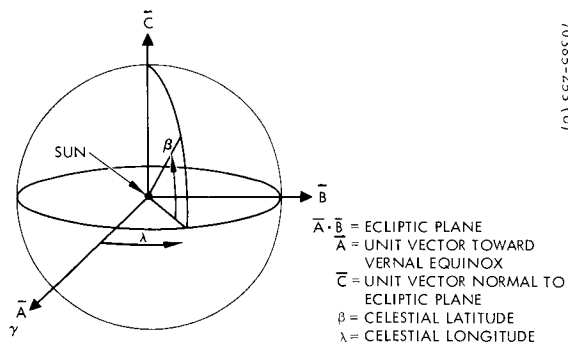


Figure 2-44. Ecliptic Coordinates

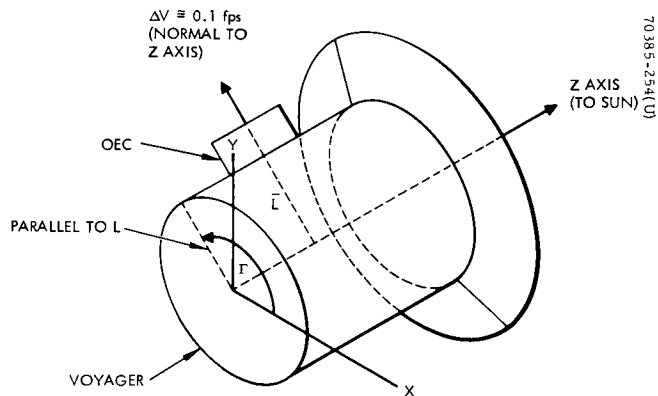


Figure 2-45. OEC Separation Relative to Voyager

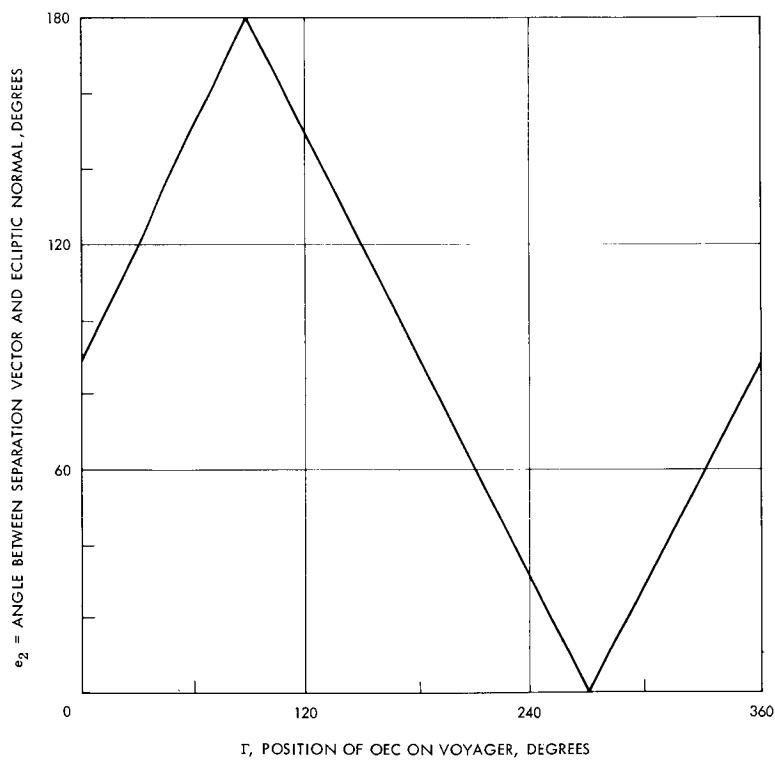


Figure 2-46. Initial Orientation to Sun

are quite accurate even for separation dates as much as 30 days on either side of the nominal date; i. e. ,  $\epsilon_2$  is insensitive to moderate changes in separation date. In fact, the maximum variation in  $\epsilon_2$  over an entire year is approximately 7 degrees.

Constraining the spin axis to be within  $\pm 5$  degrees of the ecliptic normal results in a very limited band of locations on the Voyager 180 degrees out of phase. The band itself is on the order of 5 degrees. This could be a severe constraint for the simple co-orbiter mission (no control capability) but is not so for OEC missions with attitude correction capabilities. By adding an additional degree of separation vector control, the window could be broadened. This can be accomplished by use of an adjustable OEC mounting device on Voyager.

If the separation platform could be skewed to the Voyager radius vector, a host of additional launch positions become available. Hence the results in Figure 2-46 are not conclusive evidence that the desirable mounting locations are so restricted.

Next attention is focused on the relationship between the OEC location on the Voyager and that of Voyager to its orbit plane. These results will be used to interpret the broadness of the launch windows.

Launch Window Geometry. As pointed out in Section 2. 3. 1, the angle  $\alpha$  between the separation  $\Delta V$  and the orbital velocity vector  $V_o$  is of great importance. The bounds on this angle are directly derived from the relationship of Voyager to its orbit and OEC's location on Voyager. Figure 2-47 illustrates a typical orbit and defines the angle  $\theta$  between the separation vector and the orbit plane. As can be seen, for a fixed inertial attitude of the velocity vector  $\Delta V$ , the angle  $\alpha$  can be defined to lie between

$$\theta \leq \alpha \leq 180 - \theta \quad (2-39)$$

It is immediately evident from Figure 2-47 that for  $\theta = 90$  degrees, the angle  $\alpha$  would also be 90 degrees, and hence the separation is orthogonal to the orbit velocity vector. Separation directions in this vicinity must be avoided since they do not change the OEC orbit period from that of Voyager but simply vary the inclination by some incremental value. By not changing the orbit period, it is obvious that the OEC would collide with the Voyager on the completion of one orbital revolution. Hence a limit on the value of  $\theta$  in the region of 90 degrees must be provided. A detailed discussion and error analysis is presented in Section 2. 4. 2.

Another important characteristic of Equation 2-39 is that it defines two points in each orbit at which a particular separation angle  $\alpha$  can be obtained. For a circular orbit, these positions would be 180 degrees out of phase, but for elliptic orbits the flight path angle must also be accounted for. Thus one position of injection is identified in the region of the periapsis and the other near apoapsis. Obviously the injections near apoapsis are more desirable. The underlying

reason is that the orbital velocity is smaller than for periapsis and the period or window is of greater duration. In addition, errors in the separation that propagate with velocity are smaller.

Figure 2-48 illustrates the separation geometry relative to the orbit plane. The angle  $\alpha$  is important since it determines the component of  $\Delta\bar{V}$  in the direction of the orbital velocity vector,  $\bar{V}_O$  — i. e., that component which yields a secular effect on the separation distance. It should be noted that the critical value of  $\alpha$ , i. e.,  $\alpha = \alpha_c$ , is always included in the range of possible separation angles over a complete orbit. Avoiding this condition, in this case, merely requires that separation occur at a time when  $\alpha \neq \alpha_c$ .

Examination of Figure 2-48 shows that  $\theta$  may be obtained by taking the dot product of  $\Delta\bar{V}$  and  $\bar{\eta}_O$  where both vectors are expressed in ecliptic coordinates. Let

$$\theta_1 = 90 - \theta \quad (2-40)$$

$$\cos \theta_1 = \frac{\Delta\bar{V} \cdot \bar{\eta}_O}{|\Delta\bar{V}| |\bar{\eta}_O|} \quad (2-41)$$

An expression for  $\Delta\bar{V}$  was previously obtained in terms of ecliptic coordinates,

$$\begin{aligned} \Delta\bar{V} = & (-0.98 \cos \Gamma - 0.013 \sin \Gamma) \bar{A} - (0.199 \cos \Gamma + 0.003 \sin \Gamma) \bar{B} \\ & + (0.013 \cos \Gamma - 0.999 \sin \Gamma) \bar{C} \end{aligned} \quad (2-42)$$

for a radial separation where  $\bar{A}$ ,  $\bar{B}$ , and  $\bar{C}$  are as defined in Figure 2-44. The unit vector normal to the orbit plane,  $\bar{\eta}_O$ , can also be expressed in terms of ecliptic coordinates, i. e.,

$$\bar{\eta}_O = \sin \Omega_e \sin i_e \bar{A} - \cos \Omega_e \sin i_e \bar{B} + \cos i_e \bar{C} \quad (2-43)$$

where

$\Omega_e$  = node of the orbit relative to the vernal equinox

$i_e$  = inclination of the orbit with respect to the ecliptic

Thus, as can be seen from Equations 2-40 through 2-43, the angle  $\theta$  is a function of both the location of OEC on Voyager ( $\Gamma$ ) and the orientation of the Voyager orbit with respect to the ecliptic.



The current generalities in the actual Voyager orbits make this study difficult. In order not to place any severe restrictions on the Voyager orbit, it was decided to consider all possible orientations in this analysis. Figure 2-49 indicates the range of  $\theta$  values obtainable for an orbit inclined at 45 degrees with respect to the ecliptic. The shaded area represents the possible  $\theta$  values as the node relative to the ecliptic,  $\Omega_e$ , varies from 0 to 360 degrees.

The locations in the vicinity of  $|\theta| \cong 90$  degrees must be avoided as these cases (for a particular value of  $\Omega_e$ ) correspond to separation directions perpendicular to the orbital velocity, i. e.,  $\alpha \cong 90$  degrees, regardless of location in the orbit, and admit the possibility of a collision. As an example, if  $\Gamma$  is selected as 120 degrees, then the range of possible  $\theta$  dependent on the node is 15 to 75 degrees. Selection of the launch point fixes the orientation of the velocity increment to the orbit velocity vector.

The components of the separation velocity perpendicular to the orbit velocity, both in and out of the orbit plane, result mainly in oscillatory terms and as such do not have a secular effect on the separation distance. The effect of the velocity increment on the relative distance depends upon the point in the orbit at which separation is initiated. To maintain a small separation distance, it is desirable to separate as close to apoapse as possible, where the orbital velocity is the smallest.

As noted previously, there are two points in the orbit between which separation can occur with the angle  $\alpha$  constrained between  $0 \leq \alpha \leq 180 - \theta$ . Section 2. 2. 2 shows that  $\gamma_{\max} \approx 30$  degrees for a nominal 1000 km x 10, 000 km orbit and can be as high as 45 degrees for other orbits within the range of possible Voyager orbits. For a desired value of  $\alpha$ , a separation point can be chosen within  $(90 + \gamma_{\max}/2)$  degrees of apoapsis, so that results for a separation occurring at  $\nu = 75$  degrees represent the greatest sensitivity of velocities which in turn yield the most sensitive separation ranges. Hence in the following performance discussion, a true anomaly of 75 degrees is assumed.

Voyager Mating Constraints. The constraints imposed due to the location of Voyager Orbiter subsystems largely influence the co-orbiter mission.

For the purposes of the feasibility study, an investigation into each of the three contending Voyager bus contractors was performed. The Voyager designs by General Electric, Boeing, and TRW are shown in Figures 2-50, 2-51, and 2-52. The subsystem locations on each of the spacecraft are specified in terms of the angle  $\Gamma$  measured from the positive X-axis in the direction of the positive Y-axis (Canopus pointing axis). Table 2-7 specifies the locations occupied by these external subsystems.

The random nature of subsystem locations from one configuration to the next implies that the design space is not limited and that in fact relocations of systems are possible. Thus placing too much credence on the available space is not reasonable. It is, however, established that there are available mounting locations on each of the configurations. Due to the limitation on available locations, other methods of separating in the co-orbiter mission are necessary to meet the  $\pm 5$  degree accuracy requirement. These techniques are discussed in Section 2. 4.

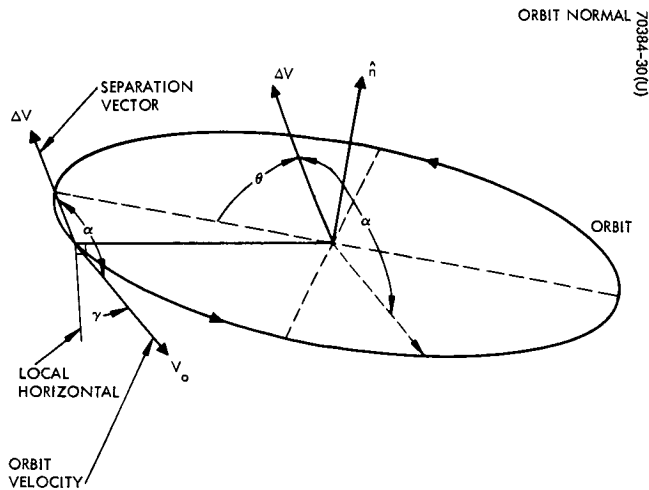


Figure 2-57. Relation of Separation Vector to Its Orbit Plane

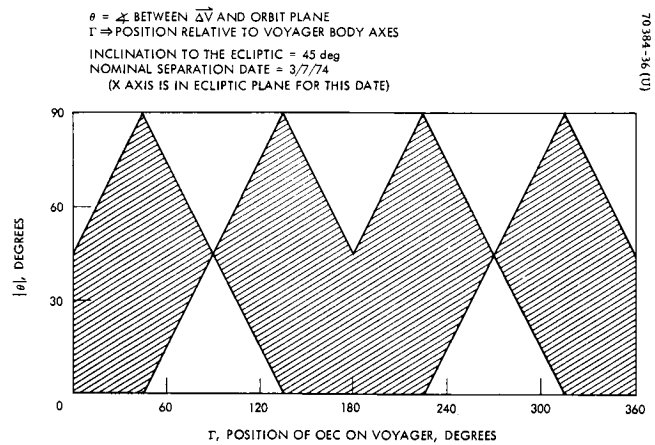


Figure 2-49. Relationship Between OEC Location on Voyager and Orbit Plane

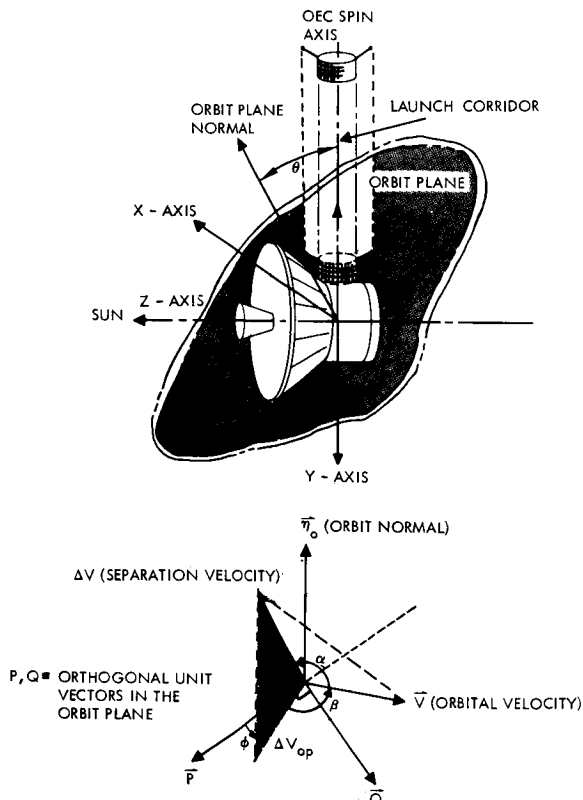


Figure 2-48. Separation Relative to Orbit Plane

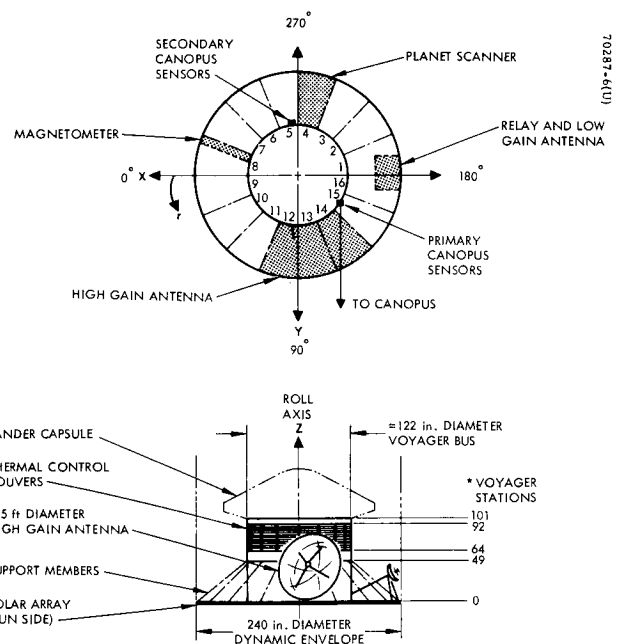


Figure 2-50. General Electric Voyager Spacecraft

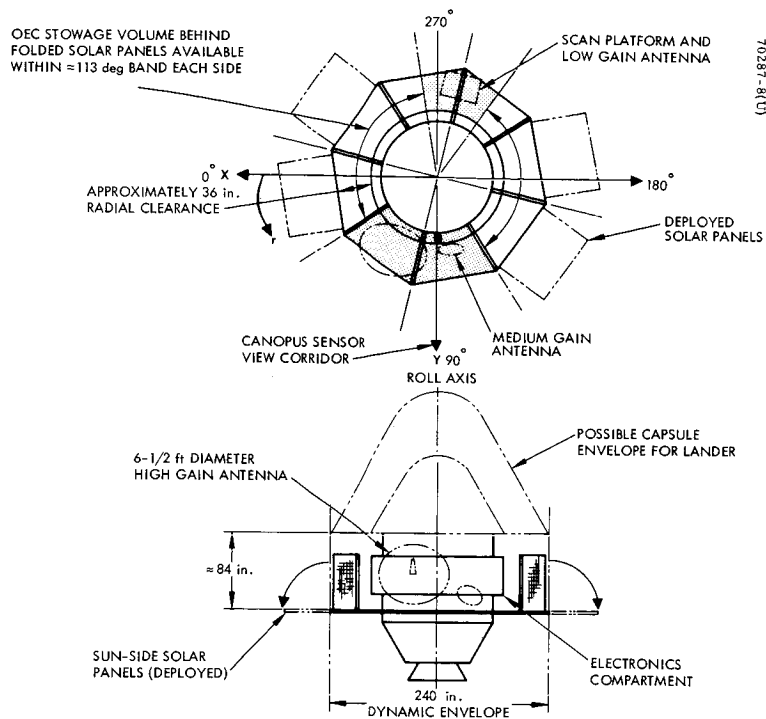


Figure 2-51. Boeing Voyager Spacecraft

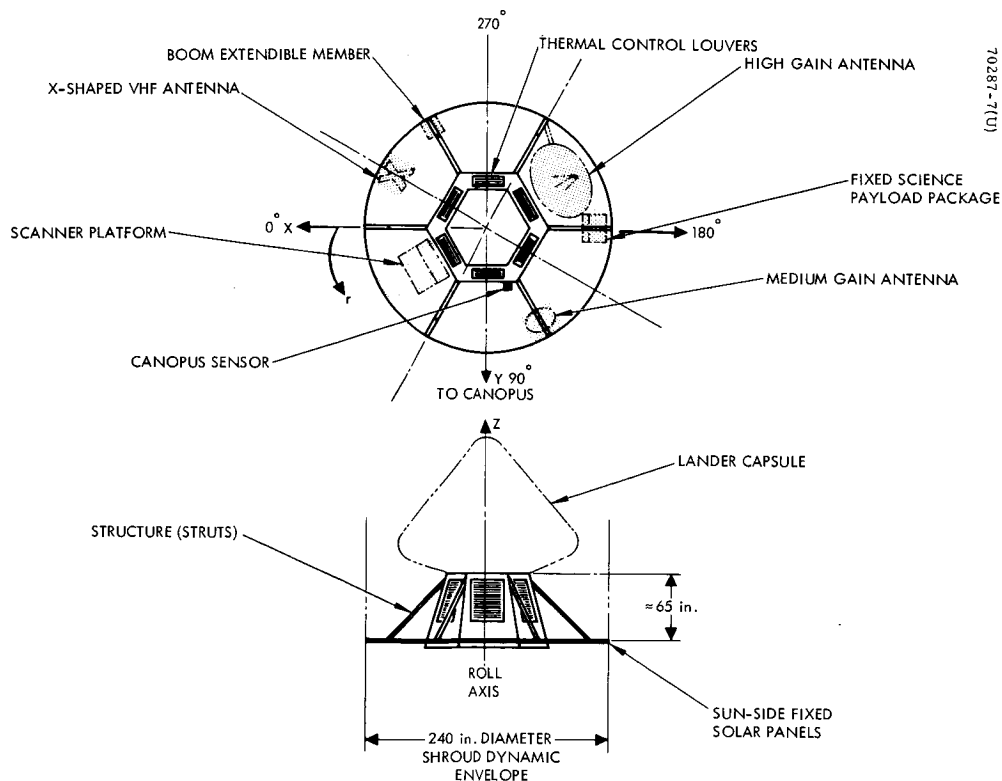
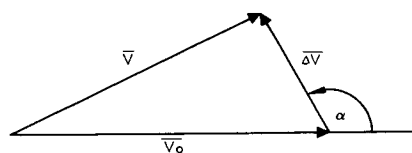


Figure 2-52. TWR Systems Voyager Spacecraft



70385-262 (U)

$|\overline{V_o}|$  = VOYAGER ORBITAL VELOCITY  
 $|\overline{\Delta V}|$  = SEPARATION VELOCITY  
 $|\overline{V}|$  = OEC ORBITAL VELOCITY

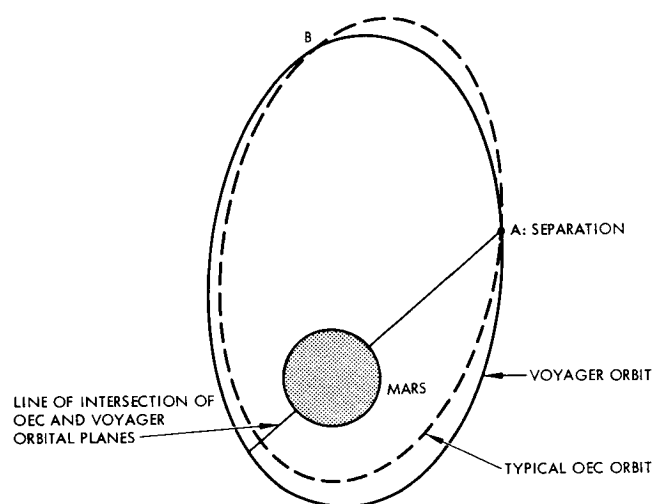


Figure 2-53. Gross Separation Geometry

TABLE 2-7. VOYAGER SPACECRAFT CONFIGURATION SUBSYSTEM LOCATIONS

Configuration	Subsystem	Angle Constraint, degrees
General Electric	High gain antenna, Canopus sensor	68 to 135
	Relay and low gain antenna	170 to 190
	Planet scanner	247 to 290
	Magnetometer	337 to 342
Boeing	High gain antenna, medium gain antenna, and Canopus sensor	31 to 121
	Scan platform and low gain antenna	234 to 278
TRW	Scan platform	0 to 63
	Medium gain antenna and Canopus sensor	109 to 132
	High gain antenna and science payload	172 to 244
	Boom extendable antenna and X-shaped VHF antenna	

#### 2.3.4 Kinematics of Separation

As the Voyager and OEC move together in orbit about Mars prior to separation, the magnitude of the component of the fixed OEC separation velocity vector collinear with the orbit velocity vector takes on different values depending on when the separation takes place. If the separation velocity is near normal to the velocity vector, the relative distance between the two vehicles after one orbit will be very small. This separation distance is proportional to the difference in the Voyager and OEC orbital periods and is especially critical during the first orbit.

In this section, the kinematic equations representing the velocity and position characteristics as a function of the particular injection geometry are established.

The general separation geometry in terms of the nominal Voyager and adjusted OEC orbits are shown in Figure 2-53. It can be shown that a change in orbit characteristics at any point in an elliptic orbit outside of periapsis or apoapsis will skew the new orbit about the reference position where the orbit velocity is changed. This is shown at point A. Adjustments in the nominal

orbit velocity at periapsis serves to increase or decrease apoapsis, whereas a change in velocity at apoapsis either lowers or increases periapsis.

From the figure it is seen that the two orbits intersect at two points. The question arises, "What are the important parameters of the separation geometry that control whether or not collision can be avoided?" A vector representation of the characteristic velocities is shown in Figure 2-53. From the Law of Cosines, the relationship between the OEC orbital velocity  $\bar{V}$  and the Voyager orbital velocity  $\bar{V}_o$  in terms of the separation velocity increment is given by

$$V^2 = V_o^2 \left[ 1 + \left( \frac{\Delta V}{V_o} \right)^2 + 2 \left( \frac{\Delta V}{V_o} \right) \cos \alpha \right] \quad (2-44)$$

where  $\alpha$  is the angle between  $\bar{\Delta V}$  and  $\bar{V}_o$  as illustrated.

For small changes in the OEC orbital velocity, the incremental change in period can be determined by simple manipulation of the orbital equation.

The period is defined by

$$P = \frac{2\pi}{\sqrt{\mu}} a^{3/2} \quad (2-45)$$

where

$\mu$  = Mars gravitational constant =  $0.428 \times 10^5 \text{ km}^3/\text{sec}^2$

$a$  = semi-major axis

For small changes in period, the following can be written:

$$\begin{aligned} \delta P &= \frac{3}{2} \frac{2\pi}{\sqrt{\mu}} a^{1/2} \delta a \\ &= \frac{3}{2} P \frac{\delta a}{a} \end{aligned} \quad (2-46)$$

From the vis-viva expression, the orbit velocity is

$$V^2 = \mu \left( \frac{2}{r_p} - \frac{1}{a} \right) \quad (2-47)$$

where  $r_p$  = radius at periapsis.

The derivation yields

$$2V \delta V = \mu a^{-2} \delta a \quad (2-48)$$

which can be written in terms of the semi-major axis as

$$\frac{\delta a}{a} = \frac{2aV\delta V}{\mu} \quad (2-49)$$

Substitution of Equation 2-49 into 2-46 gives the desired relationship

$$\delta P = \left( \frac{3PaV}{\mu} \right) \delta V \quad (2-50)$$

and the change in orbital velocity  $\delta V$  is simply

$$\delta V = V - V_o \quad (2-51)$$

where the velocities  $V$  and  $V_o$  are respectively the OEC and Voyager orbital velocities.

Equation 2-47 can also be given as

$$V^2 = \frac{\mu}{r_p} (1 + e) \quad (2-52)$$

where  $e$  = orbit eccentricity.

Doing so, it must be recognized that the coefficient is the equivalent circular orbit velocity at periapsis since

$$V_{c_p}^2 = \frac{\mu}{r_p} \quad (2-53)$$

and thus

$$V = V_{c_p} (1 + e)^{1/2} \quad (2-54)$$

can be written.

It is important here to indicate that by manipulating these equations, the objective is to show Equation 2-50 in a normalized form. Thus equating Equation 2-52 to the square of 2-54, the circular orbit velocity at periapsis altitude can be expressed as

$$V_{c_p} = \sqrt{\frac{\mu}{a(1-e)}} \quad (2-55)$$

Writing in terms of  $a$  and  $\mu$ ,

$$\frac{a}{\mu} = \frac{1}{V_{c_p}^2 (1-e)} \quad (2-56)$$

which can now be substituted into Equation 2-50 to yield the desired form

$$\delta P = \frac{3P}{(1-e)} \left( \frac{V_o}{V_{c_p}} \right) \frac{\delta V}{V_{c_p}} \quad (2-57)$$

Clearly, if the OEC orbit velocity is not changed from that of Voyager,

$$\delta V = V - V_o = 0$$

and hence there is no change in orbital period,  $\delta P = 0$ . Thus as shown in Figure 2-53, it is possible for the two vehicles to collide at the point of separation (A) at the completion of one orbit.

Collision of the two spacecraft at point B (or any other point of equal radius) is not possible. This is true either because the vehicles will not be in the same plane (i. e.,  $\Delta \bar{V}$  is not in the Voyager orbital plane) or because the time required to travel from point A to point B is not the same in orbits with different orbital parameters.

An expression which interprets the possibility of a collision in terms of the separation angle  $\alpha$  defined earlier is derived next. Dividing Equation 2-44 through by  $V_o^2$  and assuming that  $V = V_o$ ,

$$1 + \left( \frac{\Delta V}{V_o} \right)^2 + 2 \left( \frac{\Delta V}{V_o} \right) \cos \alpha = 1 \quad (2-58)$$



Regrouping and writing in terms of  $\alpha$

$$\cos \alpha = -\frac{1}{2} \left( \frac{\Delta V}{V_o} \right) \quad (2-59)$$

since

$$\sin \left( \frac{\pi}{2} - \alpha \right) = \cos (\alpha) \quad (2-60)$$

for a small angle approximation,

$$\left( \frac{\pi}{2} - \alpha \right) = -\frac{1}{2} \left( \frac{\Delta V}{V_o} \right) \quad (2-61)$$

and

$$\alpha = \frac{\pi}{2} + \frac{1}{2} \left( \frac{\Delta V}{V_o} \right) \quad (2-62)$$

where  $\alpha$  can be defined as the critical separation angle between the OEC velocity increment and the orbital velocity. Since

$$\frac{\Delta V}{2V_o} \lll 1 \quad (2-63)$$

then clearly the critical angle is, as intuition would have it,

$$\alpha_c = 90 \text{ degrees} \quad (2-64)$$

The last step in this development is the derivation of the relative separation distance between the vehicles and the sensitivity of the distance to values of  $\alpha$  near the critical value.

The sensitivity of the separation distance, at the end of one revolution, due to changes in  $\alpha$  near the critical value is developed below. The separation distance ( $\delta S$ ) can be accurately approximated by

$$|\delta S| = V_o |\delta P| = \frac{3P}{(1-e)} \left( \frac{V_o}{V_{c_p}} \right)^2 |\delta V| \quad (2-65)$$

Differentiating Equation 2-44 with respect to  $\alpha$  gives

$$\delta V = - \left( \frac{V_o}{V} \right) \Delta V \sin \alpha \delta \alpha \quad (2-66)$$

If  $V = V_o$ , operating near the critical value of 90 degrees, Equation 2-66 becomes

$$|\delta V|_{\alpha_c} \approx |\Delta V \delta \alpha| \quad (2-67)$$

The separation distance is then given by substitution of Equation 2-67 into 2-65 so that

$$|\delta S| = \frac{3P}{1-e} \left( \frac{V_o}{V_{c_p}} \right)^2 \Delta V |\delta \alpha| \quad (2-68)$$

For a typical Voyager orbit,  $h_a = 10,000$  km and  $h_p = 500$  km, the sensitivity to both the separation velocity and the critical angle is determined. It is assumed here that injection takes place at apoapsis and hence the sensitivity in separation distance is given by

$$\delta S = 170 \text{ meters/degree from critical angle/per unit } \Delta V \quad (2-69)$$

Separations occurring at other points in the orbit will yield larger coefficients because of increased orbital velocity. A representative value of the magnitude of this relative distance can be generated by assuming a velocity  $\Delta V$  and angle  $\alpha$ .

As will be shown in the latter part of this discussion, the range of separation velocities of interest are about 0.1 fps. Thus for an angle removed from  $\alpha_c$  by 10 degrees, a relative distance of 170 meters is ensured after the first orbit. The possibility of collision is then minimized by selection of the proper separation window. However, the probability of collision remains to be treated. The many uncertainties associated with the injection phase must be weighed in the final design of the separation kinematics and launch window. These are treated in detail in Section 2.4.

### 2.3.5 Voyager-OEC Relative Distance

Expressions have now been derived which indicate the relationship of the Voyager and the OEC orbits — the velocities, periods and relative ranges. The purpose of this discussion is to parametrically relate these system characteristics. A major point of emphasis is to reveal the magnitude of OEC velocity increment to maintain the minimum communication ranges for the mission as well as relating these results to launch locations on the Voyager orbiter.

Separation distance on a per orbit basis is given by combination of Equations 2-65 and 2-50:

$$\delta S = \frac{3PaV_o^2}{\mu} \delta V \quad (2-70)$$

This expression implicitly assumes that Voyager does not perform any orbital change maneuvers during the orbit. In addition, the influence of differential drag acting on the two vehicles has been studied and discussed in Section 2.2. The result is a negligible separation over the mission lifetime.

Now the results desired can be pursued. The nominal orbit altitudes of 10,000 km to 1000 km are selected as representative of the general results. This orbit has a period of 7 hours and over the 6 months makes a total 612 revolutions about Mars. Therefore, the separation distance at the completion of the mission is given by

$$\delta S = \frac{1836PaV_o^2}{\mu} \delta V \quad (2-71)$$

Figure 2-54 shows the maximum separation distance (OEC relative to Voyager) at the end of 6 months as a function of  $\alpha$ , the angle between the separation direction and the orbital velocity vector. The worst case separation conditions are assumed. This is true if separation takes place at a true anomaly  $\nu = 75$  degrees. Separation velocities up to 0.2 fps are commensurate with ranges up to 6000 km after the 6 months. Ranges less than this magnitude appear to be reasonable for the co-orbital communication system. The orbit change mission is not constrained to these minimum ranges because of the more flexible communication system contemplated.

Crossplotting the results shown in Figures 2-49 and 2-54, a curve (Figure 2-55) is generated which represents the maximum separation distance as a function of the location of the OEC on the Voyager. The orbit is assumed to be at a 45 degree inclination with respect to the ecliptic.

These results are generated for the class of orbit nodal crossings for the given inclination. This is done because of the broad nature of the possible Voyager orbits. Figure 2-55 thus represents a number of solutions to the

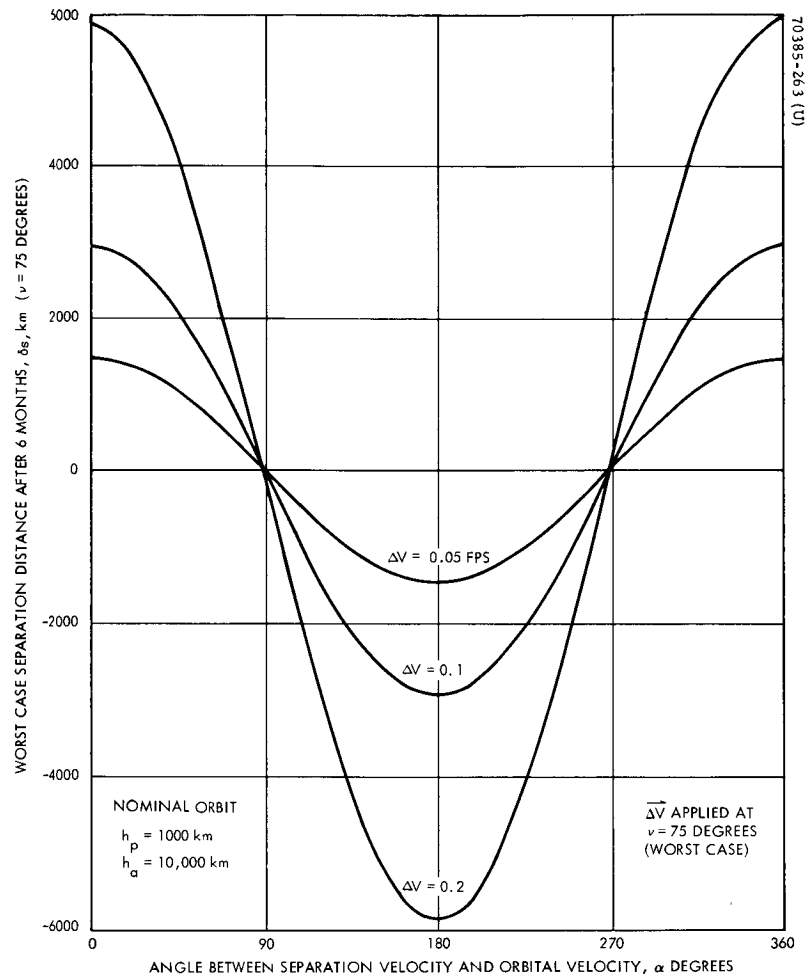


Figure 2-54. Separation Distance After 6 Months as Function of  $\alpha$

problem of finding locations on the Voyager that provide the desirable separation aspect geometry, and minimum range for a separation velocity of 0.1 fps. Results are similar in nature at other  $\Delta V$ .

For a specified  $\Gamma$ , the maximum separation distance after 6 months will be somewhere in the shaded region, regardless of the location of the ascending node of the orbit in the ecliptic. As an example of the utility of Figure 2-55, consider locating the OEC at  $\Gamma = 76$  degrees. The figure shows that, depending on the location of the node of the Voyager orbit, the separation distance after 6 months will be in the range 1500 to 2500 km. Of course, this is true only for  $\Delta V = 0.1$  fps and  $i_e = 45$  degrees. As  $i_e$  varies, a broader range of possible relative locations is generated.

It should be noted that care has already been taken to exclude the locations on Voyager which correspond to points where the separation distance is unacceptably small. This is shown as a function of the position on Voyager where  $|\theta| \approx 90$  degrees, and recalling that  $\theta \leq \alpha \leq 180 - \theta$ .

#### 2.3.6 Relative Motion

The treatment given earlier can now be extended to the motion of the OEC relative to Voyager as seen in a Voyager fixed coordinate system. Two cases are cited and illustrated in Figure 2-56.

The relative Voyager-OEC motion is determined by the magnitude and direction of the relative velocity imparted to the OEC at separation. The trajectory of the OEC, relative to the Voyager, is essentially an ever-widening spiral. The  $Y_1'$  and  $X_1'$  axes in this figure are simply in-plane axes directed along and normal to the radius vector from Mars to Voyager, at apoapsis of the orbit. The rate of growth of this spiral, as pointed out earlier, is determined by the differences in orbital period between the OEC and Voyager — caused almost entirely by the component of the separation velocity lying parallel to the orbit velocity at separation. The maximum range depends both upon the magnitude of the separation velocity and upon the point in the orbit at which separation occurs. Figures 2-54 and 2-55, as described previously, specify the range of possible separation distances for the assumed nominal orbit.

Case A presumes there are components of velocity added along the Voyager orbital vector as well as normal to it. After an initial period of "straight line motion," the OEC moves about the Voyager in an increasing spiral motion. The rate of growth of this spiral is determined by the differences in the orbit period between OEC and Voyager — caused predominantly by the parallel component of velocity (along  $V_0$ ).

Case B has no component of velocity normal to the orbit velocity vector; however, as seen, it exhibits the same rate of increase in distance from Voyager after the initial orbit. Although the figure shows a planar case, the component of separation velocity perpendicular to the orbit velocity can be in or out of the orbit plane.

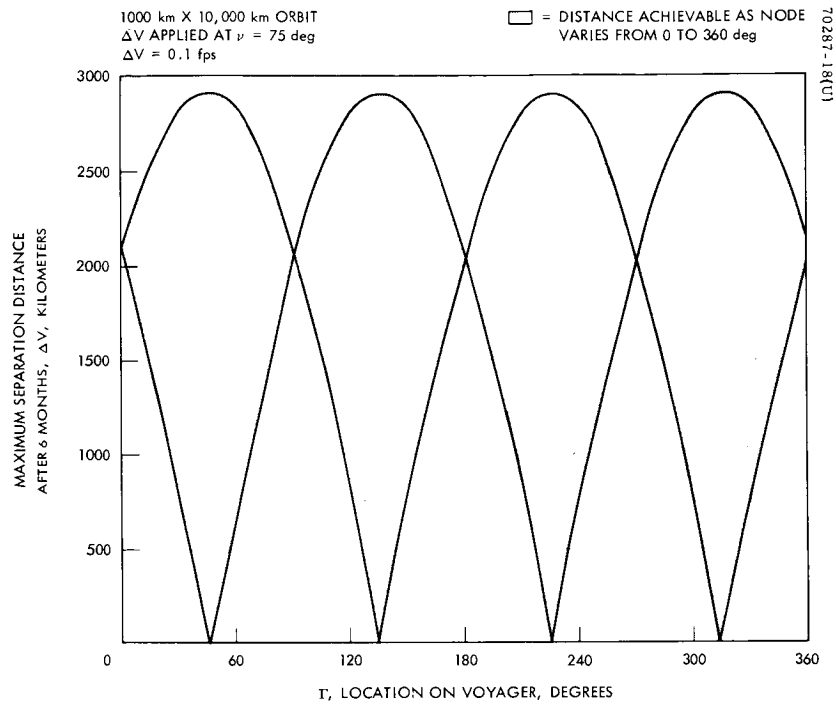


Figure 2-55. Maximum D After 6 Months Versus Location

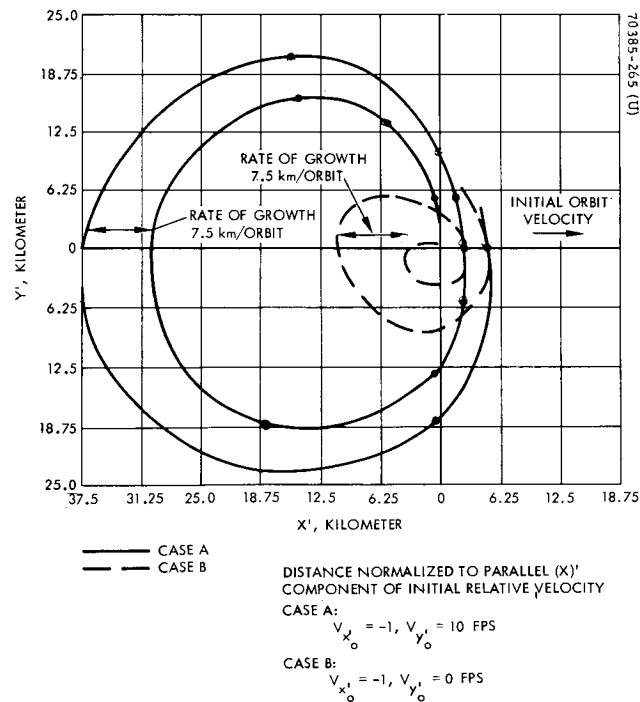


Figure 2-56. Typical OEC Relative Trajectories

## 2.4 SEPARATION STUDIES

### 2.4.1 Methods of OEC Separation

Three basic approaches are possible to place the OEC in a desirable attitude with respect to the Voyager bus. The actual selection is based on the interface possibilities with Voyager, OEC configuration, and OEC mission operation.

The first approach is based on a provision for a spin table to provide spinup prior to separation. This technique is desirable from a stability point of view and in terms of ensuring small attitude errors. However, the requirement to mount a spin table on Voyager is not preferred for several reasons: first, a large clearance envelope is required. Second, the limitations imposed on allowable OEC boom locations to ensure a safe table spinup to 60 rpm are a major consideration.

The philosophy for the OEC design is predicated on minimization of interaction or interface with the Voyager bus. For this reason a preferable approach is to first separate OEC and then provide spinup with an onboard gas system at some safe distance.

A third approach is to impart some angular rotation as well as translation with the separation system, achieving some gyroscopic stiffness. As in the previous approach, full spinup with an onboard gas system is initiated at a safe distance from Voyager.

The rationale for selection of a baseline system requires a detailed study of the configuration, system complexity, and performance. A discussion of the separation techniques follows; the spin table approach is not discussed further in this study.

#### 2.4.1.1 Nonspinning Separation

Nonspinning separation influences the attitude of the OEC through the induced tipoff rates. The final attitude is thus a function of when spinup occurs.

Provision for a small separation velocity for the co-orbital mission requires the precise design and alignment of the separation mechanism. A single-spring separation concept is proposed.

Separation Performance. In carrying forth this analysis, it is assumed that the spring is linear, and thus the following equations representing a spring under simple harmonic motion are applicable. Therefore,

$$\ddot{X} + \frac{k}{\mu} X = 0 \quad (2-72)$$

where

X = linear displacement of spring

k = spring constant

$$\mu = \text{Voyager - OEC mass ratio} = \frac{M_{\text{OEC}} M_V}{M_{\text{OEC}} + M_V}$$

and the natural frequency of the spring is

$$\omega = \sqrt{\frac{k}{\mu}} \quad (2-73)$$

The solution to Equation 2-72 is simply

$$X = A \sin \omega t + B \cos \omega t \quad (2-74)$$

where  $t$  = time the spring acts on the OEC.

Initially, the spring is compressed to a length  $d$  and at physical separation is fully extended so that the initial conditions are

$$\begin{aligned} X(0) &= d \\ X(t) &= 0 \end{aligned} \quad (2-75)$$

Substitution into Equation 2-74 yields the constants

$$\begin{aligned} B &= d \\ A &= 0 \end{aligned}$$

where for the spring fully extended

$$X = d \cos \omega t = 0 \quad (2-76)$$

and for this to hold

$$\omega t = \pi/2 \quad (2-77)$$

Since the natural frequency is known (Equation 2-73), Equation 2-77 can be rewritten as

$$k = \frac{\pi^2 \mu}{4t^2} \quad (2-78)$$

resulting in an equation representing the time varying nature of the spring. By energy relations, the total mechanical energy of the system remains constant. Equating the potential and kinetic energy gives

$$K.E. = \frac{1}{2} M \Delta V^2$$



$$P.E. = \frac{1}{2} k X^2$$

so

$$k = \frac{(\Delta V)^2}{X^2} \mu \quad (2-79)$$

where  $\Delta V$  = spring velocity and the relationship to position is apparent.

Equations 2-78 and 2-79 are plotted in Figures 2-57 and 2-58. Typically, for a velocity increment of 0.1 fps at separation, a few iterations lead to selection of a spring constant of

$$k = 150 \text{ lb/ft} = 12.5 \text{ lb/in}$$

and from the graphs

$$X = 0.168 \text{ inch}$$

$$t = 0.23 \text{ second}$$

Application of a nomograph appearing in Reference 11 leads to the following spring selection:

Mean coil diameter	4.0 inch
Free length of helix	3.2 inch
Number of active coils	7.0
Maximum stress with 2.1 pound axial load	2.5 ksi

A cross section of the coil is illustrated in Figure 2-59. The zero-twist spring is selected to minimize any lateral or rotational motion during separation. Reference 11 indicates that side force is negligible and that there is essentially no lateral spring constant for the zero-twist type spring proposed.

Attitude Accuracy. An illustration of the OEC mounting for a nonspinning separation is shown in Figure 2-60.

Errors in precisely performing separation are due to several effects:

- Transverse misalignments
- Angular misalignments
- Effects of side force
- Effects of interferences

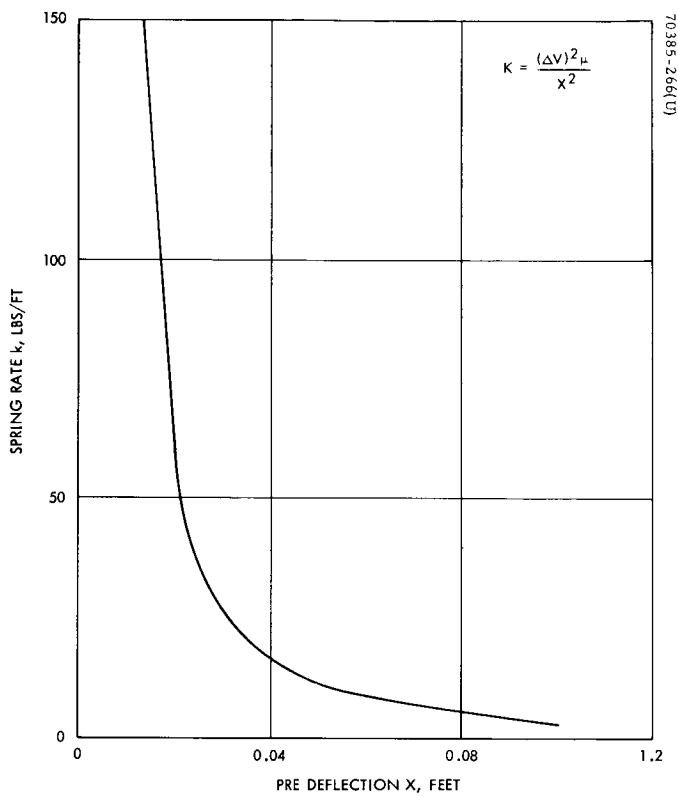


Figure 2-57. Plot of Equation 2-81

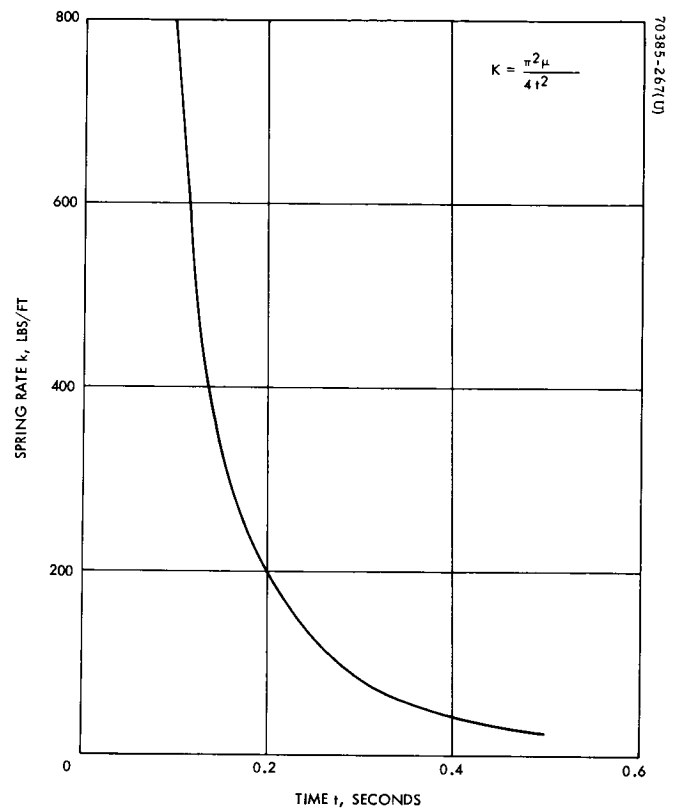


Figure 2-58. Plot of Equation 2-82

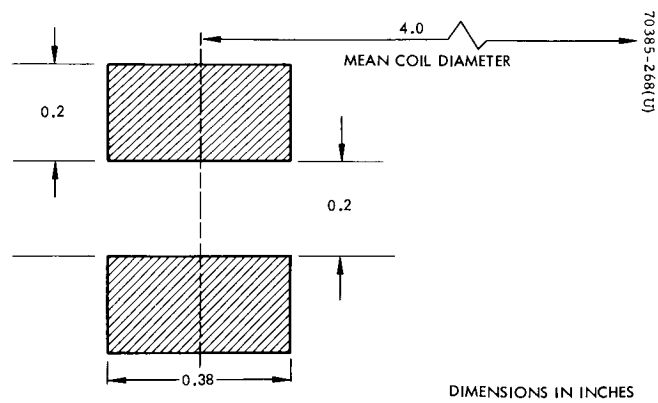


Figure 2-59. Coil Cross Section

The transverse misalignment "a" simulates assembly tolerances and center of mass uncertainty, whereas the angular misalignment "b" represents spring manufacturing tolerances and spring end location and squareness tolerances.

The first and second factors are the major contributors and for a worst case accuracy analysis can be assumed to contribute disturbances about the same transverse axis. For this case, these errors illustrated in Figure 2-61 combine to produce a misalignment factor E,

$$E = \sqrt{\left(\frac{a}{\ell}\right)^2 + (\sin b)^2} \quad (2-80)$$

where

$\ell$  = distance from CM to spring point of contact

a = transverse offset from CM at the base point

b = angular offset from nominal applied force at base point  
for small angular deviations

$$E = \sqrt{\left(\frac{a}{\ell}\right)^2 + b^2} \quad (2-81)$$

Errors representing typical alignment accuracies are substituted into Equation 2-81; for

$$a = 1/16 \text{ inch}$$

$$b = 1 \text{ degree}$$

with

$$\ell = 18 \text{ inches}$$

the misalignment function

$$E = 1.8 \text{ percent} \quad (2-82)$$

The misalignment factor given above is actually smaller since the two sources of error cited act about different axes. In any event, it is expected that a reduction can be made by providing accurate assembly tolerances and precision calibration and selection of the spring.

The effect of a misaligned separation force is a torque about an axis transverse to the OEC spin axis. The equation for the angular motion is

$$\ddot{\theta} = \frac{T}{I} \quad (2-83)$$

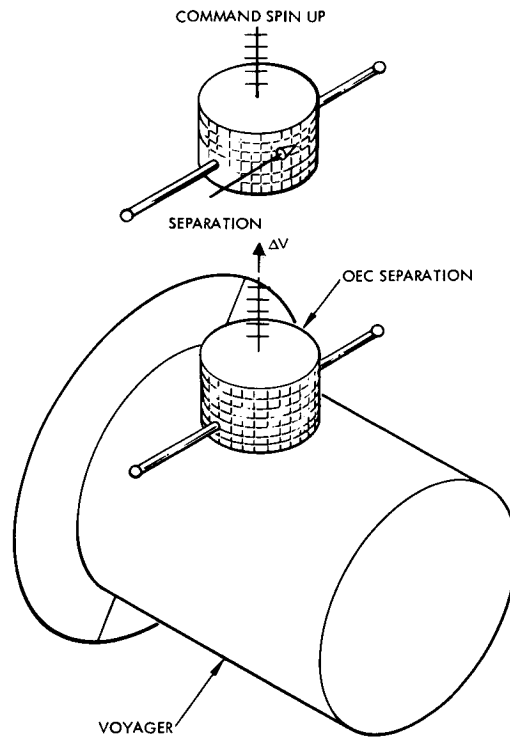


Figure 2-60. Nonspinning Separation

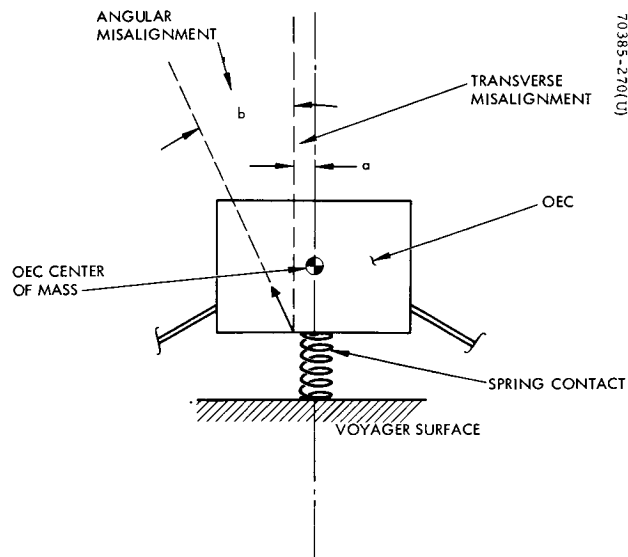


Figure 2-61. Spring Misalignments

where

$T$  = torque applied about the transverse axis

$I$  = moment of inertia about a transverse axis

For this analysis, the effect of the lateral spring force is accounted for but the lateral spring constant is assumed negligible; thus

$$T = F_x a \cos \sqrt{\frac{k}{\mu}} t + F_z c \quad (2-84)$$

where  $c$  = moment arm about  $Z$  axis.

Substitution of Equation 2-84 into 2-83 and integrating gives

$$\dot{\theta} = \frac{F_x a}{I} \sqrt{\frac{\mu}{k}} \sin \sqrt{\frac{k}{\mu}} t + \frac{F_z c}{I} ct \quad (2-85)$$

Numerical values of expected parameters are substituted into Equation 2-85 to obtain the maximum tipoff rate. Thus,

$$\begin{aligned} F_x &= kX \\ &= (150 \text{ lb/ft})(0.014 \text{ foot}) \\ &= 2.1 \text{ pounds} \\ I &= 2.5 \text{ slug-ft}^2 \text{ (minimum transverse inertia)} \\ \mu &= 3.0 \text{ slugs (assume a 100 pound OEC)} \\ \omega &= \sqrt{\frac{k}{\mu}} = \left(\frac{150}{3.0}\right)^{1/2} = 7 \text{ rad/sec} \\ t &= 0.22 \text{ second} \end{aligned} \quad (2-86)$$

Assuming the force in the  $z$ -direction is 5 percent of the axial force

$$F_z = 0.01 \text{ pound}$$

and

$$c = 17.5 \text{ inches}$$

By substitution of these parameters into Equation 2-85, the rate in terms of the transverse offset  $a$ , is

$$\dot{\theta} = (0.12a + 0.0012) \text{ rad/sec} \quad (2-87)$$

where  $a$  is in feet.

Selection of a safe distance at which to spin up limits the maximum allowable attitude error. This choice is based on guaranteeing non-interaction of the OEC booms with the bus at injection. For example, assume that the minimum separation distance prior to spinup is 10 feet and the separation velocity is 0.1 fps. Substitution of the spring misalignment of 1/16 inch into Equation 2-87 yields at tip-off rate of

$$\dot{\theta} = 0.1 \text{ deg/sec} \quad (2-88)$$

Allowing this rate error to increase over a 100 second interval creates an error in OEC attitude of 10 degrees.

Reduction of this error requires increasing the accuracy of the separation system.

Reflecting back on the mission requirements, it is noted that the attitude error using this form of separation can be greater than the  $\pm 5$  degree accuracy specification. Therefore, application for a nonspinning separation for the co-orbital mission would require the addition of an on-board attitude correction system. An alternative is to reassess the basic accuracy requirements based on the nonspinning separation accuracies. The considerations for incorporating a correction system are discussed in the attitude control section 2.7.

To complete this phase of the analysis, the lateral motion due to spring force neglecting the lateral spring constant is determined. The equation of motion is

$$\mu \ddot{z} = bF_x \cos \sqrt{\frac{k}{\mu}} t + F_z \quad (2-89)$$

for  $b \ll 1$ .

Integrating Equation 2-89 once with  $\dot{z}(0) = 0$

$$\mu \dot{z} = bF_x \sqrt{\frac{\mu}{k}} \sin \sqrt{\frac{k}{\mu}} t + F_z t \quad (2-90)$$

Assuming  $b \approx 0.5$  degree yields

$$\dot{z}(t) = 0.0022 \text{ fps at } t_s = 0.22 \text{ second}$$

and after 100 seconds or at spinup the lateral motion is

$$z(100) = 0.48 \text{ ft} = 5.8 \text{ inches} = 14.7 \text{ cm}$$

Thus the translational motion due to the separation system tolerances is small.

#### 2.4.1.2 Partial Spin Separation

Constraining the attitude error to less than  $\pm 5$  degrees over the 6 month co-orbital mission requires the investigation of another approach for separation. In the nonspinning separation, the prime moving force is along the OEC spin axis, and errors build up about either or both transverse axes. For the alternative method, to be discussed below, the prime separation force is normal to the spin axis.

As shown in Figure 2-62, the applied force lies in the center of mass plane and is offset from the center of mass by a distance limited by the radius of the OEC structural cylinder. The objective of this form of separation is not only to impart a translational impulse to yield the desired  $\Delta V$ , but in addition to build up sufficient spin momentum to provide gyroscopic stability.

The influence of a separation impulse misalignment is to build up a small free precession or nutation of the OEC body axis about the angular momentum vector. In addition, an incremental attitude deviation is developed but is small compared to that from a nonspinning separation.

Either axial or radial boom configurations can be used with this scheme; however, the axial boom lends itself better to this form of separation. For this reason, the discussion will appear to favor that configuration. A detailed discussion and analysis follows.

Requirements. The requirements basic to the nonspinning separation are also necessary to the partial spin form of separation. All of the spring characteristics identified in prior discussion are also applicable. The spring force and impulse period to impart a nominal velocity of 0.1 fps are

$$F = 2.1 \text{ pounds}$$

$$t = 0.22 \text{ second}$$

Spin Stability Analysis. Determination of the attitude error induced at separation with the partial spin technique requires the solution of the rotational equations of motion. The general form of these equations is as follows:

$$\begin{aligned} I_x \dot{\omega}_x + (I_z - I_y) \omega_y \omega_z &= M_x \\ I_y \dot{\omega}_y + (I_x - I_z) \omega_x \omega_z &= M_y \\ I_z \dot{\omega}_z + (I_y - I_x) \omega_x \omega_y &= M_z \end{aligned} \tag{2-91}$$

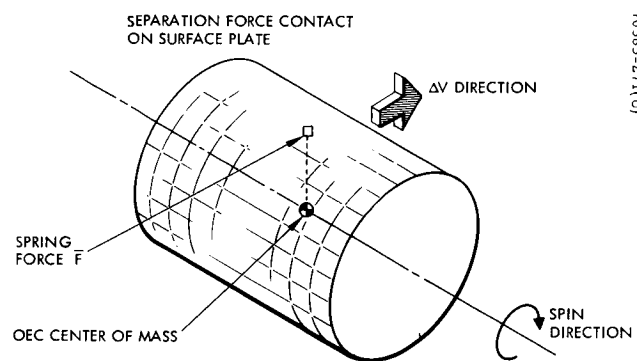


Figure 2-62. Partial Spin Separation



where

$I_x, I_y, I_z$  = OEC moments of inertia

$\omega_x, \omega_y, \omega_z$  = OEC body rates

$M_x, M_y, M_z$  = externally applied torques

This set of equations requires specifying the moments caused by the separation impulse.

Figure 2-62 illustrates the application of the separation force for the partial spin separation technique. The torque is applied at a distance  $\bar{r}$  from the center of mass and is given by

$$\bar{M} = \bar{r} \times \bar{F} \quad (2-92)$$

where

$$\bar{r} = l \hat{e}_r + a \hat{e}_z \quad (2-93)$$

$$\bar{F} = F (\sin b \hat{e}_z + \cos b \hat{e}_t) \quad (2-94)$$

and

$l$  = distance from center of mass to point of impulse application

$a$  = linear misalignment

$b$  = angular misalignment

$F$  = separation force

Carrying out the multiplication

$$\bar{M} = -lF \sin b \hat{e}_t + lF \cos b \hat{e}_z - a F \cos b \hat{e}_r \quad (2-95)$$

which indicates that the torque applied about the spin axis is

$$M_z = lF \cos b \quad (2-96)$$

and that about each of the transverse axes is

$$M_r = -a F \cos b \quad (2-97)$$

$$M_t = -lF \sin b \quad (2-98)$$

Note that the separation force essentially applies a torque impulse and

$$\begin{aligned} M_r &\sim M_x \\ M_t &\sim M_y \end{aligned} \quad (2-99)$$

where the subscript x and y can refer to an inertial reference rather than the body reference.

Substitution into the equations of motion with the applied torques presented above and the following parameters

$$I_x = I_y = 5 \text{ slug-ft}^2$$

$$I_z = 7.5 \text{ slug-ft}^2$$

$$a = 1/16 \text{ inch}$$

$$b = 1.0 \text{ degree}$$

yields

$$5\dot{\omega}_x + 2.5 \omega_y \omega_z = 0.0035 M_z \quad (2-100)$$

$$5\dot{\omega}_y - 2.5 \omega_y \omega_z = 0.0167 M_z \quad (2-101)$$

$$7.5 \dot{\omega}_z = M_z \quad (2-102)$$

Solving the last equation where  $M_z$  is treated as an impulse of finite but short duration

$$\omega_z = \frac{M_z}{7.5} t \quad (2-103)$$

which is substituted back into Equations 2-100 and 2-101

$$\dot{\omega}_x + 4.4 \times 10^{-2} \omega_y = 0.0007 M_z \quad (2-104)$$

$$\dot{\omega}_y - 4.4 \times 10^{-2} \omega_x = 0.0033 M_z \quad (2-105)$$

The solution for  $\omega_x$  and  $\omega_y$  gives

$$\omega_x = 0.013 \text{ deg/sec}$$

and

$$\omega_y = 0.126 \text{ deg/sec}$$

and the transverse body rate is found by taking the square root of the sum of the squares,

$$\begin{aligned}\omega_T &= (\omega_x^2 + \omega_y^2)^{1/2} \\ &= 0.127 \text{ deg/sec}\end{aligned}\tag{2-106}$$

The nutation buildup from this torque impulse is obtained from the relationship

$$\tan \Theta = \frac{H_T}{H_S}\tag{2-107}$$

where

$H_T$  = transverse angular momentum

$H_S$  = spin angular momentum

Thus

$$\tan \Theta = \frac{I_T \omega_T}{I_S \omega_s}\tag{2-108}$$

where

$I_T$  = transverse moment of inertia

$I_S$  = spin axis moment of inertia

By realizing that the rate about the x-axis is small compared to the y-axis, a simplification can be made.

If  $\omega_x \sim 0$  and  $\dot{\omega}_x = 0$ , then the transverse equation of motion is simply

$$I_T \dot{\omega}_T = I_{yy} \dot{\omega}_y = M_y\tag{2-109}$$

but

$$M_y = E M_z \quad (2-110)$$

where  $E$  = percent torque coupled into transverse axis due to a misalignment, and

$$I_s \dot{\omega}_s = M_z \quad (2-111)$$

Since the separation produces a torque impulse, the following can be written:

$$H_T = I_T \omega_T = M_y / t = E M_z / t \quad (2-112)$$

and

$$H_S = I_S \omega_S = M_z / t \quad (2-113)$$

Substitution of Equations 2-112 and 2-113 into 2-108 gives

$$\tan \theta = E \quad (2-114)$$

or simply stated, assuming the action of a torque impulse, the nutation angle is equivalent to the attitude error and is identically the misalignment errors of the spring system. Thus

$$\theta = \tan^{-1}(E) \quad (2-115)$$

Substitution of the maximum expected  $E$  value of 1.8 percent yields an attitude error of approximately

$$\theta = 1.0 \text{ degree}$$

which is within the desired accuracy

In summary, there are two basic reasons why this form of separation is more desirable than a nonspinning separation.

- First, the attitude errors are small and can be linearly reduced by precise alignment procedures.
- Second, the final spinup can be delayed until adequate safety margin is provided.

Thus, as a result of this analysis, the more desirable co-orbiter OEC configuration is the one with booms mounted along the spin axis. If it were possible to violate the Voyager Lander envelope, then an OEC with transverse booms could also apply this partial spinup technique.

#### 2.4.1.3 Separation System Design

Careful consideration of the separation mechanism to be selected for the coorbital OEC version is required to ensure minimum tipoff, accurate separation velocities, high reliability, long space life capability, and integrity of the system to survive the launch and boost phase environments. These requirements are not as severe for a mechanism producing larger separation velocities.

Before discussing the actual mechanism, the interface with Voyager is discussed since the design of the OEC configuration is interrelated with Voyager and the manner of separation.

Stowage of the OEC on the Voyager bus is confined to the space available between the Voyager bus structure and the dynamic shroud envelope of the launch vehicle. In addition, the OEC must be located longitudinally alongside the Voyager-Orbiter between the plane of the solar array and at the base of the spacecraft and the interface of the spacecraft with the Lander capsule. Within this region, there are four basic modes of separating the OEC from Voyager. Ramifications of the types of separation systems for each of these modes are possible, such as delayed spinup requirements, partial spinup capability, and full spinup capability. The four separation conditions are noted in Table 2-8 as Mode 1A and 1B and Mode 2A and 2B, with an itemized list of the advantages and disadvantages for each case.

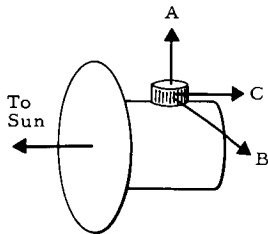
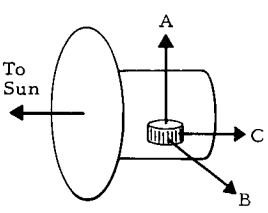
In summary, there exists only one OEC configuration, with a fixed length axial boom separated in the manner indicated as Mode 1A and 2A, that could be spunup immediately after separation due to the clearances available with the Voyager spacecraft. Mode 2A could employ an axial boom in the order of 6 feet long while Mode 1A limits the boom length to about 2.5 feet due to the launch vehicle shroud envelope constraint. For OEC configurations employing deployable booms, either axially or radially mounted, immediate spinup offers no clearance problems. Partial spinup is considered most realistically for Modes 1B and 2B. The separation force is purposely applied off the OEC center of mass to impart a spin rate as well as the separation velocity.

Techniques for providing a partial spin, such as Mode 1A and 2A, where the torque for spinup is required in a plane normal to the separation velocity vector, appear undesirable due to the additional mechanization required for such systems, i.e., spin table, helix guide rails, multiple canted springs, etc.

Ideally, a configuration with fixed length booms (either axially or radially mounted) that could be spun up immediately after separation would be most desirable. For booms in the order of 5 to 6 feet in length, there exists immediate spinup capability for 1) the axially mounted boom configuration separated in Mode 2A and 2B manner or 2) radially mounted booms, assuming that the Voyager space envelope is not restricted in the vicinity of the shroud at the Voyager-Lander interface, Mode 1A and 1B. Figures 2-63 and 2-64 depict both these concepts.

Figure 2-65 depicts the possible separation geometries of the OEC relative to the Voyager spacecraft. Assuming that the location of the OEC is constrained to the volume adjacent to the Voyager bus between the solar array plane and the Lander capsule bus interface, less complex supporting hardware is required to accomplish "radial" (Mode 1A and 2B) rather than tangential (Mode 1B and 2B)

TABLE 2-8. COMPARISON OF SEPARATION CONCEPTS

Type of System	Description	Advantages	Disadvantages
<p><b>MODE 1</b></p> <p>Spin Axis Normal to Voyager Bus</p> 	<p><u>Mode 1A</u></p> <p>Separation velocity imparted to OEC along spin axis.</p> <p><u>Mode 1B</u></p> <p>Separation velocity imparted to OEC transverse to spin axis.</p> <p><u>Mode 1C</u></p> <p>Not feasible due to Lander-Voyager interface envelope.</p>	<p><u>Mode 1A</u></p> <ol style="list-style-type: none"> <li>1) Minimum clearance window on Voyager bus required.</li> <li>2) Minimum perturbation to Voyager since separation force can be more closely aligned with Voyager cg.</li> <li>3) Requires only simple mounting adapter to Voyager bus structure.</li> <li>4) Long (approximately 6-foot fixed radial booms may be considered.</li> <li>5) Stowed booms (either radial or axial) permit immediate spinup of OEC.</li> <li>6) Launch loads path to Voyager bus structure is desirable.</li> </ol> <p><u>Mode 1B</u></p> <p>Stowed booms (either radial or axial) permit immediate spinup of OEC.</p>	<p><u>Mode 1A</u></p> <ol style="list-style-type: none"> <li>1) Fixed radial booms imply delayed spinup of OEC until clear of Voyager envelope to avoid collision.</li> <li>2) Only a short (approximately 2 to 3 foot) fixed axial boom can be considered due to the shroud envelope constraint.</li> <li>3) Deployable radial single hinged booms limited to 4.5 feet.</li> </ol> <p><u>Mode 1B</u></p> <ol style="list-style-type: none"> <li>1) Support structure weight increase and inefficient load path to Voyager structure.</li> <li>2) Larger clearance window on Voyager bus required.</li> <li>3) Longer delay in spinup required to clear Voyager envelope for fixed radial booms.</li> <li>4) Separation force cannot be aligned with Voyager cg.</li> </ol>
<p><b>MODE 2</b></p> <p>Spin Axis Tangential to Voyager Bus</p> 	<p><u>Mode 2A</u></p> <p>Separation velocity imparted to OEC along spin axis.</p> <p><u>Mode 2B</u></p> <p>Separation velocity imparted to OEC transverse to spin axis.</p> <p><u>Mode 2C</u></p> <p>Not feasible due to Lander-Voyager interface envelope.</p>	<p><u>Mode 2A</u></p> <ol style="list-style-type: none"> <li>1) Permits using long (approximately 6 foot fixed axial boom allowing immediate spinup of OEC.</li> </ol> <p><u>Mode 2B</u></p> <ol style="list-style-type: none"> <li>1) Minimum clearance on Voyager bus required.</li> <li>2) Minimum perturbation to Voyager since separation force can be more closely aligned with Voyager cg.</li> <li>3) Requires only simple mounting adapter to Voyager bus structure.</li> <li>4) Stowed radial or fixed axial booms permit immediate spinup of OEC.</li> <li>5) Launch load path to Voyager bus structure is desirable.</li> <li>6) Single hinged long booms (approximately 8 foot) may be stowed parallel to OEC spin axis, allowing immediate spinup clearance.</li> </ol>	<p><u>Mode 2A</u></p> <ol style="list-style-type: none"> <li>1) Support structure weight increase and inefficient load path to Voyager structure.</li> <li>2) Larger clearance window on Voyager bus required.</li> <li>3) Longer delay in spinup required to clear Voyager envelope for fixed radial booms.</li> <li>4) Separation force cannot be aligned with Voyager cg.</li> <li>5) Fixed radial booms limited to approximately 3 feet by Lander.</li> </ol> <p><u>Mode 2B</u></p> <ol style="list-style-type: none"> <li>1) Fixed radial booms limited to maximum length about 3 feet.</li> <li>2) Fixed radial booms imply delayed spinup of OEC.</li> </ol>

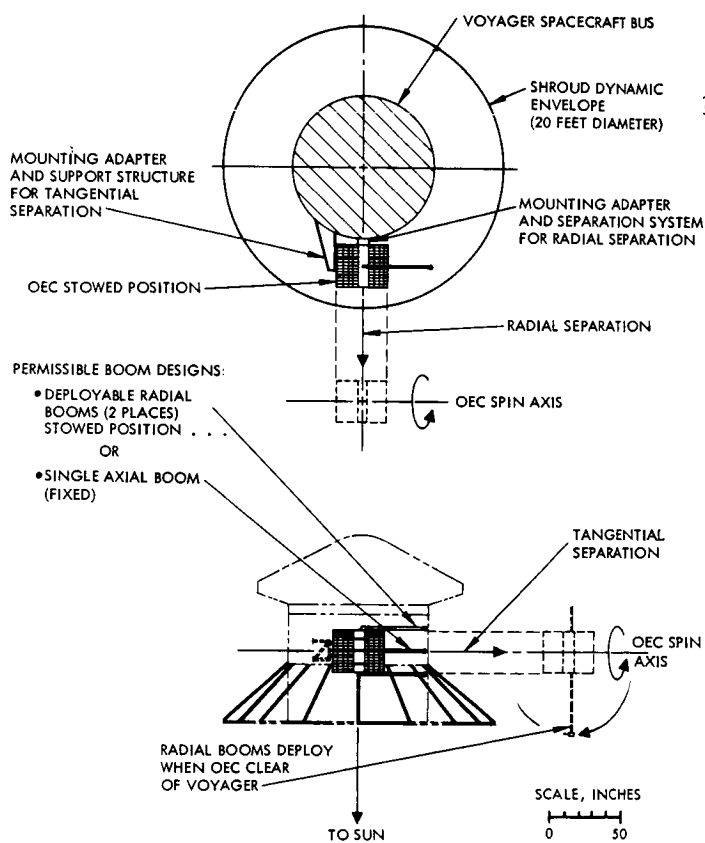


Figure 2-63. Separation Concept Permitting Immediate Spinup Capability With Fixed Length (5 Foot) Axial Booms

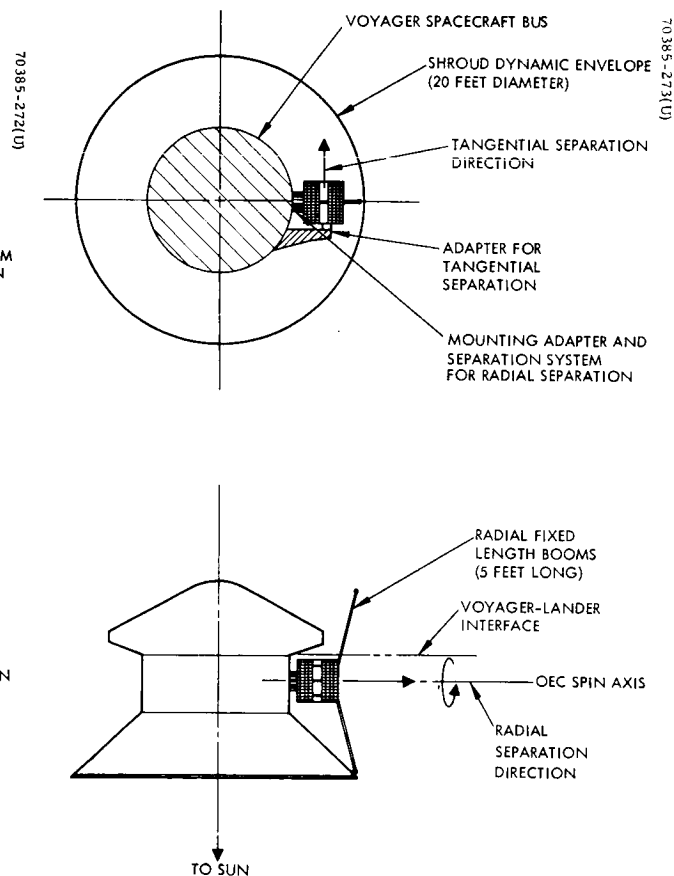


Figure 2-64. Separation Concept Permitting Immediate Spinup Capability With Fixed Length (5 Foot) Radial Booms

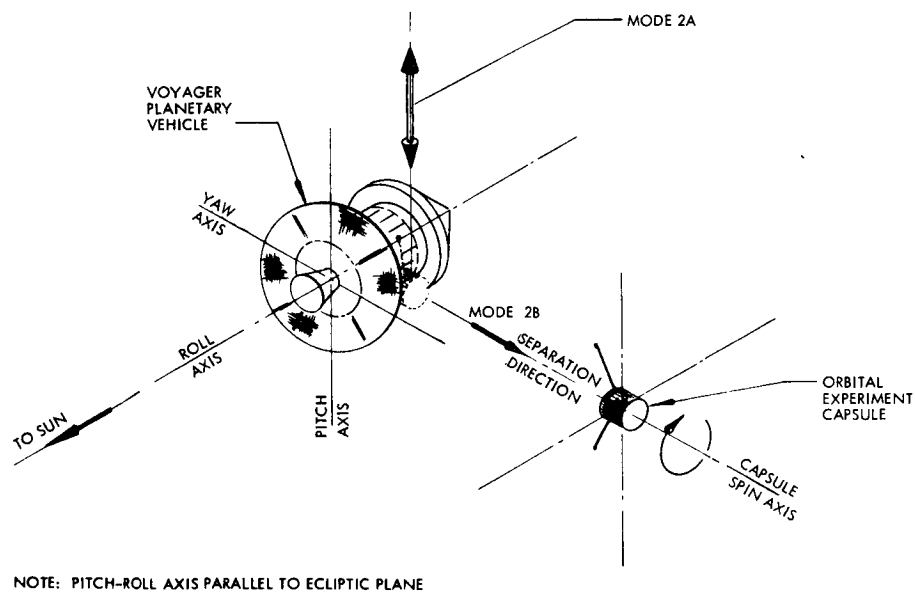
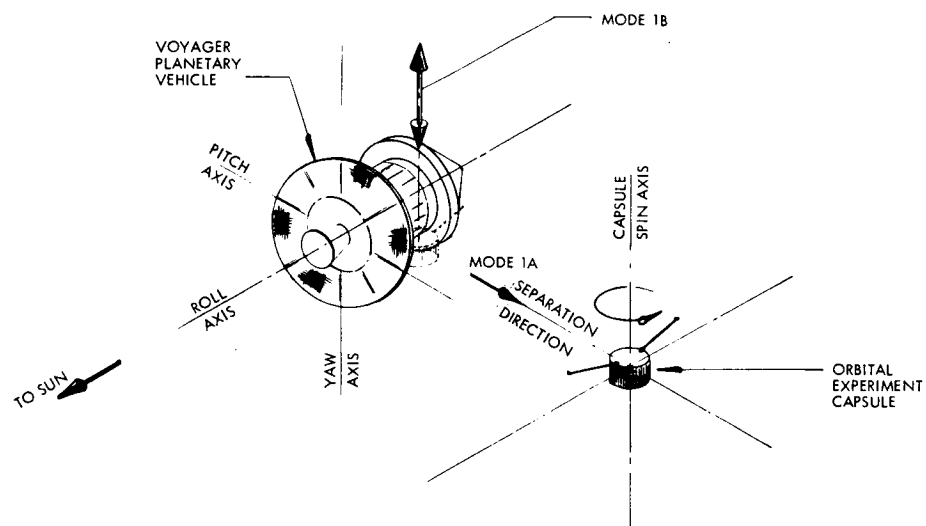


Figure 2-65. Possible OEC-Voyager Separation Geometries



separation. The radial mode of OEC ejection also minimizes the imparted disturbing impulse of separation on the Voyager.

Two separation concepts are shown in Figures 2-66 and 2-67 which utilize nonspinning separation of the OEC by means of central cable tiedown and compression springs on the separation joint periphery. Spring variation, misalignments and lateral loads are key parameters affecting the optimization of such a system.

A system that merits some discussion here is one in which only partial spinup is imparted to the OEC by the separation system. An analytical treatment of such a system is given earlier in this section. Conceivably such a system would provide the separation thrust and some rotational velocity for stability. A simple scheme by which this might be accomplished is depicted in Figure 2-68. In operation, the OEC is attached to Voyager by a tiedown cable at point B, causing a reaction at points A and C. Upon severing the cable, a spring at point C imparts a linear velocity as well as a rotation to the OEC about its normal spin axis. More complex concepts are indicated in Figure 2-69 although in application they would pose increased potential hazards due to the additional mechanisms required. Conceptually this system would employ a central spring-loaded support tube permanently attached to the Voyager bus, and by virtue of a helical race on the tube, initiate some small angular momentum to the capsule while axial motion is induced. For more precise control of the imparted velocity, a motor-driven system could accurately impart the required  $\Delta V$  in conjunction with the rotational motion desired. By virtue of the extremely small separation force required for the separation velocity in the case of the co-orbital system, the component available for initial spinup is considerably reduced, making a central spring force system questionable (alternate A of Figure 2-69). One of the advantages of such a system is the centralization along the spin axis of any possible tipoff inasmuch as they merely impart torque to the OEC while it is "guided" on what might be called a threaded shaft, in the same manner a nut is spun off a bolt. The "thread" lead can be selected to provide a range of specific  $\Delta V$ 's for a given torque.

Configuration Constraints. The following discussion is pertinent to an OEC configuration for the co-orbital mission with a single fixed boom mounted along the spin axis. A number of locations relative to the Voyager bus will satisfy the separation requirement that the OEC be separated from Voyager with its spin axis near normal to the ecliptic plane. Figure 2-70 displays five such positions (noted as A through E) typical of any one quadrant around the Voyager bus peripheral space. Each position imposes the following constraints that vary for the stowage position selected:

- 1) Boom-shroud interference distance ( $l$ )
- 2) Separation distance required for OEC to clear Voyager stowage envelope ( $l$ )
- 3) Angular clearance around Voyager periphery required ( $\beta$ )
- 4) Length of support structure required to attach the OEC to the Voyager bus ( $h$ )

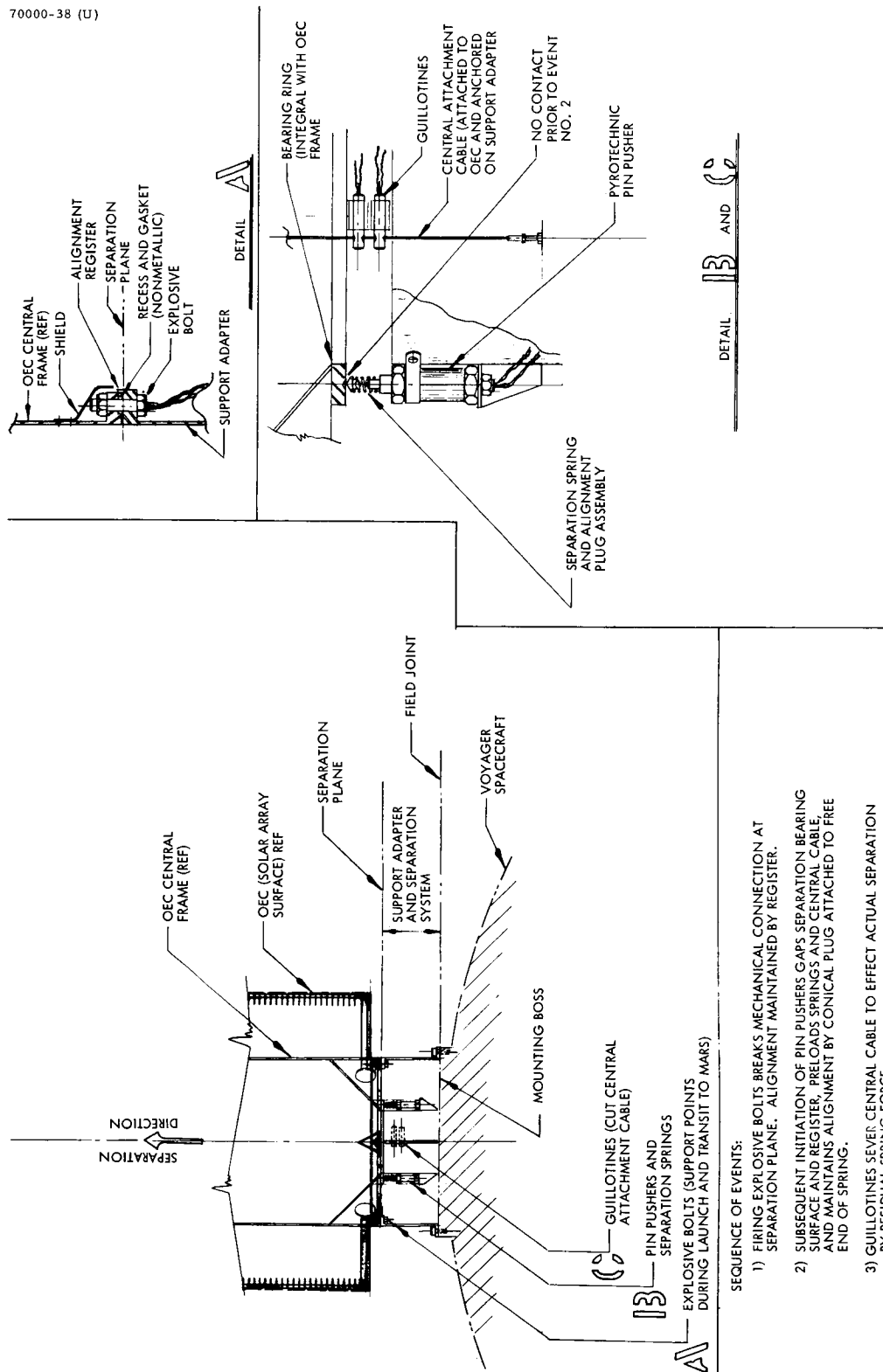


Figure 2-66. Conceptual Design of OEC Separation System

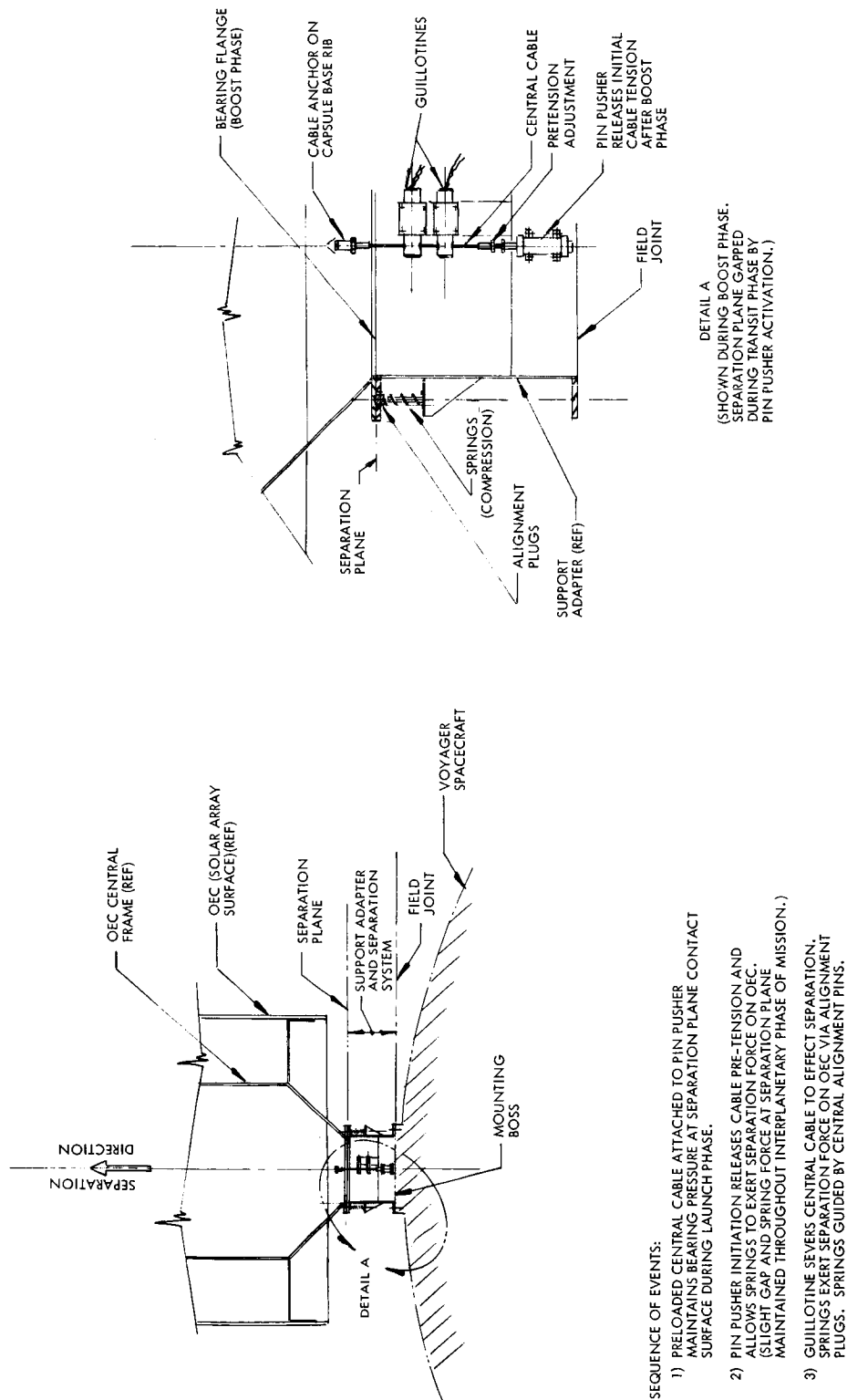


Figure 2-67. Alternate Conceptual Design of OEC Separation System

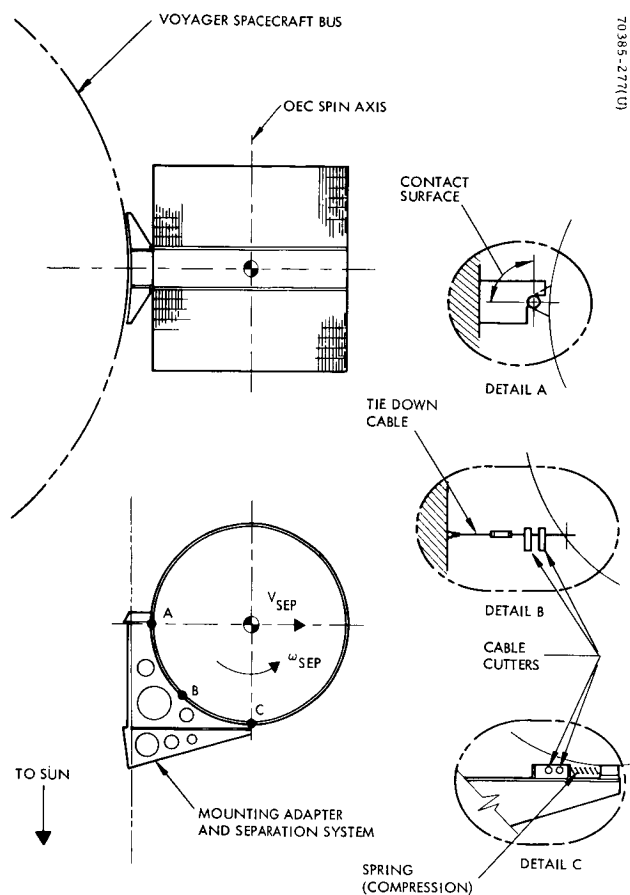


Figure 2-68. Conceptual Separation System With Low Initial Spin Rate Capability

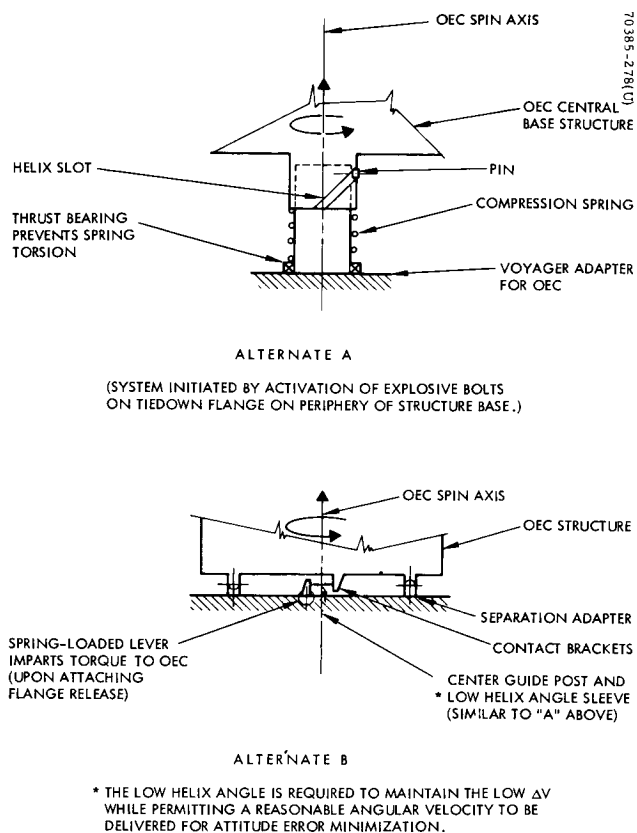
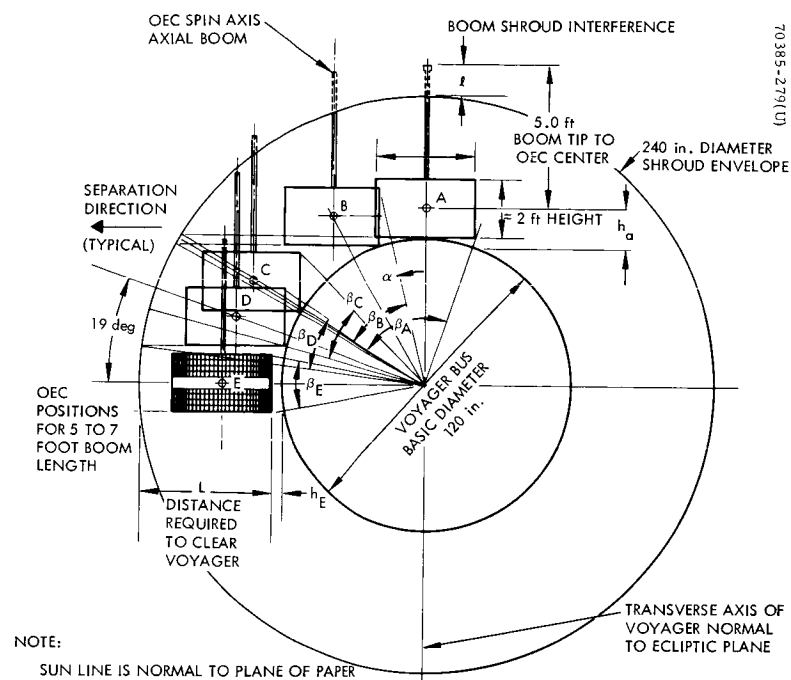


Figure 2-69. Partial Spin Induced Separation Concepts



OEC POSITION	ANGULAR POSITION $\alpha$ , DEGREES	BOOM-SHROUD INTERFERENCE $l$ , FEET	DISTANCE REQUIRED TO CLEAR $L$ , FEET	ANGULAR CLEARANCE REQUIRED $\beta$ , DEGREES	SPAN REQUIRED FOR SUPPORT STRUCTURE $h$ , INCHES
A	0	1.0	10.3	78	18
B	30	1.5	7.0	48	12
C	60	0.8	5.2	31	10
D	71	0	4.9	26	7
E	90	-2.0	4.6	21	5

Figure 2-70. Separation Parameters

The values of the parameters noted are tabulated in Figure 2-70 for the five positions indicated. The nominal OEC configuration was assumed to be a 3.5-foot-diameter cylinder 2 feet in height, with a 5-foot boom measured from the OEC center. The optimum position is clearly position E where all four of the noted constraints are minimized. It should be noted that utilization of a 5-foot (1-1/2 meter) fixed axial boom can only be realized within two 38-degree angular bands on Voyager, symmetrically located about the Voyager transverse axis which is normal to the ecliptic. The ratios of roll to pitch inertia permitting, placement of the OEC on Voyager at Location E could permit the addition of 2 feet to the boom and still stay within the shroud envelope.

The direction of separation indicated common to all the positions shown permits the separation impulse to be imparted off the OEC center of mass so as to provide a small spin rate as well as transverse separation velocity.

Separation Mechanism. Several techniques were investigated that could be employed to provide the separation function. Of the techniques considered, a simple spring force system was selected. A pyrotechnic separation system (such as shaped charges) is considered a poor choice for two reasons: 1) the high degree of uncertainty in alignment associated with the imparted separation impulse and 2) the possibility of deleterious effects of fragments and particles that could damage or cause problems for sensing devices such as the Canopus tracker on the Voyager. Particles or debris have in the past caused temporary loss of tracking, as exhibited on the Mariner IV spacecraft. A third consideration, shock, is an additional factor that would require extensive evaluation and testing.

Although explosive separation devices are available which allow full containment of all of the products and debris from separation, the shock problem remains.

The separation joint contact surfaces could pose potential cold welding problems as a result of the lengthy (12-month) space environment prior to separation of the OEC from Voyager. In a vacuum environment, metal adhesion or cohesion is enhanced for conditions typified by high temperature (above 150°C, high surface contact bearing pressure (80 percent of elastic limit), and friction resulting from relative sliding motion of the surfaces in contact. It has also been found that like metal surfaces bond more readily than unlike metals (Reference 12). The design of the OEC separation joint should therefore avoid design features that would permit these conditions to exist. The preload bearing at the separation joint can readily be controlled by sizing the mating flange to sustain the launch loading environment. Bearing pressures under 500 psi are realizable considering a contact ring approximately 12 inches in diameter by 1/2 inch wide. The possibility of high temperature at the joint is remote, and vibrations at the interface can be accepted by proper design so as not to create joint friction. Additional precaution against bonding could be taken by additionally coating the contact surfaces with an oxide film.

Experiments conducted by Ames Research Laboratory (Reference 13) indicate magnesium alloy as one of the materials least susceptible to cold welding even in the pure metal (oxide-free) contact state. Magnesium should therefore be strongly considered for the joint interface material.

#### 2.4.2 Separation and Spinup Error Analysis

Ideally, the manner in which the OEC's orbit period is changed from that of Voyager is to add or subtract some small velocity. Figure 2-71 illustrates the typical geometry of injection. The injection angle  $\alpha$  controls the component of separation velocity along the orbit velocity vector,  $\Delta V \cos \alpha$ . In reality, the added component parallel to the orbit velocity cannot be controlled perfectly. Errors in the magnitude of  $\Delta V$  and the angle  $\alpha$  must be accounted for in providing for the desired injection parameters. A summary of the sources of errors is as follows:

- Spring errors
- Spring mechanical alignments
- Orbit position uncertainties
- Voyager attitude uncertainties
- Command timing errors

Each of these sources in some way influences the value of the injection velocity component. The variation in the spring characteristics is directly proportional to changes in the magnitude of velocity increment. Misalignments of the spring mechanism tend to create an initial attitude error of the OEC spin axis.

Launch window errors are due to the latter three sources. The uncertainty of the Voyager-OEC orbit creates timing errors since the velocity vector is continually changing direction as well as magnitude. Voyager limit cycle deadband also yields timing errors. Since the attitude of Voyager is changing, so does the orientation of the OEC separation vector with respect to the orbit velocity vector. Finally, the execution errors in commanding separation yield inaccuracies in the launch window. Table 2-9 summarizes these sources of errors along with the worst case standard deviations. The errors are assumed to be gaussian distributed.

Table 2-9 is representative of the components of the uncertainty at separation. There are two additional errors that must be interpreted. Both are from the spinup thrust. One is due to a thrust mismatch while the other is created by jet misalignments. Both sources are discussed below.

##### 2.4.2.1 Spinup Error Analysis

Spinup is to be accomplished by two jets located on the periphery of the OEC and lying in the center of mass plane, as shown in Figure 2-72. Two jets are chosen to eliminate translational motion at spinup by provision of a pure couple. Because of the inherent difficulty of matching and mechanically aligning these thrusters, it is possible that a small translational impulse can be imparted to the OEC. The magnitude of the translational velocity increment is related to the thrust level of the spinup system. Hence, as will be shown, there is a desirable and undesirable level of

TABLE 2-9. SEPARATION AND SPINUP ERRORS

Source of Error	Value (1 sigma)	Comment
Spring	10 to 20% V	Possibly due to thermal variations over transit phase
Mechanical alignments	$\pm 0.5$ degree	Alignment of OEC $\Delta V$ on Voyager
Orbit position uncertainty	$\pm 4$ degrees	For maximum Voyager position volume $\pm 50$ km
Attitude errors	$\pm 0.7$ degree	Maximum Voyager attitude error in two axes, deadband $\pm 0.5$ degree
Timing errors	Negligible	50 millisecond error in execution

thrust can be chosen. This, however, requires that consideration be given to the minimization of attitude errors which build up over long spinup durations when low thrust is applied. Curves illustrating both the nutation angle and attitude error buildup following spinup as a function of the initial tip rates at separation and the thrust level selected are shown in Figures 2-73 and 2-74. These results, developed in Section 2.7, assume a symmetrical OEC (identical transverse moments of inertia) weighing 75 pounds and having spin axis and transverse moments of inertia of 7.5 slug-ft<sup>2</sup> and 5 slug-ft<sup>2</sup> respectively. A total impulse of 33 lb-sec is required to bring the OEC spin rate up to 60 rpm.

As would be expected, an instantaneous torque impulse would bring the vehicle up to spin speed with a negligible attitude error but with a nutation error. Choice of a lower thrust level, which is commensurate with an increase in spinup time, causes an increase in the attitude errors.

The translational impulse imparted by the mismatch of the spinup jets is treated in detail along with the thrust level selection in the sections to follow.

#### 2.4.2.2 Translational Effects of Spinup

The presence of a slight mismatch in jet thrust and of misalignments peculiar to the mounting of the jets provides a differential thrust effect, and hence the desirable pure couple no longer exists. To analyze the ensuing motion, the jet thrust can be treated as the equivalent to a pair of equal and oppositely directed forces



whose lines of action are separated by a distance providing a pure couple inducing rotation and a force through the center of mass providing a translational effect, as shown in Figure 2-75.

As the thrust is applied over time, the direction of translation will vary. The vector equation representing the translational force is given by

$$\begin{aligned}\overline{\delta F} &= \overline{\delta F}_x + \overline{\delta F}_y \\ &= KF \left[ \cos \theta \hat{e}_x + \sin \theta \hat{e}_y \right]\end{aligned}\tag{2-116}$$

where

$\overline{\delta F}_x$  = component of force in x-direction

$\overline{\delta F}_y$  = component of force in y-direction

$F$  = total spinup force, assumed constant

$K$  = percentage mismatch between pair of thrusters

$\theta$  = angular direction of translation

$\hat{e}_x, \hat{e}_y$  = unit vectors in the x-and y-directions

The force can be written in terms of the velocity as

$$\overline{\delta F} = M \delta \left( \frac{d\overline{V}}{dt} \right)\tag{2-117}$$

Solving for the velocity and integrating

$$\overline{\delta V}_t = M \int_0^t \overline{\delta F} dt\tag{2-118}$$

where the loss of mass due to spinup is assumed to be negligible in comparison to the overall system mass and is treated outside of the integral as a constant. The upper limit of integration represents the total interval of time over which spinup occurs.

Substitution of Equation 2-116 into Equation 2-118 leads to the expression

$$\overline{\delta V}_t = \frac{KF}{M} \int_0^{t_f} \left( \cos \theta \hat{e}_x + \sin \theta \hat{e}_y \right) dt\tag{2-119}$$

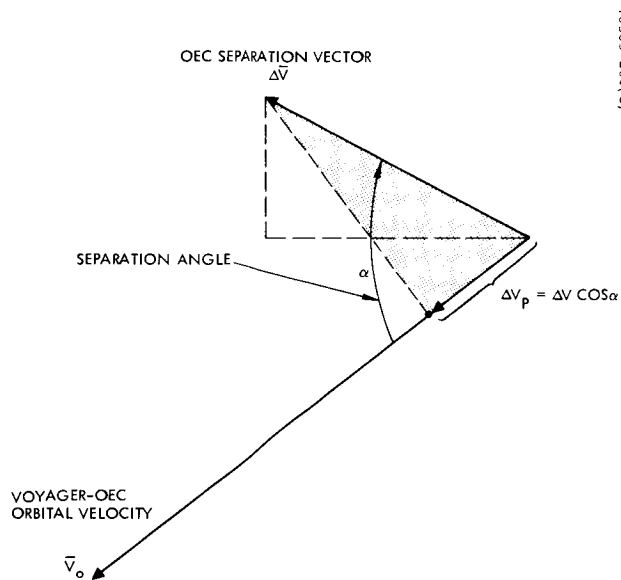


Figure 2-71. Typical Geometry of Injection

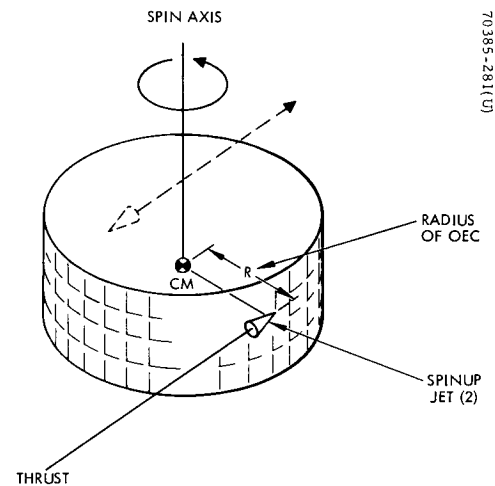


Figure 2-72. Illustration of OEC Spinup

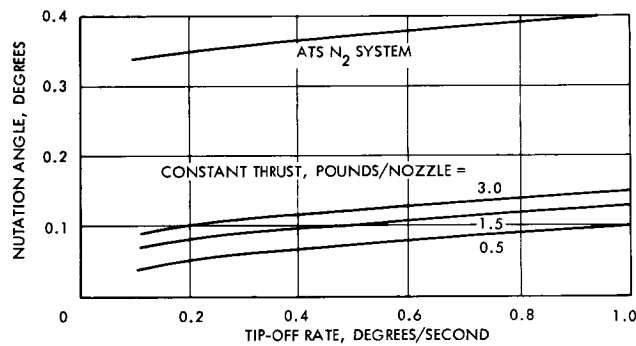


Figure 2-73. Nutation Angle Versus Initial Tipoff Rate

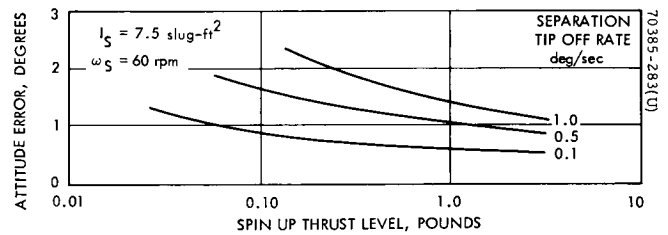


Figure 2-74. Attitude Error as Function of Initial Tipoff Rate and Spinup Thrust

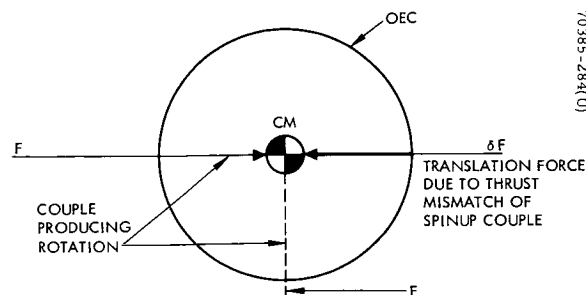


Figure 2-75. Effect of Translational Impulse at Spinup

Solution of this integral requires a relationship for the direction of translation force as a function of time. This is provided by the torque equation

$$T = I\ddot{\theta} \quad (2-120)$$

where

$T$  = applied torque (F) ( $\ell$ )

$I$  = moment of inertia about spin axis

$\ddot{\theta}$  = angular acceleration of body about spin axis

Substituting for torque and assuming a constant thrust spinup

$$T = F\ell \quad (2-121)$$

and rewriting in terms of body acceleration

$$\ddot{\theta} = \frac{F\ell}{I} \quad (2-122)$$

Integrating Equation 2-122 twice and setting the integration constants to zero (assuming quiescent initial conditions) yields

$$\theta = 1/2 \frac{F\ell}{I} t^2 \quad (2-123)$$

Recognizing that the term inside the parenthesis is just the acceleration, Equation 2-123 can be rewritten as

$$\theta = 1/2 \ddot{\theta} t^2 \quad (2-124)$$

Now that the angular position of the body is known as a function of time, it can be substituted into Equation 2-119. Therefore

$$\delta \overline{V}_t = \frac{KF}{M} \int_0^{t_f} \left\{ \cos \frac{1}{2} \ddot{\theta} t^2 \hat{e}_x + \sin \frac{1}{2} \ddot{\theta} t^2 \hat{e}_y \right\} dt \quad (2-125)$$

and by arranging the integral into a more desirable form

$$\delta \overline{V}_t = \frac{KF}{M} \int_0^{t_f} \left\{ \frac{\cos(\frac{1}{2} \ddot{\theta} t^2) \hat{e}_x + \sin(\frac{1}{2} \ddot{\theta} t^2) \hat{e}_y}{\ddot{\theta} t} \right\} (\ddot{\theta} t dt) \quad (2-126)$$

By the change in variable

$$u = \frac{1}{2} \ddot{\theta} t^2$$

$$du = \ddot{\theta} t dt$$

Equation 2-126 is rewritten as

$$\overline{\delta V}_t = \frac{KF}{\sqrt{2\ddot{\theta}M}} \int_0^t \left\{ \frac{\cos u}{\sqrt{u}} \hat{e}_x + \frac{\sin u}{\sqrt{u}} \hat{e}_y \right\} du \quad (2-127)$$

where the coefficients preceding the integral are the assumed constants of the system.

The form of the argument inside the integral is recognized as that of the well known Fresnel integral. This is a definite integral, evaluated over the interval zero to infinity, and has as its solution

$$\int_0^\infty \frac{\cos u}{\sqrt{u}} du = \sqrt{\frac{\pi}{2}}$$

$$\int_0^\infty \frac{\sin u}{\sqrt{u}} du = \sqrt{\frac{\pi}{2}} \quad (2-128)$$

Although the Fresnel integral ranges over infinity, the steady state amplitude of its solution is reached almost instantaneously and the transient position averages out after just a few cycles (a digital simulation confirms these results). Thus its solution can be admitted as the solution to Equation 2-127, where the spinup time is long compared to the transient decay.

Substitution into Equation 2-127 provides the vector solution

$$\overline{\delta V}_t = \frac{KF}{\sqrt{2\ddot{\theta}M}} \left\{ \sqrt{\frac{\pi}{2}} \hat{e}_x + \sqrt{\frac{\pi}{2}} \hat{e}_y \right\} \quad (2-129)$$

and the magnitude of the velocity due to the mismatched spinup jets is given by

$$|\overline{\delta V}_t| = \delta V_t = \frac{KF\sqrt{\pi}}{\sqrt{2\ddot{\theta}M}} \quad (2-130)$$

Substitution for  $\ddot{\theta}$  by a combination of Equations 2-120 and 2-121 finally yields

$$\delta V_t = \left( \frac{K}{M} \sqrt{\frac{\pi I}{2\ell}} \right) \sqrt{F} \quad (2-131)$$

The parameters within the parenthesis can be expressed in terms of known OEC parameters chosen to maximize this error. For example:

$$M = 2.8 \text{ slugs (minimum value)}$$

$$I = 7.5 \text{ slug-ft}^2$$

$$\ell = 1.5 \text{ foot}$$

so

$$\delta V_t = K\sqrt{F} \quad (2-132)$$

Now Equation 2-132 can be represented parametrically in terms of the thrust level assigned for spinup and the percentage mismatch,  $K$ . Figure 2-76 illustrates the range of velocity added transverse to the spin axis as a function of these parameters.

To complete the analyses, the results must be related to the attitude errors caused by spinup and shown in Figure 2-74. A combination of the results shown in Figures 2-74 and 2-76 produces a curve (Figure 2-77) of transverse velocity versus attitude error for the range of expected tipoff errors, thrust mismatch, and thrust levels. The information in the figure indicates that, for example, if it is desired to maintain spinup attitude errors below 1.0 degree, and if the OEC were separated from Voyager with a rate of 0.1 deg/sec, then a 5 percent mismatch of the jet thrust would yield a transverse velocity of approximately 0.022 fps for a thrust level of 130 millipounds.

The question, of course, is what is the criterion for selection of the thrust level. Certainly minimization of attitude errors is important. However, the effect of this transverse velocity increment must be determined in order to ascertain the acceptable level of  $\delta V$  for the mission.

Studies in Section 2.3 discuss the desirability of controlling the OEC's separation distance from Voyager. This is accomplished by selection of the injection time or position in orbit for which the orientation of the separation velocity increment,  $\Delta V$ , has a predetermined magnitude component along the orbit velocity vector. It is this component which controls the range of the OEC as a function of time. Because of the critical nature of this parameter, it must be assured that a spinup, the orbital velocity of the OEC will not be altered.

Figure 2-78 shows an assumed orientation of OEC at spinup assuming no attitude errors present. The angle  $\alpha$  lies between the orbital velocity vector  $V_o$  and the separation velocity  $\Delta V$ . If the  $\Delta V$  direction and the spin axis of OEC are coincident, then the spinup translational velocity is applied normal to the separation

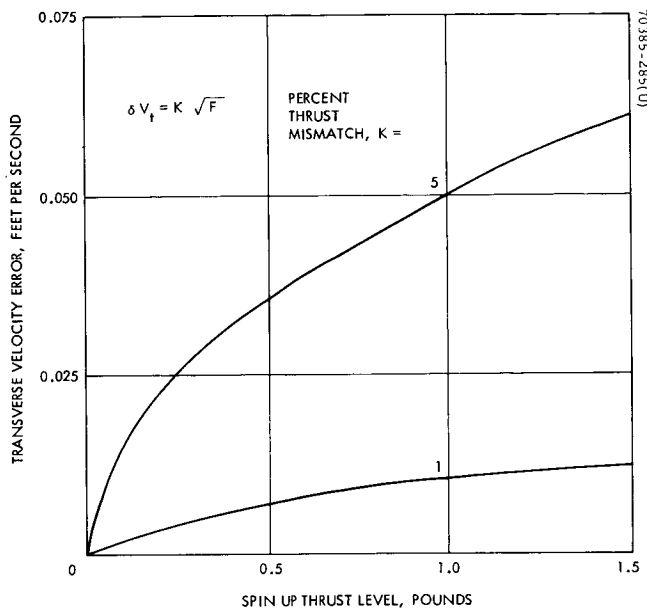


Figure 2-76. Transverse Velocity Error

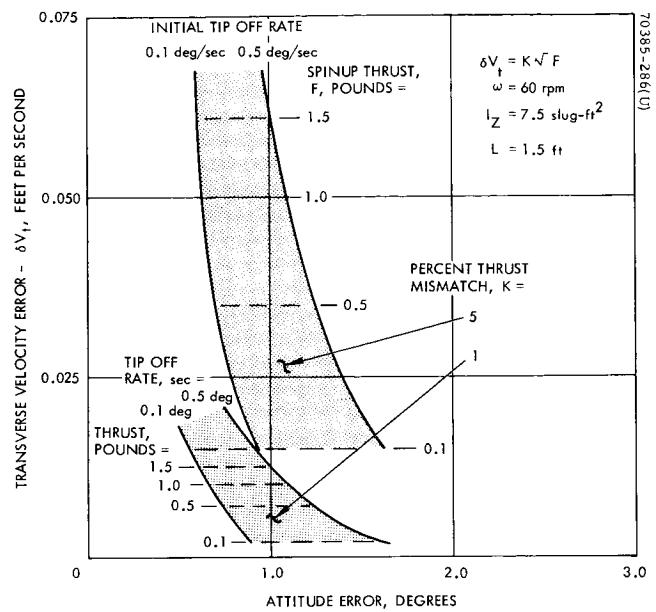


Figure 2-77. Spinup Thrust Selection Tradeoff

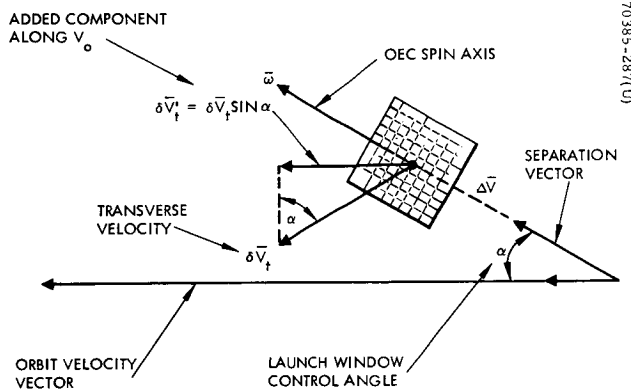


Figure 2-78. Transverse Spinup Errors

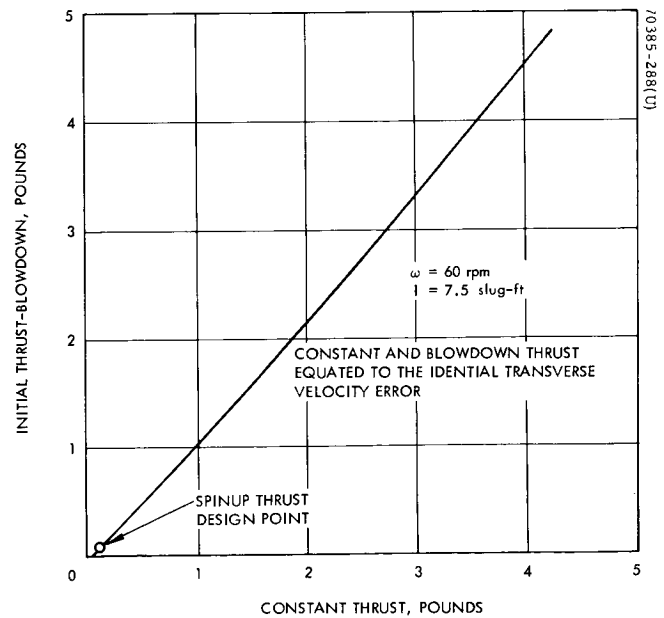


Figure 2-79. Relationship of Regulated Pressure to Blowdown Pressure Thrust Levels

vector. The critical component along the velocity vector is given by

$$\delta V'_t = \delta V_t \sin \alpha$$

This equation assumes:

- Separation  $\Delta V$  is applied ideally.
- Over the spinup interval, the angle  $\alpha$  essentially remains constant.
- In the worst case, the translational effect either decreases OEC's orbital velocity and increases the probability of collision, ... or this effect increases the velocity to the point that mission lifetime is affected.

Several important factors can be pointed out. First, the angle  $\alpha$  will never be chosen greater than some 80 degrees, and this largely due to the collision constraint, which will be discussed in the ensuing sections. Second, the translation effect could be oriented out of the orbit plane as well as in it and hence would do no more than slightly rotate the orbit plane or provide a negligible change in inclination.

The solution to the problem of spinup translation is not in whether or not the phenomenon can be better defined but rather what reduction in error can be made by a decrease in the spinup thrust. Since the range of thrust levels are all within the scope of present OEC propulsion system design, selection of small thrust, along with a slight increase in attitude error reduces the translational velocity error. Thrust levels of approximately 130 millipounds are reasonable values.

The types of spinup propulsion system considered in this study are categorized as pressure regulated or pressure blowdown gas systems. The constant thrust analysis presented here is appropriate for the regulated system design. Additional studies were required to define the equivalent effects of a blowdown system. A digital simulation of the spinup equations for a pressure blowdown system was modeled. The objective was to define the relationship between constant thrust and blowdown thrust in terms of the translational velocity imparted. The following assumptions were made:

- 1) A total impulse of 33 lb-sec is required.
- 2) An initial thrust decaying exponentially to a zero level and providing a spin of 60 rpm is selected as a blowdown model.
- 3) The translational velocity due to a blowdown system is equated to a pressure regulated system to define an equivalent constant thrust.

The results of this study are illustrated in Figure 2-79. Note that up to thrusts of 3 pounds, the blowdown and pressure regulated systems generate similar magnitudes of translational velocity. At increased levels of constant thrust, an initial blowdown thrust up to 25 percent greater than the constant case is required to produce the same velocity error.

For the 130 millipound thrust selected, an equivalent blowdown initial thrust of  $\sim 130$  millipounds is specified.

#### 2.4.2.3 Effects of Spinup Thrust Misalignment

Another source of error in the OEC orbital period is associated with the misalignment of the spinup jets. The following parameters represent typical mechanical alignment tolerances of the spinup jets:

Angular misalignment of nozzle in thrust plane:  $\leq 0.5$  degree

Angular misalignment of nozzle out of thrust plane:  $\leq 0.5$  degree

Nozzle position mismatch:  $\leq 0.06$  inch

As shown in Figure 2-80, the angular misalignment out of the cm plane is the important component. The other components affect spin speed and as such are not of interest here.

The expression that represents the added velocity due to an out of plane misalignment is developed from the conservation of linear momentum equation

$$Ft = \frac{M \delta V_a}{\sin \epsilon} \quad (2-133)$$

where

$F$  = total force applied by one jet

$t$  = period over which spinup occurs

$M$  = OEC mass

$\delta V_a$  = added velocity along spin axis due to misalignment jet

$\epsilon$  = angular misalignment

In terms of the added velocity

$$\delta V_a = \frac{Ft}{M} \sin \epsilon \quad (2-134)$$

and for the small angles expected,

$$\delta V_a \approx \frac{Ft\epsilon}{M} \quad (2-135)$$

Figure 2-81 illustrates the induced  $\delta V_a$  as a function of jet misalignment. The resulting velocity may be bounded in direction by recognizing that

- 1) If the offsets of the two nozzles are in opposite directions, they null out one another.



- 2) If the jets are biased in the same direction, then Equation 2-135 is given by

$$\delta V_a = \frac{2F\epsilon}{M} \quad (2-136)$$

and either of two extremes could occur:

- a) Offset is directed along the separation vector and in phase, adding to the  $\Delta V$  at separation.
- b) Offset is directed along the separation vector and in the opposite direction of separation, slowing the vehicle.

The velocity increment,  $\delta V_a$ , must be resolved through  $\alpha$ , the angle between the orbit velocity and separation velocity, as shown in Figure 2-82, to determine the effect on the OEC separation. Therefore

$$\delta V'_a = \delta V_a \cos \alpha \quad (2-137)$$

The influence of this error on the separation phase of the OEC mission is treated in the sections to follow.

Typical alignment errors could be as great as 0.5 degree; however, precision procedures could probably control this source of error to 0.1 degree.

#### 2.4.2.4 Separation Window

The preceding sections treated errors characteristic of the separation device. In discussing the actual separation, it is recognized that other errors must be considered.

In order to successfully perform the co-orbital mission, the component of the separation velocity along the orbital velocity vector must be controlled. As mentioned earlier, the angle  $\alpha$  between the separation vector and orbital velocity vector must be properly selected to establish a launch window. It is the selection of  $\alpha$  which fixes the parallel component of velocity increment through the equation

$$\Delta V_p = \Delta V \cos \alpha \quad (2-138)$$

where

$\Delta V$  = separation velocity

$$= \frac{\pi F}{2t k}$$

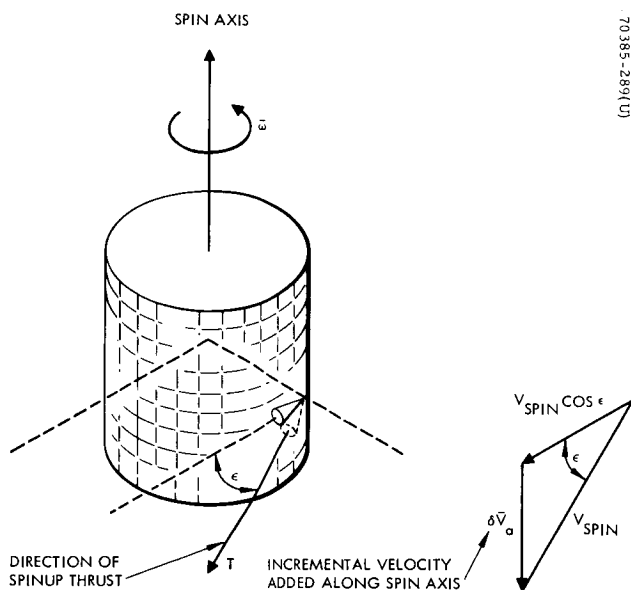


Figure 2-80. Effect of Spinup Jet Misalignment at Spinup

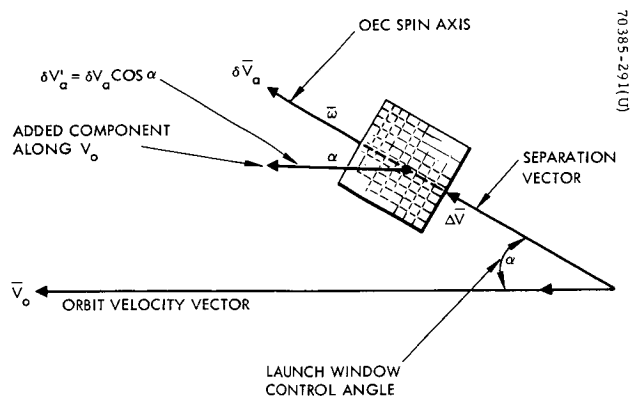


Figure 2-82. Axial Spinup Errors

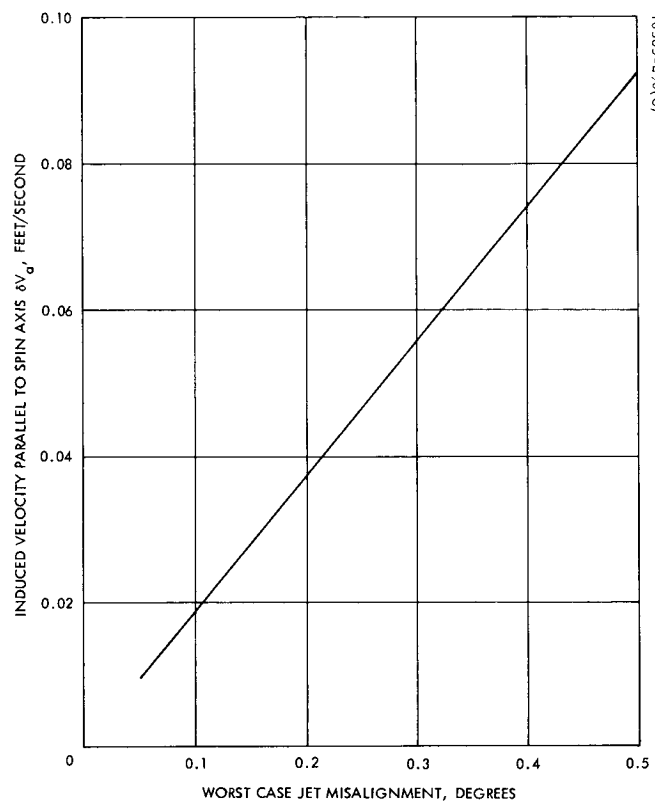


Figure 2-81. Induced  $\Delta V$  Parallel to Spin Axis Versus Jet Misalignment Angle

and

$F$  = separation force

$t$  = time separation force acts

$k$  = spring constant

so that the parallel component of velocity is

$$\Delta V_p = \frac{\pi F}{2t k} \cos \alpha \quad (2-139)$$

Several important factors are associated with relating this equation to the launch window. The spring characteristics alter  $\Delta V$ , but timing errors in execution of the separation command and uncertainty in OEC position and attitude tend to increase the uncertainty of  $\alpha$ .

There are two approaches to a separation window error analysis. The first method investigates the sensitivity of  $\alpha$  by measuring the equivalent error in the timing or application of the separation command. The second defines each of the component errors which combine in a probabilistic fashion to give  $\Delta V_p$  a bound in accuracy. The latter technique is presented in the following discussion.

The underlying assumptions applied in studying the launch window are based on results presented in Section 2.3. Necessary groundwork is presented here for additional clarification.

Figure 2-46 illustrated the relationship for a typical Voyager-OEC orbit prior to separation. A 10,000 km apoapsis — 1000 km periapsis orbit is used in the ensuing discussion. Several pertinent parameters are shown in Figure 2-28; the reference orbit plane and velocity vector, the OEC  $\Delta V$  (which is fixed to Voyager and over the period for which separation could occur is assumed inertially fixed), and the orbit plane. The angle  $\alpha$  lies between the applied  $\Delta V$  and the orbital velocity vector and represents the variable of the separation window. Selection of the maximum co-orbital OEC range requires fixing  $\Delta V_p$  and is accomplished by proper timing in the orbit to yield the desired  $\alpha$ .

The angle  $\alpha$  is constrained by the following relationship:

$$\theta \leq \alpha \leq 180 - \theta$$

which infers that it is possible to choose a value for  $\alpha$  and geometrically select two positions in the orbit for which this value occurs, the first point at  $\theta$  and the later at  $180 - \theta$ .

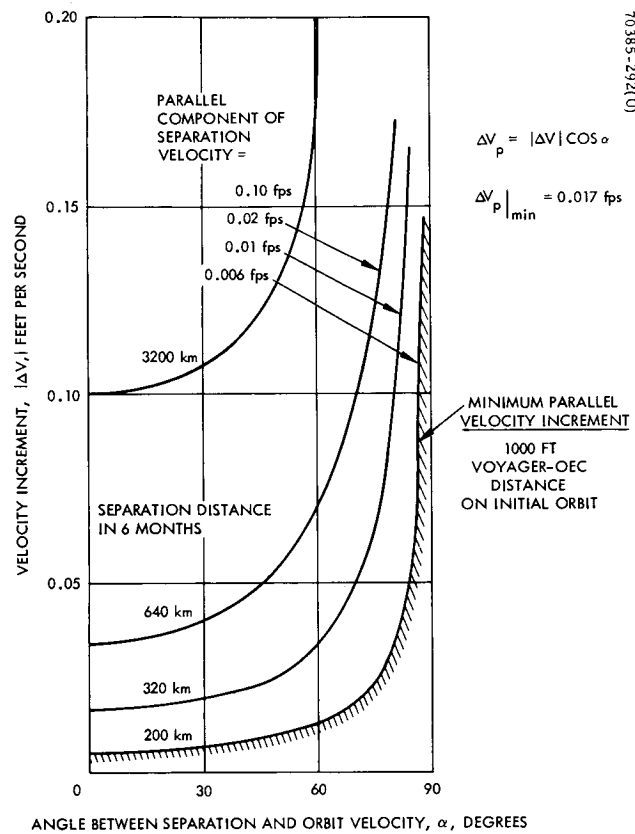


Figure 2-83. Separation Velocity Magnitudes and Angles Attainable for Fixed Minimum Parallel Component

In considering all possible values of  $\alpha$ , first let  $\theta = 0$  degree. As shown in Figure 2-46, the separation vector  $\Delta V$  then lies in the orbit plane and  $\alpha$  varies through a full revolution. Now the relationship between the orbit true anomaly and the angles  $\theta$  and  $\alpha$  can be observed. As shown,

$$\alpha = \nu + \gamma$$

where

$\nu$  = true anomaly

$\gamma$  = flight path angle of orbit velocity with respect to local horizontal

The angles  $\nu$  and  $\gamma$  are functions of the particular orbit and for the range of Voyager orbits are illustrated in Figure 2-28. To determine the range of  $\alpha$  that is within the extremes of the collision constraint and the maximum communication range constraint, the criteria for selection of  $\alpha$  must be reviewed.

To preclude collision, it was shown in Section 2.3 that a nominal safety margin in passage of OEC and Voyager after the first orbit of 560 feet would be guaranteed. This assumed a velocity increment of 0.1 fps and a 10-degree displacement from the critical 90-degree separation angle and did not account for separation errors. In the following discussions, additional margin is included and a minimum relative range of 1000 feet is assumed. Hence it can be assumed that  $\alpha$  will be no greater than 80 degrees, and the minimum allowable separation velocity is

$$\Delta V_p = 0.1 \cos 80^\circ = 0.017 \text{ fps}$$

If 0.017 fps is the minimum allowed parallel velocity component, a curve can be constructed of all possible separation velocity magnitudes, applied at different points in the orbit that yield the identical value of velocity in the orbit plane. For an error-free separation, the results in Figure 2-83 identify the non-collision constraint on  $\alpha$ . In the next section, the inclusion of deviations from the nominal will be discussed.

A summary of the expected separation-spinup errors is presented in Table 2-10 so that the separation velocity that meets all of the requirements stipulated can be selected.

#### 2.4.2.5 Error Sensitivity

A model representing the combined effects of the contributing sources of errors is formulated below. There are two identifiable modes of the separation sequence. Two sources are due to the uncertainties of the injection parameters, whereas an additional two are functions of the spinup phase.

TABLE 2-10. SUMMARY OF EXPECTED SEPARATION-SPINUP ERRORS

Error Source	Error Value ( $3\sigma$ )
Voyager OEC position in orbit	$\pm 50$ km spherical volume
Voyager attitude	$\pm 0.5$ degree per axis
Separation execution errors	50 milliseconds
Separation system transverse misalignment	1/16 inch
Separation system angular misalignment	0.5 degree
Spring impulse error	10 percent $\Delta V$
Spring constant	150 lb/ft
Spring side force	Negligible
Spinup thrust mismatch	5 percent
Angular misalignment of nozzle thrust plane	$\leq 0.5$ degree
Angular misalignment of nozzle out of thrust plane	$\leq 0.5$ degree
Nozzle position mismatch	$\leq 0.06$ inch

The separation function is given by

$$g(\Delta V, \alpha) = \Delta V \cos \alpha \quad (2-140)$$

where

$\Delta V$  = fixed velocity increment

$\alpha$  = nominal injection angle

Errors in  $\Delta V$  and  $\alpha$  are accounted for by determining the variance about the desired function  $g(\Delta V, \alpha)$ . Expanding in a Taylor series about the nominal, taking expected values, and determining second order moments neglecting higher order terms gives

$$\sigma_{g(\Delta V, \alpha)}^2 \cong \left( \frac{\partial g}{\partial \Delta V} \right)^2 \mu_{20} + \left( \frac{\partial g}{\partial \alpha} \right)^2 \mu_{02} + 2 \left( \frac{\partial g}{\partial \Delta V} \frac{\partial g}{\partial \alpha} \right) \mu_{11} \quad (2-141)$$

where

$$\mu_{20} = E(\Delta V^2) - E(\Delta V)^2 = \sigma_{\Delta V}^2 = \text{Variance } (\Delta V)$$

$$\mu_{02} = E(\cos^2 \alpha) - E(\cos \alpha)^2 = \sigma_{\cos \alpha}^2 = \text{Variance } (\cos \alpha)$$

$$\mu_{11} = E(\Delta V, \cos \alpha) - E(\Delta V) E(\cos \alpha) = \text{Covariance}$$

Assuming that the random variables are independent and uncorrelated,

$$E(\Delta V, \cos \alpha) = E(\Delta V) E(\cos \alpha)$$

so that

$$\mu_{11} = 0$$

Hence

$$\sigma_{g(\Delta V, \alpha)}^2 = \left( \frac{\partial g}{\partial \Delta V} \right)^2 \mu_{20} + \left( \frac{\partial g}{\partial \alpha} \right)^2 \mu_{02} \quad (2-142)$$

where

$$\frac{\partial g}{\partial \Delta V} = \cos \alpha$$

$$\frac{\partial g}{\partial \alpha} = -\Delta V \sin \alpha$$

and

$$\mu_{20} = \delta V^2$$

$$\mu_{02} = \delta \alpha^2$$

Therefore

$$\sigma_{g(\Delta V, \alpha)}^2 = (\cos^2 \alpha) \delta V^2 + (\Delta V^2 \sin^2 \alpha) \delta \alpha^2 \quad (2-143)$$

In a like fashion, the errors associated with the spinup can be determined and combined with those above. The two contributing sources are

$$g(V_t, \alpha) = V_t \sin \alpha$$

and

$$(2-144)$$

$$g(V_a, \alpha) = V_a \cos \alpha$$

The Taylor series expansion leads to the following expression in terms of the variances:

$$\sigma^2(V_a, V_t, \alpha) = (\sin \alpha)^2 \delta V_t^2 + (\cos \alpha)^2 \delta V_a^2 + (-V_t \cos \alpha)^2 \delta \alpha^2 + (V_a \sin \alpha)^2 \delta \alpha^2$$

where

$\delta V_t^2$  = variance of translational spinup velocity

$\delta V_a^2$  = variance of axial spinup velocity

$\delta \alpha^2$  = variance in injection angle

$V_t$  = nominal value of translational velocity

$V_a$  = nominal value of axial velocity

The nominal values of  $V_t$  and  $V_a$  are of course zero since these parameters stem from errors in the spinup thrust mismatch and alignment, which ideally are perfect. Therefore

$$\sigma^2(V_a, V_t, \alpha) = (\sin^2 \alpha) \delta V_t^2 + (\cos^2 \alpha) \delta V_a^2 \quad (2-145)$$

Combining Equations 2-143 and 2-144, the total variance is given as

$$\delta V_p^2 = \sigma_g^2(\Delta V, \alpha) + \sigma^2(V_a, V_t, \alpha) \quad (2-146)$$

or

$$\delta V_p^2 = \cos^2 \alpha [\delta V^2 + \delta V_a^2] + \sin^2 \alpha [\Delta V^2 \delta \alpha^2 + \delta V_t^2] \quad (2-147)$$

Interpretation of Equation 2-147 requires that a set of ground rules be adopted:

- Assume that the errors about the nominal have 3 sigma statistics.
- Linearly adding these errors to the nominal value yields a maximum parallel velocity increment
- Linearly subtracting these errors yields a minimum parallel velocity increment



Summarizing

$$\Delta V_p = \Delta V \cos \alpha \pm 3 \delta V_p \quad (2-148)$$

The objective of this analysis is to determine the minimum and maximum range between Voyager and OEC due to the various errors. By substitution of the error sources given in Table 2-10 into Equation 2-148, the error laden velocity increment is measured. The actual distance OEC travels on a per orbit basis or in the 6-month mission is obtained by observing the following orbit related expression.

The per orbit separation range of the Voyager and OEC is a function of the characteristic orbital parameters given by

$$\delta S = \frac{3Pa V_o^2}{\mu} \Delta V_p \quad (2-149)$$

where

P = orbital period

a = orbit semimajor axis

V<sub>o</sub> = orbital velocity

μ = gravitational constant of Mars,  $0.428 \times 10^5 \frac{\text{km}^3}{\text{sec}^2}$

ΔV<sub>p</sub> = parallel component of velocity

Based upon results discussed in Section 2.3, the worst case point of injection in the orbit occurs at a true anomaly of 75 degrees. At this point the characteristic orbit parameters for the 10,000 km x 1000 km orbit is

$$V_o = 3.3 \text{ km/sec}$$

$$P = 7 \text{ hours}$$

$$a = 8900 \text{ km}$$

and

$$\delta S = 1.7 \times 10^2 \Delta V_p (\text{km/orbit})(3\sigma) \quad (2-150)$$

The maximum distance of separation for the 6 months is

$$\delta S_{\text{max}} = 1.04 \times 10^5 \Delta V_p (\text{km})(3\sigma) \quad (2-151)$$

for ΔV<sub>p</sub> in m/sec.

These equations along with Equation 2-148 form the basis for the establishment of the lower and upper bounds on range and the selection of the appropriate velocity increment and nominal launch window.

Substitution of the errors into Equations 2-150 and 2-151 produces the numerical results shown in Figure 2-84. Both maximum and minimum values are shown. To prevent collision, a constraint on the first orbit passage for OEC and Voyager to 1000 feet (0.33 km) was assumed. This is proportional to 200 km at the completion of 6 months in orbit. The maximum range has a softer constraint, although the communication range is limited, and distances less than 4000 km are desirable. Crossplotting these results as a function of the nominal injection angle and  $\Delta V$  (Figure 2-85) illustrates the bounded nature of the nominal launch window. An upper bound of 3500 km is assumed for purpose of discussion.

A decrease in the window is apparent if lower maximum ranges are taken. Figure 2-86 summarizes the details graphically. There is an optimum selection of separation velocity increment such that a maximum window can be achieved. This point varies depending on the maximum range constraint. For the separation ranges desired, the  $\Delta V$  is in the vicinity of 0.1 fps. Assuming  $\delta S_{\max} = 3500$  km, the choice of  $\Delta V$  is 0.073 fps. However, selection of a  $\Delta V$  requires consideration be given to the spring mechanism design. There is no analytical reason why  $\Delta V = 0.073$  fps cannot be chosen, but by relieving the requirements of the spring design and selecting a slightly larger  $\Delta V$  of, say, 0.1 fps, the practical limitations of designing such a device are decreased. The window for 0.073 fps is a total 33 degrees. There is a 5-degree decrease to 28 degrees for  $\Delta V = 0.1$  fps. Note also that by decreasing the maximum constraint, the optimum point shifts closer toward larger magnitudes of velocity.

The question of what size window is reasonable with respect to an operational system can best be answered by reflecting back on the results in Section 2.3. The constraints on the injection angle  $\alpha$  are

$$\theta \leq \alpha \leq 180 - \theta$$

For a  $\Delta V = 0.1$  fps,  $40 \leq \alpha \leq 70$  degrees from Figure 2-85. Thus the minimum value of  $\theta$ , the angle between the  $\Delta V$  orientation and Voyager and the orbit plane, is

$$\theta_{\min} = 40 \text{ degrees}$$

and the range of possible  $\alpha$  is

$$40 \leq \alpha \leq 140 \text{ degrees}$$

Restricting  $\alpha \leq 70$  degrees as per the error analysis, there are two regimes of available window:

$$40 \leq \alpha_1 \leq 70 \text{ degrees (increase OEC orbit velocity)}$$

$$110 \leq \alpha_2 \leq 140 \text{ degrees (decrease OEC orbit velocity)}$$

These results are illustrated in a simple example.

Assume that OEC is mounted on Voyager so that the direction of separation makes an angle of at least 40 degrees to the chosen orbit plane, as shown in Figure 2-87. As Voyager orbits Mars, the injection angle  $\alpha$ , which is equal to 40 degrees at the assumed initial position of periapsis, increases. The first possible launch window exists from periapsis where  $\alpha = 40$  degrees to point 2 in the orbit where  $\alpha = 70$  degrees. During this time the OEC's orbit period can be made greater than Voyager's. Between 70 and 110 degrees, there is no window because of the collision constraint imposed. However, at 110 degrees the window reopens and the OEC orbit period can now be made smaller than Voyager's period. This window remains open up to the time when OEC reaches apoapsis, and  $\alpha = 140$  degrees. After passing apoapsis, the ability to adjust the period is repeated. However, this time the increase of OEC period occurs near apoapsis where  $140 \leq \alpha \leq 110$  degrees.

Obviously the errors propagate faster near periapsis because of the higher orbital velocity. This error analysis is based on these larger errors. By injecting near apoapsis, a decrease in the error is possible. Since orbit velocity decreases by some 60 percent, it is expected that a similar decrease in range occurs. Hence, the launch window will actually be of greater dimension at injections near apoapsis.

Sensitivity to Errors. The prior results are based on a set of errors that appear to be representative of a worst case. A study of Equation 2-147 indicates several important facts:

- 1) The error in velocity is not very sensitive to components proportional to  $\Delta V$  or to the launch window error. The uncertainties in spinup thrust and alignment have a greater weighting on the errors.
- 2) The largest source of uncertainty is the axial velocity increment.
- 3) Reduction of this error by careful alignment of the jets decreases the total error in velocity and increases the launch window.
- 4) Decreasing  $\delta V_a$  increases the sensitivity to the errors proportional to  $\Delta V$ , but the net effect is reduced since  $\delta V_a$  is smaller.

#### 2.4.3 Voyager-OEC Perturbation Study

Provision for a fail-safe separation is of major concern to the success of the OEC mission. The kinematics associated with this phase of mission operation was treated in the previous section. These studies assumed that the Voyager bus was an inertially fixed platform and the OEC attitude errors were due to misalignment of the separation device and spinup jets as well as differential thrust.

In this section, the steady-state operation of the Voyager bus in orbit about Mars is discussed, and both the perturbing forces of ejection of the OEC and reaction to perturbation induced in the separation phase are studied.

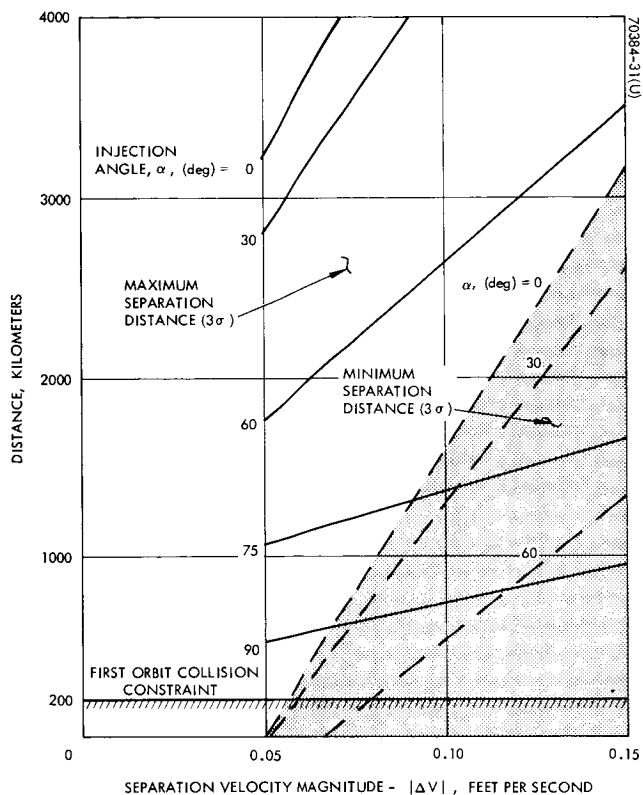


Figure 2-84. Separation Distance as Function of Injection Errors

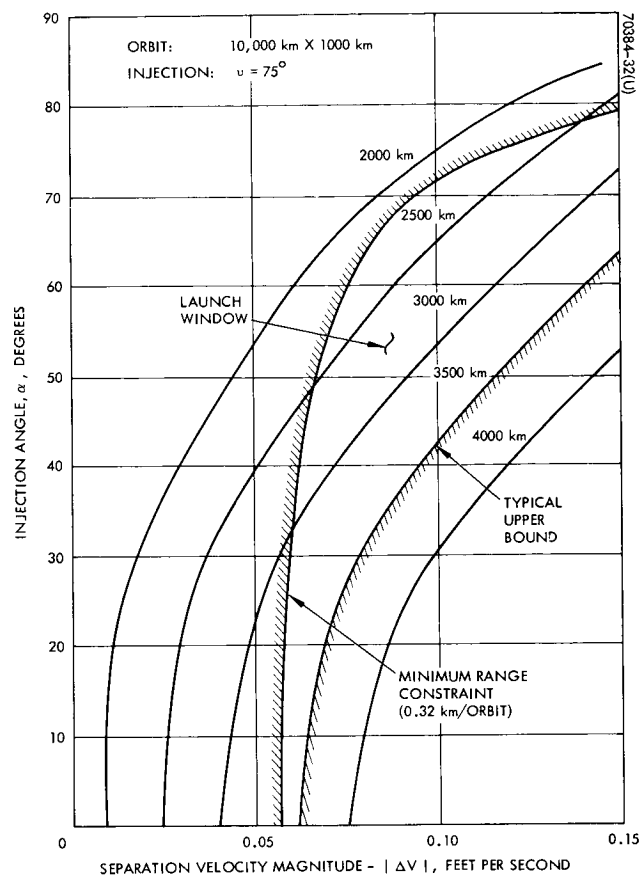


Figure 2-85. Worst-Case OEC Separation Launch Windows

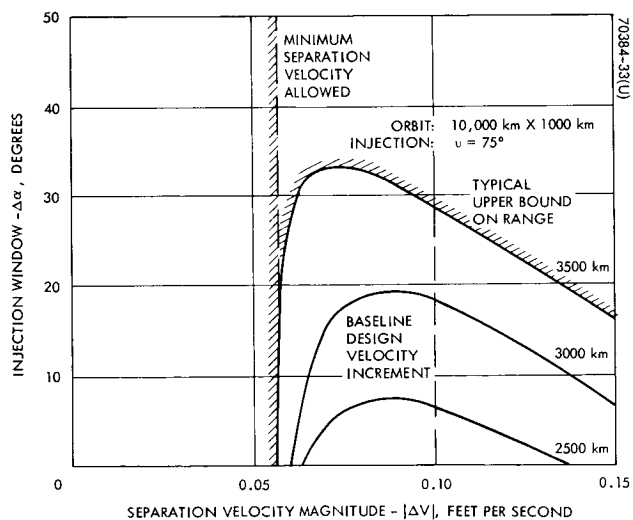


Figure 2-86. Typical OEC Injection Window

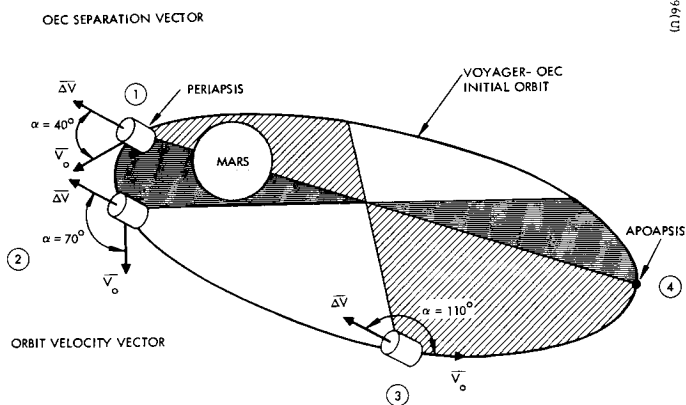


Figure 2-87. Typical Launch Window Characteristics

#### 2.4.3.1 Voyager Attitude Control

The Voyager attitude control concept proposed by each of the three present spacecraft design contractors provides operation in a limit cycle mode during the heliocentric cruise and Mars orbital phases.

The control system consists of: optical sensors (Sun sensors in pitch and yaw and Canopus sensor in roll) to determine attitude deviations from the references, gyroscopes which provide rate signals during acquisition of references and position signals during maneuvers, and electronic circuitry which processes the sensor signals to operate the appropriate solenoid valves of the gas jet subsystem.

Two operational phases of the Voyager spacecraft mission are of interest for the OEC mission. The predominant factor which establishes the separation initial conditions is the steady-state cruise limit cycle. The inertial mode, which provides Voyager the capability to reorient to any attitude, is of importance because it can be used to orient the OEC in a preferred direction at separation, but is not otherwise treated here.

Because of the near absence of disturbances in space, the optimum method by which active three-axis controlled spacecraft maintain a desired orientation is by application of the on-off reaction control system. The efficiency of the characteristic limit-cycle of this subsystem determines to a large extent the fuel required for the attitude control of the spacecraft. Typically, the cruise attitude control limit-cycle is designed to optimize jet on to off times or to minimize the fuel expended.

For purposes of illustration, the parameters associated with the GE Voyager spacecraft are used in the ensuing discussion. It is apparent that the other two Voyager configurations should be of approximately the same design in the limit cycle phase because of the similarity in control system design.

The limit cycle is characterized by the attitude deadband and the rate increment. Table 2-11 presents some of the pertinent characteristics of the GE system.

TABLE 2-11. TYPICAL VOYAGER LIMIT-CYCLE PARAMETERS

Angular deadband	$\pm 8.0$ milliradians
Rate increment	$\pm 3.4 \times 10^{-6}$ rad/sec
Control acceleration	$\pm 0.225$ mr/sec <sup>2</sup>
Valve minimum on time	30 milliseconds

#### 2.4.3.2 Effect of Limit Cycle on OEC Separation

Prior assumptions stated that perturbing effects of the Voyager limit cycle were negligible and that the spacecraft was essentially a stable platform for OEC at separation. To illustrate, the  $\Delta V$  imparted to the OEC by the limit cycling is determined. Assuming a 1 meter moment arm from the center of mass of Voyager to the location of the OEC, the velocity is

$$\Delta V = l \dot{\Delta \theta}$$

where

$l$  = moment arm = 1 meter

$\dot{\Delta \theta}$  = rate increment =  $3.4 \times 10^{-6}$  rad/sec

and

$$\Delta V = 3.4 \times 10^{-6} \text{ m/sec}$$

This velocity is about four orders of magnitude smaller than the expected separation velocity of approximately 0.03 m/sec (0.1 fps) and is negligible. Hence, the attitude of OEC will not be affected by the motion of the Voyager spacecraft steady-state operation.

#### 2.4.3.3 OEC Induced Perturbations on Voyager

The Voyager limit cycle period is approximately 1.3 hours. It is assumed that this period exists about each of the axes and that a control pulse occurs whenever the deadband is reached. As mentioned above, the limit cycle characteristics are designed to minimize fuel expenditure and still provide necessary attitude accuracies by controlling the spacecraft to point to the Sun and Canopus.

Separation of the OEC from Voyager will not cause a break of lock with the celestial references but will perturb the Voyager from its nominal attitude. The sensor fields of view are sufficiently large to provide continuous signals to the control system. Table 2-12 gives the typical sensor characteristics for the GE configuration and is expected to be very similar to the Boeing or TRW sensors.

The torque impulse applied to the spacecraft induces an instantaneous rate error

$$\dot{\theta}_D = \frac{T_D t}{I_V} \quad (2-153)$$

where

$T_D$  = disturbance torque (separation force = 0.91 kg)

$t$  = separation period - 0.3 second

TABLE 2-12. SENSOR FIELDS OF VIEW AND ACCURACIES

	Field of View, degrees	Linear Range, degrees
Sun Sensor	15	1
Canopus Sensor		
Instantaneous	4	
Slewing		
Roll	2	
Pitch	15	

$$I_V = \text{maximum moment of inertia} = 5450 \text{ kg-m}^2$$

and

$$\dot{\theta}_D = 0.49 \text{ mr/sec}$$

The position error is less than 1 percent of the deadband

$$\theta_D = 1/2 \left( \frac{T_D}{I_V} \right) t^2 = 1/2 \dot{\theta} t = 0.0735 \text{ milliradian}$$

and is negligible.

The rate error is measured about the Voyager axis where the disturbance occurs, and a closed loop control signal is initiated to pulse the proper jet. The error is removed by the control torque in about 2 seconds and the Voyager resumes steady-state operation.

There are two additional perturbative effects on Voyager that deserve consideration. First is the translational acceleration added at separation, and second is the decrease in Voyager moments of inertia at separation. Reference 1 establishes the constraints on the allowable perturbations induced on the Voyager spacecraft. In particular, the (unpredictable) translational accelerations shall not exceed an average value of  $0.6 \times 10^{-7} \text{ cm/sec}^2$  over the mission. In terms of the distance traveled over a 6-month period, this corresponds to an average velocity of 0.95 cm/sec. Assuming a separation velocity of 3.1 cm/sec imparted to the OEC, the acceleration imparted to translate the Voyager is equivalent to a velocity of about 0.13 cm/sec. The Voyager bus is assumed to weigh 1365 kg.

Separation of the OEC from Voyager changes the inertia properties of the spacecraft. This couples into the efficiency of the control system operation. Results from GE Voyager design indicate that the decrease in principal moments of inertia due to the capsule-Lander separation has a negligible effect on limit cycle operation. Hence, it is assumed that OEC, which weighs less than 5 percent of the capsule-Lander will not degrade Voyager steady-state operation.



## 2.5 ATTITUDE AND ORBIT DETERMINATION

The process of attitude and orbit determination plays an extremely important role in the OEC mission. Data assessment requires knowledge of each of these parameters. For this reason, the sensors necessary to measure both attitude and orbit are discussed in this section rather than in the attitude control section.

The basic OEC accuracy requirements are presented followed by an in-depth discussion of the expected geometry and capability to resolve ambiguities in measuring spin axis attitude and orbit position.

Techniques for establishing the attitude and orbit are presented in Sections 2.5.4 and 2.5.5. These methods are representative of possible computational algorithms which estimate the attitude and orbit parameters based on smoothing of the sensor observations. The schemes presented here are a result of two independent studies and in actuality should be combined into a single operational concept.

### 2.5.1 Requirements for Attitude and Orbit Determination

The OEC accuracy requirements are generated from both the experiment objective of defining the Mars magnetosphere and the accuracies of the experiments. These requirements are interpreted in terms of provisions for accurate relative position determination to the Mars orbit as well as vehicle attitude determination for the observed data. Table 2-13 summarizes the requirements for the OEC specified by Ames Research Center (Reference 14).

The process of attitude determination requires a precise fix of the OEC spin axis in inertial space. This can be accomplished by referencing the spin axis to any of a number of celestial objects. Ideally, a minimum of two objects is necessary to completely specify the attitude of a satellite. The position can be determined with the addition of some form of range measurement.

TABLE 2-13. OEC ATTITUDE AND ORBIT DETERMINATION REQUIREMENTS

Knowledge of spin axis attitude	$<\pm 1.0$ degree ( $3\sigma$ )
Knowledge of attitude to sun	$<\pm 0.25$ degree ( $3\sigma$ )
Knowledge of orbit position	$<\pm 100$ km ( $3\sigma$ ) apoapsis
	$<\pm 20$ km ( $3\sigma$ ) periapsis

The energy emanating from a celestial body can be detected by sensitive measuring instruments. The optics, fields of view, and other characteristic parameters of these sensors are predicated on the energy source selected and the particular sensor application. The latter plays an extremely important part in the choice of sensors. Requirements on a sensor operating from a spinning satellite are quite different from celestial tracking sensors such as those used on the Voyager bus. When applied on a spin stabilized satellite such as OEC, the sensor will view the particular source for a short time interval during the satellite spin cycle as the object passes through the sensor field of view.

The available celestial objects for attitude measurement include:

- Sun
- Planets (Mars)
- Stars

Both the Sun and the stars can be treated as point sources, whereas the planets angular subtense varies as function of closeness to the particular planet. The application of a planet sensor has different design requirements as a function of its particular environment. At Mars distances, the earth appears as a small point to a sensor, but the planet Mars has a large disc when viewed from a Mars orbit.

Orbit determination can be effected by several means. For the OEC mission, there are both direct and indirect methods. The direct method requires the inclusion of a transponder on the capsule for deep space tracking from Earth. Range and rate measurements via the Deep Space Net (DSN) can provide an accurate orbit prediction similar to the accuracies of the Voyager orbit. Position can also be indirectly determined by ranging from the Voyager bus with the data transmitted to Earth. Finally it is possible to determine position autonomously. The OEC's orbit can be established by combining planet sensor information with the spin rate and the IR disc characteristics of Mars.

The first two of the above methods of specifying OEC position requires the addition of a transponder for the basic determination scheme. The last method indicates that it is possible to use only two devices — Sun sensor and horizon sensor — to completely identify the orbit as well as the attitude.

### 2.5.2 Geometry

Conceptually, attitude and position can each be found independently, since three independent attitude measurements generally specify inertial orientation and three independent range measurements generally specify position. In analyzing the OEC mission geometry it will be shown how the problems of orbit determination and attitude determination can be interrelated.

Suppose that the position of the OEC is known; then the attitude can be defined uniquely by Sun and Mars angles. The elevation of the Sun with respect to the vehicular equator of the OEC specifies a conical locus of possible orientations, as shown in Figure 2-88. A similar conical locus is specified by the elevation of Mars and the attitude must be one of the two intersection lines of the two cones, as shown in Figure 2-89. The azimuthal difference between the Mars and Sun lines of sight specifies which of the two, as indicated in Figure 2-90, for a particular situation.

Conversely, suppose that the attitude of the OEC is known. The Martian and solar elevation angles each specify a conical locus of possible positions for the OEC; the intersection of the two cones specifies a curve of possible positions (see Figure 2-91). Once again, the azimuthal difference is used as the final piece of information, this time to fix the position of the OEC.

What if neither the position nor the attitude is known? Then, line-of-sight measurements provide the orientation of the spin axis with respect to a plane containing Mars and the Sun, but do not specify the plane (see Figure 2-92). In any such plane, there is a locus of possible positions given by the Sun-OEC-Mars angle as shown in Figure 2-93. The locus of all possible OEC positions is then the surface obtained by rotating the curve in the plane about the Sun-Mars line as shown in Figure 2-94. Given the altitude of the OEC above Mars implies a spherical locus of positions about Mars; the intersection of the surface in Figure 2-94 with the sphere provides a circular locus of positions as shown in the Figure. The circular locus of possible OEC positions is centered on the Mars-Sun line, due to the nature of the angular references used. With each possible position on the locus, there is associated a particular OEC attitude, as indicated in Figure 2-94. Thus the uncertainty is not in position alone, but an uncertainty between "coordinated position-attitude pairs."

One further datum yielding either position or attitude will uniquely specify the OEC position and attitude. Various additional sources of data can be identified which will complete the specification: range or range rate from Voyager to OEC, an additional attitude reference provided by a star sensor, or accurate range rate to earth via the DSN. All of these are feasible and, as will be seen, will definitely be required to achieve orbit position determination accuracies of the order of 5 to 20 km\* or better. It is, however, of some interest to consider the case (co-orbiter mission) where no additional data is used and to discover the expected accuracy of orbit and attitude determination in that case. For this purpose some of the numerical results to be derived in succeeding sections will be used.

It might appear that the various possible OEC positions (on the circular locus) would be sorted out by data taken over a sequence of positions as OEC orbits Mars. Some reflection on the symmetries of the "uncertainty locus,"

---

\*For the case where OEC forms one part of an occultation experiment, much better accuracies than this are said to be required; in this case DSN tracking to sufficient accuracy can be performed with the S-band occultation equipment required on the OEC with no additional weight or power penalty. This is also true of the "baseline" OEC of this report.

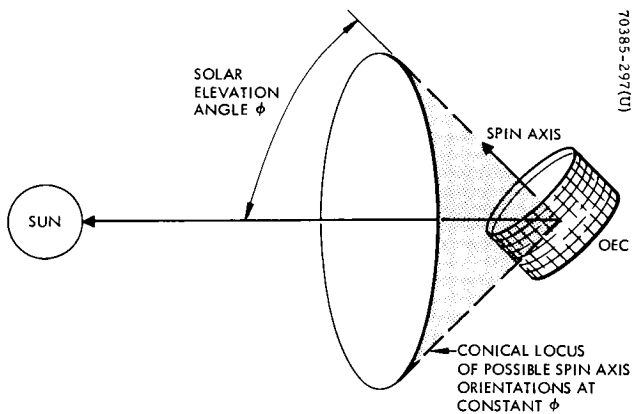


Figure 2-88. Capsule Orientation About Sun Line for Given Position

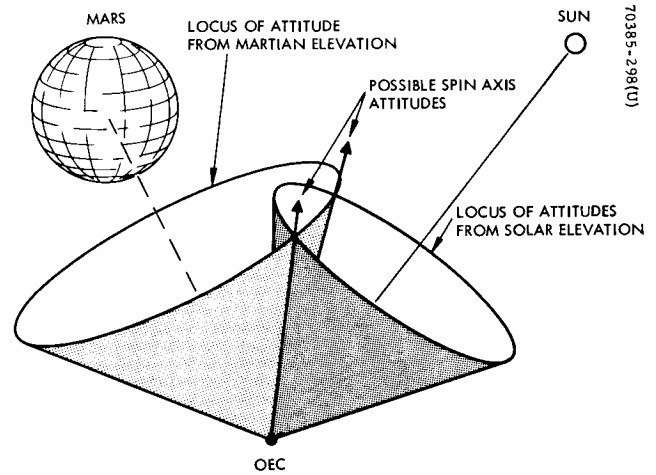


Figure 2-89. Intersection of Sun Line and Mars Cones of Attitude Uncertainty for Given Position

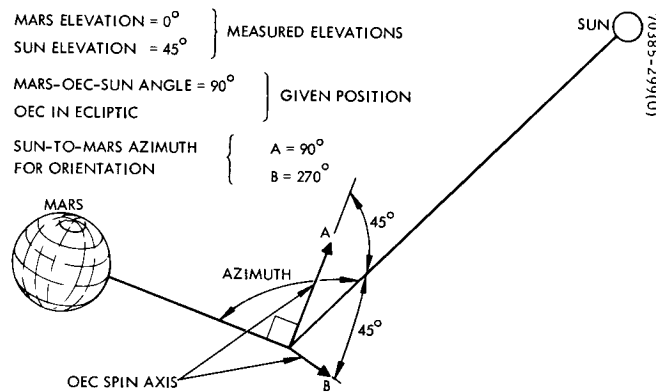


Figure 2-90. Resolving of Attitude Ambiguity

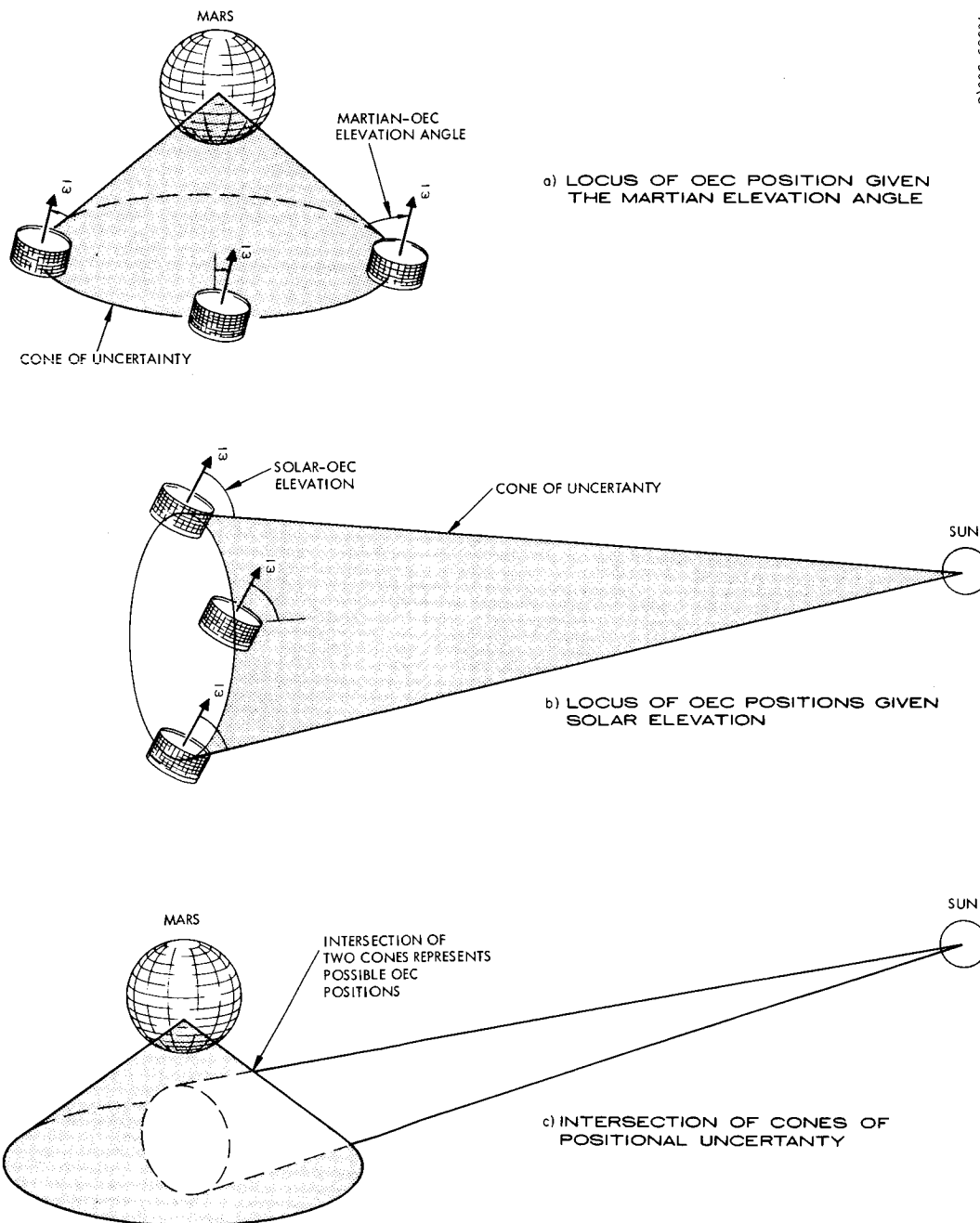


Figure 2-91. OEC Position Determination for Known Attitude

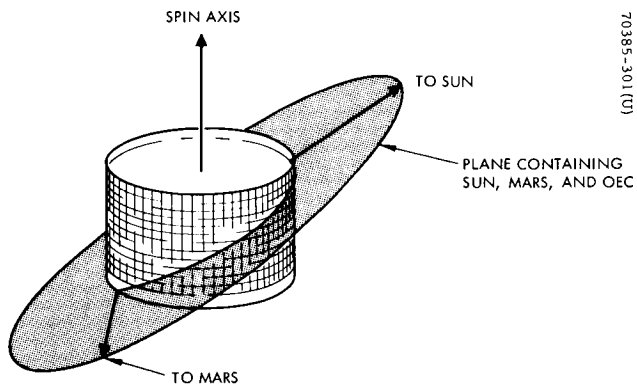


Figure 2-92. Plane Containing Sun, Mars, and OEC When Neither Position Nor Attitude is Known

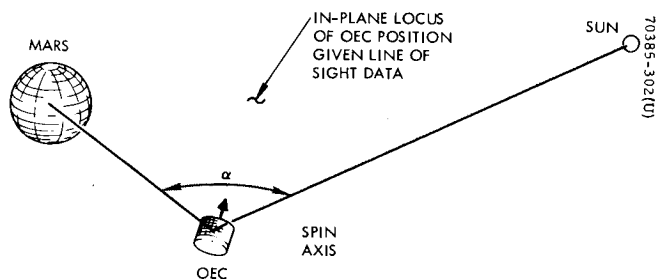


Figure 2-93. Measurement of Sun-OEC-Mars Angle Identifying Possible OEC Inertial Position

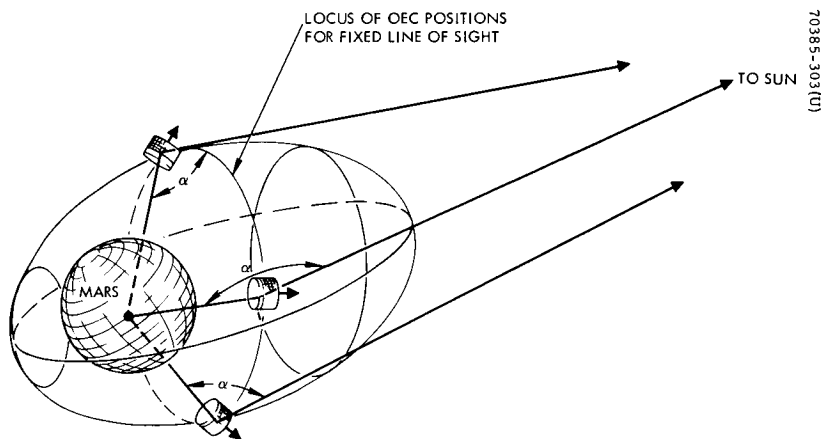


Figure 2-94. Locus of Possible Orbit Position and Attitude When Initial Conditions are not Specified

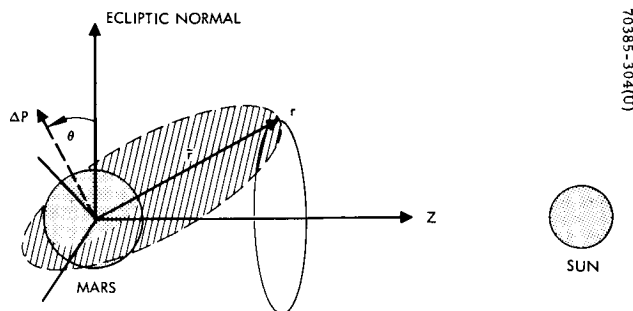


Figure 2-95. Polar Coordinate System, Mars-Centered

however, reveal that this is not the case: the possible positions of OEC at one instant lie on areocentric orbits each succeeding point of which lines on an uncertainty locus stemming from the same initial uncertainty locus. That is, the time histories of data obtained from the OEC sensors do not resolve the original ambiguity.

To see this, consider an inertial coordinate frame (instantaneously) centered on the Mars center with the Z-axis lying along the Mars sun line as in Figure 2-95. A cylindrical coordinate set  $(\rho, \theta, Z)$  will be used with the  $\theta =$  direction along ecliptic north as in the figure. At some initial time the measurements of sun and Mars sensors place the OEC on a particular circular locus as in the figure. The orbit which will be followed by an OEC on this locus depends on its velocity vector as well as its position. Neglecting perturbation terms, the gravitational attraction is a function of  $\rho$  and  $Z$ , but not of the angle  $\theta$ ; thus the whole orbital geometry is preserved under a rotation ( $\theta$  direction) about the Sun line. The spin axis angles to sun and Mars are fixed (corresponding to measured angles) but these angles, too, are preserved under such a rotation providing that position, velocity and attitude are all rotated about the Mars-Sun line. Since the symmetry is complete, the time history of altitude and angles to Sun and Mars will be the same for any of these position/velocity/attitude combinations.

The situation is, then, this: Mars and sun sensor data will determine a position and attitude locus for the OEC; the determination of which point on the locus corresponds to the actual OEC position must be made in some other way. Several ways for sorting out this ambiguity without additional sensors can be identified:

#### 2.5.2.1 Voyager Separation Conditions

Initially the OEC position is known since Voyager position was known. The problem here is that perturbing forces act on the orbit and attitude during the mission operation requiring updated estimates of new orbit and attitude to take account of "slipping" around the uncertainty locus. Thus the identification of which part of the locus OEC is on becomes gradually poorer and poorer. An upper bound on the rate at which this ambiguity increases the error in position can be obtained in the following way. Suppose that the torques on OEC due to solar pressure, gravity gradient, and aerodynamics are nominally zero (CP and cg nominally aligned.) Then any changes in the sensor data will be interpreted as due entirely to changes in the OEC orbit. This means that on the new uncertainty locus, the OEC will be located at the point corresponding to the old spin axis orientation. In reality the OEC may have been subjected to torques resulting in attitude changes as large as 0.03 degree per day (Section 2.5); therefore the uncertainty in the angular position,  $\theta$  (Figure 2-95) of the OEC might increase at a rate of up to 0.03 degree per day. Translated into position uncertainties around the uncertainty locus, this is about 5 km per day at apoapse and 2 km per day at periapse.

#### 2.5.2.2 Motion of Mars About Sun

The basic uncertainty is in rotation about the Sun line. The Mars-Sun line rotates at a rate of about 0.5 degree per day, so that a rotation of the spin axis about the Sun line will ultimately show up as a change in the elevation angle of the spin axis to the Sun. The rate at which rotation angles about the Sun line are "fed in" to elevation angles to the Sun is about 1 percent per day due to rotation of the Mars-Sun line. In a steady-state situation, then, the increase in attitude error caused by unknown torques (0.03 degree per day) would be balanced by the incremental corrections permitted by the detection of elevation angle errors (1 percent per day) when the error reached a value of  $0.03/0.01$  or 3 degrees. This corresponds to positional errors of up to 500 km at apoapse, 200 km at periapse.

#### 2.5.2.3 Orbital Regression

As shown in Section 2.2, the OEC orbits will regress at a rate of about 0.3 to 1.0 degree per day in a direction opposite to the Sun line motion. Hence, the total "feed-in" to elevation 'error' will be at a rate of 1.5 to 2.5 percent per day, yielding position uncertainties of 80 to 130 km at periapse and 200 to 330 km at apoapse.

Curve fitting (estimation) techniques might be used to reduce these uncertainties; the effectiveness of such techniques would be limited due to the unknown time variation of the disturbing torques. Clearly to achieve accuracies in the 5 to 20 km regime will require additional data, as, for example, with DSN tracking (if S-band transmitter is aboard) or with a star sensor such as that described in Appendix D.

It is important to recognize that the positional uncertainties cited above are only along the circular locus, i.e., in the  $\theta$  direction of Figure 2-95. Errors in the other axes are substantially smaller, less than 10 km near periapse with only Mars and Sun sensor data. With DSN tracking, of course, errors would be even less.

In selecting the OEC sensors, these geometrical considerations are taken into account. The choice of sensors for operating the OEC in different missions will be discussed in succeeding sections. The ultimate selection for a baseline mission design depends greatly on which combination of sensors most suitably meet the specified accuracies.

#### 2.5.3 Determination of Sensor Accuracies

A summary of the basic sensor accuracies for possible attitude sensors is presented in Table 2-14.



TABLE 2-14. ATTITUDE SENSOR ACCURACIES

Source	Accuracy ( $3\sigma$ ), degrees	Comment
Sun	$\pm 0.5$	Slit field of view spinning sensor
Star	$< \pm 0.1$	Measure field of stars during spin cycle
Planet	$< \pm 1.5$	Measure IR disc of planet

Selection of the sun as a reference source is natural for the Sun line attitude determination requirement. The  $\pm 0.5$  degree ( $3\sigma$ ) sensor accuracy can be smoothed over a number of sun sensor data pulses to values below the  $\pm 0.25$  degree ( $3\sigma$ ) specification.

A second sensor for specifying the attitude of the spin axis cannot be chosen so simply. The star sensor is quoted to have very fine accuracies ( $< 0.1$  degree) and has been used in several tracking applications such as the Mariner, Surveyor, and Lunar Orbiter and is proposed for the Voyager spacecraft. In a spinning satellite the use of only the star sensor element would suffice. In this application the sensor would not track a particular star but would map a field of known stars during a spin revolution. In particular, Canopus could serve as one of the sensed stars since it lies within 15 degrees of the ecliptic normal. A design exercise for this device is presented in Appendix D.

A Mars sensor can also be used with the sun sensor to establish the spin axis attitude. This device is generically identical to the earth horizon sensors used on the spinning TIROS satellite and the Hughes HS-308 satellite.

Both of these horizon sensors operate in the infrared spectrum of the earth's atmosphere with accuracies of much less than  $\pm 1.0$  degree ( $3\sigma$ ). Application of this type of sensor to the OEC mission requires sizing the sensor optics for the Martian IR characteristics. This is provided in Section 6.0. An unsmoothed accuracy of approximately  $\pm 1.5$  degree ( $3\sigma$ ) is sufficient for the OEC mission application as will be shown. Thus both the star and Mars sensor can provide the desired accuracies for the mission. The baseline choice is selected following the discussion of orbit determination sensors.

The determination of the orbital position of the OEC can be provided as mentioned by three methods. Table 2-15 lists these techniques and their basic accuracies.

Deep Space ranging to the OEC with coherent doppler tracking similar to that used by the Voyager spacecraft provides the most accurate position determination. This form of orbit determination requires the inclusion of additional equipment on the OEC and involves a weight penalty of approximately 11 pounds. Since the budgeted weight proposed for the OEC on Voyager ranges up to 125 pounds, it is possible to include this equipment on the capsule.

TABLE 2-15. POSITION SENSOR ACCURACIES

Source	Accuracy ( $3\sigma$ ), km	Comment
Deep Space Net (DSN)	1 to 10	Smoothed position accuracy at periapsis
Ranging from OEC to Voyager	$\pm 10$	Accuracy in range measurement
Mars sensor	100 to 300	Depends on nominal altitude; this is an error in local vertical measurement

Ranging between the Voyager and OEC is dependent on several factors. First, both vehicles must carry additional instrumentation for tracking purposes. The accuracy of the range vector can be established to  $\pm 10$  km ( $3\sigma$ ) and is limited mainly by the weight and power needed on the two vehicles.

There is one major drawback to the application of tracking between the two vehicles as a primary mode. As indicated in the Voyager specifications (Reference 1), the Voyager lifetime is nominally 6 months with a 2 month minimum. Hence this form of position measurement could not be applied over the capsule lifetime. This means of ranging could, however, be used for vernier orbit position measuring or in a backup mode.

The last form of providing for position determination is an autonomous method. The Mars sensor presented as an attitude measuring device can also be used to determine the capsule altitude above the planet. This information is then converted through the geometry into equivalent position in the orbit. The basic accuracy of this device is a function of the nominal design point in the Mars orbit. Errors attributed to the Mars horizon sensor can be suitably smoothed over a number of orbits as will be shown in Section 2.5.4 to provide the desired orbit accuracies. A desirable feature of this form of orbit determination is that the data is referenced directly to the planet and the OEC determination process can be carried on with only a sun and Mars sensor.

A summary of the solutions to the determination process is given in Table 2-16. Each of the groupings of sensor performs the attitude and orbit determination. As a basis for the analysis in the following sections, a brief description of each group is presented.

TABLE 2-16. ATTITUDE AND ORBIT DETERMINATION SENSORS

Group	Sensors
A	• Sun
	• Mars
B	• Sun
	• Mars
	• S-band to Voyager or Earth
C	• Sun
	• Mars
	• Star
D	• Sun
	• Star
	• S-band DSN

The sensors in Group A represent the nominal baseline selection. Only two sensors are required for measuring both attitude and orbit and in addition provide autonomous operation. Because of the ambiguities attributed to perturbations on the OEC orbit, another sensor is required in order to meet all of the mission accuracy specifications.

Addition of an S-band link on the OEC as a communication system backup or alternate mode suitably meets the requirement for some additional orbit information. An occasional range fix to Voyager or to the earth is all that is needed to uniquely locate the attitude and position within the specifications.

A star sensor (Group C) can also be used to resolve the geometrical ambiguity. This does require the addition of another sensor and could be considered as an alternate although is not selected because of the added backup feature of the S-band.

The same conclusion is reached for Group D. This grouping does, however, provide the most accurate measure of attitude and OEC position by the use of the Sun, star and DSN. There is only one outstanding reason for using this complement of sensors. Inclusion of an atmospheric occultation experiment on the OEC and Voyager may require exceptionally precise tracking. This could be easily achieved with the DSN.

#### 2.5.4 Attitude and Position Sensors

Having identified the alternative approaches for inertially locating the OEC spin axis, the baseline sensors are next discussed. The operation and design characteristics of these sensors are described below.

##### 2.5.4.1 Sun Sensor

The high intensity symmetrical signal emanating from the Sun presents itself as a particularly useful source for determining a satellite attitude. At Mars distances, the Sun subtends approximately 21 minutes of arc. The only major deviation from uniformity in the Sun's photosphere is due to sunspots. A conservative analysis has shown that the maximum shift in the center of radiation due to sunspots is less than 0.52 arc seconds, which is negligible for the OEC mission. The irradiance received from the Sun at the distance of Mars is approximately  $62 \text{ mw/cm}^2$ . It has a spectral distribution approximating that of a black body at  $6000^\circ\text{K}$ . Thus, the majority of the sun's radiation lies in the visual spectral range.

Design Characteristics. A simple method of measuring attitude to the Sun from a spinning vehicle is to produce a Sun pulse with a slit optics type sensor shown in Figure 2-96. The width and orientation of the slit on the vehicle define the width and shape of the sun pulse. A lower limit on pulse width is set by the angular subtense of the Sun. By aligning two of these slit fields of view at some preselected angle to one another, it is possible to measure the angle between the satellite spin axis and the Sun line. Figure 2-96 illustrates the typical orientation of the two sensors, labeled  $\psi$  and  $\psi_2$ . The plane of one fan-shaped field of view is nominally parallel to the spin axis.

By inclining the second sensor to the first, an additional piece of information regarding the aspect of the spin axis to the Sun line is observed. Figure 2-97 shows the geometrical relationship. The  $\psi$ -sensor is a spin angle sensor; its telemetered output pulse serves as a reference for spin angle. The  $\psi_2$  sensor is rotated about the X-axis relative to the  $\psi$ -sensor through the angle  $\epsilon$ .

The desired angle  $\phi$  is obtained by forming the inner product of the Sun line vector  $\bar{S}$  and the unit vector  $\hat{e}$ , normal to the inclined sensor. The unit vectors are expressed in terms of the OEC xyz coordinates as

$$\hat{S} = \hat{x} \cos (\psi - \psi_2) \sin \phi - \hat{y} \sin (\psi - \psi_2) \sin \phi + \hat{z} \cos \phi \quad (2-154)$$

and

$$\hat{e} = \hat{y} \cos \epsilon + \hat{z} \sin \epsilon \quad (2-155)$$

so

$$\hat{s} \cdot \hat{e} = -\sin(\psi - \psi_2) \sin \phi \cos \epsilon + \sin \epsilon \cos \phi = 0 \quad (2-156)$$

Regrouping and writing in terms of  $\phi$ ,

$$\cot \phi = \sin(\psi - \psi_2) \cot \epsilon \quad (-157)$$

Selection of the inclination angle between the two fields of view is based on considerations for pulse width, scan time and accuracy. An angle of 35 degrees represents an optimum angle of inclination. Hence

$$\cot \phi = \sin(\psi - \psi_2) \cot 35 \text{ degrees} \quad (2-158)$$

Typical sensor pulse outputs are illustrated in Figure 2-98 for several vehicle attitudes.

When the spin axis is aligned along the ecliptic normal, both sensors receive the solar energy at the same time. However, if the vehicle is tipped in either direction, there is a time difference between  $\psi$  and  $\psi_2$  pulses as mentioned above.

The  $\psi$  and  $\psi_2$  pulses are telemetered to Voyager (after appropriate pulse squaring), and then to Earth for ground processing and smoothing. The  $\phi$  angle can be determined to  $\pm 0.5$  degree on a per pulse basis. By ground and in-flight calibration of the actual unit, and by smoothing the data over a number of measurements, the  $\phi$  angle uncertainty can be reduced to approximately  $\pm 0.2$  degree ( $3\sigma$ ).

A detailed sensor design is presented in Section 6.5.2.

#### 2.5.4.2 Horizon Sensor

The sun sensor establishes the angle between the Sun line and the OEC spin axis within a 360 degree cone of uncertainty about the Sun line. By measuring the angle from the spin axis to Mars, the spin axis can be uniquely determined.

The horizon sensor contemplated for the OEC mission is simply a horizon crossing indicator operating in the infrared spectrum. When used in conjunction with a spinning satellite such as the OEC, a signal is produced each time the leading and trailing IR limbs of the planet are crossed. Figure 2-99 illustrates how the sensor is used. OEC attitude is determined by measuring the time difference of the leading and trailing edge crossings which is proportional to a scanned chord of Mars.

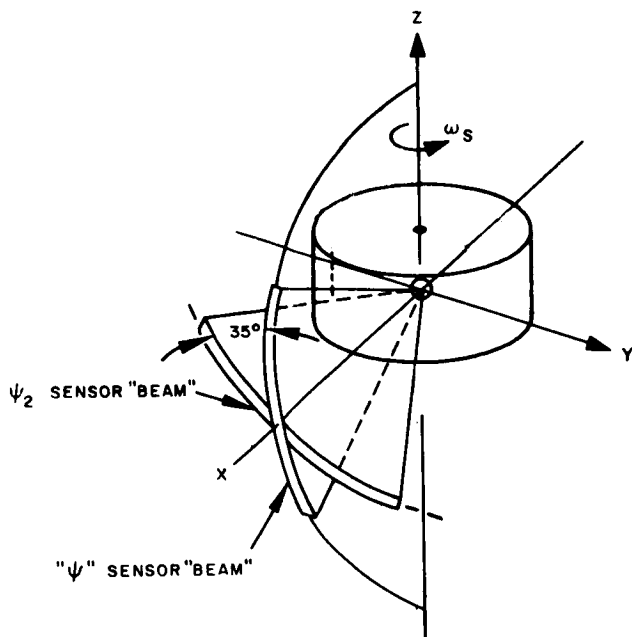


Figure 2-96. Sun Sensor Geometry

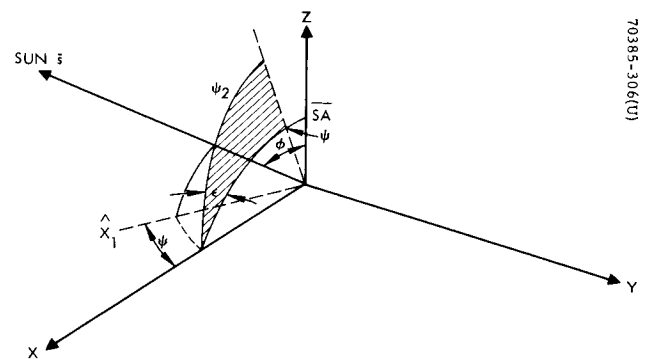
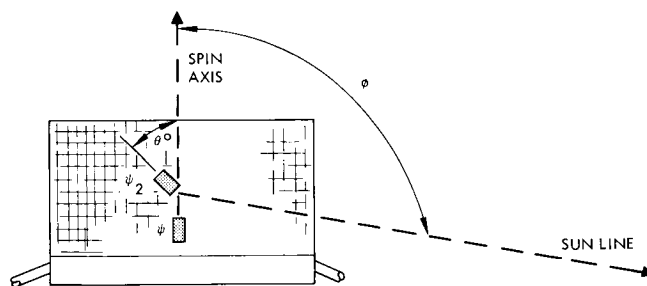


Figure 2-97. Inclined Sensor Geometry



- ANGLE BETWEEN SUN LINE AND SPIN AXIS DETERMINED BY TIME INTERVAL BETWEEN  $\psi$  AND  $\psi_2$  PULSES

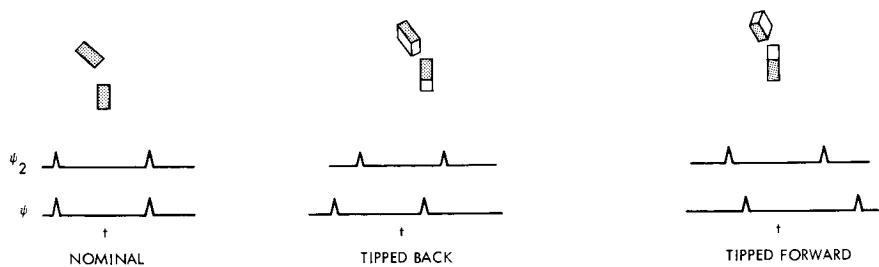


Figure 2-98. Spacecraft Attitude as It Affects Relative Position of  $\psi$  and  $\psi_2$  Pulses

Processed attitude data is used to update the initial OEC orbital information on a periodic basis. By the use of two horizon indicators inclined to one another at some fixed angle, and with knowledge of the spin speed and apparent IR disc, the altitude of the capsule above Mars can be ascertained and used to establish an updated orbit.

This form of horizon sensing for attitude or orbit determination has been applied on such earth orbiting satellites as TIROS and the Hughes HS-308 satellite. The accuracy requirements of each of these missions is greater than that of the OEC, and hence there is no limitation in terms of sensor capability.

The above mentioned satellites are in circular orbits and within an altitude regime of approximately 550 to 34,000 km. Operating with the satellite spin axis normal to the circular orbit plane, the horizon sensor provides a continuous sampled set of earth horizon pulses. Application of this sensing scheme to the OEC's mission is somewhat different in this regard. The OEC orbits are elliptic and the attitude of the capsule is not normal to the orbit plane. Therefore, there is an optimum spread angle between the two sensors so that both cross the planet at some preferred altitude, and there is also associated some particular nominal design position in the orbit. Figure 2-100 illustrates the sensor application with the spin axis shown in the plane of the orbit. For a particular orbit, the spread angle  $\beta$  is contained by

$$\beta_1 \geq \beta \geq \beta_2$$

It is desirable to cross at latitudes greater than 45 degrees because of the sensor sensitivity to chord variations. Sizing the spread angle at apoapsis means that at other positions in the orbit, the sensors will intersect at succeeding larger chords of the planet. As the chord increases in size, the sensitivity to distinguish the actual chord length decreases. If on the other hand, the angle is sized at periapsis, it is apparent that at some later position, the sensors will scan by the planet which is viewed for only a portion of an orbit.

For horizon sensor application in which the satellite spin axis is near normal to the orbit plane, the characteristic of sampling the horizon with both sensors during only a portion of the orbit also exists. This is the case in point for the OEC mission. The parameters which characterize the attitude and orbit determination process are thus interrelated with the type of orbit and OEC attitude as well as Mars characteristics.

Design Conditions. Operating altitudes ranging from 500 km at periapsis to 20,000 km at apoapsis are considered in sizing the cant angle between the two horizon sensors. The angle is defined by

$$\sin\left(\frac{\beta}{2}\right) = \frac{R_m}{h + R_m} \quad (2-159)$$

- SENSOR PROVIDES ATTITUDE AND ORBIT DATA BY MEASURING TIME BETWEEN LEADING AND TRAILING HORIZON CROSSINGS
- REQUIRES {
  - KNOWLEDGE OF SPIN SPEED
  - ANGULAR SEPARATION BETWEEN TWO FIELD-OF-VIEWS
  - PLANET DIAMETER

70287-28(U)

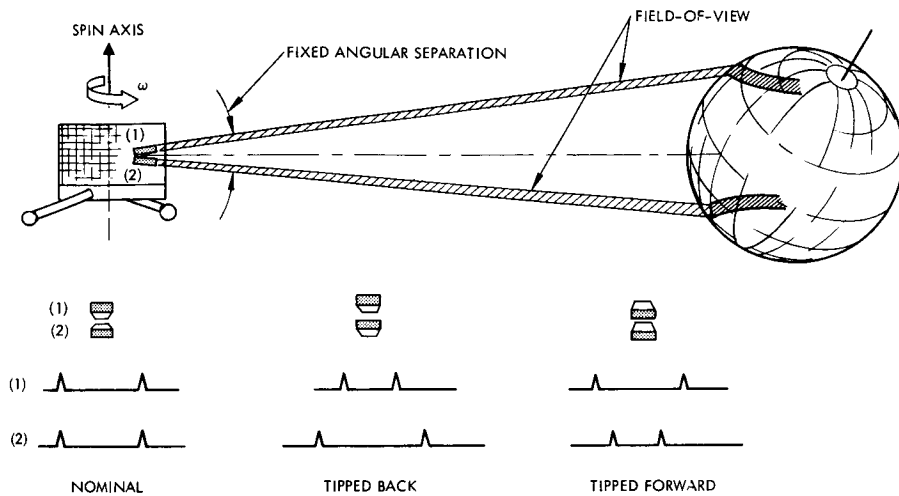
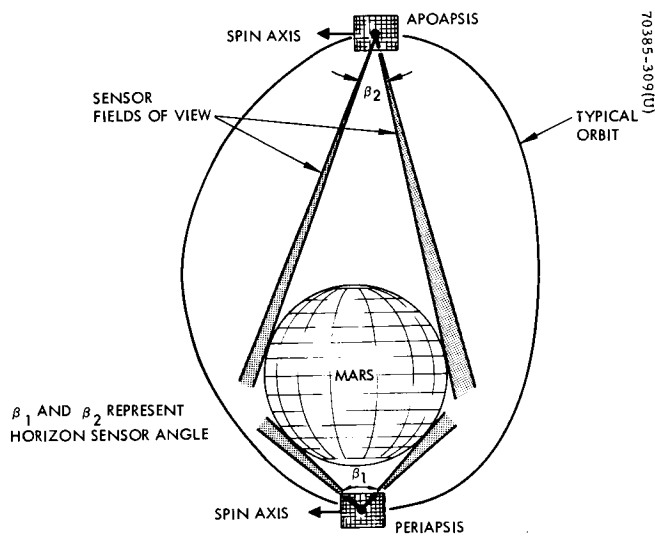


Figure 2-99. Horizon Sensor



70385-309(U)

Figure 2-100. Requirements for Sensor Spread Angle



where

$R_m$  = Mars radius = 3393 km

$h$  = altitude from surface

For the above altitude range, the angle  $\beta$  is constrained to operate between  $17 \geq \beta \geq 102$  degrees, where the angle is defined with respect to the planets actual disc.

Assuming a nominal orbit of 10,000 km at apoapsis and 1,000 km periapsis, an angle of approximately  $\beta = 51$  degrees is selected. This represents an average size spread angle and is equivalent to an orbital altitude of 4,500 km. To increase the indicator sensitivity, it is desirable to have the nominal latitude crossing near 45 degrees. This is equivalent to an optimum sensor spread of  $\beta = \pm 21$  degrees.

A summary of the pertinent design characteristics are presented in Table 2-17.

Based on these accuracies, an unsmoothed error in spin axis determination about the Mars local vertical of approximately  $\pm 1.5$  degrees ( $3\sigma$ ) is expected.

A detailed description of the sensor is given in Section 6.0.

TABLE 2-17. HORIZON SENSOR CHARACTERISTICS

Nominal Mars chord scan time	83.3 milliseconds
Nominal horizon scan time	5.6 milliseconds
Field of view	1.5 x 1.5 degrees
Objective lens	1.125 inch diameter
Minimum irradiance	0.14 microwatts
Minimum detectable signal	100 microvolts
Logic threshold	80 microvolts
Horizon indication error ( $3\sigma$ )	$\pm 0.72$ degree
Maximum horizon indication error including noise ( $3\sigma$ )	$\pm 0.8$ degree
Mars chord error ( $3\sigma$ )	$\pm 1.1$ degrees

### 2.5.5 Determination Process

The OEC mission geometry has been described in Section 2.5.2. Both the ambiguities due to locating the capsule position and attitude have been pointed out. Having described the basic performance of the sun and horizon sensors, the discussion can proceed to the manner by which the attitude and orbit locations are specified from the sensor data. Since both attitude and orbit are located with the same sensors, it is reasonable to operate in the following manner:

- 1) Transmit raw sensor data to Earth.
- 2) Smooth data to provide an attitude accuracy within the desired limits.
- 3) Use the smoothed data for orbit determination program.

#### 2.5.5.1 Attitude Determination

Raw sun sensor data is presmoothed by a single process of averaging successive readings. This technique, which is accomplished at the ground station with conventional electronic computers in a very simple and reliable manner, allows reduction of the normal rss measurement error.

The largest source of error in this device is optical and mechanical misalignment. These errors have resulted in attitude uncertainties of up to several tenths of a degree on past spacecraft and have a greater effect than the random errors. Several methods of reducing these errors are possible:

- Optical alignment or determination of the optical response of the sensor
- Control of the uniformity of the viewing slits as well as the incidence angle of illumination on the sensitive chip.
- Removal of characteristic biases by in-space calibration through comparison with the horizon sensor and through careful data reduction.

Measurements taken by the Mars horizon sensor also contain random and bias type errors. The most restrictive errors are constant bias errors since the random or noise errors are small when smoothed over a sufficient number of measurements. Bias errors affect both types of data available from the Mars sensor: the angle between the OEC spin axis and the Mars local vertical (designated  $\theta_m$ ), and the measurement of the angular separation of the spin axis - Sun line plane and the spin axis - Mars line plane (designated  $\psi_c$ ). As shown in the following discussion, these data types are independent and thus subject to different bias errors. Measurement of  $\theta_m$  is biased by misalignment of the capsule geometrical axis and its true axis of maximum moment of inertia about which it will rotate. Misalignment of the sensor mechanical axis with OEC's geometrical axis contributes to the overall error and in turn the uncertainty in the alignment of the sensor optical axis to its mechanical axis is present.

A final source of error which was discussed is the uncertainty in the Martian infrared horizon. As indicated in Section 6.0, some form of compensation could be gained with additional logic circuitry. However, variation in radiance between the leading and trailing edges of a single scan is the principal source of error in this device.

These errors are summarized together with a breakdown of the bias error sources for  $\psi_c$  data and their expected magnitudes in Table 2-18. These include radial misalignment of the sensor mechanical and optical axes, sun sensor reference pulse uncertainty, and horizon uncertainties. The horizon uncertainty represents the largest source of error.

The exact nature of the effect of each of the enumerated biases on the attitude determination process, and the data reduction techniques required to remove them, are discussed in a later section.

Sensor Equations. This section describes the exact nature of the attitude information derived from the raw measurements made on the capsule. As previously mentioned, three independent types are available:

- $\emptyset$  Data from sun sensor giving the angle between the spin axis and the Sun line
- $\emptyset_m$  Data from Mars sensor giving the angle between the spin axis and the local vertical

TABLE 2-18. MARS SENSOR BIAS ERRORS ( $3\sigma$ )

$\emptyset_m$ Data		
Spacecraft principal axis uncertainty		0.05
Sensor mechanical axis misalignment		0.05
Sensor optical axis misalignment		0.05
Horizon uncertainty effect		1.40
Root sum square		1.40 degrees
$\psi_c$ Data		
Sensor radial misalignment		0.07
Sensor optical axis misalignment		0.05
Sun sensor reference uncertainty		0.10
Horizon uncertainty effect		1.40
Root sum square		1.41 degrees

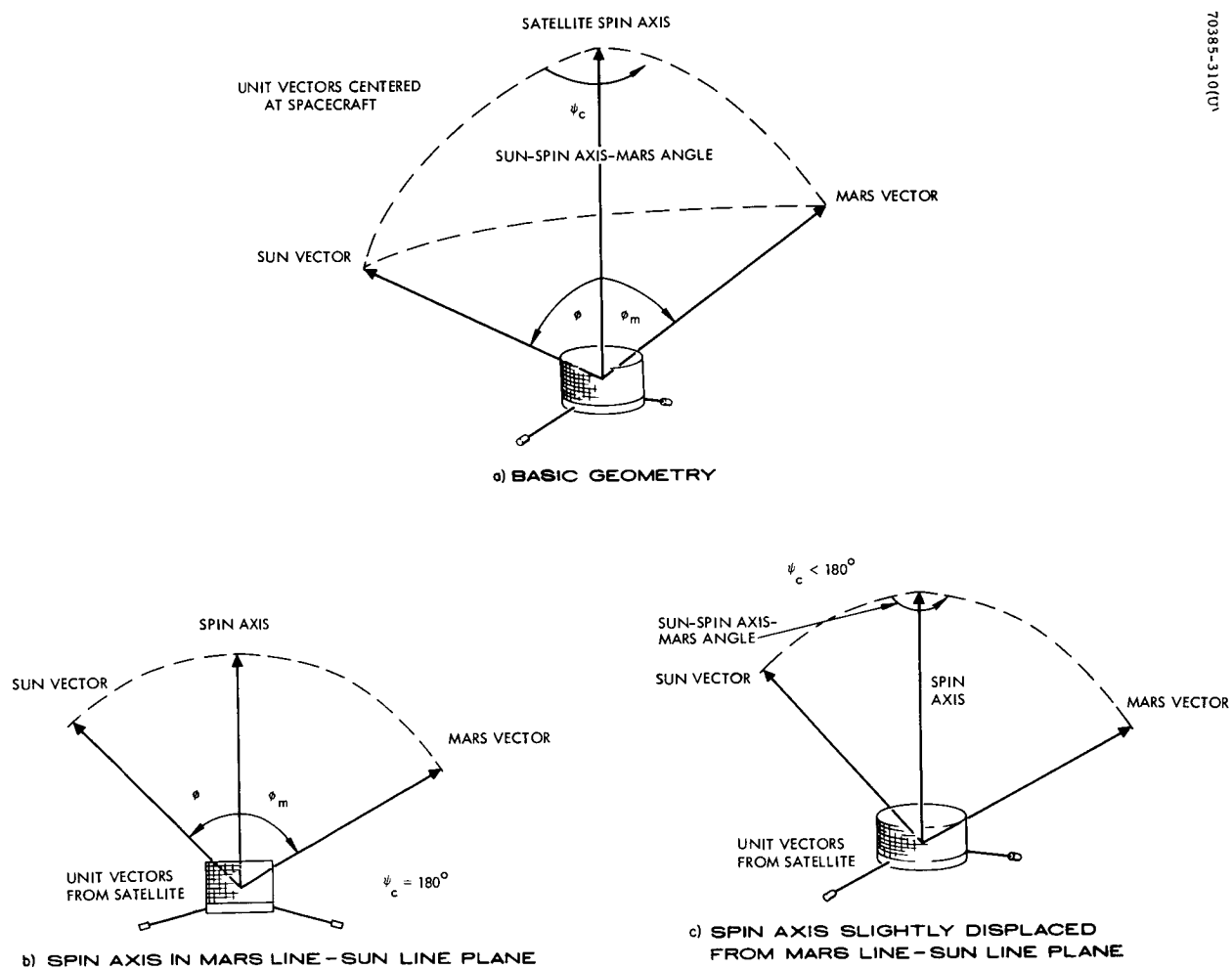


Figure 2-101. Basic Sensor Geometry and Angular Definitions

$\psi_c$  Angle through which spacecraft rotates between receipt of Sun pulse and receipt of Mars pulse

(See Figure 2-101 for illustration.)

Sun sensor or  $\emptyset$  data is obtained directly from the raw measurements of the time separation between successive main beam or  $\psi$  sensor pulses which indicate the spin period and the time delay between the  $\psi$  sensor and the second, canted beam. It is evident that the ratio of this second time to the spin period is the same as the ratio of spacecraft angular rotation during this time to 360 degrees. This rotation angle is designated  $\psi_2$  and is used directly with spherical trigonometry to give the equation for  $\emptyset$  listed in Table 2-19 and developed earlier.

The derivation of the Mars sensor equations also stems from spherical trigonometry. For a brief discussion of the derivation, refer to Appendix A. The computational equations appear in Table 2-19.

The angle  $\emptyset$  is measured in the plane of the spin axis and the Sun line; the angle  $\emptyset_m$  is measured in the plane of the spin axis and the Mars line. If these two planes coincide (Figure 2-101b), then clearly the information is redundant, and worse, neither gives an indication of any attitude component slightly out of this plane, if one is present. (That is, even if the attitude is displaced some small amount from this plane,  $\emptyset$  and  $\emptyset_m$  would change negligibly.)

Fortunately a third type of information is inherent in the sun sensor - Mars sensor combination and is designated  $\psi_c$ . It is defined as the spin angle through which the satellite rotates between receipt of the Sun pulse and receipt of the Mars center pulse. This data is calculated in the manner indicated in Table 2-19 (refer to Appendix A for the approximate derivation). This data tends to be most sensitive, and therefore most useful, when the other two types are redundant. To illustrate this, again consider the case just discussed when the Mars, Sun, and spin axis vectors are all coplanar. As qualitatively indicated in Figure 2.101c, this small out-of-plane component of the spin axis results in a definite change in  $\psi_c$  from the 180 degree (or 0) it would register if the spin axis were in the plane. That is, the partial derivative of  $\psi_c$  with respect to this out-of-plane attitude component is significant.

Attitude Determination Accuracy. The previous discussion characterized the content of data obtained from each of the sensors and the relationship to the measurement of the OEC attitude. Many data points are collected from each of the sensors; this data is then to be used to determine a best estimate of actual (inertial) OEC attitude. The method of attitude estimation adopted is a least squares fit to the expected time variation of the local vertical reference. A detailed representation of the proposed technique is discussed in Appendix A.

The attitude determination process requires only a small amount of the total sun sensor data available per orbit. Since the OEC spin speed is nominally 60 rpm, a measurement of the Sun pulse every revolution will give 3600 samples per orbit (10,000 km x 1000 km altitude). This is more than adequate since the OEC attitude remains fixed in inertial space except for the projected effects of perturbations.

TABLE 2-19. ATTITUDE SENSOR EQUATIONS

Sun sensor

$$\emptyset = \cot^{-1} \left[ \cot \epsilon \sin \psi_2 \right]$$

where  $\emptyset$  = angle between spin axis and spacecraft-to-Sun line

$\epsilon$  = cant angle between sensor beams

$\psi_2$  = spin angle between pulses from each sensor beam

Mars sensor

$$\cos \alpha_1 = \frac{\cos \alpha_o - \cos \emptyset_m \cos \eta}{\sin \emptyset_m \sin \eta}$$

where  $\alpha_1$  = one-half the scan angle of the sensor during which Mars is viewed

$\emptyset_m$  = angle between spin axis and spacecraft-to-Mars centerline

$\eta$  = angle between spacecraft spin axis and sensor optical axis

$\alpha_o$  = apparent semi-diameter of Mars as seen from satellite altitude

$$\psi_c = \cos^{-1} \left[ \frac{\bar{s} \cdot \bar{m} - (\bar{a} \cdot \bar{m})(\bar{s} \cdot \bar{a})}{\sqrt{1 - (\bar{a} \cdot \bar{m})^2} \sqrt{1 - (\bar{a} \cdot \bar{s})^2}} \right]$$

where  $\psi_c$  = spacecraft spin angle between Sun pulse and Mars center pulse

$\bar{s}$  = unit vector from spacecraft to Sun

$\bar{m}$  = unit vector from spacecraft to Mars center

$\bar{a}$  = unit vector in spin axis direction

The data requirements of the Mars sensor are sized somewhat differently since the OEC orbits the planet and does not necessarily view it continuously. The determination of the orbit requires waiting until data is received from both sensors. Obviously, each sensor individually views the planet for a duration which is much greater than the dual coverage period. The sampling rate for the horizon sensor is thus set by the necessity for dual coverage to establish the OEC orbit update.

The attitude determination process is carried forth in a continuous fashion (i. e., data is sampled over the entire mission), providing an update of the spin axis attitude. For example, data is measured over a segment of an orbit and then operated on. This is a repetitive operation. The resulting attitude accuracy is based on smoothing over the measured samples, removing the contribution of random errors. In this manner, a spin axis attitude of  $\leq 1.0$  degree ( $3\sigma$ ) and Sun line attitude of  $\leq \pm 0.2$  degree ( $3\sigma$ ) can be met.

With additional mathematical modeling, it is possible to remove some of the source of bias error. Disturbances such as solar pressure can be modeled with parameters which are estimated as a part of the attitude determination process. These methods are currently being applied on the ATS missions and have provided a greater attitude accuracy.

#### 2.5.5.2 Orbit Determination

There are two aspects of orbit determination to consider: the operational system and the preliminary accuracy analysis. These will be discussed in separate sections, though they are not completely unrelated. Briefly, the discussion of the operational system centers around the orbit determination process as related to the OEC mission, while the preliminary accuracy analysis includes the derivation of error expressions and the results of a digital computer accuracy study.

The orbit determination process consists of two phases: preliminary orbit specification and differential correction. The preliminary orbit can be found using expected injection conditions or a minimal set of measurements (e.g., six independent quantities specify a conic orbit). For the OEC, the former approach will be used, based on knowledge of the Voyager orbit and the nominal separation maneuver and orbit-change maneuver (if any). The differential-correction computations form the bulk of the orbit determination process and are contained in the remainder of this section.

The preliminary orbit will probably not agree with the actual orbit, and the differential-correction computation is a way of using additional measurements to refine the estimate of the true orbit. This is a good place to emphasize a fact that is often forgotten — the output of an orbit determination computation is an estimate of the orbit; the true orbit is never known. To specify the motion of the vehicle completely, it is necessary to know the complete dynamics, including all perturbations, the estimated orbital motion is a "best fit" of the assumed model to the measured data, where the precise meaning of best depends on the correction algorithm. Thus, a successful orbit determination requires a realistic dynamical model as well as sufficient data.

The degree of realism required in the dynamic model used for the orbit determination computation depends on such factors as type of orbit, duration of the mission, amount of measurement data, data rate, and estimation algorithm. For example, for a short-term orbit estimation a relatively crude model may suffice, but for a long-lived mission the problem is more involved. If the measurement data is sparse, a quite refined model may be required, while a greater data rate may allow a simpler model for the proper type of data processing algorithm. Specifically, the orbit determination for a long-term mission with high data rates can be performed as if it were a sequence of short-term estimations, each giving a local fit of a simple model to the latest motion. However, if the algorithm is not made to "forget" earlier data, a more complex model is necessary, even with continuous data.

To complicate the problem somewhat, there are two types of modeling errors: qualitative and quantitative. The former error can be the omission of a perturbing effect or the improper description of the physical mechanism causing a perturbation; the latter error is the use of an incorrect value for a numerical parameter describing a perturbing force. As noted in the preceding paragraph, an intentional qualitative modeling error may be used to simplify the computational complexity of the estimation process; on the other hand, a significant unintentional error can seriously degrade the orbit determination. If a parameter is not known with sufficient precision, it can be included as a quantity to be estimated, and the estimation scheme will compute the best value consistent with the rest of the model. Unknown perturbing forces can be allowed for by including a functional expansion, e.g., a Fourier series, with undetermined coefficients, where the coefficients are mode parameters to be estimated.

The preceding discussion will now be specialized to the OEC mission. The term of the OEC mission is sufficiently long that the orbit undergoes significant perturbations. Because of the two widely differing concepts advanced for the OEC, i.e., orbit-change and co-orbital, the discussion of orbit determination for the OEC is divided into two parts.

Co-Orbital Mission. The keynote of the co-orbital mission is simplicity. The separation maneuver is to be accomplished with sufficient precision that the subsequent motion of the OEC relative to the Voyager can be pre-computed with little error.\* If the inaccuracy of the pre-computed relative motion is sufficiently small, the OEC position can be inferred from the Voyager, since there is a requirement to perform an orbit determination for the Voyager. However, attitude control maneuvers may be performed by the Voyager after separation that introduce significant perturbations in its orbit; if so, the validity of the precomputed relative motion is degraded, and the approach may not provide sufficient precision in the estimate of

---

\*This possibility is considered in Appendix B. The principal error with this scheme occurs due to uncertainty in the (small) difference in orbit period between OEC and Voyager. This parameter could be measured using the Mars sensor; however, with or without Mars sensor data, the scheme is subject to serious objections, as indicated above.



the OEC position\*. Moreover, if the Voyager changes its orbit during the mapping mission, the relative-motion concept cannot be used.

Because of the present uncertainty in the planned Voyager mission, it is necessary to assume that some form of direct orbit determination will have to be performed for the OEC. The question is how? The three schemes that suggest themselves have been discussed earlier. They are Earth-based measurement, Voyager-based measurement, and autonomous or OEC-based measurement.

Orbit Change Mission. For the orbit change mission, the OEC must have sufficient autonomy to provide for the orbital adjustments which are contemplated. In Section 2.5.2, the discussion indicated that the measurement of the attitude and orbit could be accomplished with the proposed sensors.

In that same discussion it was tacitly assumed that it is necessary to measure instantaneously enough quantities to provide a unique estimate of position and attitude; the discussion was oriented to show that orbit determination and attitude determination are but obverse and reverse of a single coin. The next step is to include the dynamic aspect of the estimation, since a sequence of measurements of a changing quantity can take the place of additional measurements of different quantities.

Appendix B presents a discussion of the dynamic modeling considerations and illustrates how the differential corrections could be computed.

The basic idea of the orbit determination computation is to provide a correction to the nominal parameter set. There are a number of ways to approach the actual numerical mechanization of the orbit determination program; the choice depends on a number of factors, some theoretical and some practical.

The orbit update algorithm can be derived on the basis of different smoothed criteria, which may or may not be based on the concepts of probability theory. For the linearized approach, the details of the computations are similar for the probabilistic approaches; indeed, the only difference is in the specification of the matrix  $R$  in the more general expression of the classical least square fit

$$M = [\partial S_h / \partial p]^T R^{-1} [\partial S_h / \partial p]^{-1} [\partial S_h / \partial p]^T R^{-1}.$$

---

\*From the results of the analysis in Appendix B, it is doubtful that sufficient precision can be obtained even if the Voyager position is known exactly.

In the nonprobabilistic theory  $R$  is simply a weighting matrix assigning a measure of the relative importance of the various measurements; in the probabilistic theory  $R$  is the covariance matrix of the measurement noise and the expression

$$\left\{ \left[ \partial S_h / \partial p \right]^T R^{-1} \left[ \partial S_h / \partial p \right] \right\}^{-1}$$

is the covariance of the error in the estimate of  $\Delta p$ , a fact which will be useful for the accuracy analysis later on.

As presented thus far, the orbit determination program is a huge matrix manipulation routine; however, instead of handling the data all at once, the program can do the improvement sequentially, if it is so written. The theory and practice of sequential estimation has received much attention in the literature, and a thorough discussion is beyond the scope of this report; see, for example, References 22 and 23. Appendix B contains a detailed discussion of the sequential approach to the orbit estimation problem.

Accuracy Analysis. An orbit determination accuracy analysis provides an a priori estimate of the dispersion of the error in the orbit correction, and should not be confused with the orbit determination itself. The confusion arises from the fact that the error estimate is computed using a part of the filter; recall that one of the matrix factors relating the measurement error to the correction is the a priori covariance of the error in the estimate, just the quantity desired from an error analysis. The accuracy analysis can be performed as a single matrix computation or sequentially, just as the orbit determination itself; the choice between the approaches is strictly practical, since the resulting answers are theoretically equivalent. The differences between the accuracy program and the determination program are the following. First, there is the obvious difference that a state correction is never computed during an accuracy computation; as trivial as this may seem, it is sometimes overlooked. Second, the nominal parameters are not updated, there is no need for relinearization or iteration. The resulting accuracies are only as good as the linearization, and it may be useful to modify the nominal to ascertain the sensitivity of the covariance to such changes.

Accuracy estimates were run for an orbit with a 10,000 km apoapsis altitude and 1500 km periapsis altitude. The assumption was made that the two planet sensors were canted  $\pm 15$  degrees to the vehicular equator, i.e., 30 degrees apart. This assumption, although different from the desired separation of 41 degrees does not greatly change the results. The basic difference is the time that each sensor intersects the planet and the duration that both sensors intersect. Having specified a desired separation angle, the only two variables are the nominal position in orbit where the sensor is optimally designed and the minimum number of samples of the Mars horizon in the vicinity of this point. The portion of the orbit during which the planet is seen by the sensors depends on the attitude of the OEC with respect to the orbit. From Appendix B it follows that the altitude of the orbit must be less than 9790 km if both sensors are to see the planet. From the polar equation for a conic trajectory

$$r = \frac{a(1 - e^2)}{1 + e \cos v} \quad (2-161)$$

where  $r$  is the radial distance from the focus to the conic,  $a$  is the semimajor axis,  $e$  is the eccentricity, and  $\nu$  is the angle from the periapsis direction to the radius vector, it is easy to find the zone of possible sightings by both sensors, which is shown in Figure 2-102. Note that if the OEC spin axis is normal to the orbit plane, Figure 2-102 shows the only region of visibility. If the spin axis is in the orbit plane, aligned with the axis, the visibility regions, found graphically, are as shown in Figure 2-103(a), Orientation A. Similarly, if the spin axis is aligned with the minor axis, the visibility zones are those shown in Figure 2-103(b), Orientation B. The two-sensor region of Figure 2-103 was picked as a representative pessimistic case for the study; this case corresponds to about 20 minutes of data on each side of the 7-hour orbit.

Another important attitude-like parameter is the position of the Sun with respect to the orbit plane. For example, if the Sun vector is normal to the orbit plane, to first order, the angle between the Sun-OEC and Mars,  $\eta$ , provides no information about the in-plane parameters of the orbit. Similarly, if the Sun vector is in the orbit plane, to first order, the angle  $\eta$  provides no information about the out-of-plane parameters. Moreover, if the Sun vector is close to the orbit plane, the sun sensor may be eclipsed and solar illumination from the region behind the disc of Mars may result in the loss of planet sensor information. Three sun vectors were chosen for the accuracy estimation study; two were inclined 45 degrees to the orbit plane, one with its projection along the major axis, the other with its projection along the minor axis; the third sun vector was in the orbit plane aligned with the minor axis. The assumption was made that one entire view period per orbit was lost because of eclipsing in the last case.

The next class of inputs are the statistics of the errors in the initial state, as reflected in the initial covariance matrix; these were the most difficult to assess. The initial errors in the OEC orbit are due to three sources: the uncertainty in the Voyager orbit, the uncertainty in the separation maneuver, and the uncertainty of any orbit-change maneuver. Because of the small separation velocities envisioned, the uncertainty in the velocity increment is a negligible portion of the initial error; assuming a  $3\sigma$  value of 10 percent execution error for a nominal separation of  $10^{-3}$  km/min results in a variance of about  $0.3 \times 10^{-8}$  (km/min)<sup>2</sup>. Since orbit change maneuvers may be on the order of 200 times as large as the separation, as measured by velocity increment, the variance for an equivalent percent error is  $4 \times 10^{-4}$  as large as that for separation. The difficulty is assessing the errors due to the uncertainty in the Voyager orbit arises from the lack of definitive information about orbit determination for Voyager. However, some data is available in the form of requirements in Reference 1.

The Voyager orbit determination requirements were given in terms of the semimajor axis  $a$ , the eccentricity  $e$ , and the time of periapsis passage  $t$ . For definiteness, the initial position was assumed to be at apoapsis; as a result errors in  $a$  and  $e$  could be translated into radial errors and errors in  $t$  into in-track errors. Since no information was given about cross-track errors, they were assumed to be equal to in-track errors. The apoapsis altitude errors are found from the equation for the apoapsis radius

$$r_a = a(1 + e) \quad (2-162)$$

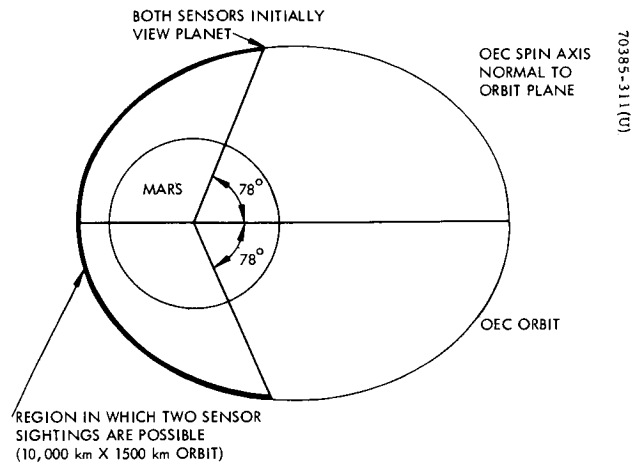


Figure 2-102. Orbit Geometry for Mars Sensor Measurements

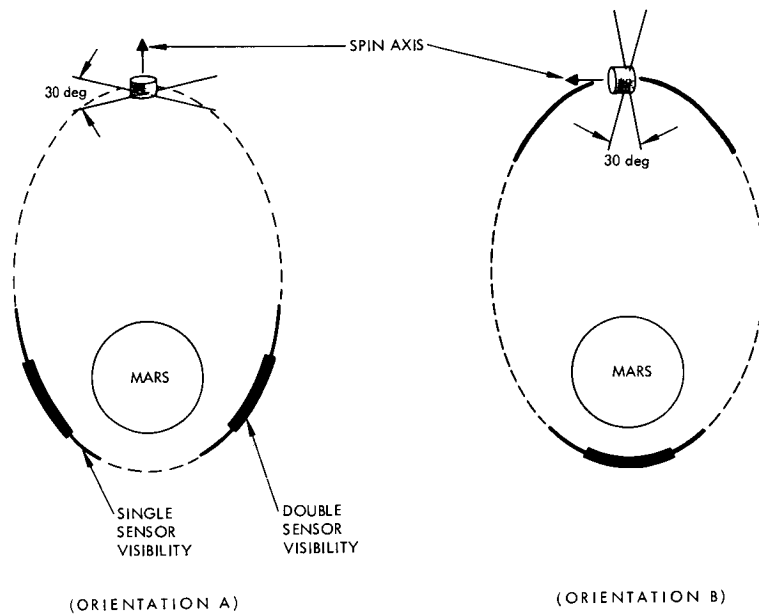


Figure 2-103. Sensor Measurements for Spin Axis in Orbit Plane

from which

$$\Delta r_a = (1 + e) \Delta a + a \Delta e \quad (2-163)$$

This error in the time of periapsis passage can be related to a position error through the periapsis velocity, which can be found from the formula for speed as a function of radial distance from the force center

$$v^2 = \mu \left( \frac{2}{r} - \frac{1}{a} \right) \quad (2-164)$$

The apoapsis position error is related to the periapsis position error by the ratio of apoapsis radius to periapsis radius, since a change of periapsis position implies a rotation of the entire line of apsides. It was further assumed that the resulting position error variance was the sum of equal in-track and cross-track errors. The worst case requirements from Reference 1 are given in Table 2-20; the resulting initial error variances, assumed uncorrelated, are given in Table 2-21. It should be noted that the design goal for Voyager is at least an order of magnitude better than the worst case requirements listed.

TABLE 2-20. VOYAGER ORBIT ACCURACY REQUIREMENTS

Quantity	3 $\sigma$ Error
Semimajor axis, a	10 km
Eccentricity, e	$10^{-4}$
Periapsis passage time, t	5 seconds

TABLE 2-21. ASSUMED INITIAL ORBIT ERROR VARIANCES

Quantity	Initial Variance
Radial position	$25 \text{ km}^2$
In-track position	$112.5 \text{ km}^2$
Cross-track position	$112.5 \text{ km}^2$
Radial speed	$0.013 (\text{km/min})^2$
In-track speed	$0.08 (\text{km/min})^2$
Cross-track speed	$0.08 (\text{km/min})^2$

The final set of inputs to the program specifies the sensor characteristics, including the spin rate of the vehicle, which is the basic limitation to the sampling rate. The minimum value, 50 rpm was used for the spin rate. The basic angle accuracy was assumed to be 1.5 degrees ( $3\sigma$ ), with three variations: all the error is bias error, all the error is random error, and the error is half bias and half random. For range measurements, the error was taken as the Voyager position uncertainty, since the measurement itself could be made much more accurate.

The first set of runs was for angle sensors only and resulted in the error curves shown in Figure 2-104. The curves in Figure 2-104a correspond to a sun vector oriented 45 degrees to the orbit plane with its projection aligned with the minor axis of the orbit. The trends shown in Figure 2-104a are generally what would be expected; errors due to biases decrease more slowly than errors due to random noise, although the ultimate behavior is nearly the same. For the situation described, the desired position accuracy can be achieved with at least a probability of 0.97 after about four and one-half orbits. The curves in Figure 2-104b correspond to a sun vector oriented 45 degrees to the orbit plane with its projection aligned with the major axis of the orbit.

Qualitatively, Figures 2-104a and 2-104b are quite similar, but the accuracy achieved by the orbit determination in the latter situation is somewhat worse; by extrapolating it appears that the desired accuracy can be reached in about five and one-half orbits. The curves in Figure 2-104a appear to be much worse than those in the preceding cases, which is understandable; the orientation of the Sun vector along the minor axis results in a solar eclipse during one measurement period, which, by the ground rules set up, is considered equivalent to a complete information blackout. Thus the estimation modeled in the computations leading to Figure 2-104a is based on half the information available in the other cases, which would suggest that the estimation takes about twice as long to reach any given accuracy. The prediction is roughly borne out by the portion of the curve shown.

Should it be necessary or desirable to improve the estimation accuracy faster than the sensors alone allow, range information can help. Ranging to Voyager for example as a vernier correction on OEC position can provide a reduction in the uncertainties in a shorter number of orbits. To demonstrate how effective ranging is, the worst-case situation was rerun, modified by the addition of seven range fixes during the first orbit, as shown in Figure 2-105. The Voyager initial state was perturbed slightly from that of OEC, 5 km in position and 0.5 km/min in velocity to simulate the effects of a small orbit change maneuver. The overall range accuracy was taken as 26 km ( $3\sigma$ ) which includes actual range imprecision plus Voyager uncertainty. Note that the Voyager position accuracy for the purpose of the range measurement was assumed to be somewhat better than that given by the maximum eigenvalue of the initial error covariance for OEC; this was done somewhat arbitrarily to account in some way for the fact that the range vector rotates and not all measurements are really as bad as the worst case would imply. In any case, the accuracy used is still quite conservative. The improvement in the estimate is dramatic, as is shown in Figure 2-106. Further improvements would result if range measurements were taken over more orbits.

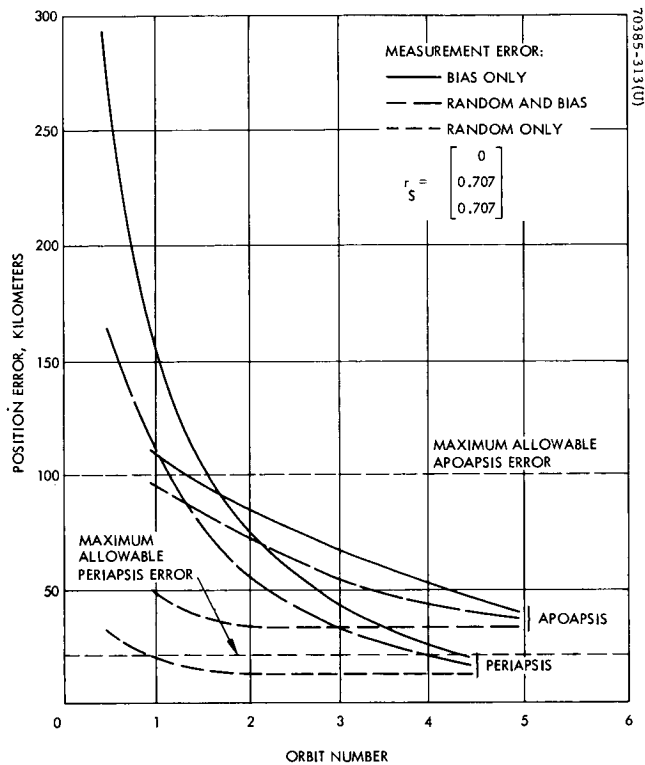
A sample run was made for a nominal orbit with a 20,000 km apoapsis altitude and a 1500 km periapsis altitude, and the results indicated that the expected accuracy is roughly equal to that obtained in the lower orbit on a per orbit basis, at least for two orbits. A complete five-orbit run could not be made because of a numerical instability problem. Because the orbit is higher, the sensor information is of poorer quality, but the speed is lower, allowing more data to be gathered; the two effects balance each other out, resulting in equivalent accuracies. However, since the higher orbit has a period which is about twice as long as that of the lower orbit, it takes about twice as long to achieve a given accuracy.

Before the discussion of the results is terminated, some comments should be made about the meaning of the number used to present the results of the accuracy computation. As noted previously, the position error was taken as three times the largest dimension of the error ellipsoid; this choice implies that the probability that the true position is within a sphere about the estimated position of radius equal to the stated error number is at least 0.971. If instead of three times the maximum  $\sigma$ , some other factor, say  $k$  times the maximum  $\sigma$ , were used the lower bound on the probability would be different. The variation of probability with  $k$  is given in Appendix B, Equation B45, and is plotted in Figure 2-107. The value chosen for  $k$  is just past the knee of the curve; increasing  $k$  does not increase probability much, but reducing  $k$  has a considerable effect. Figure 2-108 shows the behavior of the  $1\sigma$ ,  $2\sigma$ ,  $3\sigma$ , and  $4\sigma$  boundaries with time for the worst case estimate. Thus, the time to reach a given accuracy depends on how much confidence is to be placed in the accuracy figure.

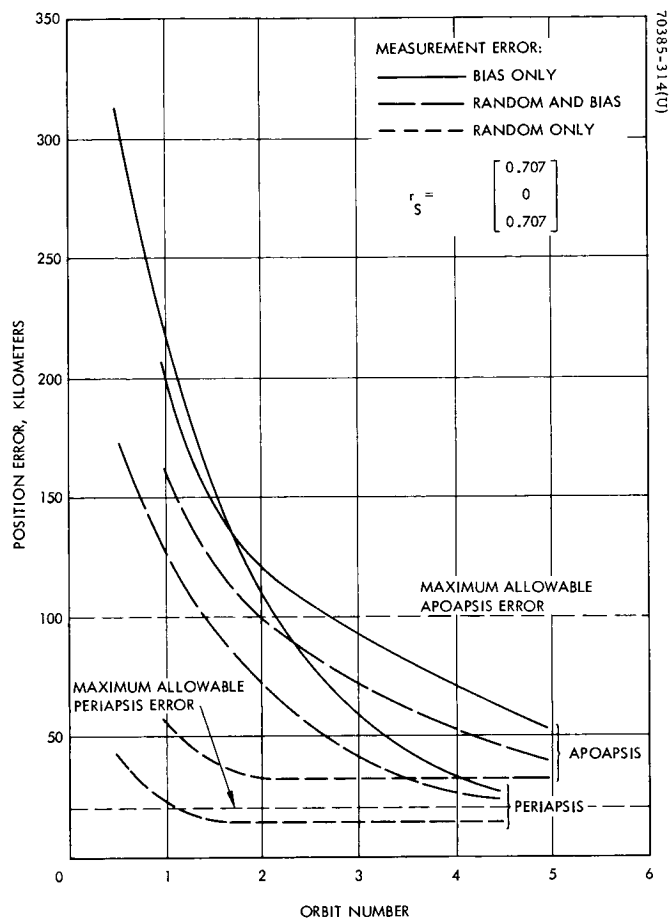
Conclusions. Based on a rather conservative estimate of the expected orbit determination accuracy for OEC, the position of the spacecraft can be specified to within 10 km at periapsis and 60 km at apoapsis, with probability greater than 0.97, after an observation period of a few days.

The exact time to achieve the desired accuracy depends on the actual orbit and sensor error characteristics. The maintenance of the precision over long periods of time depends on the type of orbit determination program and the validity of the dynamic model.

The results assume that the sun and Mars sensors uniquely define the attitude and position. For these results to apply to the OEC mission, another piece of information must be assumed to resolve the attitude/orbit ambiguity; otherwise the errors are actually greater. The baseline OEC mission does contain an S-band link, and hence the above accuracies are valid.



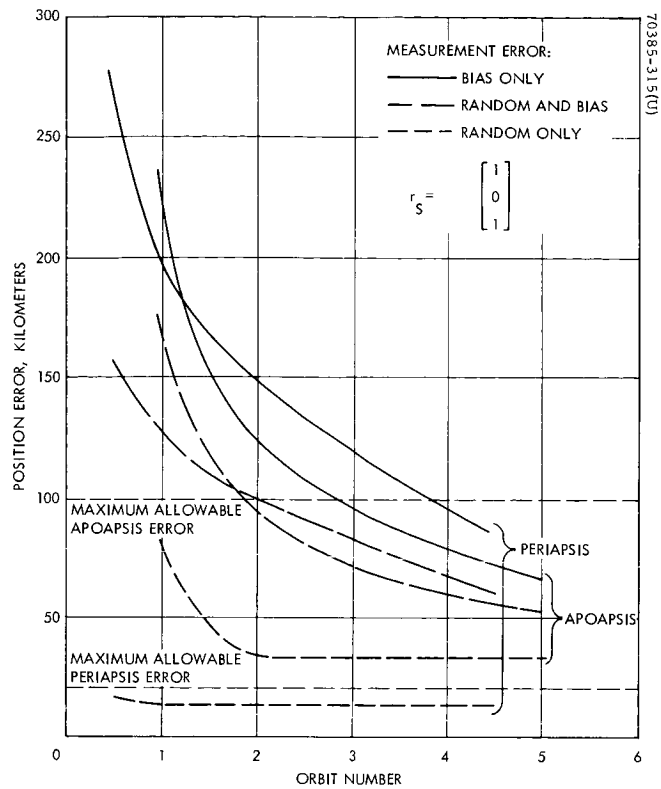
a) CASE 1



b) CASE 2

Figure 2-104. Estimation Accuracy for Mars and Sun Sensor





c) CASE 3

Figure 2-104 (continued). Estimation Accuracy for Mars and Sun Sensor

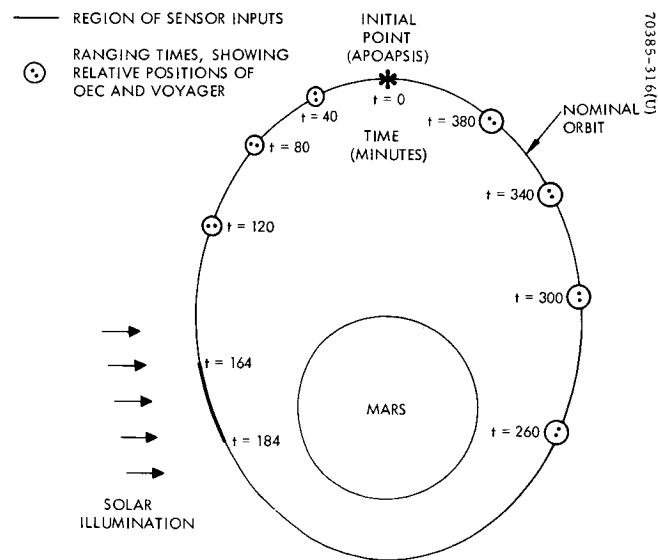


Figure 2-105. Application of Ranging to Voyager in Addition to Mars and Sun Sensor

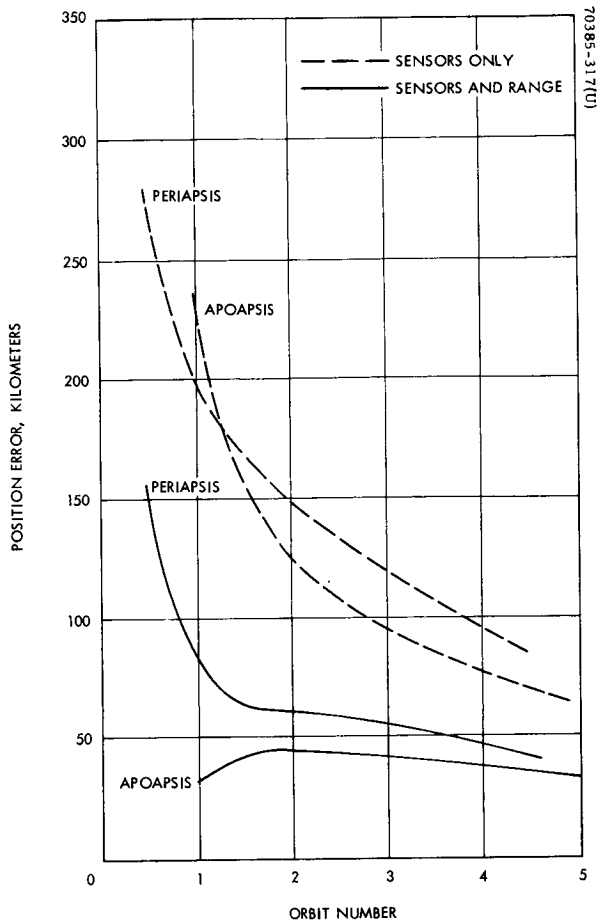


Figure 2-106. Effect of Range Measurements on Accuracy

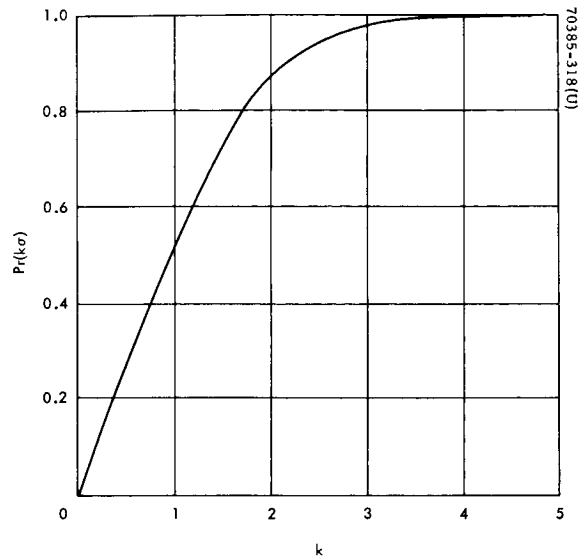


Figure 2-107. Probability Content of  $k\sigma$  Ellipsoid

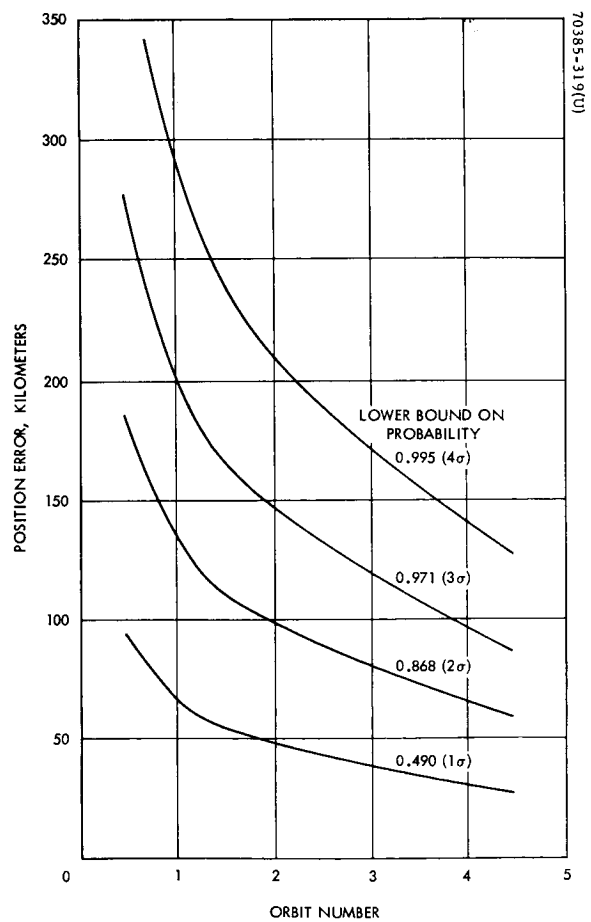


Figure 2-108. Comparison of Position Error to Criteria for Measurement

## 2.6 ATTITUDE STABILIZATION, CONTROL, AND ORBITAL MANEUVER REQUIREMENTS

In this section, the external perturbations and controlled changes which alter the OEC attitude and orbit are considered. A design requirement of the OEC mission is that the stabilization system operate over the 6 month lifetime. This is true for the co-orbital as well as orbit change systems. To determine if the attitude accuracy requirements can be met, the perturbing forces acting on the capsule and causing its attitude to deviate from the ecliptic normal must be assessed. The requirements for attitude corrections and changes preliminary to an orbit maneuver must also be determined to provide for the sizing of the propulsion system. Finally, the velocity increment requirements for changing the orbit of the OEC must be established for the various maneuvers contemplated.

### 2.6.1 Effects of External Disturbances on Attitude

Design of the attitude control system requires the determination of the attitude errors due to external disturbances such as solar radiation pressure, Martian gravitational effects, and aerodynamic drag. These disturbances are treated, but first the assumed OEC orbital environment is established.

For the purposes of discussing the stabilization tradeoffs and analyses, a nominal spacecraft and three basic elliptical orbits are assumed.

The nominal spacecraft parameters assumed for the various analyses are:

$I_z$ (spin inertia)	= 7.5 slug-ft <sup>2</sup>
$I_y$	= 7.0 slug-ft <sup>2</sup>
$I_x$	= 5.0 slug-ft <sup>2</sup>
M (mass)	= 4.1 slugs
$\omega_s$ (spin speed)	= 60 rpm

The characteristics of the three selected elliptical orbits are as follows:

#### Co-orbital Mission

Apoapsis, $h_a$	10,000 km
Periapsis, $h_p$	1000 km
Eccentricity, $e$	0.5051
Semimajor axis, $a$	8910 km

Semi-latus rectum, p	$a(1-e^2) = 6637 \text{ km}$
Period, P	7.08 hours
<u>Orbit Change Case I</u>	
Apoapsis, $h_a$	10,000 km
Periapsis, $h_p$	500 km
Eccentricity, e	0.5485
Semimajor axis, a	8660 km
Semi-latus rectum, p	6054 km
Period, P	6.79 hours
<u>Orbit Change Case II</u>	
Apoapsis, $h_a$	10,000 km
Periapsis, $h_p$	200 km
Eccentricity, e	0.5758
Semimajor axis, a	8510 km
Semi-latus rectum, p	5689 km
Period, P	6.61 hours
Mars gravitational constant, $\mu$	$4.28 \times 10^4 \text{ Km}^3/\text{sec}^2$
Orbital inclinations relative to ecliptic	$5 \text{ degrees} \leq i_e \leq 45 \text{ degrees}$

The equations used in describing the various orbital functions are:

$$r \text{ (radius)} = \frac{a(1-e^2)}{1+e \cos \theta} \quad (\theta \text{ measured from periapsis}) \quad (2-165)$$

$$\dot{\theta} \text{ (angular rate)} = \frac{\mu^{1/2} a^{1/2} (1-e^2)^{1/2}}{r^2} \quad (2-166)$$

$$V_o \text{ (tangential velocity)} = \frac{\mu^{1/2} (1+e^2 + 2e \cos \theta)^{1/2}}{a^{1/2} (1-e^2)^{1/2}} \quad (2-167)$$

$$t \text{ (time measured from periapsis)} = \frac{P}{2\pi} (E - e \sin E) \quad (2-168)$$

$$E = \sin^{-1} \left[ \frac{(1-e^2)^{1/2} \sin \theta}{1 + e \cos \theta} \right] \quad (2-169)$$

$$P = \frac{2\pi a^{3/2}}{\mu^{1/2}} \quad (2-170)$$

$$a = \frac{r_a + r_p}{2} \quad (2-171)$$

The disturbance torques acting on a vehicle which tend to precess the spin axis from its desired orientation result from gravity gradient, secular solar pressure, and, for low periapses, aerodynamic effects. Magnetic torques will be negligible because of experiment requirements for magnetic cleanliness.

#### 2.6.1.1 Solar Pressure Torques

Considerable effort has been devoted at Hughes on such programs as ATS, Syncom, and Early Bird to study and minimize the effects of solar radiation pressure on similar, but more complex, vehicle configurations. In addition, in-flight precession rate data for Syncom 2 has verified the predicted torque values for that vehicle within the attitude measurement granularity.

The simplified spacecraft model utilized in this analysis consists of a 34 x 35 inch cylinder open at both ends (4 inch openings assumed). The torque about an axis normal to the spin axis (z-axis and the Sun line of sight) is expressed as (Figure 2-109):

$$T = \rho_m F(\nu_i, r, h, h_e, \theta, L_z) \quad (2-172)$$

where

$\nu_i$  = reflectances of various surfaces

$r, h, h_e$  = spacecraft dimensions

$h_m = h + 2h_e$

$\theta$  = angle between spin axis and Sun line of sight, nominally 90 degrees

$L_z$  = distance from CP to cg

$\rho_m$  = solar pressure constant

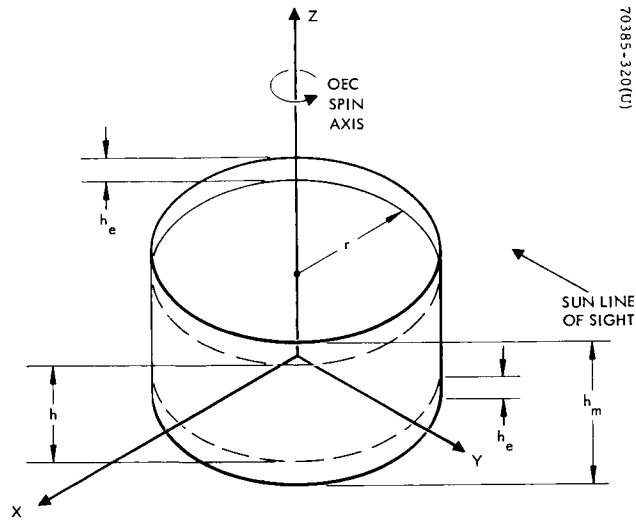


Figure 2-109. Representative Spacecraft Configuration for Solar Torque Determination

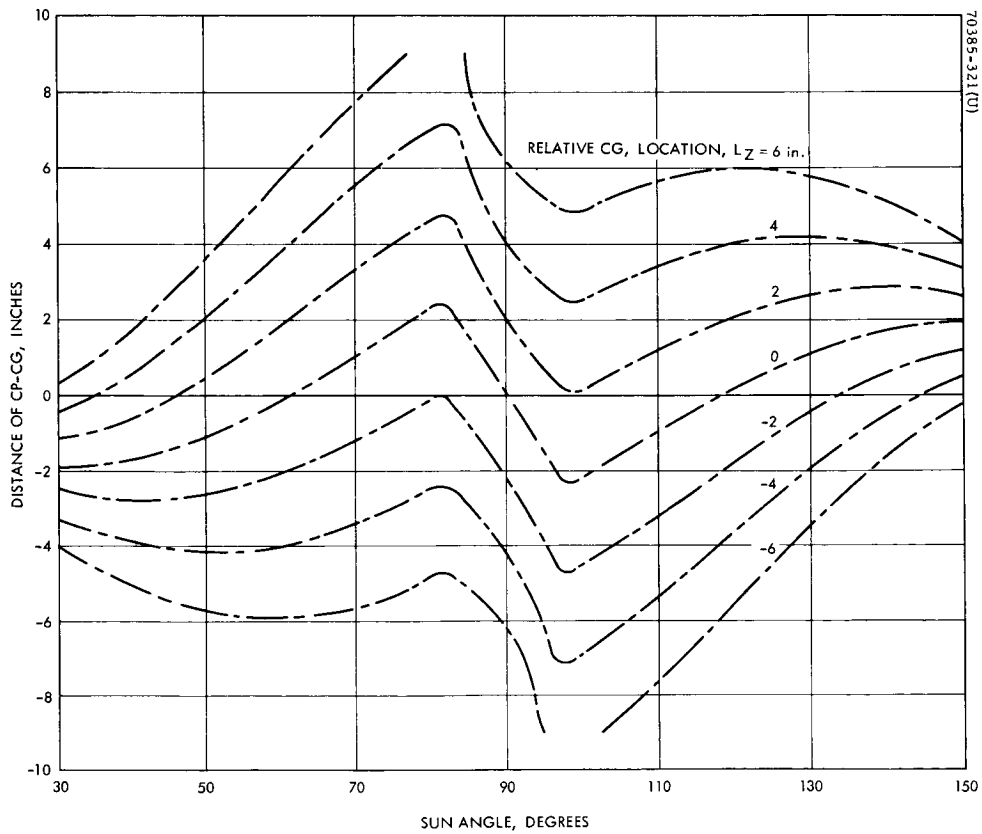


Figure 2-110. Variation of Effective Solar Pressure CP-CG With Sun Angle

$$= \rho_{\text{earth}} \left( \frac{R_e}{R_m} \right)^2 = 4.1 \times 10^{-8} \text{ lb/ft}^2$$

The booms are not included in the solar model as their effect is negligible.

The complete set of expressions implied in Equation 2-172, including shadowing effects, are programmed on the digital computer and developed in References 15 and 16. The program output yields the solar torques for various values of  $\phi$ . For purposes of parametric tradeoffs, Equation 2-172 may be expressed as:

$$T_x = \rho_m (3 + \nu_c) \left[ \frac{2rh_m}{3} \right] l(\phi, \nu_i) \quad (2-173)$$

$$= \rho_m A l(\phi, \nu_i) = 5.624 \times 10^{-7} (\text{ft-lb/ft}) l$$

where

$l(\phi, \nu_i)$  = effective CP - cg offset

computed by the digital program

$$= \frac{F(\nu_i, r, \dots)}{A\rho}$$

and

$$A\rho = \left[ (3 + \nu_c) \left( \frac{2rh_m}{3} \right) \right]$$

= effective projected area for

normal incidence ( $\phi = \pi/2$ )

The variation of  $(\phi, \nu_i)$  is illustrated in Figure 2-110 for many values of  $L$  (relative cg location). For this analysis, a vehicle CP-cg location of +2 inches is <sup>z</sup> assumed.

The resulting change in the spacecraft angular momentum per orbit as a function of  $\phi$  ( $\phi$  remains constant over several orbits) is illustrated in Figure 2-111. This change in angular momentum is periodic in inertial space with period of 1 year causing the z-axis to precess from its inertial position.

The nominal orientation of the spacecraft will determine the variation of  $\phi$  over the vehicle lifetime. For a nominal spin axis orientation normal to an orbit plane inclined 45 degrees to the ecliptic,  $45 \text{ degrees} \leq \phi \leq 135 \text{ degrees}$ . If

orientation is normal to the ecliptic, variations in  $\phi$  will be a small angle about the nominal  $\pi/2$ . The constraints for solar cell illumination and the attitude sensors will dictate the allowable variations in  $\phi$ . In order to account for the potential variations in  $\phi$ , the maximum change in the angular momentum per orbit is  $5.65 \times 10^{-3}$  ft-lb-sec/orbit (periapsis - 1000 km).

#### 2.6.1.2 Gravity Gradient Torques

The net gravity gradient torque acting on the spacecraft about an inertial axis normal to the spin axis is given by:

$$T_x = -3 \frac{\mu}{r^3} \Delta I a_{23} a_{33} \cos \theta \quad (2-174)$$

where

$\Delta I$  = effective inertia difference between the spin axis and transverse axes

$$\Delta I = I_z - \left( \frac{I_x + I_y}{2} \right) \quad (2-175)$$

$a_{23}, a_{33}$  = direction cosines relating orientation to areocentric coordinate set

Resolution of an inertial spin axis attitude error,  $\phi_\mu$ , at periapsis relative to the areocentric coordinate set results in the expressions for the direction cosines given as:

$$\begin{bmatrix} x \\ y \\ z \end{bmatrix} = \begin{bmatrix} a_{11} & a_{12} & a_{13} \\ a_{21} & a_{22} & a_{23} \\ a_{31} & a_{32} & a_{33} \end{bmatrix} \begin{bmatrix} X \\ Y \\ Z \end{bmatrix} \quad (2-176)$$

The necessary direction cosines are:

$$a_{23} = -\sin \phi_\mu \cos \theta \quad (2-177)$$

$$a_{33} = \cos \theta_\mu$$



Substituting Equations 2-175 and 2-176 into 2-174, and solving for  $T_G \Delta t$ , the angular momentum added per orbit in inertial coordinates due to gravity gradient torques, results in:

$$\begin{aligned}
 T_G \Delta t &= \frac{3 \mu \Delta I \sin 2 \phi_\mu}{2} \int_0^\tau \frac{\cos^2 \theta dt}{r^3} \\
 &= 6 \Delta I \omega_p \sin 2 \phi_G \int_0^{\pi/2} (1 + e \cos \theta) \cos^2 \theta d\theta \quad (2-178) \\
 &= 6 \omega_p \left[ I_z - \frac{(I_x + I_y)}{2} \right] \left( \frac{\pi}{4} + \frac{2e}{3} \right) \sin 2 \phi_\mu
 \end{aligned}$$

where

$$\omega_p = \dot{\theta}(p) = \text{angular velocity at } r = p$$

(see Equation 2-165)

Evaluating Equation 2-178 for various periapsis altitudes ( $h_p$ ) for the selected orbits results in the variation of the normalized gravity torque momentum change  $(T_G \Delta t)/(\Delta I \sin 2 \phi_\mu)$  for the three orbital cases considered.

The results are tabulated in Table 2-22.

Substitution of the inertia values, given previously, into the normalized angular momentum change results in Figure 2-112 which illustrates the variation of  $T_G \Delta t$  with  $\phi_\mu$  and periapsis altitudes. If the satellite transverse alignment of inertia is not identical, as might be the case, the impulse  $T_G \Delta t$  could be 20 to 30 percent larger.

The angle  $\phi_\mu$  is constrained to lie between  $\pm 45$  degrees if the spin axis orientation is normal to the ecliptic. However, for nominal orientation normal to the orbit,  $\phi_\mu$  is a small angle. Therefore the maximum gravity gradient disturbance

TABLE 2-22. NORMALIZED GRAVITY TORQUE MOMENTUM CHANGE

Orbital Periapsis, km	$(T_G \Delta t)/(\Delta I \sin 2 \phi_\mu)$ , ft-lb-sec/slug-ft <sup>2</sup>
1000	$2.58 \times 10^{-3}$
500	$3.04 \times 10^{-3}$
200	$3.39 \times 10^{-3}$

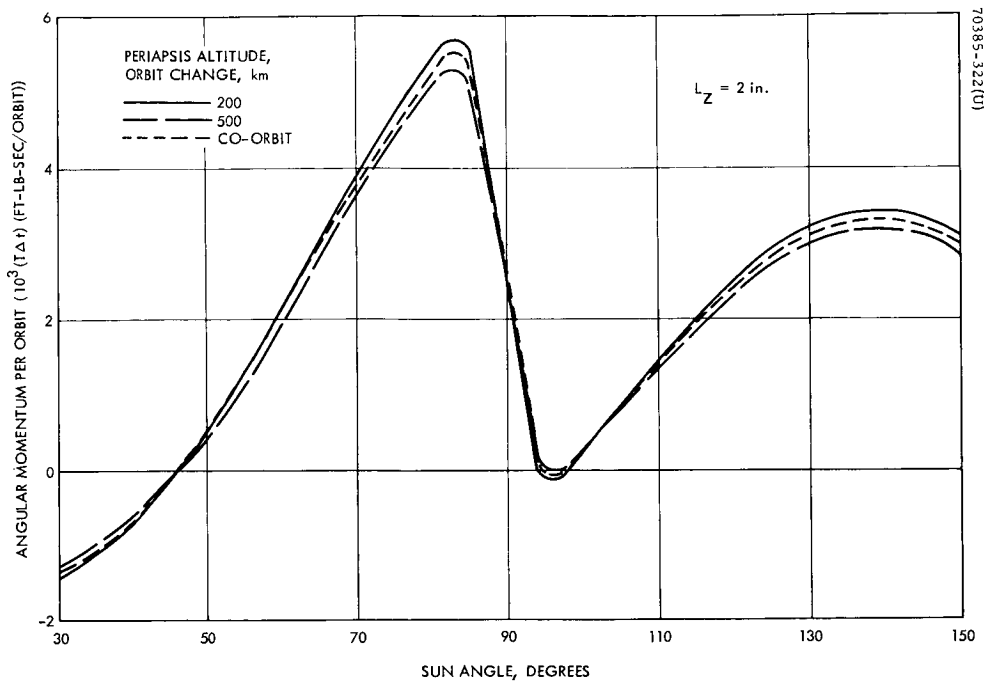


Figure 2-111. Variation of Angular Momentum Added Per Orbit Due to Solar Incidence Angle

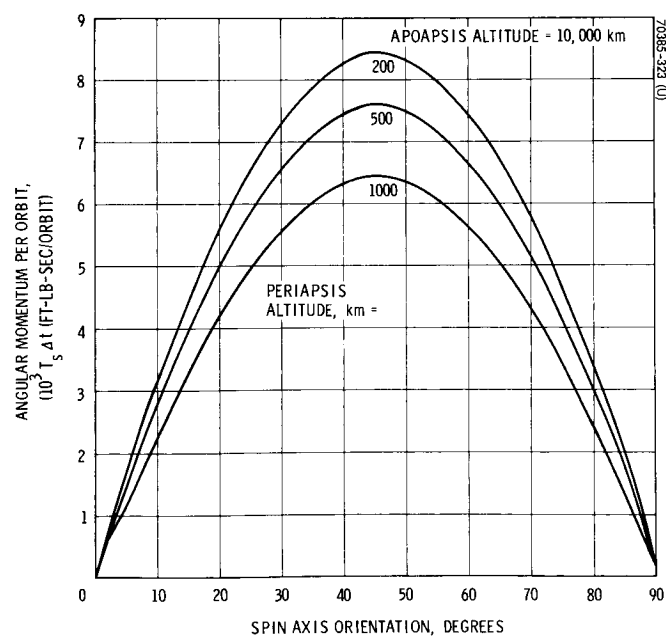


Figure 2-112. Variation of Angular Momentum Added Per Orbit Due to Gravity Torque Versus Spin Axis Orientation to Orbit Normal

torques occur at  $\phi_\mu = \pm 45$  degrees and will be used for the sizing of the control system propellant requirements. Although these torques are cyclic over a year, they appear secular for the 6 month mission projected.

### 2.6.1.3 Aerodynamic Torques

The process of solar torque estimation can be applied to aerodynamic torque estimation, assuming the effective reflectances equal to zero and replacing the solar pressure constant,  $p_0$ , with the incident pressure for free molecular flow,  $\rho V^2$ , in the direction of the orbit tangential velocity vector.

The Martian atmosphere assumed in this study is taken from the table of atmospheric characteristics given in Section 2.2. The model labeled VM-9 was shown to be the most critical with respect to lifetime requirements and is therefore chosen for this worst case analysis.

Based on the given atmospheric parameters, a power law approximation was used to determine the appropriate relationship between the density and altitude. The variation of density with altitude is used to produce Figure 2-113 where the value of  $\rho V_c^2$  lb/ft<sup>2</sup>, is given as a function of altitude for a circular orbit.

Since the density drops off very rapidly for altitudes greater than 400 km, the orbital time spent below this altitude is required; i.e., for a 400 km circular orbit,  $T\Delta t = 6.5 \times 10^{-5}$  ft-lb-sec/orbit. Converting this value to an elliptical orbit, periapsis = 400 km, will result in an angular momentum considerably less than that generated by solar and gravity gradient torques.

In order to account for the increased velocity for a 200 km periapsis altitude, over a circular orbit, the velocity expression of Equation 2-167 is utilized, giving:

$$\left(\frac{V}{V_c}\right) = \frac{(1+e^2 + 2e \cos \theta) r}{a(1-e^2)} \quad (2-177)$$

where for  $200 \text{ km} \leq h \leq 400 \text{ km}$ , the values of  $(V/V_c)^2$  are  $1.552 \leq (V/V_c)^2 \leq 1.576$ ; hence a constant value of 1.564 may be used with very little error. The resulting torque expression for normal incident is given as:

$$\frac{T}{l} = \rho V_c^2 \left(\frac{V}{V_c}\right)^2 A$$

where

(2-178)

$l$  = CP-cg offset

$A$  = effective projected area

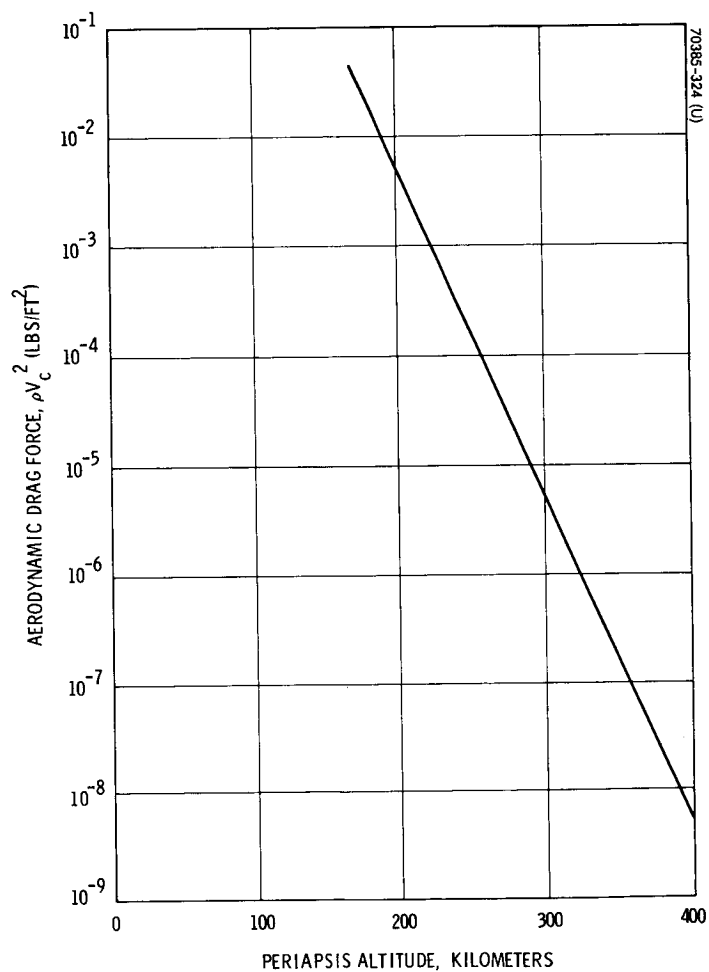


Figure 2-113. Aerodynamic Drag Force Versus Altitude for Normal Incidence and Circular Orbit

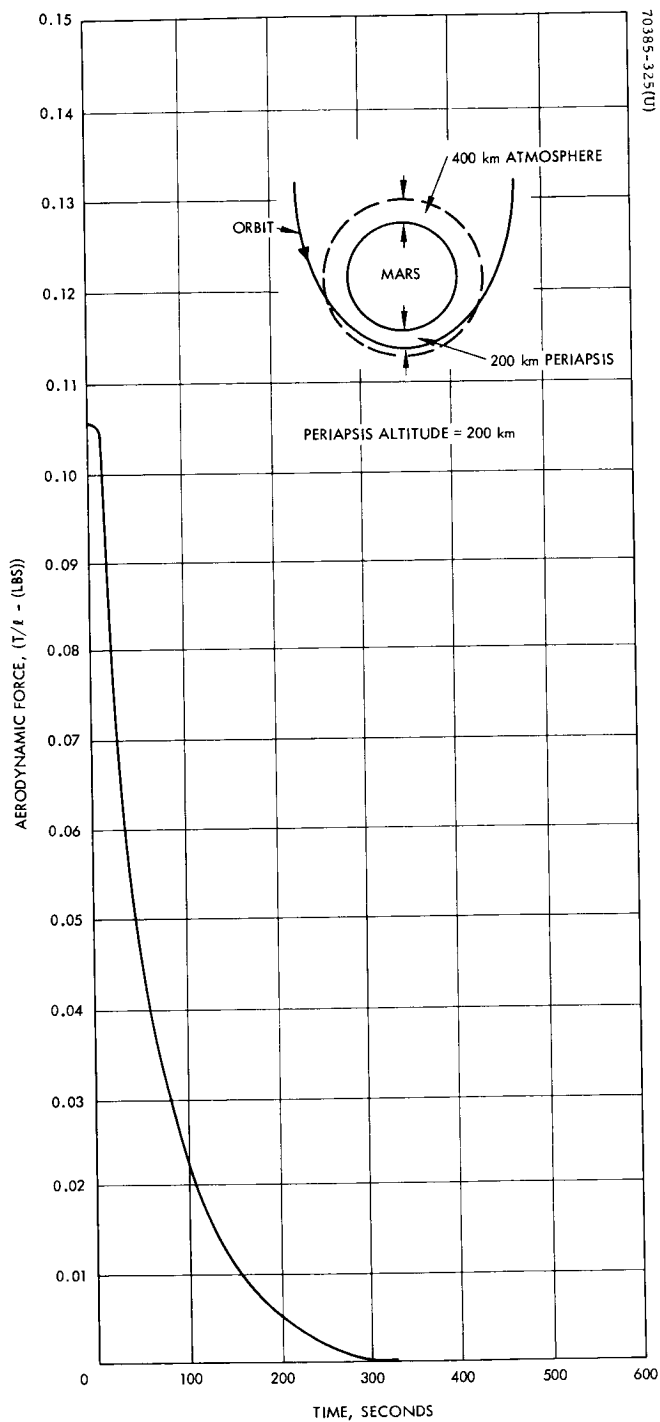


Figure 2-114. Aerodynamic Force Versus Time

A curve of the aerodynamic force,  $T/\ell$  versus  $\Delta t$ , is illustrated in Figure 2-114. The aerodynamic force builds up as the OEC enters the atmosphere. A maximum torque on the capsule occurs when the OEC passes through periapsis; however, it is the integrated torque that is important. On a per orbit basis, the total change in angular momentum is a function of the total impulse which can be found from Figure 2-113. Numerical integration of the area under the curve yields

$$T \Delta t / \ell = 14.3 \text{ lb-sec}$$

The actual aerodynamic torque experienced, of course, is dependent on the spacecraft orientation. Based on the solar torque data and the assumed CP-cg offset of 2 inches, the maximum aerodynamic angular momentum, for orbital inclinations  $\leq 45$  degrees, should be approximately

$$T \Delta t \sim \frac{(2.0) (14.3)}{6} = 4.8 \text{ ft-lb-sec/orbit}$$

#### 2.6.1.4 Disturbance Torque Summary

The normalized values of momentum change per orbit due to solar pressure,  $(T_s \Delta t) / (\ell A)$ , aerodynamics  $(T_A \Delta t) / A \ell$ , and gravity gradient  $(T_G \Delta t) / \Delta I \sin 2 \phi_\mu$  are all illustrated in Figure 2-115 for comparative purposes. (Note that the normalizing factors are not the same). The maximum values of impulses per orbit and peak torque for these disturbances are given in Table 2-23.

The maximum disturbance torque and impulse values will be utilized to determine the resulting attitude and angular momentum vector drift rates as a function of spin speed.

### 2.6.2 Spinning Body Dynamics

The inertial disturbance torques acting on a spinning body produce a drift of the spin axis (and angular momentum vector) from its desired position. The instantaneous drift rate of the spin axis from its nominal position will be greater at some times than its average drift rate (drift rate of the angular momentum vector). The effects of these drifts are discussed below.

#### 2.6.2.1 Average Drift Effects

Figure 2-116 illustrates the dynamical relationships for a spinning body under the influence of an external or internal torque. The angular momentum vector is forced to precess through an angle  $\alpha$  due to the applied torque. The equation describing this effect are given by

$$\tan \alpha = \frac{\Delta \vec{H}}{\vec{H}_s} \quad (2-179)$$

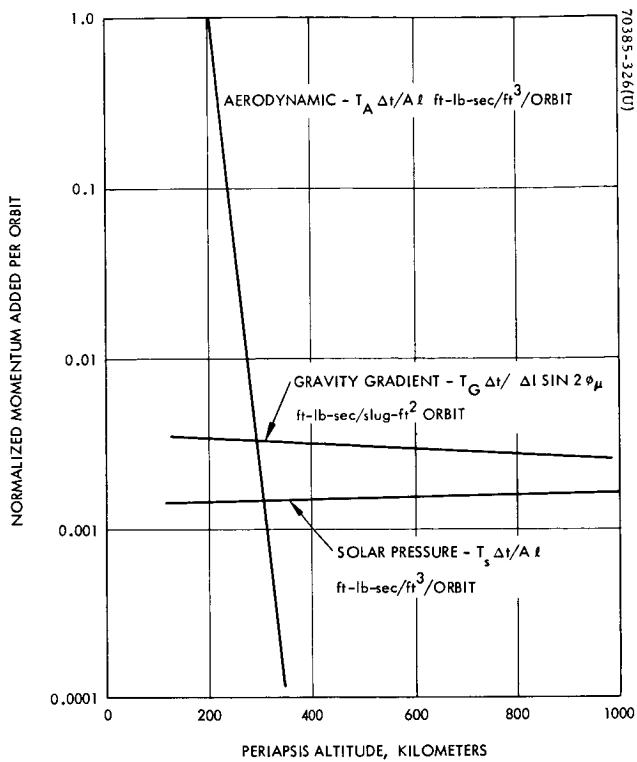


Figure 2-115. Normalized Momentum Added Per Orbit Due to Disturbance Torques as Function of Periapsis Altitude

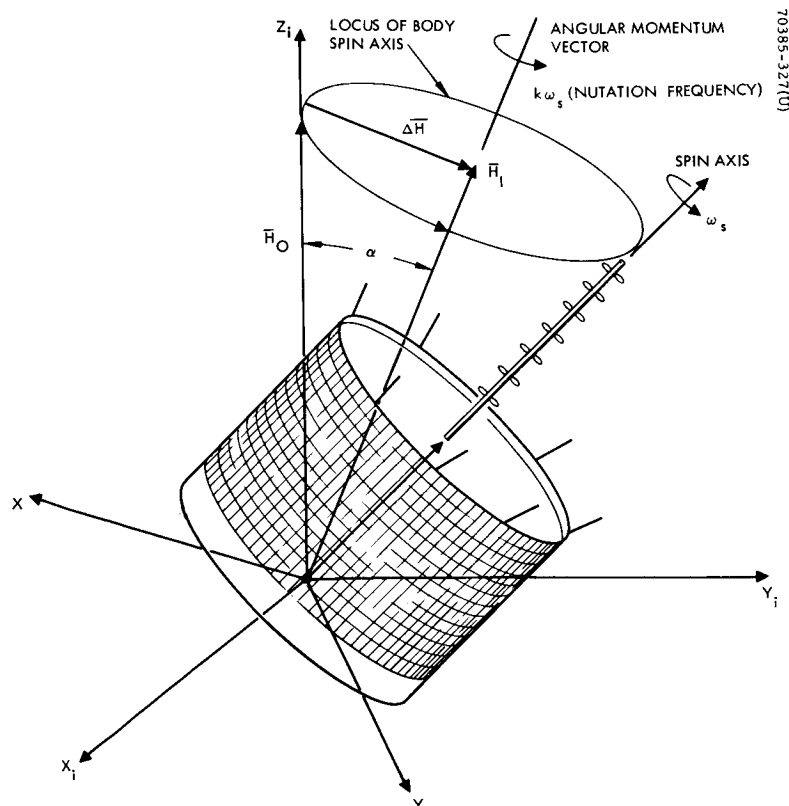


Figure 2-116. Geometry of Spinning Vehicle Dynamics as Viewed in Inertial Space

TABLE 2-23. MAXIMUM IMPULSE PER ORBIT  
(2 INCH CP-CG OFFSET ASSUMED)

Periapsis of 1000 km

Solar pressure	$T_S \Delta t \leq 5.65 \times 10^{-3}$ ft-lb-sec/orbit
Gravity gradient	$T_G \Delta t \leq 6.45 \times 10^{-3}$ ft-lb-sec/orbit
Aerodynamics	$T_A \Delta t = 0$

Periapsis of 500 km

Solar pressure	$T_S \Delta t \leq 5.50 \times 10^{-3}$ ft-lb-sec/orbit
Gravity gradient	$T_G \Delta t \leq 7.60 \times 10^{-3}$ ft-lb-sec/orbit
Aerodynamics	$T_A \Delta t = 0$

Periapsis of 200 km

Solar pressure	$T_S \Delta t \leq 5.25 \times 10^{-3}$ ft-lb-sec/orbit
Gravity gradient	$T_G \Delta t \leq 8.48 \times 10^{-3}$ ft-lb-sec/orbit
Aerodynamics	$T_A \Delta t \leq 4.8$ ft-lb-sec/orbit

where

$$\begin{aligned} H_s &= \text{spin angular momentum} \\ &= I_z \omega_s \end{aligned} \quad (2-180)$$

$$\begin{aligned} \Delta \bar{H} &= \text{applied change in angular momentum} \\ &= T_i \Delta t \end{aligned} \quad (2-181)$$

and

$\alpha$  = inertial attitude error between spin axis  
and its nominal orientation

$T_i$  = disturbance torque about inertial axis  
normal to spacecraft spin axis

$\Delta t$  = time through which  $T_i$  acts

$I_z$  = spin moment of inertia

$\omega_s$  = spin speed (assumed constant)

The influence of these external disturbances force the angular momentum vector to deviate from its desired inertial attitude. Since the change in direction of the momentum vector is incremental, a small angle approximation is valid for Equation 2-179; hence

$$\alpha \approx \frac{T_i \Delta t}{I_z \omega_s} \quad (2-182)$$

and drift rate is consequently

$$\dot{\alpha} \approx \frac{T_i}{I_z \omega_s} \quad (2-183)$$

#### 2.6.2.2 Instantaneous Drift Effects

In order to describe in detail the motions of the vehicle relative to the nominal orientation, definition of several reference coordinate sets is convenient. The reference coordinate sets are illustrated in Figure 2-116 and are described as follows:

$x_i, y_i, z_i$  - Inertial reference coordinate set with origin at spacecraft cg and defining the desired nominal orientation of the spacecraft. The  $z_i$  defines the nominal orientation of the spacecraft spin axis and the  $x_i, y_i$  plane nominally contains the transverse axis. The  $x_i$  axis is arbitrarily defined to be the axis about which an inertial disturbance torque acts on the vehicle (for small error angles).

$x y z$  - A vehicle reference set with origin at the spacecraft cg, the  $z$ -axis defining the spin axis, and  $y$ -axes along the booms.

The orientation of the  $x y z$  set relative to the  $x_i y_i z_i$  set may be expressed as a function of time by direction cosines:

$$\begin{bmatrix} x \\ y \\ z \end{bmatrix} = \begin{bmatrix} a_{11}(t) & a_{21}(t) & a_{31}(t) \\ a_{12}(t) & a_{22}(t) & a_{32}(t) \\ a_{13}(t) & a_{23}(t) & a_{33}(t) \end{bmatrix} \begin{bmatrix} x_i \\ y_i \\ z_i \end{bmatrix} \quad (2-184)$$

the spin axis motion is then defined by evaluating  $a_{13}(t)$  and  $a_{23}(t)$  and their derivatives, which represent  $(\hat{e}_z \cdot \hat{e}_{xi})$  and  $(\hat{e}_z \cdot \hat{e}_{yi})$  respectively, and for small angles,  $(a_{13}^2 + a_{23}^2)^{1/2}$  represents the angular error of the spin axis relative to the inertial reference set.



are: The rotational equations of motion for the unsymmetrical spinning vehicle

$$\begin{aligned}\dot{\omega}_x + \omega_s \omega_y \left( \frac{I_z - I_y}{I_x} \right) &= \left( \frac{T_i}{I_x} \right) \cos \omega_s t + \left( \frac{T_o}{I_x} \right) \\ \dot{\omega}_y - \omega_s \omega_x \left( \frac{I_z - I_x}{I_y} \right) &= - \left( \frac{T_i}{I_y} \right) \sin \omega_s t\end{aligned}\quad (2-185)$$

where

$\omega_s$  = spin rate (assumed constant)

$T_i$  = inertial disturbance torque (assumed about  $x_i$ -axis)

$T_o$  = body fixed disturbance torque (assumed about x-axis)

Solving Equation 2-185 for  $\omega_x(t)$ ,  $\omega_y(t)$  results in:

$$\begin{aligned}\omega_x(t) &= \omega_{xo} \cos \Omega t - \frac{\omega_{yo} (k_x - k_{yx}) \omega_s}{\Omega} \sin \Omega t \\ &+ \frac{\lambda_{ox}}{\Omega} \sin \Omega t \\ &+ \frac{\lambda_{1x}}{(\Omega^2 - \omega_s^2)} \left[ \Omega \sin \Omega t - \omega_s \sin \omega_s t \right] \\ &+ \frac{\lambda_{1y} (k_x - k_{yx}) \omega_s}{\Omega (\Omega^2 - \omega_s^2)} \left[ \Omega \sin \omega_s t - \omega_s \sin \Omega t \right]\end{aligned}\quad (2-186)$$

$$\begin{aligned}\omega_y(t) &= \omega_{yo} \cos \Omega t + \frac{\omega_{xo} \omega_s (k_x - k_{yx})}{\Omega} \sin \Omega t \\ &+ \frac{\lambda_{ox} \omega_s (k_y - k_{xy})}{\Omega^2} (\cos \Omega t - 1) \\ &+ \frac{[\lambda_{1x} \omega_s (k_y - k_{xy}) - \lambda_{1y} \omega_s]}{(\Omega^2 - \omega_s^2)} (\cos \omega_s t - \cos \Omega t)\end{aligned}\quad (2-187)$$

where

$$\begin{aligned}\frac{T_i}{I_x} &= \lambda_{1x} & \frac{T_i}{I_y} &= \lambda_{1y} \\ \frac{T_o}{I_x} &= \lambda_{ox} & \frac{T_o}{I_y} &= \lambda_{oy}\end{aligned}$$

$$k_x = I_z / I_x$$

$$k_y = I_z / I_y$$

$$k_{xy} = I_x / I_y$$

$$k_{yx} = I_y / I_x$$

$$k = 1 + (k_y - 1)^{1/2} (k_x - 1)^{1/2}$$

$$\begin{aligned}\Omega &= \text{nutaton frequency} = \omega_s (k_x - k_{yx})^{1/2} (k_y - k_{xy})^{1/2} \\ &= \omega_s (k - 1)^2\end{aligned}$$

$$\begin{aligned}\omega_{xo}, &= \text{initial angular rates about transverse axes} \\ \omega_{yo}\end{aligned}$$

Both symmetric and unsymmetric OEC design configurations are compatible with the experiment packages delineated in earlier sections. Hence, Equations 2-186 and 2-187 can also be written for an OEC having symmetric properties by letting

$$I_x = I_y \quad (2-189)$$

therefore

$$k_x = k_y = k$$

and

$$k_{xy} = k_{yx} = 1 \quad (2-190)$$

making these substitutions into Equation 2-185

$$\begin{aligned}\dot{\omega}_x + \omega_s \omega_y \left( \frac{I_z - I_y}{I_x} \right) &= \dot{\omega}_x + \omega_s \omega_y (K - 1) \\ &= \lambda_1 \cos \omega_s t\end{aligned}\quad (2-191)$$

$$\begin{aligned}\dot{\omega}_y - \omega_s \omega_x \left( \frac{I_z - I_x}{I_y} \right) &= \dot{\omega}_y - \omega_s \omega_x (K - 1) \\ &= -\lambda_1 \sin \omega_s t\end{aligned}\quad (2-192)$$

The solution to Equations 2-191 and 2-192 is then

$$\omega_x(t) = \frac{\lambda_0}{\omega_s + \Omega} \left[ \sin \Omega t + \sin \omega_s t \right] \quad (2-193)$$

$$\omega_t(t) = \frac{\lambda_0}{\omega_s + \Omega} \left[ -\cos \Omega t + \cos \omega_s t \right] \quad (2-194)$$

The instantaneous drift rates can be determined from the direction cosine derivatives where the direction cosines are those relating a vehicle reference coordinate set to an inertial reference set defining the desired nominal spacecraft orientation.

A brief digression will be made to develop the necessary relationship. In general, the vector equation of motion describing the change in angular momentum is given by

$$\frac{d(\bar{H})}{dt} + \bar{\omega} \times \bar{H} = \bar{M} \quad (2-195)$$

where

$\bar{H}$  = angular momentum vector

$\bar{\omega}$  = angular velocity vector

$\bar{M}$  = momentum vector

This vector can be described equivalently in a matrix form as

$$[\dot{H}] + [P(\omega)] [H] = [M] \quad (2-196)$$

where the angular velocity is given by the symmetric form

$$[P(\omega)] \triangleq \begin{bmatrix} 0 & -\omega_z & \omega_y \\ \omega_z & 0 & -\omega_x \\ -\omega_y & \omega_x & 0 \end{bmatrix} \quad (2-197)$$

A fundamental set of relations (Reference 17) concerning the direction cosines and their time derivatives is given in the following matrix form:

$$\frac{d}{dt} [A] + [P(\omega)] [A] = 0 \quad (2-198)$$

where  $[A]$  = direction cosine matrix.

Thus there is a set of nine differential equations in the form of Equation 2-198 which, together with Eulers equations of motion (2-195) form a set of 12 first order differential equations describing the motion of the capsule.

Writing out the directional derivatives by equating coefficients in Equation 2-198,

$$\begin{aligned} \dot{a}_{11}(t) &= \omega_z a_{21} - \omega_y a_{31} \\ \dot{a}_{12}(t) &= \omega_z a_{22} - \omega_y a_{32} \\ \dot{a}_{13}(t) &= \omega_z a_{23} - \omega_y a_{33} \\ \dot{a}_{21}(t) &= \omega_x a_{31} - \omega_z a_{11} \\ \dot{a}_{22}(t) &= \omega_x a_{32} - \omega_z a_{12} \\ \dot{a}_{23}(t) &= \omega_x a_{33} - \omega_z a_{13} \\ \dot{a}_{31}(t) &= \omega_y a_{11} - \omega_x a_{21} \\ \dot{a}_{32}(t) &= \omega_y a_{12} - \omega_x a_{22} \\ \dot{a}_{33}(t) &= \omega_y a_{13} - \omega_x a_{23} \end{aligned} \quad (2-199)$$

Equation 2-199 is then integrated to produce (rather complex) expressions for  $a_{31}(t)$ ,  $a_{32}(t)$ ; however, the value of the attitude error

$$(a_{31}^2 + a_{32}^2)^{1/2}$$

over an orbit reduces to the simple expression for  $\alpha$  of Equation 2-182 for the small disturbance torques acting on the vehicle. The instantaneous values of  $\dot{a}_{31}$  and  $\dot{a}_{32}$  are, however, of interest with respect to the maximum allowable drift rate.

By assuming that the attitude errors relative to  $x_i, y_i, z_i$  are small, the equations are given as

$$\begin{aligned}\dot{a}_{31}(t) &\approx \omega_y(t) \cos \omega_s t + \omega_x(t) \sin \omega_s t \\ \dot{a}_{32}(t) &\approx \omega_y(t) \sin \omega_s t - \omega_x(t) \cos \omega_s t\end{aligned}\quad (2-200)$$

The instantaneous drift rates are then found for the unsymmetrical vehicle configuration by substitution of Equations 2-186 and 2-187 into 2-200. For the symmetric case (from Equations 2-193 and 2-194):

$$\begin{aligned}\dot{a}_{31}(t) &= \frac{\lambda_1}{k\omega_s} (1 - \cos k\omega_s t) \\ \dot{a}_{32}(t) &= \frac{\lambda_1}{k\omega_s} (-\sin k\omega_s t)\end{aligned}\quad (2-201)$$

The instantaneous peak values are found for the unsymmetric case after some manipulation to be

$$\begin{aligned}\dot{a}_{31} &\leq \frac{2\lambda_{1x}\omega_s}{(\omega_s^2 - \Omega^2)} (k_y - 1 - k_{xy}) \\ \dot{a}_{32} &\leq \frac{\lambda_{1x}\omega_s (2 + \alpha k_x - 2k_{xy} - 2\alpha)}{(\Omega^2 - \omega_s^2)}\end{aligned}\quad (2-202)$$

where

$$\alpha = \left( \frac{k_y - 1}{k_x - 1} \right)^{1/2}$$

and inertial torques only were considered ( $T_o \approx 0$ ).

A simple form of solution for the symmetric spinning satellite exhibits peak drift rates as follows:

$$\begin{aligned}\dot{a}_{31}(t) &\leq \frac{2\lambda_1}{\omega_s} \\ &\leq \frac{2 T_i}{I_z \omega_s}\end{aligned}\quad (2-203)$$

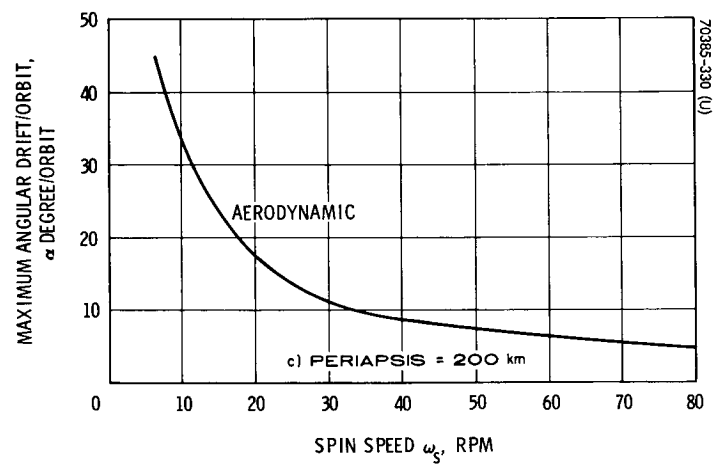
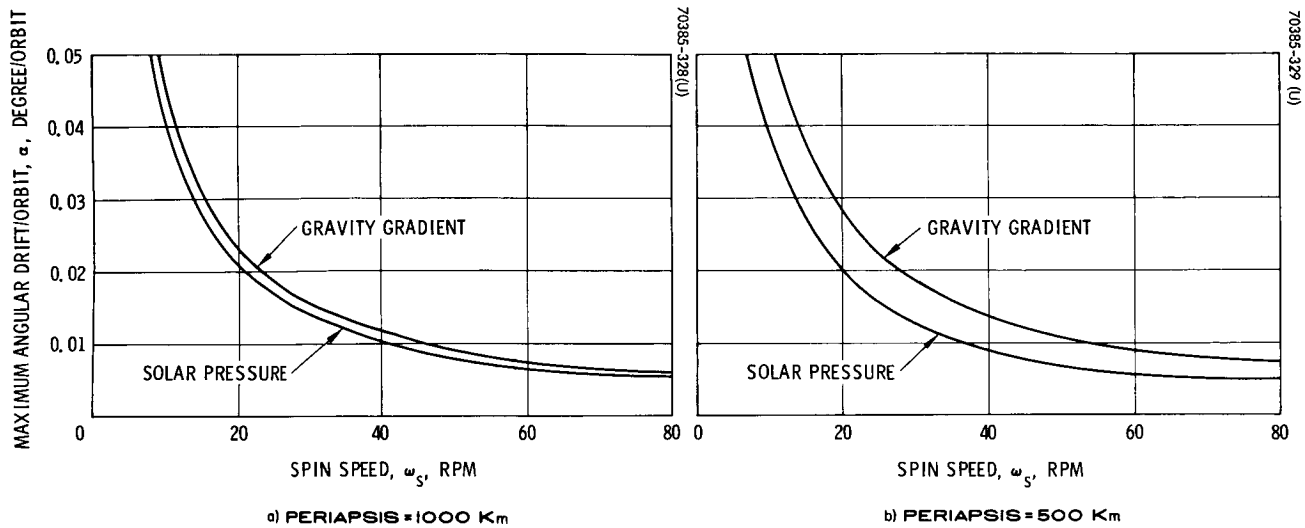


Figure 2-117. Angular Drift Per Orbit Due to Disturbance Torques Versus OEC Spin Speed

$$\begin{aligned}\dot{a}_{32}(t) &\leq \frac{\lambda_1}{\omega_s} \\ &\leq \frac{T_i}{I_z \omega_s}\end{aligned}\tag{2-203}$$

### 2.6.2.3 Effects of Disturbances on OEC Attitude

Studying the resulting expression 2-202 and 2-203, the influence of the transverse moments of inertia on the instantaneous drift rate can be readily recognized. Assuming typical inertia values of

$$\begin{aligned}I_x &= 3.5 \text{ slug-ft}^2 \\ I_y &= 7.0 \text{ slug-ft}^2 \\ I_z &= 7.5 \text{ slug-ft}^2\end{aligned}$$

the peak drift rates for the unsymmetrical case will exhibit a slight amplification in  $\dot{a}_{32}$  whereas the  $\dot{a}_{31}$  component will decrease by approximately 60 percent. Both of these rates are in an opposite sense to that of the symmetric model.

Having described both the average and instantaneous drift rates, the resulting expressions may be applied in determining the effects on the OEC attitude.

Orbital models defined in Section 2.6 are assumed. A nominal apoapse altitude of 10,000 km together periapsis altitudes of 1000, 500, and 200 km are selected to determine the attitude errors incurred as a function of the solar, gravity, and aerodynamic disturbances.

The angular drift per orbit due to each of the disturbance torques, is computed using Equation 2-182. The resulting variation of the attitude,  $\alpha$ , with the spacecraft spin speed,  $\omega_s$ , is illustrated in Figure 2-117 for periapsis of 1000, 500, and 200 km.

Since the aerodynamic perturbations exist well below 1000 km, they do not appear in Figure 2-117a. The maximum angular drift per orbit (~7 hour period) for solar pressure and gravity gradient is seen to be approximately the same magnitude. In the region of 50 to 70 rpm (desirable spin frequencies for the experiment) the attitude drift is on the order of 0.0075 degrees/orbit. At lower frequencies the attitude error builds up somewhat faster. Increasing spin speed does not decrease the per orbit attitude error by a great amount beyond 80 rpm since the attitude error is inversely proportional to spin speed and a very large number of rpm is required to further decrease  $\alpha$ .

Similarly, at a perapsis of 500 km (Figure 2-117c) the aerodynamic effects are negligible. What is apparent in this chart is that gravity disturbances increase somewhat, as is expected.

Aerodynamic perturbations based on the Martian atmospheric model VM-9 are initially effective at 400 km. A study of a lower periapsis altitude was made to determine attitude requirements in the case that orbit maneuvers to these lower altitudes were contemplated. Figure 2-117c illustrates the singular effect of the aerodynamic disturbance since it is so much greater than the combination of the solar and gravity disturbances. Notice here that the deviation of the OEC spin axis from its desired inertial reference is three orders of magnitude greater than that at the previous altitudes. In fact, the attitude requirement of  $\leq 5$  degrees to the ecliptic normal could not be realistically met at this low altitude without real time attitude control.

A more suitable attitude performance can obviously be provided for in the region between the 200 km and 500 km periapsis altitude. Referring back to Figure 2-113, it is recognized that there is greater than five orders of magnitude difference between the aerodynamic drag force between 400 and 200 km altitude. Thus increasing the minimum operational altitude from 200 km to 300 km reduces the force as well as the attitude error by a factor of 1000. Doing so, the aerodynamic disturbances are reduced to the order of those exhibited by solar and gravitational effect, approximately 0.01 degree/orbit.

The maximum drift rate is now determined for the three cases cited. Drifts due to solar pressure remain the lowest in magnitude. The error from gravity disturbances at say 60 rpm varies between 0.02 and 0.04 deg/hr depending on the minimum altitude as shown in Figure 2-118. Aerodynamic peak rates are very high at altitudes of, say, 200 km, but for the 300 km altitude (chosen earlier as a lower limit on altitude) the rate is on the same order as the gravity induced rate. A summary of the steady state and peak drift is tabulated in Table 2-24.

The selection of a best baseline spin speed between 50 and 70 rpm does not appear critical. A choice of 60 rpm is representative as a nominal and will be used to design the attitude control system parameters such as the nutation damper and propulsion system.

### 2.6.3 Attitude Corrections

Attitude correction is a basic operation in the orbit change mode. An attitude correction system can, however, also be included on the simpler co-orbital OEC. The reason for doing so is to ease the initial separation requirements so that the  $\pm 5$  degree ( $3\sigma$ ) attitude alignment to the ecliptic normal can easily be achieved. In addition, this correction system could be used to rotate the capsule into a preferred orientation so as to sense all components of the Martian magnetic field.



TABLE 2-24. MAXIMUM ATTITUDE DRIFT/ORBIT AND MAXIMUM INSTANTANEOUS DRIFT RATE

Disturbance	Attitude Drift Per Orbit	Instantaneous Drift Rate
1000 km		
Solar pressure	$\leq 0.0048$ deg/orbit	$\leq 7.9 \times 10^{-6}$ deg/sec
Aerodynamics	$\leq$ Negligible	
Gravity gradient	$\leq 0.0069$ deg/orbit	$\leq 4.6 \times 10^{-6}$ deg/sec
500 km		
Solar pressure	$\leq 0.0046$ deg/orbit	$\leq 7.9 \times 10^{-6}$ deg/sec
Aerodynamics	$\leq$ Negligible	
Gravity gradient	$\leq 0.0081$ deg/orbit	$\leq 6.5 \times 10^{-6}$ deg/sec
300 km		
Solar pressure	$\leq 0.0045$ deg/orbit	$\leq 7.9 \times 10^{-6}$ deg/sec
Aerodynamics	$\leq 0.005$ deg/orbit	
Gravity gradient	$\leq 0.0087$ deg/orbit	$\leq 7.6 \times 10^{-6}$ deg/sec
200 km		
Solar pressure	$\leq 0.00638$ deg/orbit	$\leq 7.9 \times 10^{-6}$ deg/sec
Aerodynamics	$\leq 4.8$ deg/orbit	
Gravity gradient	$\leq 0.0103$ deg/orbit	$\leq 8.3 \times 10^{-6}$ deg/sec

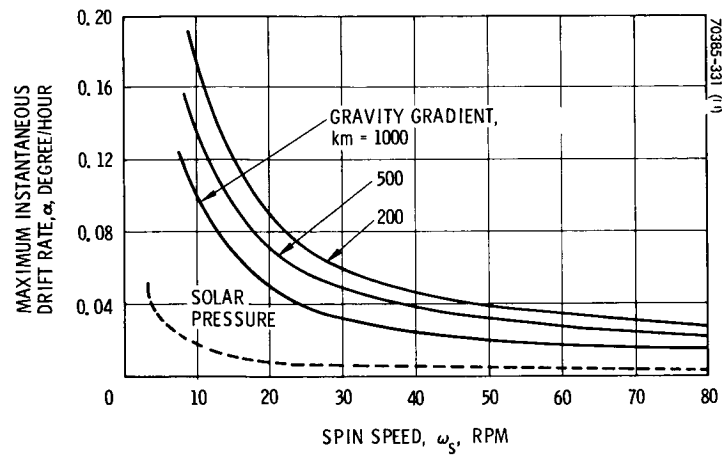


Figure 2-118. Maximum Instantaneous Angular Drift Rate Caused by Solar and Gravity Gradient Torques Versus OEC Spin Speed

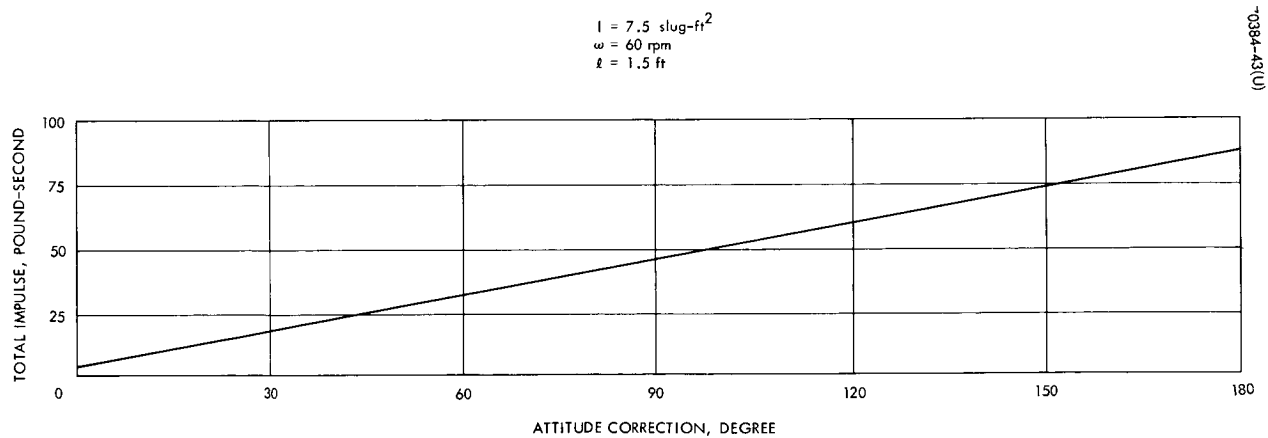


Figure 2-119. Impulse Requirements for Altitude Correction

The correction system is also used to control the OEC attitude to a new orientation so as to conduct orbit maneuvers. Requirements for these various corrections can be interpreted in terms of the total impulse necessary to achieve a change. Figure 2-119 illustrates this requirement in terms of the angular change in attitude.

#### 2.6.4 Orbital Maneuvers

The discussion in the preceding sections is pertinent to both the simple co-orbital concept and the orbit change concept. At this point in the discussion, the emphasis is shifted to illuminate the flexibility of the OEC in the orbit change concept.

There are several advantages to the orbit change mission that cannot be realized by the simpler system:

- Capability to perform atmospheric occultation experiments (mother-daughter occultation)
- Provision for adjusting the OEC orbital altitude, inclination or node
- Provision for a stationkeeping mode between Voyager and OEC

The requirements for performing maneuvers are established in the following discussion. Several orbit change maneuvers are considered: altitude changes, orbit inclination changes, and apse line rotation.

##### 2.6.4.1 Orbit Changes Dynamics

Orbital maneuvers require that energy be either added or subtracted to the orbit. The energy must be in the form of propellant carried aboard the OEC. Sizing of the quantity of fuel required is dependent on the design weight constraints. Even more, it is bounded by the velocity increment necessary to perform an orbital maneuver.

Several maneuvers are contemplated as being useful to extend the mission requirements of mapping the Martian magnetosphere. Included are changes in altitude to possibly more interesting regimes of the magnetosphere, variations in orbital inclination to observe ecliptic related experimental phenomena, and the possibility of extending the mapping feature discussed in Section 2.3 by controlled rotation of the apse line.

Altitude Changes. A derivation of the velocity requirements to provide these maneuvers is based on an evaluation of the vis-viva equation given below. For velocity changes at apoapsis,

$$v_a^2 = \mu \left( \frac{2}{r_a} - \frac{1}{a} \right) \quad (2-204)$$

where

$\mu$  = Martian gravitation constant

$r_a$  = radius at apoapsis

$a$  = semimajor axis

Differentiating with respect to  $a$ ,

$$2V_a dV_a = \frac{\mu}{a^2} da \quad (2-205)$$

Since the semimajor axis is related to the apoapsis and periapsis altitude,

$$a = \frac{h_a + h_p}{2} + R_m \quad (2-206)$$

where

$h_a$  = apoapsis altitude

$h_p$  = periapsis altitude

$R_m$  = radius of Mars

By taking the derivative of Equation 2-206

$$\frac{da}{dh_p} = \frac{1}{2} \quad (2-207)$$

and recombining with Equation 2-205, the approximate\* change in periapsis altitude due to a change in velocity at apoapsis is

$$\Delta h_p \cong \frac{4a^2}{\mu} V_a \Delta V_a \quad (2-208)$$

The term  $a/\mu$  may be replaced by evaluating the visa-viva Equation 2-204 which gives

$$\frac{a}{\mu} = \frac{1}{V_a^2} \left( \frac{1-e}{1+e} \right) \quad (2-209)$$

---

\*This approximation is good to within 10 percent of the altitude change desired.

Normalizing to the circular orbit velocity (at apoapsis)

$$V_a = V_{c_a} \sqrt{1-e} \quad (2-209)$$

it is finally observed that

$$\Delta h_p \cong \frac{4r_a \sqrt{1-e}}{(1+e)^2} \frac{\Delta V}{V_{c_a}} \quad (2-211)$$

where  $V_{c_a}$  is the magnitude of circular orbit velocity at apoapsis altitude.

In a similar fashion, changes in initial apoapsis altitude are maximized by applying a  $\Delta V$  at periapsis. In this case

$$\Delta h_a \cong \frac{4r_p \sqrt{1+e}}{(1-e)^2} \frac{\Delta V}{V_{c_p}} \quad (2-212)$$

where  $V_{c_p}$  is the magnitude of circular orbit velocity at  $h_p$ .

Figure 2-120 gives  $\Delta h_p$  as a function of  $\Delta V$  for several apoapsis altitudes and periapsis altitudes equal to 500 km and 1500 km, respectively. The results show that a capability of 500 fps is more than sufficient to reduce the periapsis altitude to any desired value from the initial Voyages periapsis altitude.

Figure 2-121 is obtained by application of Equation 2-212. A velocity capability of 500 fps appears to be sufficient to change the apoapsis altitude by at least 40 percent of the initial value. For a  $\Delta V$  of 1000 fps, the OEC orbit could be circularized at the periapsis altitude. Circularization, however, is not beneficial since changes in altitude are desirable for adequate and complete mapping of the magnetosphere.

Inclination Changes. Results in Section 2.1 indicate a desire to make the magnetic measurements between Mars inclinations of 30 to 50 degrees. This falls within the current range of possible Voyager mission inclinations, which at injection range from 30 to 70 degrees to the Martian equator. Therefore inclination changes by OEC would only result if Voyager selected the higher inclinations. Thus it would appear that changes on the order of 20 degrees might be desirable.

An expression for changes in inclination in terms of velocity added to the orbit can be obtained by application of the Law of Cosines to the illustrations in Figure 2-122.

$$\begin{aligned} \Delta V^2 &= V_o^2 + V_o^2 - 2V_o V_o \cos \Delta i \\ &= 2V_o^2 [1 - \cos \Delta i] \end{aligned} \quad (2-213)$$

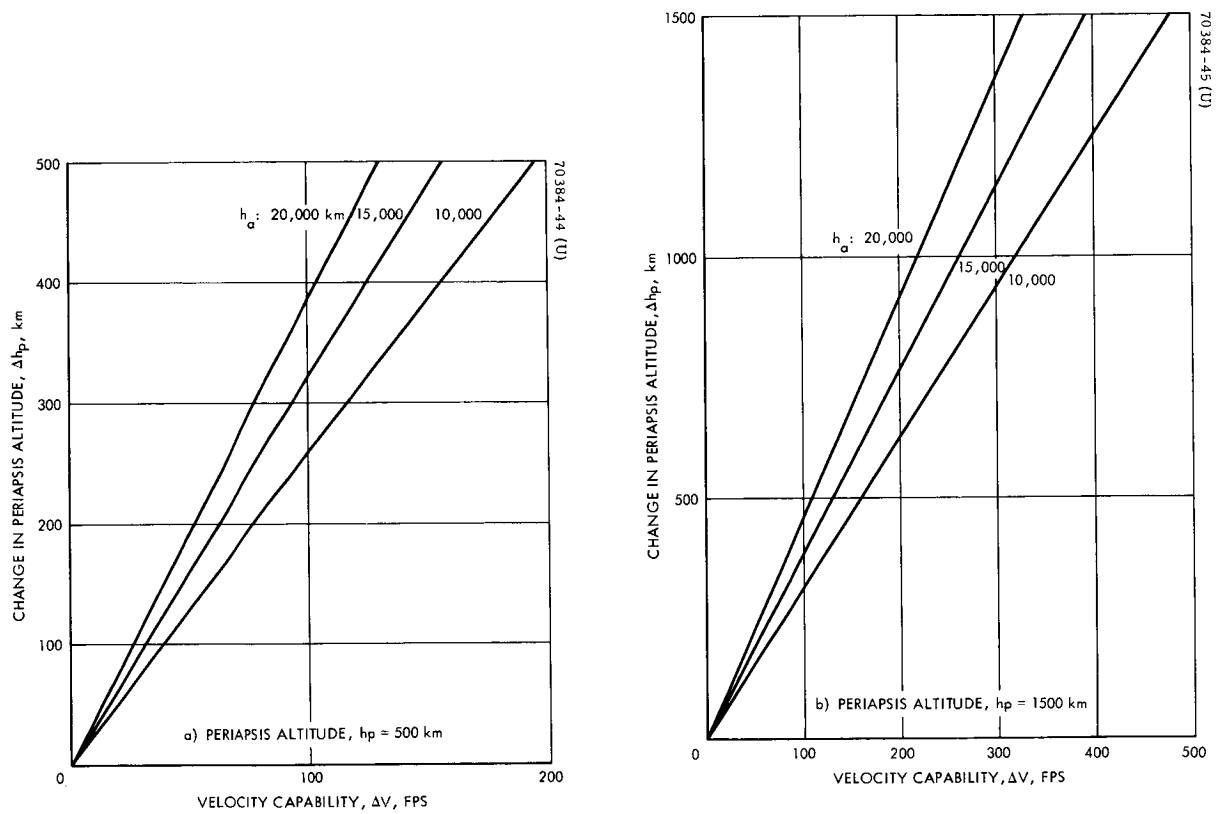


Figure 2-120. Periapsis Change Versus OEC Velocity Capability

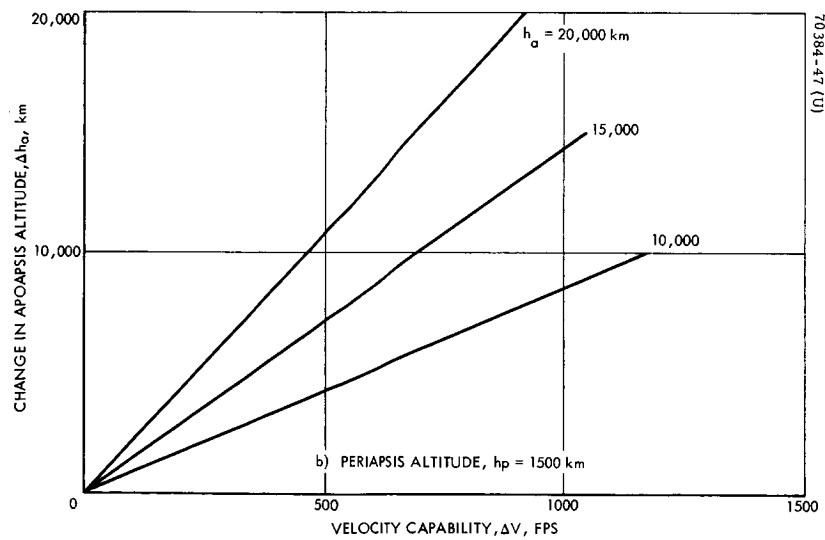
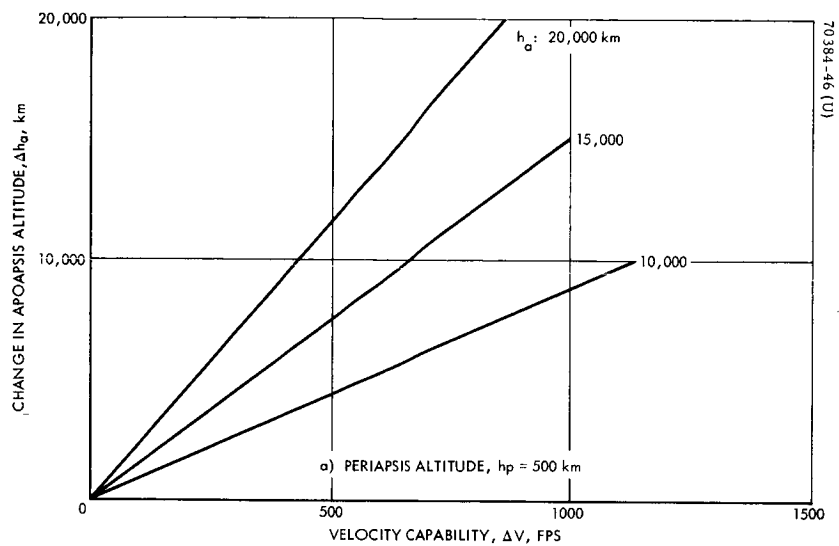


Figure 2-121. Apoapsis Change Versus OEC Velocity Capability

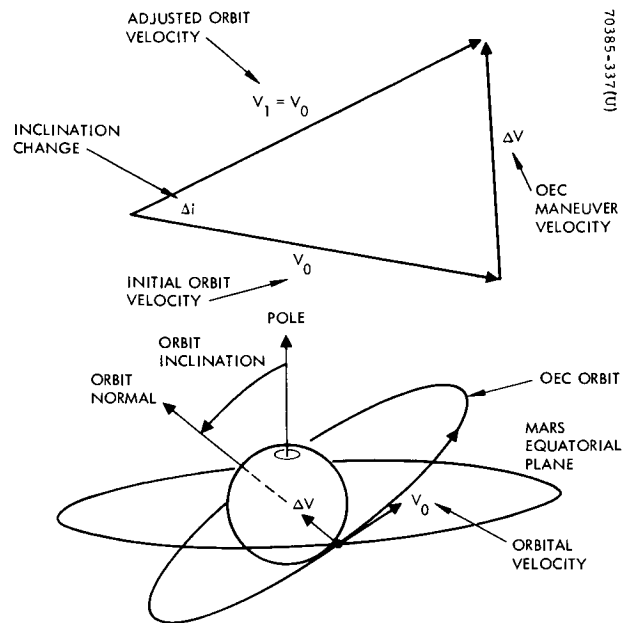


Figure 2-122. Geometry for Inclination Maneuvers

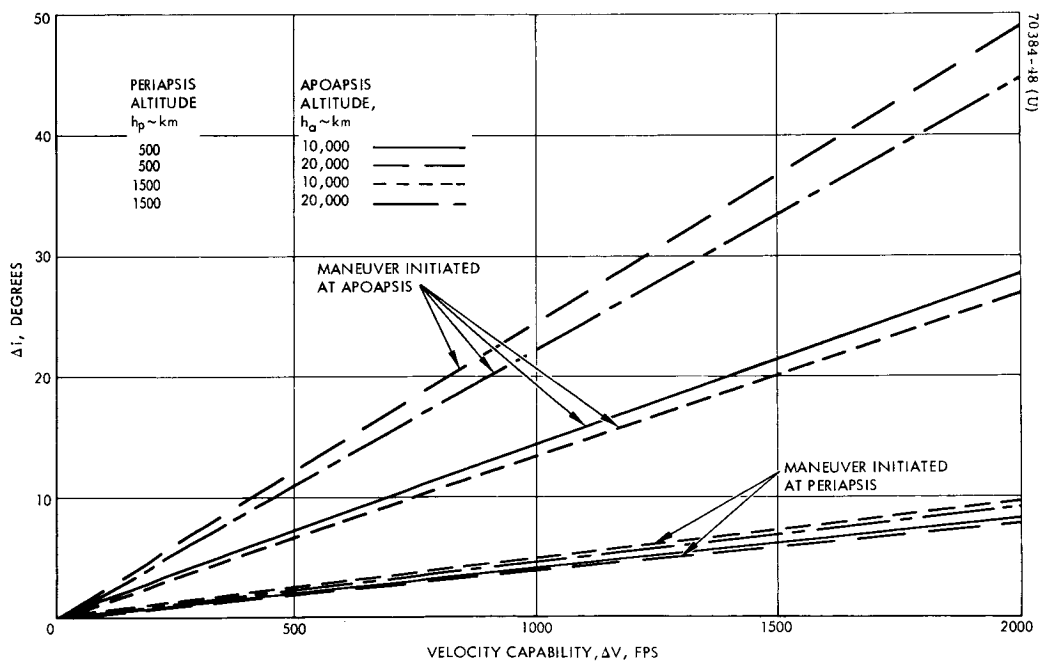


Figure 2-123. Inclination Change Versus OEC Velocity Capability



By a trigonometric identity,

$$\Delta V^2 = 2V_o^2 \left( 2 \sin^2 \left( \frac{\Delta i}{2} \right) \right) \quad (2-214)$$

can be written and, in terms of the change in inclination,

$$\Delta i = 2 \sin^{-1} \left( \frac{\Delta V}{2V_o} \right) \quad (2-215)$$

Velocity increment requirements for inclination changes are displayed in Figure 2-123. Maneuvers initiated from both apoapsis and periapsis are illustrated to show the extremes. The actual selection could be between the two sets of results. It is particularly important to point out that the inclination change obtained depends on the angular location of periapsis relative to the equator (i.e., the argument of periapsis), and therefore a complete range of inclination changes could be shown.

The general trend of the results in Figure 2-123 also points out the futility in attempting to change inclination. Costs in terms of velocity increment are extremely high. For example, a 20 degree adjustment in inclination would require a velocity increment of 1500 fps if the maneuver could be made from apoapsis (nominal 10,000 km x 1000 km altitude orbit). This requires that the apoapse of the orbit intersect the Martian equatorial plane.

Controlled Apse Line Rotation. From the point of view of the experimenter, it appears that placement of OEC periapsis at the solar subpoint at the beginning of the mission is desirable. The possibility of the Voyager orbit's being somewhat different prompted the investigation of requirements to adjust the periapsis position. Control over the location of periapsis is provided by the adjustment of the line of apsides.

Figure 2-124 shows the rotation of periapsis achieved as a function of  $\Delta V$  expended. These results are based on applying the velocity normal to the velocity vector and in the plane of motion, at apoapsis of the orbit. This appears to represent an optimum point to apply this change. The figure indicates that substantial velocity increments would be required to produce large changes in the location of periapsis. As an example, a velocity increment of 1000 fps, in a 10,000 km by 500 km orbit, will rotate periapsis only 10 degrees. If, however, the apoapsis altitude is decreased to a relatively small value prior to initiation of this maneuver, the capability for rotating periapsis will increase. A combination of this type would require additional satellite reorientation maneuvers, and would therefore increase the complexity of orbital operations. In addition, a  $\Delta V$  considerably in excess of 1000 fps would be necessary.

Thus it appears that this form of orbit correction is outside the current spectrum of OEC capability.

#### 2.6.4.2 Voyager - OEC Stationkeeping

Performance of maneuvers as an extension to the simple co-orbiter concept was initially treated as a method of broadening the OEC mission by provision for new experimental results. In this light, orbit changes provide greater data at a small cost in system weight, volume, etc. There is one valuable suggestion for an OEC mission operation which is not treated in detail but deserves mention as a promising option.

In particular, the rationale is to minimize OEC communication ranges by not only ensuring relatively short separation distances but also controlling the relative range between Voyager and OEC - in other words, "stationkeeping." The concept certainly stands out as a viable solution to minimizing power and maximizing the experimental data taken by OEC and transmitted to Voyager.

Figure 2-125 illustrates the manner in which this mission would operate. Two orbital maneuvers are required. First, the OEC must establish the proper attitude at apoapsis and maneuver to a lower periapsis. Without reorienting, the OEC is commanded at the new periapsis to increase its apoapsis. In the ideal situation, the new orbit is of the same period as the original OEC orbit in which the Voyager remains. Hence, by fixing oneself in a Voyager centered coordinate system, the OEC appears to hover relatively close to Voyager in a manner shown in Figure 2-126. Thus communication ranges can be fixed to an upper bound by the proper maneuvers.

In the actual case, both attitude and orbit trim maneuvers would be required to bring the OEC into the desired geometry and to maintain it. External disturbances such as solar pressure would continually perturb both vehicles from the desired nominal state; hence stationkeeping at some fixed interval of time would be used.

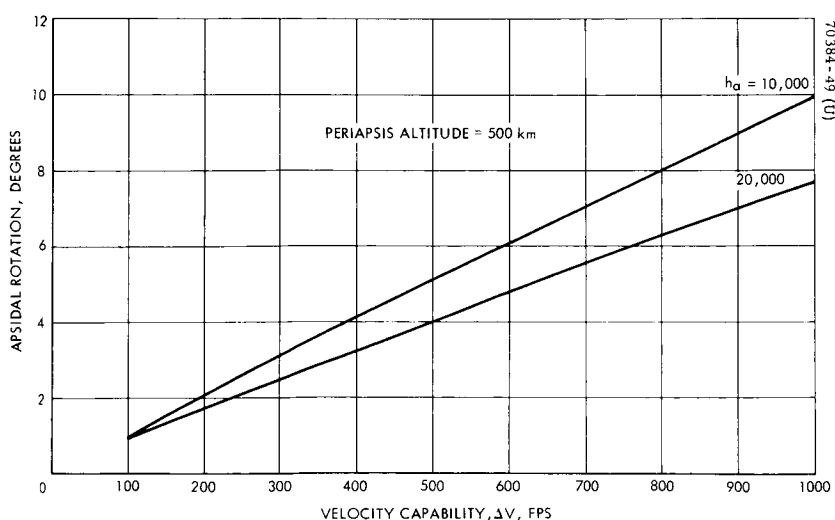


Figure 2-124. Apisidal Rotation Versus OEC Velocity Capability

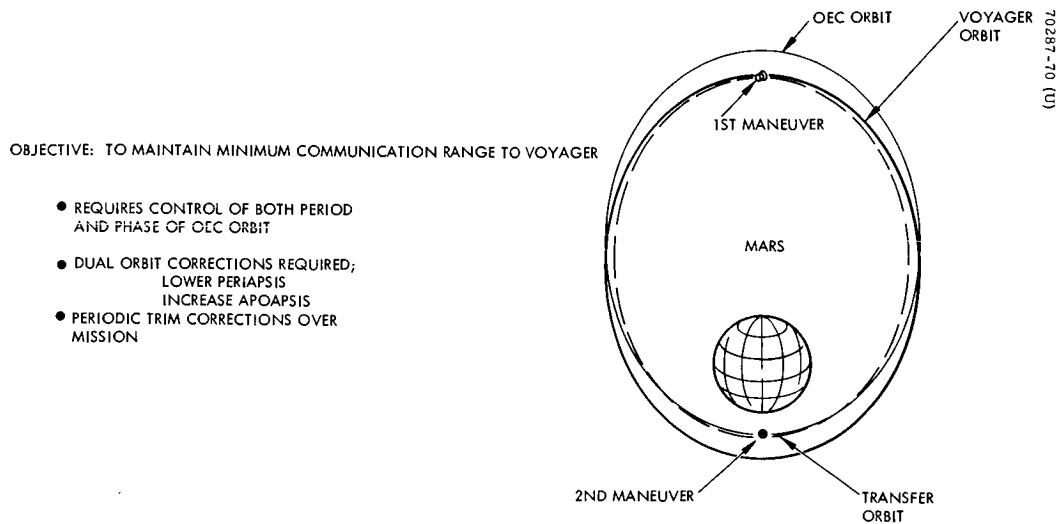


Figure 2-125. Voyager-OEC Stationkeeping

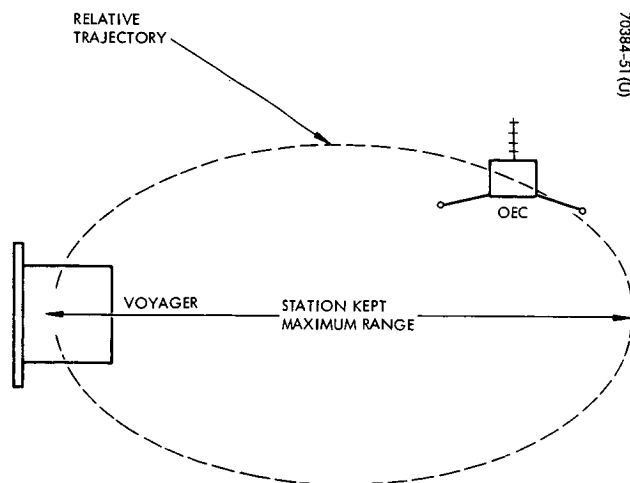


Figure 2-126. Relative Voyager-OEC Motion

## 2.7 ATTITUDE STABILIZATION, CONTROL, AND ORBIT CONTROL IMPLEMENTATION

The OEC is a spin stabilized satellite of Mars. This method of stabilization is not only the most desirable from a scientific point of view since it does provide a natural spinning platform for gathering field and particle measurements but is also the most desirable from a satellite design point of view. Stabilization as such is passive and is the least expensive and most reliable technique available.

With the addition of an active control capability, the versatility of this system increases dramatically. In its simple mode of operation (co-orbital mission), the OEC is separated, spun up to 60 rpm, and remains in a particular orbit relative to Voyager. By the addition of the active attitude control system, several important additional mission experiments can be carried out.

The desirable features of an active attitude control system are:

- 1) Capability to initially align the spin axis normal to the ecliptic plane for all viable OEC missions.
- 2) Provision for attitude corrections of external perturbations.
- 3) Capability of providing additional OEC magnetic field component measurement by reversing the direction of the spin axis attitude.
- 4) Necessary to provide orientation for orbital maneuvers.

Once the attitude control system is part of the satellite design, the extension to orbit control is rather simple.

Orbit control extends the OEC mission flexibility in many ways, for example:

- 1) Provision to map the magnetosphere at altitudes very near to the planet.
- 2) Capability to change apoapsis altitude to investigate the shock boundary in the tail of the magnetosphere.
- 3) Possibility of performing a stationkeeping mode of operation.

A summary of the basic stabilization concept and the sizing of an attitude/orbit control system are presented here.

### 2.7.1 OEC Spinup System

Following separation from the Voyager spacecraft, the OEC will be spun up to the predetermined rate. A spinup system is included on the OEC to spin the vehicle to 60 rpm. This stabilization technique provides a gyroscopic "stiffness" to the vehicle and allows relatively large thrust levels to be utilized for velocity and attitude control maneuvers without appreciably disturbing the desired orientation. In addition, this form of stabilization allows for a reasonable long period of time to pass before orientation errors due to natural disturbance torques need be corrected.

Two types of spinup system are considered here: a blowdown  $N_2$  system, and a constant thrust system. A digital program, incorporating accurate mathematical models of the systems, is used to determine the attitude history with arbitrary initial conditions under the action of a force about the axis of symmetry given by:

$$F(t) = \frac{F_i}{(1 + K_2 t)^{K_3}} \quad (2-216)$$

where, in the case of a blowdown system, the  $K$  parameters are functions of the tank and nozzle pressures and specific heat ratios, the nozzle throat area, weight of fuel, gas constant, and temperature, and  $F_i$  is the initial thrust. For constant thrust analyses,  $K_2$  is set equal to zero.

With the assumed vehicle parameters ( $I_z = 7.5$  slug-ft<sup>2</sup>,  $\omega_s = 60$  rpm, etc.), a total impulse of 33.25 lb-sec is required for spinup. This requirement in conjunction with an assumed tank pressure of 2500 psia dictates an initial thrust of ~95 pounds for the ATS  $N_2$  blowdown system. This particular system is used here largely to exemplify the differences between the two spinup systems.

Constant thrust values of 0.5, 1.5 and 3.0 pounds are studied as they represent reasonable spinup periods. The associated spinup times for each of these (all two jet systems) are:

<u>Thrust Level</u>	<u>Time to Spin Up</u>
$N_2$ blowdown (ATS)	1.4 seconds
0.5 pound constant thrust	33.25 seconds
1.5 pound constant thrust	11.08 seconds
3.0 pound constant thrust	5.54 seconds

The attitude errors and nutation angles resulting from the systems are illustrated as functions of the initial tipoff rates in Figures 2-73 and 2-74. The curves are based on a thrust plane to cg offset of 3 inches and the following tolerances:

- Angular misalignment of nozzle in thrust plane  $\leq 0.5$  degree
- Angular misalignment of nozzle out of thrust plane  $\leq 0.5$  degree
- Fractional thrust mismatch  $\leq 5$  percent
- Nozzle position mismatch  $\leq 0.06$  inch

As can be noted, significant attitude errors can build up at thrust levels below 0.5 pound. This is, of course, a function of the initial tipoff rate. The induced nutation angles appear quite reasonable for the thrust levels studied.

These results are not treated in further detail in this section since a detailed tradeoff is considered in Section 2.4 in regard to the separation-spinup phase of the OEC mission.

The final choice of thrust level based on those results is 130 millipounds. Detailed discussion on the propulsion system and the  $N_2$  spinup propellant is presented in Section 6.0.

### 2.7.2 Nutation Damping

The objective of a nutation damper is to remove the induced torque free precession (or nutation) angle of the OEC spin axis about its angular momentum vector. Nutation damping for the OEC can be provided by a nutation damper similar to that used on the Syncom/Early Bird satellites. The principal disturbances causing spacecraft nutation are separation from the Voyager spacecraft and thrusting of the reaction control system. Extensive performance analysis and testing of Syncom-type dampers have been performed at Hughes in the Syncom, Early Bird, and ATS programs, and techniques have been developed to accurately predict damping time constants for various vehicle conditions (References 18 to 21).

This type of nutation damper is a passive device consisting of a fiberglass tube partially filled with mercury and mounted some distance from the vehicle spin axis with its long axis parallel to the spin axis. The spacecraft nutation motion results in the generation of surface waves in the fluid, thereby dissipating the nutational energy via the fluid viscosity. The action of the passive energy dissipation results in variation of the nutation angle  $\alpha_n$  with time. For small angles,  $\alpha_n$  is given by:

$$\alpha_n(t) = \alpha_o e^{-t/\tau} \quad (2-217)$$

where  $\tau$  is the nutation damping time constant,  $\tau > 0$  for  $(I_z/I_x) = K > 1$ .

The damping time constant is determined as a function of the nutation frequency ( $\Omega$ ), vehicle spin speed ( $\omega_s$ ), radial distance of the damper centerline from the spin axis ( $X_O$ ), inside diameter of the tube ( $D_t$ ), fraction filled (FF) of the tube, and tube length ( $l$ ). A digital computer program is utilized to compute the time constant.

Figure 2-127 illustrates the relationship of the damper to the capsule. As indicated above, the nutation angle  $\epsilon$  is removed by the viscous energy dissipation from within the damper. Attitude errors such as  $\theta$  cannot be so removed and requires fuel expenditure. The damper proposed for the OEC is similar to that illustrated in Figure 2-128.

Figure 2-129 illustrates damper time constant versus radial distance,  $X_O$ , from the spin axis ( $\omega_s = 60$  rpm). If the OEC transverse moments of inertia are not equal, the time constant will increase slightly.

Based on these results, a damper time constant of 10 minutes is chosen since it represents a reasonable period. The characteristics of the proposed OEC damper are shown in Figure 2-127.

### 2.7.3 Control Considerations

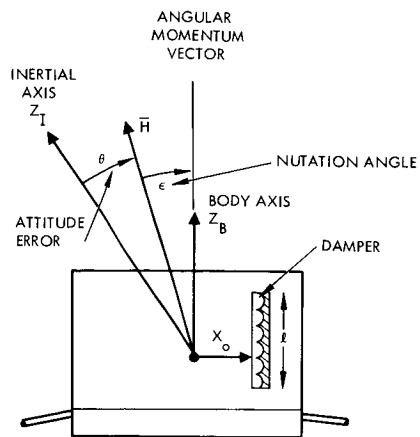
Much thought has been given to the operational aspect of the OEC mission and the ability of the capsule to maintain the nominal inertial attitude. An evaluation of the disturbances and the related attitude deviations has carefully been studied in the preceding sections. Now it remains to interpret the effects of these attitude perturbations in terms of including a correction capability as a subsystem of the experiment capsule.

#### 2.7.3.1 Attitude Control Techniques

The form of attitude correction, as well as orbit adjustment, for a spinning satellite is discussed preliminary to a detailed discussion of fuel requirements and system performance.

A body under spin is governed by the Euler rotational equations of motion. As such, it is recognized that the control of the bodies angular momentum vector (ideally collinear with the spin axis) is provided by a torque about an axis 90 degrees out of phase with the desired direction of motion. The angular momentum vector is precessed through the angle  $\theta$  to its new attitude as shown in Figure 2-130. The equation is identical with that formulated in Section 2.6, Equation 2-182, except that the attitude change is a result of an internally controlled rather than an external torque. Rewriting,

$$\delta\theta \approx \frac{Fl\delta t}{I_s \omega_s} \quad (2-218)$$

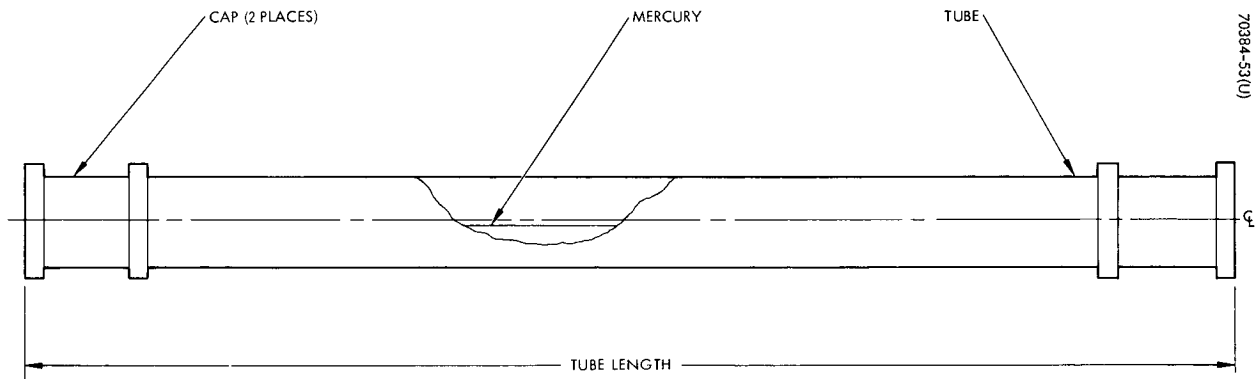


70384-52 (U)

#### CHARACTERISTICS

MERCURY WEIGHT	0.03175 kg
TUBE WEIGHT	0.01814 kg
LENGTH	18 cm
DIAMETER	0.8 cm
FRACTION FILLED	0.2569
DISTANCE FROM CM	$\geq 30.5$ cm
TIME CONSTANT	10 minutes

Figure 2-127. Nutation Damper



70384-53 (U)

INSIDE DIAMETER	= 0.787 - 0.813 cm
OUTSIDE DIAMETER	= 0.975 - 1.026 cm
LENGTH	= 17.932 cm
TUBE WEIGHT	= 0.088 kg

Figure 2-128. Syncom, Early Bird, and HS-303A Nutation Damper



where

$F$  = attitude control thrust, axial jet

$\ell$  = moment arm from center of mass to thruster

$\delta t$  = time of application

$I_s$  = spin axis moment of inertia

$\omega_s$  = capsule spin speed

The correction vector is the applied torque impulse

$$\delta \bar{H} = (\bar{\ell} \times \bar{F}) \delta t$$

As shown in Figure 2-130, the task of precessing the capsule angular momentum vector  $\bar{H}$  ideally requires the application of a pulse of thrust parallel but offset from the spin axis. In actuality, the impulse is replaced by a slightly less efficient but physically realizable thrust pulse of finite duration. The minimum pulse duration is limited only by the electrical and mechanical operation of the thruster solenoid response.

The thrust and minimum pulse on-time specifies the region of application of the axial thruster during one spin cycle. Thus

$$\delta \beta = \left( \frac{F \ell}{I_z} \right) (\delta t)^2 \quad (2-219)$$

where

$F$  = thrust level

$\ell$  = moment arm

$I_z$  = spin axis moment of inertia

$\delta t$  = minimum pulse on time

This equation establishes the minimum part of a spin revolution that can be used and indicates efficiency of the control torque to provide the desired precession. As the pulse on-time is increased, the inefficiency, which is usually small, also increases. Taken to the extreme, the thruster can be operated over a complete spin cycle. This is exactly how orbit maneuvers are provided. Discussion of this technique for making orbit adjustments is presented in subsequent sections.

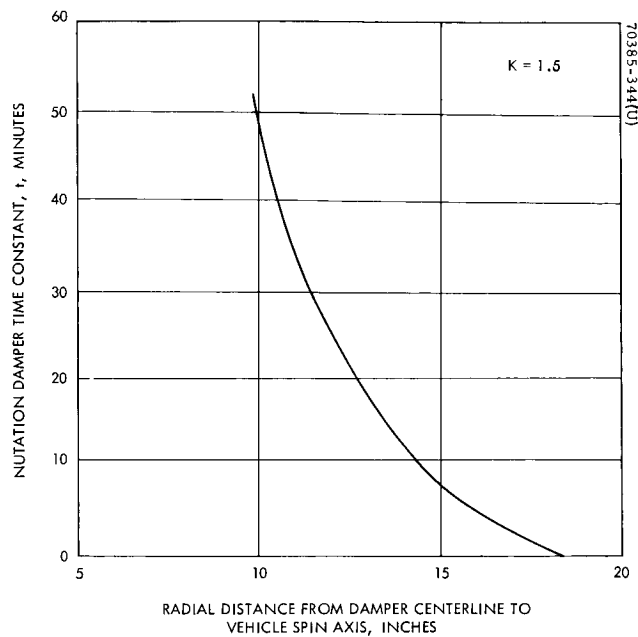


Figure 2-129. Damper Time Constant Versus Radial Distance  $X_0$

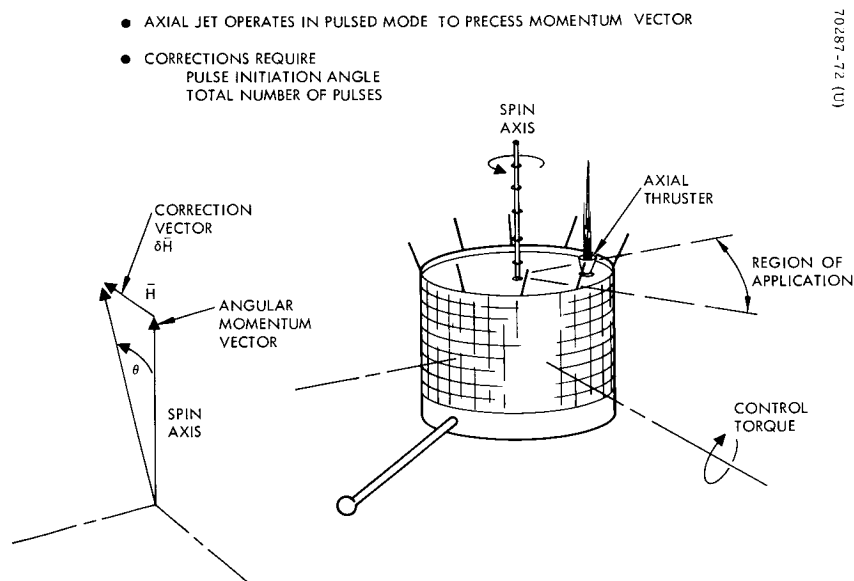


Figure 2-130. Attitude Correction Technique

In performing the actual attitude maneuver, the amount of precession per jet pulse is multiplied by the number of pulses necessary to precess the angular momentum vector from its initial reference to a new inertial attitude. Thus, the operational OEC requires storing both the pulse initiation angle (referenced to the sun sensor signal) and the total number of pulses. In similar earth satellite operations, this form of correction has been conducted in an open-loop fashion. That is, only a part of the attitude maneuver is conducted at a time. Each time the attitude sensor data is reassessed to determine accuracy of the correction. In this way, a very precise reorientation can be guaranteed.

#### 2.7.3.2 Orbit Control Technique

As part of the OEC feasibility study, the extremes of the viable missions are evaluated. The desire to adjust the initial OEC orbit from that of Voyager plays an important role in the flexible orbit change mission concept. The manner in which the capsule will perform these maneuvers is similar to that just described for attitude corrections.

There are two techniques for correcting the orbital position of a spin satellite. The first operates in a pulse mode identical to the axial thruster but instead uses a radial thruster. Referring to Figure 2-131, the application of thrust is through the center of mass of the OEC, producing a translational motion in the desired direction.

The other approach is one already mentioned — that is, to apply the axial thruster in a continuous operational mode.

There are several differences in these approaches and their applications. First, pulsed operation is inherently less efficient in producing the desired thrust level because of a slight degradation in specific impulse; thus, the continuously operated axial maneuver is more desirable. On the other hand, an orbit maneuver conducted with the radial jet has a built-in safety if an open failure occurs. For example, given that the radial jet solenoid fails to close, the fuel will be totally expended, and the average motion of the vehicle about the spin axis is cancelled.

Orbit maneuvers with the axial thruster have a slightly greater  $I_{sp}$ ; however, an open failure could occur. The choice of a baseline orbit control technique cannot be suitably made at this time. Mission performance evaluation is first required to indicate the operational modes necessary to carry out the orbit change mission. However, both methods of orbit control are chosen for the baseline because of the small cost of adding the radial thruster to the system and the redundancy afforded the orbit change mission.

#### 2.7.3.3 Operational Characteristics

The choice of thrust levels for the attitude and orbit maneuvers is not critical. A range of thrusts between 1 to 3 pounds appears satisfactory and represents values typical of a similar class and size of earth satellites. For example, jets of thrust levels similar to those used in the synchronous communications satellite program (Syncom) are chosen to illustrate operational parameters. Assuming a minimum

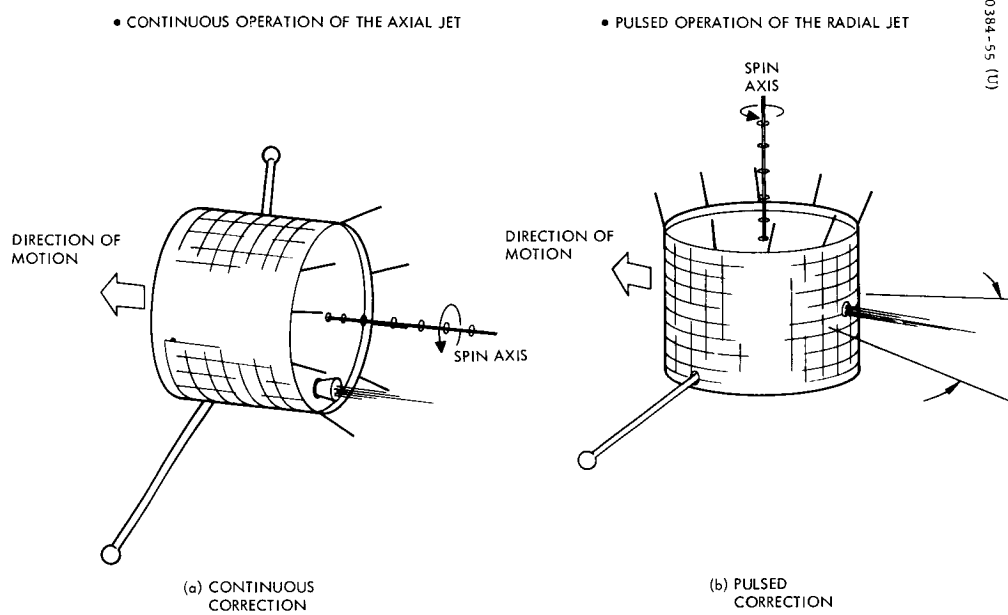


Figure 2-131. Orbit Correction

pulsed mode operation with a 60 millisecond pulse duration, the spin angle is given as 21.6 degrees. For thrust levels of 1.9 and 3.1 pounds, the velocity and attitude correction per pulse are derived and tabulated in Table 2-25. Pulse requirements for typical types of maneuvers are given in Table 2-26.

TABLE 2-25. TYPICAL CONTROL PARAMETER VALUES

	Thrust Level, pounds	
	1.9	3.1
$\Delta V/\text{pulse, fps}$	0.0367	0.0599
$\Delta \theta/\text{pulse, degrees}$	0.1386	0.2262

TABLE 2-26. TYPICAL PULSE REQUIREMENTS  
(NUMBER OF PULSES)

Maneuver	Thrust Level, pounds	
	1.9	3.1
180 degrees	1300	796
90 degrees	650	398
1 degree	7	5

#### 2.7.3.4 Attitude and Orbit Control Requirements

Assuming a nominal OEC spin speed of 60 rpm, the total impulse requirements to correct the attitude disturbances are determined. Table 2-27 summarizes the per orbit attitude error for the nominal 10,000 km apoapsis altitude model. Periapsis altitudes down to the 300 km minimum are shown. As mentioned in Section 2.6, each of the disturbances is of the same magnitude at the 300 km altitude.

To determine the total impulse to correct these errors, some rationale for combining them must be established. There are several pertinent factors to consider. The basic one is defining the correlation, if one exists between the three sources of attitude disturbance. Certainly the solar pressure is in no way correlated to either the gravity or aerodynamic torque. The solar pressure is always exerted away from the sun and about an OEC axis where the center pressure exists. It is cyclic over the year, but for the 90 degree motion of Mars over the 6-month mission can be assumed to be secular.

TABLE 2-27. DISTURBANCE TORQUE SUMMARY  
(ATTITUDE ERROR IN DEGREES PER ORBIT)

Apoapsis altitude -- 10,000 km  
Assumptions: 2 inch CP-cg offset

Source	Periapsis Altitude		
	1000 km	500 km	300 km
Solar pressure	≤0.0048	≤0.0046	≤0.0045
Gravity gradient	≤0.0069	≤0.0081	≤0.0087
Aerodynamic	Negligible	Negligible	≤0.005

Gravity gradient disturbances are cyclic and are not interrelated with aerodynamic pressure although both are Mars centered phenomena. Since the aerodynamic forces are exerted for only a short duration through the periapsis of an orbit, and since the orbit precesses (Section 2.2), the relationship could be considered random. Based on this rationale, the independent sources of error can be root sum squared to determine the net effect. The rss attitude error is given in Table 2-28. Based on these errors, the requirements to maintain the attitude to <±5 degrees are ascertained. A correction frequency of about 6 months (mission lifetime) is necessary for a nominal periapsis altitude of 1000 km for that duration. At the lower altitudes, the increased disturbance level necessitates correcting the attitude sooner.

It is very important to realize that the 5 degree constraint is only a desirable goal to meet, and that increasing this requirement by 1 degree or 5 degrees does not affect the solar plasma instrument but increases the complexity to reduce its data. Increasing this requirement by just 1 degree increases the co-orbiter flexibility by an additional month. Hence, it is definitely reasonable to operate the co-orbiter concept of the OEC for the 6 months with the desired accuracies and beyond that time for up to a year with accuracies of <11 degrees. This is limited only by the OEC subsystems ability to continue to function properly.

Establishing the total impulse is required to size the propulsion system if it is desirable to remove these inaccuracies. The total impulse requirements in Table 2-29 are determined by observing that

$$\text{Total impulse} = \frac{I_z \dot{\theta}}{g} N$$

TABLE 2-28. EFFECT OF ATTITUDE DISTURBANCE

Periapsis Altitude, km	Attitude Error, deg/orbit	Total Impulse, 6 Months, lb-sec	Fuel Weight, pounds	Correction Frequency
1000	0.0083	4.1	0.02	~6 months
500	0.0093	5.0	0.025	<5 months
300	0.011	6.2	0.03	<4 months
<ul style="list-style-type: none"> <li>• Allowable attitude error 5 degrees</li> <li>• Apoapsis 10,000 km</li> <li>• Spin rate 60 rpm</li> <li>• Pulsed axial jet Angle = 22 degree pulse Duration = 60 milliseconds</li> <li>• Thrust level T = 3 pounds</li> <li>• Correction increment <math>\Delta\theta = 0.2262</math> degrees/pulse</li> </ul>				

where

$I_z$  = spin moment of inertia

$l$  = moment arm (maximum)

$\dot{\theta}$  = per orbit attitude error

N = total number of orbits in 6 months

Assuming the nominal system parameters, the total impulse is found to vary between 4 and 6 lb-sec.

A hydrazine attitude control propulsion is presented in Section 6.0 as the baseline control propellant. Based on the performance of this fuel, Figure 6-26 is constructed and indicates that the fuel weight requirements are very small. The weights are in the range of 20 to 30 millipounds.

Capability to perform attitude maneuvers to reorient the OEC for orbital maneuvers, as well as conducting those maneuvers, is discussed next. Typical propulsion system requirements are determined for a sequence in which

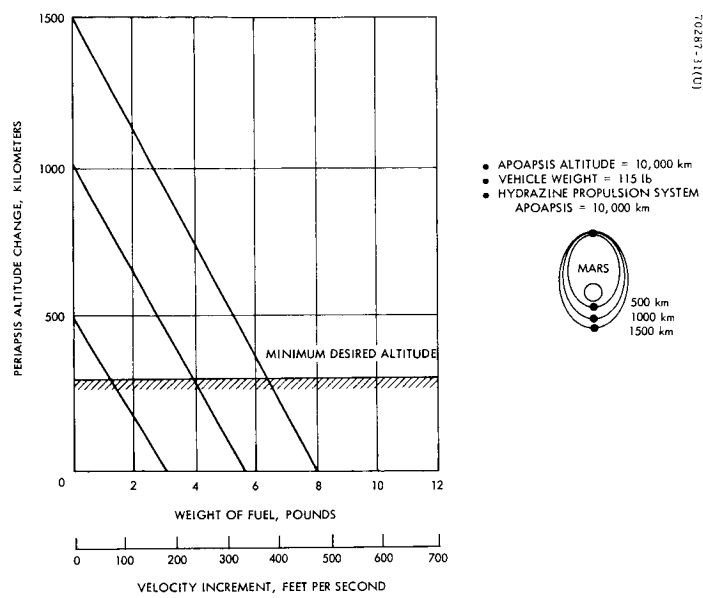


Figure 2-132. Adjustment of Periapsis Altitude



TABLE 2-29. TYPICAL ORBIT/ATTITUDE CORRECTION

Maneuver	$\Delta V$ for Orbit Change Maneuver from Periapsis, fps		
	1500 km	1000 km	500 km
Initial attitude orientation (360 degrees)	60	60	60
Attitude reorientation (90 degrees)	15	15	15
Lower periapsis to 350 km	355	205	50
Total $\Delta V$	430	280	125
Required fuel, pounds	7.7	5.3	2.5
<ul style="list-style-type: none"> <li>• Apoapsis 10,000 km</li> <li>• Spin rate 60 rpm</li> <li>• Axial jet thrust <math>T = 3</math> pounds</li> <li>• Radial jet thrust (pulsed) <math>T = 3</math> pounds</li> <li>• Pulse accuracy <math>\Delta V = 0.0599</math> fps/pulse <math>\Delta \theta = 0.2262</math> deg/pulse</li> </ul>			

- 1) An initial 360 degree OEC attitude maneuver is required after separation from Voyager.
- 2) A reorientation in attitude of 45 degrees is required to operate the axial or radial jet.
- 3) An orbit adjustment to lower periapsis altitude from 1500 km, 1000 km, or 500 km to 350 km is required.
- 4) Attitude is reestablished along the ecliptic normal by a 45 degree attitude correction.

The results are tabulated in Figure 2-132 assuming a 3 pound thrust level as well as the jet characteristics given in Table 2-29. The velocity increment and fuel requirements for the periapsis attitude correction are shown in Figure 2-132. A summary of the results in Table 2-29 indicates the minimal fuel requirements to provide attitude corrections as well as the small increase in OEC system weight to account for propellant to adjust the altitude to minimum distances from Mars which are commensurate with the 50 year lifetime constraint.

## 2.8 SYSTEM PERFORMANCE

### 2.8.1 Mission Summary

Feasibility for operating an experiment capsule about the planet Mars has been treated in detail. The extreme classes of alternative missions have been studied and each has proven to be a viable solution.

The simple co-orbital concept is a relatively light-weight vehicle and is shown to adequately meet mission accuracy requirements. This approach requires precise initial alignment on Voyager to provide an orientation of the configuration spin axis parallel to the ecliptic normal. The location on the Voyager does not appear to affect the injection since the launch platform could be properly canted from any initial position to the desired alignment.

The importance of maintaining relatively short relative ranges to Voyager has been intensively studied to ensure the desired flow of experimental data during the mission. Selection of a relatively small separation velocity of a 0.1 fps, which is commensurate with relative ranges of < 3500 km during the mission, generates communication power requirements which are within the scope of the OEC mission objectives. A detailed error analysis indicates that ranges of this magnitude can be met with launch windows on the order of  $\pm 1/2$  hour at periapsis to as great as  $\pm 1$  hour at apocapsis (nominal orbit of 10,000 km  $\times$  1,000 km). A safety factor of approximately 1/3 km passage of closest approach between Voyager and OEC on the first orbit is designed into the launch window.

Following spinup, the OEC operates as an experimental inertial platform, measuring Mars related phenomena and relaying the information via Voyager to Earth.

Whereas the co-orbital mission is qualified as being simple, it is difficult not to say that at the other extreme the orbit change mission is also relatively simple. However, in addition, it is qualified as being flexible, and brings to the mission a depth that cannot be provided in the co-orbital concept. There are several operational aspects of this more flexible approach to an OEC that must also be pointed out.

There are at least four factors in the design of this mission that stand out:

- Simple separation techniques can be used
- Voyager-OEC relative ranges are not constrained

- Collision is not a problem
- Location on Voyager is completely flexible

By the inclusion of an attitude correction capability and by provision for increased power, the OEC configuration and mission are in some ways increased in simplicity and made more flexible. Adding an attitude control system to the capsule removes the requirement for precise location and separation from the Voyager Orbiter. Following spinup, which occurs at a preselected safe distance, the attitude is assessed and corrections applied. A simple ejection technique of separation is used since attitude errors can be removed with small added fuel requirements.

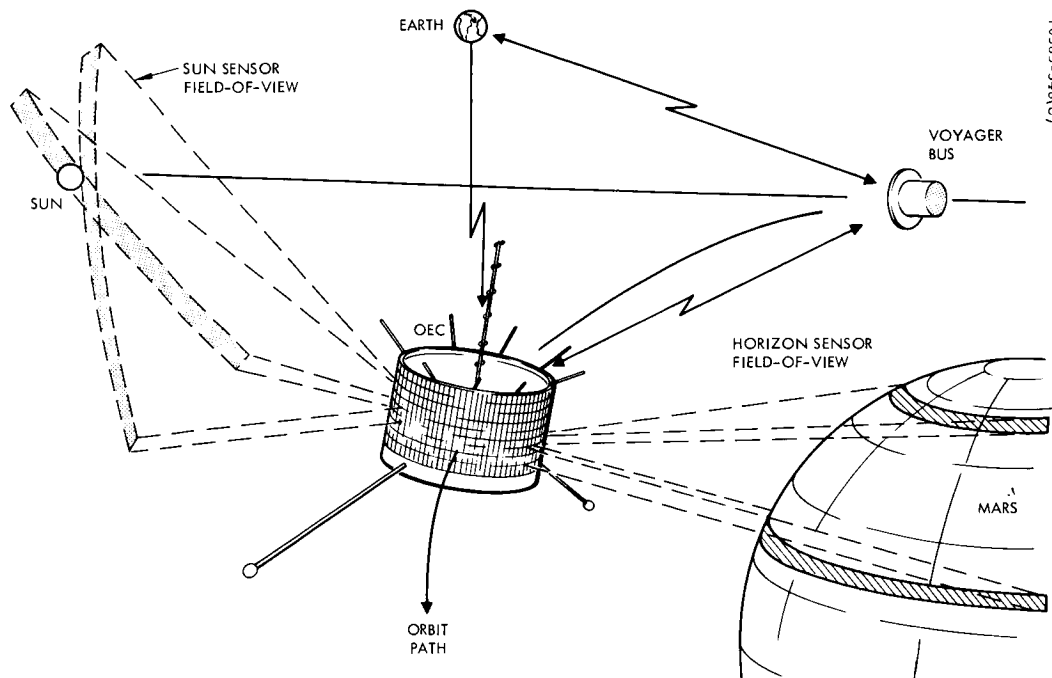
Increasing the available solar power eases the constraint on communication range. Hence a larger separation velocity increment can be applied. However, the critical separation angle (injecting normal to the Voyager orbital velocity vector) must still be observed.

The preferred design of the orbit change configuration places the experiments on booms mounted radial to the capsule spin axis. In this way stability can always be ensured in case experiment requirements change and increased accuracy of magnetic fields is desired.

Independent of the actual OEC mission, attitude and orbit determination is provided by measurements of two celestial references. A sun and Mars sensor combination is used to measure the attitude of the capsule as well as to estimate the orbital position. These sensors meet the attitude determination requirements of  $\pm 1/4$  degree knowledge of the Sun line and  $\pm 1.0$  degree for the spin axis. The smoothed data from these sensors is also used to determine the attitude and orbit control performance. Addition of an S-band communication link serves to remove attitude or positional ambiguities.

Orbit control is available from the same propulsion system used for the attitude control. A dual tank hydrazine reaction control system is designed for this task. There are several important reasons for the inclusion of orbit control besides the fact that it is a natural progression for the next step in the propulsion system implementation. First, orbit maneuvers require only that larger tanks be designed to hold the additional fuel; the jets, squibs, and other associated hardware are already available. Second, and more important, is the added dimension of flexibility to observe planetary phenomena at other conditions, and the possibility of providing a stationkeeping mode of operation. This is particularly of interest if the occultation experiment is made a part of the OEC experiment package.

Finally, the fact that increased power is available for this mission provides the OEC with a suitable communication backup system. The S-band command and receive link could be used to transmit OEC data directly to Earth. A low data rate mode will provide both the experiment and engineering data.



#### TYPICAL SEQUENCE OF EVENTS

- PRE-SEPARATION
  - SELECT LAUNCH WINDOW AND SET IN TIMING COMMAND FROM EARTH
  - ACTIVATE SUBSYSTEM OPERATION
- SEPARATION
  - EJECT OEC
  - SPINUP TO 60 RPM AFTER PRESELECTED INTERVAL
- ACQUISITION PHASE
  - TRANSMIT SUN AND MARS SENSOR DATA TO EARTH VIA VOYAGER
  - ASSESS OEC ATTITUDE AND PREPARE TRIM MANEUVER
- QUIESCENT OPERATION
  - CONTINUE ENGINEERING AND EXPERIMENT TRANSMISSION
- MANEUVERS
  - PREPARE COMMANDS FOR ATTITUDE AND ORBIT CHANGES
  - SEND COMMANDS TO OEC
  - PERFORM ATTITUDE ALIGNMENT WITH AXIAL CONTROL JET
  - PERFORM ORBIT ADJUSTMENT
  - ALIGN SPIN AXIS WITH ECLIPTIC NORMAL
  - RESUME QUIESCENT OPERATION

Figure 2-133. Typical System Operation

### 2.8.2 Baseline OEC Selection

Each of the missions suitably meet the requirements imposed. Selection of a preferred system requires that an additional constraint be imposed; otherwise, the choice would be made based purely on criteria of simplicity or flexibility. The added constraint is the nominal expected weight allotment that could be available on the Voyager 1973 bus. For present purposes, 125 pounds is provided and is broken down into the weight of the basic capsule subsystems, nominal experiment package, and S-band communication link. Sufficient weight is available for inclusion of a propulsion system; thus the following baseline vehicle design is chosen.

First, the configuration is based on a fixed length, pre-deployed pair of radial booms. This design is compatible with mating on each of the Voyager bus configurations and is separated in a radial manner. Separation in this form is chosen because of the available attitude correction capability and because it eases initial orientation requirements for this phase of the operation. Spinup occurs at a suitable distance with a single action nitrogen blowdown spinup system which nominally provides a couple using two 130 millipound thrusters. Figure 2-133 shows the typical system in operation. The attitude is reoriented at some later time after assessment of the attitude with the sun and Mars sensors.

The hydrazine propulsion system is sized with offloaded tanks which provide for up to 450 degrees of attitude reorientation and an orbit maneuver  $\Delta V = 205$  fps. By offloading the tanks, it is possible to add fuel for increased maneuverability without invoking additional redesign costs. As shown in Section 2.7, this allotment is sufficient to decrease the OEC altitude from a periapsis of 1000 km to 350 km (10,000 km apoapsis). The available propellant is sufficient to remove attitude perturbations induced at the lower altitudes. A trimming attitude is necessary after the fourth month of operation unless the OEC is maneuvered before that time.

### 2.8.3 Operation Characteristics

Prior to discussion of the sequence of baseline mission operation, the effect of the extremely large Mars-Earth communication distance must be introduced. Time delays in the reception of OEC sensor data must be evaluated to ascertain whether any basic real time operational limitations exist. The relative distance between Mars and Earth is minimum at opposition,  $56 \times 10^6$  km when Mars is at or near to the perihelion of its orbit. When conjunction coincides with the aphelion of the Martian orbit, the Earth-Mars distance has its maximum value of some  $400 \times 10^6$  km (Reference 31). Based on these extremes, the time delay associated with communications between these planetary distances lies between 3 and 22 minutes. For the Voyager 1973 mission, a time delay of approximately 15 minutes is assumed. Hence, a minimum round trip time of 30 minutes is required to receive data and transmit a command from Earth to the OEC in orbit about Mars.

The process of real time attitude or orbit determination could be complicated by the time delay. This is largely of importance during a maneuver. Assuming a 15 minute command transmittal delay time, the confirmation of

command reception would take a total of 30 minutes. Evaluation of the maneuver requires reception and processing of both the sun and Mars sensor data taken for a period following the completion of the maneuver. This period depends on the geometry and whether Mars is in the horizon sensor field of view. The time necessary to process this data and establish the proper altitude correction could then take on the order of 2 to 4 hours. This, of course, depends to a great extent in the magnitude of the orbit maneuver contemplated. To better understand the pseudo-real-time maneuver operation, an example of the attitude-orbit control sequence for the case cited in Section 2.8.2 is developed.

A  $\Delta V = 205$  fps is sufficient to lower periapsis of the nominal orbit to 300 km. This requires reorientation of the OEC and thrusting at apoapsis. Procedure for the reorientation maneuver is similar in nature to initial orientation. Since the attitude and orbit are well established prior to this maneuver, the magnitude of attitude correction can be stored in the OEC central sequencer at any time prior to initiation. In the worst case, a change in attitude of 90 degrees might be necessary. The total time to make this maneuver is found by observing the total number of axial jet pulses required. From Section 2.7, the 3 pound axial jet was sized to provide 0.14 degrees/pulse.

The total number of pulses (equivalent to spin revolutions) required is 640. Therefore, 12 minutes is necessary to perform this change for the nominal OEC spin speed of 60 rpm. Because of the importance of precise attitude alignment prior to a maneuver, the adjustment could be extended over a longer period of time by dividing it into several corrections, each being studied prior to commanding the next. In this way, overshoot can also be avoided.

Upon completion of the attitude correction, the orbit maneuver is initiated. Either the axial or radial jet is applied. If a pulsed radial jet is used, the per-pulse correction of  $\sim 0.04$  fps indicates the execution of 5650 pulses. At 60 rpm, the total time required is 95 minutes.

For this case, the orbit maneuver is conducted at apoapsis. From Section 2.2, it is seen that the OEC period spent near the apoapsis ( $\pm 20$  degrees) of this particular orbit is almost 2 hours. The orbit correction is completed and verified within the first orbit. Following confirmation of the change, the attitude is redetermined and corrections to reestablish the spin axis collinear with the ecliptic normal are made.

The identical sequence is followed when using the axial thruster. However, the continuous mode operation must be used. The  $\Delta V$  added per revolution in the continuous operation is 17 times greater than that in the pulsed mode since the pulse spin angle is 21 degrees. Therefore, the maneuver could be completed in just 6 minutes. This is a far more reasonable operation time.

Another method of decreasing the maneuver time when using the pulsed radial jet is to increase the thrust level. For example, a choice of 10 pounds decreases the maneuver period to  $< 20$  minutes. This is mentioned only to show that the radial jet could be used to raise the apoapsis of the orbit also. Assuming the requirement to increase apoapsis with  $\Delta V = 205$  fps, it is readily recognized

from Section 2.2 that only 20 minutes is available in the vicinity of periapsis ( $\pm 20$  true anomaly). A 3 pound pulsed jet would require 95 minutes or up to five orbits to accomplish this, whereas a thrust increase to 10 pounds would allow maneuver completion in one orbit. There is but one additional alternative: to increase the pulse spin angle. This increases the  $\Delta V$  per cycle, but at the cost of greater inefficiency. Axial jet operation is again an obvious solution for the orbit changes.

There is one additional constraint imposed on maneuvers that deserves mention. If the correction is made over several orbits, the attitude to the Sun must be preserved to maintain the solar array at the minimum allowable solar aspect.

Maneuvers may require reorientation of the spin axis normal to or into the plane of the orbit about Mars. This change is bounded by the inclination of the orbit to Mars, which is 30 to 70 degrees. Hence, for low inclined orbits, the attitude adjustment could be as great as 45 degrees. There is then a solar array peak power degradation of 30 percent during this orientation. In this case it is required to establish a maneuver mode.

#### 2.8.4 Sequence of Events

Based on the previous discussions, the sequence of events and the associated time intervals are established. To illustrate the differences between the co-orbital concept and the baseline orbit change, two sequences are defined. Tables 2-30 and 2-31 list the events. A time history is illustrated for the baseline OEC in Figure 2-134. The important events are shown at the respective orbital positions. Although the attitude correction need not be conducted immediately, it is shown as part of the acquisition phase.

TABLE 2-30. TYPICAL SEQUENCE OF EVENTS - CO-ORBITAL SYSTEM

- |   |
|---|
| <ol style="list-style-type: none"><li>1) Transit to Mars<ol style="list-style-type: none"><li>a) OEC temperature controlled using Voyager power</li><li>b) Batteries under continuous trickle charge (NiCd); precharged for (AgCd)</li></ol></li><li>2) Voyager in Mars orbit, Lander operation complete</li><li>3) Optimum separation time determined (Earth computation)</li><li>4) OEC systems activated, internal power connected (Earth command)</li></ol> |
|---|

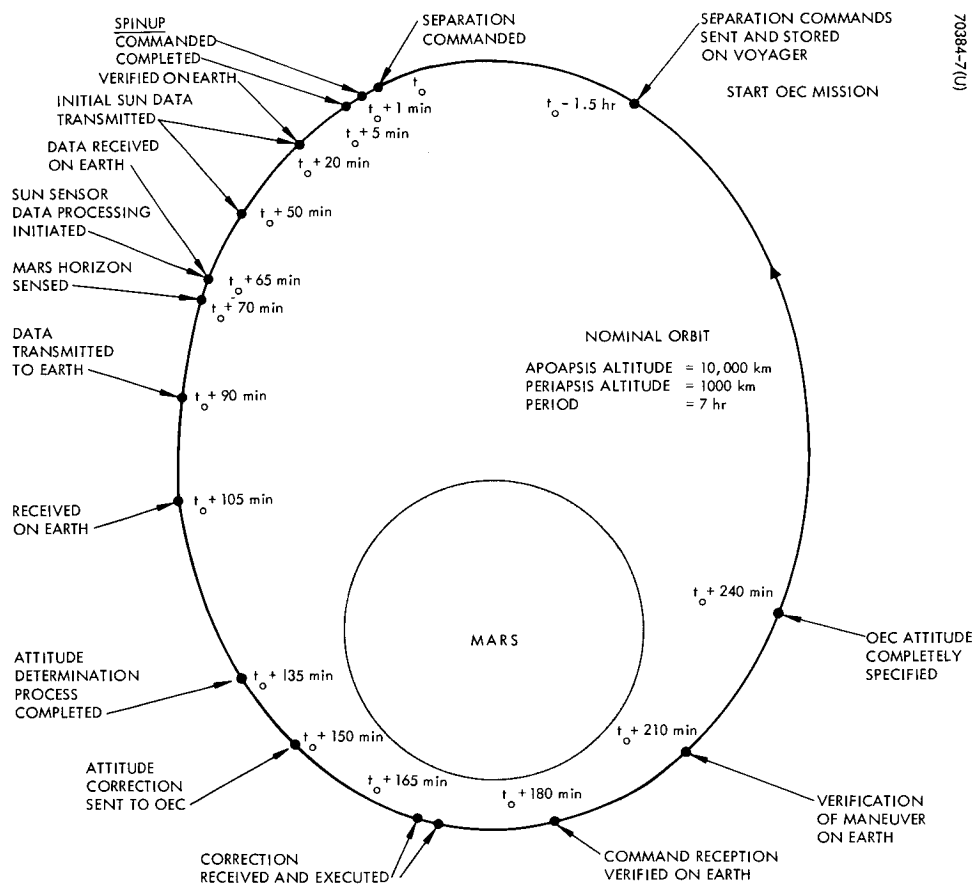


Figure 2-134. Orbital Time History for Baseline OEC



Table 2-30 (continued)

- 5) Separation sequence initiated, timer started (Earth command)
  - a) Main structural support of OEC removed (OEC timer)
  - b) Power umbilical separated (OEC timer)
  - c) Final release, springs push OEC off (OEC timer)
  - d) Fire squibs to release spinup gas (OEC timer)
  - e) OEC spinup to 60 rpm (automatic consequence of squib firings)
  - f) Switch to operational mode (OEC timer)
- 6) Operational mode
  - a) Sample scientific instruments (spin-cycle counter)
  - b) Sample sun and Mars sensors (spin-cycle counter)
  - c) Sample housekeeping data (spin-cycle counter)
  - d) Transmit data to Voyager (continuous-real time)
  - e) Control OEC temperature (passive control – power to boom sensors)
  - f) Charge batteries (battery controller, as needed)
  - g) Provide regulated power (power subsystem)
- 7) Solar eclipse mode
  - a) Switch to battery power (battery controller)
  - b) Continue sampling and transmitting (as in (6))
  - c) Control OEC temperature (passive control – power to boom sensors)
  - d) Provide regulated power (power subsystem)
  - e) Absorb power surge on emergence from eclipse (bus limiters)
  - f) Use horizon sensor pulse to activate plasma probe (sensor logic)
- 8) Data received and stored on Voyager (continuous)
- 9) Data transmitted from Voyager to Earth (Earth command)
- 10) Sensor data processed to determine OEC attitude and position (Earth computation)

#### EARTH COMMANDS REQUIRED

Activate OEC (1 on-off)	1 time only
Start separation (on-off)	1 time only
Transmit data to Earth (1 on-off)	Depends on Voyager storage

#### VOYAGER COMMANDS REQUIRED

Relay "activate OEC" (1 on-off)	1 time only – umbilical
Relay "start separation" (1 on-off)	1 time only – umbilical

TABLE 2-31. TYPICAL SEQUENCE OF EVENTS - ORBIT  
CHANGE SYSTEM

- 1) Transmit to Mars
  - a) OEC temperature controlled using Voyager power
  - b) Batteries under continuous trickle charge (NiCd); precharged for (AgCd)
- 2) Voyager in Mars orbit, landing operation complete
- 3) Optimum separation time determined (Earth computation)
- 4) OEC system activated, internal power connected (Earth command)
- 5) Separation sequence initiated, OEC sequencer started (Earth command)
  - a) Main structural support of OEC removed (OEC sequencer)
  - b) Umbilical separated (OEC sequencer)
  - c) Final release, springs push OEC off (OEC sequencer)
  - d) Fire squibs to activate propulsion (OEC sequencer)
  - e) Spinup to 60 rpm (OEC sequencer)
  - f) Activate attitude control system (OEC sequencer)
  - g) Switch to acquisition (OEC sequencer)
- 6) Acquisition Mode
  - a) Sample and store scientific instruments (spin-cycle counter)
  - b) Sample and store sun and Mars sensors (spin-cycle counter)
  - c) Sample and store housekeeping data (spin-cycle counter)
  - d) Receive ranging pulse(s) (Voyager command)
  - e) Transmit ranging pulse(s) (command decoder to telemetry transpond mode)
  - f) Receive transmit data command (Voyager command)
  - g) Switch to transmit data mode (command decoder to data and telemetry subsystems)
  - h) Switch out of data transmit mode (Voyager command or OEC sequencer)
  - i) Assess OEC attitude and provide correction commands (earth computation)
  - j) Orientation maneuvers set in OEC sequencer (Earth command through S-band)
  - k) Process to stored Sun-spin axis angle (OEC sequencer)
  - l) Process about Sun line by stored number of pulses parallel with ecliptic normal (OEC sequencer)
- 7) Operational Mode
  - a) Sample scientific instruments (spin-cycle counter)
  - b) Sample housekeeping data (spin-cycle counter)
  - c) Transmit data to Voyager

Table 2-31 (continued)

d)	Control OEC temperature (passive control power to boom sensors)	
e)	Charge batteries (battery controller as needed)	
f)	Provide regulated power (power subsystem)	
8)	Solar Eclipse Mode	
a)	Switch to battery power (battery controller)	
b)	Continue sampling and transmitting data (as in (8) )	
c)	Switch off attitude control system (attitude control logic)	
d)	Control OEC temperature (passive control – power to boom sensors)	
e)	Use horizon sensor pulse to activate plasma probe	
f)	Provide regulated power (power subsystem)	
g)	Absorb power surge on emergency from eclipse (bus limiters)	
9)	Data (including ranging pulses) received and stored on Voyager Earth command, relayed to OEC – or Voyager sequencer)	
10)	Data transmitted from Voyager to Earth (Earth command)	
11)	Maneuvers sensor and range data processed to determine OEC attitude and position (Earth computation)	
a)	Time and direction of the attitude and orbit change impulse determined (Earth computation)	
b)	Attitude and orbit change impulse duration set in OEC sequencer (Earth command to OEC S-band)	
c)	Precess to stored Sun-spin axis angle (OEC sequencer)	
d)	Precess about Sun line by stored number of pulses (OEC sequencer)	
e)	Fire orbit change engine for stored duration (OEC sequencer)	
f)	Precess about Sun line, reversing (c) (OEC sequencer)	
g)	Precess spin axis to perpendicular to Sun line and parallel to ecliptic normal (OEC sequencer, attitude control logic)	
EARTH COMMANDS REQUIRED		
Orientation maneuvers (2 magnitudes)		
Orbit change impulse duration (1 magnitude)		
Activate OEC (1 on-off)		1 time only
Start separation (1 on-off)		1 time only
Obtain ranging data (1 on-off)		Several times only
Obtain data from OEC (1 on-off)		Every orbit
Transmit data to Earth (1 on-off)		Depends on Voyager storage

Table 2-31 (continued)

VOYAGER COMMANDS REQUIRED

Relay orientation maneuvers (2 magnitudes)	1 time only — umbilical
Relay orbit change impulse duration (1 magnitude)	1 time only — umbilical
Relay "activate OEC" (1 on-off)	1 time only — umbilical
Relay "start separation" (1 on-off)	1 time only — umbilical
Relay "obtain ranging" (1 on-off)	Several times only
Relay "obtain OEC data" (1 on-off)	Every orbit
Command OEC data stop (1 on-off)	Possibly every orbit

## 2.9 REFERENCES

1. Performance and Design Requirements for the 1973 Voyager Mission, General Specification for, Jet Propulsion Laboratory, SE002 BB001-1B21, 1 January 1967.
2. T. Gold, "The Magnetosphere of the Moon. The Solar Wind," edited by Robin J. Wakin and Marcia Neugebauer, Pergamon, 1966, pp. 381-391.
3. C. G. Barnett, "Voyager Spacecraft Orbit Data," Hughes IDC No. 2293.1/7.
4. Richard Battin, "Astronautical Guidance," McGraw and Hill, 1964.
5. G. P. Kuiper and Middlehurst, "The Solar System - Vol. I, Planets and Satellites," Chapter 3, The University of Chicago Press, Chicago, 1967.
6. 1973 Voyager Capsule System Constraints and Requirements Document, JPL SE002 BB02-2A21, January 1967.
7. D. F. Spencer, "Our Present Knowledge of the Martian Atmosphere," Jet Propulsion Laboratory, Contract No. NAS7-100, Presented at AIAA/AAS Stepping Stones to Mars Meeting, 28-30 March 1966.
8. B. H. Billik, "Survey of Current Literature on Satellite Lifetimes," ARS Journal, November 1962.
9. Mildred M. Moe, "Solar-Lunar Perturbations of the Orbit of an Earth Satellite," ARS Journal, May 1960.
10. The American Ephemeris and Nautical Almanac, 1966.
11. "Design and Purchase Manual - Soehner Springs," Kinemotive Corp., Lynbrook, New York, 15 June 1966.
12. "Study of Adhesion and Cohesion in Vacuum," Hughes Aerospace Group Report Number P65-94, Materials Technology Department, Contract NAS8-11066.
13. W. P. Gilbreath and H. T. Sumsion, "Solid-Phase Welding of Metals Under High Vacuum," NASA, Ames Research Center.

14. "Specification for an Orbital Experiment Capsule Study," NASA Ames Research Center Specification No. A-12506.
15. R. J. McElvain and L. Schwartz, "Minimization of Solar Radiation Pressure Effects for Gravity-Gradient Satellites," Journal of Basic Engineering (ASME, Vol. 88, No. 2, pp. 444-450, June 1966).
16. L. Schwartz, Hughes IDC 2223/723, "Solar Pressure Torque Computation Routines," 21 January 1965.
17. E. I. Ergin, V. D. Norun, T. G. Windeknecht, Techniques for Analysis of Nonlinear Attitude Control Systems for Space Vehicles, Volume I, "Characteristics of the Spacecraft Attitude Control Problem," Aeronautical Systems Division Technical Documentary Report No. ASD-TDR-62-208, Volume I, June 1962.
18. D. D. Williams, "Nutation Dampers," Hughes IDC 2720.7/5, 6 June 1961.
19. D. D. Williams, "Analysis of a Simplified Nutation Damper Model at Small Amplitudes," Hughes IDC 2280.03/192, 6 June 1961.
20. R. J. McElvain, "ATS Nutation Dampers - Performance Evaluation Summary," Hughes IDC 2223/1132, 14 May 1965.
21. R. J. McElvain, "ATS S/S Nutation Damper Predicted Performance - Unsymmetrical Vehicle Configuration," Hughes IDC 2223/1582, 14 September 1965.
22. I. A. Gura, "An Algebraic Approach to Optimal State Estimation," Hughes Report No. SSD 70072R, March 1967.
23. C. B. Solloway, "Elements of the Theory of Orbit Determination," Jet Propulsion Laboratory Engineering Planning Document No. 225, 9 December 1964.
24. L. Schwartz, "Approximate Continuous Nonlinear Minimal-Variance Filtering," Hughes Report No. SSD 60472R, December 1966.
25. I. A. Gura, "Attitude Determination for Advanced Spinning Satellites," Hughes IDC No. 2281.1-16, 25 May 1967.
26. W. M. Sinton and John Strong, "Radiometric Observation of Mars," Astronomical Journal, 1960.
27. J. H. Spotts, "Optical Attitude Sensors for Space Vehicles Application," UCLA Thesis, 1965.
28. G. DeVaucouleurs, Physics of the Planet Mars, McMillan, 1950.

29. "Earth Sensor for a Spinning Vehicle," Barnes Engineering Company Proposal BEC P-1092, 9 August 1966.
30. J. Duncan, et al., "Infrared Horizon Sensors," Institute of Science and Technology, University of Michigan, April 1965.
31. S. Glasstone, Source Book on Space Sciences, Van Nostrand Co. Inc., 1965.

### 3.0 COMMUNICATIONS AND DATA HANDLING STUDIES AND TRADEOFFS

#### 3.1 GENERAL

Communication links to and from the OEC will provide for transmission of data to earth via the Voyager orbiting spacecraft for commands to the OEC and, possibly, at substantially reduced data rate transmitted directly to DSN in an emergency mode. The commands could be sent directly from earth or by spacecraft relay. Figure 3-1 shows a sketch of these routes with indications of link capabilities for the illustrative design. Following are the considerations that influence selection of RF power, duty cycles, modulation methods, frequencies, orbit preference, and equipment selection.

The illustrative design is based on mission requirements outlined in Table 3-1. Parametric curves are presented that allow equipment characteristics to be deduced for changes in these requirements which are bound to occur as the design of experiments becomes firm.

#### 3.2 UHF/VHF RELAY LINK FOR PRIMARY DATA MODE

The primary data link will use the Voyager vehicle as a relay so that the large antenna and power capability of the large spacecraft will bridge the long path to earth. A glance at the subsequent discussion describing the direct OEC link for a backup mode will illustrate the need for relaying OEC data gathered at rates exceeding 500 bits/sec. In the co-orbital mission, OEC separation is controlled so that the two orbiting vehicles do not drift sufficiently apart that the line of sight is occulted by Mars during the 6 months operational requirement. This implies ranges less than 7000 km (3000 km at 6 months for the baseline example), so that real time data can be transmitted using modest transmitter power. In the orbit change mission Mars will intervene and the two vehicles may only have unobstructed line of sight at distances as great as 23,000 km and then for only 30 percent of the time. Provisions must be made to store data during most of the orbit and transmit at an accelerated rate when the opportunity occurs. The transmitters will consume energy levels of at least 110 watt-hours every 7 hours for the baseline design and correspondingly more if unfavorable frequencies are used or if data requirements grow.



TABLE 3-1. COMMUNICATIONS REQUIREMENTS

• Sampling rate for experiments	550 bits/sec or 1 frame/spin
Distance between samples	<4.4 km at periapsis, <1.3 km at apoapsis
• Mars sensor data	8 bits/sec, averaged
• Clock - Sun sensor	15 bits/sec
• Engineering data	50 bits/sec, averaged
• Data rate	630 bits/sec or 16 megabits in 10,000 km orbit; 32 megabits in 20,000 km orbit
• Commands	
Set magnitudes into sequencer	7
Start sequences	4
Select data readout modes	4
Backup capability on-off	16 (32 commands)

### 3.2.1 Frequency Selection

On the one hand, frequency selection depends upon the frequency varying terms of the range equation, which are: noise temperature, transmitter power efficiencies, and receiving antenna coverage requirements. On the other hand, the frequency choice involves practical wavelength dimensions for achieving the antenna coverage required for both vehicles and also must lie in bands that have been allocated for these purposes. The latter consideration would not appear to be important for Mars applications; however, Earth testing problems make it advisable to observe these regulations. Analysis leading to a quantitative evaluation of the particular terms is described in the succeeding paragraphs.

It will be observed that receiving antenna coverage is listed among the frequency dependent terms. This arises from the fact that coverage for both sending and receiving antennas is set by the orbital geometry; therefore gain of the transmitter is constant with respect to frequency and the effective receiving area increases as  $\lambda^2$  for constant coverage angle.

### 3.2.2 Galactic Noise

The total noise temperature seen by the receiver is composed of receiver noise, normal and abnormal solar temperature, and galactic noise.

The galactic noise seen by the vehicle receiving antenna was derived by superimposing typical antenna beamwidths on a galactic plot of noise, measured at 100 MHz by John Bolton\* and averaging for the worst case. These values were then interpolated across the UHF/VHF band using other researcher's measurements of the peak noise at the galactic nucleus. Figure 3-2 shows the integrated effect for three different antenna beamwidths; noise temperatures for present uncooled receivers have been plotted against the same ordinate. Antenna patterns are surfaces of revolution, henceforth termed omnidirectional. Only the wider beamwidths appear suitable for the OEC geometry,

### 3.2.3 Solar Noise

Temperatures for the normal sun were derived from the relationship

$$T_{k^0} = \frac{(290) (675)}{f \text{ Gigahertz}}$$

This value represents the noise temperature seen by an antenna with beamwidth sufficiently narrow to precisely include the sun (41 db gain) and must be adjusted for the wider antenna beamwidths used here. This adjustment is most readily achieved by forming the ratio of gains for the two antennas and was found to augment the noise temperature by 1.6 db in the 30 degree - 100 MHz case.

Types III (synchrotron radiation) and IV (plasma radiation) will add to the normal solar temperature for limited periods. Type III radiation is concentrated in the first few minutes of a storm and is characterized by spikes of energy spaced at 5-second intervals and lasting 1 to 2 seconds, followed by spikes of energy spaced at 10 second intervals, 1 to 2 seconds long. Their effect is to raise the noise temperature 7 to 13 db at 136 Mz. The plasma radiation will last for 1 to 6 hours but the total power reduction will be less than 0.6 db.

The more extreme power loss caused by Type III is not shown in the data links since discussions with ARC indicated that these short term dropouts are tolerable and the entire system should not be penalized by the additional weight needed to override such transient noise.

---

\*"The Distribution of Cosmic Radio Background Radiation," Proc IRE, Vol. 46, pp. 208-215, January 1958.

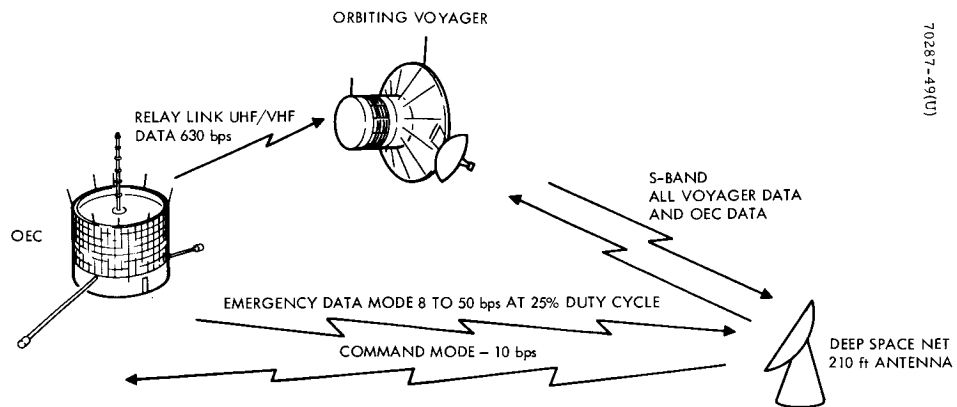


Figure 3-1. Signal Flow Paths

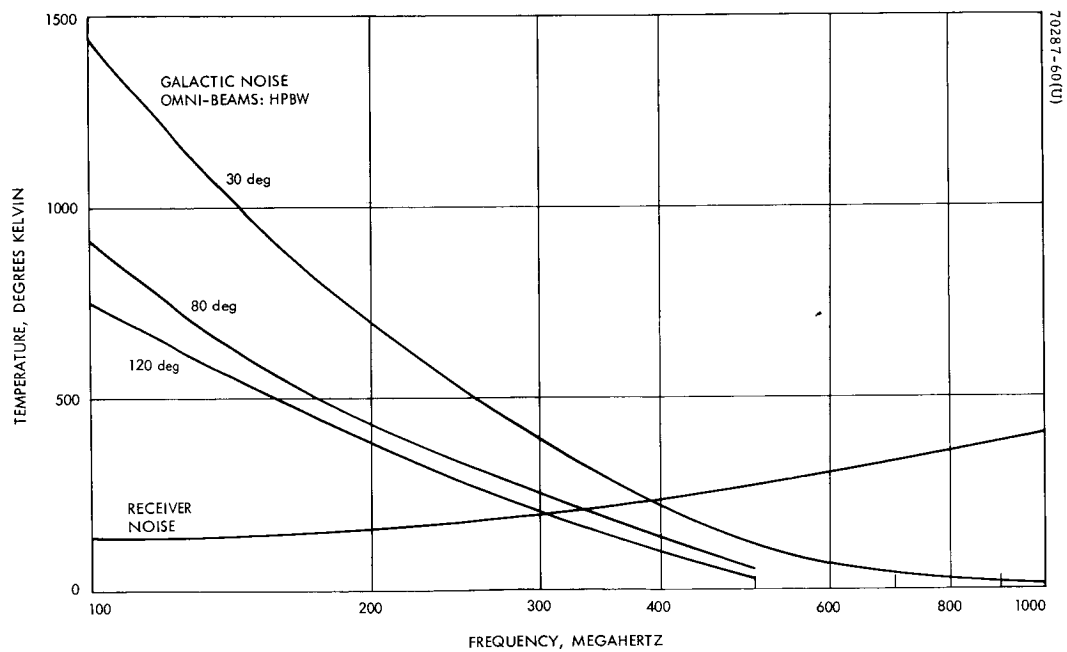


Figure 3-2. Galactic and Receiver Noise Temperature Versus Frequency

### 3.2.4 Summary of Frequency-Dependent Parameters

Figure 3-3 shows the conversion losses presently attainable in producing RF power from solar panel or battery prime power sources. Figure 3-4 shows the combined effect of all the frequency-dependent terms. Arrows indicate the three frequencies in the range that are available for telemetry according to international agreement. The positive direction of the ordinate represents increasing link capability.

### 3.2.5 Modulation Method

Two modulation techniques have been considered for the relay link. The fact that the Orbiter relay equipment is unattended suggested the use of a simple discriminator for detecting noncoherent FSK of binary data on the carrier. The penalty to the link couched in logarithmic terms is:

$$\text{db [carrier/noise]}_{R'Q'D} = 15.0 + 10 \log (\text{bit rate}) + 10 \log [(M+1)^2] \\ - 10 \log (3M^2)$$

Added bandwidth to allow for oscillator instability will raise this requirement significantly. At 10 parts per million or 3 ppm if an oven is used, an additional 2 kHz or 600 Hz must be provided, and these bandwidths are comparable to those required for transmitting the information.

A similar representation of link stress for coherent PCM/PM in which the data are bi-phase modulated on a subcarrier oscillator is:

$$\text{db carrier/noise}_{R'Q'D} = 6.8 + 10 \log (\text{bit rate}) + 10 \log (2 J_1^2)$$

Substituting numerical values for the real time case involving data rates of 630 bits/sec with a bit error rate of  $10^{-3}$ , it is found that the noncoherent method requires 10.6 db to 6.3 db more power than the coherent case, depending on use of an oven.

This difference may have little significance if power is low as is the situation with some combinations of short ranges and optimum frequencies displayed below, but for other situations shown even the 6 db penalty may result in data compromise.

There is still uncertainty in the demodulation method carried on the orbiting vehicle for relay of descent data from the landing vehicle, but the very high data rates expected for that phase indicate that high power levels would also encourage the use of the most efficient modulation method. In this application the RF power breakdown in Mars atmosphere causes a limitation that will not yield appreciably even if weight were not limited.

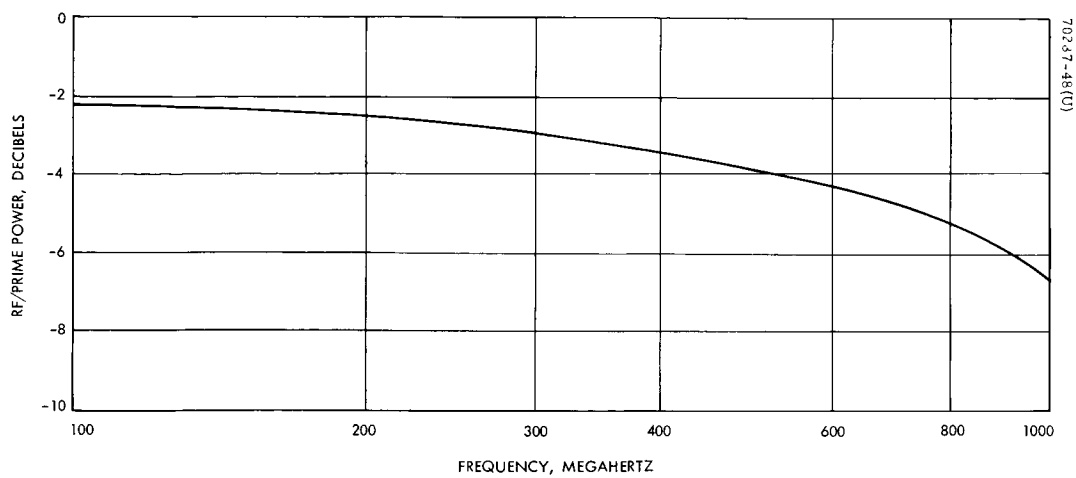


Figure 3-3. Present Capability for Power Conversion

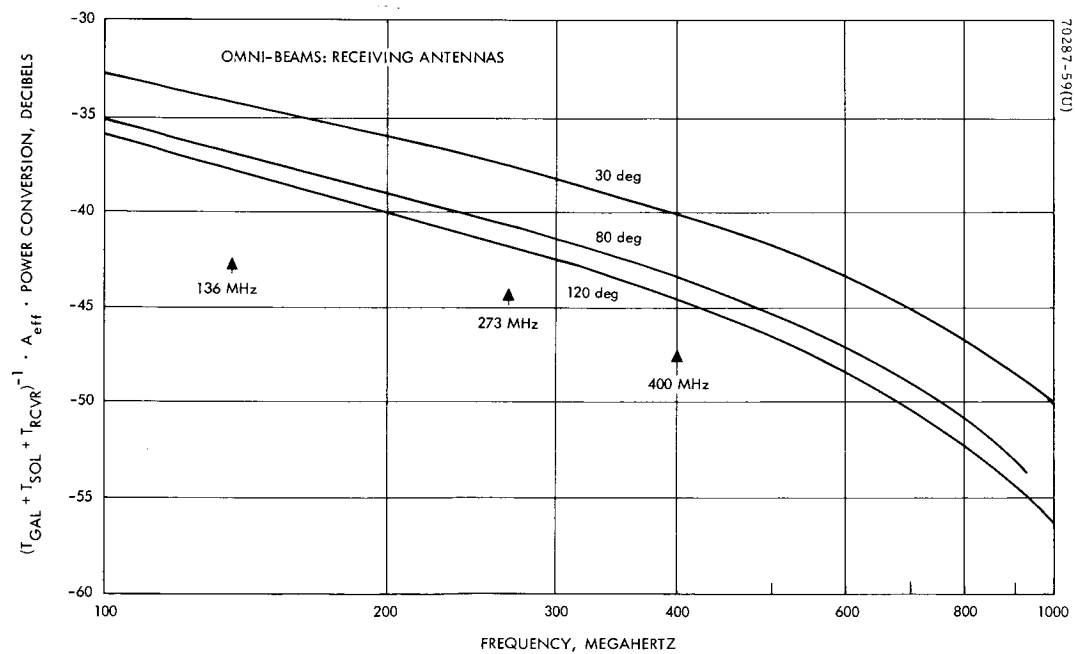


Figure 3-4. Frequency-Dependent Factors Affecting Link Capacity

### 3.2.6 Coding

A good case is made for using coding in the subsequent discussion of the backup data link operating directly into DSN. The possibility of using similar techniques on the relay link was discarded because of the uncertainty in acquiring bit synchronization. In order to realize a power advantage it is necessary to send the coded binit at such a low energy level that the received signal is from 1 to 4 db below the noise. Therefore binit synchronization must be achieved before decoding can be started. The entire RF signal band can be recorded on the ground and binit synchronization can be acquired at leisure with monitoring and repetition if difficulty arises. This approach on the Voyager spacecraft is felt to involve too much risk to be recommended in view of the present amount of inexperience.

### 3.2.7 Power Requirements for Alternate Cases in Co-orbital Mode

Table 3-2 shows combined effects for all of the frequency-independent terms for the three types of modulation methods discussed above. These db sums added to those shown in Figure 3-4 for the frequency-dependent terms give the -dbw value for prime power required to transmit 630 bits/sec from 1000 km. Figure 3-5 shows the prime power required for the several frequencies and modulation methods as range increases.

The maximum range for each of nine data link parameters is determined by the range at which the pertinent power line is intersected. These ranges are important to the co-orbital tradeoff concerning separation forces and to the occultation experiment. Occultation distances can only be achieved in the real time data transmission mode if the coherent phase-modulation and 135 MHz option is used and if 13 watts can be used for the transmitter.

If an FSK noncoherent system were specified for ease of spacecraft data handling and if 400 MHz were dictated, then the co-orbital OEC could not be permitted to drift more than 1000 km away from the spacecraft for full data transmission capability.

### 3.2.8 Orbit Change Mode

The preceding calculations can be adapted to the orbit change mode in which spacecraft and capsule can be regarded as having roughly the same orbit but with changing phase relationship in that orbit. Data collected at the 630 bits/sec rate amount to 15 to 30 megabits for the orbital extremes under consideration. Since the energy required to transmit a given amount of data is independent of transmission rate, it is instructive to examine energy requirements versus range shown in Figure 3-6. This graph shows the watt-hours that will be expended by the transmitter in transmitting various amounts of data to the Voyager Orbiter. Next, the actual ranges that will be encountered for two vehicles in similar orbits but with different periods was examined and summarized in Figure 3-7.

Here is shown a day-to-day history of ranges for readout opportunities as the two vehicles drift into and out of orbital phase. The lower curve shows ranges for 2 hour readout intervals when the Voyager orbit has 10,000 km apoapsis and

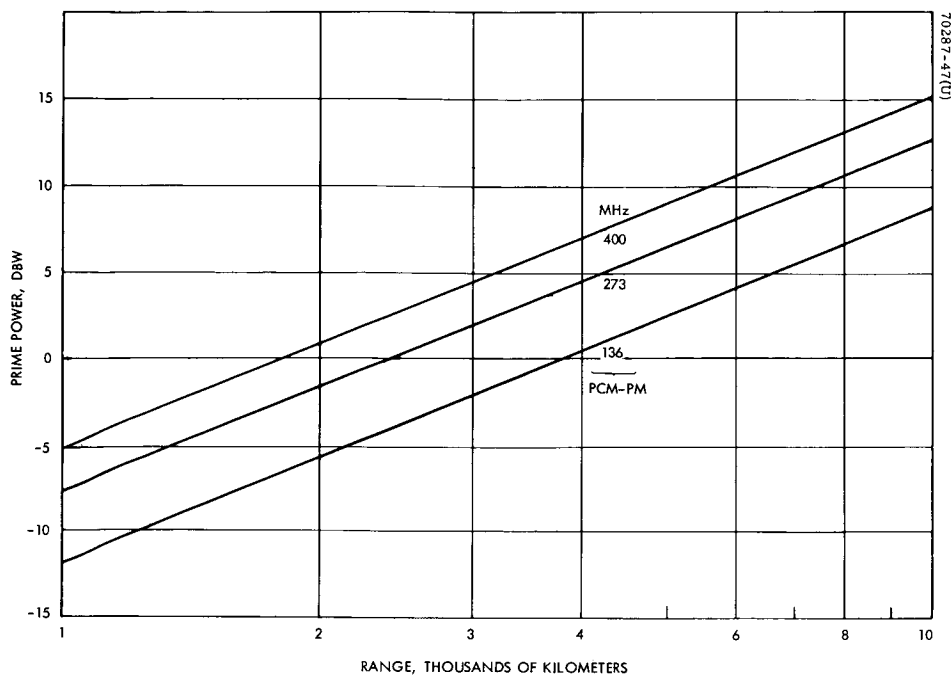


Figure 3-5. Transmitter Power Requirements Versus Range for Transmitting 630 bits/sec

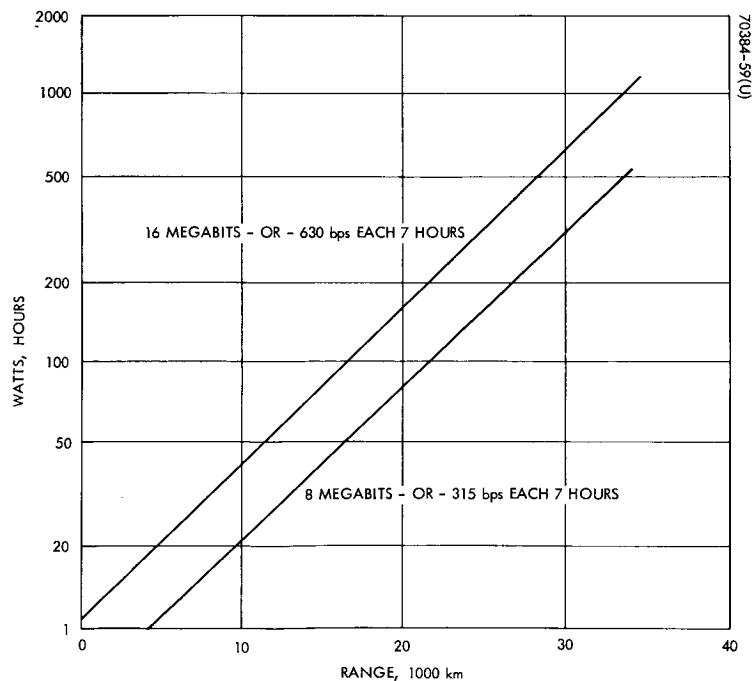


Figure 3-6. Energy Required to Transmit Various Amounts of Data Versus Range

TABLE 3-2. DATA LINK FREQUENCY INVARIANT TERMS

Frequency invariant terms normalized for:

Power            1 watt  
 Range            1000 km  
 Data rate        630 bits/sec

	PCM/PM	FSK-FM No Oven	FSK-FM Oven
OEC gain and losses, db	- 6.0		
$4\pi R^2$ with respect to a meter, db	-131.0		
Boltzman's Constant, dbw/Hz	+228.6		
Margin, db	- 4.0		
Data requirements, dbw	+ 87.6	87.6	87.6
Modulation loss or improvement, db	- 3.2	- 3.3	- 3.3
Bandwidth (630 bits/sec), db	- 28.0	-28.0	-28.0
Threshold for bit error rate of $10^{-3}$ , db	- 6.8	-10.0	-10.0
Oscillator instability, db	0	- 7.3	- 3.0
	*49.6 dbw	*39.0 dbw	*42.3 dbw

\*These values may be combined with the frequency-dependent terms shown in Figure 3-3. Prime power required may then be deduced by reversing the resulting sign.

1000 km periapsis but the OEC orbit has apses of 10,000 km and 500 km. The upper curve gives ranges for 4 hour readout intervals for the same periapses, but apoapses are both 20,000 km. These readout intervals were chosen to represent the same duty cycle for each case since the orbit period is 7 hours for the lower curve and 14 hours for the upper curve. Curves for the intervening Voyager orbits lie between these two extremes if duty cycles are maintained at 0.29.

These curves represent one cycle of the synodic period which is repeated with the period of earth days plotted respectively along the two abscissas. In both cases the discrepancy between vehicle orbits is about 24 minutes. If a more dramatic orbit shift is effected, then the range histories (or ordinates) will remain the same but the synodic period will be shortened; i. e., the two vehicles will drift into and out of phase more quickly.



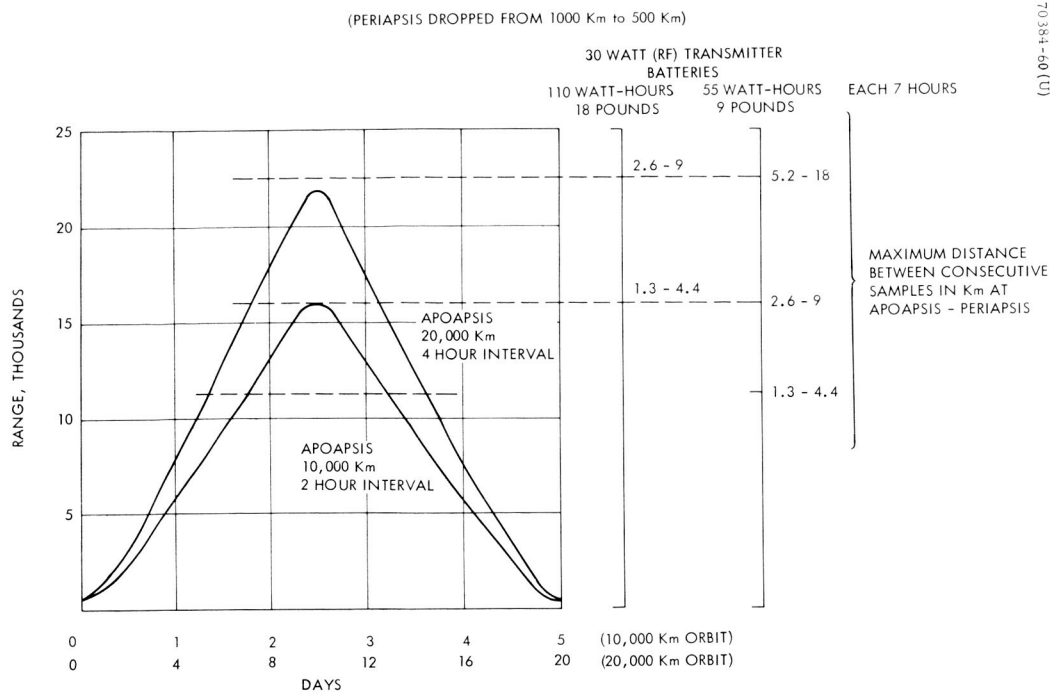


Figure 3-7. Communication Readout Ranges and Sampling Spacing for Typical Orbit Range

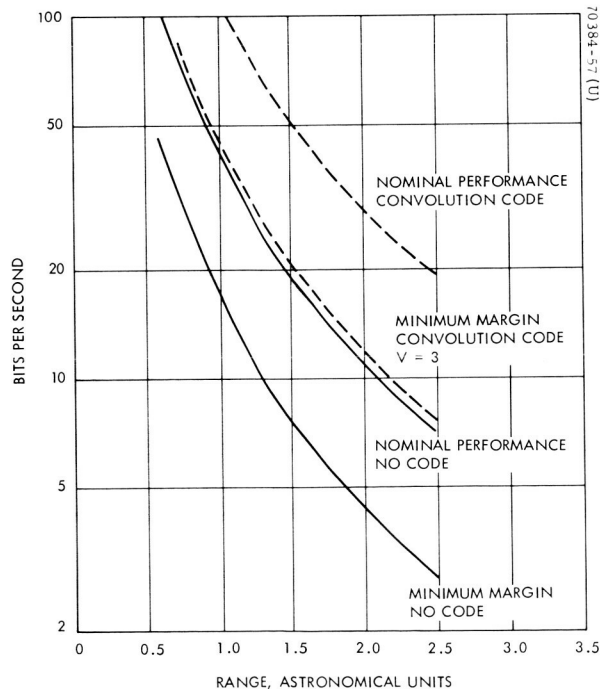


Figure 3-8. Link Capability for 10-watt TWT into DSN Versus Range

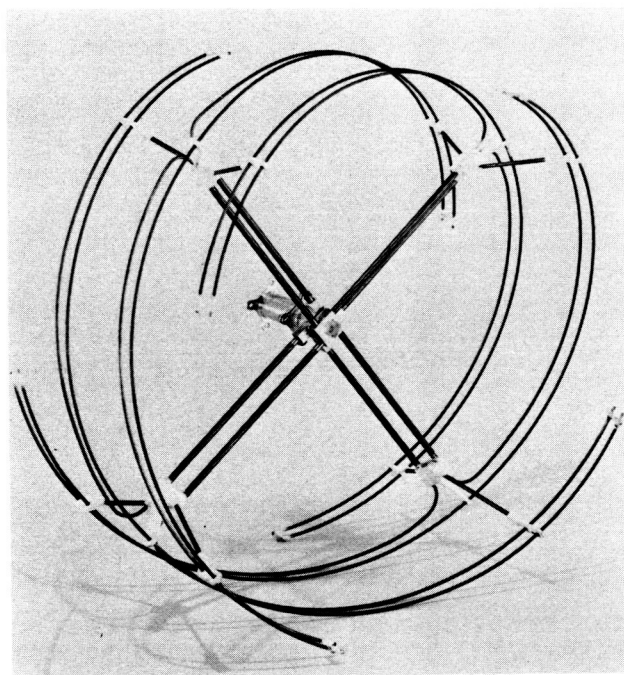


Figure 3-9. Circularly Polarized Radiating Element (Photo R116236)

At any particular day of a cycle it is possible to discover the energy necessary to transmit data by reading range from the ordinate and entering this value on Figure 3-6. The illustrative design has assumed that the batteries and solar array are capable of collecting and storing transmitter energy of 110 watt-hours each 7 hours. Figure 3-6 shows that this energy is sufficient to transmit all of the experiments data for ranges up to 16,000 km. All of the data corresponds to sampling experiments each vehicle spin or at distances of 1.3 to 4.4 km. This line has been transferred to Figure 3-7 to show those days of the synodic cycles when all data may be retrieved. If half the battery weight, or 55 watt-hours capability every 7 hours, is used the maximum amount of data can be retrieved only when ranges are less than 11,300 km. This is also indicated by a horizontal line with the 1.3 to 4.4 km inter-experiments sampling distance marked. Lines marked with greater inter-experiments sampling distances indicate one way the volume of data might be diminished to permit transmission when distances are too great for the energy available. Experimenters could be given the option of reducing the sampling rate with attendant increase in distance between consecutive samples or sampling rate could be maintained with concentration on some portions of the orbit. The above discussion is further covered for the baseline OEC power system in Section 5.2 of Volume I.

### 3.3 S-BAND LINK FOR BACKUP DATA MODE

#### 3.3.1 Analysis and Design

A direct link to the DSN can be provided with the addition of equipment shown in Table 3-3. Table 3-4 gives the calculations for link capability at the maximum Mars range of 2.5 AU, and Figure 3-8 shows the performance for ranges down to the closest range for either 1973 and 1975 launch opportunities. The curves for no coding and for a convolutional code are presented to show the range of capability that can be offered.

The curves designated minimum margin represent the case for all negative tolerances agglomerated. The spread of values for various distances and system performance levels indicates that provisions for several data rates should be included to optimize data return. If coding were used, the rates might be 8, 48, 96, 200, and 300 bits/sec. Similarly, the sequencer could be programmed for a variety of sampling modes that might be elected by the experimenters. With coding, options could be provided so that data could be sampled from 1/2 to 1/70 as often as in the primary data mode, or orbital segments of particular interest might be sampled with the primary mode density.

The equipment weights shown are those of an existing transponder which has been flight qualified for Surveyor and also flown on Atlas-Centaur tests for doppler tracking. The antenna will be a stacked array of about  $6\lambda$  with a 10 degree half-power omnidirectional beam. The calculations are shown for circular polarization which can be achieved with the element shown in Figure 3-9. This element has been used at UHF frequencies in an array configuration, and scaling to the Goldstone frequency presents no problem.

TABLE 3-3. ADDITIONAL COMPONENTS FOR S-BAND MODE

Components	Weight, pounds	Power Input, watts
TWT amplifier	0.95	--
Electronic conversion unit	2.5	53
Drive chain	2.15	9
Receiver and transponder	3.9	3
Diplexer	0.5	--
Decoder selection circuits	0.3	--
Cables and connectors	0.2	--
Structure	0.7	--
Totals	11.2	65

Should it be decided to measure the capsule attitude by sensing polarization, then it would be necessary to use a linearly polarized antenna. The existing Syncom communications satellite design can be readily extended to provide a 10 degree beam.

TABLE 3-4. TELECOMMUNICATION DESIGN CONTROL TABLE

Number	Parameter	Value	Tolerance, db		Source
1	Total Transmitter Power (12 watts)	+10.8 dbw	+1.0	-0.8	TWT specification
2	Transmitting Circuit Loss	-1.7 db			
3	Transmitting Antenna Gain (6λ, circular polarization)	10.5 db		-0.5	
4	Transmitting Antenna Pointing Loss	-3.0 db	+3.0	-0.0	
5	Equation Constant $\lambda^2(4\pi R)^{-2}$ with respect to a meter at 2295 MHz, $R = 37.5 \cdot 10^8$ km	-271.1 db	+3.2	-0.4	
6	Polarization Loss				
7	Receiving Antenna Gain (including losses)	+60.9 db	+1.2	-1.2	
8	Receiving Antenna Pointing Loss	0.0 db			
9	Receiving Circuit Loss	0.0 db			
10	Net Circuit Loss	-204.4 db	+7.4	-2.1	
11	Total Received Power	-193.6 dbw	+8.4	-2.9	
12	Receiver Noise Spectral Density (N/B) T System = $45^\circ \pm 10^\circ$	+212.0 dbw/Hz	+1.1	-0.9	
13	Carrier Modulation Loss 1.2 R	-3.4 db	+0.2	-0.2	
14	Received Carrier Power	-197.0 dbw	+9.7	-4.0	
15	Carrier APC Noise Bandwidth ( $2B_{LO} = 5$ Hz)  CARRIER PERFORMANCE-TRACKING (ONE-WAY)	-7.0 db			
16	Threshold SNR in $2B_{LO}$	-2.0 db			
17	Threshold Carrier Power				
18	Performance Margin  CARRIER PERFORMANCE-TRACKING (TWO-WAY)				
19	Required Threshold SNR in $2B_{LO}$	4.0 db			
20	Required Threshold Carrier Power	201.0 db			
21	Performance Margin	4.0 db	+9.7	-4.0	
22	Threshold SNR in $2B_{LO}$	-4.0 db			
23	Threshold Carrier Power	+8.4 db			
24	Performance Margin	+4.4 db	+9.7	-4.0	
	DATA CHANNEL				
25	Modulation Loss	-3.1 db	+0.2	-0.2	
26	Received Data Subcarrier Power	-196.7 dbw	+9.7	-4.0	
27	Bit Rate (1/T) (2.8 bits/sec)	-4.5			
28	Required ST/N/B	-6.8 db			
29	Required Threshold Subcarrier Power	-200.7 dbw			
30	Performance Margin	4.0 db		-4.0	
	SYNC CHANNEL				
31	Modulation Loss				
32	Receiver Sync Subcarrier Power				
33	Sync APC Noise Bandwidth ( $2B_{LO} =$				
34	Threshold SNR in $2B_{LO}$				
35	Threshold Subcarrier Power				
36	Performance Margin				

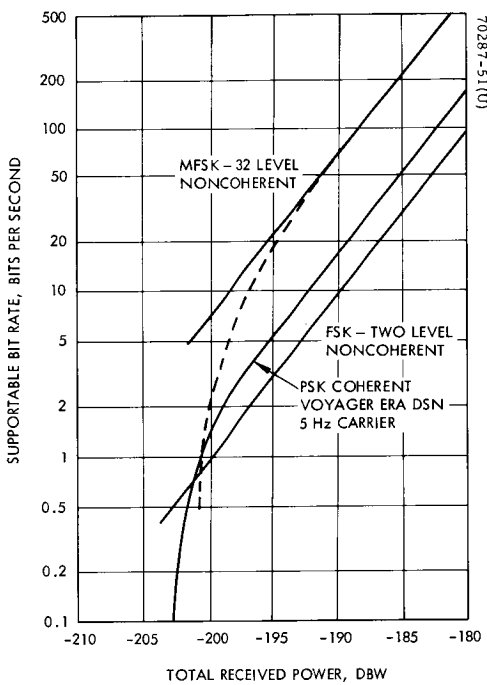


Figure 3-10. Comparison of Modulation Methods

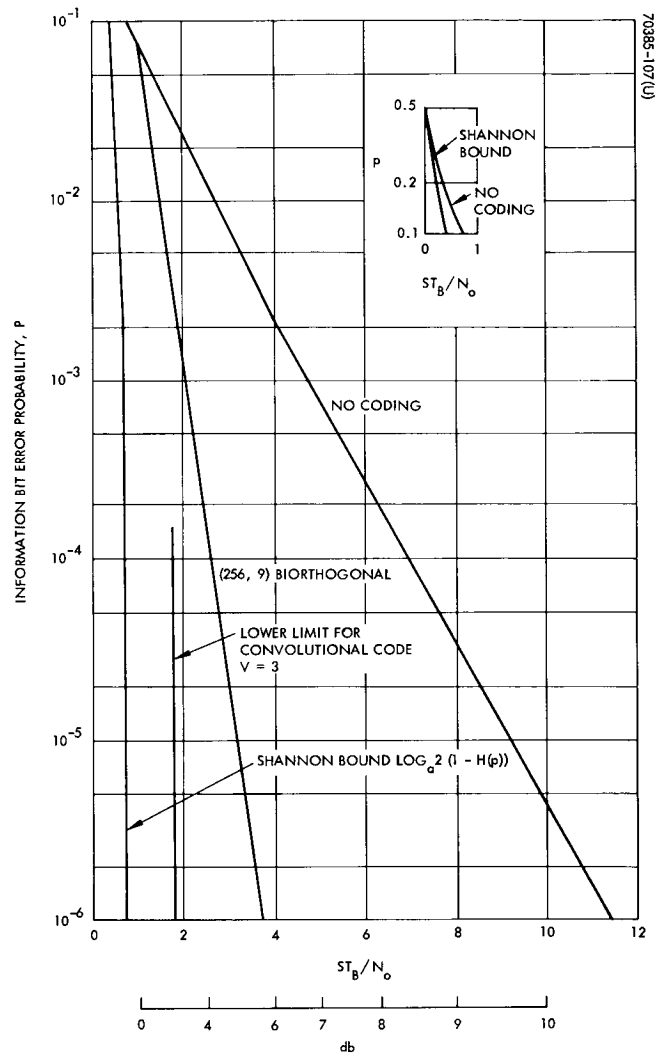


Figure 3-11. Probability of Bit Error Versus Received Energy per Bit/Noise Spectral Density

### 3.3.2 Modulation Methods

The link computation for an OEC S-band transmitter to be used with the DSN for a "backup" data mode shows that the minimum margin worst range case affords a bandwidth  $\times$  S/N product in excess of 11 db. This represents the power in the subcarrier after threshold has been met in a 5 Hz carrier tracking loop ( $2 B_o$ ) for a total received power of -197.6 dbw.

The first question that arises is that of modulation method, and in particular whether the link is sufficiently weak to warrant multiple frequency shift keying (MFSK), instead of proven phase shift keying of a subcarrier frequency. The succeeding arguments were made in rejecting inclusion of this modulation method.

If only the statistical effects of thermal noise are considered, then the two straight line performance curves for MFSK and FSK of Figure 3-10 are obtained. The 32 level modulation would then offer an improvement factor of four over PSK; however, when oscillator drift is taken into account, as shown in Appendix C, the dotted curve performance is obtained and the method offers little improvement in the critical low data region. In addition, PSK has the advantage that it is the DSN method which is compatible with doppler tracking and proven data acquisition.

### 3.3.3 Data Enhancement Achievable With Coding Techniques

Enhancement of data rates by coding was then studied for this mission and results were found to be favorable. The few codes discussed in the following paragraphs are selected to give comparative advantages of block coding and sequential (e.g., convolutional) coding for the present application. The additional equipment in the spacecraft is modest for all of the codes cited, and the ground decoding equipment varies for different codes as indicated below.

The capability of a code is expressed basically in terms of its error rate as a function of received energy per bit/noise spectral density. In Figure 3-11 the information bit error rate probability  $p$  is plotted against  $ST_B/N_o$ , where  $S$  is the average received power in watts,  $T_B$  the bit time in seconds, and  $N_o$  the noise spectral density in watts/Hz. Two codes are indicated in addition to the no coding case: the (256, 9) biorthogonal code (Viterbi, "Digital Communications") and the convolutional code with sequential decoding. The biorthogonal code uses word correlation decoding, and requires 256 correlators to decode according to one mode of decoding.

It may be important to note that each binit will have 1/28 the energy in a binit, and hence synchronization could be a problem. For example, at  $p = 10^{-3}$ ,  $ST_B/N_o = 2.1$  and the binit signal to noise ratio is -11 db.

For the convolutional code the notation of Wozencraft and Jacobs\* is used. For  $V = 3$ , essentially error-free performance could be achieved for values of  $ST_B/N_o$  quite close to the Shannon bound, but it is felt that the lower

---

\*"Principles of Communication Engineering."

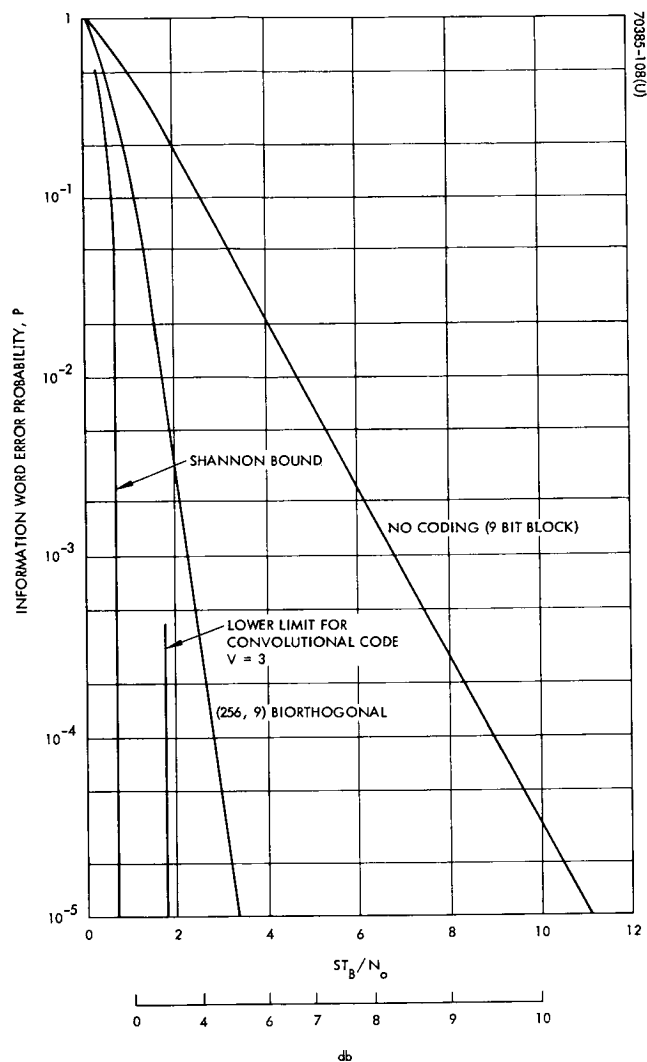


Figure 3-12. Probability of Word Error  
Versus Received Energy per Bit/Noise  
Spectral Density

limit on  $ST_B/N_0$  is about 1.75 due to computational difficulties. At this point  $R_{comp} = 1/3$  for  $V = 3$ , and the average number of computations per bit becomes infinite. Note that energy/binit is much higher than for the biorthogonal code. The cutoff point of 1.75 assumes 8-level quantization of each binit at the receiver.

It is also useful to determine the word error rate because it is sometimes more meaningful to think of a word as a single entity. In Figure 3-12 the word error rate for 9-bit blocks is plotted. The word error rate does not have any significant effect on the cutoff energy/bit for the convolutional code, and hence 1.75 remains the lower limit.

Enhancement is defined as the ratio, for given error probability, of the no coding  $ST_B/N_0$  to the  $ST_B/N_0$  for the code in question. For the convolutional code, the latter quantity is taken to be  $ST_B/N_0 = 1.75$  for all values of error rate. The no coding case is considered to be the reference for measuring enhancement. Figure 3-13 shows the enhancement plotted against information bit error probability and word error probability respectively. The enhancement is different for block codes depending on whether the bit error criterion or word error criterion is used.

The interpretation of enhancement is that it is the factor by which the power can be reduced for the same information bit rate or the factor by which the information bit rate can be increased for the same power. The enhancement curves should be used in the following way for block codes. For a bit error probability of, say,  $10^{-5}$ , the enhancement in Figure 3-13a is 2.9. This bit error probability corresponds to a no coding word error probability of  $10^{-4}$ , and this yields an enhancement of 4.1 in Figure 3-13b. Which one will be used is a question the user must decide. For a bit error probability of  $10^{-3}$ , the two enhancements are nearly the same.

For the convolutional code, enhancement offers a comparison between the energy required for a certain no coding error rate and the least energy required to produce essentially error-free performance, under conditions that make decoding reasonable. Recent developments suggest that it may be possible to trade computing difficulty for some non-negligible error rate for these low energy levels. This problem is being further studied and with the help of the Hughes simulator, now being developed, it will be possible to state what additional performance can be obtained. However, as of this time, the block codes are shown having greater enhancement than the convolutional code for high error rates, but it is the opinion of experts in the field that convolutional codes will outperform block codes in every aspect.

Other block codes have been considered, but the results are not included here. For example, the Hamming (13, 9) code using two level binit quantization (BSC channel) would produce a very modest enhancement (around 1.3). The decoding for this code is trivial compared to the above codes. Another code might be (24, 9) code consisting of adjacent (16, 5) and (8, 4) biorthogonal codes. The energy/binit would be high enough to ensure bit synchronization, and the analysis is manageable.



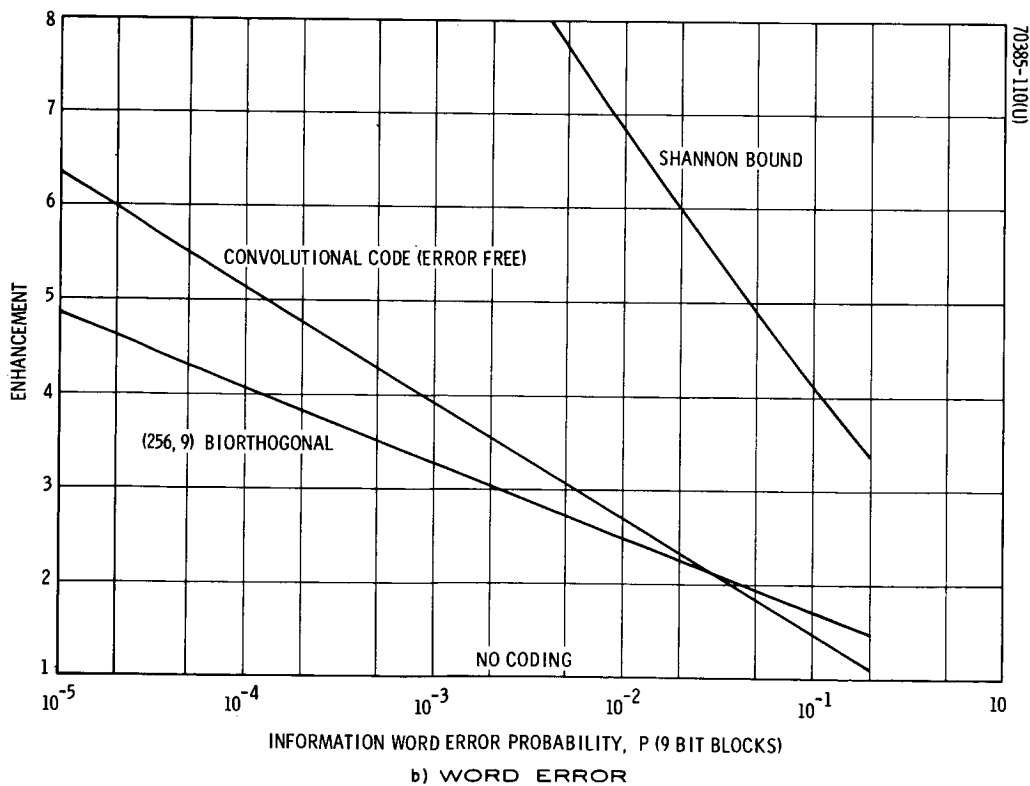
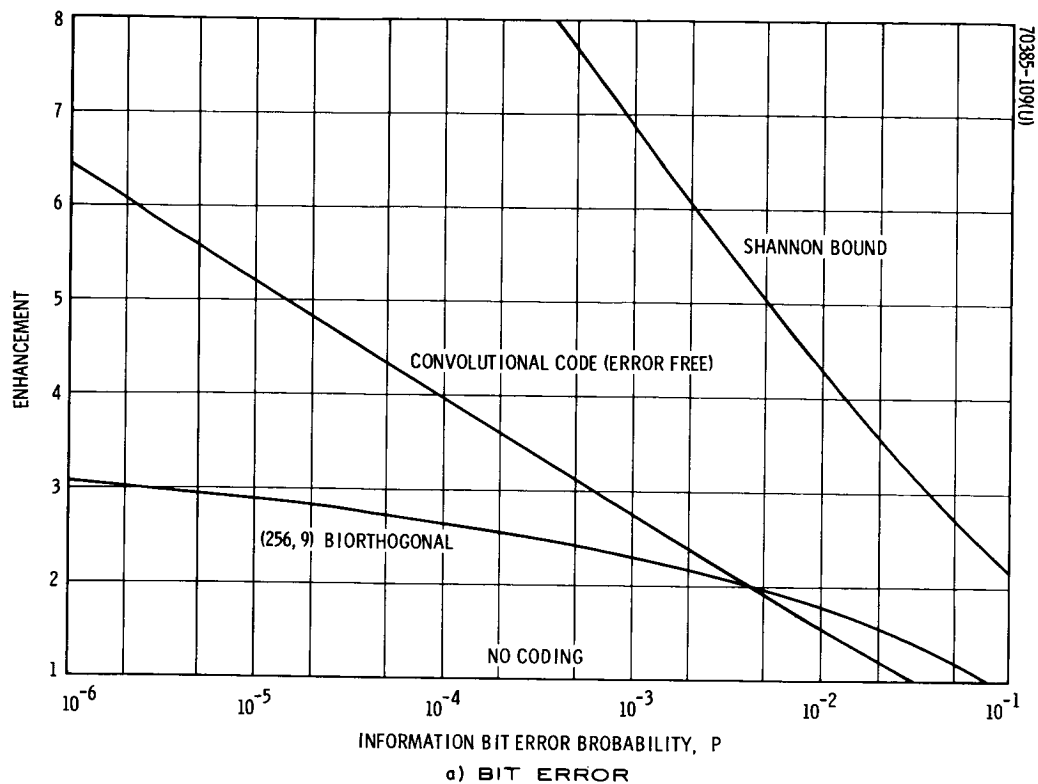


Figure 3-13. Information Enhancement

### 3.3.4 Command Link

The illustrative design makes use of the direct link from the Deep Space Net (DSN) for sending commands to the vehicle. This path was selected in preference to a Voyager relayed link for a number of reasons, but none forces the choice decisively, and a relayed link would be adequate. First, present Voyager plans have not included a VHF/UHF transmitter for commands to the Lander capsule, and the OEC effort has been directed toward sharing relay equipment as much as possible. Second, the inclusion of an S-band transmitter for emergency data retrieval makes it desirable to carry an S-band receiver so that the OEC can be entirely independent of the Voyager Orbiter. Once this equipment has been added, it is reasonable to connect the two in a transponder mode so that the excellent DSN doppler tracking capability can be employed to accelerate acquisition of OEC orbital information. The orbital considerations are discussed in Section 4.0\* where the conclusion is drawn that this capability is not necessary for inferring positional data, but it would facilitate assessment of the OEC orbit after orbit changes have been commanded.

Disadvantages of relaying commands through the orbiting vehicle are that the equipment necessary for the relay portion adds in series for reliability purposes and that the possibility of Mars occultation between Voyager and OEC will increase the time during which commands may not be sent to the OEC.

A range calculation verified that this link would indeed be adequate for the purpose. This calculation is shown in the JPL format (Table 3-5) using a pessimistic projection of DSN capability for the Voyager era and presuming the use of an OEC receiver with a tunnel diode amplifier and a 20 Hz carrier tracking loop. Maximum Mars-Earth range was used in the calculation.

Investigation of coding techniques for this link led to the following recommendations. Codes that offer increased data rate are probably not worth the incorporation of extra equipment in the OEC since the uncoded link supports sufficient data rates to permit any command sequences envisioned. On the other hand, error correction codes do offer the advantage that they significantly diminish the probability that commands having errors will arrive and be rejected by the OEC, thus requiring repetition of the command. Since the round-trip time for a command and rejection may take 30 minutes, it is desirable to reduce the incidence of such an occurrence.

The effect of using a (15, 10) Hamming "distance 4" code implemented so that single errors in a word are corrected and double errors are detected is of interest. If a carrier to noise level and information rate is selected so that the uncoded stream will experience an erroneously accepted word in  $10^5$  words, then the (15, 10) code using the same carrier to noise level and command rate will result in a rejected and retransmitted word in  $10^6$  words.

Execution of an erroneous command will not occur more than once in about  $10^{10}$  words. If only error detection were implemented, then the rejection rate, with attendant time lost, would rise to one word in  $10^3$ . Figure 3-14 shows the probability of these events occurring as a function of  $ST_B/N_0$ , where

---

\* Volume I.

TABLE 3-5. TELECOMMUNICATION DESIGN CONTROL TABLE

Number	Parameter	Value	Tolerance, db		Source
1	Total Transmitter Power	40.0 dbw	+0.0	-1.0	
2	Transmitting Circuit Loss	-0.5 db	+0.1	-0.1	
3	Transmitting Antenna Gain	60.0 db	+0.8	-0.8	
4	Transmitting Antenna Pointing Loss	-0.2 db	+0.0	-0.1	
5	$\lambda^2(4\pi R)^{-2}$ with respect to meter at 2113 MC, $R = 270 \times 10^6$ KM	-267.6 db	+0.4	-0.4	
6	Polarization Loss	-0.7 db	+0.3	-0.3	
7	Receiving Antenna Gain	0.0 db			
8	Receiving Antenna Pointing Loss				
9	Receiving Circuit Loss	-0.4 db	+0.5	-0.5	
10	Net Circuit Loss	-269.4 db	+1.3	-1.4	
11	Total Received Power	-169.4 dbw	+2.2	-3.2	
12	Receiver Noise Spectral Density (N/B) T System = 410°K	202.5 dbw/Hz	+1.0	-1.0	
13	Carrier Modulation Loss	-3.2 db	+1.0	-1.0	
14	Received Carrier Power	-172.6 dbw	+3.2	-4.2	
15	Carrier APC Noise BW( $2B_{LO} = 20$ Hz)	-13.0 db	+0.7	-0.7	
	CARRIER PERFORMANCE-TRACKING (ONE-WAY)				
16	Threshold SNR in $2B_{LO}$	-6.0 db			
17	Required Threshold Carrier Power	-183.5 dbw	+1.7	-1.7	
18	Performance Margin	10.9 db	+4.9	-5.9	
	CARRIER PERFORMANCE-TRACKING (TWO-WAY)				
19	Threshold SNR in $2B_{LO}$				
20	Threshold Carrier Power				
21	Performance Margin				
	CARRIER PERFORMANCE				
22	Threshold SNR in $2B_{LO}$				
23	Threshold Carrier Power				
24	Performance Margin				
	DATA CHANNEL				
25	Modulation Loss 1.16 radians	-3.2 db	+0.6	-0.6	
26	Received Data Subcarrier Power	-172.6 dbw	+2.8	-3.8	
27	Bit Rate (1/T)	-10.0 db	+1.0	-1.0	10 bits/sec
28	Required ST/N/B	-11.0 db	+1.0	-1.0	$10^{-5}$ bit error rate
29	Required Threshold Subcarrier Power	-180.5 dbw	+2.0	-2.0	
30	Performance Margin	+7.9 db	+4.8	-5.8	
	SYNC CHANNEL				
31	Modulation Loss				
32	Receiver Sync Subcarrier Power				
33	Sync APC Noise BW( $2B_{LO} =$				
34	Threshold SNR in $2B_{LO}$				
35	Threshold Subcarrier Power				
36	Performance Margin				

S is signal power, B bandwidth, T time per binit, and  $N_0$  noise spectral density. This quantity represents the product of energy/binit and bandwidth which occur in the range equation. The uncoded case, represented by (10, 10), will be sent at 10 bits/sec and the coded case (15, 10) will be sent at 15 binit/sec to effect the same information rate. The abscissa has been selected so that a single value represents the same link stress or energy for both cases. This may also be regarded as energy per word, where the information per word is equivalent for both cases.

The matter of transit time between sending and executing commands presents the question of whether this delay could affect the mission adversely. The command philosophy as shown in Section 4.0\* has been to make the spacecraft essentially automatic, with commands used for changing the mission sequences or selecting alternate modes. Separation from the Voyager spacecraft will be initiated by a command to that vehicle, but subsequent operations will be controlled by a sequence stored on the OEC. Similarly, attitude changes will be controlled by stored sequences which are initiated by clock magnitudes set into the OEC by magnitude commands that can be sent as much as one orbit prior to execution. Instances when the mission is redirected involve examination of engineering data which have been stored on the Voyager spacecraft. The time lapse involved in storing and relaying information is more significant than command transit times.

### 3.4 SUMMARY

Figure 3-15 is a block diagram of the communications components necessary to implement the orbit change baseline design. The proposed weights, powers, and functional characteristics are now met in existing components or represent simple modifications of existing components. Simple modifications include stripping unwanted capability from more complex designs, adding existing circuitry to augment capability, or scaling in frequency. The type of equipment or modification is listed in Volume I.

---

\* Volume I.

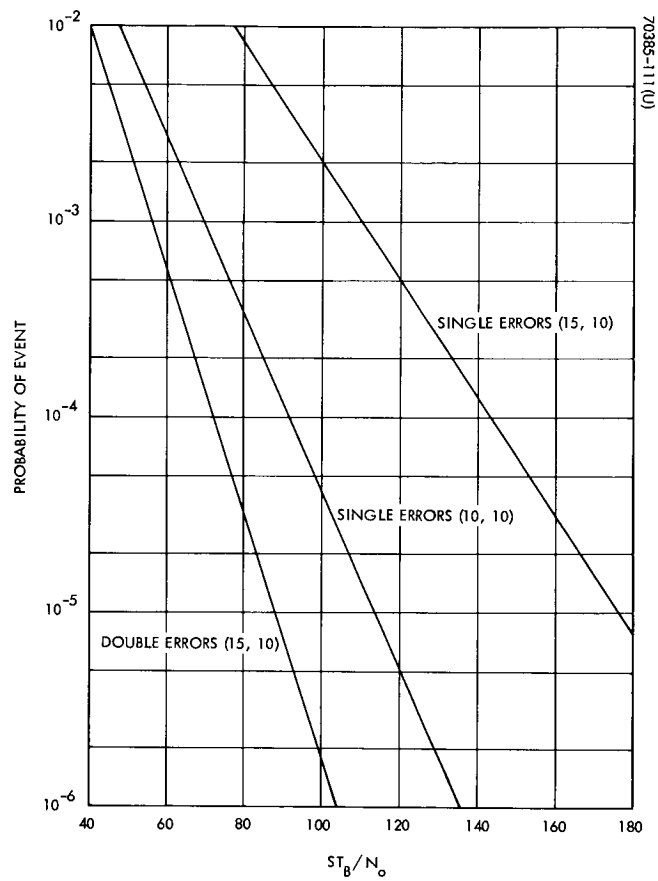


Figure 3-14. Combined Error Detection-Correction Capability

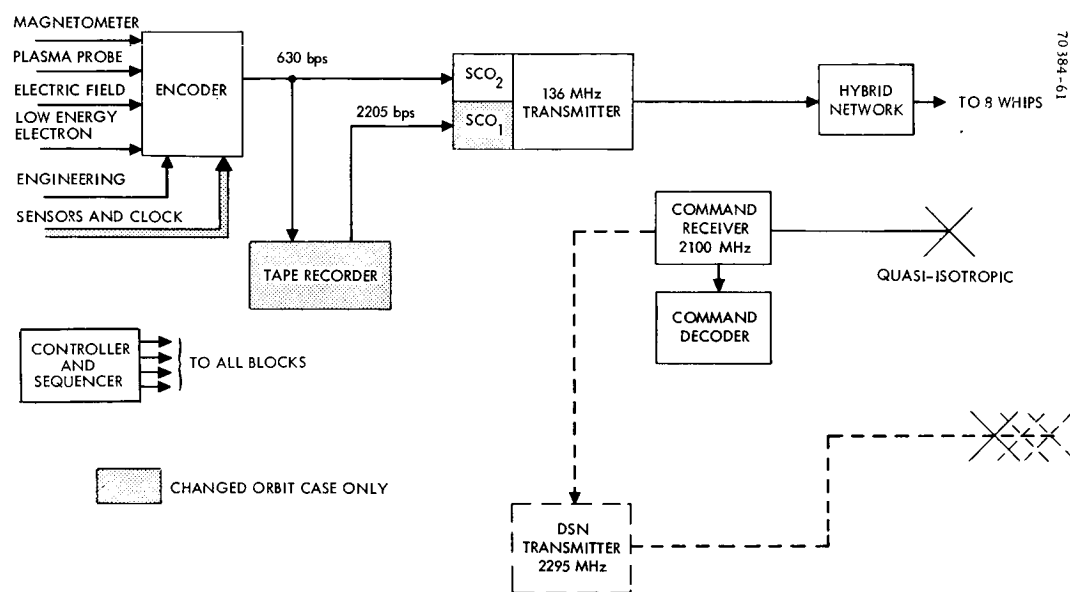


Figure 3-15. Communications Block Diagram

## 4.0 CONFIGURATION STUDIES AND TRADEOFFS

### 4.1 GENERAL

Prior to the selection of a baseline OEC configuration, key areas needed to be studied and explored so as to ensure that the conceptual design selected for the OEC could feasibly satisfy the overall mission requirements. The purpose of this section is to document the studies conducted during the course of the feasibility study that provided the groundwork for selection of the baseline configuration.

The establishment of a baseline configuration for the Orbital Experimental Capsule rests primarily on meeting problems associated with the following aspects of the system design:

- Experiment requirements and constraints
- Environmental conditions
- Voyager interface
- Gyroscopic stability
- Separation concept considerations
- Solar power considerations
- Boom mounted sensors
- Overall integration of OEC subsystems required to satisfy mission requirements

The design effort required to integrate the OEC experiments and the capsule subsystems could meaningfully evolve only after these interrelated areas were evaluated and their implications on the capsule configuration fully understood.

In the pursuit of establishing a conceptual OEC configuration, certain design freedom was constrained by the following specified OEC system requirements:

- Compatibility of the OEC with the 1973 Voyager mission spacecraft.
- A life requirement of 12 months in transit to Mars stowed on Voyager with a 6 month life in orbit about the planet.

- Spin stabilization at 50 to 70 rpm.
- A 0.25 gamma or less magnetic field at the magnetometer sensor due to the capsule's inherent field.
- A scientific payload consisting of a complement of instruments which could be represented by a magnetometer, solar plasma probe, and electric field meter totaling 15 pounds and requiring 10 watts of power continuously.
- A nominal weight of 100 pounds with potentially a contingency of 15 percent.
- A stipulation that the capsule's spin axis be normal within  $\pm 5$  degrees to the ecliptic plane while in orbit about Mars.

The requirements of spin stabilization and spin axis orientation for the OEC immediately suggest that the capsule's shape be cylindrical to accommodate an optimum shaped solar cell array. There are then basically two concepts for the capsule internal arrangement: an integrated design approach where the experiments and supporting subsystems are intermingled, or a modular design approach where the experiments and subsystems are essentially isolated from each other by an arrangement that allocates a certain portion of the cylindrically enclosed volume for each. Certain ramifications result, and are discussed later in this section, by electing to locate the experiment module centrally on the capsule or at one end of the cylinder.

The requirement that the magnetometer and the electric field meter sensors be located away from the capsule bus by booms also implies possible configuration variations: 1) an axially mounted boom along the spin axis for both sensors, 2) two radially mounted booms, and 3) drooped radially mounted booms.

The fact that the feasibility study considered both the co-orbital OEC system and the orbit change OEC concept did not significantly affect the configuration studies since only the propulsion subsystem requirement is significantly different. Basically, the choice of an OEC configuration rests with satisfactorily integrating the overall system into a simple and reliable design utilizing qualified equipment and subsystems, after having explored the key interrelated areas to ensure flexibility and compatibility of the design choice.

#### 4.1.1 Experiment Requirements

For the purposes of configuration evaluation and studies, three experiments were defined as the baseline payload: a magnetometer, solar plasma probe, and electric field meter. Both the magnetometer and electric field meter require that their sensing elements be located some distance from the capsule electronics for valid measurements to be made. The consideration of booms as part of the OEC therefore is a firm requirement in light of the 0.25 gamma limit for the magnetometer. The sensors for both these experiments could conceivably share the same mast.



The plasma probe considered for the OEC mission requires a window through the capsule to permit scanning the plasma, primarily in the plane of the ecliptic. In addition to the three experiments mentioned, a low energy electron detector may also be required in the payload. Upon reviewing the typical scientific experiments, the nominal physical parameters were found to be approximately as follows:

#### Magnetometer

Sensor	1.0 pound
Electronics	5.0 pounds (10 x 10 x 3 inches)

#### Solar plasma probe

Weight	8.0 pounds
Size	≈ 6 inch cube

#### Electric field meter

Sensor	1.0 pound
Electronics	2.0 pounds (3 x 4 x 5 inches)

For the solar plasma probe, the required unobstructed acceptance window corridor is assumed to be 30 degrees equatorial by 160 degrees polar with respect to the capsule.

The nominal physical parameters used for the scientific equipment specified as the baseline payload compare very closely to the equipment used by Ames Research Center on the Pioneer program.

## 4.2 ENVIRONMENTAL CONSIDERATIONS

Although the environmental conditions the OEC would be exposed to do not play a major role in dictating configuration selection, they are certainly of utmost concern in the conceptual design of the overall system. The thermal environment was studied for both the transit phase and in-orbit operation of the OEC. During the transit phase, the OEC is mounted on the Voyager spacecraft bus and by necessity (available stowage volume) must be placed on the nominal shade side of the Voyager solar panels. For in-orbit operation, the thermal studies had to investigate power variations for extreme modes of operation as well as eclipse periods. The studies resulted in findings and conclusions that recommended special design features for incorporation in the baseline configuration. These conclusions are covered in detail in Section 6.4 of this volume.

Due to the current uncertainty of the actual 1973 Voyager spacecraft design to be selected from the present three contractors involved, a dynamics analysis of the OEC launch environment was felt to be of little credibility at this

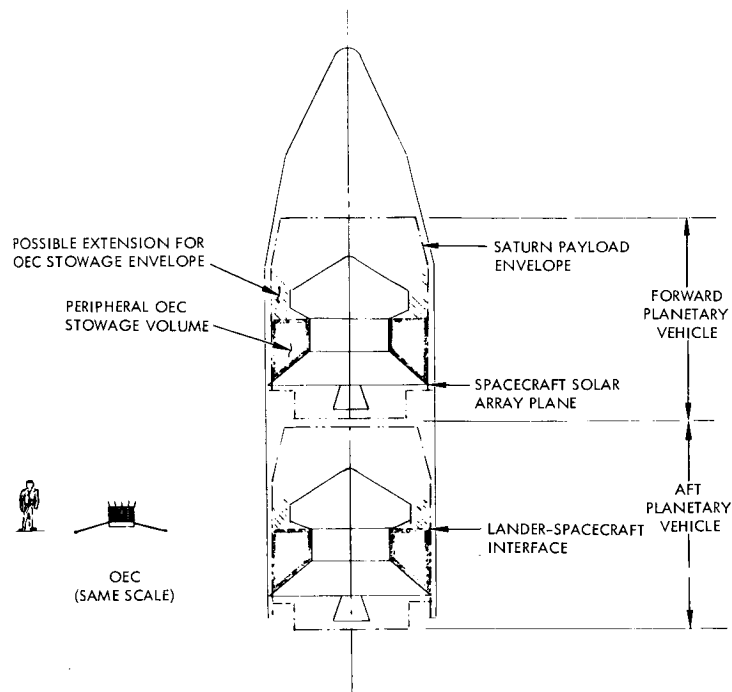


Figure 4-1. Voyager Envelope Considerations for Stowage of OEC

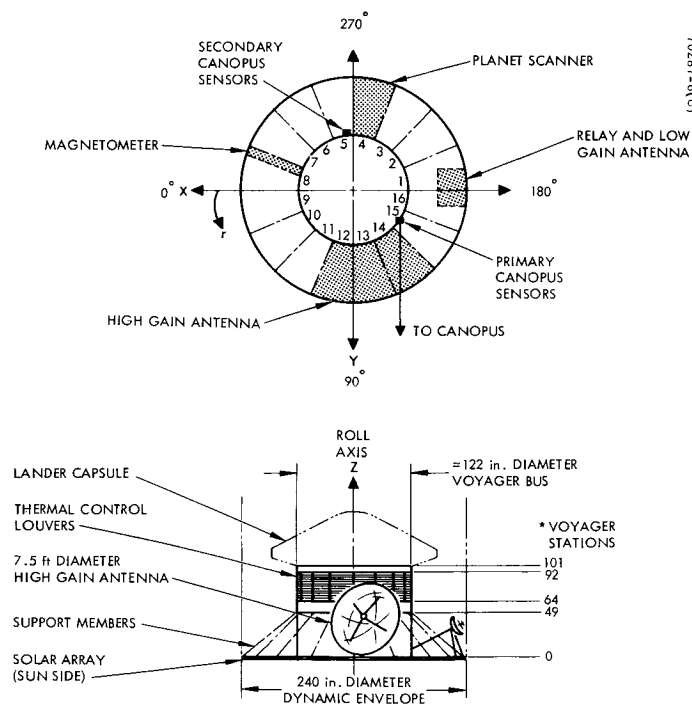


Figure 4-2. General Electric Voyager Spacecraft

time. Information on the structural dynamic characteristics of the Voyager bus would require thorough assessment before a meaningful study of the OEC launch environment could be undertaken. In concept there do not appear to be insurmountable problems in attaching an OEC mounting adapter to a portion of the Voyager structure, realizing that the Voyager bus itself requires that certain of its equipment be mounted externally of the bus structure, i.e., scanner platform, high gain antenna, etc.

#### 4.3 VOYAGER SPACECRAFT CONSTRAINTS

In order to define a baseline OEC configuration, the preferred spacecraft design of each of the three candidate contractors (General Electric, Boeing, and TRW Systems) was studied so as to establish the physical constraints that each design imposed on the OEC. The commonality of the three designs with respect to their solar array, spacecraft bus, and Lander capsule placement established the fact that the OEC could only be attached to the Voyager bus in the peripheral space between the bus and the Saturn V shroud. The longitudinal position of the OEC is restricted between the Lander capsule bus interface and the shade side of the solar array. Figure 4-1 depicts the typical overall Voyager envelope. There may very likely be additional stowage space forward of the Lander-spacecraft interface should the selected Lander design for the 1973 Voyager mission not fully utilize the launch vehicle cylindrical dynamic envelope of 20 feet in diameter. Since the Lander design is presently undergoing design development, the stowage volume for the OEC was assumed to be constrained to the peripheral space around the Voyager bus so as not to violate space in the forward area that may be required by the Lander or its separation mechanism and interface with Voyager.

Figure 4-2 depicts the GE Voyager design and placement of subsystems that could negate stowage of the OEC in those areas. Figures 4-3 and 4-4 show the same information for the TRW Systems and Boeing designs respectively.

The radial space between the Voyager bus and the shroud dynamic envelope is approximately 5 feet, with the exception of the Boeing design which is more restrictive. The Boeing design utilizes solar panels that are stowed parallel to the longitudinal axis of the Voyager during the launch phase, further reducing the radial space in local regions to approximately 3 feet available for stowage of the OEC.

Figure 4-5 summarizes these physical constraints for all three designs with a superimposed plan view. To maintain a common reference on all three designs, the location of the spacecraft transverse axis normally pointing to Canopus was used since the axis nomenclature used by the three contractors varied.

In summary, it appears that at least within the present Voyager spacecraft concepts proposed by the three contractors, the most OEC stowage space is available in the GE design. The TRW design offers slightly less space because the longitudinal dimension of the bus is reduced over the GE design. The most restrictive envelope for stowage of the OEC is offered by the Boeing

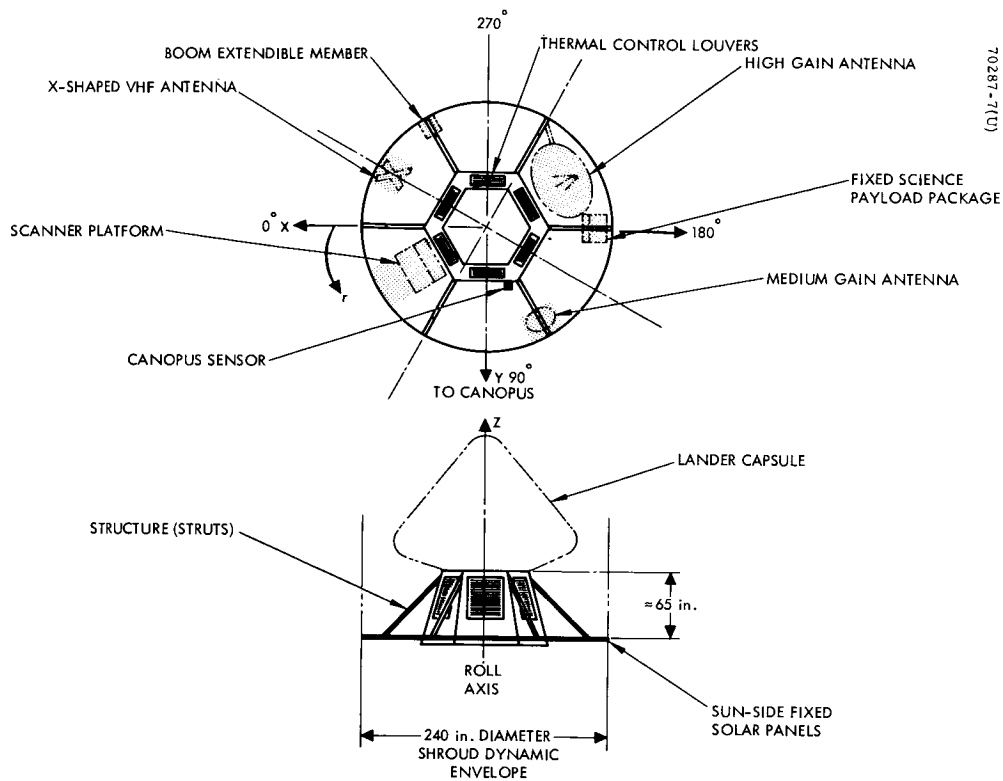


Figure 4-3. TRW Systems Voyager Spacecraft

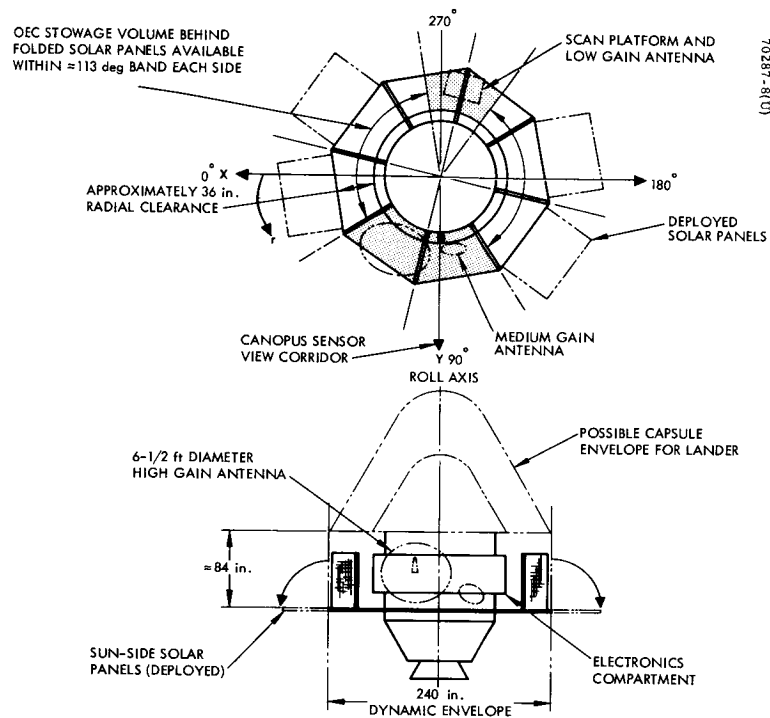


Figure 4-4. Boeing Voyager Spacecraft

design, primarily due to their solar panel design concept and electronics compartment that extends farther outboard from the basic bus structural envelope. Nevertheless, it appears that with any of the present Voyager designs, adequate space is available for stowage of the OEC.

#### 4.4 GYROSCOPIC STABILITY CONSIDERATIONS

The specified requirement that the OEC be a spin-stabilized capsule requires that the mass moment of inertia about the spin axis be greater than the moment of inertia about any transverse axis for stability to be inherent. During the course of this feasibility study, the implications of the inertia ratio criteria ( $I_{\text{roll}}/I_{\text{transverse}} \geq 1.0$ ) was investigated for alternate configuration approaches (integrated or modular design) and various boom mounting schemes to the capsule - axial, radial, and drooped radial booms.

The fact that the size of the cylindrical solar cell array basically dictates the capsule envelope required an assessment of the volume requirements of the internal equipment and experiments. Based on preliminary studies, the total packaging volume required was established nominally at 4 cubic feet. A solar array capable of 37.5 watts appeared to be required to provide the necessary power for the capsule equipment and subsystems. Based on the capsule diameter and effective packaging height, Figure 4-6 relates inertia ratio to capsule aspect ratio (diameter/effective height).

For increased power demands, the effect of increasing the length of the cylindrical solar array has only a negligible net result on the moments of inertia of the capsule, although the added feature of booms to support sensors remotely from the bus does significantly affect the capsule's inertia ratios. Figure 4-6 shows the range of inertia ratios ( $I_{\text{roll}}/I_{\text{pitch}}$ ) for four Hughes spin-stabilized spacecrafts. The approximate increase of 50 percent in the Early Bird satellite's solar panel length does not contribute any substantial change in inertia ratio over its predecessor, the Syncom satellite, yet outwardly a large change in apparent aspect ratio (diameter/actual height). The UCLA satellite inertia ratio is significantly lower than Early Bird or Syncom by virtue of the two long ( $\approx 3$  meters), drooped booms required. The curve on the figure is for a classical model cylinder shaped capsule assuming uniform packaging density.

The effects of both axially mounted booms and radially oriented booms are shown in Figures 4-7 through 4-12. Figure 4-7 presents moments of inertia of the OEC in roll and pitch versus capsule diameter for the single axially mounted boom concept. Figure 4-8 is a plot of axial boom length versus OEC diameter for varying roll to pitch inertia ratios. Figure 4-9 relates cylindrical height for the basic bus and solar arrays of 20 and 30 watt capabilities to OEC diameter. Figure 4-10 indicates the axial boom length variation for various OEC basic diameters for a desirable roll to pitch inertia ratio of 1.10. Figure 4-11 is a plot of roll to pitch inertia ratio versus radial boom length for a fixed volume OEC and also for a fixed weight (varying volume) OEC. The same data is presented in Figure 4-12 for dual radial booms drooped 30 degrees for a fixed height OEC capable of satisfying the modular "stacked" configuration concept.

SPACES OCCUPIED BY  
VOYAGER SUBSYSTEMS

GENERAL ELECTRIC  
SPACECRAFT  
TRW SPACECRAFT  
BOEING SPACECRAFT

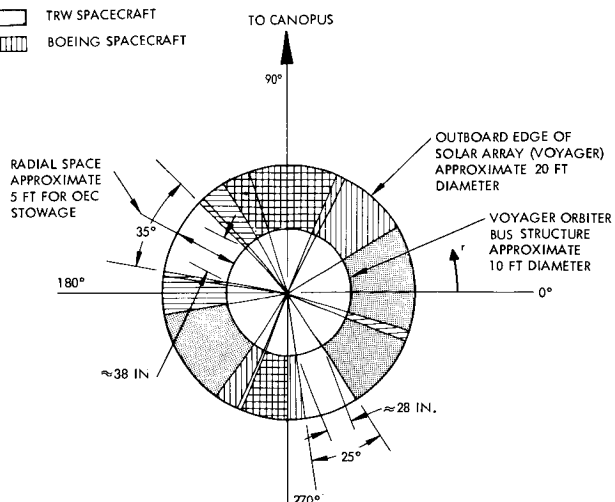


Figure 4-5. Peripheral Space Allocations of Voyager Orbiter Subsystems

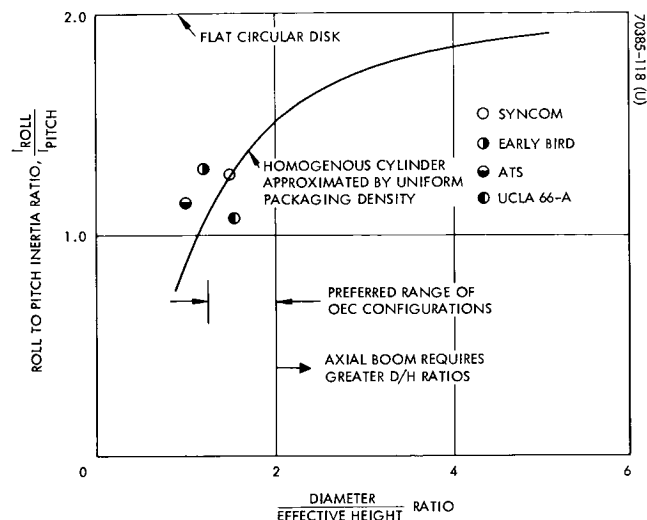


Figure 4-6. Roll to Pitch Inertia Ratio Versus OEC Diameter to Height Ratio

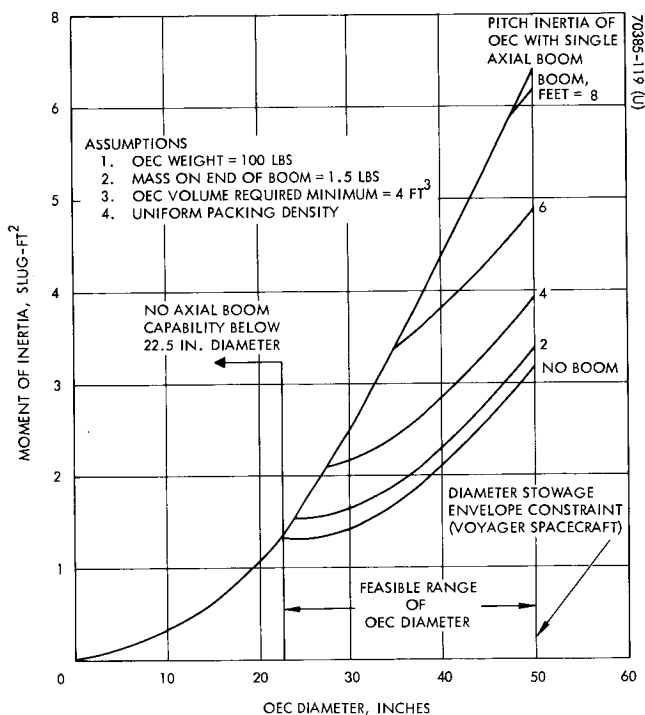


Figure 4-7. Moments of Inertia Versus OEC Diameter for Constant Volume OEC (4 square feet)

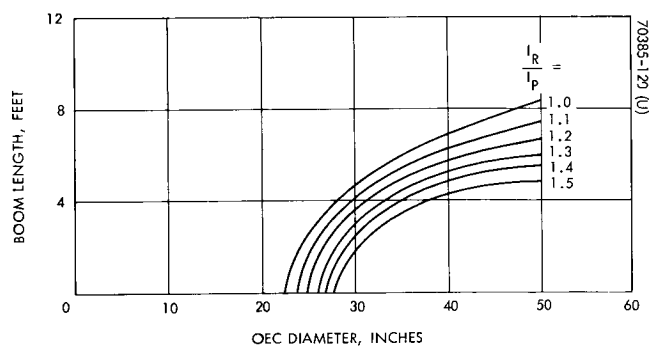


Figure 4-8. Single Axial Boom Length Versus OEC (4 square feet) Diameter for Range of Roll to Pitch Inertia Ratios ( $I_R/I_P$ )

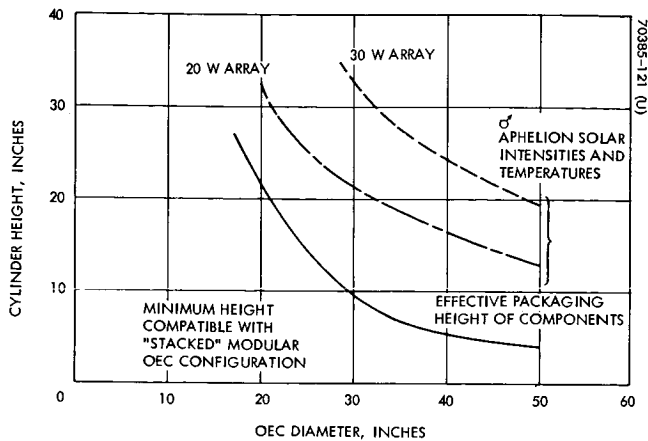
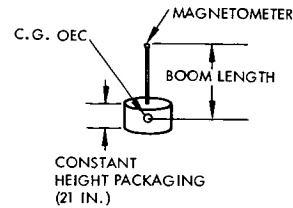


Figure 4-9. Cylindrical Height Versus OEC Diameter



70385-122 (U)

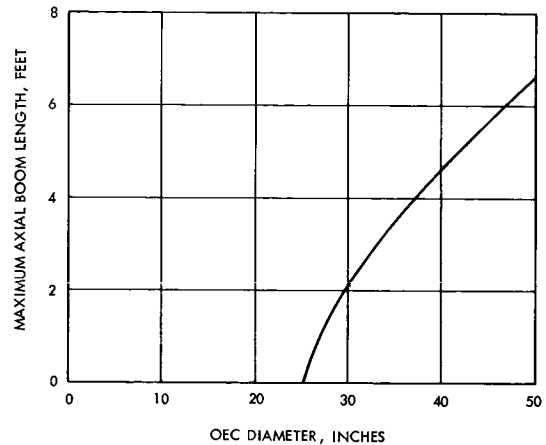
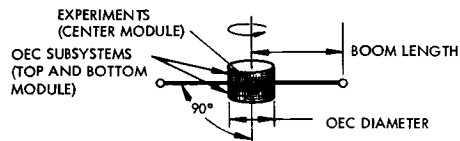


Figure 4-10. Maximum Axial Boom Length Versus OEC Diameter for Constant Height OEC to Retain  $I_R/I_P = 1.10$



70385-123 (U)

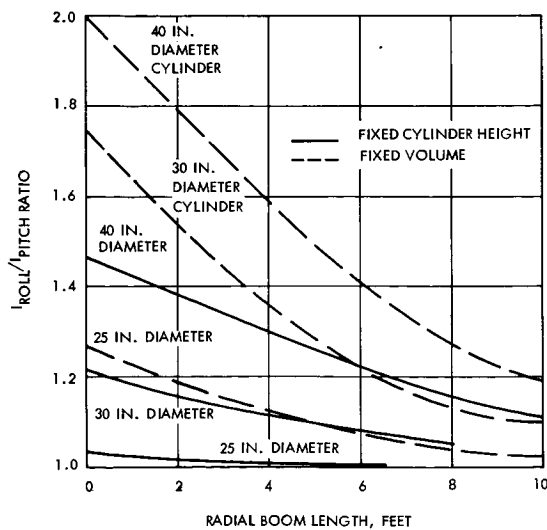
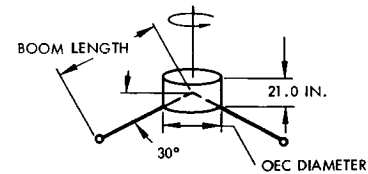


Figure 4-11. Roll to Pitch Inertia Ratio Versus Radial Boom Length for Fixed Volume (4 square feet) and Fixed Cylindrical Height (21 inches) OEC Configurations



70385-124 (U)

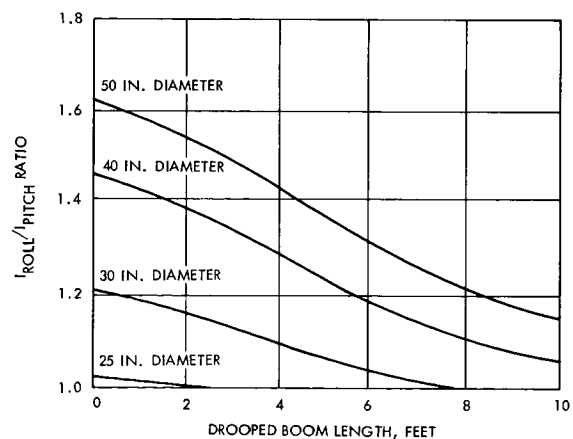


Figure 4-12. Roll to Pitch Inertia Ratio Versus Drooped Radial Boom Length for Fixed Height (21 inches) OEC

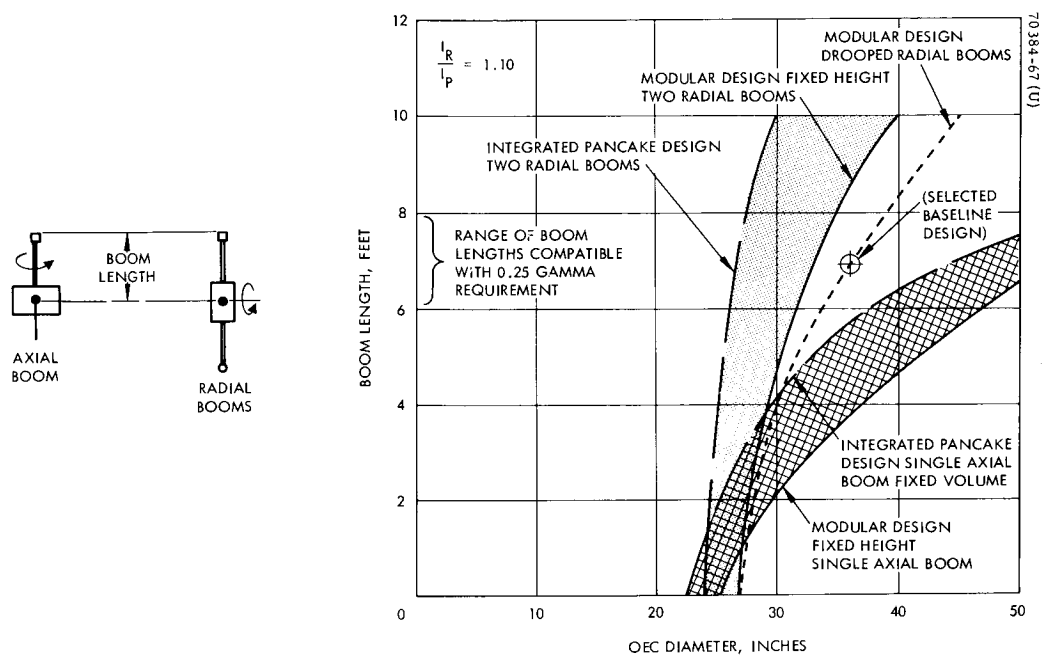


Figure 4-13. Boom Implications on Inertia Ratios

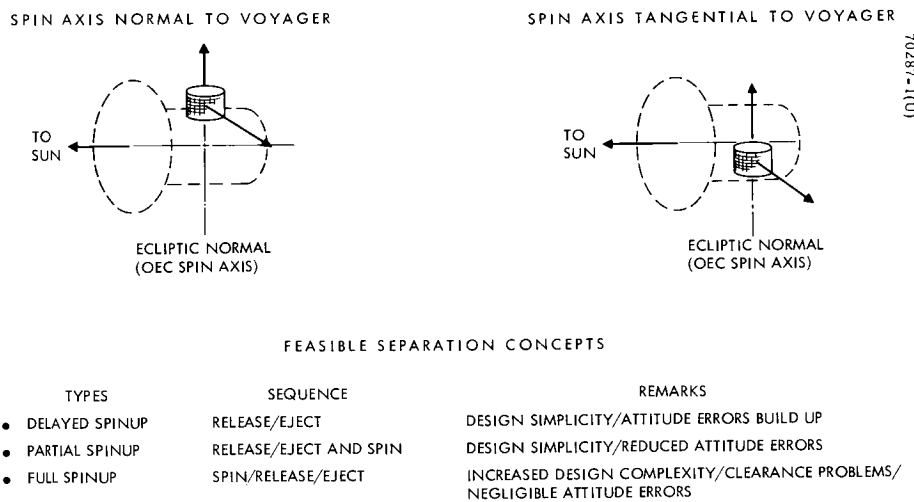


Figure 4-14. Spectrum of Separation Modes



Figure 4-13 in effect summarizes the investigations of boom implications on inertia ratios. From the data presented, it is evident a serious disadvantage of the axial boom concept exists in contrast to radial booms since the capsule diameter would have to greatly increase above approximately 4 feet in diameter should a 7 foot boom be required.

#### 4.5 SEPARATION CONCEPTS

As part of the OEC configuration studies, the manner in which the capsule is attached to the Voyager, and the direction and technique considered for separation had to be studied. In a separate section of this report, the problems involved with separation are treated in detail; the discussion here is aimed at the facets of separation most pertinent to and influencing configuration selection.

Figure 4-14 shows the variety of ways separation of the OEC cylindrical capsule could be achieved. The scheme evolved, considered to be the most simple and straightforward, is briefly described below.

The OEC is attached to an adapter which in turn is mounted to an appropriate surface on the Voyager bus. The separation joint is held in contact by utilizing multiple explosive bolts at the flange. Upon command, prior to actual separation, the pyrotechnic attachments are activated, which releases the loading at the separation flange. Following this, small fixed stroke thrusters (pinpushers) are activated which push the OEC mounting flange off the adapter flange so as to ensure no adhesion at the joint. The amount of clearance need not be great since it is merely the assurance of no adhesion between the surfaces that is desired. A single cable at this time holds the OEC to the adapter. Upon initiating a pyrotechnic guillotine, which severs the cable, a single spring imparts the separation impulse to the capsule. Should it be considered undesirable to have the separation spring loaded throughout the transit phase of the mission, it is quite feasible to design into the system a means of loading (compressing) the spring as a result of the thrusters' function of gapping the separation plane.

The technique described above would be utilized for pure separation without imparting any spin rate or, by a slight modification of the OEC mounting, could be utilized to impart a partial spin (torque-impulse) with the separation impulse (force impulse). In concept, the two schemes are shown in the sketches in Figure 4-15. It is felt that the conceptual design of the OEC should be of a nature that either scheme can be considered. The baseline configuration as discussed in Volume I in fact could accommodate either mounting technique since the structural frame could be attached to an adapter at either the cylinder end (for nonspinning separation) or on the cylinder edge at the bulkheads (for partial spinning separation).

The most straightforward and simple utilization of booms is to provide rigid nonmoving members attached to the capsule structure. An assessment of the stowage volume available on the Voyager spacecraft indicated that fixed booms could be accommodated within the assessed available space. Figure 4-16 shows a sketch of the possible placement of the OEC on the Voyager bus utilizing

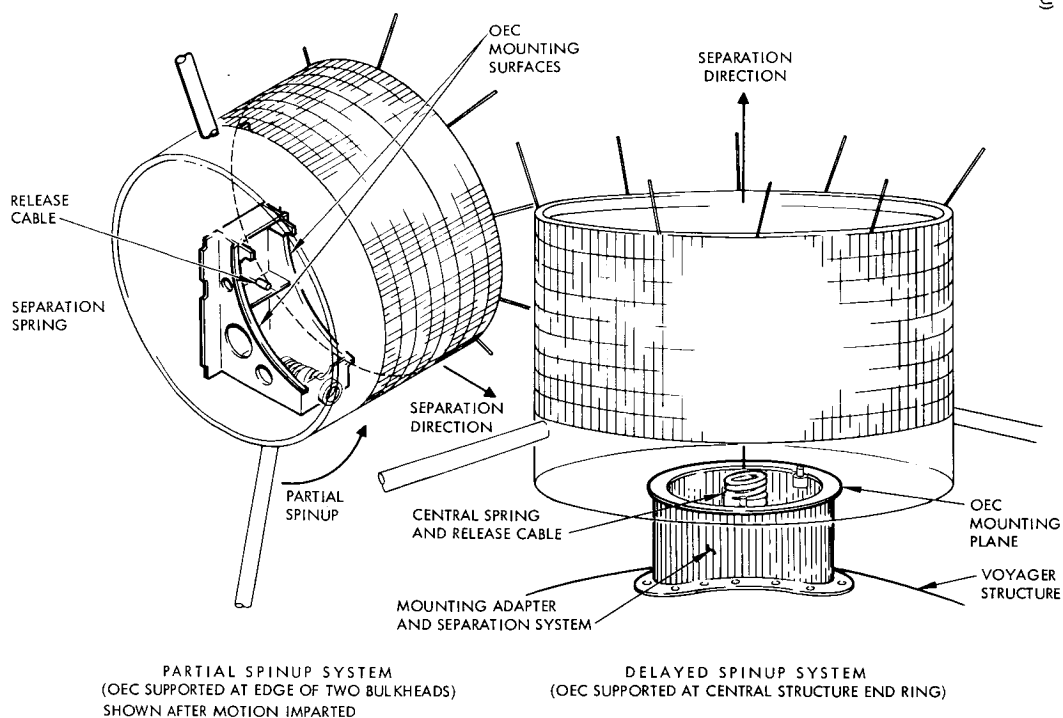
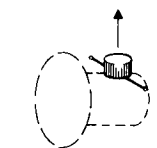
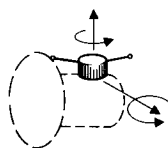


Figure 4-15. Conceptual Arrangement of Mounting Adapter and Separation System

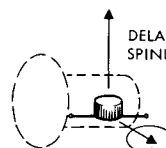
RADIAL BOOMS:



a) DELAYED SPINUP

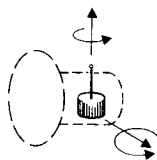


b) PARTIAL SPINUP  
OR FULL SPINUP



c) DEGRADED  
PARTIAL  
SPINUP

AXIAL BOOM:



d) PARTIAL SPINUP  
OR FULL SPINUP

NOTE:  
METHODS DEPICTED FOR BOOM LENGTHS  
OF APPROXIMATELY 6 feet

Figure 4-16. Candidate Separation Modes for Fixed Length Radial and Axial Boom Configurations

both radial and axial booms. Of the candidate separation modes indicated, the recommended technique considering radial booms is for the nonspinning (delayed spinup) type of separation. The selection of fixed radial booms as the type considered for the baseline OEC configuration definitely limits the orientation of the capsule on Voyager to a manner such that the booms do not extend beyond the Lander-bus interface.

#### 4.6 SOLAR POWER CONSIDERATIONS

As mentioned earlier in this section, the requirement of providing a solar array around the external surface of the OEC essentially established the capsule's external profile and space envelope. The fact that the solar array surface area encloses a volume sufficiently larger than that required by the OEC equipment offers alternative approaches to the packaging of experiments and subsystems. Figure 4-17 depicts the OEC configuration alternatives which were explored leading to the selection of a baseline configuration.

Of importance in consideration of boom placement on the capsule is potential shadowing of the solar array by radial booms. The modular design, in which the experiment module is placed below the subsystem module, readily ensures that booms mounted off the experiment compartment will not shadow the array.

Due to the relatively light weight of the solar array, the extension of the cylindrical array has negligible effect on the moments of inertia of the basic capsule. Hence any increased power requirements could easily be met with negligible changes to the basic configuration and arrangement.

#### 4.7 BOOM CONSIDERATIONS

A prime factor in the selection of a baseline OEC configuration is the necessity of providing the capsule with booms to position experiment sensing elements such as a magnetometer sensor and electric field meter antennas away from the magnetic field generated by the OEC electronics. The incorporation of booms on satellites is a state-of-the-art technique utilized on numerous artificial satellites for various reasons — i. e., sensor mounting, gravity gradient stabilization techniques, and various antenna designs.

Ideally, constraints permitting, the simple fixed boom concept provides maximum assurance of operation because no mechanisms or moving parts are required in the system. Other techniques recognized as feasible are: hinge or multiple-hinged booms such as those typically provided by Comstock and Wescott, Inc., Cambridge, Massachusetts; storable tubular extendible member (STEM) devices built by DeHavilland Aircraft of Canada Limited; and telescopic extendible members.

The fixed double boom weighs approximately 3.0 pounds, considering sensor positions in the order of 2.0 meters from the OEC center. Hinged booms of equivalent length would weigh about 2.5 to 3.5 pounds for each assembly

- SOLAR ARRAY REQUIRED SURFACE AREA DEFINES BASIC ENVELOPE
- EXPERIMENTS AND SUBSYSTEMS REQUIRE PACKAGING VOLUME OF 4 cubic feet (MINIMUM)
- POSSIBLE PACKAGING ALTERNATIVES

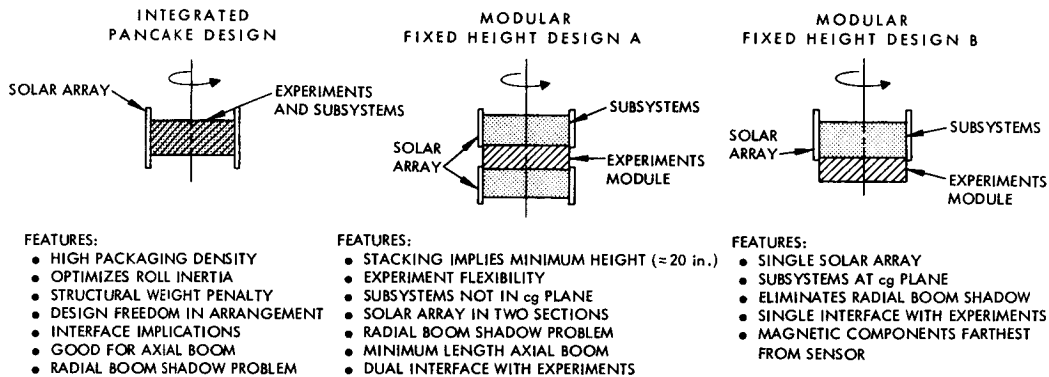
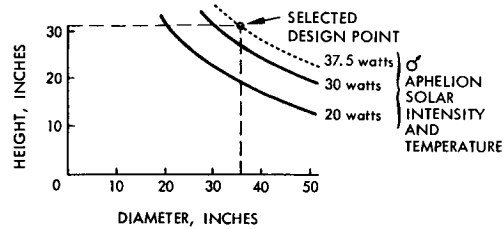
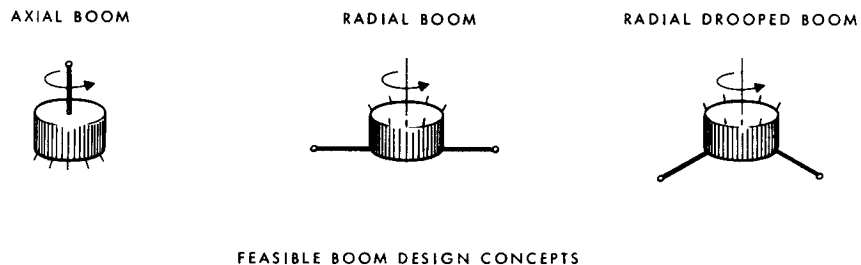


Figure 4-17. OEC Configuration Alternatives



TYPE	WEIGHT (POUNDS)	SENSOR POSITION ACCURACY	DESIGN COMPLEXITY
FIXED	3.0	EXCELLENT ( $< 1$ deg)	SIMPLE
HINGED	6.0	GOOD	REQUIRES RELEASE ACTUATION AND LOCKING
S.T.E.M. (DEPLOYABLE)	9.0	FAIR (TORSIONALLY POOR 3 deg MINIMUM)	SPACE QUALIFIED BUT MORE COMPLEX
TELESCOPIC	6.0	GOOD	SIMILAR TO HINGED TYPE

Figure 4-18. OEC Boom Configuration Alternatives

considering hinge and locking mechanisms. The DeHavilland STEM device poses the largest system weight, in the order of 7.5 to 9.0 pounds for a dual extending boom package. A magnetometer boom for a 20 foot extension built by DeHavilland weighed 9.4 pounds and utilized a beryllium copper element 1.25 inches in formed diameter. The retracted envelope was 6 by 7 by 18 inches. Position accuracy of the deployed sensor axis poses a serious problem in the STEM (storable tubular extendible member) principle since the element's torsional qualities cannot be controlled to under 3 degrees for the lengths considered for the OEC application. Some improvement in the torsional uncertainty is being sought by the manufacturer by a technique of multiple concentric elements.

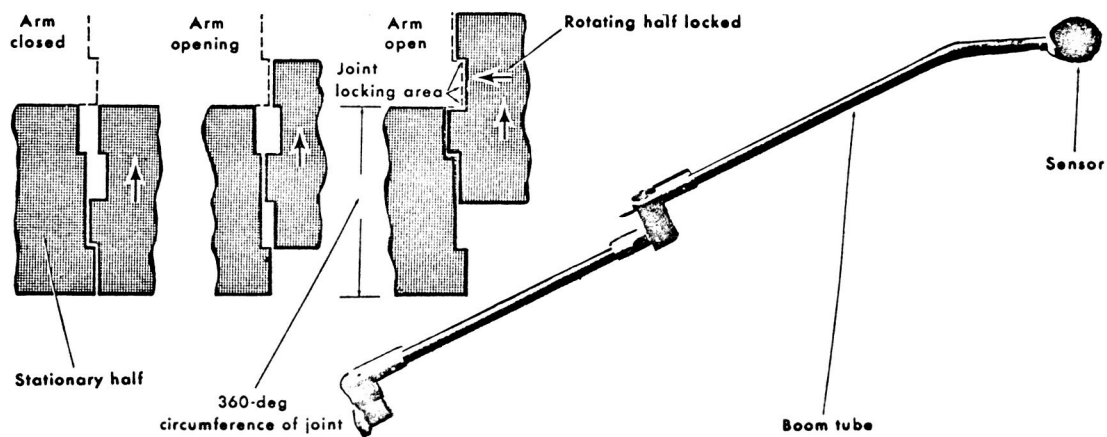
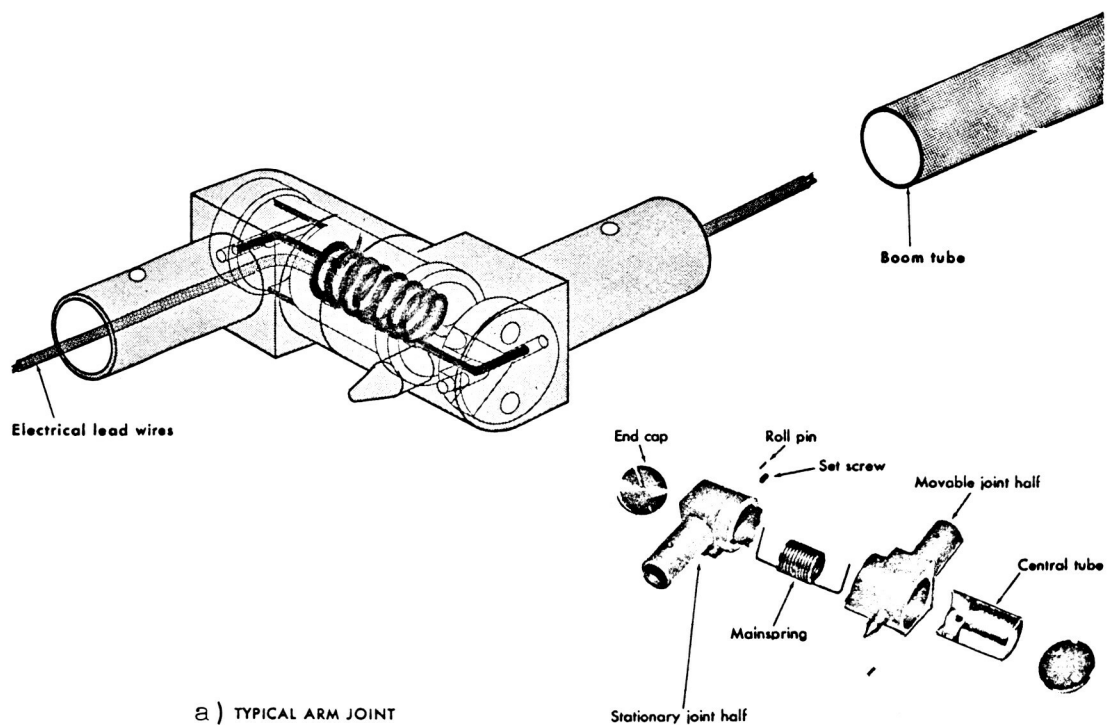
Figure 4-18 illustrates the boom configuration alternatives considered as candidate design concepts. Having investigated the ramifications involved for each configuration, the suggested approach for the OEC mission is to utilize radial drooped booms, in light of the serious lack of growth capability in length for axial booms. The advantage of the drooped booms over purely radial booms is that shadowing of the solar array is virtually eliminated.

The possibility certainly exists that during further development of the Voyager spacecraft itself, envelope allowances for the OEC may become more restrictive, requiring the use of stowed booms in transit to be deployed once the OEC is separated from Voyager. Should this constraint become a reality, the radial boom could be designed as a single hinged member, folded adjacent to the capsule surface and parallel to the spin axis while in transit.

A manufacturer specializing in space application instrument booms such as Comstock and Wescott could provide boom assemblies comparable to the units described above. A brief description of their design follows; Figure 4-19 shows a typical boom hinge of Comstock and Wescott design:

A coil spring of music wire acts in torsion and extension to operate a self-opening and locking joint. Used in a series of self-extending boom systems for ionospheric sensors from spacecraft or sounding rockets, the design permits wires from remotely mounted probes to pass through the joints without exposure or interference.

The joint consists basically of stationary and movable body halves connected by a central tube fixed to the stationary body portion. An end cap in each body half is retained by the close-wound spring, which exerts a twisting and pulling force on the two halves. Rotating the caps during assembly provides initial spring windup. Roll pins prevent the end caps from rotating in the body halves and thus transmit the torque to open the joint. When the caps have rotated fully, the spring operates in tension to move them axially toward each other. This causes engagement of locking lugs that prevent rebound or oscillation. An external pin in the movable body half seats in a hole in a stationary mounting block and holds the boom system in its folded position. In a multisection probe, the pins assure sequential unfolding of each section.



b) arm and joints in probe's extended position.

Figure 4-19. Comstock and Wescott Boom Hinge Design

The two body halves and end caps are machined from aluminum to reduce weight. The central tube is made of stainless steel for added strength, and the main spring is close-wound music wire. Thin-walled aluminum tubing is used for the boom sections. The body halves are hard-coated to avoid galling at points of sliding contact, and the central tube is chrome-plated for a satisfactory low-friction bearing surface.

For comparison, Figure 4-20 shows the STEM type of boom mechanization which utilizes the principle of a prestressed element that takes on a tubular shape once unrolled from a storage drum.

#### 4.8 CONFIGURATION DEVELOPMENT

The iterations leading to the recommended configuration proposed for the OEC are best envisioned by briefly covering some of the initial configuration concepts evolved in the study. Four configurations (A through D) are described here which were later rejected on the basis that the recommended configuration offered the greatest flexibility and best satisfied the OEC mission objectives.

##### 4.8.1 Configuration A

Configuration A (Figure 4-21) is basically a modular type design which centrally allocates the midportion of the capsule for the housing of scientific equipment. This central section would permit flexibility in the selection of alternate scientific equipment and provide the capability for full circumferential position selection of instrument sensing equipment.

The capsule is basically a cylinder approximately 36 inches in diameter by 38.5 inches in length equipped with two diametrically opposed booms that support the magnetometer and electric field sensing elements. The booms are indicated as part of the central science instrumentation module structure and extend radially from the OEC spin axis. The placement of the booms and sensor on the geometric center of the capsule also reduces their inertia contribution to the transverse axis of maximum inertia, helping enhance the roll to pitch inertia ratio of the capsule. The booms are rigid and fixed to the capsule fully extended, eliminating the added complexity of articulated or deployable boom mechanization which would increase the overall complexity of the system. With fixed-extended booms, more consideration of launch and boost phase dynamic environments is necessary than with stowed boom configurations. Dynamic loads and vibrations could satisfactorily be controlled by providing additional support lines from the boom to the capsule and/or snubbers mounted on the Voyager bus.

The maximum length of the booms from the capsule centerline is about 2 meters, limited by the launch vehicle shroud dynamic envelope. The slight increase in boom semispan that could be realized ( $\approx 1$  foot) by locating the booms on the OEC closer to the base or separation plane does not appear attractive for an OEC without attitude correction capability since the separation distance required prior to OEC spinup is also increased. Clearance requirements between the Voyager and the boom extremities will dictate "safe"

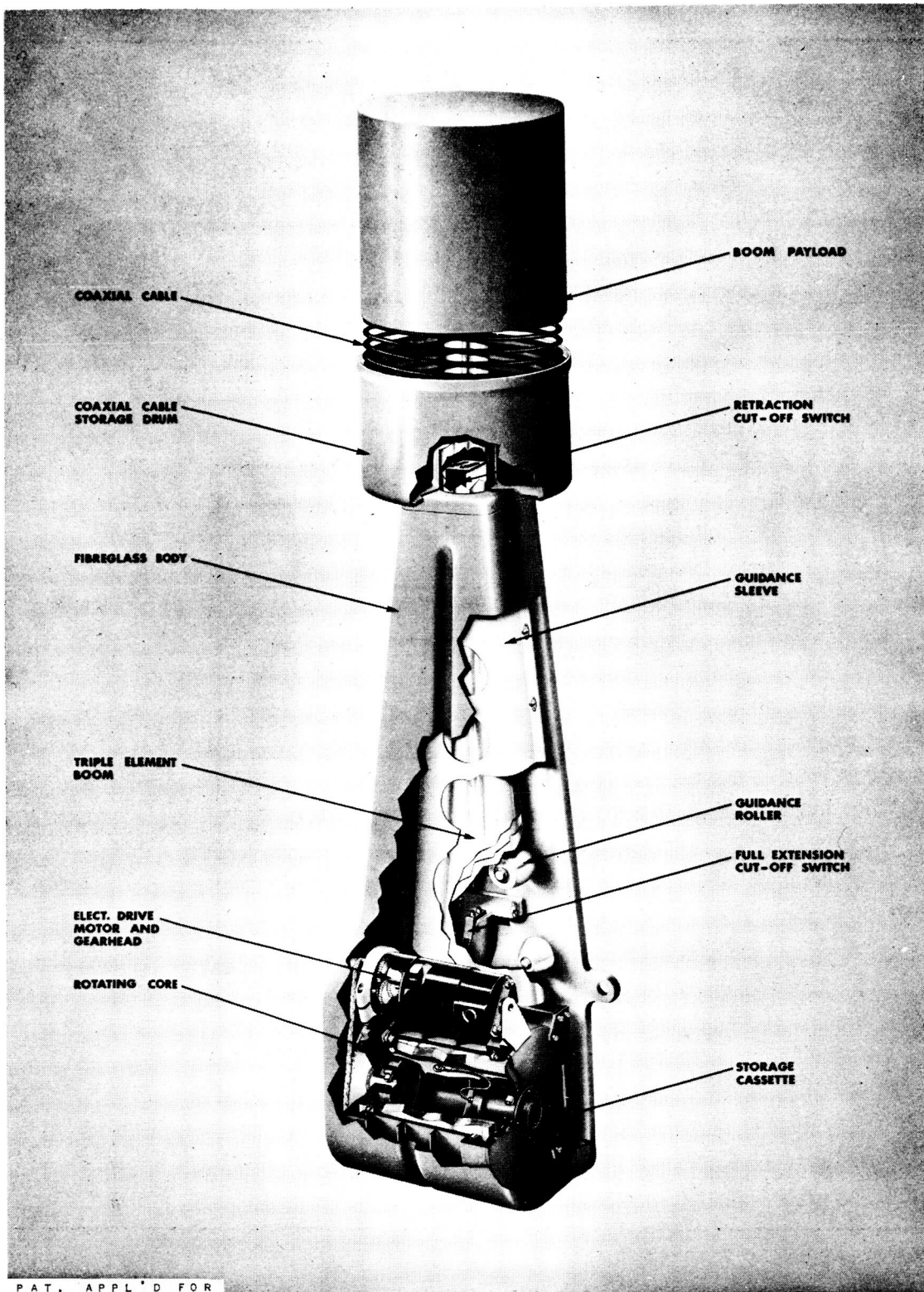


Figure 4-20. DeHavilland STEM — Typical Design



separation distances prior to spinup. Although this clearance problem is not present if spinup is effected prior to boom deployment, the added complexity of stowed deployable booms does not show any other significant advantages.

An attractive feature of the modular configuration approach is flexibility in assembly, testing, checkout, and replacements. By virtue of the stacked assembly, each module can be handled separately. The modular approach also provides for minimum experiment-subsystem interfacing, which would facilitate accommodation of alternate instruments for future planetary missions. Future interchanging of experiments also will have a minimum effect on mass properties of the OEC. Figure 4-22 shows a conceptual arrangement for the modular OEC configuration. Figure 4-23 shows a structural arrangement for this design, and Figure 4-24 describes a typical experiment module layout for this configuration.

#### 4. 8. 2 Configuration B

Configuration B (Figure 4-25) differs from the modular approach of Configuration A primarily in that the scientific equipment is integrated with the capsule subsystem components. This design concept imposes packaging constraints on both the science equipment and the capsule subsystems since the internal arrangement of components is interdependent. Experiment viewing requirements and acceptance angle variation of sensors also affect the solar array design.

The solar array, extending the full length of the cylindrical shaped capsule, limits attachment of the booms, whether fixed or deployable, to the capsule structure at either end of the cylinder to avoid penalties to the power system from solar cell shadowing.

As is true for Configuration A, the booms could be designed as simple hinged members supported at the capsule structure. Increasing the length of the booms and stowing them at an angle of approximately 45 degrees with respect to the capsule longitudinal axis would permit individual boom lengths up to 3.5 meters (tip of boom to capsule centerline). In order to minimize the failure probability of the boom hinge and tiedown mechanization, the boom support and release mechanism might be activated to orient the booms perpendicular to the capsule spin axis upon termination of the launch vehicle boost phase, thereby eliminating the 12-month transit storage life requirement of such a system.

#### 4. 8. 3 Configuration C

Configuration C (Figure 4-26) utilizes a central antenna mast to extend the magnetometer and electric field sensors from the capsule body along the spin axis. To compensate for the transverse inertia growth due to the antenna mast and tip mounted sensors, the internal arrangement of experiment electronics and subsystem components requires more extreme peripheral mounting within the capsule than the two previous arrangements. A diameter constraint of 48 inches for the OEC seems reasonable, based on stowage envelope capability of the three candidate Voyager spacecraft designs. Assuming 48 inches as a maximum diameter and power requirements for the cylindrical solar cell array area

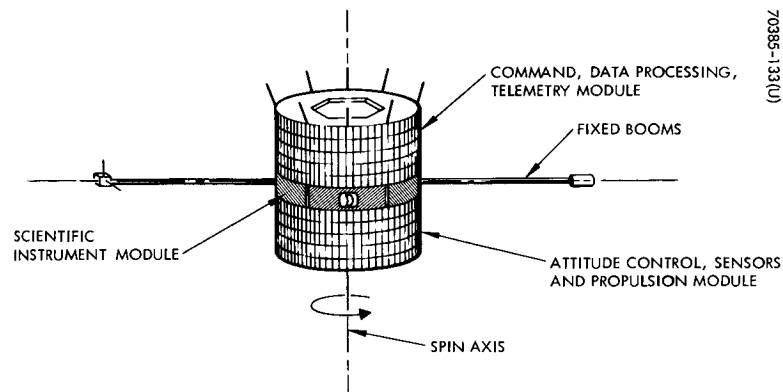


Figure 4-21. Configuration A

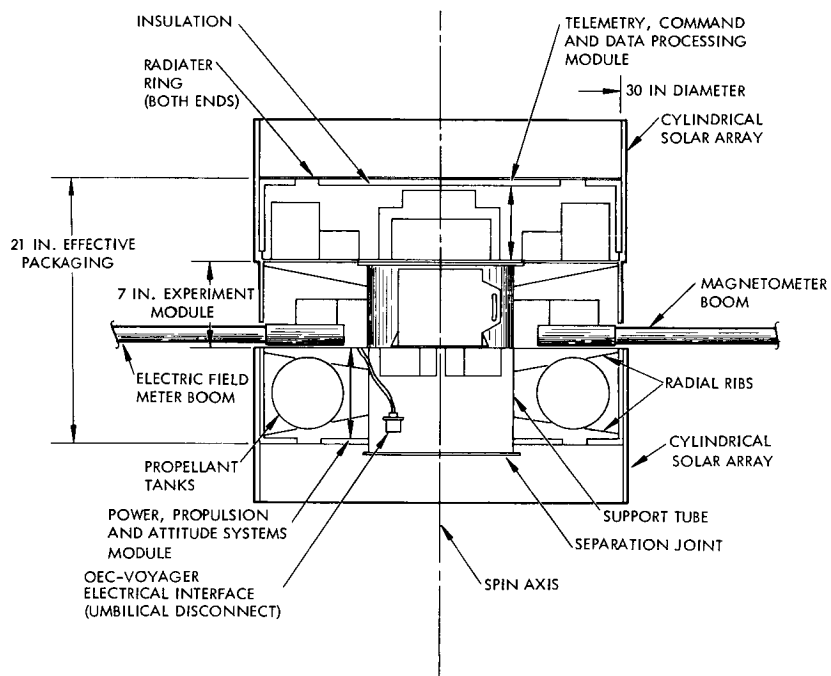


Figure 4-22. OEC Modular Conceptual Configuration

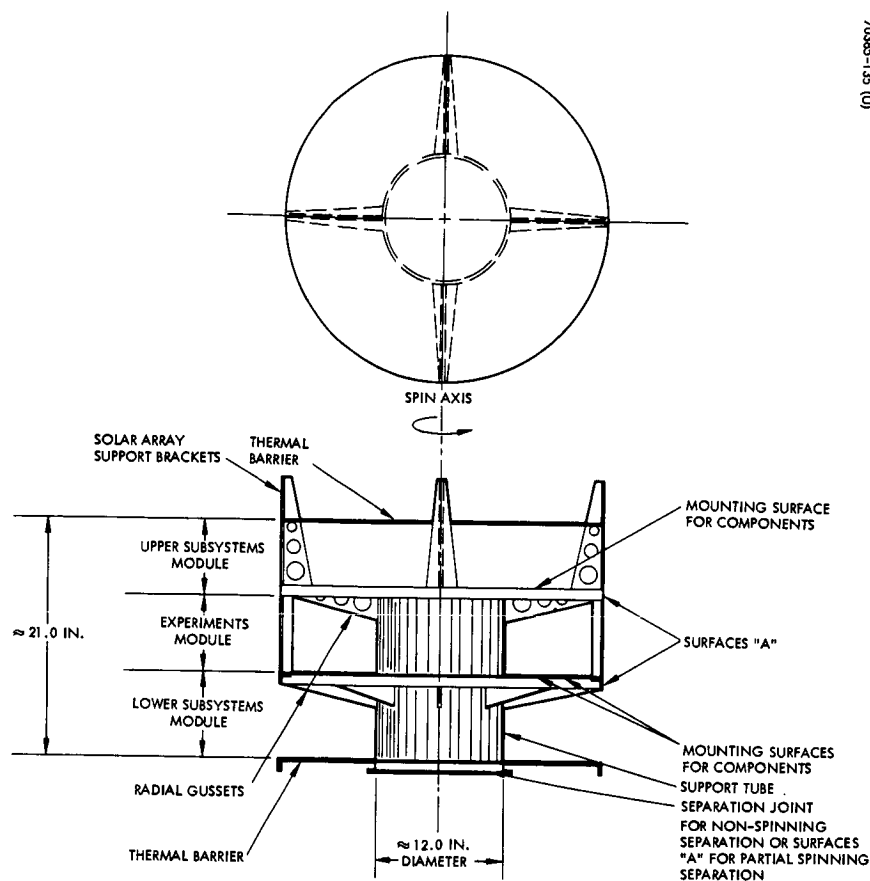


Figure 4-23. Conceptual OEC Structural Arrangement for Stacked Modular Configuration

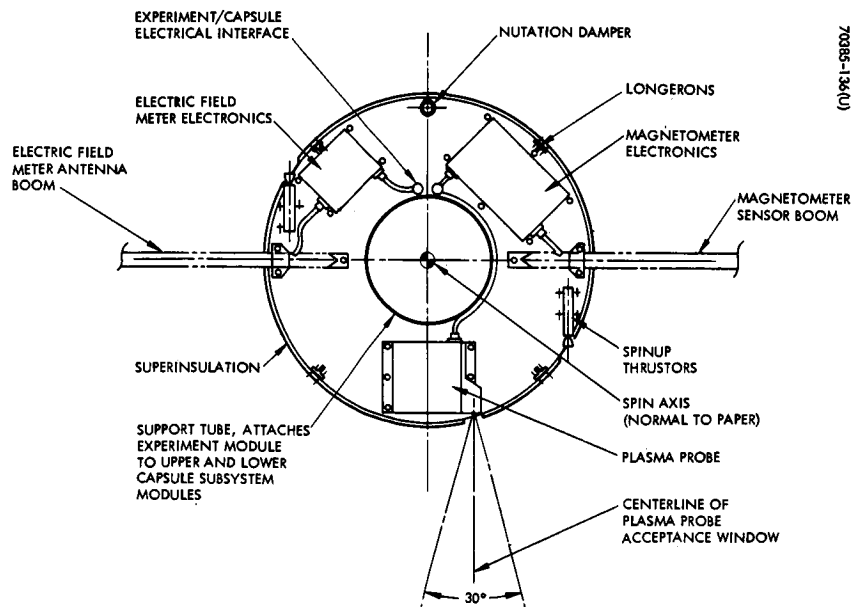


Figure 4-24. Typical Experiment Module Layout

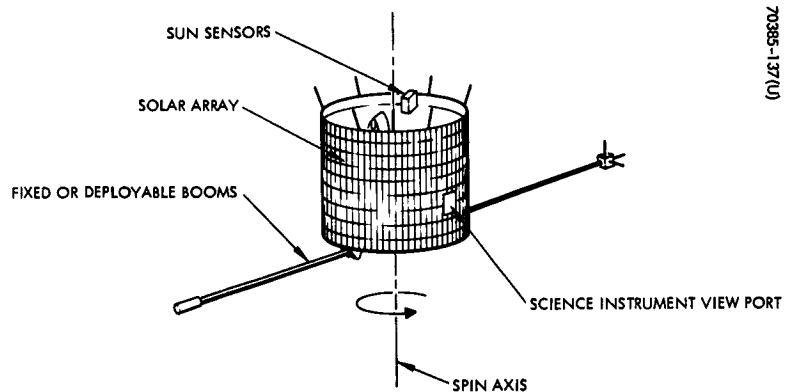


Figure 4-25. Configuration B

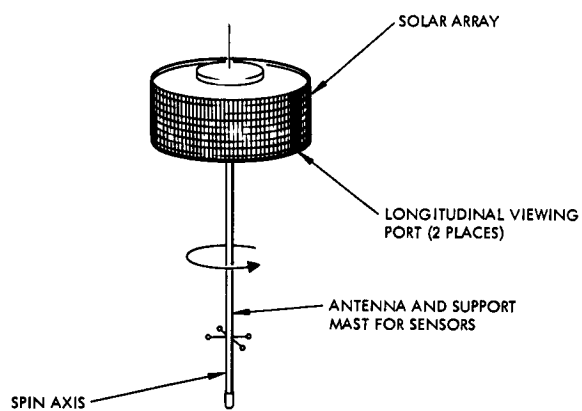


Figure 4-26. Configuration C

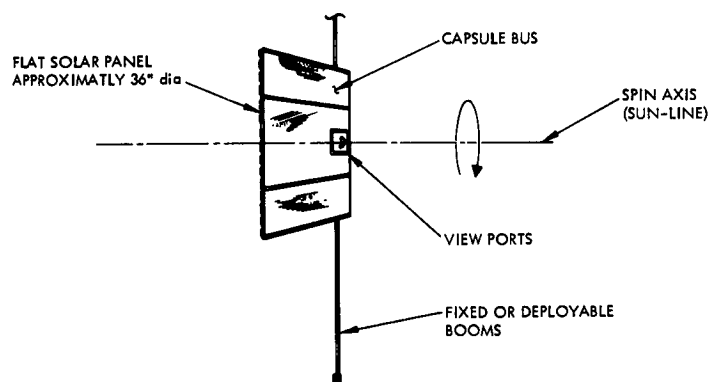


Figure 4-27. Configuration D

comparable to the two previous configurations, the cylindrical array height would be approximately 24 inches.

The penalties of Configuration C include the difficulty of maintaining proper thermal control due to the ineffective coupling because of the inefficient packaging considerations required and structural weight penalties that would result in providing support for the components at greater distances from the desired central support region. With the mast serving as the supporting member for the sensors, it is necessary to size the member so that any possible initial eccentricity of the mast about the spin axis will not induce centrifugal loads on the shaft greater than its bending (deflection) capability. For zero-gravity environment, the critical speed - natural frequency consideration does not establish the stiffness criteria for the mast member; consequently the member's stiffness is selected to accommodate possible induced centrifugal loads and launch/boost environments.

The modular approach, as utilized in Configuration A, if applied to Configuration C would yield a highly inefficient structural design due to structural redundancy of each module with inherent stability problems. An alternate modular approach could consider separate pie-shaped bays reserved for experiments and OEC subsystem components. Radial viewing requirements of experiments could be accommodated by a longitudinal viewing slot through the solar array.

Integration of the Configuration C type OEC with the Voyager spacecraft does result in increased mechanical interface complexity, merely due to the larger capsule profile. Clearance requirements of the Voyager bus subsystems may complicate the mechanical interface considerations. The present Boeing design concept imposes OEC stowage envelope constraints not present in the GE or TRW design because the solar array is initially stowed at four radial positions at the base folded parallel to the Voyager bus. Since the solar panels are stowed parallel to the launch vehicle axis, it is possible to position the capsule in the space between the Voyager bus and folded panels; the penalty would be the increased distance the OEC must travel prior to initiation of spinup to assure ample clearance of the outboard edge of the deployed solar array.

Since the propellant required to spin up the capsule is less than 1 pound (assuming  $\text{GN}_2$  or  $\text{CF}_4$ ), the increase in the torquing radius provided by this configuration results in only minor propellant weight savings, at the expense of an increase in the systems fixed weights. Similarly, placing the spinup thrusters on radial booms does not warrant the added complexity of flexible lines and associated line weights incurred.

#### 4.8.4 Configuration D

No serious consideration was given to the configuration depicted in Figure 4-27 since the required attitude is in violation of that stipulated by the Ames OEC specifications. The sun-line oriented spin axis does imply attitude control requirements for the OEC, although only a minor number of corrections (two or three) would be required throughout the 6 months life in orbit, accepting

slight power degradation due to off-normal incidence. The desired field of view best satisfying the plasma probe experiment would be only partially attainable with this configuration inasmuch as the fields of interest lie in the ecliptic plane. No serious thermal control problems are introduced by this configuration that could not be controlled by a passive system. One feature of the fixed-flat solar array concept is a weight reduction by over a factor of three for the solar panels over the other configurations discussed. No telecommunications advantages are gained by this configuration.

## 5.0 RECOMMENDED CONFIGURATION

A spectrum of configurations has been discussed which lead to the design approach presented here as the most suitable OEC arrangement in light of the numerous interrelated areas that needed to be satisfied. The recommended OEC configuration is shown in Figures 5-1 and 5-2. A detailed discussion of the general arrangement is presented in Volume I of this final report.

Table 5-1 represents a weight breakdown of the baseline system by major subsystems and components. In block form, Figure 5-3 shows the same data, indicating the flexibility of the OEC mission and the associated weight increment increase for additional capability imposed on the basic co-orbital system.

Some of the major advantages provided by the configuration selected are:

- The modular arrangement approach lends flexibility to the experiments since they are isolated from the major capsule subsystems.
- Radial booms mounted from the experiment module virtually eliminate any potential shadow problems on the solar cells.
- Separation schemes are flexible without significant modification to the capsule design.
- The solar array may be a single unit design and need not be fabricated by sub-units.
- The components of high magnetic properties can be located remotely from the magnetometer sensor.
- The propulsion systems tankage can readily be mounted in the plane of the capsule's cg.
- Exhaust impingement by the propulsion system jets is avoided since they are directed and located away from the experiments.
- Minimum interface between the experiments and subsystems is required.

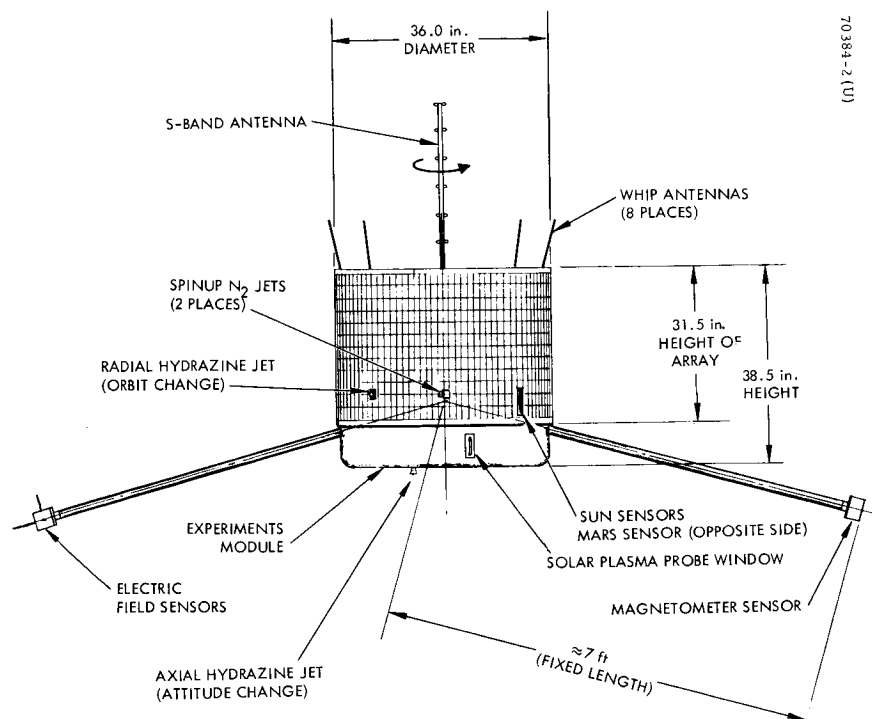


Figure 5-1. OEC Recommended Configuration External Profile



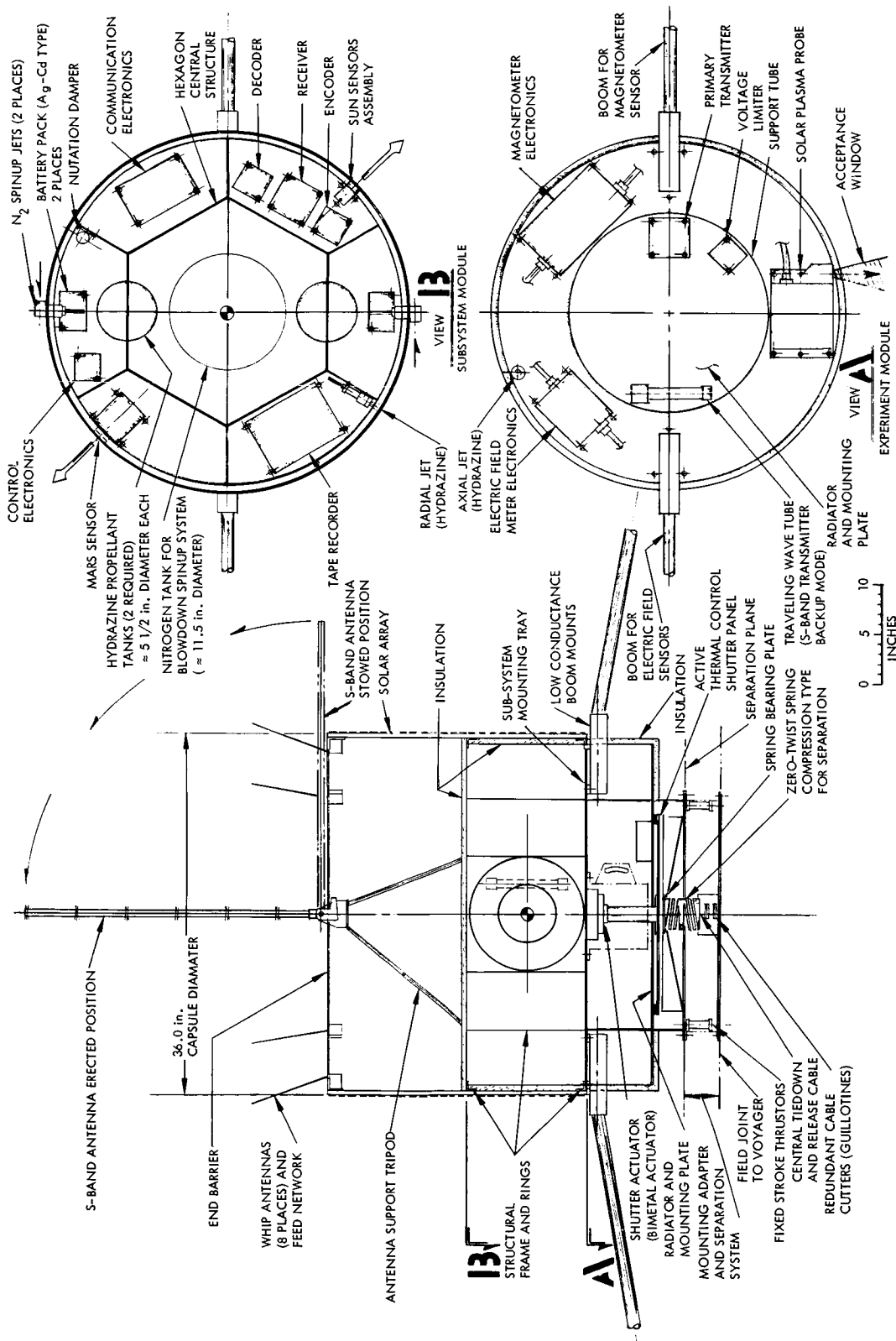


Figure 5-2. OEC Recommended Configuration General Arrangement

TABLE 5-1. OEC WEIGHT BREAKDOWN

		<u>Weight, pounds</u>	
CO-ORBITAL MISSION SYSTEM (NO ATTITUDE CORRECTION CAPABILITY)			
• Scientific payload		15.0	
• Communication system		9.7	
• Power system		15.1	
• Attitude determination and N <sub>2</sub> spinup		8.4	
• Electrical harnesses		2.5	
• Structure and fixed radial booms		15.0	
• Thermal control		4.5	
• Support adapter and separation system		5.0	
	Total	<u>75.2</u>	
FOR ATTITUDE CORRECTION CAPABILITY			
		<u>Additional Weight</u>	
• Hydrazine system (preferred)		3.5	
or			
• Nitrogen system		<u>4.2</u>	
FOR ORBIT CHANGE AND INCREASED COMMUNICATION CAPABILITY			
• Hydrazine system		8.0	
	(includes 3.5 pounds above)		
• Tape recorder		7.0	
• Logic electronics, harness, and bracketry		2.0	
• Power system		18.1	
Additional array	4.6		
Batteries	13.5		
		<u>35.1</u>	
FOR S-BAND BACKUP COMMUNICATION MODE			
• Components, harness, antenna		12.5	
SUMMARY			
<u>Co-orbital Without Attitude Correction</u>	<u>Co-orbital With Attitude Correction</u>	<u>Orbit Change Without S-Band</u>	<u>Orbit Change With S-Band</u>
75.2 pounds	78.7 pounds	110.3 pounds	122.8 pounds

- Should stowed booms be required resulting from Voyager design development restricting the OEC stowage envelope, the optimum length can still be achieved by providing a single hinge and folding the booms along each side of the capsule.
- A straightforward spring energy separation scheme is feasible.
- The choice of radial booms allows additional growth capability should additional separation distance of the magnetometer sensor be necessary, stowage envelope permitting.

In summary, the configuration recommended provides the greatest flexibility and, as studies have indicated, offers the most feasible approach for the design development phase of an OEC.

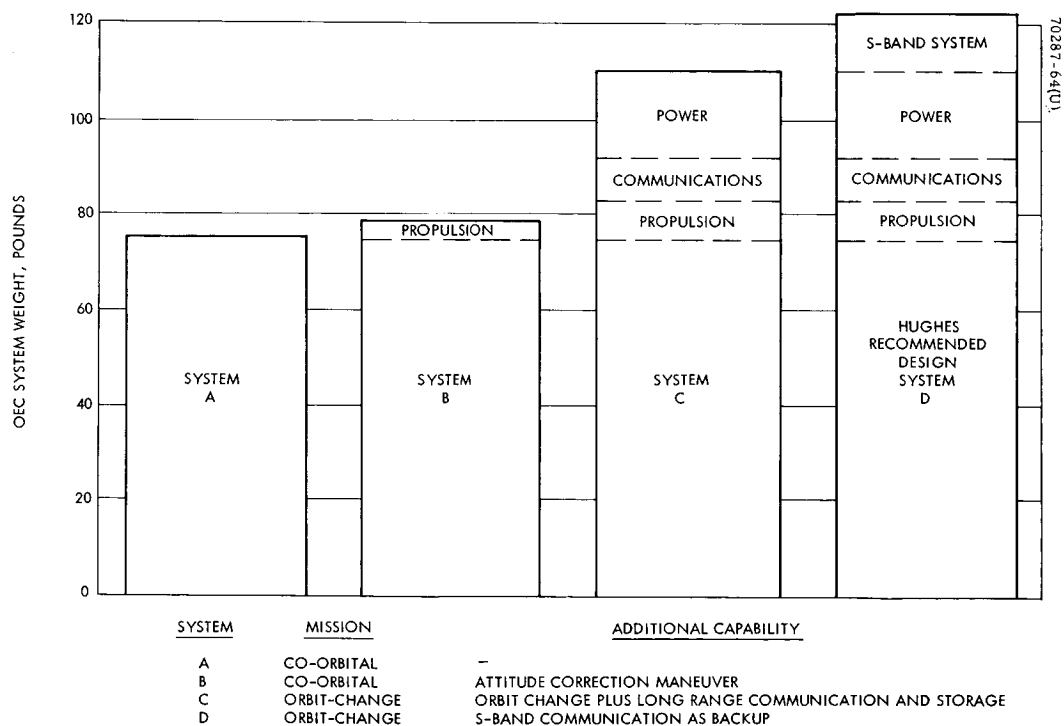


Figure 5-3. OEC System Weight Comparison

## 6.0 SUBSYSTEMS STUDIES AND TRADEOFFS

### 6.1 POWER SUBSYSTEM

#### 6.1.1 General

Three OEC power systems configurations capable of being designed to suit the OEC mission requirements are indicated in the following sections. Discussed herein are the power system configurations considered, the solar panel design approach, battery, and battery charge-discharge control electronics suitable for the OEC system. The power subsystem studies were conducted to encompass the spectrum of power requirements discussed and tabulated here. The data presented will enable formulation of a specific power subsystem suitable for, and pending the establishment of, a specific and definitive OEC mission profile.

#### 6.1.2 Design Concepts

During this feasibility study three different design concepts capable of meeting the OEC mission requirements were explored. They are presented in block diagram form in Figures 6-1, 6-2, and 6-3. A brief description of the three concepts follows.

##### 6.1.2.1 Configuration A

Configuration A consists of a single cylindrical solar panel, two batteries, and associated electronics for battery charging and discharging.

The solar panel supplies power to the spacecraft electronics system during the sunlight portion of the orbit. At the beginning of solar eclipse periods, the battery control circuit senses the bus voltage drop and connects the batteries to the bus. As the spacecraft reenters sunlight, the solar panel forces the bus voltage to a higher potential, causing the battery control circuit to switch from the battery discharge to the battery charge condition. This configuration was selected as the baseline system.

##### 6.1.2.2 Configuration B

Configuration B is identical in operation to configuration A. In configuration B, however, the solar panel is divided into two parts, leaving a clear mid-section between the two portions of the panel for placement of experiments. This configuration becomes considerably less desirable than configuration A where objects placed in the experiment section are allowed to protrude beyond the surface of the solar array and thereby cast shadows on the array and reduce its power output. There are several methods available to minimize the solar panel losses due to shadowing, or to provide battery power to make up for the losses during shadowing, but all of the methods increase the weight and complexity of the system and cause a corresponding reduction in reliability as compared with configuration A.

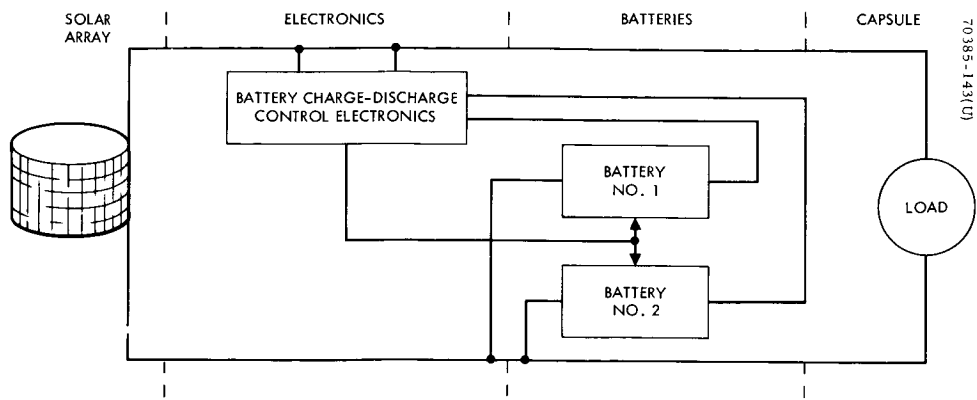


Figure 6-1. Concept "A"

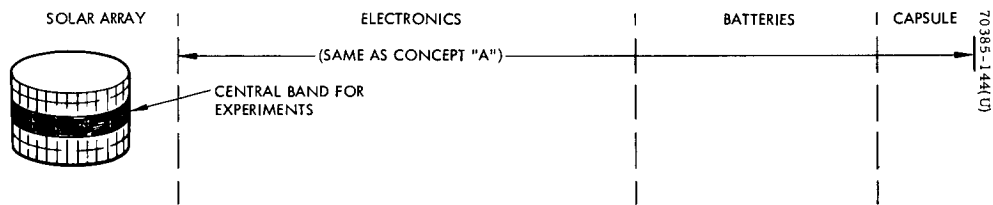


Figure 6-2. Concept "B"

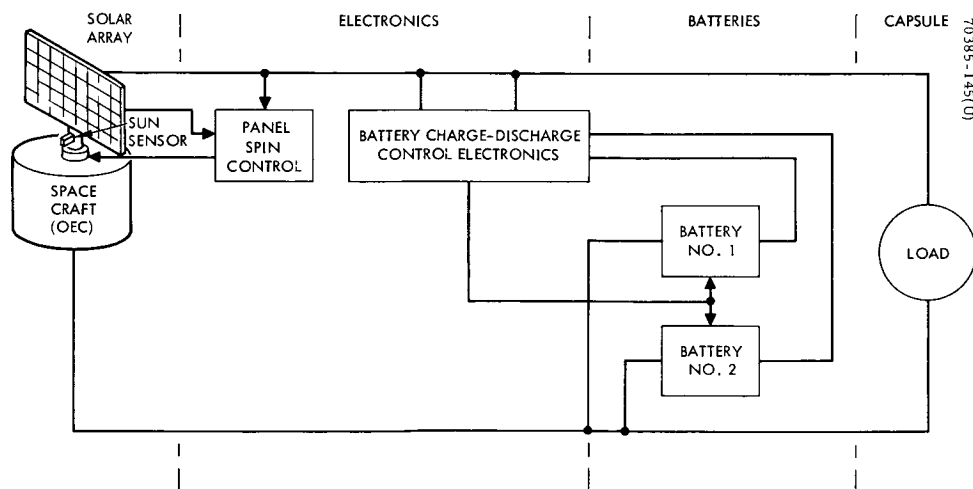


Figure 6-3. Concept "C"

If the on-board experiments are such that the "separated array" configuration is desirable, care should be taken to minimize protrusions beyond the solar array surface.

#### 6.1.2.3 Configuration C

In configuration C the solar array is considered as a flat panel, and the electronics would require a spin-control system for keeping the solar panel oriented toward the sun. The flat array will deliver approximately three times the power of a cylindrical array having the same number of cells; however, the present cost of the despin mechanism and associated spin-control circuits makes it unattractive for solar panels below 400 watts. Consideration of orienting the spin axis along the sunline with a flat array normal to the spin axis enhances neither experiment requirements nor communication capabilities of the capsule bus, making a flat array normal to the spin axis unattractive. Attitude corrections throughout the 6 months mission are also implicit of such a configuration to maintain proper OEC-Sun attitude.

#### 6.1.3 Solar Panel

##### 6.1.3.1 Design Considerations

Selection and optimization of the solar panel configuration and power requirements is dependent on the accurate assessment of numerous factors. The principal factors to be considered include: spacecraft power and weight requirements, spacecraft configuration and envelope constraints, mission environments and induced transients, orbital requirements, and current solar cell and materials technology. The objective is to provide a reliable and predictable power source for the spacecraft which incorporates design simplicity and experience based on other successful spacecraft programs.

The capability to produce a reliable and predictable power source is illustrated in Figure 6-4 which compares the predicted and measured performance of solar panels for communication satellites. The close correlation between the predicted and measured performance is of special significance as the size of the panels shown in Figure 6-4 encompasses the OEC panel size and provides a firm basis for study and design.

Several candidate solar panel configurations were briefly evaluated, including orientated flat panels, cylindrical solar panels, and extendable solar panels.

The cylindrical solar panel configuration was selected as the optimum configuration for the OEC mission and the spin-stabilized spacecraft configuration on the basis of simplicity, reliability, and minimum weight. Each of the other configurations would require despin and orientation mechanisms, which would introduce added weight and added complexity to spacecraft command and control elements. Based on previous studies, the cylindrical panel configuration is more efficient on a spacecraft power-to-weight basis than the other two configurations up to a power level of 400 watts.

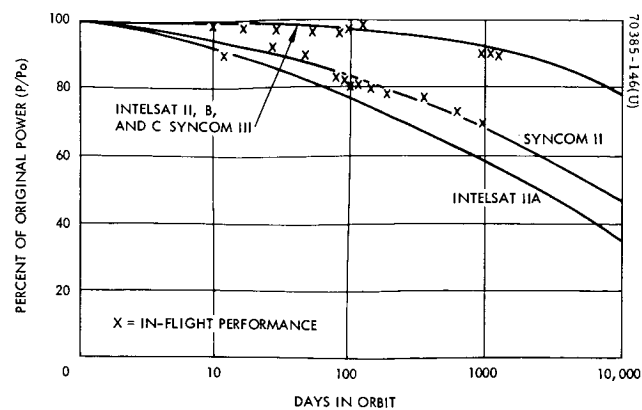


Figure 6-4. Solar Array Performance in Orbit

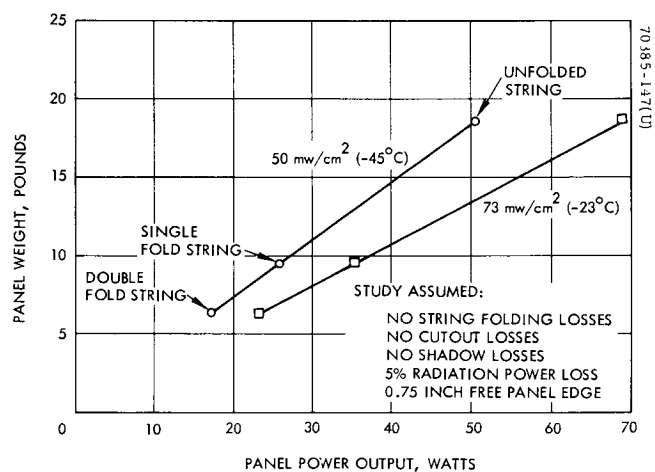


Figure 6-5. Solar Panel Weight Versus Power Output

The power delivered to the spacecraft system by the solar panel depends on several factors, as shown by Figures 6-5 through 6-8. These factors are grouped into those dictated by the environment and those dictated by the system. The environmental factors are solar intensity, temperature, and radiation. Those dictated by the system are cylindrical shape (and edge effect); holes cut in the panel for jets, etc.; shadowing; allowable panel dimensions; series string folding; spacecraft Sun angle variations; and system and voltage requirements.

The environment in which the solar panel might operate is variable due to the eccentricity of the Martian orbit. Solar intensity will have a range of 50 to 75 mw/cm<sup>2</sup>, and the temperature will correspondingly be from -23 to -45°C (minimum temperature -157°C at emergence from eclipse). The radiation degradation is anticipated to be approximately 5 percent during the 1-year transit and 6-month Martian orbit.

System requirements at this time are, in some cases, not yet fixed. Panel shape, sun angle, and voltage are considered fixed. The 36-inch-diameter cylindrical shape and edge losses affect power by factors of  $1/\pi$  and 0.97. The sun angle of incidence is to be normal to the panel ( $\pm 5$  degrees) and voltage delivered to the blocking diodes (loss = 0.7 volt) is 25.5 volts. Bypass diodes may be used to limit any shadowing loss.

The analysis assumes a continuous series string pattern of solar cells and does not include the effect of panel cutouts for the jet nozzles and Sun and planet sensors, which are considered relatively minor. The effect of boom shadowing is not included since the boom orientation selected for the OEC virtually eliminates shadowing of the solar array. During the design phase, the performance of specific panel lengths should be optimized in relation to the series-parallel cell assemblies and also includes the effect of folding the series strings.

Based on the above assumptions, studies were made of specific solar panel configurations. For purposes of evaluation, both the 1x2 cm and 2x2 cm silicon n on p type solar cells were considered in the study. Based on the reduction in assembly losses resulting from fewer interconnections and economic considerations, including initial cell and panel fabrication costs, the 2x2 cm was selected for use in the panel sizing studies. The cells recommended are 2x2 cm shallow diffused, silicon n on p junction type, with nominal 10 ohm-cm bulk resistivity. Quartz coverglasses employing antireflectant and ultraviolet filters will be used to provide reasonable protection from severe radiation degradation. Based on radiation degradation assessments, 0.006 inch thick coverglasses are recommended. The cells have a minimum average output with coverglasses installed of 56.75 milliwatts at 0.445 volt at standard temperature (77°F) and illumination (139.6 mw/cm<sup>2</sup> at air mass zero).

The electrical performance of the 36-inch-diameter solar panel at the orbit operating temperature and illumination conditions is shown in Figure 6-7 as a function of panel height. Figures 6-5 and 6-6 depict the corresponding solar panel weight and length relationship.



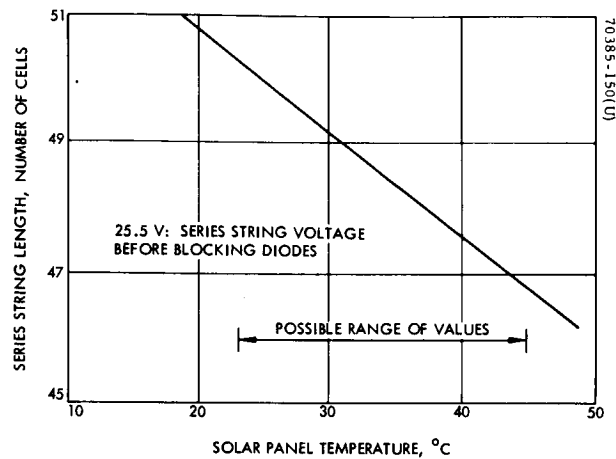


Figure 6-6. Solar Panel Weight Versus Height for 2x2 cm Solar Cells

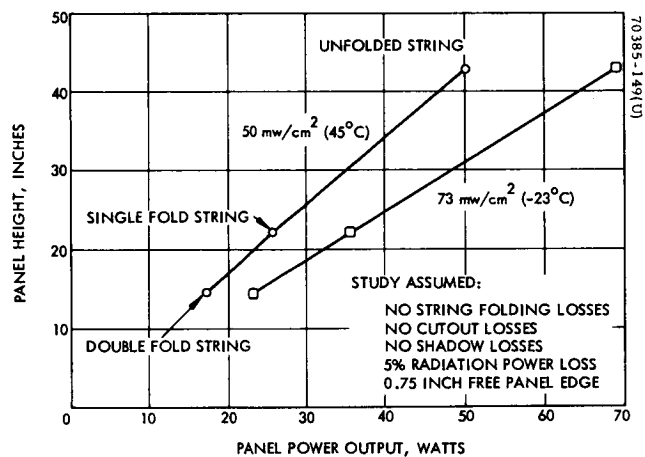


Figure 6-7. Solar Panel Power Output Versus Height

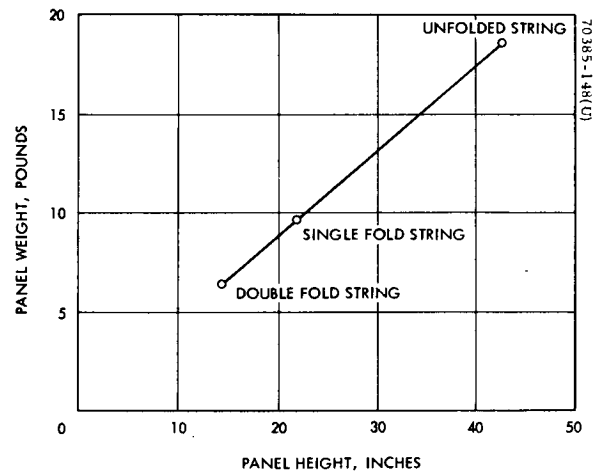


Figure 6-8. Number of 2x2 cm Solar Cells in Series Versus Solar Panel Temperature

#### 6.1.3.2 RF Shielding

RF shielding, for purposes of minimizing antenna pattern distortion, can readily be accomplished by bonding a thin metallic foil to the internal surface of the cylindrical solar panel. The RF shielding technique has been successfully used on the Hughes communication satellite program.

The effect of solar panel induced magnetic fields, which could affect the experiments and spacecraft electronics, will be minimized by alternating the polarity of the individual series-parallel solar cell group. By alternating the cell groups, and paralleling busses of opposite polarities, induced magnetic fields are essentially cancelled.

#### 6.1.3.3 Solar Panel Voltage Ripple

The magnitude of the voltage ripple produced by the cutouts in the panel for the control system jets will be minimized through selective grading and placement of high performance solar cells. The selective grading and placement technique has been successfully used by Hughes on the Syncom, ATS, and HS-303A series of communication satellites.

#### 6.1.3.4 Solar Panel Weight

The solar panel weights shown in Figure 6-5 are based on the use of a 36-inch-diameter cylindrical substrate fabricated using 3/8 inch thick aluminum honeycomb and 0.003 inch thick impregnated fiberglass face sheets. Based on the radiation damage assessment, 0.006 inch thick solar cell coverslides were selected for study purposes. A weight breakdown for a 28.95 inch and 36 inch long solar panel is given in Table 6-1.

The OEC panel analysis was based on the technology established for the fabrication of a 56 inch diameter by 26-1/2 inch long solar panel for the HS-303A (Intelsat II) communication satellite. The HS-303A solar panel utilizes a 1/2 inch thick substrate. The estimated design weight of the solar panel for a specific satellite (F-4) which used 6596 solar cells (2x2 cm) with 0.012 inch thick coverslides is as follows:

Substrate (56 inch outside diameter by 26-1/2 inch length)	7.37
Cell, coverslides, and interconnection	10.56
Cell adhesive	1.02
Wiring, connectors, brackets, and diodes	0.52
Thermal surface	0.39
Thermal barrier, ground plane, and attach brackets	1.44
F-4 total weight	<hr/> 21.33 pounds

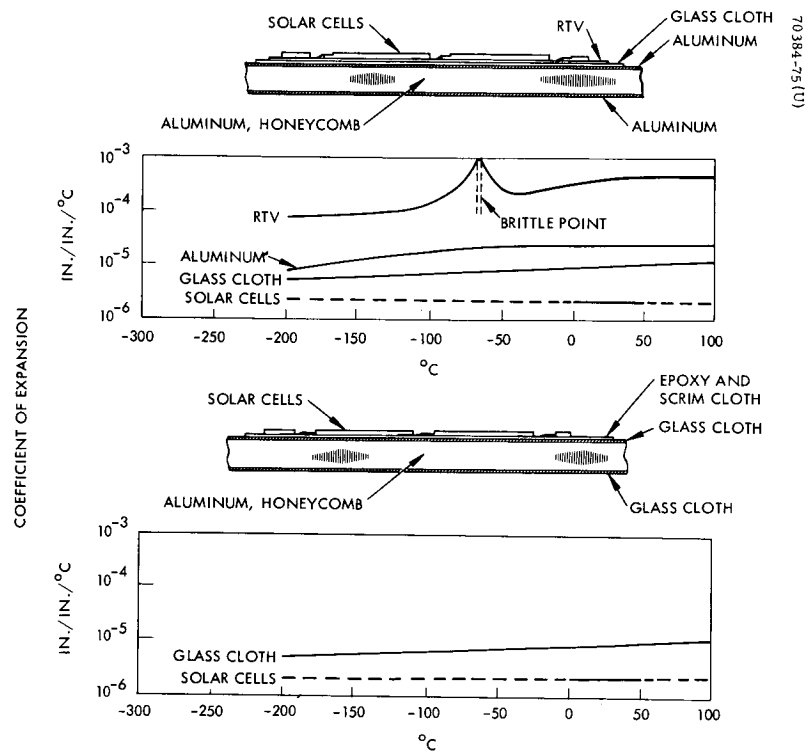


Figure 6-9. Comparison of Solar Panel Fabrication Techniques

TABLE 6-1. SOLAR PANEL WEIGHT BREAKDOWN (POUNDS)

Component	28.95 Inch Panel	36 Inch Panel
Fiberglass substrate	5.90	7.34
Honeycomb	1.11	1.38
Glass cloth	1.63	2.03
Bus bars	0.25	0.31
Edge fill	0.44	0.55
Inserts	0.41	0.51
Adhesive	1.04	1.29
Connectors, brackets, and wire	1.02	1.27
	<u>5.90</u>	<u>7.34</u>
Cells, coverslides	5.25	6.86
Cell adhesive	1.11	1.38
Interconnectors and diodes	0.23	0.30
TOTAL	<u>12.49</u>	<u>15.88</u>

Upon completion of fabrication, the F-4 solar panel weighed 21.57 pounds.. The maximum weight of the first four HS-303A panels, which used 1x2 cm solar cells, was 22.1 pounds.

Based on fabrication experience with the fiberglass faced substrates on the HS-303A and ATS programs, the weight estimates for the OEC solar panel are considered to be realistic.

#### 6.1.3.5 Environmental Capabilities

Based on thermal studies of the OEC mission, it is estimated that the solar panel unit can be exposed to temperatures as low as  $-192^{\circ}\text{C}$  ( $-314^{\circ}\text{F}$ ) during transfer orbit, if a passive thermal control technique is used. While on station, the panel must be capable of delivering power to the spacecraft during exposure to temperatures ranging from  $-22^{\circ}$  to  $-157^{\circ}\text{C}$  ( $-8^{\circ}$  to  $-25^{\circ}\text{F}$ ).

As shown in Tables 6-2 and 6-3, Hughes has successfully tested solar panels and representative solar panel sections to temperatures ranging from  $-200^{\circ}$  to  $-315^{\circ}\text{F}$ . The Hughes developed communication satellite utilized the fiberglass faced substrate construction shown in Figure 6-9 and a Hughes modified epoxy adhesive system. Panel sections have been successfully subjected to repeated cycling to liquid nitrogen temperatures without degradation. A typical aluminum faced substrate construction is also shown in Figure 6-9. Hughes has fabricated solar panel sections using the RTV adhesive system for cell bonding and has successfully subjected the sections to repeated cycling to liquid nitrogen temperatures without degradation.

TABLE 6-2. SOLAR PANEL PERFORMANCE DATA  
(denotes specimen test)

Project	Panel Diameter, inches	Panel Rated Power, watts	Duration of Space Operations as of 7-6-67, days	Temperature Limits, °F	
				Operating	Test
Surveyor	Flat	101.9	210	-300	-270 (-320)
Syncom 2	28	30.0	1441	-80	-150
Syncom 3	28	33	1051	-80	-320
Early Bird (HS-308)	28	46.5	811	-80	-120 (-320)
Intelsat (HS-303A (3))	56	104	176	-150	-80 (-290)
ATS-A	56	139	91	-200	-200 (-250)
ATS-B	57.7	175	212	-80	(-250)
HS-308	111.3	1050	Design phase	-190	-200 (-320)

TABLE 6-3. TEST DATA ON HUGHES ADHESIVE SYSTEM

Program	Temperature, °F	Number of Temperature Cycles	Remarks
Advanced Syncom	+250 -250	500	Coupon (typical panel segment) 150°F/minute
Advanced Syncom	+250 -320	25	Hot plate to LN <sub>2</sub> immersion
Syncom 3	150	35	Panel (typical quadrant of cylindrical array) 20°F/minute
ATS	+250 -250	5000	Coupon (typical panel segment) 16°F/minute

Although not shown in Figure 6-9, the solar panel for the Surveyor project consisted of a flat panel, using an RTV adhesive system to bond cells to a titanium faced honeycomb substrate. The ability of the solar panel to withstand extreme temperatures was vividly demonstrated by the continued performance of SC-1 after several lunar nights.

Due to the close relationship between the thermal expansion coefficient of the fiberglass and the silicon solar cells, the fiberglass substrate is recommended. The Hughes modified epoxy system and the RTV adhesive systems are both usable with the fiberglass substrate. The selection of the adhesive and cell interconnection systems for the OEC mission will be established through developmental testing.

#### 6.1.4 Battery

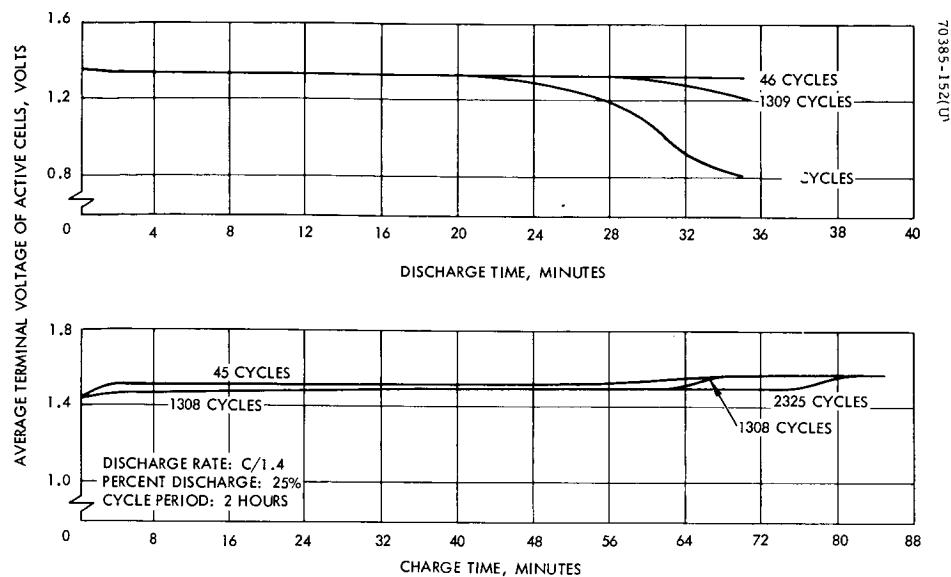
##### 6.1.4.1 Battery Candidates

Although there are many different types of batteries in existence, only three types have been used since the beginning of the space program. These are the nickel-cadmium (Ni-Cd), silver-cadmium (Ag-Cd), and silver-zinc (Ag-Zn) types. The selection of the type of battery system is based on consideration of capacity, coupled with cycle life and availability.

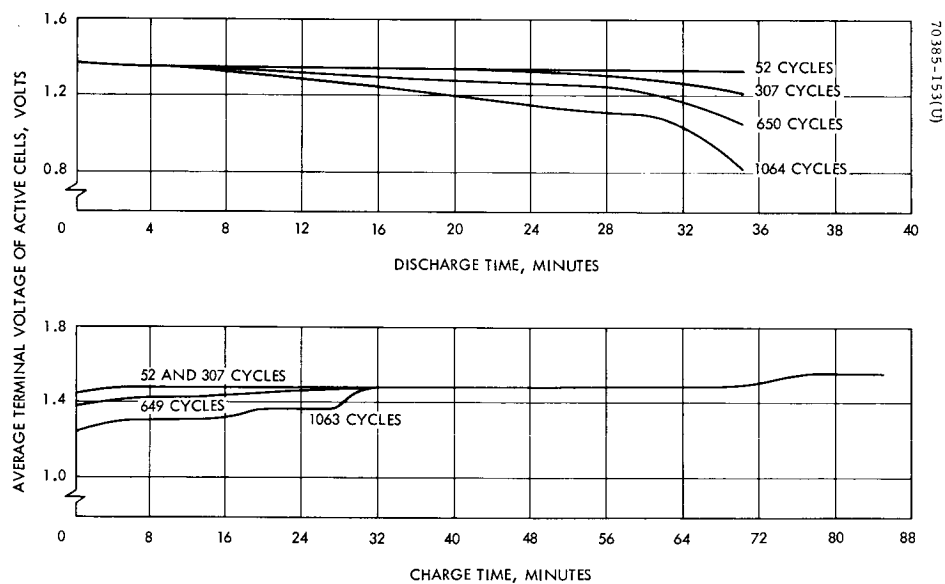
With excellent cycle life, coupled with good performance at low temperatures, nickel-cadmium cells are hermetically sealed to prevent loss of electrolyte and give maintenance-free performance, are easily recharged, and can provide fairly high peak currents. Limitations include a low energy output per unit of weight and volume. In addition, the Ni-Cd cell requires an overcharge for a full capacity input and exhibits limited charge retention.

Silver-cadmium cells combine some of the best features of the silver-zinc and nickel-cadmium types - i.e., they can provide a high capacity with a fairly long life. These cells also exhibit a high specific energy-to-weight ratio, usually one and a half to two times greater than the nickel-cadmium cell, and have a greater charge retention. The silver-cadmium cell can be discharged to greater depths than the nickel-cadmium cell, can provide extended shelf life in both wet and dry conditions and a flat output voltage, and is mechanically rugged. Compared to silver-zinc, its limitations include lower cell voltage, lower specific energy ratio, and availability. The most significant feature of the silver-cadmium cell is that it is basically non-magnetic and therefore highly desirable for the OEC application.

The advantage of the silver-zinc cell as compared to Ni-Cd and Ag-Cd cells, lies principally in the ability to provide higher specific energy-to-weight ratios. In addition, the Ag-Zn cells have an extremely high rate discharge capability.



a) AT 5°C



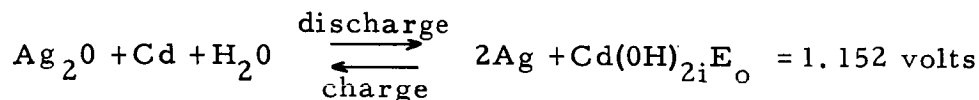
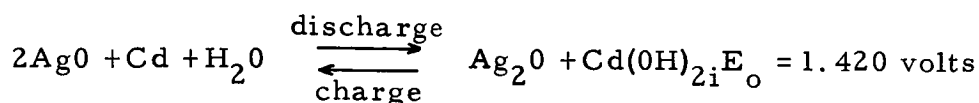
b) AT 25°C

Figure 6-10. Voltage Characteristics of Silver-Cadmium Cells

#### 6.1.4.2 Selection of Battery

Batteries containing silver-cadmium cells have been chosen for the Orbital Experimental Capsule power system because of their nonmagnetic nature, relatively high reliability, excellent charge efficiency, and ease of charge control.

Silver cadmium cells exhibit two cell reactions which account for the charge-discharge curves:



The upper plateau (1.420 volts, open circuit) provides approximately 40 per cent of the nominal capacity. It can be seen from Figure 6-10 that all voltages are a function of 1) the number of cycles a cell has experienced and 2) temperature. Figure 6-10 represents test data, performed on groups of eight cells, as reported in Report No. AF APL-TR-65-42. From data in this figure, a cycle-voltage graph showing end-of-discharge voltages has been constructed (Figure 6-11). It is significant that for the maximum number of cycles for OEC (730), the cell voltage will be as follows: 1.20 volts at 5°C and 1.01 volts at 25°C. However, with the lower discharge rate planned for the OEC batteries, the cell voltages should be somewhat higher than indicated in Figure 6-11. Use of the results from Figure 6-11 should therefore provide a conservative voltage estimate.

#### 6.1.4.3 Cell Requirement

As shown in Figure 6-11, a minimum cell voltage of 1.01 volts can be expected at the end of 730 cycles at 25°C — a more severe cycling regime than might be expected for the OEC system. At 5°C, the voltage would be 1.2 volts. Utilizing 27 cells in series, the minimum voltage will be 27.0 volts at 25°C.

#### 6.1.4.4 Power Demands on Batteries

Four basic power profiles have been considered based on the average orbital power requirements indicated in Table 6-4, where the batteries supply a minimum voltage of 27.0 volts. The battery loads are as follows:

- 1) 7 hour orbit: 1.5 hour period at 19 watts or 28.5 watt-hr
- 2) 7 hour orbit: 2.0 hour period at 57 watts or 114 watt-hr
- 3) 15 hour orbit: 2.65 hour period at 19 watts or 50.4 watt-hr
- 4) 15 hour orbit: two 2.5 hour periods at 57 watts, separated by 5 hour or 143 watt-hr per period



TABLE 6-4. OEC POWER REQUIREMENTS

	Average Constraint Power, watts
Experiments	10.0
Tape recorder	3.0
Encoder	2.0
Phase lock loop	0.5
Receiver and decoder	3.5
Total	19.0 plus transmitter*

\*Additional power of 55 watts required periodically for high power transmitter for orbit change system, or additional power of 57 watts required periodically for S-band transmission.

Battery requirements for the four power profiles are summarized in Table 6-5.

#### 6.1.4.5 Battery Characteristics Summary

Cell type	Silver-cadmium, hermetically sealed
Cells per battery	27
Discharge voltage	1.2 volts/cell nominal; 1.1 volts/cell worst case
Charge rate	C/10
Temperature range	$60 \pm 20^{\circ}\text{F}$ — orbiting; $0 \pm 20^{\circ}\text{F}$ — transit storage
Depth of discharge	25 percent
Charge-discharge cycles	730 (620 cycles maximum for orbits considered in study)
Number of batteries	2

TABLE 6-5. BATTERY REQUIREMENTS, 25 PERCENT DEPTH OF DISCHARGE

Profile	Output, amp-hr	Capacity, amp-hr	Capacity per Battery, amp-hr	Weight per Battery, pounds	Volume per Battery, cubic inches
1	1.0	4	2	4.7	80
2	4.1	20	10	18.6	254
3	1.8	10	5	9.6	147
4	5.1	20	10	18.6	254

#### 6.1.4.6 Cycle Life

As indicated earlier, the maximum duty cycle considered was for 7 months of orbiting with a 7-hour orbital period yielding a total of 730 cycles. Test data, presented in Table 6-6, were gathered during the period for 1962 to 1965, and these data indicate that a depth of discharge of 25 percent (to 75 percent of nominal capacity) at temperatures of 5° and 25°C provides a satisfactory cycle life; this depth of discharge has been selected for this design.

Recent major advances in cell construction have resulted in cycle lives much longer than the data presented here. It is expected that by virtue of the actual 6 month lifetime requirement and advancements in cell technology, a greater depth of discharge may be considered in the advanced program phases.

#### 6.1.4.7 Open Circuit Storage During Transit

Figure 6-12 presents approximate open circuit storage loss data for silver-cadmium cells. Thus, at the extremes of the proposed storage temperature range, the capacity loss on open circuit should be approximately 1.15 percent per month at -7°C and approximately 0.1 percent per month at -29°C. It is therefore proposed that the batteries be fully charged prior to launch and stored in an open circuit condition during transit.

#### 6.1.4.8 Battery Capacity and Charge Rate

Battery capacity as a function of temperature is shown in Figure 6-13. In the operating range from 4 to 27°C, the capacity will range from 90 to 117 percent of nominal capacity. Therefore, even at the low end of the temperature span, no serious loss of capacity will be encountered.

Figure 6-14 represents battery capacity versus battery weight. The relationship is linear with a slope of 28 watt-hr/lb. Charging at the C/10 rate to a limiting voltage of 1.55 volts per cell (41.9 volts battery voltage) is planned for all cases.

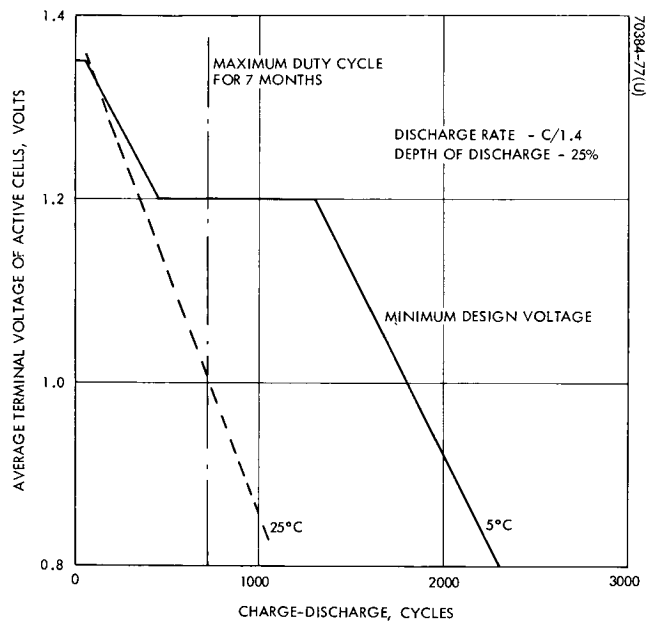


Figure 6-11. Average Silver-Cadmium Cell Voltage Versus Cycles as a Function of Temperature

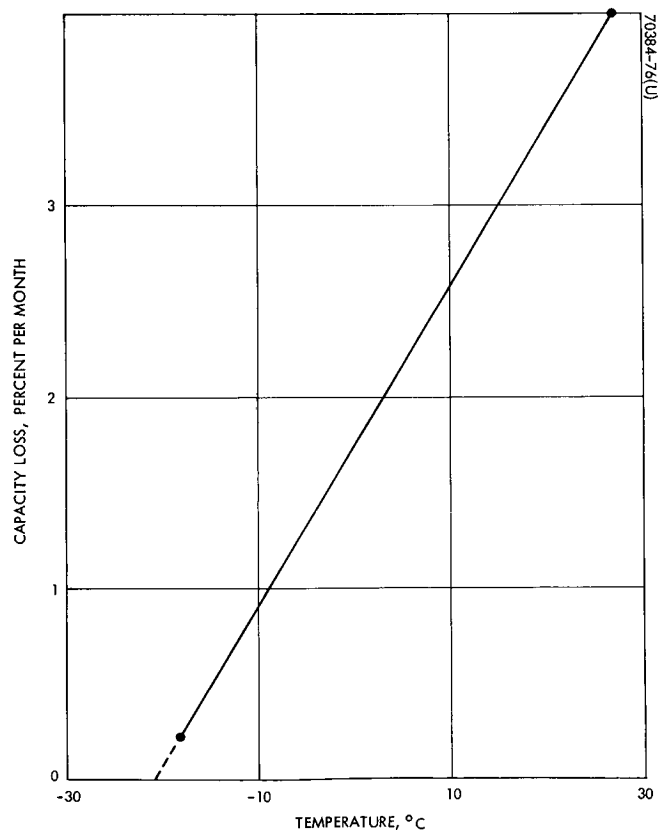


Figure 6-12. Estimated Open Circuit Stand Loss for Silver-Cadmium Batteries

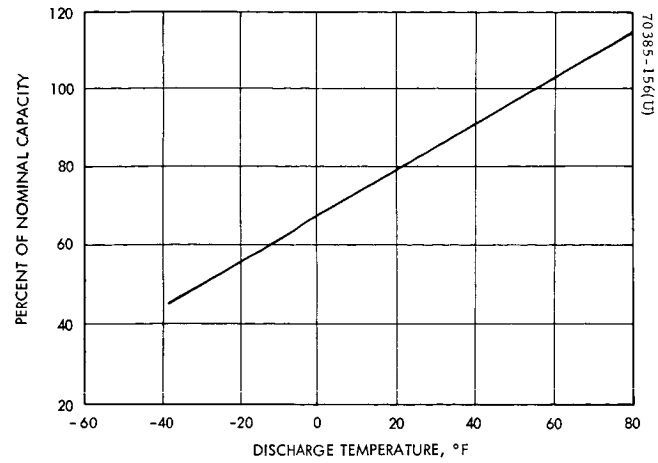


Figure 6-13. Battery Capacity Versus Temperature

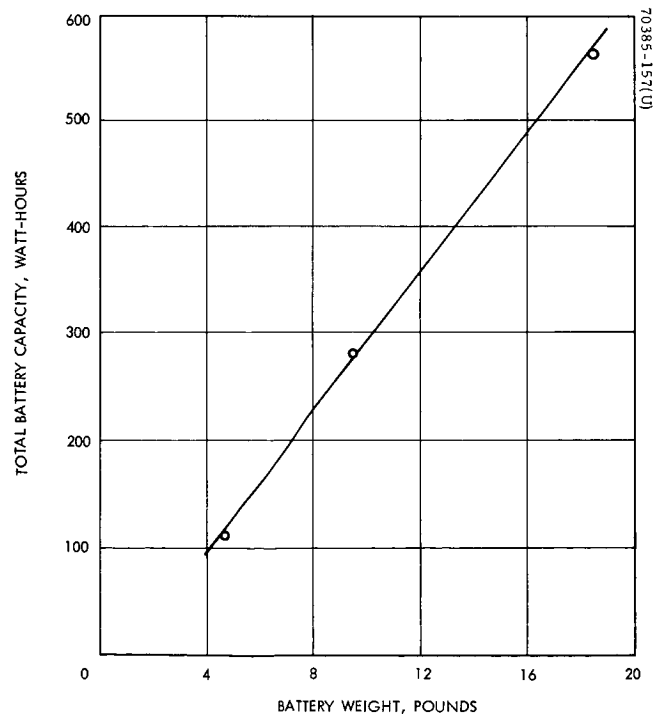


Figure 6-14. Silver-Cadmium Battery Weight Versus Capacity for OEC Mission

TABLE 6-6. CYCLES TO FAILURE FOR AG-CD CELLS  
(85 minute charge, 35 minute discharge)

Temperature, °C	Depth of Discharge, percent	Cycles to Failure for 50 Percent of Cell Group*			
5	25	1185	1124	2366	2366
5	50	72	72	74	156
25	25	652	1021	1067	1081
25	50	72	74	74	156

\*Failure defined as E < 0.80 volt. (See Report No. AF APL-TR-65-42.)

#### 6.1.5 Battery Charge-Discharge Controller

##### 6.1.5.1 Description of Operation

The battery controllers provide control for both charge and discharge. The two batteries and controllers are interconnected to provide constant current charge to both batteries, even if one controller fails. A schematic block diagram is shown in Figure 6-15.

##### 6.1.5.2 Detail Operational Characteristics

The controllers are designed to provide a number of functions as follows.

When the solar panel bus voltage is high, it supplies power directly to the load. During this period, solar panel power is also fed to a boost supply in each controller. This supply provides two separate secondaries, each of which is used to boost the solar panel voltage sufficiently for battery charging. This boosted voltage is then controlled by the charge control to provide the required current limited charge current. When the battery terminal voltage exceeds a predetermined upper limit, the charge control is turned off, terminating battery charging.

As the solar panel voltage decreases below the desired switching point, the bridge circuit will sense this decrease in voltage and override the normal charge control to open up the charge circuit. The purpose is to permit optimum usage of the solar panel to provide energy for the loads. As the solar panel voltage continues to drop, a bridge circuit senses this falloff in voltage and causes the discharge control to deliver from the battery that portion of the load current that cannot be supplied by the solar panel.

The two batteries are constrained to discharge at a ratio of 60/40 or better by use of a common control reference and small resistor networks in series with each controller downstream of the sensing network. Diodes across the resistors provide pulse power capability.

The baseline design for the voltage boost portion of the battery charge control will be of the boost-add configuration. This configuration has been used with much success on the HS-308 program. It is a highly efficient system, since only the boost voltage is handled by the boost dc to dc converter. A series regulator operated via a differential amplifier comparing output voltage and current against a reference will provide the output regulation and charge cutoff required to ensure proper battery charging.

The two boost supplies are interconnected to provide boost voltage to charge both batteries even if one supply should fail. This interconnection greatly improves overall system reliability with a very minimum increase in part count and system weight.

A modulation type discharge controller, which permits only that power which cannot be supplied by the solar panel to be drawn from the batteries, is proposed for the baseline design. This permits the batteries to be operating as close to full charge as possible during all phases of operation. To control the depth of discharge of both batteries within acceptable limits, consistent with their life requirements, a single common reference voltage source is required for both discharge controllers. The need for this single reference can best be visualized by referring to Figure 6-16.

As the discharge set point separates between the controllers, the current sharing variation also increases. For the condition shown in Figure 6-16, controller 1 is supplying all of the load current, since its set point is higher than the other controller. Set point C would have to be increased to slightly above point B before any of the load current ( $I_L$ ) would be drawn from the second battery. At the condition where set points A and B coincide, equal current sharing will exist (assuming equal values of load sharing resistors). Increasing the load sharing resistors ( $R_{S1}$  and  $R_{S2}$  in Figure 6-15) would reduce the current share spread; however, it would also increase the power dissipated in this added source resistance.

To provide for pulse power capability from the batteries, a diode is connected across the series load sharing resistors to limit the voltage drop at high pulse currents.

To reduce the possibility of system failure, resulting from failure of the single voltage reference, redundancy will be designed into the system such that catastrophic failure of a minimum of two parts will be required before performance would be affected. Since the probability of two catastrophic part failures is remote, the reliability of this system will be extremely high.

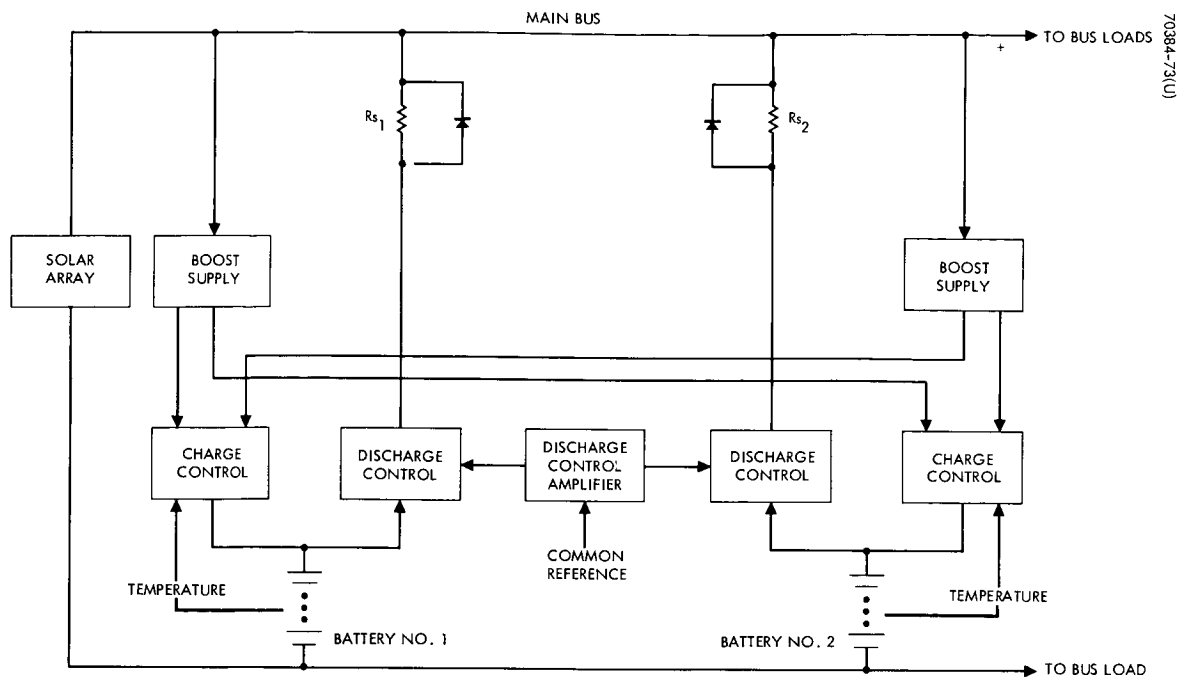


Figure 6-15. Charge-Discharge Control Block Diagram

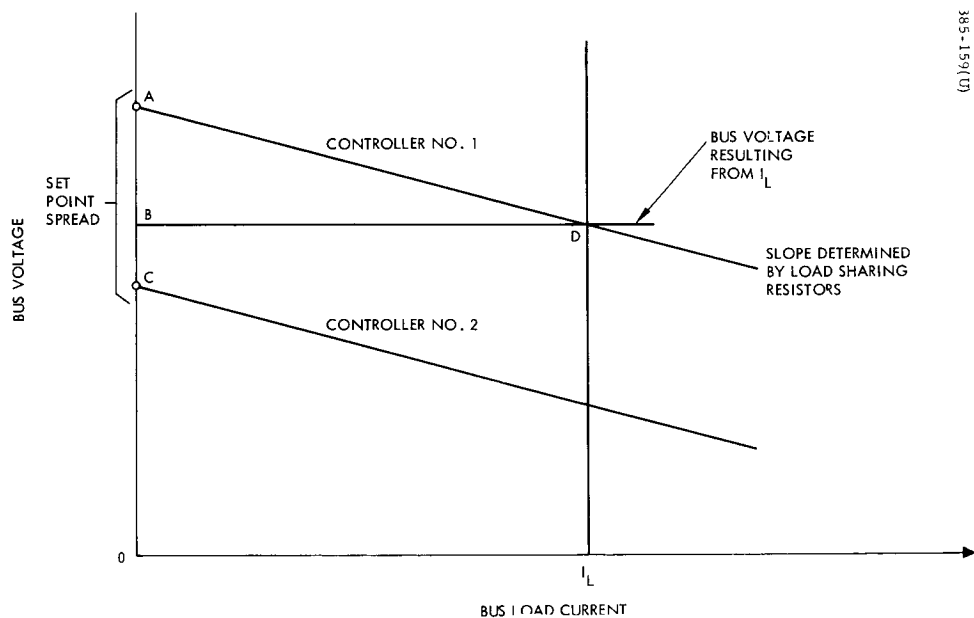


Figure 6-16. Load Current Sharing Versus Controller Set Point

### 6.1.5.3 Electronics Characteristics Summary

#### Electrical Characteristics

Charge voltage                      Above 24.5 volts

Discharge voltage                  Below 24.5 volts

#### Physical Characteristics

	<u>Weight</u>
Limiter	0.3
Charge boost	0.3
Controller	0.3
Discharge control	0.5
Total	<u>1.4 pounds</u>



## 6.2 PROPULSION SUBSYSTEM

### 6.2.1 General

Several candidate propulsion systems have been examined for each of the possible requirements evolved from the OEC feasibility study. Volume I describes the preferred systems; this section describes system characteristics and tradeoff studies which lead to the selection of the recommended propulsion systems.

The following systems were examined:

#### Co-orbital spinup

- 1) Conventional solid propellant
- 2) Ammonia vaporjet
- 3) Cold gas
- 4) Monopropellant hydrazine (as part of orbit change system)

#### Orbit change system

- 1) Monopropellant hydrazine for all functions
- 2) Monopropellant hydrazine with one of the above spinup systems

Other possible spinup systems, including bipropellant, resistojet, and electrical propulsion, were not considered desirable because of their added complexity and lack of a weight advantage for the size of system considered for the OEC. Subliming solids are a remote possibility if thrust levels of the order of  $10^{-3}$  lbf or less are tolerable; higher thrust would require substantial electrical power to accelerate the sublimation process. The weight of such a device would be intermediate between a conventional solid rocket and a cold gas system.

A monopropellant hydrazine system is considered the only good choice for the orbit change system. Bipropellants, because of extra tankage, lines, and valves, are less reliable and do not show a weight advantage in small systems. Hydrogen peroxide is space-proven in spinning satellites but has lower performance than hydrazine and is less stable chemically. Decomposition of the propellant would require a provision to vent gas under zero gravity conditions while in transit aboard the Voyager spacecraft. Electrical propulsion systems are not sufficiently advanced in development to be of interest for the present mission and require extremely large amounts of power for higher thrust levels. Cold gas results in a severe weight penalty, and vaporizing liquid or resistojet systems require more power than will be available. Conventional solid propellants could supply the orbit change impulse but would still require an auxiliary attitude control system.

### 6.2.2 Spinup Systems

The feasibility of alternate propulsion techniques is discussed in the following paragraphs and system parameters defined for spinup of the OEC to the required  $60 \pm 10$  rpm after separation from the Voyager spacecraft.

#### 6.2.2.1 Solid Propellant Spinup System

Several units are currently or recently in production which deliver a total impulse in the general range of interest. Any could be modified to give a slightly different impulse without an extensive development effort. Unfortunately, all of these available rockets have a rather high thrust level, as shown in Table 6-7. Other suitable motors may be available but Atlantic Research Corporation, who manufactures the models shown, has provided virtually all of the operational motors of this type. Other suppliers would not be expected to offer a substantially different product.

If a development program were undertaken, it should be possible to make a motor more suited to the requirements. One example is shown in Figure 6-17, an Aerojet General Corporation conceptual design for a motor which delivers 50 lbf-sec at a thrust of 2.18 lbf. This particular motor uses a nonaluminized JATO propellant, AN-584, which is capable of sterilization. Since sterilization is not required, the lower burning rate ANP-2874 HO Mod 1 could be used with an attendant reduction in thrust to about 0.7 lbf. If still lower thrust is required, an ammonium nitrate based composition such as LFT-3 or AMT-2091 could give a thrust of 0.1 lbf or lower in a slightly smaller diameter grain.

The lower limit of thrust would be determined by the lowest chamber pressure that gives stable combustion and the smallest nozzle that does not suffer detrimental buildup of deposits during the firing. Determining these parameters would require a substantial experimentation and testing program. Adjustment of total impulse is accomplished simply by changing the length of the end-burning grain. In the above example, a 25 lbf-sec motor would be 3.43 inches long and weight approximately 0.25 pound.

#### 6.2.2.2 Ammonia Vaporjet Spinup System

A vaporjet, which offers the advantage of liquid propellant storage and attendant reduction in tank weight over cold gas, would not appear to be the system of choice for the OEC mission. The three versions described below may offer some weight savings but are not actually state-of-the-art. Propellants other than ammonia may offer some slight advantages in performance but not enough to deserve additional analysis (Reference 1).

Significant problems which must be resolved are:

- 1) Propellant management under the initial zero gravity conditions must include thermal control.

TABLE 6-7. QUALIFIED SPIN ROCKETS

Model Number	Qualified for	Total Impulse, lbf-sec	Thrust, lbf	Burning Time, seconds	Propellant, pounds	Total Weight, pounds	Envelope (Length x Diameter), inches
MARC 18 B1	Skybolt	15.6	34.8	0.438	0.069	0.49	4.126 x 1.25
MARC 18 A1	Skybolt	17.6	40.9	0.41	0.078	0.49	4.38 x 1.25
MARC 18 D1	Thor-Delta	22.8	38	0.6	0.117	0.48	4.24 x 1.53
MARC 4C2	Scout	25	41.7	0.6	0.117	0.70	6.83 x 1.53
MARC 15 A1	Discoverer	26	34	0.75	0.130	0.71	5.27 x 1.53
MARC 4C1	Thor-Delta	28	46	0.6	0.117	0.50	4.78 x 1.53

- 2) Heat exchanger design information may be required and is very meager.
- 3) A significant amount of heat is required to vaporize the liquid. This introduces complexity and/or uncertainty in the design.

#### 6.2.2.3 Equilibrium Boiling System

The first and simplest system extracts the heat of vaporization from the propellant itself. A minor quantity of sensible heat is also available from the tankage, bracketry, and propellant vapor. Equilibrium boiling occurs until all of the liquid is frozen. Subsequently, gas production will probably depend primarily on heat soak into the system because at temperatures below the freezing point the sublimation process is relatively slow.

#### 6.2.2.4 Electrically Heated System

A second configuration of the vaporjet system utilizes a battery to supply the latent heat of vaporization. This system will boil at constant temperature and thus have a constant specific impulse.

#### 6.2.2.5 Water Heat Source System

The third configuration is similar to the first but uses a properly shaped and sealed container of water in the tank as a heat source. This water will cool down with the ammonia and contribute sensible heat. At the triple point of the water (about 32°F), however, a first order phase transition will occur, and this conversion of liquid water to ice will yield a substantial heat of fusion isothermally. The weight of this system should lie somewhere between the two cases previously stated.

	<u>Fired Weight, pounds</u>
Lines	1.0
Squib	0.6
Burst diaphragm	0.2
Pressure transducer	0.3
Fill valve	0.2
Screen for zero-g	0.05
Thrusters	0.8
Battery only heaters (2)	<u>0.05</u>
	3.20

PREDICTED PERFORMANCE AT 70°F AND VACUUM		PROPELLANT BALLISTIC PROPERTIES		WEIGHT SUMMARY, POUNDS	
DURATION, sec	22.3	STD $I_s$ , sec	216.0	CHAMBER	0.051
TOTAL IMPULSE, lb-sec	50.0	DELIVERED $I_s$	247.0	INSULATION	0.082
THRUST, lbf	2.18	BURNING RATE AT 200 psia in./sec	0.19	NOZZLE	0.049
PRESSURE, psia	200.0	PROPELLANT DENSITY, lb/in. <sup>3</sup>	0.0606	IGNITER	0.020
DESIGN DATA				TOTAL INERTS	0.202
THROAT AREA, in. <sup>2</sup>	0.0063			PROPELLANT	0.202
EXPANSION RATIO	20:1			TOTAL MOTOR	0.404
THROAT DIAMETER, in.	0.090				

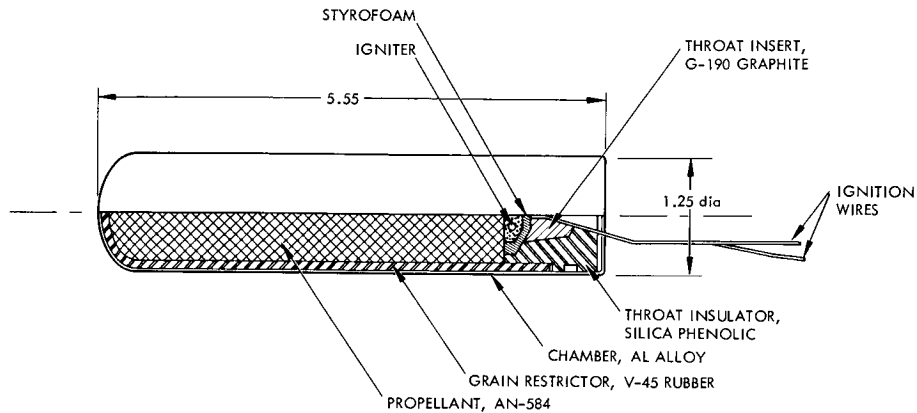


Figure 6-17. Aerojet General Conceptual Motor Design

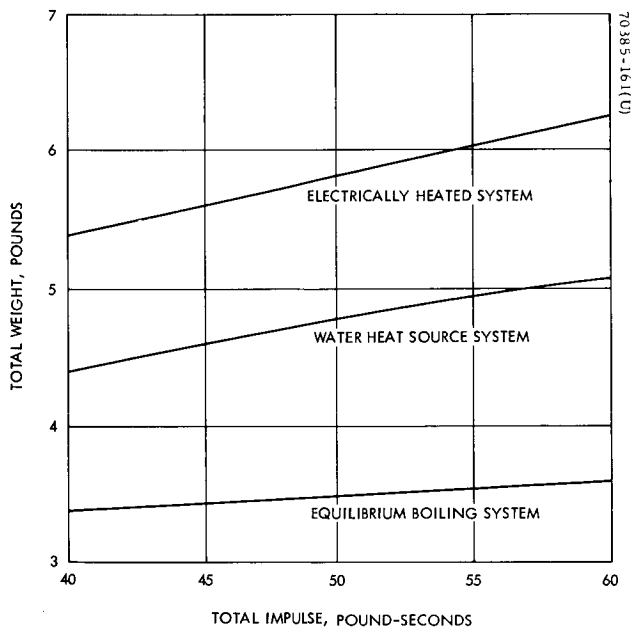


Figure 6-18. Ammonia Vaporjet Systems Weight Versus Impulse

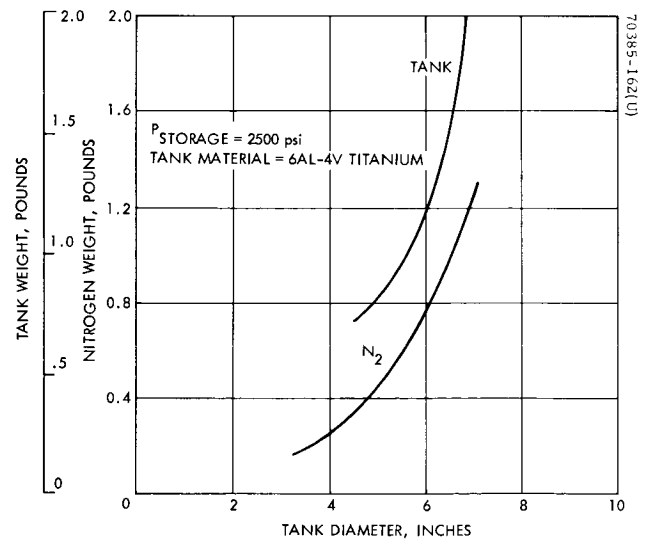


Figure 6-19. Nitrogen Spinup System Parameters

Figure 6-18 relates total system weight for the above systems to total impulse.

#### 6.2.2.6 Cold Gas (GN<sub>2</sub>) System

As an alternative to the baseline nitrogen system described earlier, a 2500 psi blowdown system of the type used by Hughes on the Applications Technology Satellite program was considered. Design parameters and weights are given below and in Figure 6-19.

Tank material	6AL-4V titanium
Tank pressure	2500 psia
Tank inside diameter	5.29 inches
Chamber pressure	~2000 psia
Nozzle area ratio	40
Vacuum thrust coefficient	1.7
Throat diameter	0.19 inch
Specific impulse	62.5 seconds
Total impulse	33.25 lb-sec
Initial thrust	~95 pounds
Squib valves (2)	0.6
Nozzles (2)	0.7
Amplifier, gauge, temperature sensor	0.3
Tank (1)	0.9
Plumbing	1.0
Nitrogen	0.54
Total	<hr/> 4.0 pounds

It is seen that no significant weight or envelope reduction is gained over the proposed nitrogen low pressure (250 psi) unregulated blowdown baseline system described in detail in Volume I.

### 6.2.3 Attitude Control and Orbit Change Propulsion System

The following discussion presents parametric design information for a monopropellant hydrazine system using typical state-of-the-art components. The baseline system described in detail in Volume I is slightly below the range of data in some of the figures but was computed by the same technique as described below.

The use of the figures is contingent on knowledge of the following system parameters:

- 1) Thrust level
- 2) Spin speed (established as 60 rpm)
- 3) Pulse duration
- 4) Number of pulses required per maneuver
- 5) Total impulse required in pulse mode
- 6) Total impulse required in steady state mode

Figure 6-20 illustrates the linear relationship between total propellant weight and corresponding system weight with and without spinup capability. The difference between the spin and no-spin cases is the additional weight required for spinup thrusters and valves. If spinup is required, a screen device may be needed to guarantee liquid feed to the thrusters at startup.

Figures 6-21 and 6-22 give tank sizes and weights based on propellant weight for one- and two-tank system configurations.

The propellant weight consists of contributions from both steady state and pulse mode operation. It is therefore necessary to analyze these components separately; the total propellant required is the sum of the two.

Figure 6-23 shows the dependence of steady state specific impulse on engine thrust level. Figure 6-24 is based on Figure 6-23 and can be used to establish the steady state propellant requirement for a given thrust level and total impulse.

Figure 6-24 illustrates the effect of spin speed on effective specific impulse for various pulse durations. The effective specific impulse is reduced proportionally to the geometric cosine loss due to rotation of the thrust vector. It can be seen that for 60 rpm, a wide range of pulse widths will give good performance. For a 60 degree arc, the pulse duration will be 0.167 second, which is near optimum.

Figure 6-25 shows effective specific impulse versus pulse width. Figure 6-26 based on Figure 6-25, gives 60 rpm pulse mode propellant requirement for a given pulse width and total impulse. If a spin rate other than 60 rpm is required, a new set of curves may be derived from the basic data in Figure 6-24.

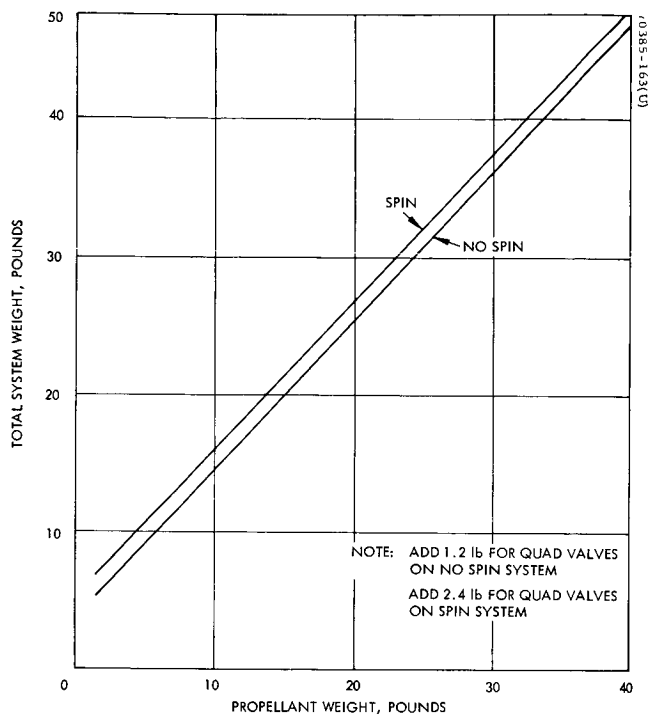


Figure 6-20.  $N_2H_4$  System Weight Versus  $N_2H_4$  Propellant Weight

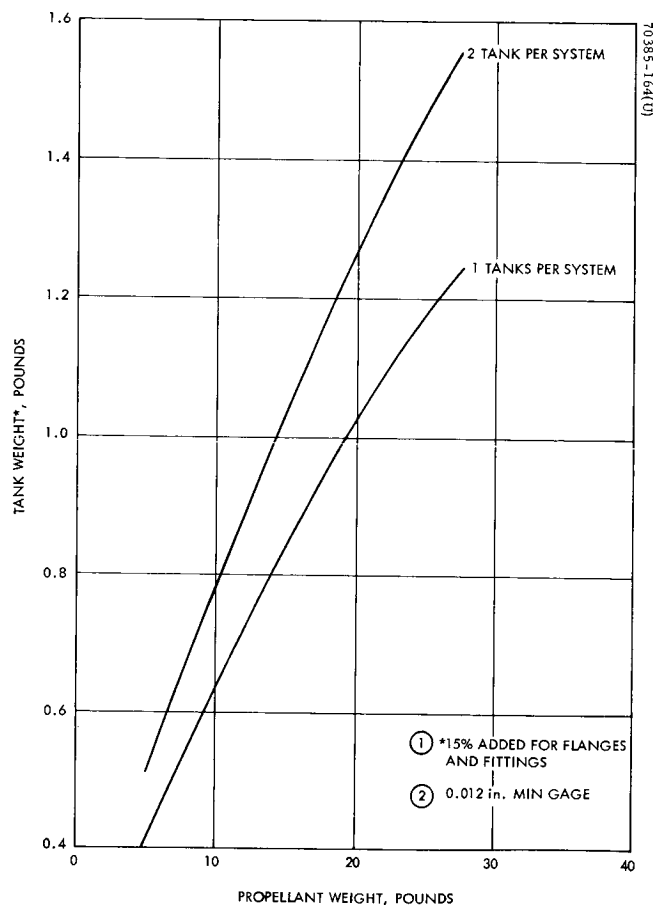


Figure 6-21.  $N_2H_4$  Tank Weight Versus Propellant Weight

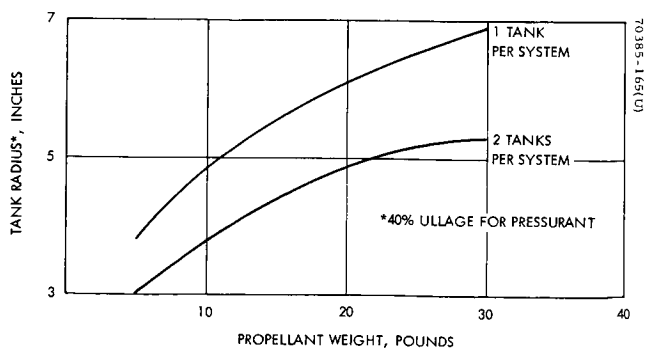


Figure 6-22.  $N_2H_4$  System Tank Radius Versus Propellant Weight

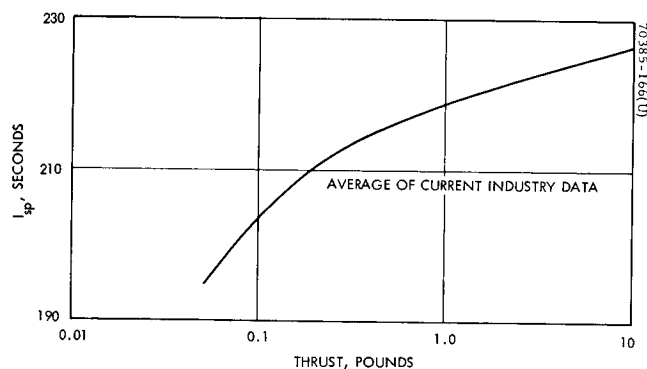


Figure 6-23.  $N_2H_4$  Steady State Specific Impulse Versus Thrust



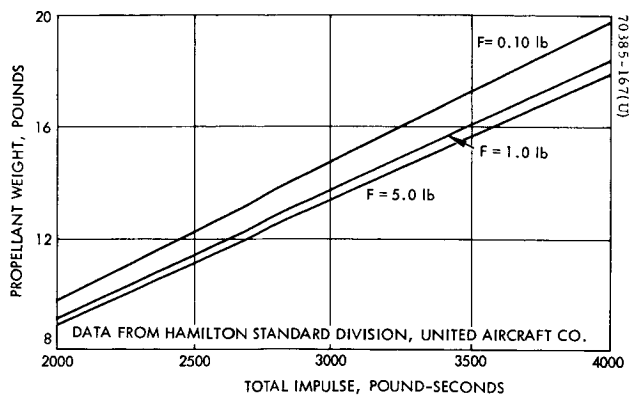


Figure 6-24.  $N_2H_4$  Propellant Weight Versus Total Impulse (Steady State)

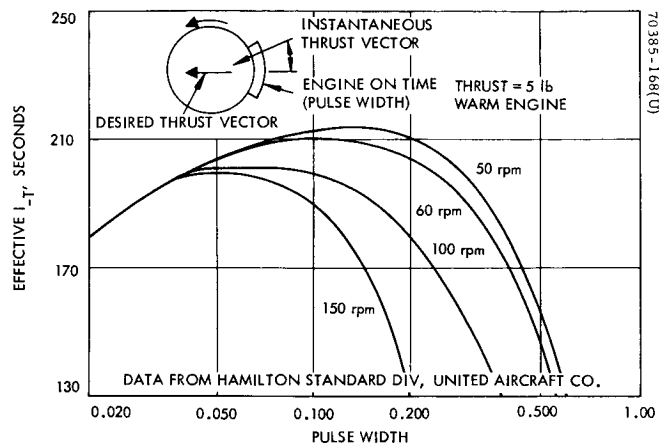


Figure 6-25.  $N_2H_4$  Effective Specific Impulse Versus Pulse Width

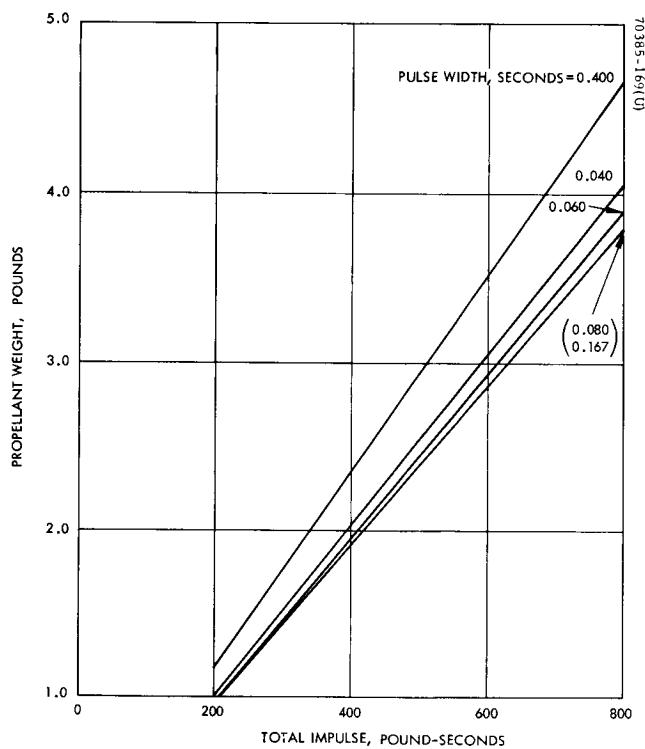


Figure 6-26. Propellant Weight Versus Total Impulse for 60 rpm Pulse Mode

Figures 6-27 and 6-28 show the effect of cold starts on performance for a 5 pound thrust hydrazine engine. As the engine heats up through successive pulses, the specific impulse reaches an equilibrium value, the magnitude of which is dependent on pulse width. It is therefore possible from Figure 6-27 to evaluate the additional propellant required because of thermal inefficiencies in the first 30 pulses. From the number of pulses and weight of propellant required for any maneuver, the amount of additional propellant required can be calculated. It is quite likely, however, that the number of pulses will be large enough to make this correction unimportant.

In summary, a typical sequence in determining the weight of an attitude control system would be as follows:

- 1) For each steady state maneuver, establish the propellant requirements from Figure 6-24 for a given thrust level and steady-state total impulse. Note that the thrust level should be an average over the blowdown experienced in the maneuver.
- 2) Establish the pulse mode propellant requirement from Figure 6-26 for a given pulse width and pulse mode total impulse.
- 3) Establish the propellant loss due to thermal inefficiencies in pulsing for a given number of pulses and a given propellant weight from (2). This may require iteration because of the variation of specific impulse during the first 30 pulses. Also, if thrust level is very different from 5 lbf, adjustment of effective specific impulse must be made. Little data is available, but the change in specific impulse may be assumed to follow the steady-state performance.
- 4) Establish total system weight from Figure 6-20 where propellant weight is the sum of (1), (2), and (3).

#### 6.2.3.1 System Considerations

A considerable improvement in overall reliability can be achieved by redundancy in system functions. In most cases this has been accomplished by two or more completely separate independent systems. A recent study of spacecraft propulsion systems (Reference 1) has shown, however, that the reliability of systems which are required to valve a gaseous or liquid propellant may benefit as much from utilizing quad valves as from incorporating a complete additional system. A substantial weight saving results.

Specifically, a 3600 lbf-sec capacity nitrogen system with quad valves weighed 142 pounds and had a 5 year projected reliability of 0.962 to 0.986 (limiting cases). The weight penalty over one single valve system was only 7 pounds; yet the reliability was higher than for a 389 pound system composed of two complete single valve systems, each containing 1-1/2 times the required propellant (as used in Ranger and Mariner to protect against one open failure).

It is recommended that the quad valve or, if a developed valve is not available, a series-parallel arrangement of four single valves be considered as one

possible alternative. If further study indicates a possible response problem with four independent valves, it may be desirable to consider a series dual arrangement of only two valves. It is likely that the system will have adequate reliability with dual valves. In an all-welded system, rupture or leakage of tanks and lines should be an unlikely event, and there is little benefit in improving the reliability of that portion of the system, particularly when a substantial weight penalty results.

One other observation should be made pertaining to the spinup system. The solid propellant units proposed weigh so little that they might be considered as an emergency backup for whatever system or systems are eventually selected even if the thrust levels ordinarily might be too high.

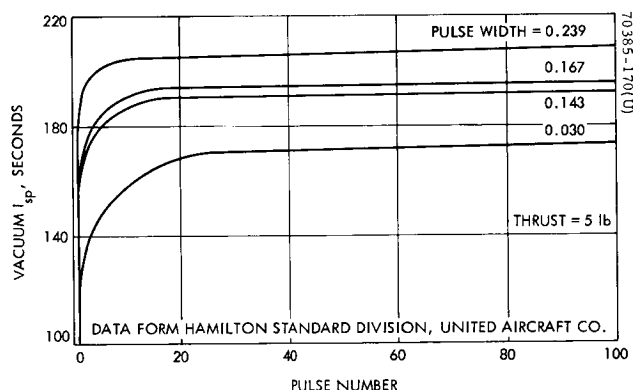


Figure 6-27.  $N_2H_4$  Specific Impulse Versus Pulse Number

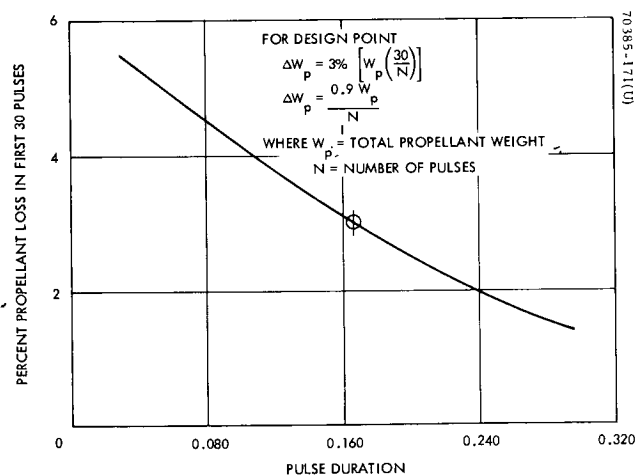


Figure 6-28.  $N_2H_4$  Percent Propellant Loss (First 30 Pulses) Versus Pulse Duration

## 6.3 STRUCTURE SUBSYSTEM

### 6.3.1 General

As part of the overall configuration studies conducted throughout this feasibility study for an OEC, the structural aspect and relationships of the structure geometry with packaging, mounting, and separation system features and basic envelope constraints had to be evaluated. The extent of this feasibility study excluded any structural analysis since a definitive static and dynamic environment has not yet been established for the OEC. Pending the advancement of the Voyager spacecraft design and overall system environment definition, a meaningful study of the OEC structure could be implemented. The structural considerations for this feasibility study were limited to establishing a conceptual framework that satisfied equipment and subsystem arrangements, thermal control considerations, and attachment and separation techniques selected.

A brief description of the OEC structure is presented in the following paragraphs.

### 6.3.2 Structure Description

The structural frame for the recommended OEC configuration would consist basically of the following major sections:

- 1) Central hexagonal support structure
- 2) Central mounting tray bulkhead
- 3) Base mounting/radiator tray
- 4) Solar array support rings
- 5) Support tripod for stacked array antenna (S-band)
- 6) Base support tube
- 7) End closure bulkheads/thermal barriers
- 8) Mounting interface adapter incorporating the separation mechanism and providing the OEC-Voyager mechanical interface

The booms are not considered here as part of the primary structural subsystem but are discussed in detail in the configuration studies material presented in both Volume I and this volume.

The primary supporting structure is the central hexagonal frame to which all members are attached and loads are transmitted and carried through to the base support tube which is attached to the mounting interface adapter. Connected to the hexagon structure is the primary mounting tray bulkhead which extends outboard to

support the base of the cylindrical solar cell array. At the top of the central frame, a lightweight bulkhead provides the upper closure and secondary attachment surface for the solar array. So as to provide a surface and support for the S-band antenna mount and deployment device at the top of the capsule, a tripod is mounted off three corners of the hexagon frame and extends upward to a central point at the top edge of the solar panel. Below the main tray a cylindrical support tube extends downward to the separation flange. Within this tube, near the base, a mounting tray/radiator surface is provided to support the high power dissipation components.

In addition to being the primary support structure, the central hexagon frame serves as the mounting structure for the propulsion systems tankage, which must be located on the capsule's center of mass.

Within the base cylinder of the structure a circular plate is centrally supported by three light gusset plates and serves as the bearing surface for the separation compression spring.

The proposed structure is considered to be fabricated using nonmagnetic aluminum alloys, with an additional oxide coating provided at the mounting surface to minimize any potential solid phase welding (cold welding) occurring at the contact surfaces that might jeopardize successful separation of the OEC. In view of the low compressive stresses and low temperature conditions at the static contact surfaces, solid phase welding is considered quite a remote possibility.

An assessment of the weight of the proposed structure, excluding bracketry, attachments, and separation adapter system, is as follows:

Central hexagon structure	1.7
Central mounting tray	2.1
Base tray	0.6
Array support rings	1.7
Support tripod	0.2
Base tube	1.9
End bulkhead	1.4
<hr/>	
Total	9.6 pounds

A budget has been established for the OEC structure (including 3.0 pounds for two radial booms plus an additional 2 to 3 pounds for bracketry and attachment) at 15 pounds. Satellite structures have been built that weigh less than 10 percent of the total system weight; therefore, the allocation of 12+ percent for the OEC structure based on the baseline configuration weight of 122.8 pounds seems conservative. The complete support adapter and separation mechanism was estimated at 5.0 pounds, which is also felt to be quite conservative.

In order to maintain a desirable ratio of roll to transverse moments of inertia for inherent spin stabilization of the OEC, the recommended configuration was developed with this criterion as one of the prime considerations. Calculated values of moments of inertia for the orbit configuration OEC are as follows:

$$I_{\text{roll}} = 7.5 \text{ slug-ft}^2$$

$$I_{\text{transverse (max)}} = 6.8 \text{ slug-ft}^2 \text{ (axis normal to booms)}$$

$$I_{\text{transverse (min)}} = 2.0 \text{ slug-ft}^2 \text{ (axis parallel to booms)}$$

A minimum ratio of roll to transverse inertia of 1.10 results.

## 6.4 THERMAL CONTROL SUBSYSTEM

### 6.4.1 General

The thermal environment and thermal control requirements during transit and operation including eclipse conditions for the OEC were analyzed and alternate means of satisfying thermal requirements were investigated. The following basic assumptions were used in the analysis:

- 1) The OEC will be carried to Mars on the side of the Voyager spacecraft and will remain on Voyager for the first 4 weeks orbiting Mars.
- 2) After separation from Voyager, it will be spunup and will orbit Mars at an altitude of 300 to 1500 km at periapsis to 10,000 to 20,000 km at apoapsis.
- 3) The solar direction assumed in this analysis was  $90 \pm 25$  degrees from the spin axis.
- 4) The infrared flux and reflected solar flux from Mars are only about 4 percent and 1.5 percent of the solar flux respectively at an altitude of 5,000 km, and they were neglected in this thermal analysis.

### 6.4.2 Design Summary

Two methods of passive temperature control and an active method were considered for the capsule's internal equipment for the transit and operational phases of the mission.

The first method uses an uninsulated cylindrical region at the spacecraft mid-section for temperature control. This region would be coated to produce the desired ratio of solar absorptance to infrared emittance for the temperature required. The major part of the internal power dissipation would be radiated out to space from this region. The disadvantage of this design is that the variable solar intensity and range of possible solar directions causes a large temperature range. Also, the large uninsulated area causes a large temperature drop in an eclipse.

The second method of passive temperature control uses small radiators on the ends of the spacecraft. This design is better than the first because the range of solar intensity and possible solar directions has less effect on the spacecraft internal temperature. However, the internal power dissipation must be some given mean steady state value  $\pm 1.3$  watt to control the internal mounting surface temperatures to  $4^{\circ}$  to  $27^{\circ}\text{C}$  ( $40^{\circ}$  to  $80^{\circ}\text{F}$ ) which is required by the batteries (this includes  $6^{\circ}\text{C}$  uncertainty at each end of the temperature range).

The recommended temperature control method is to use a rotating shutter on the end of the spacecraft similar to the type used on the Applications Technology Satellites.

During the transit phase of the mission, the spacecraft is shaded by Voyager. The batteries require  $-29^{\circ}$  to  $-7^{\circ}\text{C}$  ( $-20^{\circ}$  to  $20^{\circ}\text{F}$ ) in transit. The electrical power required from Voyager to keep the inside of the OEC spacecraft at  $-29^{\circ}$  to  $-7^{\circ}\text{C}$  is approximately 9 watts for the design with a movable shutter on the end of the OEC spacecraft. The two passive temperature control designs would require more power from Voyager. The minimum solar panel temperature in transit is  $-192^{\circ}\text{C}$  ( $-314^{\circ}\text{F}$ ). The solar panel can withstand temperatures at least as low as  $-184^{\circ}\text{C}$  ( $-300^{\circ}\text{F}$ ) and probably can be designed to withstand  $-192^{\circ}\text{C}$  ( $-314^{\circ}\text{F}$ ), which is the minimum predicted temperature.

For the booms the primary concern is deflection caused by temperature gradients since the scientific instrument sensors would provide their own thermal control system. The drooped radial booms will be heated on one side more than the other. However, the angular deflection of the sensors on the ends of the booms will be kept within 0.12 degree angle (12 percent of the maximum allowable) without using insulation, by using aluminum booms (1.25 inch diameter tubes with 0.020 inch thick walls) instead of plastic booms. Thermal gradient effects are negligible in the case of the boom located along the spin axis.

The weight penalties associated with the thermal control of the OEC are minimal. The end of the spacecraft in this study was 0.024 inch thick aluminum sheet (or aluminum honeycomb sandwich with 0.012 inch thick facesheets) to prevent large internal temperature gradients. This weight, 2.4 pounds, would be divided between thermal control and structures weight. The insulation and cover sheet weight would be 2.46 pounds. The paint for the inside of the ends of the spacecraft and internal packages would be 0.31 pound. The rotating shutter type of active temperature control (bimetallic strip, linkage, shutter, etc.) would be approximately 0.94 pound. The electrical heater and heater control electronics for the transit phase is 0.2 pound, totaling approximately 5 pounds for the entire system.

#### 6.4.3 Solar Panel

The solar cells were assumed to be the type used on the Applications Technology Satellites ( $\alpha_{\text{solar}} = 0.75$ ,  $\epsilon = 0.78$ ) with a packing factor of 88 percent. The solar panel temperatures shown in Figure 6-29 were calculated assuming they were insulated on the back side. Figure 6-29 shows the solar panel temperature variation due to the seasonal variation in the solar flux and the range of possible solar directions in one Martian year. It did not appear desirable to thermally couple the inside of the spacecraft to the solar panel or part of the solar panels because of their large temperature excursion.

The solar panel steady state temperatures shown in Figure 6-29 were calculated from the following energy balance equation

$$\frac{SA}{\pi} \alpha_1 \cos \theta = \epsilon_1 AF \sigma T^4$$



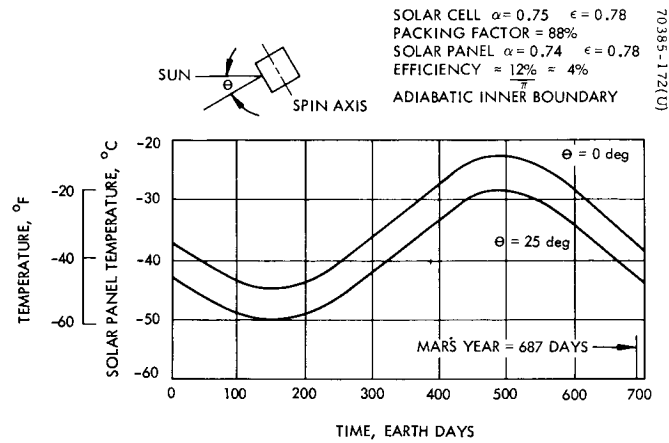


Figure 6-29. Solar Panel Temperature

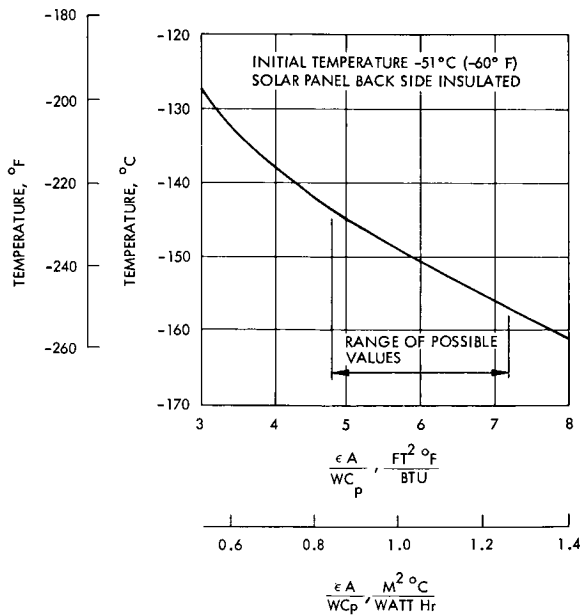


Figure 6-30. Solar Panel Temperature After 2.65-Hour Eclipse

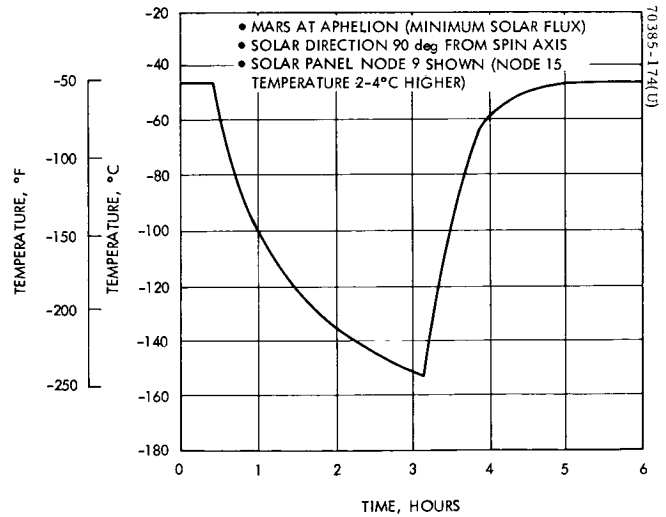


Figure 6-31. Solar Panel Temperature During 2.65-Hour Eclipse Each 15-Hour Orbit

where

$S$  = solar flux

$\alpha_1$  = solar panel effective absorptance, 0.74

$$= \alpha_2(1-N) P + \alpha_3(1-P)$$

$\alpha_2$  = solar cell absorptance, 0.75

$\alpha_3$  = effective absorptance of area between solar cells = 0.95

$N$  = solar panel efficiency  $12\%/\pi \approx 4$  percent (cell efficiency is about 12 percent in direct sunlight but solar panel is rotating)

$P$  = fraction of area covered with solar cells = 88 percent

$\theta$  = angle between plane normal to spin axis and solar direction, degrees

$\epsilon_1$  = solar cell emittance = 0.78

$$= \epsilon_2 P + \epsilon_3(1-P)$$

$\epsilon_2$  = solar cell emittance = 0.78

$\epsilon_3$  = effective emittance of area between solar cells = 0.80

$F$  = view factor to space = 1.0

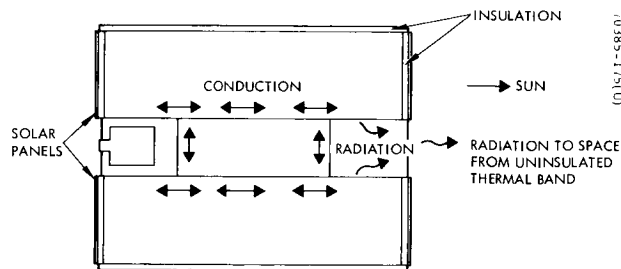
$\sigma$  = Stefan-Boltzmann constant

$T$  = solar panel temperature

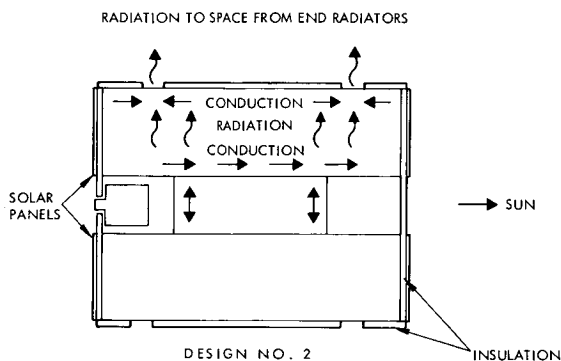
The solar panel temperatures possible after a 2.65 hour eclipse are shown in Figure 6-30. This range of solar panel temperatures was calculated for the range of properties shown in Table 6-8. Figure 6-31 shows the solar panel temperature as a function of eclipse time.

#### 6.4.4 Internal Equipment

The batteries have the smallest range of allowable temperature, and therefore the temperature control system is designed to meet their requirements (see Table 6-9). The batteries require a range of only  $23^{\circ}\text{C}$  ( $4^{\circ}$  to  $27^{\circ}\text{C}$ ) in orbit.



DESIGN NO. 1



DESIGN NO. 2

Figure 6-32. Passive Thermal Designs

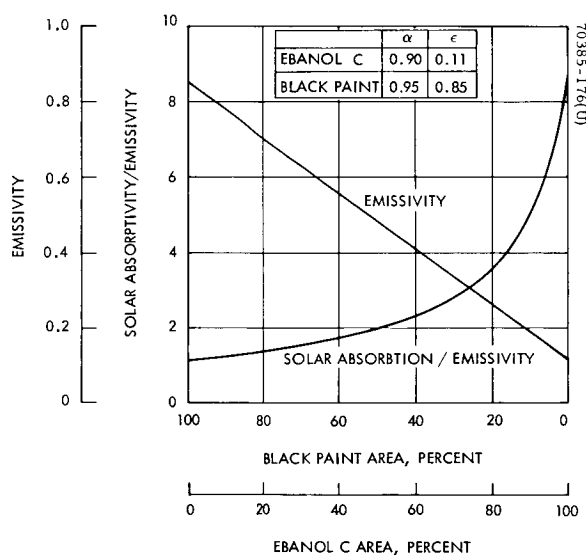


Figure 6-33. Thermal Control Coating Properties

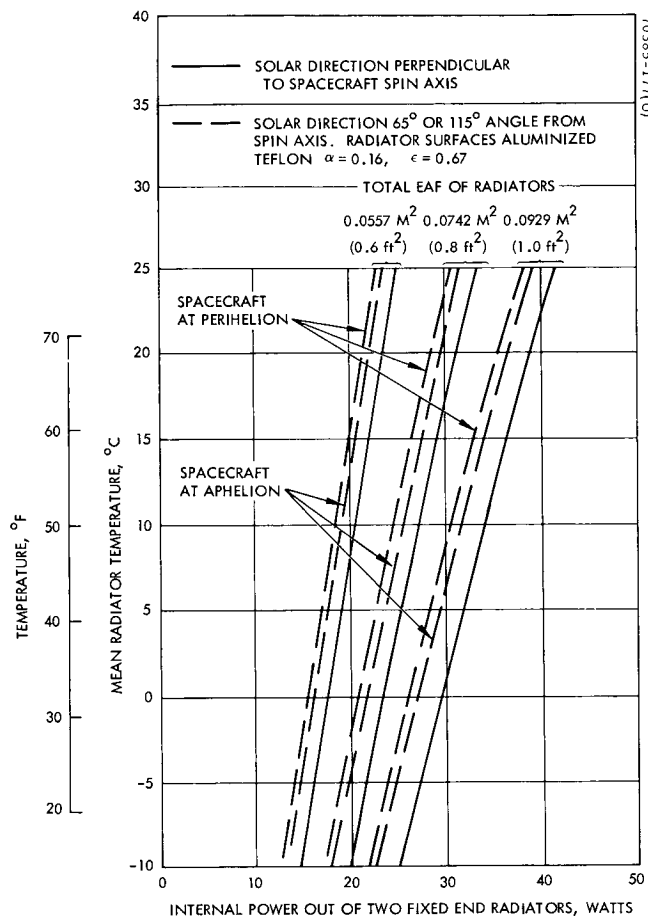


Figure 6-34. Steady State Radiator Temperature Versus Heat Radiated Out to Space

TABLE 6-8. SOLAR PANEL PARAMETERS

Effect of booms neglected; view factor to space assumed to be 1.0

	Value Used in This Study	Probable Range of Values
Emmissivity	0.78	$0.80 \pm 0.02$
Weight per unit area, lb/ft <sup>2</sup>	0.72	$0.72 \pm 0.05$
Mean specific heat, Btu/lb°F	0.2	$0.19 \pm 0.02$
$\frac{\epsilon A}{WC_p}$ , ft <sup>2</sup> °F/Btu	5.4	$6.0 \pm 1.2$

Two passive thermal designs were considered, both with the back of the solar panels insulated (see Figure 6-32). The first design is with the mid-section between the solar panels (approximately 34 inch diameter and 6 inches wide) uninsulated and 70 percent of the area coated with black paint and the remaining area ebonal "C", which is an oxidized copper coat. This will produce a ratio of solar absorptance to infrared emittance ( $\alpha/\epsilon$ ) of 1.5 (see Figure 6-33). This area would radiate out to space the major part of the internal power dissipation. If the net radiated heat flux from this mid-section radiator was about 5 watts per square foot and the internal power dissipation changed 10 watts, the temperature would change 42°C in one Martian year including the effect of the seasonal variation in the solar flux and the unpredictability in the solar direction (90 ± 25 degrees from the spin axis). The temperature drop of the inside of the spacecraft would be about 33°C in the 2.65 hour eclipse.

The second passive design (Figure 6-32) has insulation behind the solar panels and the midsection except where there are small experiment windows. The major part of the internal power dissipation is radiated to the ends and radiated out to space. If the total product of emittance, area, and view factor to space ( $\epsilon AF$ ) of the radiators on the two ends is 0.8 square foot and the internal power dissipation change is 10 watts, then the radiator temperature change would be 33°C in one Martian year (see Figure 6-34). This is 9°C less variation than that of the first design for the same variation in internal power and duration. The change in the internal temperature gradient (total conduction and radiation temperature gradients inside the capsule) for a 10 watt change in power dissipation is less for the second design; if this were included in the comparison, the second design would be even more attractive than the first. In addition, the temperature drop of the spacecraft interior would be only about 14°F in a 2.65 hour eclipse for the second design.

TABLE 6-9. THERMAL CAPABILITIES AND PREDICTED TEMPERATURES

	Thermal Capabilities, °C		Predicted Temperatures, °C***	
	Non-Operating	Operational	Transit Phase Non-Operating	Orbiting Mars Operational
• Batteries (silver cadmium)	-29 to -7 (-20 to 20°F)	4 to 27 (40 to 80°F)	-29 to -7 (-20 to 20°F)**	4 to 27 (40 to 80°F)**
• Experiments*	-50 to 80 (-58 to 176°F)	-10 to 55 (14 to 131°F)	-34 to -1 (-30 to 30°F)**	4 to 32 (40 to 90°F)**
Solar plasma probe				
Electric field meter electronics				
Magnetometer electronics				
• Spacecraft electronics	-32 to 57 (-25 to 135°F)	-18 to 52 (0 to 125°F)	-32 to -1 (-25 to 30°F)	-1 to 38 (30 to 100°F)
• Tanks and valves for hydrazine	-73 to 60 (-100 to 140°F)	4 to 60 (40 to 140°F)	-34 to -1 (-30 to 30°F)**	4 to 32 (40 to 90°F)
• Solar panel	-184 to +120 (-300 to 248°F)	-184 to +120 (-300 to 248°F)	-192 to 65 (-314 to 150°F)	-157 to -22 (-250 to -8°F)

\*The allowable temperature limits of the experimenter's equipment inside the spacecraft will be specified by the equipment unit engineers. The temperatures shown are the limits presently assumed.

\*\*Mounting surface temperatures.

\*\*\*With the active temperature control system.

The third design or recommended approach (Figure 6-35) is an active temperature control system using a movable shutter at one end of the capsule. The shutter is rotated by a bi-metal actuator. The steady state temperature change at the equipment mounting surface inside of the spacecraft is only  $9.4^{\circ}\text{C}$  per 10 watts (assuming the shutter is not full open or closed) compared to  $42^{\circ}\text{C}$  per 10 watts for the second design. (The  $42^{\circ}\text{C}$  change is  $33^{\circ}\text{C}$  radiator temperature change plus  $9^{\circ}\text{C}$  internal gradient change.) These temperature changes include the effect of the sun angle uncertainty of  $\pm 25$  degrees and the seasonal variation in the solar flux from aphelion to perihelion. The total area of the circular shutter is 2 square feet with 1 square foot of its area consisting of pie-shaped holes. The radiator under the shutter is 1 square foot of pie-shaped areas painted white located so that when the bi-metal actuator is  $21^{\circ}\text{C}$  ( $70^{\circ}\text{F}$ ) the shutter is "open;" i.e., the holes in the shutter are over the white painted pie-shaped areas of the radiator. When the bi-metal actuator is  $13^{\circ}\text{C}$  ( $55^{\circ}\text{F}$ ) the shutter is closed;" i.e., the pie-shaped areas are covered by the shutter. The predicted temperatures with this active temperature control system are shown in Table 6-9. Information on the detailed analysis of this active system is given later in this section (see 6.4.6).

#### 6.4.5 Internal Power Dissipation

The electrical power dissipation inside of the spacecraft is a constant 19 watts plus intermittent operation of the primary transmitter that dissipates 22 watts. With the primary transmitter off and the OEC operating in the S-band mode, a constant 16 watts and an intermittent 47 watts for the S-band transmitters are dissipated (see Table 6-10). The possible combinations of power dissipations and eclipse durations are shown in Table 6-11. The maximum temperature cases are those without eclipse and the minimum temperature cases are with a long duration eclipse and assuming that the transmitter is not operated. A computer thermal analysis of the spacecraft nodal model was made for these extreme transient temperature cases at aphelion and perihelion with the solar direction 90 degrees from the spin axis.

#### 6.4.6 Thermal Model

Sixteen lumped masses or nodes were used for the mathematical model of the OEC to calculate the capsule's temperatures with the active temperature control system. The passive temperature control systems were not considered in this much detail because it was obvious they could not satisfy the temperature requirements with the large variations in power dissipation. The nodes are described in Table 6-12. The radiation and conduction heat transfer connections between the nodes are shown in Figure 6-36. The values of the node heat capacities, conductance between nodes, and radiation coefficients between nodes are given in Table 6-13.

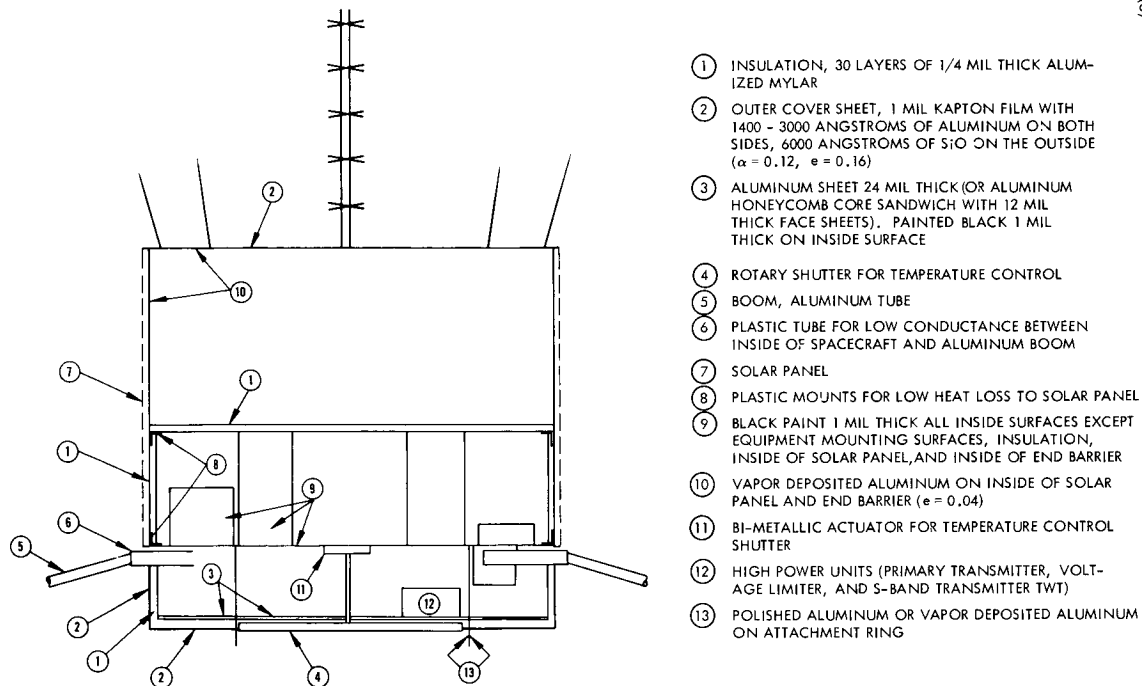


Figure 6-35. Thermal Design No. 3 - Active Temperature Control

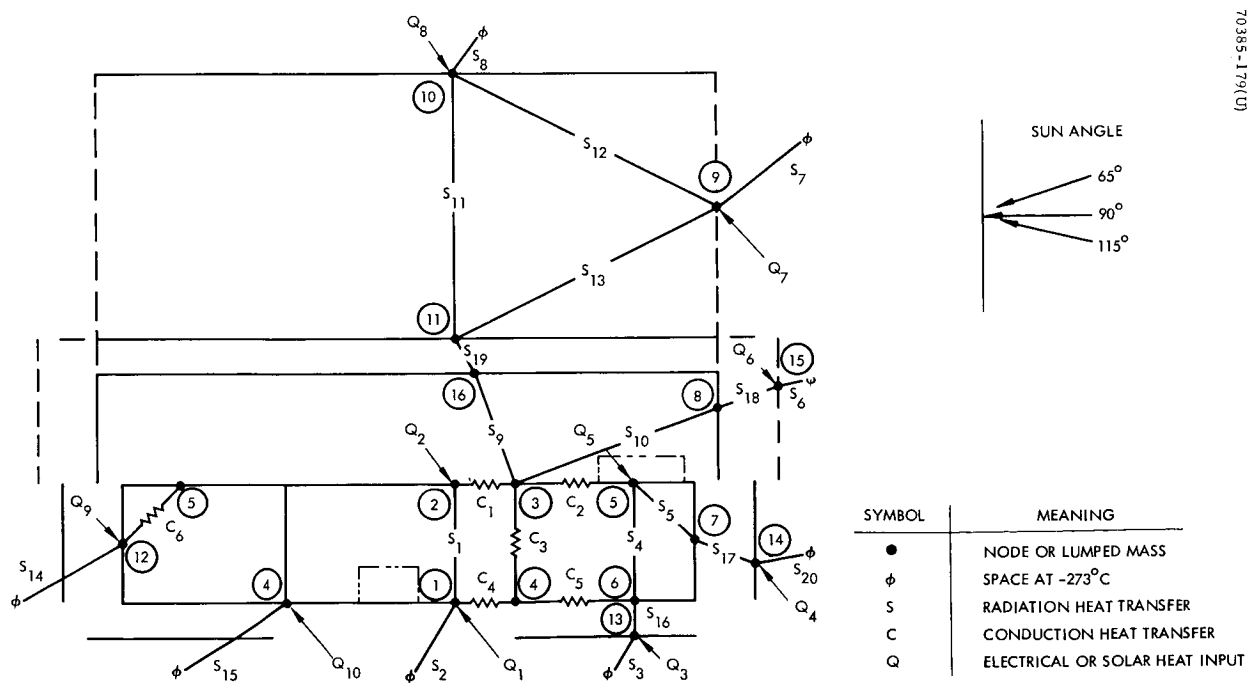


Figure 6-36. Radiation and Conduction Connections Between Spacecraft Nodes

TABLE 6-10. ORBIT-CHANGE SYSTEM INTERNAL POWER DISSIPATION

<u>Primary Mode</u>	
Experiments	10.0
Tape recorder (average)	3.0 (2 watts for 5 hours; 5 watts for 2 hours)
Encoder	2.0
Phase lock-loop	0.5
Receiver and decoder	<u>3.5</u>
Total	19.0 watts constant
Primary transmitter	22.0 watts (55 watts in, 33 watts out)
<u>S-Band Mode</u>	
Experiments	10.0
Encoder	2.0
Phase lock-loop	0.5
Receiver, transponder, and decoder	<u>3.5</u>
Total	16.0 watts constant
S-band transmitter	47.0 watts (57 watts in, 10 watts out)

TABLE 6-11. POSSIBLE POWER DISSIPATIONS AND ECLIPSE DURATIONS

	In Sunlight			In Eclipse	
	Hours	Constant Power, watts	Transmitter Power, watts*	Hours	Watts
<u>With Primary Transmitter</u>					
7-hour orbit					
Maximum temperature case	7	19	22 for 2 hr	0	
Minimum temperature case	5.5	19	0	1.5	19
15-hour orbit					
Maximum temperature case	15	19	22 for 4 hr	0	
Minimum temperature case	12.35	19	0	2.65	19
<u>Orbit with S-Band Transmitter</u>					
7-hour orbit					
Maximum temperature case	7	16	47 for 2 hr	0	
Minimum temperature case	5.5	16	0	1.5	16
15-hour orbit					
Maximum temperature case	15	16	47 for 2 hr twice per orbit	0	
Minimum temperature case	12.35	16	0	2.65	16

\*The power into the primary transmitter is 55 watts, but the power dissipation is only 22 watts. The input to the S-band transmitter is 57 watts and the power dissipation is 47 watts.



#### 6.4.6.1 Thermal Model Results

The capsule steady state heat balances for "cold" and "hot" examples are shown in Table 6-14. The cold conditions are for the spacecraft at aphelion, solar direction 65 degrees from the spin axis (sunlight on the antenna end of the spacecraft), and low power dissipation. The hot conditions are for the spacecraft at perihelion, solar direction 115 degrees from the spin axis (sunlight on the experiment section end of the spacecraft), and high power dissipation. The capsule internal steady state temperatures for cold conditions, nominal conditions, and hot conditions as a function of internal power dissipators are shown in Figure 6-37.

The solar panel transient temperatures during a 2.65 hour eclipse are shown in the discussion of the solar panel temperatures. The interior of the OEC has a mean temperature drop of only 2°C in the 2.65 hour eclipse because the minimum internal power dissipation (16 watts) is almost equal to the heat losses to space from the insulated section of the capsule.

The OEC interior temperatures with the primary transmitter assumed to be operating 4 hours each 15-hour orbit are shown in Figure 6-38a. The temperatures of the capsule interior structure modes that are not shown in these figures are within the limits shown. The capsule interior temperatures satisfy the equipment requirements but the battery mounting surface maximum temperature is at the maximum allowable temperature.

The interior temperature with the S-band transmitter operating at 47 watts dissipation for 2 hours each 7-hour orbit is shown in Figure 6-38b. The constant power dissipation was assumed to be 19 watts; later analysis indicated this value to be 16 watts.

The temperatures in the last two figures would be higher if the solar angle were 115 degrees (sunlight on the radiator) rather than 90 degrees. This would cause the battery to be overheated. Lowering the temperature range at which the shutter opens and closes by 10°C and possibly reducing the duration of S-band transmitter operation should keep the battery temperatures within allowable limits.

#### 6.4.6.2 Transit Phase

In transit, the capsule is attached to the Voyager and the shutter is covered by this attachment region. Only 9 watts of electrical power is required from Voyager. Four watts at node 1 makes the temperature inside of the capsule  $-18 \pm 2^\circ\text{C}$  ( $0 \pm 4^\circ\text{F}$ ) and the solar panel  $-192^\circ\text{C}$  ( $-314^\circ\text{F}$ ) at node 15. Five watts at node 11 makes the solar panel temperature  $-185^\circ\text{C}$  ( $-301^\circ\text{F}$ ) at node 9. These calculations were based on the worst case condition, which assumes no infrared heat input and conduction input from the Voyager. These minimum solar panel temperatures actually would occur only on the outboard side facing space.

The worst thermal shock on the solar panel would be at a midcourse correction if the Voyager maneuvered so that the sunlight direction would be normal to the solar panel surface. The solar panel rise rate would depend on the distance to the Sun at that time and the rate of change of the Voyager direction; it would be less

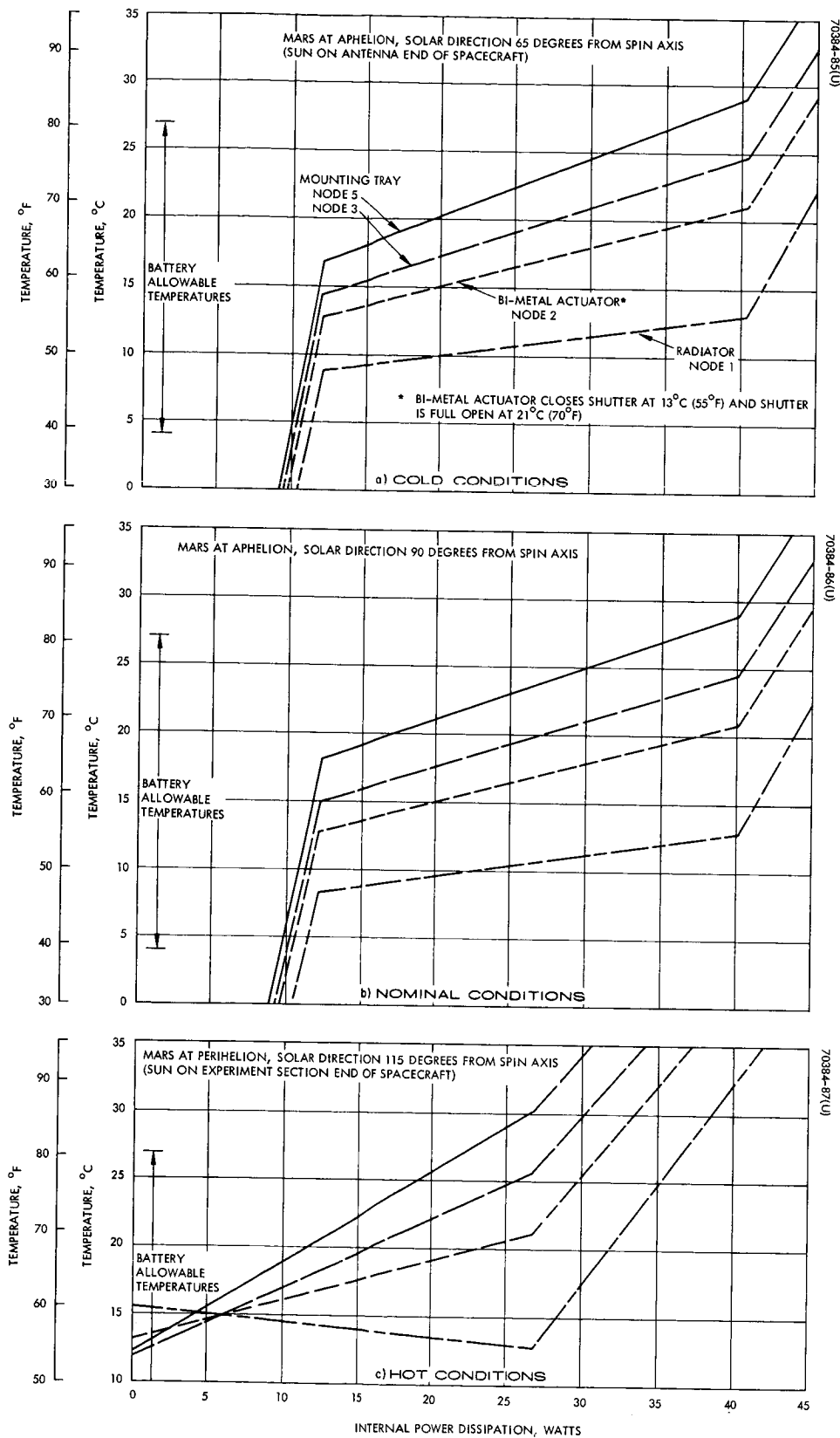


Figure 6-37. Spacecraft Steady State Temperatures

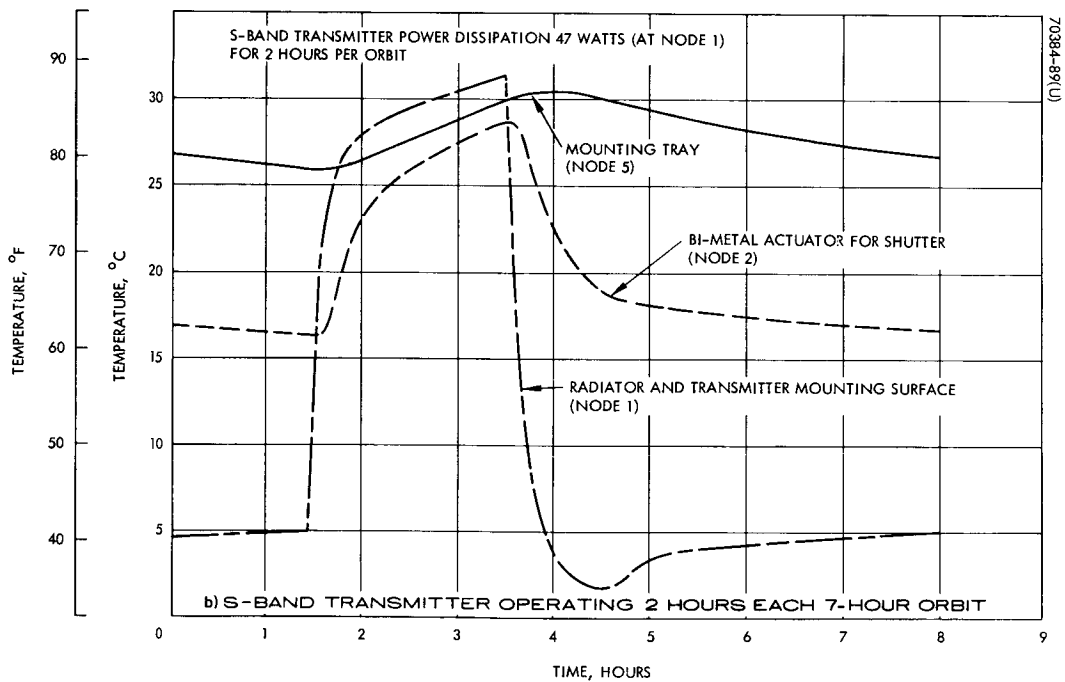
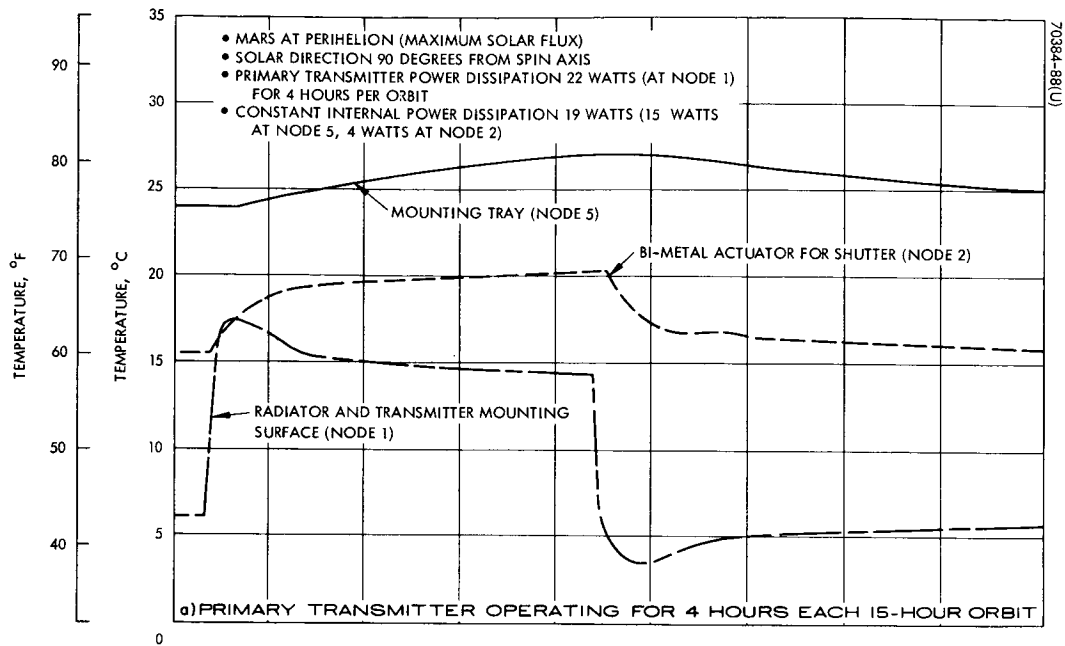


Figure 6-38. Spacecraft Interior Temperatures

than 21°C/minute (38°F/minute) which was calculated assuming a solar distance of 1 AU, the solar direction normal to the solar panel surface, and neglecting the reradiation heat loss from the solar panel.

The present plan is to fabricate the solar panels to withstand -314°F (the minimum calculated temperature) and the thermal shock. If this cannot be accomplished by 1973, two design alternatives available:

- 1) Use electric heaters on the back side of the solar panels and use about 12 watts from Voyager to keep the solar panel temperature above some temperature such as -160°C (-250°F) which would provide a margin of safety.
- 2) Use a sheet of insulation to cover the outboard side of the solar panels during the transit phase.

#### 6.4.7 Materials, Hardware, and Weights

Insulation. The insulation is 30 layers of 1/4 mil thick aluminized mylar with an effective emittance from the inside sheet to the outer sheet of 0.01 (see Figure 6-39). The insulation weighs 0.081 lb/ft<sup>2</sup> for 30 layers.

Outer Cover Sheet. The outer sheet of the insulation for the experiment section and the antenna end of the spacecraft can be 1-2 mil thick Teflon or Kapton film, both sides aluminized 1400 to 3000 angstroms thick and 6000 angstroms of silicon monoxide on the outside. The outside solar absorptivity will be 0.12 and emissivity 0.16.

Paint for Inside of Spacecraft. The black paint for the inside of the spacecraft (except insulated and mounting surfaces) will be 1 ± 1/4 mil thick. It will have an emissivity of 0.86.

Comparison of White Thermal Coatings for Active Temperature Control Radiator. Four possible coatings for the active temperature control radiator are 1) Z-93, which is zinc oxide (PS-500) pigment and potassium silicate binder; 2) Hughes white, which is aluminum silicate (clay) pigment and potassium silicate binder; 3) H-10, a Hughes developed coating that is a clay pigment in a silicone binder; and 4) modified S-13G, a potassium silicate sealed zinc oxide pigment in a silicone binder.

The Z-93 coating will be manufactured from the raw materials. The SP-500 zinc oxide is available from New Jersey Zinc, and the PS-7 electronic grade potassium silicate is obtained from Sylvania Electric. Care must be exercised during manufacturing to prevent the yellowing that occurs when the ZnO undergoes excessive grinding or mechanical working. The shelf life problem of this paint must also be considered. The major effect here is loss of adhesion with increased time between manufacture and application of the paint. Excellent adhesion is obtained for coatings applied within 3 days of paint manufacturing. The adhesion is good if the paint is applied within 6 days after it is manufactured. Paint older than 6 days should not be used. The surface is prepared for application of Z-93 type coatings by sandblasting

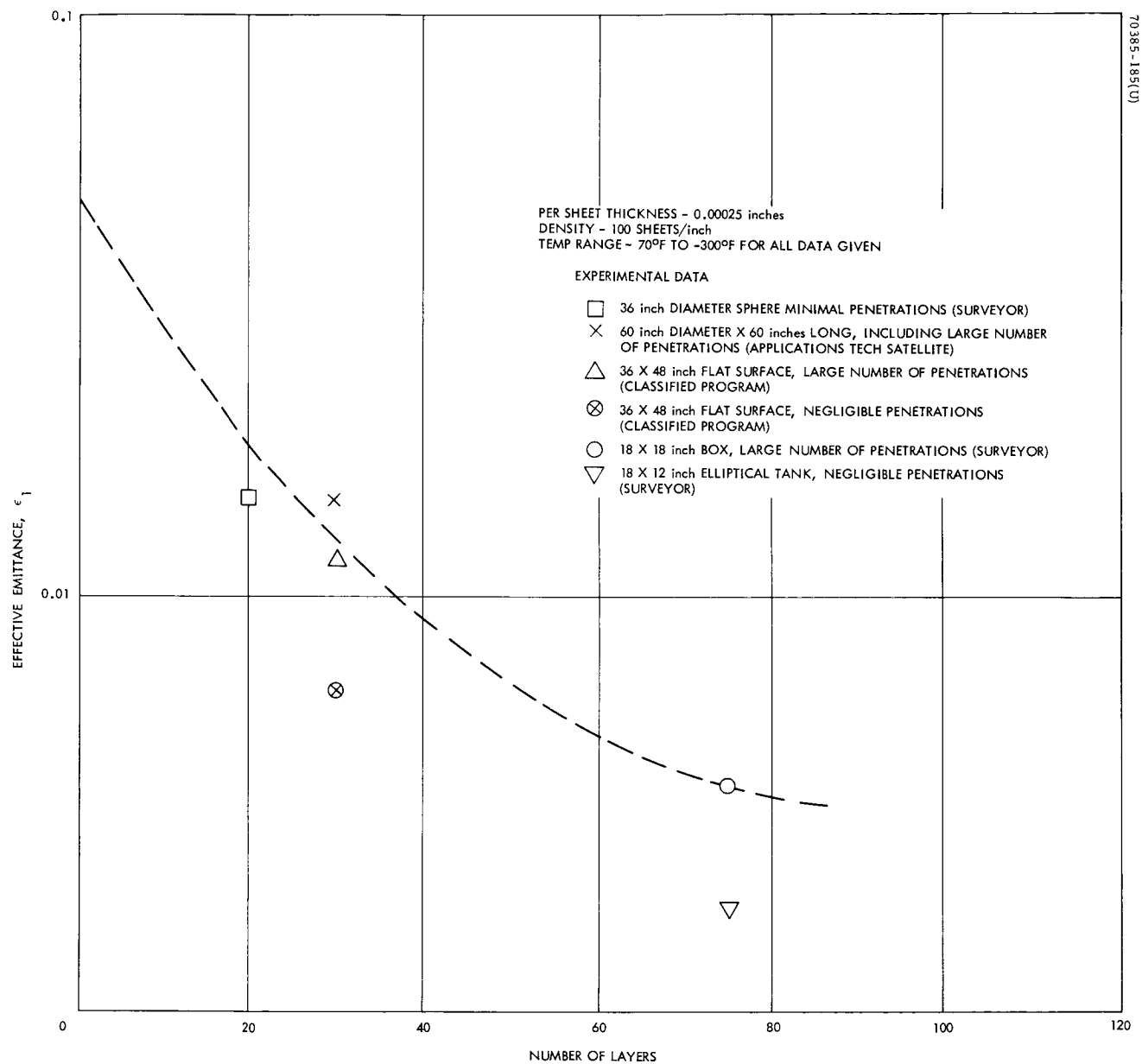


Figure 6-39. Performance of Multiple Layer Aluminized Mylar Insulation

TABLE 6-12. SPACECRAFT NODE DESCRIPTION

Node	Description
1	2 square foot active temperature control radiator; high power units (transmitters and voltage limiter) are mounted here.
2	Area on mounting tray adjacent to 2 square foot active temperature control; shutter bi-metal actuator is located here.
3	Mounting tray and central structure.
4	Structure; a fixed radiator can be located here if it is needed.
5	Mounting surface for electronic equipment and experiments (except solar plasma probe which is at node 12).
6	Aluminum sheet 0.024 inch thick.
7	Inside surface of insulation on side of the experiment section.
8	Inside surface of insulation on back of 10 inch high section solar panel.
9	Solar panel, 16 inch high section, with vapor deposited aluminum on back side (inside $\epsilon = 0.04$ , outside $\alpha = 0.74$ , $\epsilon = 0.78$ ).
10	End barrier, vapor deposited aluminum (VDA) on inside ( $\epsilon = 0.04$ ), VDA and $\text{SiO}_2$ on outside ( $\alpha = 0.12$ , $\epsilon = 0.16$ ).
11	Outer surface of insulation facing end barrier ( $\epsilon = 0.04$ ).
12	Solar plasma probe and its window.
13	Outer surface of insulation on end of experiment section ( $\alpha = 0.12$ , $\epsilon = 0.16$ ).
14	Outer surface of insulation on side of experiment section ( $\alpha = 0.12$ , $\epsilon = 0.16$ ).
15	10 inch high section of solar panel insulated on back side.
16	Inside surface of insulation facing electronic equipment ( $\epsilon = 0.04$ ).

TABLE 6-13. THERMAL PARAMETERS

Number	Heat Capacity, Btu/°F	Conductance, Btu/hr °F	Radiation Coefficient, $10^{-10}$ Btu/hr °R <sup>4</sup>
1	0.63	2.3	20.0
2	0.78	3.62	3.4 if shutter closed 16.4 if shutter open
3	2.32	0.55	14.0
4	0.45	1.48	52.0
5	7.3	2.3	2.6
6	0.23	3.8	105.0
7	0.11		16.9
8	0.16		20.0
9	1.53		4.6
10	0.17		5.0
11	0.15		1.34
12	1.1		2.09
13	0.11		2.1
14	0.11		0.065
15	0.95		0 (no fixed radiator)
16	0.15		0.86
17			0.95
18			1.35
19			1.2
20			15.0

TABLE 6-14. SPACECRAFT STEADY STATE HEAT BALANCE

Location	$\alpha$	$\epsilon$	Net Heat Loss, Watts	
			Cold Example*	Hot Example**
Insulated solar panel, 10 inches high x 36 inches diameter			2.0	1.7
Solar panel outside	0.74	0.78		
Insulation inside surface	--	0.04		
Experiment section side, 7 inches high x 36 inches diameter			1.4	1.3
Outside surface	0.12	0.16		
Inside surface	--	0.04		
Experiment section end, 36 inch diameter			2.2	1.2
Outside surface	0.12	0.16		
Inside surface	--	0.04		
Insulated bulkhead at mid-section	--	0.04	1.4	1.4
Active temperature control			7.9	24.3
Radiator	0.2	0.86		
Shutter	0.2	0.1		
Solar plasma probe window			0.1	0.1
Cavity painted black	0.96	0.86		
Gold plate around cavity	0.28	0.03		
TOTAL			15.0	30.0

\*At aphelion, internal power dissipation 15 watts (at node 5), ATC shutter in closed position, solar direction 65 degrees from spin axis (Sun on antenna end of spacecraft).

\*\*At perihelion, internal power dissipation 30 watts (11 watts at node 1, 15 watts at node 5, and 4 watts at node 9), ATC shutter in open position, solar direction 115 degrees from spin axis (Sun on experiment section end of spacecraft).



with a #120 grit aluminum oxide. Hand scrubbing of surfaces does not adequately clean the surface for application of the paint. Final baking of paint is done at 250° to 270°F for 1 to 2 hours. The adhesion of the coating as well as its hardness are directly related to this required final bake.

The Hughes white coating is similar to the Z-93 type coating. The clay pigment is obtained from Standard Industrial Minerals located in Bishop, California. Manufacturing and shelf life are not critical items in preparation. Normal ceramic practice is followed in calcining, then grinding the pigment into a usable paint. The shelf life of the material is in excess of 60 days. The surfaces are prepared by hand scrubbing, although sand blasting can be used. Application and curing are similar to the Z-93 type coating.

Both Z-93 and Hughes white paints become contaminated quite easily. The contamination soaks into the porous coating and is difficult to remove. The Hughes white has an advantage over the Z-93 type in that it can be sanded to remove contamination. The Z-93 must be cleaned using great care. Sanding with two heavy a grit sandpaper produces a mechanical strain in the ZnO crystals and produces a yellowish coating.

The white coat properties are shown in Table 6-15. There may be some additional increase in the solar absorptivity due to the solar wind damage.

The maximum solar ultraviolet inputs to the white coat on the active temperature control radiator surface during 6 months in the Mars orbit at the minimum and maximum solar intensities at Mars are equivalent to 7000 to 1100 hours respectively at one astronomical unit from the Sun. These maximum times were calculated assuming that the active temperature control shutter was open all of the 6 months in orbit and for the worst solar direction (25 degrees from the plane of the white surface).

TABLE 6-15. WHITE COAT PROPERTIES

	Emissivity	Solar Absorptivity		
		Initial	After 500 ESH*	After 1000 ESH*
Z-93	0.88	0.16	0.18	0.18
Hughes white	0.87	0.18	0.22	0.23
H-10	0.88	0.18	0.19	0.20
Modified S-13G	0.88	0.18	0.19	0.19

\*Equivalent solar hours of ultraviolet radiation at one astronomical unit from the Sun, test sample at 38°C (100°F)

The white coat properties used in the thermal analysis for the OEC radiator were 0.2 solar absorptivity (constant) and 0.86 emissivity. An increase in the white coat solar absorptivity from 0.2 to 0.24 will increase the heat input to the spacecraft by 1 watt and will increase the spacecraft temperature by 1°C if the shutter is open.

Active Temperature Control. The rotating shutter for temperature control is 19.7 inch diameter circle with 50 percent of the area cut open with pie-shaped holes. The shutter is of the type used on the Hughes Applications Technology Satellites. It is a sandwich constructed of 0.012 inch thick face sheets and aluminum honeycomb core 0.34 inch and would weigh 0.68 pound. The bi-metal actuator was assumed to weigh 0.2 pound. The shaft from the actuator to the shutter would be 0.01 pound. Miscellaneous items were assumed to be 0.05 pound, giving a total weight of 0.94 pound

Weights. The weights for temperature control are shown in Table 6-16.

TABLE 6-16. WEIGHTS FOR THERMAL CONTROL

• Electric heater and heater control for transit phase*	0.2
• <u>Shutter</u> – (ATS type) and bi-metal actuator	0.94
• <u>Paints</u> – 1 mil thick 30 square feet inside of spacecraft, 6 mil thick 1 square foot for radiator under shutter	0.31
• <u>Multilayer insulation</u> – 30 sheets of 1/4 mil thick aluminized mylar, 25.6 square feet total area	2.08
• <u>Cover Sheet</u> – 2 mil thick plastic (Teflon or Kapton) for experiment section and antenna end 17.7 square feet	<u>0.38</u>
	3.91 pounds
• <u>Radiator</u> (under shutter) and end bulkhead for experiment section, assumed 0.24 inch thick aluminum, 7 square feet. Major portion of this weight can be charged to structural weight. Large thickness might not be neces- sary for good thermal control; therefore this weight might be reduced.	

\*Same as type used on Surveyor spacecraft.

#### 6.4.8 Nomenclature

G	Heat capacity, $WC_P$
C	Conductance, $\frac{KA_c}{L}$
S	Radiation coefficient, $\sigma \bar{t} A_R$
W	Weight
$C_P$	Specific heat
$A_C$	Conducting area
$A_R$	Radiating area
K	Thermal conductivity
L	Length of conducting path
$\bar{t}$	$e\bar{F}_s$ , or $e_i e_j F_{ij}$ , or overall radiation interchange factor
e	Emissivity
F	Geometric shape factor
$F_s$	View factor to space
Q	Heat input. electrical power dissipation or solar heat
$\sigma$	Stefan-Boltzman constant

## 6.5 SENSORS SUBSYSTEM

### 6.5.1 General

The requirement to establish the inertial location and attitude of the OEC necessitates the consideration and selection of on-board OEC equipment to furnish such data. For the information required to provide such data, a number of techniques were investigated and are discussed in this section and Section 2.5.4 of Volume II.

The implementation of these techniques is covered here. For the baseline OEC configuration, two types of sensors, a Sun sensor and Mars horizon sensor, were selected. The consideration of a third data source to improve required accuracies, such as the addition of a star sensor or the use of ranging techniques, is covered in Section 2.5.4 of Volume II. A preliminary evaluation of incorporating a star sensor has been made; it appears to offer a substantial improvement to the baseline system for relatively small weight and power demands. A preliminary design using Canopus as a reference is presented in Appendix D.

### 6.5.2 Sun Sensors Description

The sun sensor assembly consists of two identical sensor units, as depicted in Figures 6-40 and 6-41.

The sensor assembly is a small, rugged package that is well able to withstand typical launch and orbital environments. The cell is bonded to the sensor housing with an epoxy cement -- fiberglass combination that protects the cell from any damage due to thermal expansion effects in addition to securely holding it in the proper position. The width of the viewing slits is very stable once they are adjusted, due to the mechanical strength of the sensor halves and the use of metal shims. Each sensor unit consists of an n-on-p silicon photovoltaic cell, a load resistor, and two clam-like aluminum shells. A narrow gap between the clam shells defines the narrow, fan-shaped field of view of the sensor. When the sun-line and the sensor field of view coincide, the silicon cell is illuminated and an output pulse produced. When the spin axis is aligned along the ecliptic normal, both sensors receive the solar energy at the same time. However, if the vehicle is tipped in either direction, there is a time difference between the two pulses ( $\psi$  and  $\psi_2$ ), as indicated in Figure 6-42. The plane of one fan-shaped field of view is nominally parallel to the spin axis, while the other is canted to it as indicated in Figure 6-43. Selection of the inclination angle between the two fields of view is based on considerations for pulse width, scan time, and accuracy. An angle of 35 degrees represents an optimum angle of inclination.

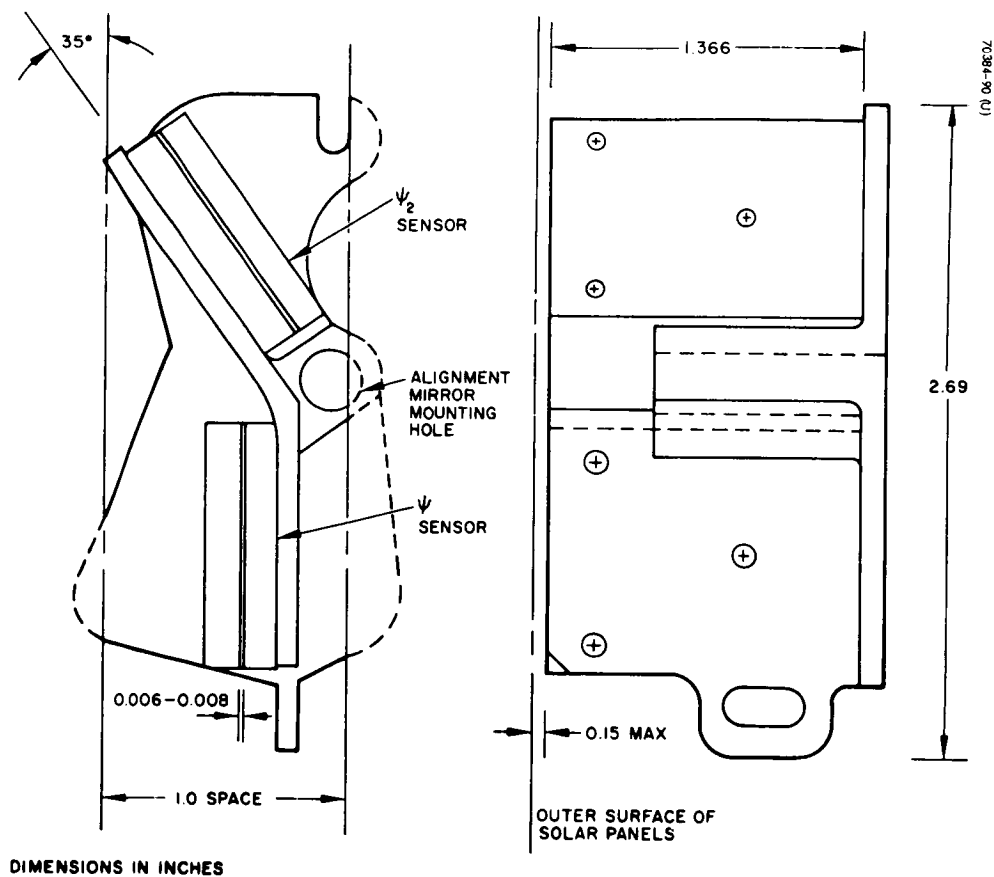


Figure 6-40. Sun Sensor Assembly

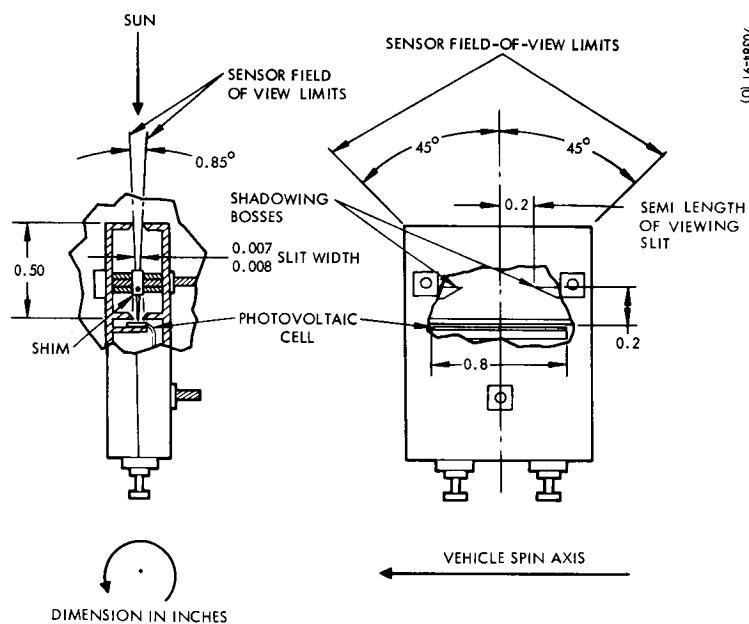
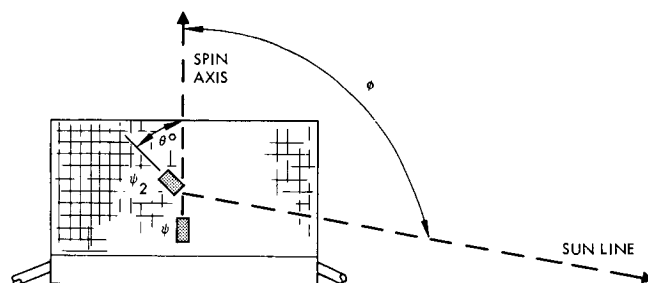


Figure 6-41. Schematic Diagram of Sensor Unit



- ANGLE BETWEEN SUN LINE AND SPIN AXIS DETERMINED BY TIME INTERVAL BETWEEN  $\psi$  AND  $\psi_2$  PULSES

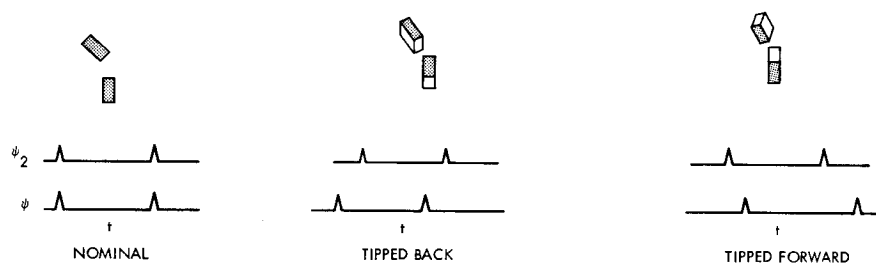


Figure 6-42. Spacecraft Attitude as It Affects Relative Position of  $\psi$  and  $\psi_2$  Pulses

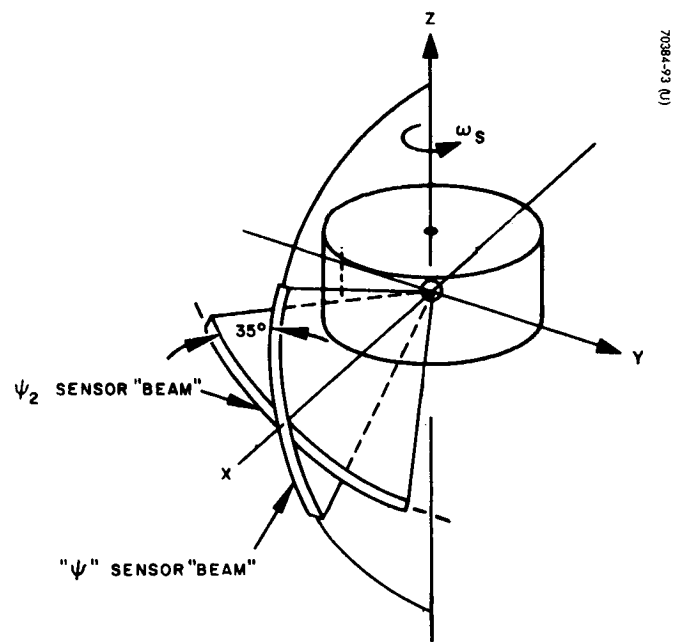


Figure 6-43. Sun Sensor Geometry

The electrical output signal from the sensor is a function of the input energy from the sun that falls on the cell, the load resistor, and the diode loading effect of the unilluminated area of the cell. A typical sensor output pulse is shown in Figure 6-44, and the voltage output at the  $\psi$  and  $\psi_2$  sensors is shown in Figure 6-45. This width, plus the 21-arc minute angular size of the sun at Mars distance, results in a nominal  $\psi$  pulse width of approximately 1.25 degrees. (Due to the 35-degree inclination of the  $\psi_2$  sensor, its nominal pulse width is  $1.25/\cos 35 \text{ degrees} = 1.53$  degrees).

As shown in Figure 6-41, the length of illuminated cell area is approximately 0.4 inch. Thus the nominal illuminated area is  $0.4 \times 0.0075 \text{ inch} = 0.003$  square inch. The defined field of view of the sensor is  $\pm 45$  degrees from the normal to the cell's surface. At angles greater than 45 degrees to the cell, the illuminated area (and consequently the sensor output) drop off sharply. The complete sensor assembly weighs approximately 0.15 pound. The angle between the spin axis and sunline ( $\phi$ ) can be determined to  $\pm 0.5$  degree on a per pulse basis. By ground and in-flight calibration of the actual unit, and by smoothing the data over a number of measurements, the  $\phi$  angle uncertainty can be reduced to approximately  $\pm 0.2$  degree ( $3\sigma$ ).

### 6.5.3 Horizon Sensor Description

The basic Mars sensor unit is similar to the unit being developed for the Hughes HS-308 satellite. This Mars sensor system assembly is shown in Figure 6-46. Two narrow-beam IR sensors in a common housing assembly are arranged with one unit pointing at 21 degrees above and one unit 21 degrees below the central line of sight.

Each of the two sensor units has three mounting bosses that define a plane whose relationship to the sensor optical axis is constructed to be within 0.05 degree. These mounting bosses in turn mate with accurately located bosses on each sensor assembly housing. The housing for each unit incorporates alignment references (such as an accurate hole and slot) that accommodate an alignment fixture. The alignment fixture has mirrors that permit the use of autocollimation techniques for alignment during the final assembly of the vehicle. The weight of the two sensor units is less than 3 pounds.

The sensor consists of a coated germanium optical system, a multilayer interference filter, an immersed thermistor bolometer detector, and processing electronics. The detector element is masked to precisely define the sensor field-of-view limits. The most fragile part of the sensor units is in the IR telescope, including the optics, filter, and detector. The front part of the sensor in which the telescope is located will be supported to ensure that resonance amplification is negligible. The vibration and shock environments for this mission are expected to be consistent with the environments normally encountered by similar sensors.

A nominal OEC spin speed of 60 rpm is assumed to determine Mars scan time. The scan angle at 10,000 km distance is 30 degrees and the duration is 83.3 milliseconds. These values vary with the OEC orbit position or altitude.



Various types of indicators could be considered for this task, but most visible light indicators have difficulty contending with diurnal effects. By operating in the infrared spectrum, these effects are avoided. Many successful satellite designs implementing infrared horizon sensing technology have proven the concept in an earth environment. The differences between the IR characteristics of Earth and Mars require adaptation of such a sensor to the expected Mars environment. There are, however, certain uncertainties in establishing the characteristics of the planet Mars that must be established. Information about Mars is generated from Earth based measurements. The difficulty of defining the horizon characteristics exists because many areas of the spectrum are opaque as measured through the Earth's atmosphere. Much of the available data falls within a 7 to 13 micron portion of the spectrum. Because this data is the only source of spectral information available pertaining to the Martian atmosphere, it appears reasonable to design the instrument for this known spectral region.

Because of the OEC's wide range of possible attitudes, the sensor will at some times scan the Mars poles. Because of the lack of sufficient atmospheric detail, a conservative design approach is to account for the worst case temperature variation.

Based on actual observations, the temperature varies from  $300^{\circ}$  K in the summer at the Mars equator to a low of  $200^{\circ}$  K at the winter pole. An analytic comparison of the minimum stratospheric temperature of Earth to Mars establishes a slightly lower minimum value of  $170^{\circ}$  K. The expected Mars radiance level can be determined using the above extremes of  $170^{\circ}$  to  $300^{\circ}$  K. As a result, an expected dynamic range of radiance ratio of 1:19 is obtained.

At the lower extreme of  $170^{\circ}$  K, Mars will radiate  $390 \text{ microns/cm}^2$  in the 10 to 12.5 micron spectral range. A thermistor bolometer and optical system similar to that used in HS-308 is used as a basic reference design model. This sensor is similar to the TIROS sensor but has increased accuracy.

The Mars horizon sensor design is optimized for the operational conditions specified above. The optical system is comprised of a germanium immersed bolometer, spectral filters, and a germanium objective lens which attenuates the peak signal by about a factor of 4. The schematic is shown in Figure 6-47.

A square field of view is sized with dimensions of 1.5 degrees on a side. This yields a scan path of approximately 2.1 degrees. Selection of an objective lens of 1.125 inch diameter will provide 0.14 microwatts minimum irradiance to the bolometer detector. The minimum signal of approximately 100 microvolts is generated when operative on an assumed 170 volt dc bias. This signal is sufficiently above the noise level for proper instrument operation.

Generally the signal that occurs when viewing the planet is capacitive coupled to the amplifier input to cause a "pip" for the ON and OFF transition. As the horizon sensor views the transition region from space energy levels to the planet, a signal builds up from the nominal off level to the peak expected signal. The actual location of the horizon falls between the minimum and maximum extremes of this signal.

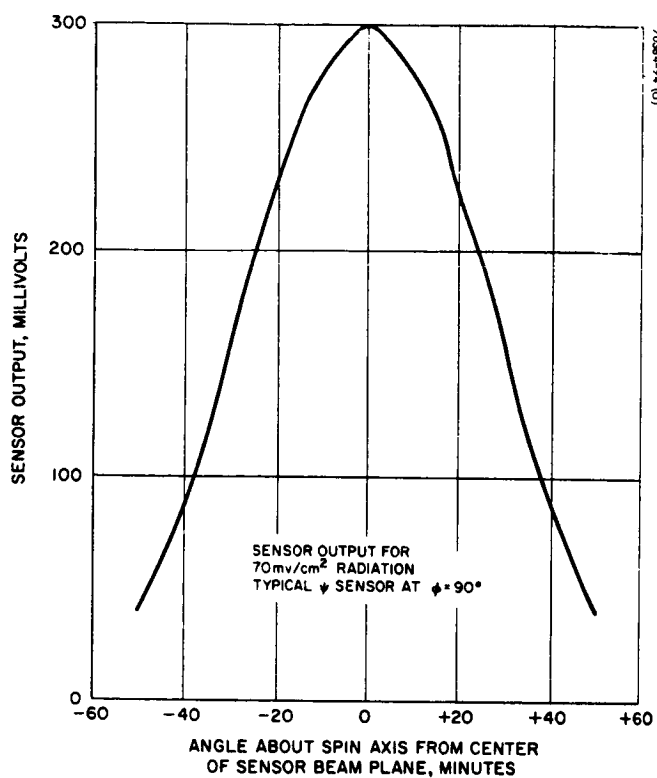


Figure 6-44. Typical Sun Sensor Output

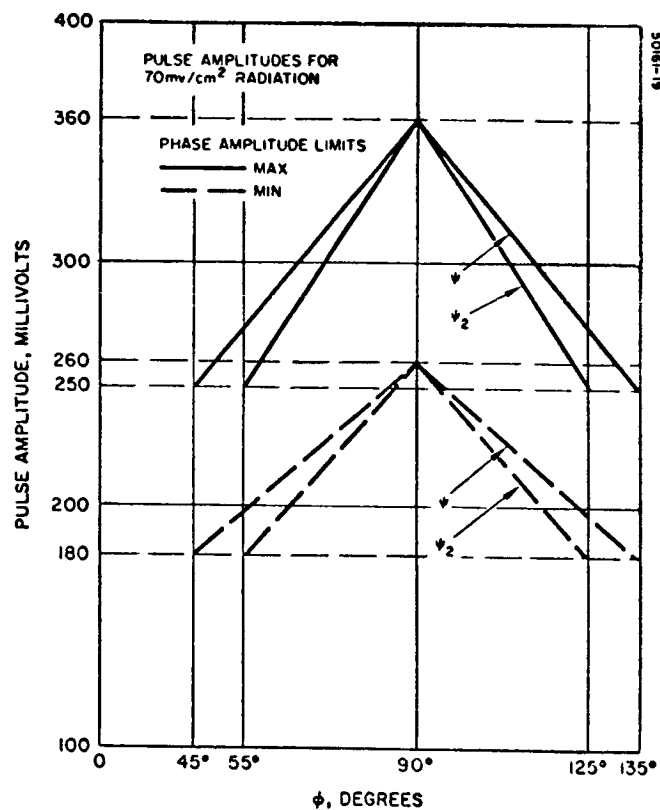


Figure 6-45. Solar Sensor Output Versus  $\phi$  Angle

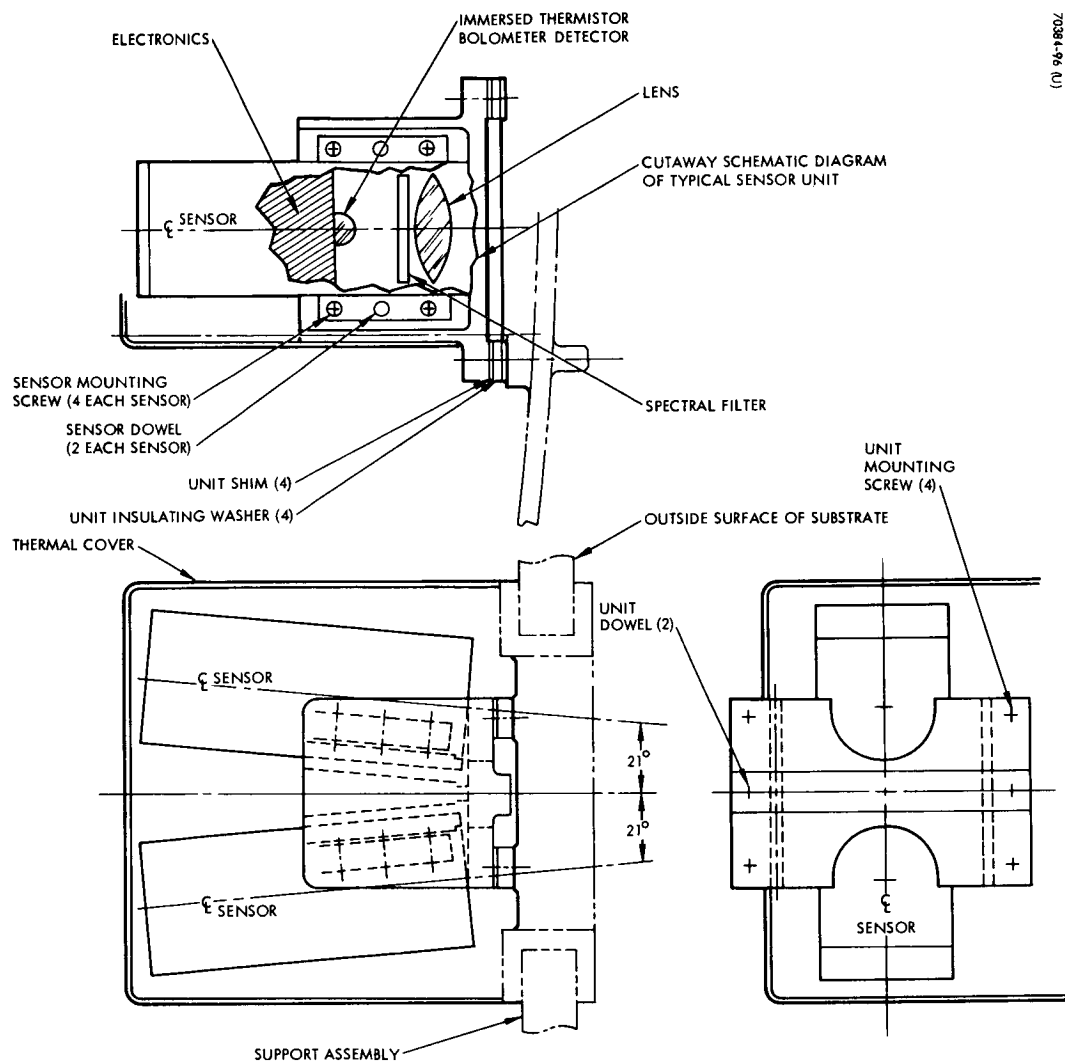


Figure 6-46. Mars Sensor Assembly

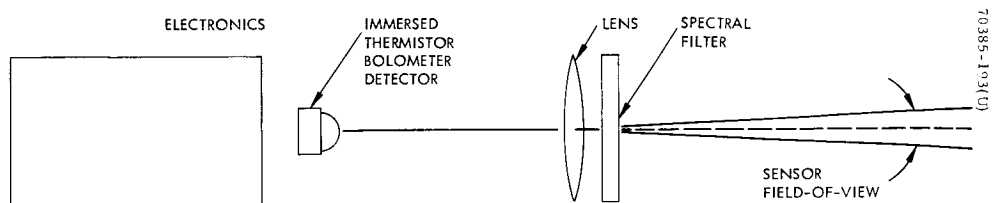


Figure 6-47. Schematic Diagram of Pencil Beam Horizon Crossing Indicator

The minimum allowable voltage level required to trigger the Mars sensor has been established as 100 microvolts. In designing the circuit logic, it is desirable to allow for uncertainties in the expected signal such as cold spots on the planet by thresholding at a lower voltage level; for this design, a 80 microvolt level was chosen.

In determining the horizon, it is required to establish the signal change mentioned above. To do so does not require measuring the total signal amplitude. It suffices to measure only a portion of the signal that is necessary to establish a pulse representing the ON or OFF planet condition. A 200 microvolt upper bound is used to clip the signal, which is then differentiated in the sensor circuitry to provide the pulse.

The minimum signal level is a bound in the uncertainty in horizon crossing. This is because the sensor aperture must be almost completely illuminated before the threshold is exceeded, meaning that the sensor line of sight has passed the horizon. Conversely, if a very hot horizon is observed, only a partial illumination of the aperture is required to exceed the 80 microvolt threshold. The uncertainty in horizon crossing is the difference in angle or time between these two extremes.

Errors due to the constant voltage threshold are a direct function of spin speed. At 60 rpm, the crossover time is 5.6 milliseconds. By normalizing the position of the horizon with respect to the threshold point, the error of the horizon indication would be about  $\pm 0.72$  degree. Instrument noise error could increase the sample to sample error to about  $\pm 0.8$  degree ( $3\sigma$ ). However, by using data smoothing techniques, most of the noise errors would be averaged out. Thus it appears that a chord measurement of  $\pm 1.1$  degrees ( $3\sigma$ ) is possible on a particular spin cycle. In terms of spin axis accuracy about the local vertical, an unsmoothed error of  $\pm 1.5$  degrees is expected.

There are other facets of the sensor design that should be accounted for. The basic uncertainty in the atmospheric characteristics of Mars warrants a similar design study in, say, the 14 to 40 micron spectral bandpass. In this regime, the radiance levels are not as sensitive to thermal variations. In addition, consideration should be given to application of circuit logic indicating when the trailing edge signal should occur. This could increase the sensor accuracy.

Since the horizon sensing detector is a thermal device, the environmental temperature variations are important. Generally,  $0^{\circ}\text{F}$  minimum temperature is considered necessary to ensure a high reliability. Detector temperatures above  $140^{\circ}\text{F}$  accelerate the aging of the detector and in addition, there is a permanent increase in the instrument noise. These requirements are not severe and should require no special provisions except for eclipse periods. Such passive techniques as the use of thermal insulators on mounting feet should suffice to maintain acceptable temperatures during eclipse.

Sensor power requirements are small. Depending on the isolation and regulation specifications, a power of 1 to 1.5 watts would be required. The total weight of the instrument would be less than 1.5 pounds.

#### 6.5.4 Reliability

All existing earth sensor units use either components or subassemblies in a building block manner from units for which extensive test and flight data exists. The basic simplicity of the unit--no moving parts, passive thermal control--lends further to the confidence of the reliability estimates.

Estimates based on extensive failure mode analyses of the components, and on the test and flight experience of the components on existing sensor designs, indicate reliabilities of  $>0.99$  for 6 months of operation.

#### 6.6 REFERENCES

1. W. W. Butcher, et al, "Spacecraft Attitude Control/Gas System Analysis," Final Report, JPL Contract 95170, April 1967.

## 7.0 MAGNETIC CONTROL STUDIES

The desire to perform accurate measurements of the very weak Martian magnetic field is a prime motivation for the OEC mission. In general, the achievability of a particular level of magnetic cleanliness is not susceptible to paper analysis; magnetic cleanliness is achieved only by a thorough and painstaking program of controlling design, parts, materials, processes, and techniques backed by a comprehensive testing program to assure that every nut and bolt is as magnetically clean as it can be consistent with performing the basic mission.

Feasibility, then, can only be demonstrated on the basis of past performance – and rests on the implicit assumption of magnetic controls equalling or surpassing in effectiveness those used in the cited performances. The first three parts of this section are devoted to attempting to evaluate the OEC goal (0.25  $\gamma$ ) in light of previous experience – Pioneer, IMP, and Mariner series spacecraft. Comparison is first made on the basis of total spacecraft, then on the basis of the specific OEC equipment complement. The fourth part is a brief description of the type of magnetic control program needed to achieve the OEC goals; this brief description is supplemented by a preliminary outline of a Magnetics Control Plan in Volume III.

A qualitative discussion is included of the magnetic measurement accuracy to be expected with the OEC and several possible techniques for improving the accuracy of the magnetic measurements. Finally, a tabulation is given of the boom lengths required to obtain the same quality magnetic data from the Voyager Orbiter.

### 7.1 OVERALL SPACECRAFT FIELDS

The OEC spacecraft magnetic fields are required to be less than 0.25 gamma (1 gamma is  $10^{-5}$  gauss) at the location of the (boom-mounted) magnetometer. One perspective on the feasibility of achieving this low level is gained by a comparison with magnetic contamination levels achieved on comparable spacecraft. Table 7-1 gives a comparison with Pioneer and IMP spacecrafts, both comparable in size and complexity to OEC. It can be seen that the OEC magnetic requirement, while severe, appears feasible.

In general, designers of magnetically clean spacecrafts have been successful in eliminating almost all sources of permanent magnetism and ferromagnetic materials. Some notable exceptions are the traveling-wave tubes for telemetry transmission and jet solenoids for attitude control; magnetic contamination from these few "special cases" have been controlled by compensation or other techniques. Stray fields caused by current loops in solar cell arrays and electronic units have been reduced well below critical levels by careful design and control procedures.

TABLE 7-1. OVERALL COMPARISON OF MAGNETIC CLEANLINESS

Spacecraft	Weight, pounds	Boom, inches	Field
Pioneer VI	140	83	0.58Y (TRW data)
IMP I	140	82	0.8Y
IMP F and G	~150	82	0.25Y (specification)
OEC	123	84 (can go to ~96)	0.25Y (specification)

## 7.2 MAGNETIC ENVIRONMENT

The major remaining source of magnetic contamination fields is thought to be spacecraft magnetism induced during launch and early flight in the Earth's magnetic field. Table 7-2 shows test data obtained on several spacecraft in a de-permed state and after application of a steady (perming) field. Studies\* have indicated that the launch phase magnetic exposure is roughly equivalent to a 5 gauss perm or, alternately, that a rough measure of the effect of this launch exposure is 1/5 of the post 25 gauss measurement, also listed in the table. It is evident that the induced field is substantially larger than the "permanent" field (i.e., post-de-perm) for all the examples.

Since the major portion of contaminants is produced in the magnetic environment to which the spacecraft is exposed, this environment will be briefly examined.

- 1) Fabrication, handling, and prelaunch environments are not an important factor — the spacecraft is thoroughly de-permed shortly before being installed on the Voyager spacecraft and is not exposed to strong fields thereafter. After final de-perm, tight control is exercised to ensure that no contamination can occur. Equivalent field exposure is less than 1 gauss.
- 2) Launch and early flight environments are the most severe; equivalent exposure is taken as a 5 gauss perm.
- 3) Transit flight environment includes long term exposure to both the interplanetary field and the Voyager spacecraft field. The interplanetary field level is extremely low (1 to 10Y) and is not of

---

\*"Proceedings of the Magnetics Workshop," Jet Propulsion Laboratory  
TM 33-216, April 1965.

significance relative to the other stronger fields during prelaunch and launch exposure. Estimates of the possible Voyager fields have been made by extrapolating the magnetic moments of several existing spacecraft, yielding the values in Table 7-3. Scaling from these smaller spacecraft was done on a mass ratio basis (to a 15,000 pound Voyager); the field after exposure to launch environment was taken as four times (as in Table 7-2) the de-permed values in the ATS and OGO cases.

The likely case for Voyager is the "worst" case of Table 7-3 since no strict magnetic controls are planned for the Voyager spacecraft. Even here the field intensity at the OEC location is an order of magnitude less than the normal Earth field and should be a much less severe exposure than that during the launch period. However, measurements should be made of the Voyager field at the OEC location to ensure that the OEC is not located in a local "hot spot" of the Voyager field.

TABLE 7-2. COMPARISON OF CAUSES OF CONTAMINATION

Spacecraft	B at 1 meter, Post 25 gauss	Equivalent after Launch Exposure	Post-de-perm
Explorer XVIII (IMP I)	37.7	7.5	3.1
IMP C	63	12.6	2.6
IMP B	49	9.8	1.9
Pioneer IV (non-operating array)	22.5	4.5	2.4

TABLE 7-3. ESTIMATES OF POSSIBLE VOYAGER FIELDS IN TRANSIT

Case	Moment, pole-cm	Scaled from	B at 5 feet, gauss
Worst	100,000	OGO-A	0.02
Average	48,000	ATS	0.01
Controlled	7,500	IMP, Mariner	0.001



- 4) Martian magnetic environments are expected to be extremely low — less than 100 to 200 gamma even at the periapse point — and should not be critical.
- 5) OEC stray fields, produced by electronics and solar array currents, can pose a magnetic environment to the remainder of the spacecraft. These fields are, however, carefully controlled in design and their effects are thoroughly tested before flight including prime failure modes so that this need not be considered an "external environment."

### 7.3 MAGNETIC BUDGETS — DETAILED ESTIMATE

Evaluation of the OEC's environmental exposure reveals that the dominant periods are launch and early flight. Design and evaluation of OEC units and assemblies should therefore be directed at achieving the 0.25 gamma contamination level after exposure to this environment. Since this goal is identical to that set for the IMP (F and G versions), the specification levels used for IMP sub-assemblies can be used as a reference here. The IMP Test Criteria are reproduced as Table 7-4.\* Using the "1/5 of post 25 gauss" criterion, this reference subassembly yields a field contribution of 0.06 gamma a distance of 7 feet.

In order to further assess the difficulty of meeting the OEC requirement, preliminary estimates of the field contributions of individual units comprising the OEC equipment have been made. Table 7-5 lists data on various pieces of equipment obtained from Pioneer and Mariner programs. Comparing these data with the IMP specification (Table 7-4) reveals that most of the units are well under the post 25 gauss specification; the command distribution unit exceeds the de-permed allowance but the net after 25 gauss perm is sufficiently low that this exception is probably allowable. The traveling-wave tube and tape recorder are far in excess of the de-perm allowance; both units, however, fall in the category of "special cases" with permanent magnetic characteristics so that their total field contribution is largely in the de-permed state; the contributions to the net OEC field from these two items are substantial, with the tape recorder a distinctly critical item.

TABLE 7-4. MAGNETIC TEST CRITERIA FOR IMP SUBASSEMBLIES

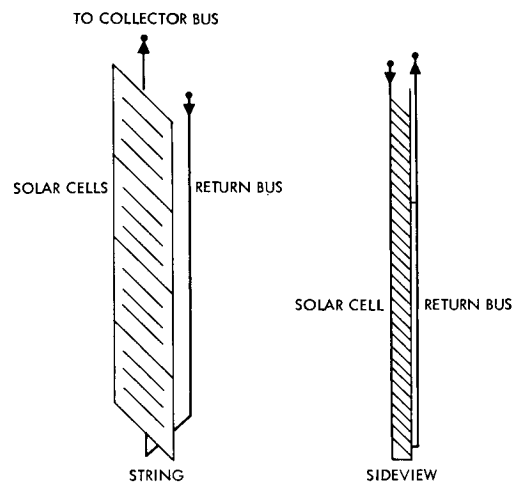
	Applied Field, gauss	Maximum Magnetic Field Disturbance, gamma	
		18 inches	36 inches
Post 25 gauss exposure	0	32	4
Post 50 gauss de-perm		2	0.25
Stray-power on versus power off	0	4	0.50

\*From "Magnetic Field Restraints for IMP's F and G," Normal F. Ness, NASA TMX-55444, July 1964.

TABLE 7-5. TYPICAL MAGNETIC FIELDS OF VARIOUS COMPONENTS

B field at 3 feet

Item	Magnetized post 25 gauss, gammas	Demagnetized post 50 gauss de-perm, gammas
PIONEER VI		
Receiver	0.404	0.055
Transmitter converter	XY 0.48	0.22 to 0.147
	XZ 0.18	0.147 to 0.036
Transmitter drive	0.42	0.088
Decoder	1.30	0.22
Command distribution unit	1.38	0.40
	As received	
Batteries (Ag-Cd)	0.147	-0.09
Antenna		0.029
	As received	
Sun sensor	XY 0.007	-0.007
	XZ 0.017	-0.007
	Each half illuminated	
Solar array	0.007	0.024
Traveling-wave tube	(<2 est.)	0.64 to 1.44
MARINER VENUS		
Tape recorder	(~3.5 est.)	3.36



70385-194(U)

Figure 7-1. Solar Cell Wiring

When the solar panels are activated by exposure to solar radiation, electric currents are set up that form current loops and produce magnetic moments. Solar cells are usually prepared in modules which in turn are mounted in strings, depending on the voltage level desired as shown in Figure 7-1.

The equation for the magnetic moment of a current loop is

$$M = N A (\Delta i)$$

where

$$N = 1 \text{ (number of turns)}$$

$$A = 1.5 \times 10^{-4} \text{ m}^2 \text{ (area)}$$

$$i = 5 \times 10^{-2} \text{ amperes (current in the loop)}$$

Then the sub-field B represented by:

$$M = 1.5 \times 10^{-4} (5 \times 10^{-2}) = 7.5 \times 10^{-6} \text{ amp m}^2$$

$$= 7.5 \text{ pole-cm per string}$$

Arranging the solar cell strings by reversing the current in adjacent strings, the individual magnetic moments would be cancelled except for the possible 3 percent error in current due to manufacturing tolerances. This means that the residual sub-field between two adjacent loops would be 0.225 pole cm.

Around the spacecraft there are a possible 134 strings of solar cells of which only half will be illuminated. Since there is a cosine effect on the illuminated half, the effective number of strings is 42. This constitutes 21 pairs that have self-cancelling of magnetic moment vectors. The total contribution to the magnetic field is  $21 (0.225) = 4.7$  pole cm if all differentials act in the same direction. If 25 percent are assumed to be in a given direction, the total magnetic moment reduces to 1.4 pole cm. This in turn produces a sub-field flux density at 1.8 meters (magnetometer position) of 0.025 gamma.

Since the magnetic moment vector is tangential to spin, a radially mounted magnetometer will "observe" a cyclic field due to the solar cells having an off-center contribution. The "observed" sub-field is estimated to vary between 0.04 and 0.01 gamma. The axial magnetometer will "observe" a constant average value of the solar cell contribution; however, the data will be modulated due to the variability of individual strings.

In the baseline OEC configuration, the magnetometer is mounted 7 feet from the spacecraft center. A preliminary equipment arrangement within the spacecraft is shown in Section 5.0, Figure 5-2; in this layout some attempt was made to locate the primary magnetic offenders as far away as possible from the magnetometer. Table 7-6 lists the principal units and assemblies in the OEC and

TABLE 7-6. PRELIMINARY MAGNETIC BUDGET

Item	Distance, inches	Field gammas	Comments
Reference	84	0.06	Taken from specification for IMP F and G
Tape recorder	97	0.17	Critical item — consistent with Mariner 67
Control jets (2)	96, 99	0.02 each	Measured on ATS
Communication electronics	72	0.10	Consistent with Pioneer VI and IMP specifications
Power electronics	80	0.074	Consistent with Pioneer VI and IMP specifications
Magnetometer electronics	75	0.06	Consistent with Pioneer VI and IMP specifications
Other electronics	90	0.05	Consistent with Pioneer VI and IMP specifications
Traveling-wave tube	90	0.05	Pioneer VI
Structure, har- ness, etc.	84	0.08	
Arithmetic sum		0.62	
RSS sum		0.24	

tabulates their estimated magnetic field contributions at the magnetometer. As expected from the data of Table 7-5, the tape recorder is the prime offender, even when located as far as possible from the magnetometer. A review of Table 7-5 and Figure 5-2 indicates possible improvements by a further rearrangement — for example, moving the (low field) batteries closer to the magnetometer and the communication electronics farther away. However, in light of the preliminary nature of the magnetic data available, efforts to completely optimize the detailed layout were not felt to be warranted.

The preliminary budgets given in Table 7-6 yield a "worst possible field" of 0.6Y when added together arithmetically; if the individual field contributions are root sum squared, a "best possible field" of 0.24Y results. Excluding the two special cases (tape recorder and traveling-wave tube), the values are 0.4Y arithmetic and 0.17Y rss'd. If the magnetometer were placed 8 feet from the spacecraft center, these values would decrease to 0.45Y arithmetic, 0.17Y rss with the tape recorder and traveling-wave tube and 0.28Y arithmetic, 0.12Y rss without them.

These results do not provide assurance that the 0.25Y goal set for OEC will be met; as always in a spacecraft program, many compromises are required in the interest of cost, schedule, or particular interface and performance criteria. The preliminary estimates, however, show that both on the basis of previous spacecraft achievements and on the basis of data on the particular units the 0.25Y goal should be regarded as a feasible one.

#### 7.4 ACHIEVEMENT OF MAGNETIC CLEANLINESS – MAGNETIC CONTROL

The achievement of the OEC magnetic goals is no simple task. To meet the specified levels the elimination of magnetic contributions must be pursued throughout the design, development, and assembly of the OEC. Basically, a magnetic control program must be adopted that will have as its prime objectives:

- Total elimination of permanent magnets and ferromagnetic materials from the spacecraft except where absolutely required
- Careful control, supplemented by testing, of materials, processes, and components to ensure that the spacecraft contains an absolute minimum of magnetically permeable material
- Careful control and test to ensure that design of electronic units, wiring harnesses and connectors, etc., produce fields well below critical levels in all their possible operating modes
- Arrangement of units within the spacecraft so as to minimize the contaminating field at the magnetometer

Criteria for the design of magnetically clean spacecraft have been developed on the basis of the experience gained in implementing (successfully) such programs as IMP and Pioneer. These data are available in such publications as the IMP Magnetic Field Restraints document; maximum use should be made of such information in the OEC program, supplemented by results of testing for items specific to OEC.

A magnetic control plan must be an integral part of the overall spacecraft hardware planning and must contain at least the following items:

- 1) Control organization
- 2) Specifications

- 3) Procedures and tests
- 4) Fabrication and assembly
- 5) Handling

To implement a strict magnetics control program, an organization should be formed to have a responsibility on a parallel with the spacecraft design, quality assurance, and experiment integration functions. This group would have responsibilities for

- Maintaining and augmenting, as appropriate, a Magnetic Requirements document based on best available information and continually updated to take account of data generated by test. Close liaison with NASA personnel should be maintained to assure maximum utilization of experience with magnetically clean design and fabrication techniques acquired during the IMP, Pioneer, and other programs.
- Reviewing and approving circuit design, layout, and selection of materials and components to assure compliance with magnetic requirements. Approval of exceptions to these requirements or of new or unusual materials or techniques should be granted only after consultation with the NASA project office; such approvals, with supporting data, should be carefully documented.
- Reviewing and approving procurement specifications and vendor processes and facilities to ensure compliance with magnetic requirements. Certification and on-site surveillance of vendors should probably be accomplished in conjunction with the overall quality control function, monitored and reviewed by the Magnetic Control organization.
- Formulation and implementation of a plan for magnetic inspection of parts and components. It is likely that many (if not all) parts will require 100 percent magnetic inspection (50 gauss de-perm followed by measurement after 25 gauss perm and after subsequent 50 gauss de-perm). Establishment of criteria for selection of magnetically acceptable parts should be closely coordinated with NASA.
- Formulation, coordination, and implementation of a plan for magnetic testing of subassemblies. Tests should be performed as early as possible in the development cycle to permit the identification and rectification of any trouble areas. All questionable items or techniques should be proven by testing unless adequate assurance of magnetic acceptability can be otherwise provided.

A preliminary outline for an OEC Magnetic Control Plan is presented in the Program Plan section of Volume III.

## 7.5 ACCURACY OF MEASUREMENT

The preceding discussion has related to the achievement of a minimum level of spacecraft-generated fields. To assess the accuracy of the measured data, the fact that the spacecraft is spinning, thus modulating the (external) measured fields, must also be considered. Figure 7-2 shows the idealized form of the fields as seen by the three magnetometer sensors and indicates the modulation imposed on the (radial and tangential) external fields by the spacecraft spin. Clearly it is possible during data reduction to distinguish between the satellite residual field, producing a static bias, and the external field, as a spin frequency sinusoidal.

The instrument to be used in the baseline OEC payload is that developed by Ames Research Center for the Pioneer spacecraft. This instrument\* incorporates as a part of the sensor electronics a spin demodulation function so that the data output from the magnetometer is the demodulated version of that shown in Figure 7-2. In this case, the spacecraft residual fields would appear in the demodulated data as oscillating fields at the spin frequency; here too, they can readily be distinguished from external fields.

Thus the contamination fields present in the plane normal to the spin axis should produce an error in the (reduced) data much smaller than the actual contaminant fields. No modulation exists naturally for the field component parallel to the spin axis.

As indicated earlier, the prime contributor to the spacecraft field is expected to be the magnetism induced during the launch and near-earth portions of the trajectory. This being the case, the spacecraft field may be expected to be fairly stable over its 6 months in Martian orbit. It is suggested, therefore, that the spacecraft field be calibrated shortly after placement of the OEC in orbit by a 180 degree "flip" of the entire OEC. This would require approximately 1/2 pound of propellant and would provide a calibration of the spacecraft field in the direction parallel to the spin axis. The maneuver should be performed near apoapsis of the OEC orbit to ensure a fairly stable ambient field.

One other possible technique that has been evaluated but does not appear attractive is in-flight de-perming. Conceivably it could be accomplished in a similar manner to the laboratory procedure, by ring-down with a coil around the spacecraft as shown in Figure 7-3.

The size of the coil is determined by the power supply and the field intensity required. The spacecraft before launch would be de-permed to reduce the field to the design level. In traversing the Earth's field during the launch phase the spacecraft is permed with a field equivalent to a dc 5 gauss field. It is assumed that this is the design field for the coil. A plot was made of the average turn required per winding versus coil weight with up to 5 amperes available, as shown in Figure 7-4

---

\*Ames Magnetometer for Pioneer C and D, Specification A-10201, Revision B, Ames Research Center, May 1967.



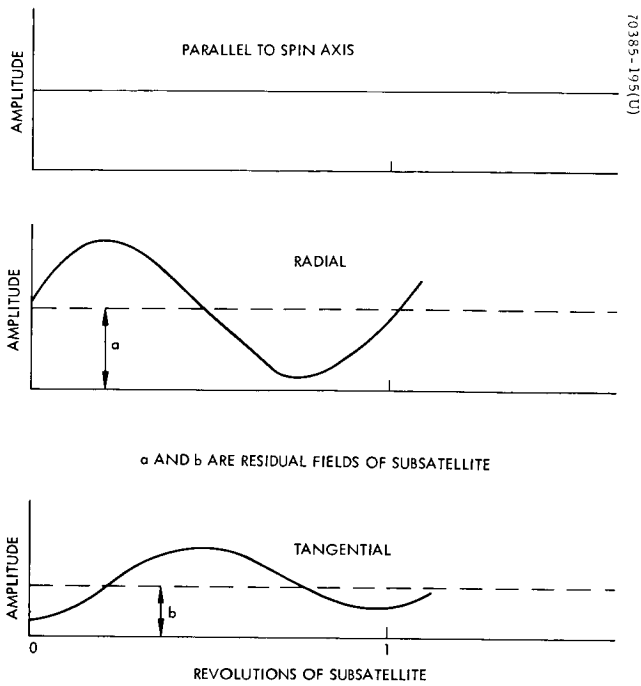


Figure 7-2. Illustration of Modulation Components of Magnetic Field

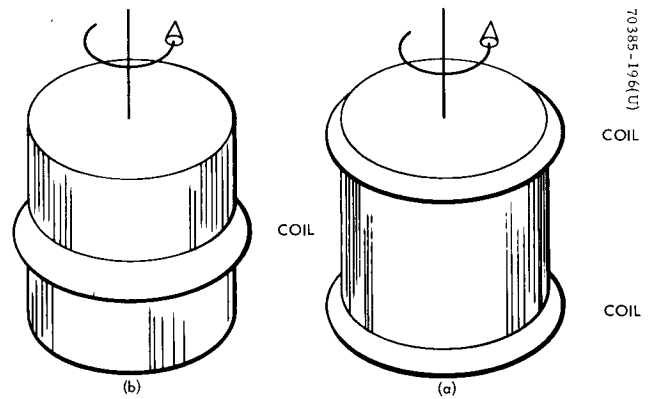


Figure 7-3. Coil Locations for De-perming

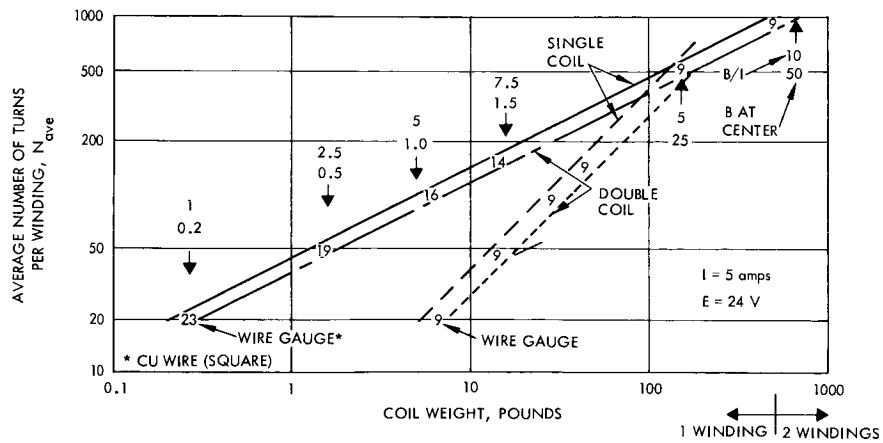


Figure 7-4. Weight of Spacecraft-Mounted De-perming Coil System

for single coil and double coil systems. Also shown in the value of gauss per ampere developed and the corresponding wire size. A coil that would produce 5 gauss for 5 amperes of current would weigh about 5 pounds, exclusive of the coil frame and associated ring-down electronics. The time required to de-perm would be about 11 minutes.

## 7.6 VOYAGER BOOM LENGTHS

One alternate method for providing measurements of the Mars magnetosphere would be to mount the magnetometer sensor on a long boom attached to the Voyager orbiter. The period of interest is after the Voyager flight capsule (including Lander) has separated from the Orbiter; at this time the Voyager Orbiter is about one-third the mass of the "Earth-Mars transit phase" spacecraft, so that the Voyager magnetic moments should be roughly one-third those of Table 7-3.

Table 7-7 lists the boom lengths that would be required to achieve the 0.25Y field level specified for OEC. The extreme lengths could pose problems, not only in deployment but also in alignment of the sensor axis in the deployed position and in dynamic flexing causing spurious measurement "errors."

TABLE 7-7. ESTIMATED BOOMS REQUIRED FOR VOYAGER TO  
CONDUCT MAGNETOSPHERIC MEASUREMENT

Case	Moment, pole-cm	Boom Length Required to Yield 0.25 Y Contamination, feet
Worst	33,000	78
Average	16,000	61
Controlled	2,500	33

## 8. OEC RELIABILITY

### 8.1 RELIABILITY ASSESSMENT

The goal set for the OEC is 0.75 reliability over a 12-month transit period, stowed on the Voyager spacecraft, followed by a 6-month orbit operational period. This requirement is relatively modest as space systems go and appears to be well within the present state of the art. Hughes satellites, generally of comparable or greater size and complexity than the OEC, have presently accumulated 11 satellite years in space, with all those placed in their specified orbits still fulfilling their intended functions. The earliest of these satellites, Syncom 2, has been in orbit for over 3 years. Thus, the feasibility of achieving the OEC goal can be indicated by analogy to other space systems.

Another approach to demonstrating the feasibility of achieving the desired OEC reliability is through a block diagram reliability assessment using the specific OEC equipment with failure data estimated or extrapolated from experience with similar units. Such an assessment, reported below, has been performed, yielding a prediction of 0.78 for the baseline OEC over its 18-month life (6 months in orbital operation plus 12 months in stowed condition). This prediction should be considered pessimistic since detailed failure mode analysis and determination and incorporation of optimum redundancies have not been performed in this feasibility study.

The baseline OEC has been configured to have a number of capabilities not absolutely essential to meeting a minimum mission function. Such capabilities include the orbit change propulsion and the tape recorder for data storage. Considering this same spacecraft operated in its simplest mode (real time data transmission, no propulsion except spinup) yields a reliability of 0.92 for the 18 months

Reliability block diagrams for the recommended OEC configuration and for the same spacecraft operated in its simplest ("co-orbital") mode are shown in Figures 8-1 and 8-2.

### 8.2 RELIABILITY OF ALTERNATE MODES OF OPERATION

Four additional reliability block diagrams and estimates for the 12-month transit and 6-month orbital mission are presented in Figures 8-3 through 8-6 to show the relationship of reliability to:

- 1) The different levels of performance
- 2) The various functional capabilities of the system design
- 3) The circumstances influenced by mission orbit

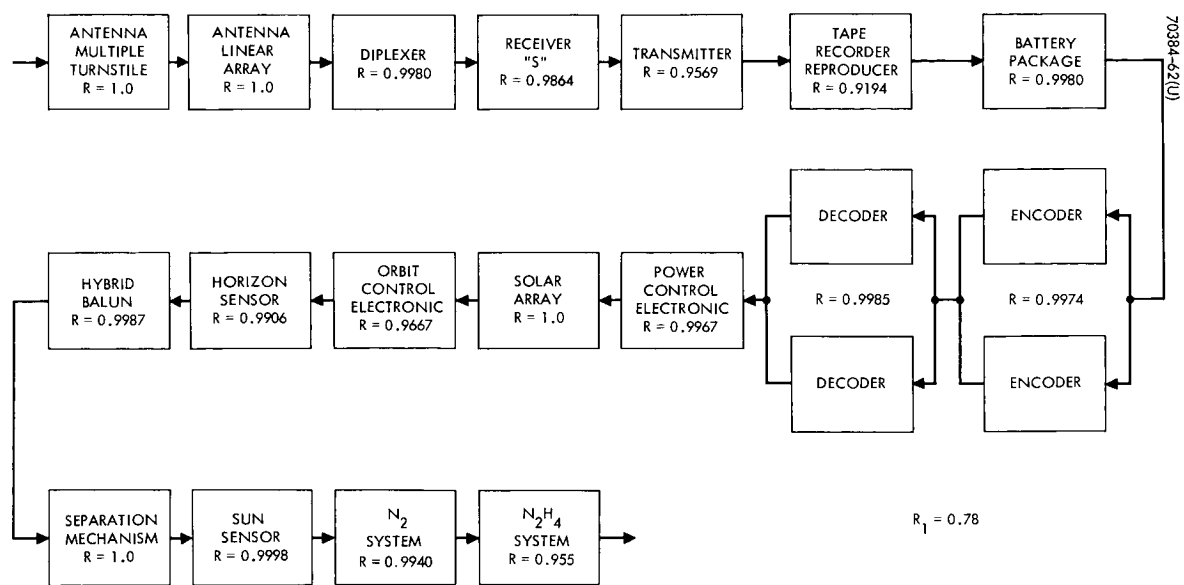


Figure 8-1. Reliability Block Diagram for Primary Communication Mode With Orbit Change  
(High speed data transmission rate capability)

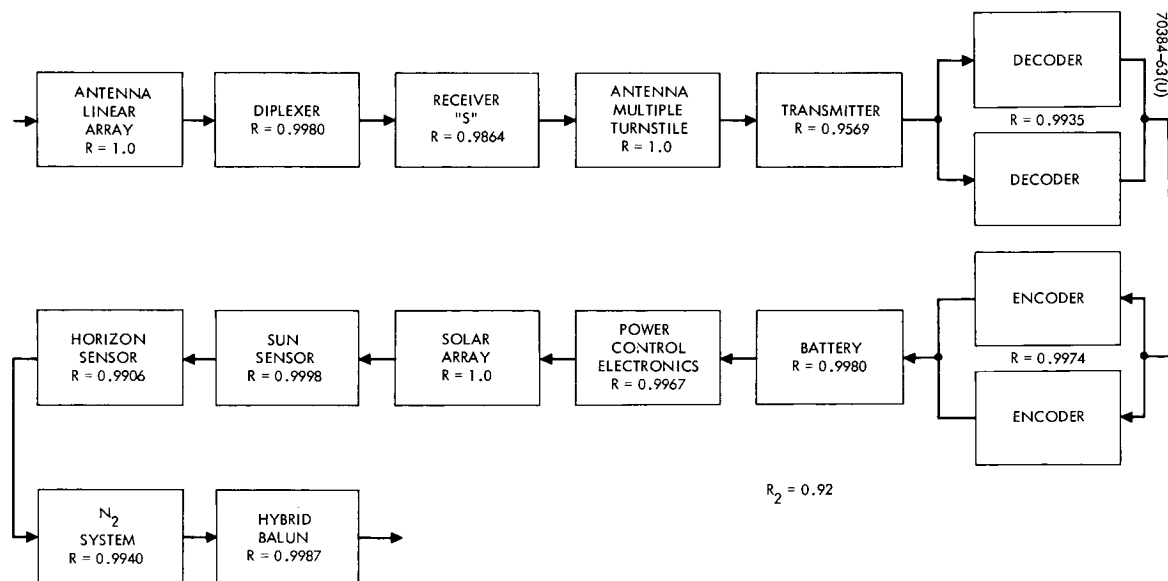


Figure 8-2. Reliability Block Diagram for Primary Communication Mode Without Orbit Change  
(Continuous data transmission capability)

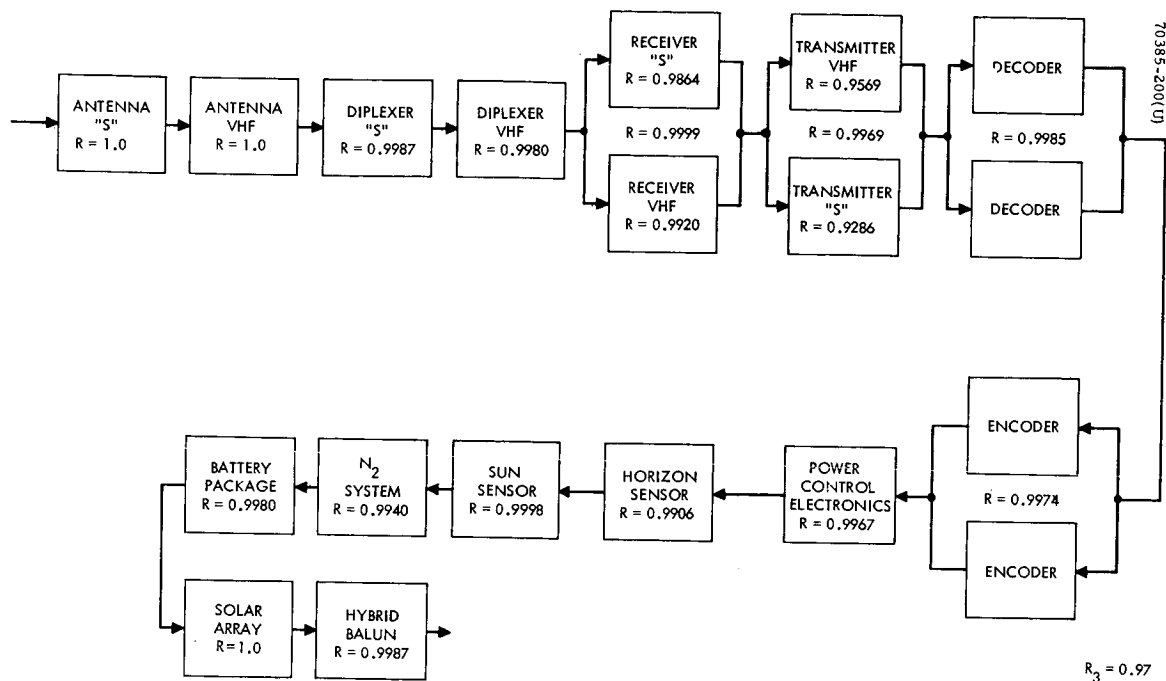


Figure 8-3. Reliability Block Diagram for Primary Communication Mode Considering S-Band Transmitter and VHF Voyager Link Receiver as Redundant Channels – Without Orbit Change

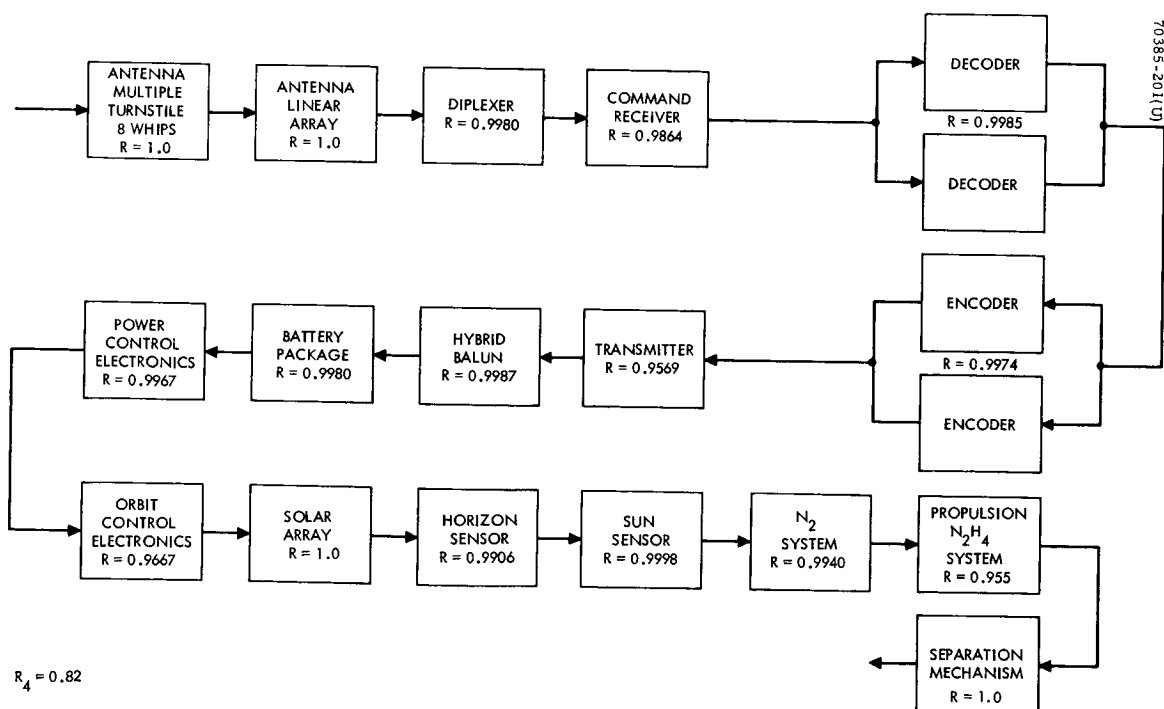


Figure 8-4. Reliability Block Diagram for Primary Communication Mode at Low Data Transmission Rate – With Orbit Change

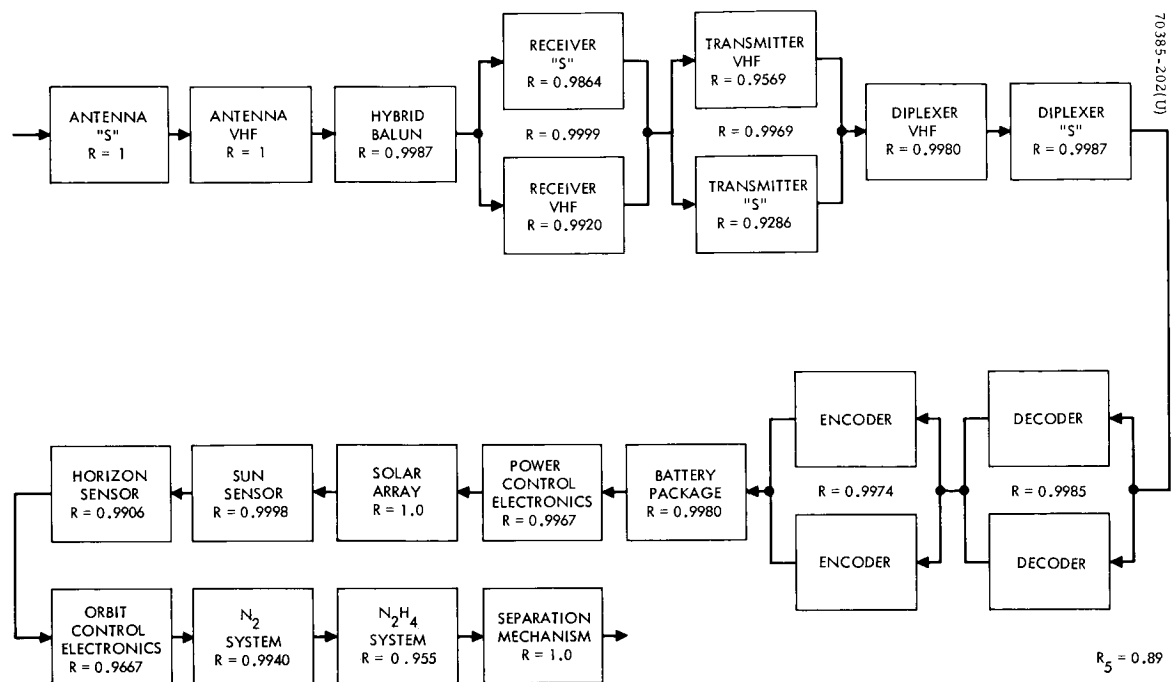


Figure 8-5. Reliability Block Diagram for Primary Communication Mode at Low Data Rate Considering S-Band Transmitter and VHF Voyager Link Receiver as Redundant Channels

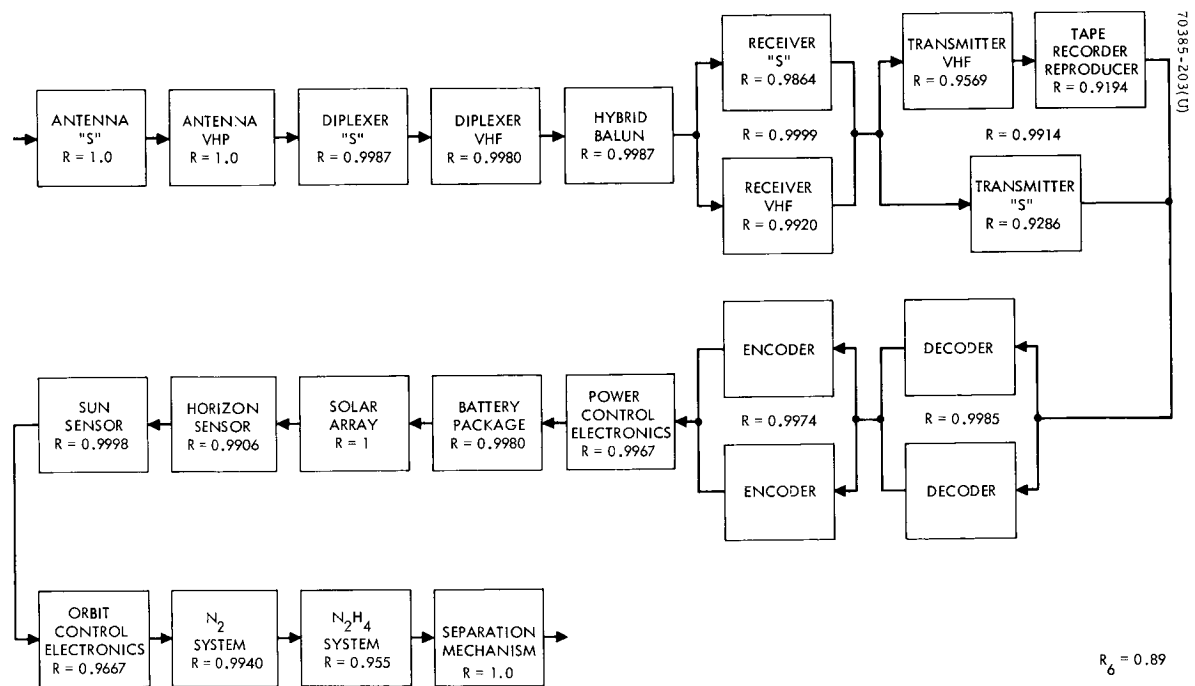


Figure 8-6. Reliability Block Diagram for Primary Communication Mode at High Speed Data Rate and Considering S-Band Transmitter at Low Data Rate and VHF Voyager Link Receiver as Redundant Channels - With Orbit Change

The reliability block diagram of Figure 8-3 considers the UHF Voyager link command receiver and the S-band transmitter link to earth DSN as redundant units for the primary communication equipment. This is for a condition without orbit change and no requirement for data recording or reproducing. The reliability estimate of this "mode" is 0.97.

The reliability block diagram of Figure 8-4 considers the case with orbit change, and the primary communication channels at low data transmission rate. This is the same as block diagram for the basic requirement shown by Figure 8-1 without the tape recorder providing the capability for optimum data transmission rate. The reliability estimate is 0.82.

The reliability block diagram in Figure 8-5 considers the conditions of orbit change, primary communication mode at low data transmission rate, with the S-band transmitter and UHF Voyager link command receiver as redundant equipment to the primary communication units. The reliability estimate is 0.89.

The reliability block diagram in Figure 8-6 considers the conditions of orbit change, the primary communication mode with optimum data recording and transmission speeds, the S-band transmitter at low data transmission rate redundant to the primary UHF transmitter at high data rate, and the UHF Voyager link command receiver redundant to the S-band command receiver. The reliability estimate is 0.89.

### 8.3 FAILURE RATE DATA

The baseline for the component failure rates used in estimating reliability is taken from Hughes Space Systems Division Bulletin R22-100DC (May 1967) entitled, "Space Systems Component Basic Failure Rates and Derating Curves." Current values of the "Operational Experience Factor" applied to the basic failure rates are a result of the latest updating supplement to Bulletin R22-100DC-Space Systems Division report entitled "Hughes Satellite Operational Data Analysis," dated 21 June 1967, Reference 2207.1/10. This current data represents results of actual performance of Hughes satellite systems to 31 May 1967--a total of 277 million component hours functioning in the operational mode and 200 million component hours in the space environment nonoperational mode.

The reliability estimates previously cited were based on calculations that included failure rates for both the "operating" and "non-operating" conditions of the mission time profile.

The specific equipment reliabilities used are listed in Table 8-1, together with the sources for part types, parts counts, and/or life data.

Table 8-2 provides the basic data pertinent to OEC. It also shows a comparison between the basic  $\lambda_b$  or operational failure rate and the corresponding  $\lambda_d$  or dormant failure rates. The conditions of comparison are:

$\lambda_b$  temperature 25° C, 20 percent of rated stress

$\lambda_d$  temperature 25° C

TABLE 8-1. OEC RELIABILITY ESTIMATES

Unit	Failure Rate, percent per 1000 hours		Reliability	Reference Source
	On	Off		
Receiver	0.1541	0.0136	0.9920	Drawing 457210-100
Transmitter	0.8338	0.0847	0.9569	Power amplifiers 3080013 and 475220-101
Decoder	0.57514	0.1616	0.9613	ATS drawings
Encoder	0.6267	0.2849	0.9488	IDCSP/A
Tape recorder reproducer	1.60	0.16	0.9194	Performance data-space
Orbit control electronics	0.3876	0.1904	0.9667	IDCSP/A
Horizon sensor	0.1775	0.0177	0.9906	IDCSP/A
Sun sensor	0.0064	0.0006	0.9998	IDCSP/A
Diplexer	0.0404	0.0020	0.9980	ATS drawings
Power control electronics	0.0877	0.0076	0.9967	IDCSP/A
Hybrid balun	0.0245	0.002	0.9987	ATS drawings
Battery package	—	—	0.9980	Performance analysis
N <sub>2</sub> spinup system	—	—	0.9940	JPL Contract 951720
N <sub>2</sub> H <sub>4</sub> propulsion system	—	—	0.955	JPL Contract 951720
Solar array	—	—	1.0	Performance studies
Antenna — 8 whips	—	—	1.0	Performance analysis
Receiver — S-band	0.2580	0.0250	0.9864	Drawing 231900 — less transponder
Transmitter — S-band	1.4000	0.1424	0.9286	Drawing 263220 — less transponder
Diplexer — S-band	0.0244	0.0024	0.9987	Drawing 231872
Antenna — linear array	—	—	1.0	Syncom



TABLE 8-2. OEC RELIABILITY DATA

Part Type Description	988XXX Part Numbers	Operational Failures/ 10 <sup>9</sup> hr	Dormant Failures/ 10 <sup>9</sup> hr
Capacitors	9885XX (average satellite)	7	0.1
Ceramic	504, 25, 26, 30, 41	5	0.02
Glass-mica	502, 03, 28, 40	5	0.02
Mylar-plastic	501, 07-10, 47	10	0.05
Paper	505, 42	50	0.2
Tantalum	500, 06, 46	20	1
Variable	520-22, 43, 45	20	1
Magnetics: coils, chokes, trans- formers	9884XX (average satellite)	20	0.5
Connectors	9882XX (average satellite)	25	2.5
Coax	211-17, 20, 26-31	20	2
All others	2XX	200	20
Crystals	660-68	40	0.1
Diodes	9887XX, 9889XX (average satellite)	13	2
Power rectifier	714, 16, 17, 19, 28, 39, 45, 48	50	5
Detector (mixer)	909, 19, 27, 28, 43, 44, 50	200	20
Switching	702, 03, 11, 13, 18, 27, 40, 43	2	1
General purpose*	700, 01, 22, 23, 30, 36, 51; 914, 16	5	1
Silicon controlled rectifier	900, 01, 12, 15, 17, 21, 26	50	5
Tunnel	710, 12; 940, 41	200	20
Zener	704-09, 25, 26, 29, 31, 32, 34, 35, 38 41, 42, 46, 47, 49, 902	20	2
Varactor	903-05, 13, 24, 29, 36, 42	200	20
Resistors	9886XX (average satellite)	1.3	0.08
Carbon com- position	600-605	1	0.1
Film	610-24, 74-75, 77-79, 92, 93, 97	2	0.02
Power wire- wound	630-37, 91	5	0.01
Precision wire- wound	607-09, 40-49, 90, 94	3	0.01
Transistors	9888XX (average satellite)	10	1
Switching npn	800, 02-04, 06, 07, 24, 33, 38, 40, 48, 66, 78, 939	5	1
All pnp	801, 05, 09, 20-23, 25, 29, 31, 35, 37, 39, 42, 43, 47, 53, 54, 64, 67, 71	20	2
General purpose npn	819, 45, 49	10	1

Table 8-2 (continued)

Part Type Description	988XXX Part Numbers	Operational Failures/ 10 <sup>9</sup> hr	Dormant Failures/ 10 <sup>9</sup> hr
Power npn	813, 16, 17, 30, 34, 44, 46, 50, 60, 65, 74, 76	100	10
High-frequency RF npn	811, 12, 26, 28, 36, 52, 73, 79	20	1
FET	857, 59, 62, 69, 75, 77	100	10
Integrated circuits	(average satellite)	50	25
DTL**	932(6), 34(4), 33(3)	10	5
MOS	204671, 251373, 251372	70	30
Solder and weld connections		0.2	0.2
Traveling-wave tube***		2000	2000

\*General purpose diodes used in digital application may be classified "switching."

\*\*Failure rate given for complexity of 1.0 (complexity factors in parentheses).

\*\*\*Inherent failure rate of traveling-wave tube. Does not include power supply interface failures.

The 988 part numbers refer to Hughes space-approved parts. In addition to the basic failure rate data, figures are given for "average satellite" complements of these parts.

In addition to the Hughes documents referenced above, data are based in part on the following two reports:

- 1) RADC Reliability Notebook, Volume II, January 1967 (unpublished Hughes draft), C&M Laboratory.
- 2) D. F. Cottrell, et al, "Dormant Operating and Storage Effects on Electronic Equipment and Part Reliability," Technical Report RADC-TR-66-348, October 1966, Martin-Marietta Corporation.

## 8.4 CRITICAL UNIT RELIABILITIES

### 8.4.1 Tape Recorder

Magnetic tape recorder units with functional characteristics that are adaptable to the requirements of the OEC mission have been developed for previous space programs by the following manufacturers:

Raymond Engineering Laboratory, Inc.

Kinelogic Corporation

Lockheed Electronics Company

Leech Corporation

Ralph M. Parsons Company

A number of the units are accumulating sufficient operating time in the space environment to establish the required reliability assurance of this unit for the OEC mission. Based on information available, the failure rate is presently estimated at 1.6 percent per 1000 hours.

The recording speed requirement of 0.5 ips and the short time interval playback at 4.0 ips are known to be favorable conditions for long periods of operation with minimum of wear. The thermal control of this unit is an important factor directly related to its reliability.

### 8.4.2 Batteries

The OEC system requires two 25 cell batteries for normal operation. In order to improve reliability, it is planned to include three additional cells per battery so that each battery can tolerate a short circuit condition within three of the 28 cells and continue its normal function. Reliability will also be enhanced by inserting a suitable diode in parallel with each cell to provide an alternate circuit path if an "open" should occur. With this arrangement normal battery function would be possible even if two such failures should occur.

Due to the weight and spare restrictions that influence battery design, the relative occurrence of "open circuits" to "short circuits" is estimated to be one-to-ten, respectively.

The reliability of one of these batteries can be expressed as

$$R_B = (R_0^{28} + 28R_0^{27} (1 - R_0)) \times (R_S^{28} + 28R_S^{27} (1 - R_S) + \frac{28 \cdot 27}{2} R_S^{26} (1 - R_S)^2 + \frac{28 \cdot 27 \cdot 26}{2} R_S^{25} (1 - R_S)^3)$$

where  $1 - R_S$  is the probability of cell short and  $1 - R_0$  is the probability of cell open. If a nickel-cadmium battery is used, a failure rate of 0.05 percent/1000 hours may be assigned to a cell, apportioned as 0.045 short and 0.005 open.

The reliability for a mission of 1-1/2 years (the failure rate on is essentially a dormant failure rate since total cycles will be minimal compared to a 5000 cycle wearout life) is then computed as  $R_B^2 = 0.998$  for the two batteries in series.

Silver cadmium batteries should be used in OEC in order to reduce magnetic contamination. The art of achieving long life with these batteries is dependent on the temperature environment both during transit and operational phases. The OEC thermal control system for both phases takes into account the Ag-Cd battery requirements.

#### 8.4.3 Propulsion

Co-Orbital Mission. The single function of the propulsion system in the co-orbital mission is spacecraft spinup. Three different designs were considered:

- 1) Solid propellant motors (2 units)
- 2)  $N_2$  jet system
- 3)  $N_2$  jet system with solid propellant motors as backup

The solid propellant motors would consist of two independent units 180 degrees apart, both required to function to obtain full spinup to 60 rpm. Solid propellant motors of this type have demonstrated a high degree of reliability, a typical reliability value being 0.999\*. The reliability for two "in series" would be  $(0.999)^2 = 0.998$ .

The nitrogen jet design would consist basically of the components listed in Table 8-3, with the assigned failure rates, obtained from the RADC Reliability Notebook previously cited.

---

\* Falcon missiles have had no two solid propellant failures in 4000 trials. Atlantic Research reports one failure in 1580 trials for motors of this type.

TABLE 8-3. NITROGEN JET SPINUP FAILURE RATES

Number Used	Component	Failure Rate
1	Tank	0.016
1	Manifolding	$0.057/10^5$ hours
1	Squib valve	0.0005/operation
2	Thruster	$0.000/10^5$ hours

Because of the large margin of force available from the explosive charge used to open the  $N_2$  valve, it can be assumed that the reliability of this function is essentially that of the pyrotechnic initiator. The Apollo dual bridge wire pyrotechnic initiator has demonstrated a reliability of 0.9995.

The reliability of this system, assuming spinup occurs 1 year after launch, is:

$$0.9995 \exp \left[ (0.016 \times 10^{-5} + 0.057 \times 10^{-5}) \times 0.0876 \times 10^{-5} \right] = 0.994$$

For the nitrogen jet system with solid propellant motors as a backup, assuming a switching reliability of 0.99,

$$R = 1 - (1 - 0.994) (1 - 0.998 \times 0.99) = 0.99993$$

Orbit Change System. The orbit change propulsion design under consideration consists of a hydrazine system with quad valves for attitude control. A quad valve is a preferred method of obtaining maximum reliability for minimum weight through use of internal redundancy, consisting of four independent valves. The reliability of a quad valve can be computed as follows.

A single valve may fail in two modes (open or closed) or both since it is possible for an inoperable valve to leak. The reliability in the closed position of a single valve is denoted by  $R_c$ ; the reliability in the open position, by  $R_o$ . For failure in the closed position of a quad valve, there must be at least one failure in each branch. The reliability of a quad valve against closed failures is given by:

$$Q^{R_c} = 1 - (1 - R_c^2)^2 \quad (1)$$

For failure in the open position, there must be two open failures in at least one branch; thus the reliability of a quad valve against open failures is:

$$Q^{R_o} = (1 - (1 - R_o)^2)^2 \quad (2)$$

Thus, assuming these failure modes to be independent:

$$Q^R = (1 - (1 - R_o)^2)^2 \cdot (1 - (1 - R_c^2)^2) \quad (3)$$

assuming independent failure modes of valves. If non-independent failure modes can occur with probability  $1 - R_s$ , the equation becomes

$$Q^R = (1 - (1 - R_o)^2)^2 \cdot (1 - (1 - R_c^2)^2) \cdot R_s^*$$

\* The major producer of quad valves has found no occurrences of non-independent failures in their production of over 1200 quad valves. This event will be assumed to have probability zero.

Table 8-4 lists the failure rates for elements of the reaction control system configuration for orbit change. The operational rates are based on the RADC Reliability Notebook.

Assuming a mission of 8760 hours dormant and 4380 hours operational for the  $N_2H_4$  system, the reliabilities are, assuming exponential time to failure:

1) Series Elements

$$\begin{aligned} & \text{Exp} + (0.017 + 0.057 + 0.020) \text{ failures}/10^5 \text{ hours} \times 8760 \text{ hours} \\ & + (0.017 + 0.057 + 0.02) \text{ failures}/10^5 \text{ hours} \times 4380 \text{ hours} \\ & + \times 1 \text{ cycle} + 2 \times 16 \text{ failures}/10^6 \text{ cycles} \times 10 \text{ cycles}^* \\ & = e^{-0.512} = 0.970 \end{aligned}$$

\* Ten cycles are used as a nominal for this analysis. The actual number of pulses required of the  $N_2H_4$  jets depends on the implementation of the orbit change propulsion system—whether a radial or axial jet is used. In this sense, the cycles have been interpreted as initiating a jet pulse train, whether the train is one long pulse or many short repetitive pulses. The failures, then, are attributed primarily to startup of the thruster from a cold condition.

TABLE 8-4. ORBIT CHANGE SYSTEM RELIABILITY

Component	Number per System	Operational Failure Rate	Dormant Failure Rate
$N_2$ squib valve	1	0.005/cycle	--
$N_2H_4$ tank	1	$0.017/10^5$ hr	$0.017/10^5$ hr
$N_2H_4$ manifolding	1	$0.057/10^5$ hr	$0.057/10^5$ hr
$N_2H_4$ burst diaphragm (open mode)	1	$0.020/10^5$ hr	$0.020/10^5$ hr
$N_2H_4$ thruster (catalyst bed)	2	$16/10^6$ cycles	$0.000/10^6$ cycles
$N_2H_4$ solenoid			
Open	2	0.467	0.200
Closed		0.140	0.140

2) Valves (each)

From Equation 3:

$$\begin{aligned} Q^R &= \left( 1 - (1 - e^{-[0.467 \times 0.0438 + 0.200 \times 0.0876]})^2 \right)^2 \\ &\quad \left( 1 - (1 - e^{-2[0.014 \times 0.0876 + 0.014 \times 0.0438]})^2 \right) \\ &= (1 - (1 - 0.9628)^2)^2 \cdot (1 - (1 - 0.9635)^2) = 0.9959 \end{aligned}$$

The total reliability for the  $N_2H_4$  orbit control propulsion is then:

$$(0.970) (0.9959)^2 = 0.961$$

With  $N_2$  spinup included:

$$R = 0.961 \times 0.994 = 0.955$$

## 8.5 RELIABILITY CONSIDERATION FOR LOW TEMPERATURE EXPOSURE DURING ECLIPSE

The exposure of the OEC to a temperature extreme of  $-250^\circ\text{F}$  during eclipse periods is recognized as a significant design factor related directly to reliability. However, with adequately designed thermal control for certain units and all other items qualified to the temperature extremes by specification requirements, it is known from past experience that the reliability problems created by this condition can be solved.

In general, in most instances, low temperatures result in less reliability degradation to components than temperatures on the high side of normal. The component parts used in Surveyor were qualified to survive at least five cycles of temperature shock from  $70^\circ$  to  $-375^\circ\text{F}$  to  $257^\circ$  to  $70^\circ\text{F}$  without physical damage or change in characteristic, as indicated in the following paragraph from a typical Surveyor specification control document for a quartz crystal, part number 988660.

"4.5.3 Thermal Shock - Before the test, the frequency and equivalent resistance shall be measured. The crystal units shall be subjected to 5 complete cycles of thermal shock, in accordance with the following procedure: While at room temperature, the crystal units shall be quickly immersed in liquid nitrogen ( $-375^\circ\text{F}$ ). After ten minutes of immersion, the crystal units shall be removed and placed, within one minute, in an air chamber held at  $+257^\circ\text{F}$ . After ten minutes the crystal units shall be removed from the chamber and shall be exposed to room temperature for five minutes. Upon completion of the 5 cycles, the crystal units shall be examined for physical damage and the frequency and equivalent resistance shall be measured. (See 3.2.2.)"

The low temperature conditions for OEC must be further explored in the program definition to ascertain units that might be significantly affected; in spacecraft development, the OEC test regime should include these low temperature environments to ensure viability of the spacecraft design and manufacture. Based on present studies, the feasibility of meeting such a low temperature environment is not in question.



## DETERMINATION PROCESSES

The detailed results of the attitude and orbit determination processes are illustrative of possible solutions to the inertial determination of the OEC spin axis as well as its estimated orbit. Due to the nature and complexity of these problems, two individual analyses were conducted and are detailed in Appendices A and B. Basically the foundations for each of these studies is identical; however, owing to the simultaneous period to which the results were generated there is some repetition which, for the sake of clarity, is left in the text.

## APPENDIX A. ATTITUDE DETERMINATION

### A.1 Basic Relationships\*

It is convenient to derive the formulas for the general estimation problem by first considering the simple case where the unknown parameters are constant, and then extending the results obtained\*\* to the time varying case. To facilitate any attempt at following these derivations, this order has been adopted here in presenting the key relationships needed for attitude determination.

Let  $x$  be an  $n$ -vector of unknown parameters to be estimated and  $y$  be an  $m$ -vector of given data values. For the attitude determination problem  $m \gg n$ . In general, the relationship between  $x$  and  $y$  takes the form

$$y = h(x) + v \quad (A1)$$

where  $h(x)$  is a nonlinear vector function dependent on the physical situation, and  $v$  is a vector of sensor "noise." Assume that it is possible to guess a vector  $x^0$  sufficiently "close" to the true value of  $x$  so that the linearized relationship

$$y = h(x^0) + H(x - x^0) + v \quad (A2)$$

where

$$H = \begin{bmatrix} \frac{\partial h_1}{\partial x_1} & \frac{\partial h_1}{\partial x_2} & \cdots & \frac{\partial h_1}{\partial x_n} \\ \frac{\partial h_2}{\partial x_1} & \frac{\partial h_2}{\partial x_2} & \cdots & \frac{\partial h_2}{\partial x_n} \\ \cdots & \cdots & \cdots & \cdots \\ \frac{\partial h_m}{\partial x_1} & \frac{\partial h_m}{\partial x_2} & \cdots & \frac{\partial h_m}{\partial x_n} \end{bmatrix}_{x=x^0} \quad (A3)$$

\*In this section upper case letters refer to matrices, unsubscripted letters (except  $t$  which denotes time) refer to vectors, and subscripted lower case letters refer to scalars. The asterisk is used to denote matrix transposition.

\*\*I. Gura, "An Algebraic Approach to Optimal State Estimation, Hughes Report No. SSD 70072R, March 1967.

holds. Using the methods of Gura\*, it can be shown that a better approximation of  $x$  is given by

$$x^1 = \left( P_o^{-1} + H^*WH \right)^{-1} H^*W(y - h(x^0)) \quad (A4)$$

where  $P_o$  is the covariance matrix of the initial guess  $x^0$  and  $W$  is a matrix of weighting numbers on each data point. (The inverse of the covariance matrix of the "noise" in Equation A2 can be used as an appropriate weighting matrix.) The theory shows that the covariance matrix of  $x^1$  is given by

$$P_1 = \left( P_o^{-1} + H^*WH \right)^{-1} \quad (A5)$$

Thus Equations A4 and A5 can be used recursively to generate a sequence of approximations to  $x$ . In most practical situations this sequence will converge to the best estimate of  $x$  for the nonlinear configuration of (A1).

Recall that since  $m \gg n$ , the matrix  $H^*WH$  is relatively "small" in dimension ( $n \times m$ ) compared to its factors  $H$  and  $W$  ( $n \times m$  and  $m \times m$ , respectively). It is therefore desirable to avoid direct computer storage of the latter quantities. If the matrix  $H$  and the corresponding vector  $y$  are partitioned in some consistent manner, i. e.,

$$H = \begin{bmatrix} H_1 \\ H_2 \\ \vdots \\ H_q \end{bmatrix}, \quad y = \begin{bmatrix} y^1 \\ y^2 \\ \vdots \\ y^q \end{bmatrix} \quad (A6)$$

so that the weighting matrix can be taken as\*\*

$$W = \begin{bmatrix} W_1 & & 0 \\ & W_2 & \\ 0 & & \ddots \\ & & & W_q \end{bmatrix} \quad (A7)$$

---

\*Op cit.

\*\*This kind of weighting matrix results when the groups of data  $y^1, y^2, \dots, y^q$  are statistically independent of each other. The further simplification that  $W_1 = W_2 = \dots = W_q$  can usually be made for most physical problems.

the formulas

$$H^*WH = \sum_{i=1}^q H_i^* W_i H_i \quad (A8)$$

and

$$H^*W[y - h(x^0)] = \sum_{i=1}^q H_i^* W_i [y^i - h^i(x^0)] \quad (A9)$$

will hold identically. Then by using

$$x^1 = P_1 \sum_{i=1}^q H_i^* W_i [y^i - h^i(x^0)] \quad (A10)$$

and

$$P_1 = \left( P_0^{-1} + \sum_{i=1}^q H_i^* W_i H_i \right)^{-1} \quad (A11)$$

instead of Equations A4 and A5, and forming the indicated sums as soon as the appropriate partial derivatives are computed, the need for storing the large matrix  $H$  is avoided.

This basic theory can be extended to the case where the parameters  $x$  are not really constant, but vary according to some known differential equations. That is, if  $x$  obeys

$$\dot{x}(t) = f[x(t)] \quad (A12)$$

and corresponding measurements of the form

$$y(t) = h[x(t)] + v(t) \quad (A13)$$

are available at  $t = t_1, t_2, \dots, t_\mu$ , a guess of the initial condition,  $x^0(t_0)$ , for Equation A12 can be improved by application of the formulas

$$x^1(t_0) = P_1^{-1} \sum_{j=1}^{q_j} \Phi^*(t_j, t_0) \sum_{i=1}^{q_j} H_i^*[x(t_j)] W_i(t_j) \{y^i(t_j) - h^i[x(t_j)]\} \quad (A14)$$

$$P_1^{-1} = P_o^{-1} + \sum_{j=1}^{q_j} \Phi^*(t_j, t_o) \left\{ \sum_{i=1}^{q_j} H_i^*[x(t_j)] W_i(t_j) H_i[x(t_j)] \right\} \Phi(t_j, t_o) \quad (A15)$$

where

$$\Phi(t_j, t_o) = \begin{bmatrix} \frac{\partial x_1(t_j)}{\partial x_1^o(t_o)} & \frac{\partial x_1(t_j)}{\partial x_2^o(t_o)} & \dots & \frac{\partial x_1(t_j)}{\partial x_n^o(t_o)} \\ \frac{\partial x_2(t_j)}{\partial x_1^o(t_o)} & \frac{\partial x_2(t_j)}{\partial x_2^o(t_o)} & \dots & \frac{\partial x_2(t_j)}{\partial x_n^o(t_o)} \\ \dots & \dots & \dots & \dots \\ \frac{\partial x_n(t_j)}{\partial x_1^o(t_o)} & \frac{\partial x_n(t_j)}{\partial x_2^o(t_o)} & \dots & \frac{\partial x_n(t_j)}{\partial x_n^o(t_o)} \end{bmatrix} \quad (A16)$$

and  $x(t_j)$  is found by direct integration of Equation A12 using the "guessed" initial condition. The  $q_j$  in Equations A14 and A15 refer to the number of submatrices in the partitions of  $y(t_j)$  and  $H[x(t_j)]$ .

The remainder of this report is concerned primarily with the application of Equations A14 and A15 to the attitude determination problem.

## A.2 Definition of Variables

For OEC it is not only necessary to estimate attitude as it changes due to the effect of solar radiation pressure, gravity gradients, and aerodynamic torque but also parameters in an arbitrarily input model for each. A capability for estimating possible biases in sensor measurements is also desired. Since attitude is determined by a unit vector in the direction of the spin axis, only two independent parameters are needed for its complete specification. (For example, right ascension and declination in some inertial coordinate system would suffice.)

The  $x$ -vector of Equations A12 and A13 thus takes the form

$$\left. \begin{matrix} x_1 \\ x_2 \end{matrix} \right\} \text{attitude parameters}$$

$$\left. \begin{matrix} x_3 \\ x_4 \\ \vdots \\ x_r \end{matrix} \right\} \text{solar pressure, gravity gradient, aerodynamic torque parameters}$$

$$\left. \begin{array}{c} x_{r+1} \\ x_{r+2} \\ . \\ . \\ . \\ x_n \end{array} \right\} \text{ measurement biases}$$

The effects of external disturbances enter the problem through the differential equations of Equation A12. Note that only  $x_1$  and  $x_2$  (the attitude parameters) are time varying. The remaining variables are governed by trivial differential equations of the form

$$\dot{x}_k = 0 (k = 3, 4, \dots, n) \quad (\text{A17})$$

Thus

$$f(x) = \begin{bmatrix} f_1(x) \\ f_2(x) \\ 0 \\ . \\ . \\ . \\ 0 \end{bmatrix} \quad (\text{A18})$$

where the functions  $f_1(x)$  and  $f_2(x)$  are derived in Section 5.0.

The  $y$ -vector of Equation A13 is a vector of measurement data related to the capsule attitude at  $t = t_j$ . Since the effect of radiation pressure is very small, several hours could pass and a large amount of data could be obtained before a change in attitude is significant. Thus as far as the differential equations of Equation A12 are concerned, time remains essentially unchanged in this period. Small changes in time, however, are very significant in interpreting sensor output because of the relatively rapid changes in orbital position of the satellite. This difference between the various data points suggests a natural way of partitioning the  $y$ -vector so that Equation A14 can be applied. That is, each subvector  $y^i$  should contain all data gathered at a specific instant in the satellite's orbit (such "instants" could be of 3 or 4 minutes duration). For OEC with a sun sensor and two Mars sensors, a typical  $y^i$  would be

$$y_1^i(t_j) = \text{sun sensor data}$$

$$y_2^i(t_j) = \text{first Mars sensor data}$$

$$y_3^i(t_j) = \text{second Mars sensor data}$$

$$y_4^i(t_j) = \text{data indicating satellite rotation between Mars and sun observation.}$$

Note that the superscripts  $i = 1, 2, \dots, q_j$  refer to specific "instants" within the basic time interval defined by  $t_j$ . Thus the estimation procedure requires two "levels" of measuring time — a coarse one to describe external pressure affects and a finer one to describe satellite position changes.

The  $h^i$ -vectors in Equation A14 correspond element for element to the  $y^i$ -vectors, but whereas the latter come from actual measurement data, the former come from computing the sensor outputs from "guessed" values of attitude and other parameters. (See Section A.4 for deviations of the appropriate relationships).

In general, the  $H_i$  matrices used in Equations A14 and A15 may have to be computed by numerically differentiating  $h^i(x)$ . For the typical sensors described above, however, analytical expression for the required partial derivatives can be easily derived and should be used in the new attitude determination program.

Finally, the functions in  $\Phi(t_j, t_0)$  are computed from the definition given in Equation A16 by numerically perturbing the differential equations of Equation A13. Note that if the  $f(x)$  functions are all zero, the  $\Phi(t_j, t_0)$  matrices become identity matrices and Equations A14 and A15 reduce to Equations A10 and A11 respectively.

### A.3 Discussion of Flow Diagram (See Figure A-1)

The input and output format for this process are expressed in terms of right ascension and declination in a fixed inertial system. To avoid ambiguities and permit convenience in computation, these vectors are transformed to a coordinate system such that the positive direction of the third axis (z-axis\*) coincides with the initial guess of the satellite spin axis. The corrected satellite attitude vector is determined in this system by specifying components along the two other axes. The third component is always

$$+ \sqrt{1 - x_1^2 - x_2^2}$$

because attitude must be a unit vector. (Note that the positive square root is taken because attitude corrections will be small.)

Attitude maneuvers are permitted at some time  $t = t_1$  after the initial guess, but before any data are used. The effect of a maneuver is to change the attitude guess in some predetermined way. The parameter covariance matrix is, of course, adjusted to account for the increased uncertainty.

The remaining computations on the first page of the flow diagram (Figure A-1) concern integration of the solar radiation equations. The scheme shown was specially derived to permit efficient sequential computation of the matrices  $\Phi(t_1, t_0)$ ,  $\Phi(t_2, t_0)$ , ...,  $\Phi(t_\mu, t_0)$  and the attitude parameters  $x_1(t_1)$ ,  $x_1(t_1)$ ;  $x_2(t_2)$ ,  $x_2(t_2)$ ; ...;  $x_1(t_\mu)$ ,  $x_2(t_\mu)$ .

---

\*Where necessary, the usual x, y, and z-axis designations have been suppressed in favor of the first, second and third axis to avoid confusion with the x- and y-vectors of the estimation scheme.

On the second page of Figure A-1 the details of applying Equations A14 and A15 to the attitude determination problem are shown. Note that the data at  $t = t_j$  has been broken down into  $q_j$  sets of four data points. The computations implied symbolically in the "sensor" block are described in detail in the following pages.

#### A.4 Sensor Relationships

In each case below, the sensor output is interpreted as a spacecraft rotation angle. Formulas for these angles in terms of an assumed attitude and the known sensor configuration are then derived. The actual angles correspond to the components of the  $y^i$ -vectors in Equation A14, while the angles computed from the assumed attitude correspond to the components on the  $h^i$ -vectors.

For the convenience in presenting the derivations, the symbols  $a = (a_1, a_2, a_3)$ ,  $m = (e_1, e_2, e_3)$  and  $s = (s_1, s_2, s_3)$  are used to denote unit vectors in the direction of the satellite spin axis, the satellite-Mars line and the satellite-Sun line, respectively. Note that the  $a$ -vector is always the "present" guess of the satellite attitude. Its components are computed as

$$x_1, x_2, \sqrt{1 - x_1^2 - x_2^2}$$

where the quantities  $x_1$  and  $x_2$  should be interpreted as  $x_1(t_j)$  and  $x_2(t_j)$ . They are evaluated from the guessed attitude parameters  $x_1^0(t_0)$  and  $x_2^0(t_0)$  by direct integration of Equation A13.

##### Sun Sensor

The sensor configuration consists basically of two long sun-sensitive "slits" — one in a plane containing the spin axis and the other in a plane inclined with respect to the spin axis by an angle  $\xi$ . A pulse is transmitted to earth whenever the Sun's rays directly penetrate a slit. The spacecraft rotation angle between sensor pulses is effectively the "output" of the instrument for it can be directly computed as

$$\Psi = \frac{\tau_2}{\tau_1} 2\pi \quad (A19)$$

where

$\tau_1$  = time between pulses of the same sensor (the sensor containing the spin axis is usually used as the reference)

$\tau_2$  = time elapsed between the spin axis sensor pulse and the inclined sensor pulse.

To compute a corresponding value of  $\Psi$  from an assumed attitude, consider the geometry of Figure A-2. At the instant the sun activates the inclined sensor, the sun direction vector must be perpendicular to the normal to this sensor plane.



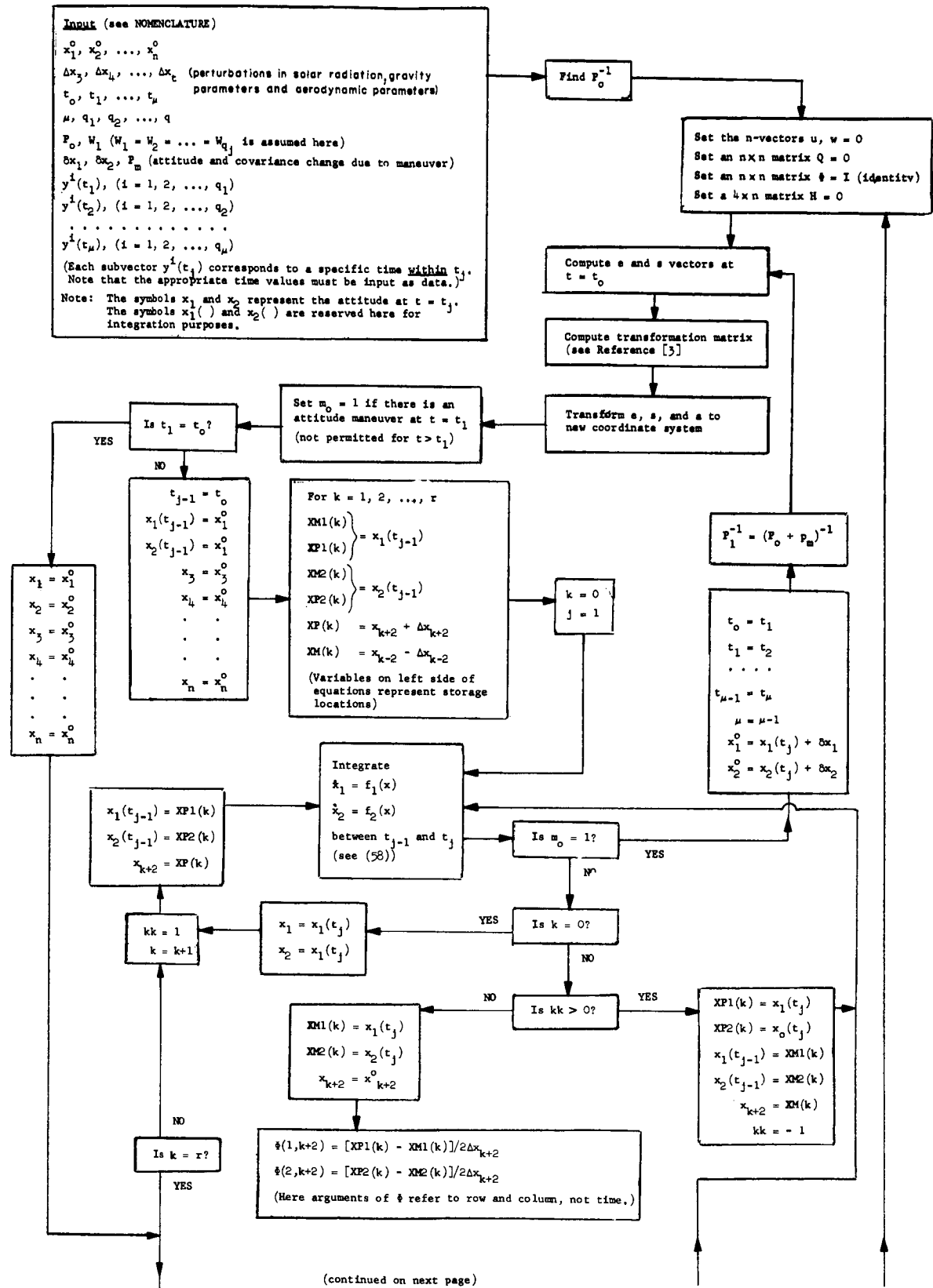


Figure A-1. Flow Diagram for Attitude Determination

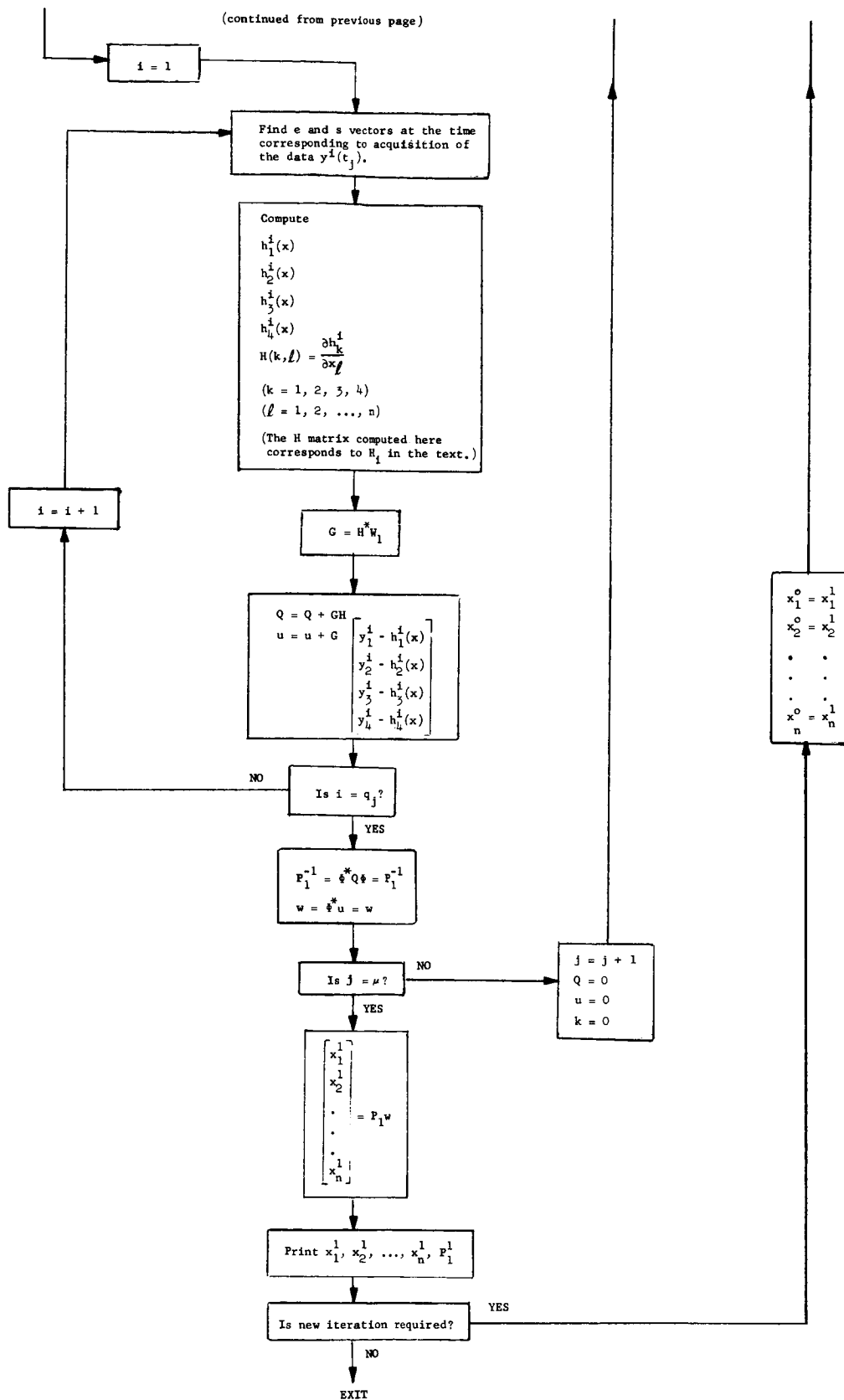


Figure A-1 (continued). Flow Diagram for Attitude Determination

From the diagram, the unit vector in the direction of the sun is  $(\cos \Psi \sin \phi, -\sin \Psi \sin \phi, \cos \phi)$ , and the unit normal to the inclined sensor is  $(0, \cos \xi, \sin \xi)$ .

Thus

$$(\cos \Psi \sin \phi, -\sin \Psi \sin \phi, \cos \phi) \cdot (0, \cos \xi, \sin \xi) = 0 \quad (\text{A20a})$$

$$-\sin \Psi \sin \phi \cos \xi + \cos \phi \sin \xi = 0, \quad (\text{A20b})$$

$$\sin \Psi = \frac{\cot \phi}{\cot \xi} \quad (\text{A20c})$$

Now since the vectors  $a$  and  $s$  are known,  $\phi$  is also known from

$$\cos \phi = a \cdot s \quad (\text{A21})$$

so that

$$\cot \phi = \frac{a \cdot s}{\sqrt{1 - (a \cdot s)^2}} \quad (\text{A22})$$

Then Equation A20c becomes

$$\Psi = \arcsin \left[ \frac{a \cdot s}{\cot \xi \sqrt{1 - (a \cdot s)^2}} \right] \quad (\text{A23})$$

In general, the inclined sensor plane may be rotated about the spacecraft by an angle  $\Psi_s$  with respect to the other sensor plane (measured in the spin direction). For such a case,

$$\Psi = \arcsin \left[ \frac{a \cdot s}{\cot \xi \sqrt{1 - (a \cdot s)^2}} \right] + \Psi_s \quad (\text{A24})$$

In terms of the estimated attitude parameters,  $x_1$  and  $x_2$ , Equation A24 becomes

$$\Psi = \arcsin \left[ \frac{s_1 x_1 + s_2 x_2 + s_3 \sqrt{1 - x_1^2 - x_2^2}}{\cot \xi \sqrt{1 - (s_1 x_1 + s_2 x_2 + s_3 \sqrt{1 - x_1^2 - x_2^2})^2}} \right] + \Psi_s \quad (\text{A25})$$

For use of sun sensor data in Equations A14 and A15, identify Equation A19 with  $y_1^i$  and A25 with  $h^i(x)$ . \*

Now even if  $x_1$  and  $x_2$  were very close to the true value of the attitude parameters, the value of  $\Psi$  from Equation A24 could be in considerable error because of misalignments in specifying  $\xi$  and  $\Psi_s$ . These "biases", however, can be estimated in the same way attitude is estimated. That is, assume them to be  $x_{r+1}$ ,  $x_{r+2}$ \*\* and use the function

$$\Psi = \arcsin \left[ \frac{s_1 x_1 + s_2 x_2 + s_3 \sqrt{1 - x_1^2 - x_2^2}}{\cot(\xi + x_{r+2}) \sqrt{1 - (s_1 x_1 + s_2 x_2 + s_3 \sqrt{1 - x_1^2 - x_2^2})^2}} \right] \quad (A26)$$

$$+ \Psi_s + x_{r+1}$$

for  $h_1^i(x)$  in Equation A14. Note that if the  $a$  and  $s$  vector do not vary much, the parameter  $x_{r+2}$  could be eliminated and any bias in  $\xi$  would be included in  $x_{r+1}$ .

#### Mars Sensors

The Mars horizon sensor is essentially a narrow infrared sensitive tube mounted so that its axis passes through the center of the spacecraft. As the satellite rotates, the field of view through this tube traces out a cone in space. A pulse is transmitted when this sensor first "sees" the edge of Mars and then again when it leaves the Mars' disk. The spacecraft rotation angle ( $2\alpha_1$ ) between these pulses is clearly computed from

$$\alpha_1 = \frac{\pi \tau_3}{\tau_1} \quad (A27)$$

where

$\tau_1$  = rotation period

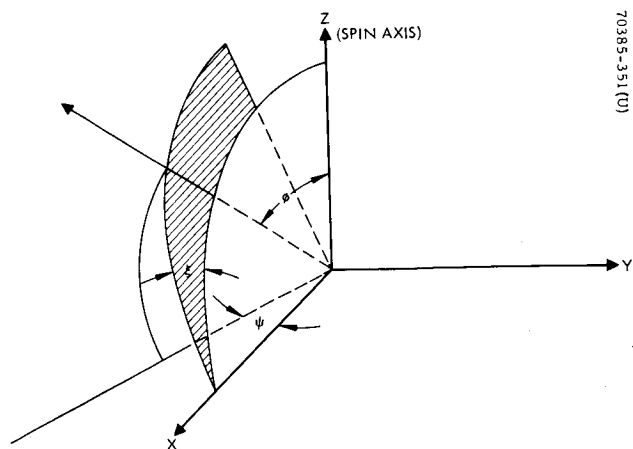
$\tau_3$  = time between horizon pulses.

To derive a formula for computing  $\alpha_1$  from an assumed attitude, note that, in addition to  $\eta_1$ , the angle between the spin axis and the Mars satellite line ( $\gamma$ ) and the half angle subtended by the Mars disk ( $\alpha_0$ ) will be known. The former is computed from

$$\cos \gamma = a \cdot m \quad (A28)$$

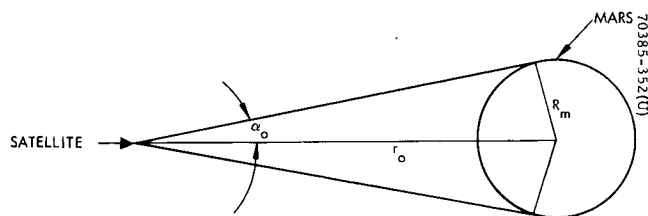
\*The superscript  $i$  as used here refers to the time at which the  $s$ -vector is computed.

\*\*Recall that  $x_1$  and  $x_2$  refer to attitude parameters while  $x_3, x_4, \dots, x_r$  refer to solar radiation model parameters.



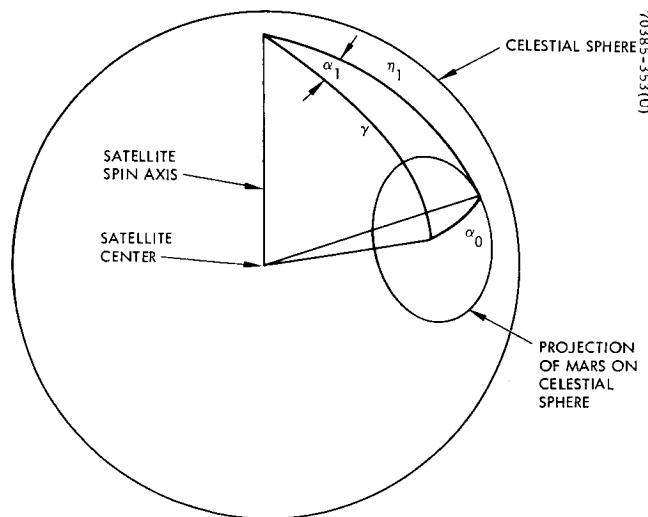
70385-351 (U)

Figure A-2. Sun Sensor Geometry



70385-352 (U)

Figure A-3. Angle Subtended by Mars at Satellite Altitude



70385-353 (U)

Figure A-4. Mars Sensor Configuration (Spherical Trigonometry)

and the latter from

$$\sin \alpha_o = \frac{R_m}{r_o} \quad (A29)$$

where  $R_m$  is the radius of Mars and  $r_o$  is the orbital altitude from the center of Mars. (See Figure A-3.)

The desired formula for  $\alpha_1$  is derived next.

Consider the celestial sphere centered at the spacecraft as shown in Figure A-4. The known angles  $\alpha_o$ ,  $\eta$ ,  $\phi_m$ , and the unknown angle  $\alpha_1$  are appropriately labeled.\* By direct application of the Law of Cosines to the spherical triangle shown in the diagram, a formula for  $\alpha_1$  can be found immediately. Thus

$$\cos \alpha_1 = \frac{\cos \alpha_o - \cos \phi_m \cos \eta}{\sin \phi_m \sin \eta} \quad (A30a)$$

or, using Equations A28 and A29,

$$\alpha_1 = \arccos \left[ \frac{\sqrt{r_o^2 - R_m^2}/r_o - (a \cdot m) \cos \eta}{\sin \eta \sqrt{1 - (a \cdot m)^2}} \right] \quad (A30b)$$

For use in the estimation procedure, the basic Mars sensor equation (A30b) should be expressed as

$$\alpha_1 = \arccos \left[ \frac{\sqrt{r_o^2 - R_m^2}/r_o - (e_1 x_1 + e_2 x_2 + e_3 \sqrt{1 - x_1^2 - x_2^2}) \cos(\eta + x_{r+3})}{\sin(\eta + x_{r+3}) \sqrt{1 - (e_1 x_1 + e_2 x_2 + e_3 \sqrt{1 - x_1^2 - x_2^2})^2}} \right] \quad (A31)$$

where  $x_{r+3}$  is a possible bias in the value of  $\eta$ . (If changes in  $a$  and  $e$  are small,  $x_{r+3}$  can be as an additive bias as  $x_{r+1}$  is used in Equation A26.)

In actual practice, an OEC will have two independent Mars sensors — one mounted at an angle  $\eta$  with the spin axis and another at an angle  $\eta_2$  with the spin axis. These angles are chosen so that the sensor paths cross Mars in opposite

\*Angles on the surface of the sphere refer to angles between planes passing through the center of the sphere. Lines on the surface refer to angles between lines passing through the center of the sphere.

hemispheres. By analogy to Equation A27, the spacecraft rotation angle ( $2a_2$ ) between pulses of the second sensor is computed from

$$a_2 = \frac{\pi \tau_4}{\tau_1} \quad (A32)$$

where  $\tau_4$  is the time between these pulses. Similarly by analogy to Equation A31, a value of  $a_2$  based on the assumed attitude

$$a = \left( x_1, x_2, \sqrt{1 - x_1^2 - x_2^2} \right)$$

is found from

$$a_2 = \arccos \left[ \frac{\sqrt{r_o^2 - R_m^2 / r_o} - (e_1 x_1 + e_2 x_2 + e_3 \sqrt{1 - x_1^2 - x_2^2}) \cos(\eta_2 + x_{r+4})}{\sin(\eta_2 + x_{r+4}) \sqrt{1 - (e_1 x_1 + e_2 x_2 + e_3 \sqrt{1 - x_1^2 - x_2^2})^2}} \right] \quad (A33)$$

where  $x_{r+4}$  represents the bias in  $\eta_2$ . Note that Equations A27 and A32 represent  $y_2^i$  and  $y_3^i$  of A14, respectively, while Equations A31 and A33 correspond to the functions  $h_2^i(x)$  and  $h_3^i(x)$  used in that same basic equation.

#### Separation Between Sun and Mars Pulses

To this point it has been shown that the Sun and Mars sensors each contribute an element to the  $y^i$  and  $h^i$  vectors. For a spacecraft having both types of sensors, an additional independent data point is usually available. If  $\tau_5$  is the time between the reference Sun sensor pulse and the leading pulse of one of the Mars sensors (say, the one whose output is  $\tau_3$ ), the corresponding spacecraft rotation angle is

$$\lambda = \frac{2\pi}{\tau_1} (\tau_5 + \tau_3) \quad (A34)$$

This angle is clearly independent of the angles  $\Psi$ ,  $a_1$ , and  $a_2$  and provides more information for estimating the unknown parameters.

A corresponding value of  $\lambda$  can be computed from an assumed attitude vector by use of the formula

$$\lambda = \lambda_r - \lambda_s, \quad (0 \leq \lambda \leq 2\pi) \quad (A35)$$

where

$\lambda_s$  = angle from the Sun sensor to the Mars sensor in the spin direction  
( $0 \leq \lambda_s \leq 2\pi$ )

$\lambda_r$  = angle from the Sun-satellite axis plane to the Mars-satellite axis plane in the spin direction ( $0 \leq \lambda_r \leq 2\pi$ )

Now the angle  $\lambda'_r$  computed from the formula

$$\cos \lambda'_r = \frac{(a \times s) \cdot (a \times m)}{\sin \phi \sin \phi_m}, \quad (A36)$$

or more simply from

$$\cos \lambda'_r = \frac{(s \cdot m) - (a \cdot m)(a \cdot s)}{\sqrt{(1 - (a \cdot m)^2)(1 - (a \cdot s)^2)}}, \quad (A37)$$

will indeed be the angle between the two planes of interest, but it will not necessarily be in the spin direction. That is either  $\lambda_r = \lambda'_r$  or  $\lambda_r = 2\pi - \lambda'_r$  is possible. This ambiguity can be removed by the following considerations.

The vectors  $(a \times s)$  and  $(a \times e)$  are in the spin plane. Thus  $(a \times s) \times (a \times e)$  is either in the same direction as the  $a$ -vector or in the opposite direction. If it is in the same direction,  $\lambda_r = \lambda'_r$  as computed from Equation A30 is the desired angle. If it is in the opposite direction,  $\lambda_r = 2\pi - \lambda'_r$ . Since

$$(a \times s) \times (a \times m) = -(\det U)a, \quad (A38)$$

where

$$U = \begin{bmatrix} s_1 & a_1 & e_1 \\ s_2 & a_2 & e_2 \\ s_3 & a_3 & e_3 \end{bmatrix}, \quad (A39)$$

$$\lambda_r = \lambda'_r \quad \text{if } \det U < 0$$

$$\lambda_r = 2\pi - \lambda'_r \quad \text{if } \det U > 0. \quad (A40)$$



Note that Equations A35, A37, and A38 can be expressed more compactly as

$$\lambda = \left\{ \pi - \arccos \left[ \frac{(s \cdot m) - (a \cdot m)(a \cdot s)}{\sqrt{[1 - (a \cdot m)^2][1 - (a \cdot s)^2]}} \right] \right\} \frac{\det U}{|\det U|} - \lambda_s + \pi, \quad (0 \leq \lambda \leq 2\pi). \quad (A41)$$

Thus Equation A34 corresponds to  $y_4^i$ , and A41 in the form,

$$\eta = \frac{\det U}{|\det U|} [\pi - \arccos \beta] + \lambda_s + x_{r+5} + \pi \quad (A42)$$

where

$$\beta = \frac{(s \cdot m) - (e_1 x_1 + e_2 x_2 + e_3 \sqrt{1 - x_1^2 - x_2^2})(s_1 x_1 + s_2 x_2 + s_3 \sqrt{1 - x_1^2 - x_2^2})}{\sqrt{[1 - (e_1 x_1 + e_2 x_2 + e_3 \sqrt{1 - x_1^2 - x_2^2})^2][1 - (s_1 x_1 + s_2 x_2 + s_3 \sqrt{1 - x_1^2 - x_2^2})^2]}}, \quad (A43)$$

corresponds to  $h_4^i(x)$ . Note that  $x_{r+5}$  is a possible bias in  $\lambda_s$ .

#### Summary of Sensor Relationships\*

##### Sun Sensor

$$y_1^i = \frac{\tau_2}{\tau_1} 2\pi \quad (A44)$$

$$h_1^i(x) = \arcsin \left[ \frac{s_1 x_1 + s_2 x_2 + s_3 \sqrt{1 - x_1^2 - x_2^2}}{\cot(\xi + x_{r+2}) \sqrt{1 - (s_1 x_1 + s_2 x_2 + s_3 \sqrt{1 - x_1^2 - x_2^2})^2}} \right] + \Psi_s + x_{r+1} \quad (A45)$$

\*During the interval described by  $t = t_j$  there are  $i = 1, 2, \dots, q_j$  "sets" of sensor measurements. The equations of this section refer to any one of these sets. The sets are distinguished from one another by the particular  $e$ - and  $s$ -vectors used in the computations.

First Mars Sensor

$$y_2^i = \frac{\tau_3 \pi}{\tau_1} \quad (\text{A46})$$

$$h_2^i(x) = \arccos \left[ \frac{\sqrt{r_o^2 - R_m^2}/r_o - (e_1 x_1 + e_2 x_2 + e_3 \sqrt{1 - x_1^2 - x_2^2}) \cos(\eta + x_{r+3})}{\sin(\eta + x_{r+3}) \sqrt{1 - (e_1 x_1 + e_2 x_2 + e_3 \sqrt{1 - x_1^2 - x_2^2})^2}} \right] \quad (\text{A47})$$

Second Mars Sensor

$$y_3^i = \frac{\tau_4 \pi}{\tau_1} \quad (\text{A48})$$

$$h_3^i(x) = \arccos \left[ \frac{\sqrt{r_o^2 - R_m^2}/r_o - (e_1 x_1 + e_2 x_2 + e_3 \sqrt{1 - x_1^2 - x_2^2}) \cos(\eta_2 + x_{r+4})}{\sin(\eta_2 + x_{r+4}) \sqrt{1 - (e_1 x_1 + e_2 x_2 + e_3 \sqrt{1 - x_1^2 - x_2^2})^2}} \right] \quad (\text{A49})$$

Sun-Mars Separation Data

$$y_4^i = \frac{2\pi}{\tau_1} (\tau_5 + \tau_3) \quad (\text{A50})$$

$$h_4^i(x) = \frac{\det U}{|\det U|} [\pi - \arccos \beta] + \lambda_s + x_{r+5} + \pi, \quad (\text{A51})$$

where

$$\beta = \frac{(s \cdot m) - (e_1 x_1 + e_2 x_2 + e_3 \sqrt{1 - x_1^2 - x_2^2})(s_1 x_1 + s_2 x_2 + s_3 \sqrt{1 - x_1^2 - x_2^2})}{\sqrt{[1 - (e_1 x_1 + e_2 x_2 + e_3 \sqrt{1 - x_1^2 - x_2^2})^2][1 - (s_1 x_1 + s_2 x_2 + s_3 \sqrt{1 - x_1^2 - x_2^2})^2]}} \quad (\text{A52})$$

and

$$U = \begin{bmatrix} s_1 & x_1 & e_1 \\ s_2 & x_2 & e_2 \\ s_3 & \sqrt{1 - x_1^2 - x_2^2} & e_3 \end{bmatrix} \quad (A53)$$

#### A.5 Solar Radiation Effects

Let  $\mathcal{H}$  be the angular momentum vector of a spinning spacecraft. The torque due to solar pressure (T) will cause a change  $d\mathcal{H}$  in the direction defined by  $(s \times \mathcal{H})$  and of magnitude

$$|d\mathcal{H}| = T dt \quad (A54)$$

Then

$$\frac{d\mathcal{H}}{dt} = T \frac{(s \times \mathcal{H})}{|s \times \mathcal{H}|} \quad (A55)$$

is a vector differential equation describing the change in angular momentum with time. Assuming that the  $\mathcal{H}$ -vector is coincident with the a-vector, and that  $|\mathcal{H}|$  is constant, the equation

$$d\mathcal{H} = |\mathcal{H}| da \quad (A56)$$

will be valid and Equation A55 becomes the more useful expression

$$\frac{da}{dt} = \frac{T}{|\mathcal{H}|} \frac{(s \times a)}{|s \times a|} \quad (A57)$$

Now the solar torque is generally a function of the Sun-satellite angle  $\phi$ . Over a several week period, this curve can be approximated sufficiently well by a low order polynomial in  $\phi$ . Since it is desired to estimate this curve, the unknown parameters  $x_3, x_4, \dots, x_r$  are introduced to represent the coefficients. Then, using

$$a = x_1, x_2, \sqrt{1 - x_1^2 - x_2^2}$$

Equation A57 becomes

$$\frac{dx_1}{dt} = \frac{T(x_3, x_4, \dots, x_r; \phi)}{|\mathcal{H}|} \frac{\left[ s \times \left( x_1, x_2, \sqrt{1 - x_1^2 - x_2^2} \right) \right]}{\left| s \times \left( x_1, x_2, \sqrt{1 - x_1^2 - x_2^2} \right) \right|} \text{ 1st component} \quad (\text{A58a})$$

and

$$\frac{dx_2}{dt} = \frac{T(x_3, x_4, \dots, x_r; \phi)}{|\mathcal{H}|} \frac{\left[ s \times \left( x_1, x_2, \sqrt{1 - x_1^2 - x_2^2} \right) \right]}{\left| s \times \left( x_1, x_2, \sqrt{1 - x_1^2 - x_2^2} \right) \right|} \text{ 2nd component} \quad (\text{A58b})$$

The right-hand side of Equations A58a and A58b are the functions  $f_1(x)$  and  $f_2(x)$  in Equation A13.

## A.6 Nomenclature

a	Unit vector in the direction of the satellite spin axis
m	Unit vector along satellite-Mars line
f(x)	n-vector function defined by Equation A12
$h[x(t_j)]$ or $h(x)$	m-vector of predicted sensor measurements at $t = t_j$ based on guessed values of the unknown parameters. It is partitioned into subvectors $h^i(x)$ , ( $i = 1, 2, \dots, q_j$ ) of four elements each.
H	$m \times n$ matrix of partial derivatives defined by (A3). It is partitioned into $4 \times n$ submatrices $H_i$ ( $i = 1, 2, \dots, q_j$ ).
$\mathcal{H}$	Angular momentum of satellite
i	Index used to describe the partitioning of $y(t)$ , $h(x)$ , and $H$ . ( $i = 1, 2, \dots, q_j$ )
j	Index used to $t$ . ( $j = 1, 2, \dots, \mu$ )
m	Total number of measurements at $t = t_j$
n	Total number of parameters to be estimated
$P_o$	Covariance of guessed parameters

$P_1$	Corrected parameter covariance matrix
$q_j$	Number of submatrices in the partitions of $y(t)$ , $h(x)$ , $H$ at $t = t_j$
$r$	Two more than the number of parameters in the solar torque curve
$R_m$	Radius of Mars
$r_o$	Distance from center of Mars to satellite
$s$	Unit vector along satellite-Sun line
$t$	Time
$t_o$	Time at which guessed attitude is valid
$t_j$	Times at which data are available. Each $t_j$ represents a several hour period (i. e., $t_j$ could be the midpoint of this period). The equations $\dot{x} = f(x)$ must be integrated between $t_{j-1}$ and $t_j$ .
$v$	m-vector of sensor noise
$w_i$	Weighting matrices
$x(t)$	Parameter vector. The argument is omitted whenever possible.
$x^o(t_o)$	Guess of parameter vector at $t = t_o$ . By integration with this as an initial condition, the corresponding attitude at $t = t_j$ can be found.
$x^1(t_o)$	Corrected parameter vector at $t = t_o$
$y(t_j)$ or $y$	m-vector of measurements taken in the several hour period defined by $t = t_j$ . This vector is partitioned into subvectors $j^i(t_j)$ , ( $i = 1, 2, \dots, q_j$ ) of four components each. Note that each subvector corresponds to data taken at a specific time within the interval covered by $t_j$ .
$\alpha_o$	Half-angle subtended by disk of Mars at the satellite
$\alpha_1, (\alpha_2)$	Half the spacecraft rotation angle between pulse at first (second) Mars sensor
$\beta$	Defined by Equation A49
$\phi_m$	Angle between spin axis and satellite-Mars line
$\phi$	Angle between spin axis and satellite-Sun line
$\xi$	Angle between planes containing the Sun sensor slits
$\eta, (\eta_2)$	Angle between spin axis and first (second) Mars sensor axis

$\lambda$	Spacecraft rotation angle between reference Sun sensor pulse and leading pulse of 1st Mars sensor. ( $0 \leq \lambda \leq 2\pi$ )
$\lambda_r$	Spacecraft rotation angle from Sun-satellite axis plane to Mars-satellite axis plane measured in the spin direction ( $0 \leq \lambda_r \leq 2\pi$ )
$\lambda_r'$	Angle between Sun-satellite axis plane and Mars satellite axis plane
$\lambda_s$	Rotation angle from reference Sun sensor to first Mars sensor measured in the spin direction ( $0 \leq \lambda_s \leq 2\pi$ )
$\Psi$	Spacecraft rotation angle between reference and inclined Sun sensor pulses
$\Psi_s$	Rotation angle between Sun sensor planes measured in the spin direction
$\mu$	Number of times at which data are available
$\tau_1$	Time between pulses of reference Sun sensor (rotation period)
$\tau_2$	Time between reference and inclined Sun sensor pulses
$\tau_3, (\tau_4)$	Time between horizon pulses of first (second) Mars sensor
$\tau_5$	Time between reference Sun sensor pulse and leading pulse of first Mars sensor

## APPENDIX B. ORBIT DETERMINATION

### B.1 Differential Correction

The manner in which differential corrections are computed is presented below.

The nominal orbit is given by a set of  $n$  orbital parameters, represented by the  $n$ -vector (column matrix)  $p$ . The set of orbital parameters may contain the classical parameters or initial position and velocity or any equivalent set; in addition, the set includes all constants to be estimated and, if attitude determination is accomplished concurrently, whatever parameters are used for specifying the attitude. The assumption is made that given  $p$  and a time  $t$ , the position, velocity, and attitude can be computed for that time.

Let the vector  $x$  represent the state of the system; then  $x = x(t, p)$ . Note that  $x$  will contain the state of Voyager if Voyager ranging information is to be used. Given the state at time  $t$ ,  $x(t, p)$ , it is possible to compute each measurement taken at that time. Let  $h = h(t, x(t, p))$  be the  $m$ -vector with components equal to the set of  $m$  measurements taken at time  $t$ . Let  $p_N$  denote the nominal orbit parameter set; the nominal measurement at time  $t$  is  $h_N(t) = h(t, x(t, p_N))$ .

Assume that measurements are taken at times  $t_i$ ,  $i = 1, \dots, k$  giving a set of vectors  $h(t_i)$ . For each measurement vector there is a corresponding nominal,  $h_N(t_i)$ . Now, define an operation called "stack," denoted  $S$ , where, for  $\phi$ -vector arguments  $v^i$

$$S(v^1, \dots, v^j) \triangleq \begin{bmatrix} v_1^1 \\ \vdots \\ v_l^1 \\ \vdots \\ v_1^j \\ \vdots \\ v_l^j \end{bmatrix} \quad (B1)$$

In other words, stack forms a "super vector" whose components are the components of its arguments, taken in order. Let

$$\epsilon \triangleq S_h - S_{h_N} \triangleq S(h(t_1), \dots, h(t_k)) - S(h_N(t_1), \dots, h_N(t_k)) \quad (B2)$$

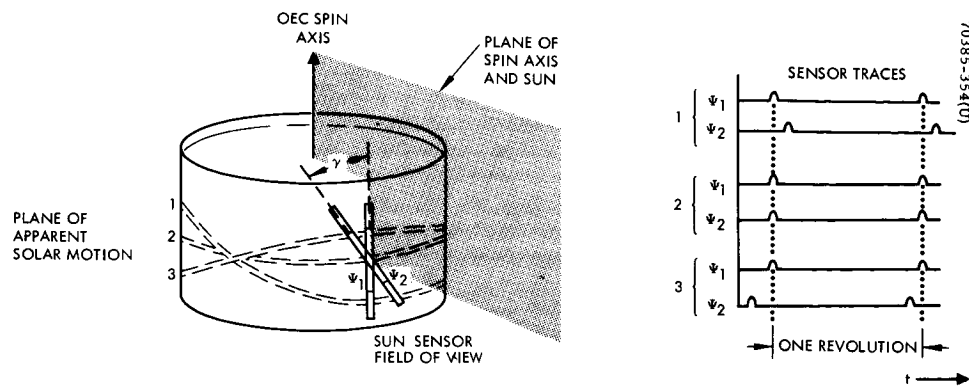


Figure B-1. Sun Sensor Measurement

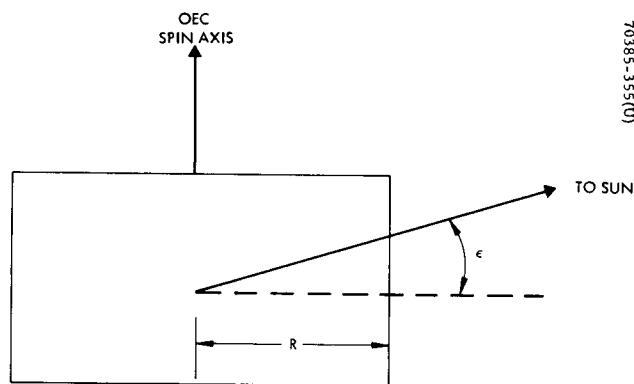


Figure B-2. Spin Axis Relation to Sun

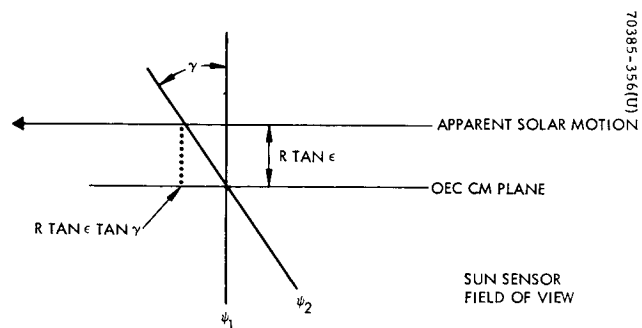


Figure B-3. Motion of Sun Across Sun Sensor Field of View



The differential correction scheme, in essence, computes a change in  $p$  based on the stacked measurement error as follows:

$$\Delta p = M\epsilon \quad (B3)$$

where  $M$  is an  $n \times m_k$  matrix that depends upon the form of  $h$  and upon which differential correction method is used. The classical least squares technique results in a matrix

$$M = \left\{ \left[ \partial S_h / \partial p \right]^T \left[ \partial S_h / \partial p \right] \right\}^{-1} \left[ \partial S_h / \partial p \right]^T \quad (B4)$$

where

$$\left[ \partial S_h / \partial p \right]$$

denotes the matrix of partial derivatives evaluated at  $p_N$ , of the elements of  $S_h$  with respect to the elements of  $p$ , and where  $T$  denotes matrix transpose.

The reason for the preceding description of the differential correction is to show explicitly that the orbit determination algorithm does not need a complete position/attitude measurement each time data is taken. Indeed, if the definition of  $M$  is modified by replacing the inverse in (B4) by the pseudo-inverse, assuming  $\partial S_h / \partial p$  is not zero, some improvement in  $p_N$  is available after only a single data point is obtained. Generally, however, the greater the amount of independent data taken at each measurement instant, the faster the accuracy of the estimate improves. In fact, the choice of sensors can be based on the time it takes to reach a desired accuracy level for each candidate sensor package.

## B.2 Interpretation of Sensor Pulse Data

The basic element in the sun sensor has a slit opening offering a fan-shaped field of view; it provides a signal when the sun is in the field of view. A single sensor would be useful only to generate an azimuth reference pulse. But two of them can provide elevation information also. The operation of this dual element device is shown schematically in Figure B-1. One element, labeled  $\Psi_1$  is mounted parallel to the spin axis, the other, labeled  $\Psi_2$  is canted at an angle  $\gamma$  in such a way that for zero elevation the signals from both sensors occur at the same time (case 2 in Figure B-1). If the sun is at a non-zero elevation, the  $\Psi_2$  signal is displaced from the  $\Psi_1$  signal by an interval that depends upon the elevation.

From Figure B-2 it is seen that the sun intersects the side of the vehicle at a height  $R \tan \epsilon$  above the equator of the vehicle, where  $R$  is the radius of the OEC and  $\epsilon$  is the elevation. From Figure B-3 it is seen that the arc between the intersection of the apparent sun with  $\Psi_1$  and  $\Psi_2$  is  $R \tan \epsilon \tan \gamma$ . If the spin rate is  $\omega$ , the temporal separation between the pulses is then

$$\Delta t = (\tan \epsilon)(\tan \gamma) / \omega \quad (B5)$$

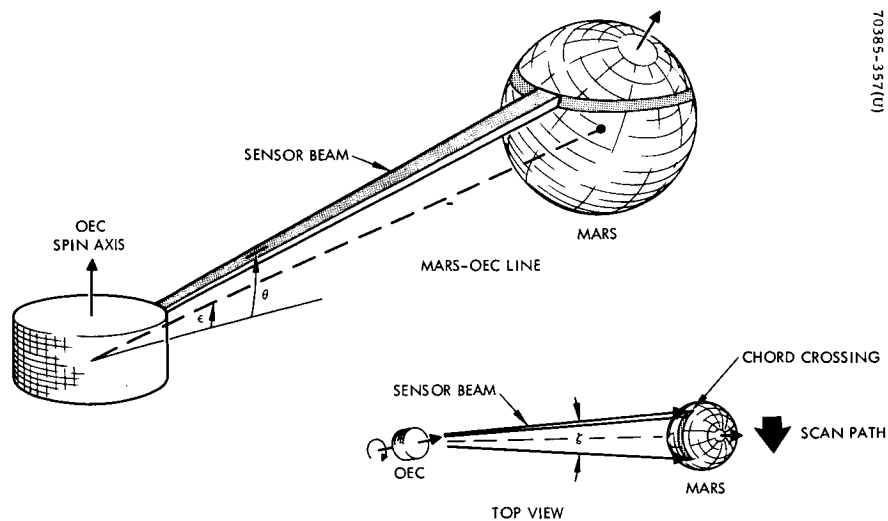


Figure B-4. Mars Sensor Measurement Geometry

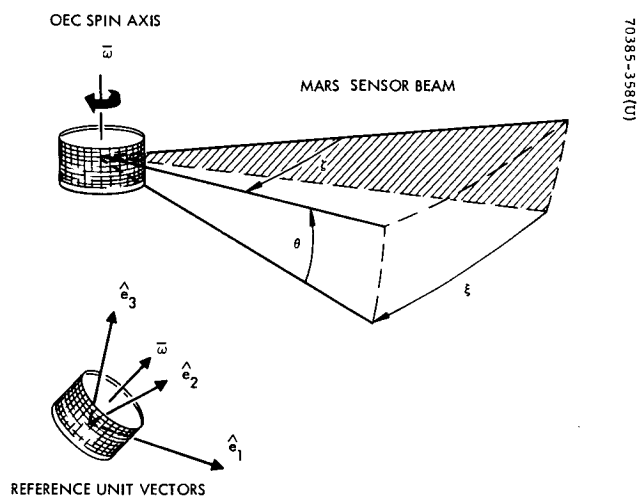


Figure B-5 Scan Path Geometry

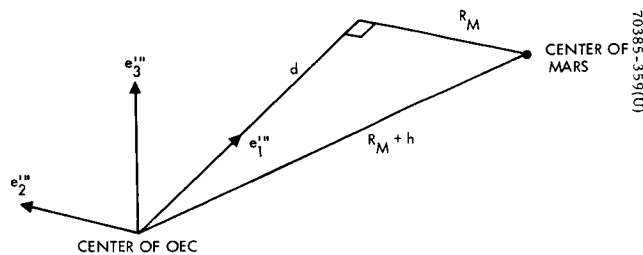


Figure B-6. Geometry for Mass Measurements

Inverting Equation B5 provides an expression for  $\epsilon$  in terms of the measured time interval and the assumed known values of  $\gamma$  and  $\omega$ .

The planet sensor can be considered a narrow beam that generates a pulse when the beam encounters an edge of the planet, i.e., when the area viewed changes from the black of space to the albedo of the planet and viceversa. The interval between pulses depends on both the altitude above the planet and the elevation of the planet, as will now be shown. For reasons that will be discussed subsequently, the sensor beam is assumed to be canted at an angle  $\theta$  from the vehicular equator. The situation is depicted in Figure B-4; since the beam traces out a cone in space with vertex angle  $\pi - 2\theta$ , the path of the beam across Mars is the intersection of the cone with Mars, assumed to be spherical.

To compute the time interval between pulses it is necessary to compute the spacecraft azimuthal change  $\xi$  corresponding to the angle  $\zeta$  between the beams that graze the planet, as shown in Figure B-4. The relationship between  $\zeta$  and the corresponding azimuthal change in the spacecraft is depicted in Figure B-5, from which it can be shown that

$$\xi = 2 \sin^{-1} \left[ \tan(\zeta/2) / \cos \theta \right] \quad (B6)$$

Define a right-handed, spacecraft-centered triad, as follows: the 1-axis points toward the center of Mars and the 2-axis is along the cross product of the spin-axis with the 1-axis. The resulting 3-axis is in the plane of the spin-axis and the 1-axis, pointing generally "up," as defined by the positive direction of the spin-axis (see Figure B-6). The following sequence of rotation takes the  $e_1$  axis into a unit vector along the grazing beam:

- 1)  $+\epsilon$  about  $e_2$ , giving the  $e_1', e_2', e_3'$  triad
- 2)  $+\xi/2$  about  $e_3'$ , giving the  $e_1'', e_2'', e_3''$  triad
- 3)  $-\theta$  about  $e_2''$ , giving the  $e_1''', e_2''', e_3'''$  triad.

#### Orbit Determination for OEC

The final situation is shown in Figure B-6, where  $R_M$  denotes the radius of Mars and  $h$  denotes the altitude of OEC. Figure B-6 reflects the fact that the condition for grazing is that the beam be perpendicular to a radius at the point of intersection. It is evident from the drawing that the distance from OEC to the graze point is equal to the  $e_1'''$  component of the vector from OEC to the center of Mars, and that the length in question is given by

$$d^2 = (R_M + h)^2 - R_M^2 \quad (B7)$$

Let  $\Omega$  denote the rotation matrix defined by the three rotations described in the preceding paragraph. The  $e_1'''$  component of the OEC-Mars vector is given by

$$\begin{bmatrix} 1 & 0 & 0 \end{bmatrix} \begin{bmatrix} \Omega_{11} & \Omega_{12} & \Omega_{13} \\ \Omega_{21} & \Omega_{22} & \Omega_{23} \\ \Omega_{31} & \Omega_{32} & \Omega_{33} \end{bmatrix} \begin{bmatrix} R_M + h \\ 0 \\ 0 \end{bmatrix} = \Omega_{11} (R_M + h) \quad (B8)$$

Since

$$\Omega = \begin{bmatrix} \cos \theta & 0 & \sin \theta \\ 0 & 1 & 0 \\ -\sin \theta & 0 & \cos \theta \end{bmatrix} \begin{bmatrix} \cos \frac{\xi}{2} & \sin \frac{\xi}{2} & 0 \\ -\sin \frac{\xi}{2} & \cos \frac{\xi}{2} & 0 \\ 0 & 0 & 1 \end{bmatrix} \begin{bmatrix} \cos \epsilon & 0 & -\sin \epsilon \\ 0 & 1 & 0 \\ \sin \epsilon & 0 & \cos \epsilon \end{bmatrix} \quad (B9)$$

It follows that

$$\Omega_{11} = \cos \theta \cos \epsilon \cos \frac{\xi}{2} + \sin \theta \sin \epsilon \quad (B10)$$

Substituting Equation B10 into B8 and equating the right-hand side of B8 with the square root of the right-hand side of B7 provides

$$\sqrt{(R_M + h)^2 - R_M^2} = (\cos \theta \cos \epsilon \cos \frac{\xi}{2} + \sin \theta \sin \epsilon) (R_M + h) \quad (B11)$$

Solving Equation B11 for  $\xi$  provides

$$\xi = 2 \cos^{-1} \left[ \frac{1}{\cos \theta \cos \epsilon} \left( \sqrt{1 - \left( \frac{R_M}{R_M + h} \right)^2} - \sin \theta \sin \epsilon \right) \right] \quad (B12)$$

If the spin rate is  $\omega$ , the time between pulses is  $\xi/\omega$ .

Since  $R_M$ ,  $\theta$  and  $\omega$  are assumed to be known constants, Equation B12 shows that the time interval between planet-sensor pulses depends upon altitude and elevation. The reason for including the arbitrary cant angle  $\theta$  is to allow the use of two such sensors, each with a different value of  $\theta$ , thereby providing two independent measurements, so that both altitude and elevation can be computed.

It is evident from symmetry that the Mars sensor is pointed directly toward Mars at the instant halfway between the two planet pulses. The azimuthal difference  $\nu$  between the Sun and Mars can be derived from the interval between the  $\Psi_1$  Sun pulse, the Mars pulses, the known azimuthal separation  $\phi$  between the Sun and

Mars sensors, and the spin speed, using the diagram in Figure B-7. Assume  $t = 0$  corresponds to the occurrence of the sun pulse; the first Mars pulse occurs an interval

$$\Delta t_1 = (\phi - \nu - \xi/2)\omega \quad (B13)$$

later. The next pulse occurs an interval

$$\Delta t_2 = \xi/\omega \quad (B14)$$

after that. Given  $\Delta t_1$  and  $\Delta t_2$  as measured quantities, the azimuthal difference  $\nu$  is computed as

$$\nu = \phi - \omega(\Delta t_1 + \frac{1}{2} \Delta t_2) \quad (B15)$$

The details of the star sensor will not be discussed here since it is not presently considered to be a prime candidate for inclusion in the sensor package. It can be considered to be a device that specifies the azimuth and elevation of a star, if it becomes necessary to augment the other sensors.

### B.3. Computational Algorithm

The following is a quick sketch of the sequential approach. Usually, the quantity of interest in sequential estimation is  $x(t, p)$  rather than  $p$  itself, and the algorithm specifies a value of  $\Delta x(t_i)$  for each measurement instant  $t_i$ . Suppose the measurement is  $h(t_i)$ ; the estimated correction to  $x_N(t_i)$  is

$$\begin{aligned} \Delta x(t_i) = & P(t_i)H^T(t_i) \left[ H(t_i)P(t_i)H^T(t_i) \right. \\ & \left. + R(t_i) \right]^{-1} \left[ h(t_i) - H(t_i)\Phi(t_i, t_{i-1})\Delta x(t_{i-1}) \right] + \Phi(t_i, t_{i-1})\Delta x(t_{i-1}) \end{aligned} \quad (B16)$$

where

$$H(t_i)$$

is the matrix of the partial derivatives of the measured quantities with respect to the state variables;  $R(t_i)$  is the covariance matrix of the measurement noise at  $t_i$ ;  $\Phi(t_i, t_{i-1})$  is the fundamental solution matrix for the linearized equations for the correction to the state evaluated at  $t_i$  and  $t_{i-1}$ ; equivalently  $\Phi(t_i, t_{i-1})$  is the matrix of partial derivatives of the state at  $t_i$  with respect to the state at  $t_{i-1}$ ;  $P(t_i)$  is the covariance matrix of the error in the estimate of  $x(t_i)$ , and is given by

$$\begin{aligned}
P(t_i) = & \Phi(t_i, t_{i-1})P(t_{i-1})\Phi^T(t_i, t_{i-1}) \\
& - P(t_{i-1})\Phi^T(t_i, t_{i-1})H^T(t_i)\left[H(t_i)\Phi(t_i, t_{i-1})P(t_{i-1})\Phi^T(t_i, t_{i-1})H^T(t_i) \right. \\
& \left. + R(t_i)\right]^{-1}H(t_i)\Phi(t_i, t_{i-1})P(t_{i-1})
\end{aligned} \quad (B17)$$

Equation B17 can run into computational stability problems and there are some alternative mechanizations, which need not be considered herein.

The discussion has thus far considered only the linearized equations for orbit determination, but the problem is really nonlinear, and there are several ways to account for the nonlinear effects. The first problem arises from the fact that a linearization is adequate in a region about the nominal but is inaccurate outside that region. For the nonsequential estimation the usual approach is to perform the estimation iteratively, as follows. Using  $p_N$ ,  $\Delta p^{(1)}$  is computed using Equation B3;  $p^{(1)}$  is defined as  $p_N + \Delta p^{(1)}$ ,  $M^{(1)}$  is defined in a manner similar to  $M$ , except that the partials are evaluated about  $p^{(1)}$  instead of about  $p_N$ , and  $\epsilon^{(1)}$  is similarly updated;  $\Delta p^{(2)}$  is computed from Equation B3 with  $M^{(1)}$  and  $\epsilon^{(1)}$ ; the process is repeated until  $\epsilon^{(n)}$  reaches a sufficiently small value.

For the sequential estimation there are several common approaches. The simplest technique is to relinearize the state update equations at each time, giving a modified  $\Phi$  matrix for the next measurement time. A more complicated approach is to update the nominal path back to the initial times and carry out the linearized sequential analysis over again using the new nominal. A different type of approach is the use of higher order expansions for the nonlinearities, though a discussion of such filters is beyond the scope of this report.\*

The choice between sequential and nonsequential depends upon data rates, the interval between desired updated estimates, and available computer time and storage; there should be no significant difference in the ultimate accuracy. Additional considerations are whether to use a simple model with "forgetting" or a sophisticated model, and whether to actually treat the attitude estimation and orbit estimation as completely equivalent or to handle them separately with crossfeed of the latest estimate. It is suggested that the decision about just how to mechanize the estimation program be studied further, when more is known about the overall system, including supporting ground facilities for data handling and processing.

#### B.4. Orbit Accuracy Estimation

The remainder of this discussion is devoted to the derivation of the elements of an accuracy estimation program for the OEC mission. For the present study the sensor outputs are not modeled in detail; rather than the time pulse computations described previously, it is assumed that the sensors provide OEC

---

\*See E. Schwartz, "Approximate Continuous Nonlinear Minimal-Variance Filtering, Hughes Report No. SSD 60472R, December 1966.

altitude and the Sun-OEC-Mars angle directly. The accuracy program is a mechanization of the sequential formula given in Equation B17, so that the discussion considers  $P(t_0)$ ,  $\Phi(t_i, t_{i-1})$ ,  $H(t_i)$ , and  $R(t_i)$ , in addition to specifying the nominal.

The state of the system at  $t_i$  is composed of the position and velocity of OEC and any constant parameters being estimated; for the problem at hand it is assumed that the only constants estimated are an altitude bias factor and a Sun-OEC-Mars angle bias. The program uses an existing subroutine to compute the position and velocity of the satellite given the initial values and the time increment. For the OEC orbit, the program uses a subroutine that computes the  $\Phi(t_i, t_{i-1})$  matrix along with the state. The Voyager orbit is computed when necessary for range measurement updating by another subroutine, which does not compute the  $\Phi$ .

To find  $H(t_i)$ , the first step is to find  $h(t_i, x(t_i))$ . For the Sun/Mars sensor package, the two elements of  $h$  are the altitude  $a$  and the Sun-OEC-Mars angle  $\alpha$  plus their biases  $a_0$  and  $\alpha_0$ , i.e.,

$$h = \begin{bmatrix} a + a_0 \\ \alpha + \alpha_0 \end{bmatrix} \quad (B18)$$

Let the position of OEC with respect to an aerocentric coordinate system be denoted

$$r = \begin{bmatrix} r_1 \\ r_2 \\ r_3 \end{bmatrix} \quad (B19)$$

The altitude of OEC above Mars

$$a = \sqrt{r_1^2 + r_2^2 + r_3^2} - R_M \quad (B20)$$

where  $r_M$  denotes the radius of Mars. Let the unit vector toward the Sun in the same coordinate system be denoted

$$r_s = \begin{bmatrix} r_{s1} \\ r_{s2} \\ r_{s3} \end{bmatrix} \quad (B21)$$

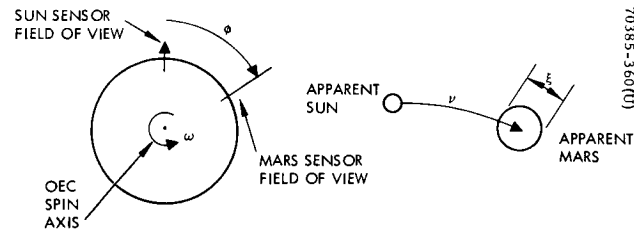


Figure B-7. Application of Sensors for Measuring Azimuthal Angle Between Sun and Mars

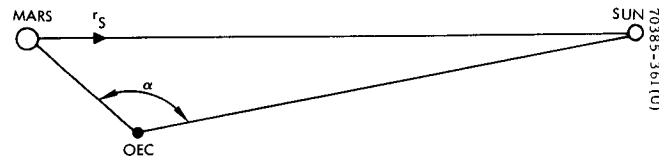


Figure B-8. Geometry of Mars-OEC-Sun Angle

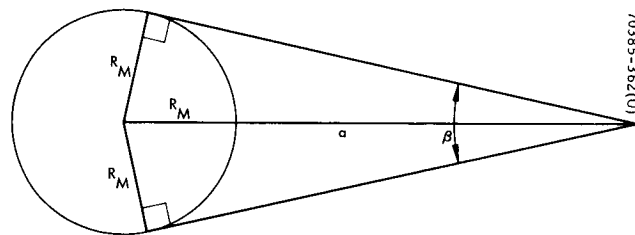


Figure B-9. Mars Sensor Altitude Measuring Geometry



The angle  $\alpha$  can be found from the drawing in Figure B-8, but to a very high degree of accuracy (one part in  $10^8$ ) the OEC-Sun line can be considered parallel to the Sun-Mars line, resulting in a much simpler expression:

$$\alpha = \pi - \cos^{-1} \left( \frac{r \cdot r_s}{|r|} \right) \quad (B22)$$

Substitution of Equations B22 and B21 into B19, with some additional manipulation, results in

$$h = \left[ \frac{\sqrt{r_1^2 + r_2^2 + r_3^2} - R_M + a_o}{\pi - \cos^{-1} \left( \frac{r_1 r_{s1} + r_2 r_{s2} + r_3 r_{s3}}{\sqrt{r_1^2 + r_2^2 + r_3^2}} \right)} + \alpha_o \right] \quad (B23)$$

Next, the form of the bias terms have to be specified. In reality, both bias terms result from errors in the measurement of intervals between sensor pulses, but in the accuracy program they are modeled as equivalent angle errors. Thus  $\alpha_o$  is simply considered a constant; to derive an equivalent model for altitude error as a function of angle measurement error, consider Figure B-9. It is easy to show

$$a = R_M \left( \frac{1}{\sin \beta/2} - 1 \right) \quad (B24)$$

so that

$$\frac{\partial a}{\partial \beta} = - (a + R_M) \sqrt{\left( \frac{a + R_M}{R_M} \right)^2 - 1} \quad (B25)$$

and

$$a_o = \frac{\partial a}{\partial \beta} \beta_o \quad (B26)$$

where  $\beta_o$  is the assumed equivalent angular measurement error. It is not necessary to take  $\alpha_o$  and  $\beta_o$  equal, even though they both represent an equivalent angle error of the combined sensor package, since they are actually computed differently from the raw pulse data.

The assumption has been made that a pair of Mars sensors are available to compute altitude directly, even though it is not necessary for the state estimation. The present configuration was chosen for several reasons: single-sensor measurements over a larger portion of the orbit, additional information when both sensors see Mars, and no complete loss of planet information in case a sensor

fails. By proper choice of parameters the program can be made to simulate a single-sensor system, so that generality is not lost.

The measurement vector is now

$$h = \begin{bmatrix} \sqrt{r_1^2 + r_2^2 + r_3^2} \left( 1 - \beta_o \sqrt{\frac{r_1^2 + r_2^2 + r_3^2}{r_M^2}} - 1 \right) - r_M \\ \pi - \cos^{-1} \left( \frac{r_1 r_{s1} + r_2 r_{s2} + r_3 r_{s3}}{\sqrt{r_1^2 + r_2^2 + r_3^2}} \right) + \alpha_o \end{bmatrix} \quad (B27)$$

For expected values of  $\beta_o$ , about 0.01 radians, even at the maximum value of the square root multiplying  $\beta_o$ , which is about 4, the quantity in parentheses in  $h_1$  can be approximated by unity in finding the  $\partial h_1 / \partial r_i$ . The resulting elements of H are found to be

$$\begin{aligned} \frac{\partial h_1}{\partial r_i} &= \frac{r_i}{a + R_M} \\ \frac{\partial h_1}{\partial v_i} &= 0 \\ \frac{\partial h_1}{\partial \beta_o} &= - (a + R_M) \sqrt{\left( \frac{a + R_M}{R_M} \right)^2 - 1} \\ \frac{\partial h_1}{\partial \alpha_o} &= 0 \\ \frac{\partial h_2}{\partial r_i} &= \frac{1}{\sqrt{(a + R_M)^2 - (r \cdot r_s)^2}} \left[ r_{si} - \frac{r_i (r \cdot r_s)}{(a + R_M)^2} \right] \\ \frac{\partial h_2}{\partial v_i} &= 0 \\ \frac{\partial h_2}{\partial \beta_o} &= 0 \\ \frac{\partial h_2}{\partial \alpha_o} &= 1 \end{aligned} \quad (B28)$$

where the  $v_i$  are the components of the velocity.

For Voyager ranging let the position of Voyager be denoted by

$$\mathbf{r}_v = \begin{bmatrix} r_{v1} \\ r_{v2} \\ r_{v3} \end{bmatrix} \quad (\text{B29})$$

Then  $h$  is a scalar given by

$$h = |\mathbf{r} - \mathbf{r}_v| \quad (\text{B30})$$

From Equation B30 it is easy to find the elements of  $H$ :

$$\begin{aligned} \frac{\partial h}{\partial r_i} &= \frac{r_i - r_{vi}}{|\mathbf{r} - \mathbf{r}_v|} \\ \frac{\partial h}{\partial v_i} &= 0 \\ \frac{\partial h}{\partial \beta_o} &= 0 \\ \frac{\partial h}{\partial \alpha_o} &= 0 \end{aligned} \quad (\text{B31})$$

The noise covariance matrix  $R$  is found next. Let  $\sigma_a^2$  denote the measurement noise variance for altitude measurements and  $\sigma_\alpha^2$  denote that of the sun-OEC-Mars angle. Since the angle measurement uses sun sensor information while the altitude measurement does not, and since the computations performed on the raw data are different for the two measurements, it seems reasonable to assume that the noises on the two quantities are uncorrelated, so that

$$R = \begin{bmatrix} \sigma_a^2 & 0 \\ 0 & \sigma_\alpha^2 \end{bmatrix} \quad (\text{B32})$$

As was done with the bias errors, both noises are related to equivalent angular quantities;  $\sigma_\alpha^2$  is constant, but  $\sigma_a^2$  is related to a constant  $\sigma_\beta^2$  by

$$\sigma_a^2 = \left( \frac{\partial a}{\partial \beta} \right)^2 \sigma_\beta^2 \quad (\text{B33})$$

For the range measurement,  $R$  reduces to a scalar, denoted  $\sigma_R^2$ , where  $\sigma_R^2$  is assumed to be a sum of range measurement error plus Voyager orbit determination error.

The initial error covariance matrix is assumed to be diagonal, to simplify program input requirements. The position elements approximate the variance in the position vector components, and reflect the uncertainty in the knowledge of Voyager at separation plus the position uncertainty due to the errors in separation that may have accumulated by the time the program is initiated. Similarly, the velocity variances represent the initial velocity uncertainty plus the uncertainty in any orbit change maneuvers. The bias variances reflect the expected dispersion in the corresponding constants.

The description of the accuracy program is now complete, but some additional comments are in order. The recursion algorithm given by Equation B17 is theoretically stable, but is well known to be susceptible to numerical instabilities, particularly when many measurements are taken of slowly changing quantities. The instability may result in a diverging or a sign-indefinite covariance matrix. A number of approaches have been devised to circumvent the difficulty. For example, if the instability arises, the simulated measurement times can be decreased in number and the accuracy of each measurement be increased an equivalent amount using the well known least-squares result that the error variance for a measured parameter decreases as the number of measurements increases. Thus ten measurements can be replaced by one measurement with one-tenth the variance of the original measurement. A scheme that guarantees that the covariance remain non-negative definite computes a matrix  $E$  such that  $E^T E = P$ . A third approach which is apparently more stable does not take inverses in the sequential computation loop, but works with  $p^{-1}$ , inverting  $P^{-1}$  only for input/output purposes. Finally, the computations could be done in double precision. The program used for this report computes  $P$  using Equation B17 and relies on input modification to avoid the instability problem. Since the Sun/Mars sensor data is taken once per revolution at 50 to 70 rpm, the modification is necessary.

A flow chart of the program is given in Figure B-10. The branch alluding to a singularity in the computation of the observation of the observation partials is necessary because the expression for  $\partial h_2 / \partial r_i$  in (B28) is useless for  $\alpha = \pi$  radians. Physically, the partials of  $\alpha$  with respect to the position variables are meaningful, if taken as one-sided derivatives, since  $\alpha$  is taken  $0 \leq \alpha < \pi$ ; the program is designed to compute equivalent information using a fictitious sun vector rotated  $\pi/2$  radians from the true sun, thereby avoiding the singularity.

The operation of the program is roughly as follows:

- 1) The initial condition parameters are read in.
- 2) Each following card specifies a time and some options.
  - a) The first option specifies range information, planet/sun sensor information, or simple updating without measurement.

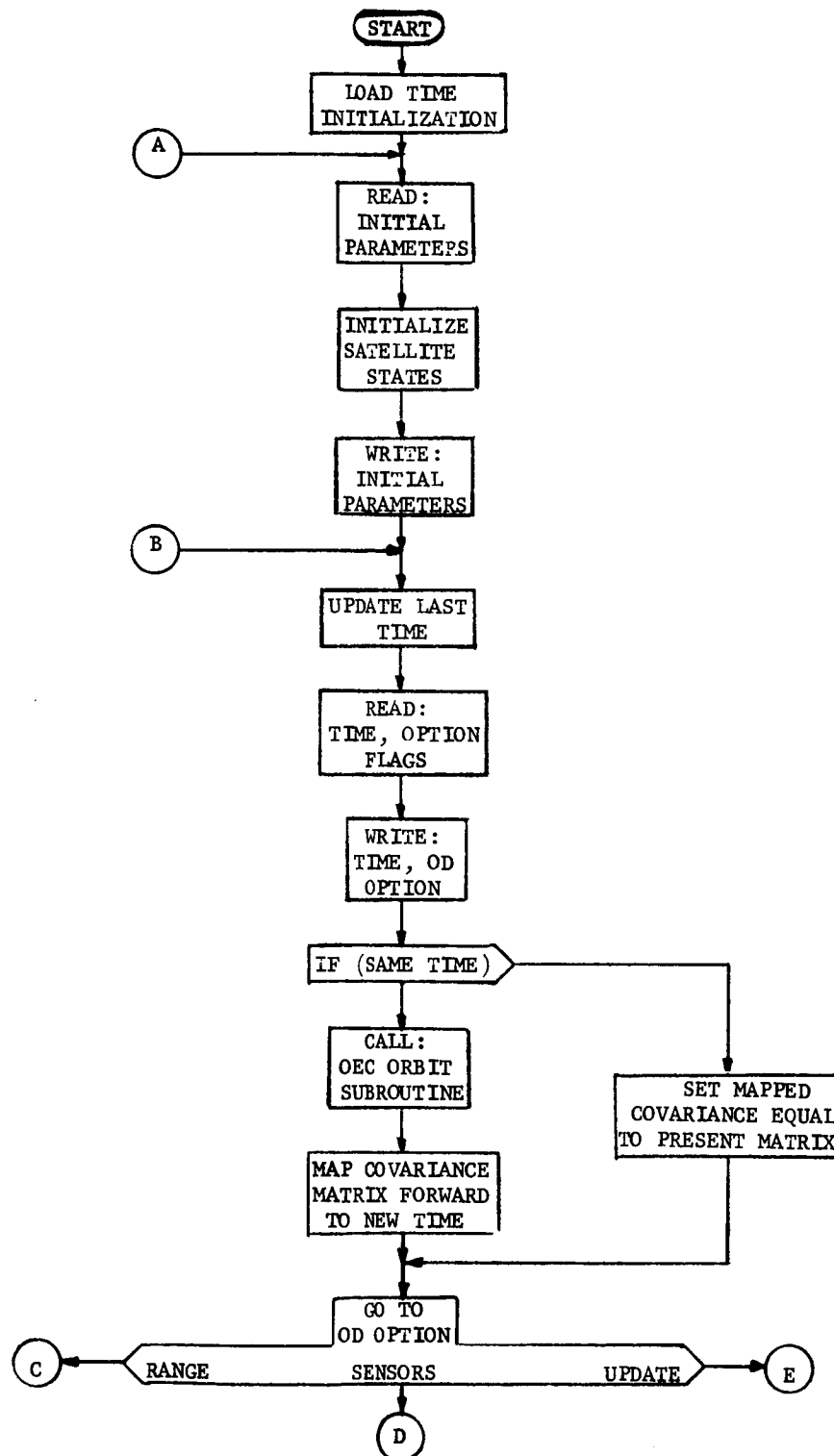


Figure B-10. Orbit Accuracy Program  
Computer Flow Diagram

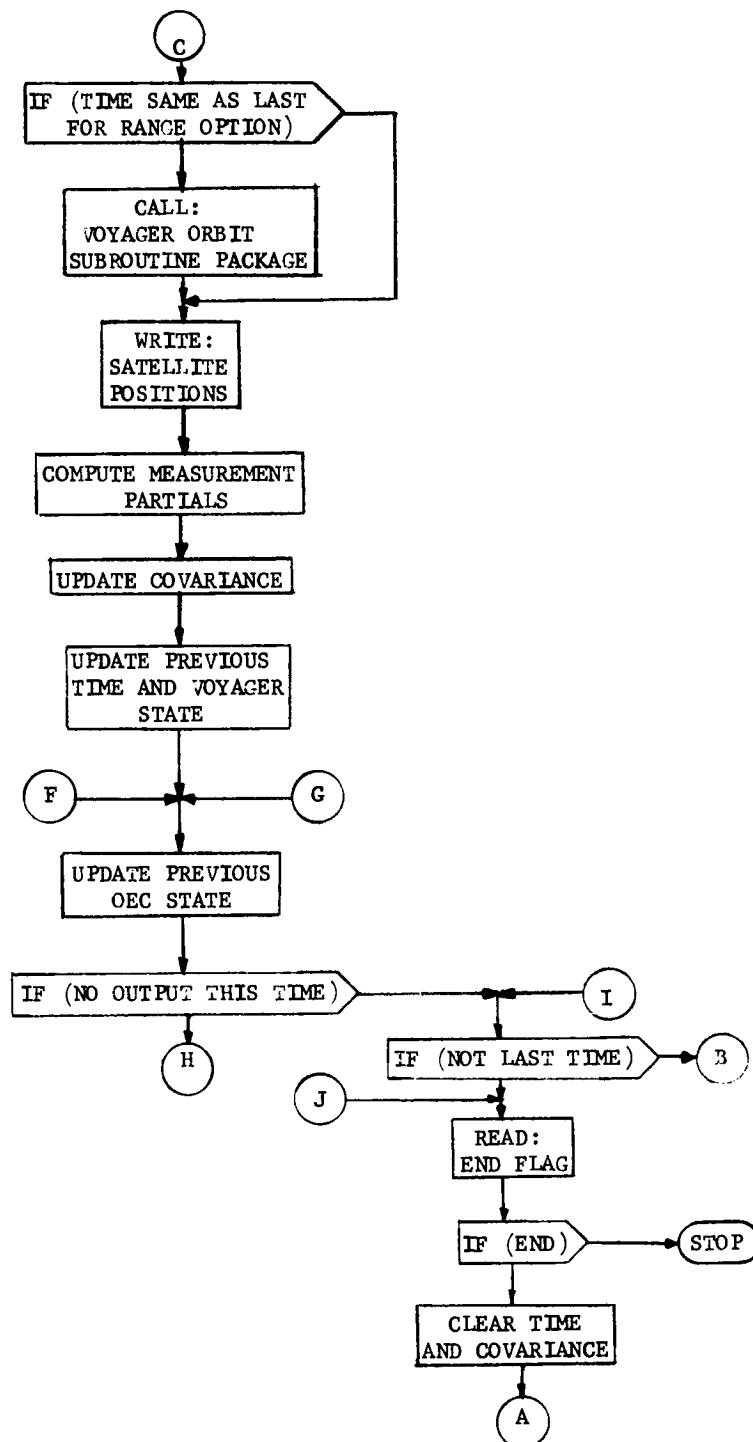


Figure B-10 (continued). Orbit  
Accuracy Program Computer  
Flow Diagram

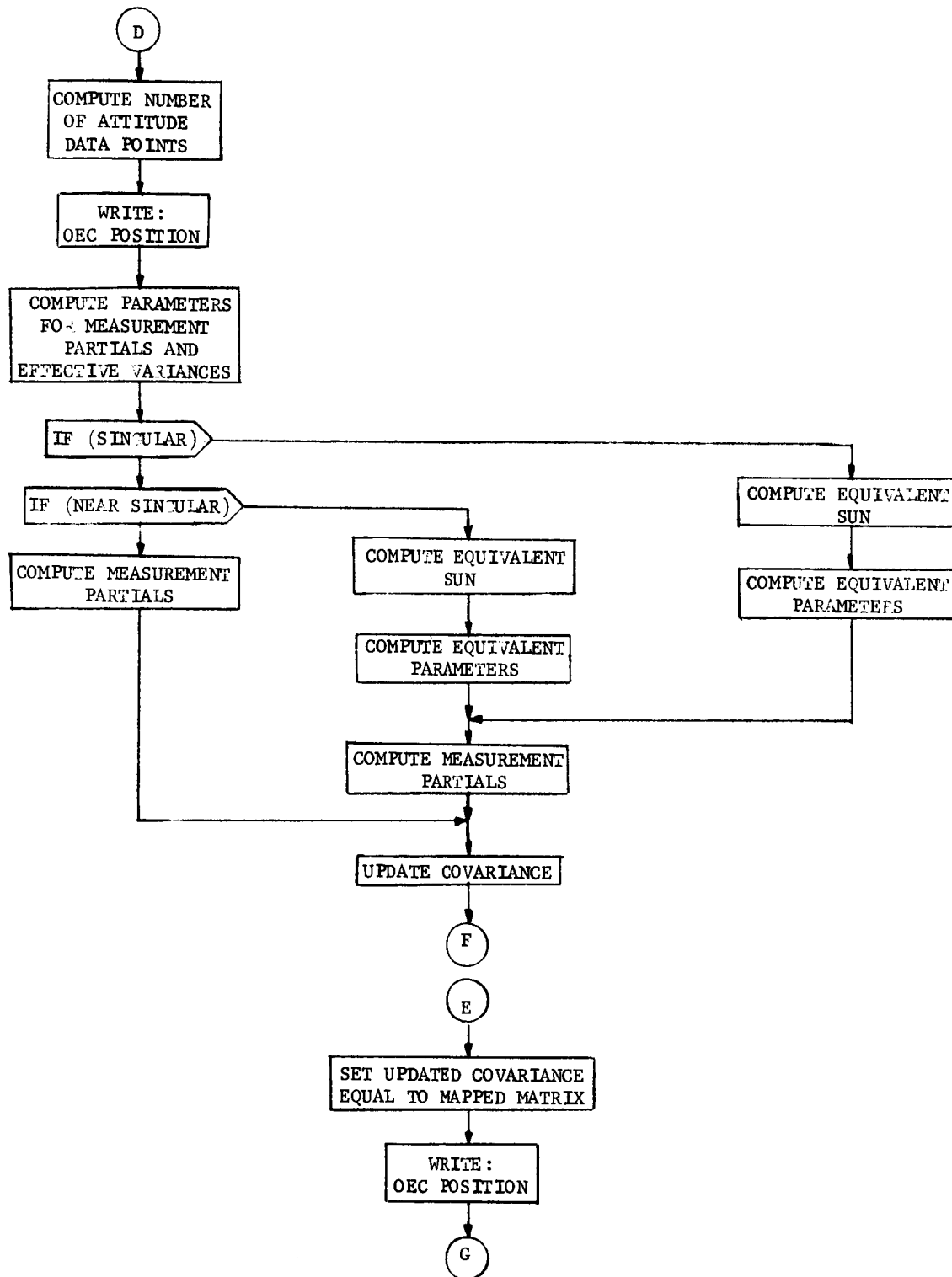


Figure B-10 (continued). Orbit Accuracy Program Computer Flow Diagram

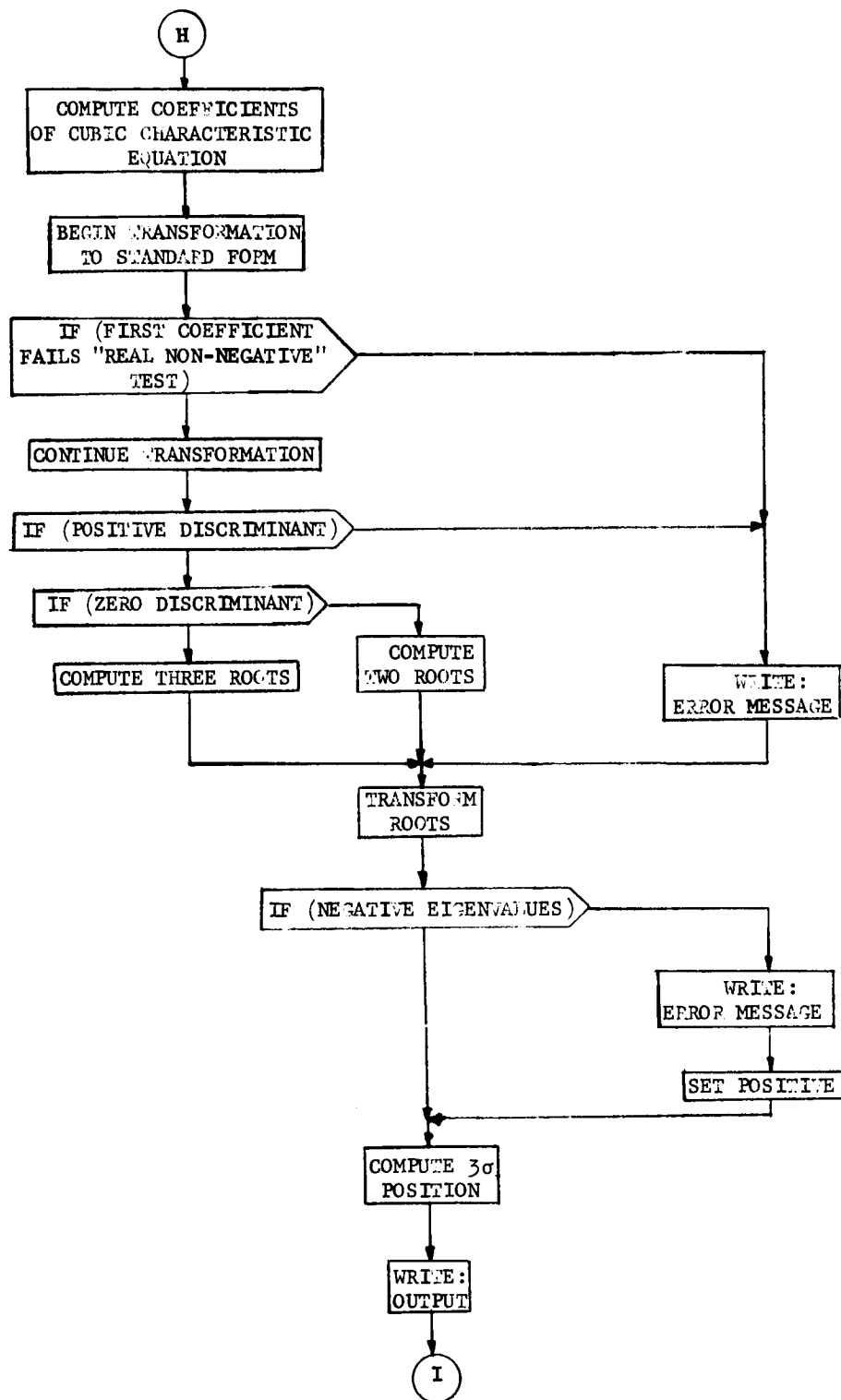


Figure B-10 (continued). Orbit  
Accuracy Program Computer  
Flow Diagram



- b) The second option specifies whether to print output data.
- c) The last option tells if any more time cards follow.

The specified operations are executed after each card is read in; when the last computation for each case is completed, the program tests for the existence of additional cases; if there are none, the program stops. The update operations are given by the equations presented earlier in this section; the only computations not yet discussed are those associated with the output.

The primary output is the covariance matrix itself. Recall that this matrix is  $E[(\Delta x)(\Delta x)^T]$ , where  $\Delta x$  is the difference between the true state and the estimated state. The question, then, is how to interpret the covariance matrix to determine the accuracy with which the position can be estimated. To answer the question, note that the differential equations used to find the evolution of the difference between the true state and the nominal are linear. If the initial errors are assumed to be normal random variables and if the measurement errors are also assumed to be normally distributed, it follows that the errors are normally distributed for all time, so that the statistics of  $\Delta x$  are completely specified by its expectation (which is zero, since the initial errors and the noise are assumed to be of zero mean) and its covariance. Since the position error components are obtained from  $\Delta x$  by a linear transformation, the position error is a normally distributed vector random process. In particular, the transformation is

$$\Delta r = \Psi \Delta x \quad (B34)$$

where  $\Psi$  is the projection matrix

$$\begin{bmatrix} 1 & 0 & 0 & 0 & 0 & 0 & 0 & 0 \\ 0 & 1 & 0 & 0 & 0 & 0 & 0 & 0 \\ 0 & 0 & 1 & 0 & 0 & 0 & 0 & 0 \end{bmatrix}$$

Then, from Equation B34 the expected value of  $\Delta r$ ,  $E(\Delta r) = 0$  and

$$\begin{aligned} E(\Delta r \Delta r^T) &= E(\Psi \Delta x \Delta x^T \Psi^T) \\ &= \Psi E(\Delta x \Delta x^T) \Psi^T \end{aligned} \quad (B35)$$

Evaluation of Equation B35 shows that the covariance of  $\Delta r$  is simply the upper diagonal  $3 \times 3$  submatrix of the covariance of  $\Delta x$ . Let the position error covariance matrix be denoted  $\Lambda$ ; since  $\Delta r$  is a zero-mean normal random vector, its probability density function is

$$p_{\Delta r}(\rho) = \frac{1}{(2\pi)^{3/2} |\Lambda|^{1/2}} e^{-1/2 \rho^T \Lambda^{-1} \rho} \quad (B36)$$

The accuracy figure-of-merit will be based on Equation B36.

\* $E(\cdot)$  denotes expectation or mean value.

One way to specify the accuracy of the estimate is to find a number  $R$  such that the probability that  $|\Delta r| \leq R$  is some specified value. For a scalar normal random variable that much abused  $3\sigma$  value  $R$  is that number that guarantees a probability of 0.997 that the variable is less than  $R$  in magnitude. For the vector random variable the equivalent specification is somewhat more complicated and often misunderstood. The first problem is to find the proper generalization to higher dimensions of the idea of bounding the magnitude of a scalar with given probability; the use of the bound on the length of the vector, as suggested at the beginning of the paragraph is not the commonly adopted generalization. The usual approach is based on the idea of maximal likelihood; for a normal distribution, the random variable is most likely to be near the mean, the region of greatest probability density. The likelihood of finding the variable near a given point decreases as the probability density decreases. Given the facts that the normal density is symmetric about the mean and decreases monotonically away from the mean, it is reasonable to use surfaces of equal likelihood, i.e., surfaces of constant probability density as boundaries, and to find the one that bounds the random vector with given probability.

From Equation B36 it is easily seen that a constant probability density implies a constant value for the quadratic form  $\rho^T \Lambda^{-1} \rho$ , that is, the boundary surface is of the form

$$\rho^T \Lambda^{-1} \rho = k^2 \quad (\text{B37})$$

Since  $\Lambda^{-1}$  is a positive-definite, symmetric matrix, as a consequence of its definition, it follows that Equation B37 specifies an ellipsoid. The remainder of the analysis can be simplified by rotating the coordinate system to coincide with the axes of the ellipsoid; mathematically, doing so amounts to diagonalizing the  $\Lambda$  matrix; probabilistically, doing so amounts to finding a random vector with uncorrelated components. Let the resulting rotated covariance matrix be

$$\Sigma = \begin{bmatrix} \sigma_1^2 & 0 & 0 \\ 0 & \sigma_2^2 & 0 \\ 0 & 0 & \sigma_3^2 \end{bmatrix} \quad (\text{B38})$$

In the new coordinate system Equation B36 becomes

$$p_{\Delta r}(\rho) = \frac{1}{(2\pi)^{3/2} \sigma_1 \sigma_2 \sigma_3} e^{-1/2(\rho_1^2/\sigma_1^2 + \rho_2^2/\sigma_2^2 + \rho_3^2/\sigma_3^2)} \quad (\text{B39})$$

It can now be seen that Equation B37 specifies an ellipsoid with semi-axes of length  $k\sigma_1$ ,  $k\sigma_2$ , and  $k\sigma_3$ , which is called a  $k\sigma$  ellipsoid and is the desired generalization of the  $k\sigma$  number for scalar random variables.

The next problem is to compute the probability associated with a given value of  $k$ . Let  $E_k$  denote the  $k\sigma$  ellipsoid; the probability of being within  $E_k$  is given by the three-dimensional integral

$$\int_{E_k} p_{\Delta r}(\rho) d\rho \quad (B40)$$

Define a new set of variables

$$\tau_i \triangleq \rho_i / \sigma_i \quad i = 1, 2, 3 \quad (B41)$$

and let  $s_k$  denote the sphere

$$\tau^T \tau = k^2 \quad (B42)$$

In the new variables Equation B40 becomes simply

$$\int_{s_k} \frac{1}{(2\pi)^{3/2}} e^{-1/2(\tau_1^2 + \tau_2^2 + \tau_3^2)} d\tau \quad (B43)$$

Note that the integrand in Equation B43 is spherically symmetrical, a fact which allows a relatively simple evaluation by integration of nested differential spheres, a technique used to find the mass of spherically symmetrical bodies. The differential volume of a sphere of radius  $s$  and thickness  $ds$  is simply  $4\pi s^2 ds$ , the surface area times the thickness; since the differential mass is the density times the differential volume, Equation B43 becomes

$$2 \int_0^k s^2 \frac{e^{-1/2 s^2}}{\sqrt{2\pi}} ds \quad (B44)$$

Evaluating Equation B44 provides the following expression for the probability associated with a  $k\sigma$  ellipsoid:

$$\text{erf}\left(\frac{k}{\sqrt{2\pi}}\right) = \frac{2k}{\sqrt{2\pi}} e^{-1/2 k^2} \quad (B45)$$

where  $\text{erf}(\cdot)$  is the tabulated error function. From Equation B43, the probability associated with a  $3\sigma$  ellipsoid is 0.971, which is less than the probability associated with a  $3\sigma$  scalar number.

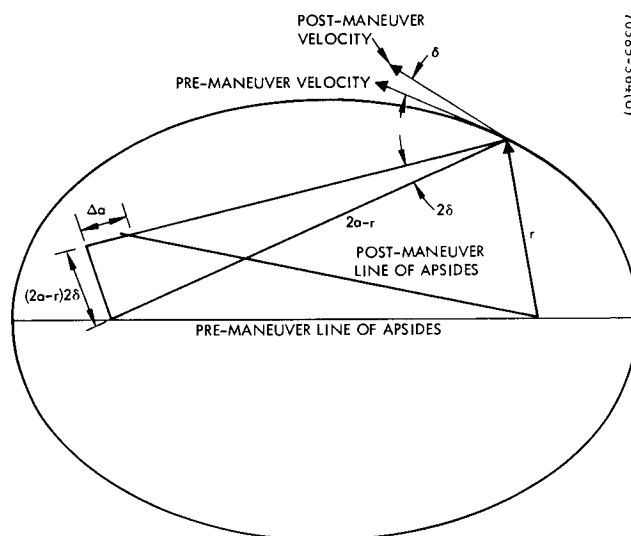


Figure B-11. Geometry for Orbit Extrapolation Accuracy

The final aspect of the accuracy specification stems from the fact that it is rather cumbersome to have to specify three vectors representing the three axes of the ellipsoid; it is much more convenient to specify a spherical radius associated with a given probability. Unfortunately, the computation of the probability of being in a given sphere is much more difficult, and must be done numerically. However, if the semi-major axis of the  $k\sigma$  ellipsoid is taken as the radius of a sphere, the probability of being in the sphere is at least as big as that of being in the ellipsoid. Thus, the probability associated with the  $k\sigma$  ellipsoid is a lower bound on the probability associated with the circumscribed sphere. The results of the orbit determination accuracy computation are given as the semi-major axis of the  $3\sigma$  ellipsoid; the effect of choosing different values of  $k$  was presented in the text of this section.

#### B.5 Orbit Extrapolation Accuracy for OEC Co-Orbital Mission

Essentially, the problem considered herein is as follows: Given a nominal initial Voyager-OEC position and a nominal initial Voyager-OEC velocity, what is the position error introduced by a perturbation at OEC separation in the initial velocity. There are two types of orbit change to consider. The first type of change results in displacements of the perturbed orbit that are time-invariant; the other change results in a time-varying displacement that grows to a maximum approximately equal to the major axis of the orbit. It will be shown that the time-invariant displacements are small, while the time-varying displacement places a severe restriction on the separation maneuver tolerance. This analysis presumes that no orbit determination sensors are used at all. The following results only apply to the very simplest of co-orbital missions where only the initial Voyager orbit data and OEC separation are used.

The total fixed displacement is most simply looked at as the sum of several components. For the purpose of the present investigation, it suffices to find rather crude upper bounds on the various orbit changes. First, consider a change in the plane of the orbit, which is brought about by rotating the velocity vector. For a velocity increment of magnitude  $\Delta V$  that is small with respect to the orbital speed  $S$ , the maximum angle of rotation is approximately  $\Delta V/S$  radians. The amount of out-of-plane displacement of any point on the orbit is certainly bounded by the quantity

$$\left| \frac{\Delta V}{S_a} r_a \right| \quad (B46)$$

where 'a' refers to apares, since  $S \geq S_a$  and  $r \leq r_a$  for any  $S$  and  $r$  in the orbit. Now, consider in-plane distortions. A quick estimate of the magnitude of such effects can be found using the vis-viva integral, Equation B45, and the geometrical properties of the ellipse. The nomenclature is given in Figure B-11.

Since, to a first approximation, the  $\Delta V$  can be considered to be applied impulsively,  $r$  does not change during the maneuver and Equation B45 implies that

$$|\Delta a| = \left| \frac{2S_a^2}{\mu} \Delta V \cos \alpha \right| \quad (B47)$$

where  $\alpha$  is the angle between the incremental velocity and the original orbital velocity. Thus the change in semi-major axis is bounded by the right-hand side of Equation B47 evaluated with  $\alpha = 0$ . If the  $\Delta V$  is used to rotate the velocity vector in the plane of the orbit, the effect is to move the vacant focus, thereby changing the ellipse. The motion of the vacant focus can be computed using the fact that a tangent to an ellipse is normal to the bisector of the angle formed by the lines from the point of tangency to the two foci. Since the vector from the central body to the vehicle is considered fixed and since the velocity is always tangent to the ellipse, the line from the vacant focus to the vehicle must rotate through an angle twice that given by the rotation of the velocity vector,  $\delta$  in Figure B-11. Also, since the sum of the lengths of the lines from the foci to any point on the ellipse equals that of the major axis, there is an additional motion of the vacant focus along the rotated line through a distance  $\Delta a$ . For small angles  $\delta$ , the two motions are essentially at right angles, and the total motion is given by the expression

$$\sqrt{\Delta a^2 + 4(2a - r)^2 \delta^2} \quad (B48)$$

As noted earlier, the rotation of the velocity vector is bounded in magnitude by  $|\Delta V/S_a|$ ; using this, and the bound on  $|\Delta a|$  provides the following bound on Equation B48:

$$\sqrt{\frac{4S_p^2 a^4 \Delta V^2}{\mu^2} + 4(2a - r_p)^2 \frac{\Delta V^2}{S_a^2}} = 2\sqrt{\frac{S_p^2 a^4}{\mu^2} + \frac{(2a - r_p)^2}{S_a^2}} |\Delta V| \quad (B49)$$

where 'p' denotes periares. If the distance between foci before the maneuver is denoted  $d$ , the maximum rotation of the line of apsides is then given approximately by Equation B49 divided by  $a$ . Also, from the elementary property of ellipses that the eccentricity  $e = d/2a$ , and the evident fact that  $d$  cannot change by an amount greater than that given by Equation B49,  $\Delta e$  is bounded by (B49) divided by  $2a$ . To bound the position change resulting from a change in  $a$  and  $e$ , differentiate the polar equation of the ellipse

$$r = \frac{a(1 - e^2)}{1 + e \cos \nu} \quad (B50)$$

\*The semi-major axis.

$$\Delta r = \frac{1 - e^2}{1 + e \cos v} \Delta a - a \frac{2e + (1 + e^2) \cos v}{(1 + e \cos v)^2} \Delta e \quad (\text{B51})$$

so that

$$|\Delta r| < (1 + e) |\Delta a| + a \frac{2e + (1 + e^2) \omega}{(1 + e \omega)^2} |\Delta e| \quad (\text{B52})$$

for some  $\omega$  between -1 and +1. Also, the position change caused by the in-plane rotation is certainly less than the apares radius times the angle of rotation.

Combining all the in-plane terms provides the following bound on the in-plane change:

$$|\Delta r| \leq \left[ (1 + e) \left| \frac{2S_p a^2}{\mu} \right| + \left( \frac{1 + e}{e} + \frac{2e + (1 + e) \omega}{(1 + e \omega)^2} \right) \sqrt{\frac{S_p^2 a^4}{\mu^2} + \frac{(2a - r_p)^2}{s_a^2}} \right] |\Delta V| \quad (\text{B53})$$

where use was made of the fact that  $d = ae$  and  $r_a = a(1 + e)$ . Since the out-of-plane motion is approximately normal to the in-plane motion, the total change can readily be bounded by the rss of Equations B46 and B53. Substituting values given by the orbit with  $r_a = 23510$  km and  $r_p = 4910$  km provides, after the maximizing Equation B53 with respect to  $\omega$ ,

$$|\Delta r| < 3300 |\Delta V| \quad (\text{B54})$$

With a nominal separation velocity of 0.002 km/min and with a 10 percent error, the resulting bound on the time-invariant position uncertainty is about 0.76 km, which is less than the 20 km requirement.

The time-varying error can be found immediately from the separation range plots given in Section 2.0, which shows that the nominal separation velocity results in a range of about 2700 km after 6 months. Because of the linearity of the analysis, a 10 percent uncertainty in the velocity implies a 10 percent uncertainty in the range, hence position, i.e., about 270 km, which is an order of magnitude worse than the acceptable uncertainty. Thus this form of estimating the co-orbital OEC orbit from the Voyager orbit does not meet the accuracy requirements.

## APPENDIX C. EFFECTS OF OSCILLATOR DRIFT ON MULTIPLE FREQUENCY SHIFT KEYING

Figure 3-10, Section 3.3.2, shows the data rates that can be supported by three modulation methods operating with a bit error rate of 1 per 1000. In the case of the two noncoherent modes (2- and 32-level FSK), the straight lines represent capability calculated solely in terms of statistical computation for thermal noise. The dotted curve line breaking away from the MFSK line shows performance that can be expected if an oscillator drift of 0.25 Hz is assumed. This value represents drift measured at X-band between two thermally stabilized laboratory oscillators. The value stated was inferred for S-band. Derivation for general expressions from which the curves are computed follows. It is recognized that some coding techniques might be used to alter the results, but the following analysis indicates that the value of noncoherent MFSK diminishes at low data rates much as coherent PSK does, but for different reasons.

Let us presume an MFSK system having the listed characteristics:

Oscillator drift =  $R$  Hertz

Character transmission rate =  $\eta$ /sec

Time between calibration characters =  $T$

Drift between calibrations =  $RT$

Number of calibration characters per second =  $1/T$

Number of information characters per second =  $(\eta - \frac{1}{T}) = C$

Required S/N for character detection =  $(S/N)_R$

Noise density of receiver =  $N_d$

Signal power delivered at receiver =  $P_d$

The bandwidth required must be augmented to provide for frequency drift and can be expressed:

$$\Delta B = (\eta + R \cdot T) \text{ Hertz}$$



The signal to noise requirement then fixes the bandwidth which can be supported at the receiver with the following relationship:

$$\left(\frac{S}{N}\right)_R = \frac{P_d}{N_d (\eta + R \cdot T)}$$

For convenience, set  $P_d/N_d \cdot (N/S)_R = k$ , since these are constant for a given link and bit error situation.

Now  $\eta = k - RT$ , which can be substituted into the expression for  $C$  which is the quantity to be optimized.

$$C = K - RT - \frac{1}{T}$$

$$\frac{dC}{dT} = -R + \frac{1}{T^2} \text{ or } T = \frac{1}{\sqrt{R}} \text{ for maximum } C$$

$$C = -\sqrt{R} \text{ and } \Delta B = +R$$

In order to relate these values to the curves based on thermal noise, it must be recognized that the signal level sufficient to accommodate  $B$  would appear to support a character rate of  $\eta + \sqrt{R}$  per second, but actually only  $(\eta - \sqrt{R})$  characters per second could be realized.

## APPENDIX D. USE OF CANOPUS SENSOR AS ROLL REFERENCE

This appendix presents some preliminary calculations on the use of a Canopus sensor as a roll reference for a spinning satellite in which the Canopus line of sight is roughly perpendicular to the spin vector. A slit field of view pointing radially outward would, if properly placed, cross Canopus once per spacecraft revolution. By sensing the time of the Canopus crossing, the roll position of the satellite could be determined. This information, plus Sun tracking, would provide the spacecraft attitude in all three axes. As a result of these calculations it is concluded that a relatively simple (and hence reliable) all solid state, no moving part Canopus sensor is feasible for this application.

Canopus star sensing as a roll reference has been used in a number of space vehicles. Surveyor, Mariner, and Lunar Orbiter are three examples. These vehicles are three axis stabilized, and hence their Canopus sensors are really trackers which generate either a mechanical or electrical scan (i. e., image dissectors). A Canopus sensor on a spinning satellite offers the potential of being simpler in concept by using the spin motion of the spacecraft to generate the required scanning. An example of the proposed scheme is shown in Figure D-1. A sensor slit  $\alpha$  degrees in length (along the spin axis) and  $\beta$  degrees wide is scanned through the celestial sphere at the rate of one complete  $2\pi$  scan per satellite revolution. If a stellar source of sufficient intensity were within the swath cut by the scanning slit, it would generate a signal pulse approximately  $\beta/\omega$  seconds long (where  $\omega$  is the spin rate of the spacecraft). The question of Canopus intensity and sensor sensitivity will now be examined.

### CANOPUS INTENSITY

The visible magnitude of Canopus,  $m_r$ , is -0.83. The magnitude scale can be related to the intensity scale by

$$m_a - m_b = -2.5 \log \frac{H_A}{H_B} \quad (D-1)$$

where  $m$  is magnitude and  $H$  is intensity and the subscripts represent two stars A and B. The intensity of a star of first magnitude is  $1.5 \times 10^{-13}$  w/cm<sup>2</sup> in the spectral passband of the human eye. Rearranging Equation D-1,

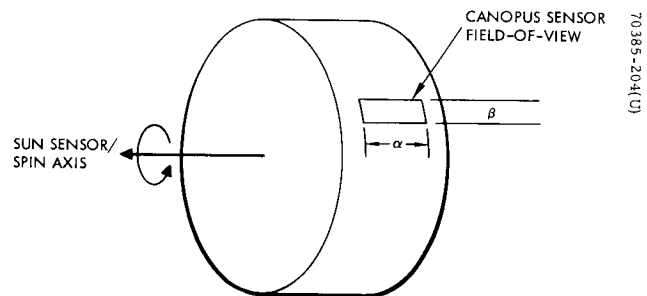


Figure D-1. Proposed Sensor Configuration

$$H_B = 1.5 \times 10^{-13} \text{ anti log } \left[ 0.4 - \frac{m_b}{2.5} \right] \text{ watts/cm}^2 \quad (D-2)$$

and Canopus has an intensity in the visible band of  $8.1 \times 10^{-13} \text{ watts/cm}^2$ .

#### RADIOMETRIC RELATIONSHIPS

If a photoconductive or photovoltaic sensor is employed as the sensing element for the Canopus sensor, then it is appropriate to write the noise equivalent power of the detective element as

$$NEP = \sqrt{\frac{A_D \Delta f}{D^*}} \quad (D-3)$$

where

$A_D$  = detector area,  $\text{cm}^2$

$\Delta f$  = noise bandwidth, Hertz

$D^*$  = normalized sensitivity of detector element chosen,  $\text{cm-cps}^{1/2} \text{ watt}^{-1}$

The detector area may be related to the field of view by the focal length of the optical system,  $F$

$$A_D = (F\alpha) (F\beta) = F^2 \alpha\beta \quad (D-4)$$

The bandwidth may be conveniently related to the dwell time by the near optimum design decision to make

$$\Delta f = (\text{dwell time})^{-1} = \frac{\omega}{\beta} \quad (D-5)$$

Combining Equations D-3, D-4, and D-5,

$$NEP = \frac{F (\alpha\omega)^{1/2}}{D^*} \quad (D-6)$$

The signal power  $S$  received at the detector from a star of irradiance  $H_S$  is related to the aperture by (assume unity transmission)

$$S = H_S \frac{\pi D^2}{4} \quad (D-7)$$

Combining Equations D-6 and D-7 and utilizing the optical relationship that  $F/D =$  focal length,  $f$ , the signal-to-noise ratio may be written

$$\frac{S}{NEP} = \frac{\pi H_S D D^*}{4f (\alpha \omega)^{1/2}} \quad (D-8)$$

Equation D-8 should be thought of as representing peak signal to rms noise since this is a pulse detection system. The implicit assumption is the peak signal out of the predetection filter will be equal to the equivalent steady state signal. This is comparable to a visibility factor of unity in the analysis of pulse detection signals.

Equation D-8 enables the radiometric relationships to be examined parametrically. One aspect of interest is that the signal to noise is independent of slit width. This is a result of the fundamental sensitivity relationship of Equation D-3. In essence, the extra noise introduced by wider detectors is compensated by the use of narrower noise filters allowable with the resulting longer signal pulses (consistent with detector response times and noise frequency distribution).

Consider an  $f/2$ , 2 inch aperture optical system. This system is sufficiently small and light-weight to represent a negligible perturbation on spacecraft weight. Assume the spacecraft spinning at 60 rpm, which should provide a pointing accuracy somewhat less than 1 degree. However, the sizing of  $\alpha$  is based on the variation in Canopus position observed during a typical flight. Since the spacecraft will have its spin axis essentially normal to the ecliptic, the field of view,  $\alpha$  can be assumed to be about 3 degrees.

Primary consideration for the detection element is given to a solid state detector because of the inherent reliability advantage over the more sensitive photomultiplier tubes. Cd S is the most sensitive of the alternatives with a  $D^*$  of  $3.5 \times 10^{14}$  watts<sup>-1</sup>-cm-cps<sup>1/2</sup>. However, the Cd S detector has a relatively slow time response and its polycrystal structure creates a potential stability problem for long term operation. Photovoltaic silicon has a fast time constant and relatively good sensitivity. A  $D^*$  of  $1.0 \times 10^{13}$  cm-cps<sup>1/2</sup>-watt<sup>-1</sup> has been reported by Electro-Nuclear Laboratories for their 602 detector. Values of  $D^*$  as high as  $5 \times 10^{13}$  have been measured by Mike Braun of the Hughes Electro-Optical Laboratories. A silicon detector is quite stable in performance and hardy in withstanding severe environments. It is even capable of looking at the Sun without performance

degradation. This obviates the need for a mechanical Sun shutter as required for photomultipliers — with a resulting incremental reliability.

To review the selected parameters:

$$D = 2'' = 5 \text{ cm}$$

$$D^* = 1 \times 10^{13} \text{ watts}^{-1} \text{ cm-cps}^{1/2}$$

$$H_S = 8.1 \times 10^{-13} \text{ watts/cm}^2$$

$$f = 2$$

$$\alpha = 3 \text{ degrees} = 0.052 \text{ radian}$$

$$\omega = 360 \text{ deg/sec} = 6.28 \text{ rad/sec}$$

Applying Equation D-8,

$$\frac{S}{NEP} = 28$$

This is a satisfactory signal to noise for the proposed application, and hence it is concluded that it is feasible to use an all solid state, no moving part Canopus sensor for OEC.

#### DETECTOR SIZE

It is of interest to compute the detector size required. The length,  $l$ , and the width,  $d$ , are computed:

$$l = F\alpha$$

$$d = F\beta$$

The value of  $\beta$  should be chosen small so as to enhance background discrimination capability and maximize angular accuracy. However, it should not be so small as to provide severe fabricating problems. Somewhat arbitrarily, the value chosen is aspect ratio 50:1, i. e.,

$$\alpha = 3 \text{ degrees}$$

$$\beta = 0.06 \text{ degree}$$

hence

$$l = 0.52 \text{ cm}$$

$$d = 0.01 \text{ cm}$$

## FURTHER CONSIDERATIONS

The preceding calculations are very approximate and must be carried out in further detail (along with more detailed design) before feasibility is fully substantiated. Among the areas that should be investigated further are the spectral distribution of energy of Canopus and the spectral responsivity of silicon. These factors have been ignored for simplicity by using only the visible component of Canopus normalized to the response of the human eye. However, silicon's spectral responsivity is significantly different from that of the human eye, peaking at about 0.85 micron. To properly compute the sensitivity, the spectral irradiance of Canopus must be integrated with the spectral responsivity of silicon.

Another factor that has not been taken into account is the potential increase in detector sensitivity due to the lower ambient photon flux that will be experienced in space. The new planar silicon detectors will be limited only by amplifier noise in this environment. Sample calculations given below indicate that this represents a significant potential enhancement in performance.

Other factors such as variations of noise with frequency, optimizing optical and electrical design, etc., should also be taken into account with a detailed design.

This same application could be accomplished with a photomultiplier tube receiver. However, the use of silicon detectors is more attractive from both a simplicity and a reliability standpoint.

## SENSITIVITY OF AMPLIFIER NOISE LIMITED SILICON CANOPUS SENSOR

For a good planar silicon detector with a space background, the limiting noise should be from the detecting amplifier. The rms noise current will be

$$i_{\text{rms}} = F \sqrt{\frac{4 kT \Delta f}{R_L}} \quad (\text{D-9})$$

where

$i_{\text{rms}}$  = amplifier noise current, amperes

$k$  = Boltzmann's constant ( $1.38 \times 10^{-23}$  joules/ $^{\circ}\text{K}$ )

$T$  = temperature (300 $^{\circ}\text{K}$ )

$\Delta f$  = noise bandwidth, Hertz

$R_L$  = load resistance, ohms

$F$  = amplifier noise factor (assumed as 1.5)

The noise equivalent power will be

$$\text{NEP} = \left( \frac{1}{\eta_s q} i_{\text{rms}} \right) \times \left( \frac{hc}{\lambda} \right) \quad (\text{D-10})$$

where

$\eta_s$  = responsive quantum efficiency (electrons/photons) 0.5 (according to M. Braun)

$q$  = electron charge ( $1.6 \times 10^{-19}$  coulombs/electron)

$h$  = Planck's constant ( $6.6 \times 10^{-34}$  joule-sec)

$c$  = velocity of light ( $3 \times 10^{10}$  cm/sec)

$\lambda$  = wavelength of visible light ( $\sim 5 \times 10^{-3}$  cm)

Hence:

$$\text{NEP} = \frac{F h c}{\eta_s q \lambda} \sqrt{\frac{4 kT \Delta f}{R_L}} \quad (\text{D-11})$$

Substituting numbers

$$\text{NEP} = 9.5 \times 10^{-12} \sqrt{\frac{\Delta F}{R_L}} \quad (\text{D-12})$$

Good frequency response can be obtained with  $R_L = 10^8$  ohms. For this value

$$\text{NEP} = 9.5 \times 10^{-16} \sqrt{\Delta F} \quad (\text{D-13})$$



For this case, NEP is independent of detector size, so that Equation D-8 must be rewritten for

$$S = \frac{\pi D^2}{4} H_s \quad (D-14)$$

$$\Delta F = \frac{\omega}{\beta} \quad (D-15)$$

Combining Equations D-13, D-14, and D-15,

$$S/NEP = \frac{\pi D^2 H_s}{4 \times 9.5 \times 10^{-16}} (\beta/\omega)^{1/2} \quad (D-16)$$

It is interesting to note that in this case the signal to noise is independent of  $\alpha$ .

The following values will be used:

$$D = 5 \text{ cm}$$

$$H_s = 8.1 \times 10^{-13} \text{ watts/cm}^2$$

$$\beta = 0.06 \text{ degree} = 0.001 \text{ radian}$$

$$\omega = 360 \text{ deg/sec}$$

For these values

$$S/NEP = 220$$

and a substantial increase in signal to noise is effected.

The importance of these results is that they indicate that good planar silicon detectors operating in a low photon flux environment will produce a substantial increase in the performance computed in the main body of this report. Such detectors have come on the market and will eventually replace models such as the ENL 602 detector used as a reference for the calculations.